Technische Universität München
Lehrstuhl für Anorganische und Metallorganische Chemie

Defects in Functional Porous Materials

Ruthenium and Rhodium HKUST-1 Analogues as Case Study for Precious Group Metal-Organic Frameworks

-

Synthesis, Characterization, Defect-Engineering and Catalysis

Werner Reinhold Heinz

Vollständiger Abdruck der von der Fakultät für Chemie der Technischen Universität München zur Erlangung des akademischen Grades eines

Doktors der Naturwissenschaften (Dr. rer. nat.)

genehmigten Dissertation.

Vorsitzender:		Prof. Dr. Dr. h. c. Bernhard Rieger
Prüfer der Dissertation:	1.	Prof. Dr. Dr. h. c. Roland A. Fischer
	2.	Prof. Dr. Klaus Köhler

Die Dissertation wurde am 26.03.2021 bei der Technischen Universität München eingereicht und durch die Fakultät für Chemie am 17.05.2021 angenommen.

Defects in Functional Porous Materials

Ruthenium and Rhodium HKUST-1 Analogues as Case Study for Precious Group Metal-Organic Frameworks

-

Synthesis, Characterization, Defect-Engineering and Catalysis

Werner Reinhold Heinz

“We are only what we know, and I wished to be so much more than I was, sorely.”

“And only as you gasp your dying breath shall you understand,
your life amounted to no more than one drop in a limitless ocean!
Yet what is any ocean but a multitude of drops?”

David Mitchell, Cloud Atlas

This dissertation describes the work carried out at the Chair for Inorganic and Metal-Organic Chemistry at the Technical University of Munich between January 2017 and October 2020. The project described in this thesis was supervised by *Prof. Dr. Roland A. Fischer*.

The results chapters of this thesis were published:

"Mixed Precious-Group Metal–Organic Frameworks: A Case Study of the HKUST-1 Analogue $[Ru_xRh_{3-x}(BTC)_2]$", W. R. Heinz, T. Kratky, M. Drees, A. Wimmer, O. Tomanec, S. Günther, M. Schuster and R. A. Fischer *Dalton Transactions* **2019**, *48*, 12031-12039.

"Thermal Defect-Engineering of Precious Group Metal-Organic Frameworks: A Case Study on Ru/Rh-HKUST-1 Analogues", W. R. Heinz, I. Agirrezabal-Telleria, R. Junk, J. Berger, J. Wang, D. I. Sharapa, M. Gil-Calvo, I. Luz, M. Soukri, F. Studt, Y. Wang, Ch. Wöll, M. Drees and R. A. Fischer *ACS Applied Materials & Interfaces* **2020**, 12, 36, 40635–40647.

"Thermal Defect Engineering of Precious Group Metal-Organic Frameworks: Impact on the Catalytic Cyclopropanation Reaction", W. R. Heinz, R. Junk, I. Agirrezabal-Telleria, B. Bueken, H. Bunzen, T. Gölz, M. Cokoja, D. De Vos and R. A. Fischer Catalysis: Science and Technology **2020**, 10, 8077 – 8085.

"Defect Engineered Ruthenium MOFs as Versatile Hydrogenation Catalysts", K. Epp, I. Luz, W. R. Heinz, A. Rapeyko, F. X. Llabres i Xamena and R. A. Fischer *ChemCatChem* **2020**, 12, 1720-1725.

"Scrutinizing Ligand Exchange Reactions in the Formation of the Precious Group Metal-Organic Framework $Ru^{II,II}$-HKUST-1: The Impact of Diruthenium Tetracarboxylate Precursor and Modulator Choice", W. R. Heinz, D. Staude, H. Bunzen, D. Mayer and R. A. Fischer, *Dalton Transactions* **2021**, accepted manuscript, DOI: 10.1039/D1DT00118C.

"Defective Metal-Organic Frameworks", S. Dissegna,[*] K. Epp,[*] W. R. Heinz,[*] G. Kieslich and R. A. Fischer *Advanced Materials* **2018**, 1704501. [*]equally contributing

Acknowledgement

There are many people, colleagues, friends, and relatives that had their contribution in making this thesis possible.

…And it wasn´t me if I kept this short!

My deepest gratitude deserves my supervisor and professor for his continuous support throughout the whole period of my time at the AMC chair. For his trust in my abilities, quality of work and character. For offering me an exceptional freedom to operate, any budget and support imaginable and *precious* times at conferences worldwide in the context of my academic work finally peaking in this thesis. Beyond this, I got the unique opportunity to develop valuable skills within an industrial collaborative project on skin tumor radiotherapy. These great experiences and responsibilities already turned out to be priceless for entering my professional future at Pharmpur GmbH. For all these reasons and because he strongly promotes the personal development of any of his PhD students: My deepest gratitude to **Prof. Dr. Dr. Roland A. Fischer**

I also acknowledge the other members of the examination commission Prof. Dr. Bernhard Rieger (chairman) and Prof. Dr. Klaus Köhler (2nd examiner).

Many thanks deserves the whole academic staff of the AMC chair lovely joking called “the hateful eight” among them particularly Christian Gemel, Mirza Cokoja and Markus Drees for sharing their experience and scientific input for our publications, for a productive working atmosphere and for an open ear anytime.

Turning to the ones who strongly contributed with enormous efforts in the lab and beyond: Many thanks to the great people who intentionally joined my research activities and hopefully never regretted doing so. Who put their trust in me as a lab course supervisor, who worked hard to address the questions of chemistry and always kept their smile: Dominik Staude, Thorsten Gölz, Martin Fredrich, Wolfgang “Yogi” Büchele and Raphael Junk.

Filling me with deep pride and honor for joining me again for their Master theses: Dominiks strong courage and creativity made that time productive and funny. Dominik: The mandelate route is dedicated to you! Raphael: Thank you for your trust, loyalty, respect, inspiration, and courage! You enabled the success of this thesis to large extents!

Colleagues from AMC that became friends in and outside university: Stefano Dissegna, Konstantin Epp, Zahid Mian Hussain (thanks for the Siddharta and all the good time in past and future), Miguel Rivera Torrente, and Marcone Baron. I´ll always remember our time in Italy, New Zealand, France, the Netherlands, Belgium and at AMC.

Greatly appreciated is the whole AMC group including all PhDs, permanent academic staff, technicians and secretaries particularly for the blistering parties, group trips (hiking to the Kampenwand, Kolbensattel and Mittenwald, rafting in Lenggries), the collegiality, barbecues and conference contributions (docMOF and AC get together@Raitenhaslach; EuroMOF2017@Delft; DEFNET workshop@Utrecht; MOF2018@Auckland; EuroMOF2019@Paris) and not to forget the unique X-Mas parties!

Using the MOF terminology, the secretary of a chair could be imagined as a multitopic linker. It´s the very crosslink, the heart of the framework. For a very long time, there was a missing linker defect and most of the lattice was held together mostly by Martin Schellerer alone. Thank you so much! Meanwhile the vacancy was filled by Dana and the framework stability has risen. I strongly recognize and appreciate the

efforts of both of you! Many thanks also to all technicians of AMC and the department of chemistry in general. I´d like to highlight the extraordinary kindness, competence, experience, and great curiosity around each and every sample of Ulrike Ammari, Jürgen Kudermann and the single crystal diffraction specialists Alexander Pöthig, David Mayer and Philip Altmann. Highly appreciated is the uncomplicated help with technical equipment by Anika Kwiatkowski and Richard Wetzel with his whole team!

At this point there shall be room for acknowledging the numerous collaborators:

@TUM: Jan Berger, Tim Kratky, Prof. Sebastian Günther, Andreas Wimmer, Prof. Michael Schuster, Matthias Nobis, Katia Rodewald, Prof. Bernhard Rieger. Special thanks deserve my PhD mentor and great inspirator Sergei Vagin as well as Carsten Troll for their outright willingness to help solving theoretical challenges with practical solutions that always inspired me!

In Germany: Yuemin Wang, Prof. Christof Wöll (Karlsruhe Institute of Technology), Prof. Birgit Weber (University of Bayreuth). Finally, Hana Bunzen (University of Augsburg) who raised my experiences of research collaborations on a completely different level with her passion, rapid response and excellent quality of work! It´s been a pleasure!

In Europe: Iker Aguirrezabal Telleria (University of Bilbao, ESP), Prof. Francesc X. Llabres i Xamena (University of Valencia, ESP), Mian Zahid Hussain (ex University of Exeter, GBR), Paul Iacomi, Prof. Philip Llevellyn (University of Marseille, FRA) and Ondřej Tomanec (Oloumuc, CZE).

In Leuven where I had a great great research stay: Prof. Dirk De Vos, thank you so much for your instant and generous rescue with accommodating Konstantin and me when CRC was down! Annelies Vanlasseler for the organization of literally everything. Bart Bueken and Simon Smoulders for great scientific assistance! Mikael Henrion, Min Tu and the whole COK group for simply having a fantastic time at the campus, the bioengineering bar and the Oude Markt.

Worldwide: Prof. Suresh Kalindindi (India), Ignacio “Nacho” Luz & Mustapha Soukri (RTI International, USA), Mai Hosoi and Mahiro Yoshioka.

Former colleagues I am grateful having met in the past that inspired me and influenced my way through science and life:

Veronika Mader: Danke für Dein inspirierendes Organisationstalent, die tolle Kameradschaft während der Ausbildung und auch noch zehn Jahre danach! Richard Kaspar: Danke für die Inspiration, die Energie und die Neugier, die Du stets in mir geweckt und gefördert hast! Du hattest einen enormen Anteil an meiner beruflichen Entwicklung von 2006 bis heute!

Großer Dank gilt meinen Freunden und Mitbewohnern aus München und Umgebung, die mir während Studium und Promotion das Erarbeiten von Frustrationstoleranz immer erleichtert haben: Alex (das nestbauende Muttertier), Hardrock Bernie Halleluja, Steffi (ich konnte mich bei der Vielzahl an Möglichkeiten für keine der liebevollen Neckereien entscheiden…), Chilli-Lilly (tiefenentspannt am Strand), Rugby-Tom, Jens, der Kino-Tanja, dem Judiehasen tanzend auf dem Pferderücken, Paul, sowie der besten WG mit vielen Pizza und Spieleabenden: Jasmine (Tennis & Wein), Susi (Pflanzenflüsterin und Spezialistin für Hosenkäufe) sowie Maxi (Käseliebhaber und Gelaterist). Ich werde die gemeinsame Zeit für immer in schöner Erinnerung behalten!

Besonderer Dank, ja gar ein dickes Lob verdienen meine Freunde vom TSV Königsbrunn – Tischtennis: Egal ob spätnachts telefonische Verfügbarkeit für Fragen zu experimenteller Durchführung (Simon), dem Zaubern von eleganten Formulierungen aus dem Handgelenk weit über den Dienst nach Vorschrift hinaus (Petro), Inspiration zur Erforschung gänzlich neuartiger Verbindungen (Angelo) sowie die Beratung zu unternehmerischen (Stefan), juristischen (Kathi) und didaktischen (Vicky) Fragestellungen aller Art, das schafft – nur der TSV!

Unbeschreiblich, die Dankbarkeit für den unverrückbaren Rückhalt meiner Familie, die stete Unterstützung und das Urvertrauen daraus: Meinen Eltern Gerlinde und Norbert sowie Jürgen, Stefan, Chrissi, Marie und Gerd: Danke. Für alles.

Zu guter Letzt, meine Liebe Eva: Meine tiefste Dankbarkeit für Deine Unterstützung, Deinen Humor, und für Deine bedingungslose Liebe.

Wer ich bin und wo ich stehe, verdanke ich Euch.

Werner R. Heinz, März 2021

Abstract

Material science has largely fueled the technological evolution during the last century, now being found in everyday consumer products. Prominent examples range from functional clothing and sports equipment to electronic devices such as personal computers, notebooks, tablets, smartphones, and LED screens. One new class of functional materials that gained increasing scientific attention are metal-organic frameworks (MOFs). The modular assembly of organic and inorganic secondary building blocks – termed linkers and nodes – into porous crystalline coordination networks comes along with an enormous design freedom regarding structure, porosity, composition, morphology, and related physicochemical properties. In this regard, the combination of the two orthogonal dimensions of linker and metal node choice represents a fusion of both organic and inorganic worlds: the almost infinite wealth of organic chemistry is paired with metal secondary building units (SBUs) of different nuclearity available from elements covering large parts of the periodic table. This unique parameter space allows for the tailor-made design of MOF materials. Consequently, academic research identified numerous fields of applications where MOFs could potentially outperform other conventional materials such as in catalysis, gas sorption, storage, or separation, sensing, and in the fields of energy and electronics.

In recent years, the perception of defects within MOF materials has changed significantly: In early days, researchers strived for the highest structural perfection trying to minimize defects and disorder in newly discovered porous crystalline coordination polymers. However, once the strong and often beneficial impact of defects on many material properties started to be uncovered, the paradigm changed with an awakening interest in not only utilizing but intentionally introducing and controlling defective sites – termed defect-engineering (DE) – as a third dimension in MOF property design.

The central motif of this thesis are the precious group metal (PGM)-based analogues of the iconic MOF $[M_3(BTC)_2]_n$ (HKUST-1, Hong-Kong University of Science and Technology, BTC = 1,3,5-benzene tricarboxylate). While the assembly of defined dimeric paddlewheel-type (PW) metal nodes comprising PGMs such as Ru and Rh with suitable organic linkers towards MOFs represents a sound opportunity for their utilization as heterogeneous catalysts, their respective 3-D connected porous frameworks are largely dominated by defects. In contrast to their isostructural rather defect-free Cu-HKUST-1 analogue, the kinetic inertness with respect to ligand exchange at Ru- and Rh-based PWs renders their “defect-free” synthesis a challenging yet open quest. Former works by *Olesia Kozachuk* and *Wenhua Zhang* were dedicated to the synthesis and characterization of the mixed-valence $Ru^{II,III}$- and the univalent $Ru^{II,II}$-HKUST-1 analogues. Both the concepts of modulated synthesis (using acetic acid as coordination modulator) and the controlled secondary building unit approach (CSA; using preformed isolated PW complexes of the type $[M_2(OAc)_4]$ for the MOF synthesis) were established to yield materials with certain structural order and high porosity. Intriguingly, the use of acetic acid modulator is Janus-faced: On the one hand, it is a key requisite for the efficient self-assembly towards structurally ordered materials and thus, crystallinity. On the other hand, its necessary use in large concentrations provokes a significant incorporation of acetate-based defects within the materials. In addition, the potential of DE to further tune materials properties in the context of open metal sites (OMS), porosity and catalysis was explored by the truncated mixed-linker approach to yield Ru-DE-MOFs. Their properties were studied and found superior to the parental, less-defective MOF, for instance, in the catalytic dimerization of ethene, the olefin hydrogenation or for CO sorption.

This thesis represents a continuation of these former works. Yet open questions and new directions and developments are equally addressed. The versatility of defect-engineered Ru-HKUST-1 was further demonstrated with different catalytic hydrogen transfer reactions. Both, the mixed-linker approach for

DE as well as a hydrogen pretreatment of the materials was found to boost the catalytic performance by progressive open metal site (OMS) and metal hydride formation. The family of HKUST-1 analogues was expanded by a series of mixed-metal RuRh-MOFs comprising mixtures of Ru and Rh-PWs finally peaking in the first report of a crystalline purely monometallic $Rh^{II,II}$-HKUST-1. These materials were characterized regarding their structure, porosity, composition, elemental distribution, and oxidation states.

Equipped with these Ru-, RuRh- and Rh-HKUST-1 analogues as chemical playground, the main objective of this thesis is structural control of the defects. On the one hand, defect control was targeted through defect minimization. The intrinsically most defective and thus, most challenging case of the univalent $Ru^{II,II}$-HKUST-1 was selected to systematically investigate the impact of the precursor ligand and modulator choice. The respective pK_a of the carboxylate precursor ligand was found to be one important aspect governing the ligand exchange efficiency. Improved structural order, ideal porosity and a fourfold increase in MOF particle size were accessible by using benzoate- or L-mandelate-based PW precursors in the MOF synthesis. On the other hand, the high intrinsic defectiveness of the PGM-HKUST-1 analogues was deliberately exploited. Ways to create, control, and utilize imperfect structures by defect-engineering were investigated and can be classified into *de novo* synthesis of defective MOFs and the postsynthetic defect creation. The *de novo* synthesis of DE-MOFs was studied following the mixed-linker approach by doping the synthetic mixture with an additional competing defective linker which is incorporated into the structure giving rise to modified PW defects. On the contrary, a process of controlled thermal defect-engineering (TDE) was established to postsynthetically introduce defects to a given PGM-MOF (Ru, Rh and mixed-metal RuRh) in a controlled manner. Comprehension of the defective materials was achieved through intensive material characterizations utilizing a plethora of different analytical methods from the fields of microscopy, diffraction techniques, chromatography, computational chemistry, and other more indirect methods. Their careful combination revealed the formation of partially reduced metal nodes featuring additional OMS. In this regard and compared with Rh-PWs, the Ru-PWs offer much broader redox flexibility and have a pronounced hydride generating ability (HGA) upon defect creation.

The applicability of pristine and defective materials was investigated using several catalytic test reactions such as the dimerization of ethene, two hydrogen transfer reactions and the cyclopropanation reaction. In all cases, DE-MOFs outperformed their pristine counterparts. While the former catalysis examples showed strong dependence on the materials HGA, the latter reaction was found to represent a convenient analytical probe for investigating the defect chemistry of the used PGM-MOFs. The characteristics such as activity, chemo- and diastereoselectivity of the well-understood catalytic cyclopropanation reaction of styrene using ethyl diazoacetate are found sensitive to probe the chemical environment of defective PWs within the heterogeneous catalyst materials. Conclusions on the density of OMS (as a measure of their oxidation state), their nature (perfect or modified PW), and stability can be valuable insights to this complex class of materials.

In short, PGM-analogues of the well-known highly stable HKUST-1 structure type were studied and crystalline mixed-metal RuRh- and monometallic Rh-HKUST-1 were first described. Ways to control and utilize the pronounced structural defectiveness of these compositionally complex MOFs were investigated. In this regard, a new method for the thermal defect-engineering of MOFs complementing other DE techniques was established. Structure-property relations with respect to solid-gas interactions, catalytic performance, and both chemical and thermal stability of these PGM-MOFs were investigated. The obtained fundamental insights into the role of defects in porous crystalline coordination polymers based on catalytically relevant PGMs could stimulate the investigation of yet unexplored MOFs of heavier metals and their utilization in practically relevant applications.

Zusammenfassung

Der technologische Fortschritt des letzten Jahrhunderts wurde mitunter maßgeblich durch die Entwicklung neuer Materialien geprägt, welche längst in viele Produkten des täglichen Gebrauchs Einzug erhielten. So reichen zahllose Beispiele von Funktionswäsche und Sportausrüstung bis zu elektronischen Geräten wie PCs, Notebooks, Tablets, Smartphones oder LED-Bildschirmen. Eine bestimmte Klasse funktionaler Materialien, die sogenannten metallorganischen Gerüstverbindungen (engl. *metal-organic frameworks*; MOFs), erhalten seit einigen Jahren besondere Aufmerksamkeit. Die modulare Assemblierung von organischen und anorganischen Sekundärbausteinen (engl. *secondary building units*; SBUs) – genannt Linker und Knoten – zu porösen, kristallinen Koordinationsnetzwerken birgt einzigartige Gestaltungsmöglichkeiten in Hinblick auf Struktur, Porosität, Zusammensetzung, Morphologie und verwandte physikochemische Eigenschaften. Hierbei verkörpert die Kombination der beiden orthogonalen Dimensionen bezüglich der Auswahl von Linkermolekül und Metallknoten buchstäblich eine Verheiratung von Organik und Anorganik: der schier unendliche Reichtum der organischen Molekülchemie gepaart mit SBUs verschiedenster Nuklearität beinahe jedes metallischen Elements des Periodensystems ergeben einen einzigartigen Parameterraum für maßgeschneiderte MOF Materialien. In diesem Zuge gelten MOFs für zahlreiche Anwendungsfelder als vielversprechende Alternativen, um konventionelle Materialien zu ersetzen. Mögliche Einsatzgebiete sind Katalysatoren, Gassorption, -separation und -speicherung, Sensoren, aber auch die Bereiche der Energiematerialien und der Mikroelektronik.

Die Wahrnehmung von Defekten und Fehlstellen in MOF-Materialien hat sich innerhalb der letzten Jahre stark gewandelt: vor zehn bis zwanzig Jahren strebten Forscher bei der Entwicklung neuer poröser, kristalliner Koordinationspolymere noch ausschließlich nach höchster struktureller Perfektion und der Minimierung oder Vermeidung von Defekten. Mit der zunehmenden Erforschung der tragenden Rolle von Fehlstellen auf viele Materialeigenschaften ging ein Paradigmenwechsel einher. Mittlerweile werden nicht nur vorhandene Defekte bewusst genutzt, sondern darüber hinaus gezielt Fehlstellen implementiert und kontrolliert. Diese sogenannte Defektmanipulation (engl. *defect-engineering;* DE) kann als dritte Dimension zur Gestaltung bestimmter Materialeigenschaften betrachtet werden.

Das zentrale Strukturmotiv dieser Arbeit sind die Edelmetallanaloga (*precious group metal*; PGM) der bekannten HKUST-1 Familie $[M_3(BTC)_2]_n$ (HKUST-1, *Hong-Kong University of Science and Technology*, BTC = 1,3,5-Benzoltricarbonsäure). Die Assemblierung molekular definierter Schaufelradkomplexe (paddlewheels; PWs) des Rutheniums oder des Rhodiums mit entsprechenden organischen Linkermolekülen hin zu MOFs verkörpert eine solide Strategie zu deren Verwendung als heterogene Katalysatormaterialien. Jedoch sind die resultierenden dreidimensional vernetzten, porösen Gitterstrukturen maßgeblich durch den Einbau von Defekten dominiert. Im Gegensatz zum vergleichsweise defektfreien Kupfer-basierten HKUST-1 Analogon, erschwert die hohe kinetische Inertheit von Edelmetallen (wie Ru oder Rh) den nötigen Ligandenaustausch während der MOF-Synthese. Eine Synthese von relativ defektfreien PGM-HKUST-1 Analoga ist entsprechend knifflig und bislang ungelöst. Bisherige Arbeiten durch *Olesia Kozachuk* und *Wenhua Zhang* waren der Synthese und Charakterisierung des gemischtvalenten $Ru^{II,III}$- und des univalenten $Ru^{II,II}$-HKUST-1 gewidmet. Die Anwendung der Konzepte von Koordinationsmodulation (Einsatz von Essigsäure zur modulierten MOF-Synthese) und kontollierten SBUs (Einsatz vorgeformter, isolierter Schaufelradkomplexe des Typs $[M_2(OAc)_4]$ zur MOF-Synthese; engl. *controlled SBU approach*; CSA) ermöglichen Materialien mit einer moderaten strukturellen Ordnung und hoher Porosität. Interessanterweise ist die Essigsäure zur Koordinationsmodulation janusköpfig: einerseits ist deren Einsatz eine Grundbedingung der effizienten Selbstassemblierung zu strukturell geordneten und somit kristallinen Materialien. Andererseits führen die notwendigen hohen

Essigsäurekonzentrationen in der Syntheselösung zwangsläufig zum Einbau signifikanter Mengen Acetat-basierter Defekte innerhalb der Materialien und limitieren somit die erreichbare Netzwerkperfektion. Darüber hinaus wurden Ru-DE-MOFs erzeugt, um den Einfluss von Defektmanipulation (mittels gekürzten Defektlinkern) auf die Anzahl ungesättigter Metallzentren (engl. *open metal sites*; OMS), Porosität und Katalyse untersucht. Die Eigenschaften der defektmanipulierten Ru-DE-MOFs übertrafen jene der defektärmeren MOFs bei der Ethendimerisierung, der Hydrierung von Olefinen sowie der Adsorption von Kohlenstoffmonoxid.

Diese Dissertation knüpft an die vorangegangenen Arbeiten an und adressiert gleichermaßen bislang ungelöste Fragestellungen ebenso wie neue Forschungsaspekte. So wurde die Vielseitigkeit von defektmanipulierten Ru-HKUST-1 Katalysatormaterialien im Rahmen verschiedener Wasserstofftransferreaktionen untermauert. Sowohl der Einsatz von Defektlinkern zur Synthese defektmanipulierter MOFs, sowie eine postsynthetische Wasserstoffbehandlung der Materialien führten zur Steigerung der Katalysatoraktivität. Diese konnte auf die zunehmende Bildung von OMS und Metallhydriden zurückgeführt werden. Die Familie der HKUST-1 Analoga konnte durch eine gemischt-metallische Serie von RuRh-MOFs (feste Lösungen von monometallischen Ru_2- und Rh_2-Dimeren) sowie erstmalig durch ein kristallines, rein monometallisches Rh-HKUST-1 erweitert werden. Die erhaltenen Materialien wurden bezüglich ihrer Struktur, Porosität, Zusammensetzung, elementarer Verteilung und Oxidationsstufen analysiert.

Innerhalb der so geschaffenen chemischen Plattform der Ru-, RuRh- und Rh-HKUST-1 Analoga liegt die Hauptzielsetzung dieser Dissertation in der strukturellen Defektkontrolle. Diese wurde zum einen durch Defektminimierung angestrebt. Hierfür wurde die intrinsisch defektreichste und somit herausforderndste Struktur des univalenten $Ru^{II,II}$-HKUST-1 ausgewählt. Der Einfluss der Wahl von Vorläuferligand und jeweiliger freier Carbonsäure als Koordinationsmodulator wurde systematisch untersucht. Hierbei zeigte der pKa-Wert des Carboxylatvorläuferliganden einen starken Einfluss auf die Ligandenaustauscheffizienz. Mit Hilfe von Benzoat- sowie L-Mandelatliganden am Schaufelradkomplex konnten MOF-Proben mit verbesserter struktureller Ordnung, idealen Porositäten und bis zu vierfachen Partikelgrößen (verglichen mit der etablierten Acetat-basierten Synthese) gewonnen werden. Zum anderen wurde der hohe intrinsische Defektgrad der Edelmetall-HKUST-1 Analoga gezielt ausgenutzt.

Die studierten Ansätze zur Erzeugung, Kontrolle und gezielten Verwertung lassen sich unterteilen in *de novo* Synthesen defekter MOFs und postsynthetische Defekterzeugung in bereits existierenden Strukturen. Die *de novo* Synthese von DE-MOFs wurde mittels der gemischten Linkerstrategie untersucht. Hierbei wird ein Teil der zur Synthese notwendigen Linkerstoffmenge durch einen zusätzlichen Defektlinker substituiert. Dieser kompetitive Defektlinker greift in das Gleichgewicht des Ligandenaustauschs ein und wird bei der Entstehung der ausgedehnten Gerüststrukturen des MOFs in sogenannten modifizierten Schaufelradkomplexen mit eingebaut. Gegenteilig zur *de novo* Strategie wurde außerdem ein postsynthetisches Verfahren zur kontrollierten thermischen Defektmanipulation (engl. *thermal defect-engineering;* TDE) entwickelt. Die Orchestrierung verschiedener analytischer Methoden aus Mikroskopien, Beugungsexperimenten, Chromatographien, quantenchemischen Rechnungen und anderen, eher indirekten Methoden ermöglichte ein tiefgreifendes Verständnis der erzeugten komplexen Defektstrukturen. TDE führt demnach zu einer partiellen Reduktion der enthaltenen Metallknoten unter Bildung zusätzlicher, freier Koordinationsstellen. Verglichen mit Rhodiumzentren zeigen Ruthenium-basierte Metallknoten eine starke Redoxflexibilität und Hydridbildungsfähigkeit (engl. *hydride generating ability*; HGA) bei deren Defektmanipulation.

Die Anwendbarkeit von ursprünglichen sowie defektreicheren Materialien wurde mittels verschiedener katalytischer Testreaktionen wie der Dimerisierung von Ethen, zwei unterschiedlichen Wasserstofftransferreaktionen und der Cyclopropanierung untersucht. In allen Fällen waren DE-MOFs

ihren ursprünglichen, defektärmeren Varianten überlegen. Während die ersten drei genannten katalytischen Testreaktionen stark von einer vorhandenen Hydridbildungsfähigkeit profitieren, konnte die Cyclopropanierungsreaktion als sensitive, analytische Sonde identifiziert werden. Die charakteristischen Parameter dieser Reaktion, nämlich Aktivität, Chemo- und Diastereoselektivität, lassen sich praktischerweise zur Untersuchung der Defektstrukturen der komplex zusammengesetzten Edelmetall-MOFs ausnutzen. Die in der Literatur bereits intensiv studierte Cyclopropanierung von Styrol mit Ethyldiazoacetat zeigt sich empfindlich gegenüber der chemischen Umgebung defekter Metallzentren im Netzwerk der heterogenen Katalysatormaterialien. Diese Informationen ermöglichten Schlussfolgerungen bezüglich der Anzahl freier Koordinationsstellen (und der Oxidationsstufen der Metalle), deren Natur (perfekt oder modifzierte PWs) und Stabilität und erlauben somit wertvolle Einblicke in diese vielschichtige Klasse neuer Materialien.

Zusammengefasst wurden Edelmetallanaloga der bekannten, metallorganischen Gerüstverbindung HKUST-1 untersucht und kristalline gemischt- (RuRh) und monometallische (Rh) Varianten erstmalig beschrieben. Strategien zur Kontrolle und Nutzbarmachung der ausgeprägten strukturellen Defekte dieser kompositionell komplexen MOFs wurden untersucht. Hierzu wurde eine neuartige Methode zur kontrollierten, thermischen Defektmanipulation entwickelt, welche bestehende Ansätze zur Defektmanipulation und -generierung komplementiert. Erforscht wurden Struktur-Eigenschafts-Beziehungen mit Schwerpunkten auf Festgas-Wechselwirkungen, Katalysatoreignung und chemische wie thermische Beständigkeit dieser Edelmetall-MOFs. Die gewonnenen, grundlegenden Erkenntnisse zur Rolle von Defekten in porösen, kristallinen Koordinationspolymeren auf Basis von katalytisch relevanten Edelmetallen könnten zukünftig die Erforschung neuer MOFs schwererer Metalle stimulieren und eine Basis für mögliche, praktische Anwendungen bilden.

List of Abbreviations

0-D	Zero-dimensional
1-D	One-dimensional
2-D	Two-dimensional
3-D	Three-dimensional
AAS	Atom absorption spectroscopy
ADMET	Acyclic diene metathesis polymerization
AFM	Atomic force microscopy
ATR	Attenuated total reflection
BINAP	2,2'-bis(diphenylphosphino)-1,1'-binaphthyl)
BDC	1,4-benzene dicarboxylate
BET	*Brunauer-Emmet-Teller*
bipy	bipyridine
BM	Bohr magneton
BO	Bond order
BTC	1,3,5-benzen tricarboxylate
CM	Cross metathesis
CP	Cyclopropane / cyclopropanation
CP	Coordination polymer
CSA	Controlled secondary building unit approach
CUS	Coordinatively unsaturated sites (equally used as OMS)
DABCO	1,4-Diazabicyclo[2.2.2]octane
DAniF	*N,N'*-di(*p*-anisyl) formamidinate
DCM	Dichloromethane
DE	Defect-engineering
DEF	Diethyl formamide
DFT	Density functional theory
DIPAMP	ethane-1,2-diylbis[(2-methoxyphenyl)phenylphosphane]
DMF	Dimethyl formamide
EA	Elemental analysis
EDA	Ethyl diazo acetate
EDX	Energy dispersive X-ray spectroscopy
EoA	Energy of Adsorption
EPR	Electron paramagnetic resonance spectroscopy
ESI	Electronic supporting information
EXAFS	Extended X-ray absorption fine structure analysis
FID	Flame ionization detection
FT	Fourier Transform
GC	Gaschromatography
HAADF	High angle annular dark-field
HGA	Hydride generating ability
HKUST-1	Hong Kong University of Science and Technology 1
HPLC	High performance liquid chromatography
hpp	Hexahydropyrimidinopyrimidine
HR	High resolution
ICP	Inductively coupled plasma
ICP-OES	Inductively coupled plasma – optical emission spectroscopy
IPA	Isophthalate / 1,3-benzene dicarboxylate
IR	Infrared (spectroscopy)

IUPAC	International Union of Pure and Applied Chemistry
LA	*Lewis* acid
LB	*Lewis* base
LP	Large Pore
mand	Mandelate
MAS	Magic angle spinning
MIL	Matériaux de l'Institut Lavoisier
MOF	Metal-organic framework
MOP	Metal-organic polyhedra
MPG	Mixed-precious group
MPV	*Meerwein-Ponndorf-Verley*
MS	Mass spectrometry
NDC	Naphthalene dicarboxylate
NMR	Nuclear magnetic resonance
NP	Nanoparticle
OAc	Acetate
OBz	Benzoate
OMS	Open metal site
PALS	Positron annihilation lifetime spectroscopy
PCN	Porous coordination network
PDF	Pair distribution function
PGM	Precious group metal
POM	Polyoxometalate
ppb	Parts per billion
ppm	Parts per million
PSD	Pore size distribution
PSM / PST	Post-synthetic modification / treatment
PTFE	Poly (tetrafluoroethene)
PW	Paddlewheel
PXRD	Powder X-ray diffraction
PyDC	3,5-pyridine dicarboxylate
ROM(P)	Ring-opening metathesis (polymerization)
SALE	Solvent-assisted linker exchange
SALI	Solvent-assisted linker incorporation
SAME	Solvent-assisted metal exchange
SBU	Secondary building unit
SEM	Scanning electron microscopy
SP	Small pore
STM	Scanning tunneling microscopy
TA	Thermal annealing
TD	Time dependent
TDE	Thermal defect-engineering
TEM	Transmission electron microscopy
TFA	Trifluoro acetate
TGA	Thermogravimetric analysis
THF	Tetrahydrofurane
TOF	Turn-over frequency
TON	Turn-over number
TUM	Technical University of Munich
UHM	University of Hawaii at Manoa

UHV	Ultra-high vacuum
UiO	Universitaet i Oslo
UV	Ultraviolet
Vis	Visible light
XPS	X-ray photoelectron spectroscopy
XRD	X-ray diffraction
XRF	X-ray fluorescence spectroscopy
ZIF	Zeolitic imidazolate framework

Table of Contents

1. Motivation

The rise of *homo sapiens* started roughly 70'000 years ago with the cognitive evolution. According to the popular philosopher *Yuval Noah Harari*, this was the first of four revolutions with the agricultural (≈10'000 years ago), the cultural (≈800 years ago) and the scientific revolutions (started ≈500 years ago) following.[1] The latter strongly gained momentum during the last 200 years with enormous technological advances giving rise to increasing wealth of humankind. However, the vastly rising human population is associated with socio-economic, energy and environmental challenges considering the limited resources of the planet. The quest for new materials fulfilling the increasing demand for energy efficient, environmentally friendly solutions is apparent and finally found its ways to politics. Chemistry in general and particularly material sciences impart a decisive role in this regard!

In the field of new materials, the emerging class of MOFs has gained increasing attention while their first reports just date back to the early 2000s. Although industrial use is yet prenatal, academic research is continuously growing with already tens of thousands of new structures being just the tip of the iceberg with endless possibilities regarding future applications of these tailor-made structurally ordered, porous hybrid materials as a subclass of coordination polymers. MOFs are considered interesting in the fields of catalysis, gas sorption, separation, and storage, but also in sensing applications, magnetics, electronics, and medicine such as the targeted drug delivery.[2-3]

While the early research focused on the beauty of structural perfection, a shift in paradigm took place towards the recognition and appreciation of defects and disorder often governing the properties of MOFs. Although the terms defects or disorder have an almost exclusive negative connotation in society, they can be a key requisite in materials to valuable properties and functions. Some impressive examples are the doping of highly pure silicon with trace impurities of group three and group five elements causing defects within the materials. When such defects are intentionally introduced to the materials, the emerging properties of p- and n-doped silicon semiconductors can be applied in transistors as core element of any advanced microelectronic device seen in everyday life. Other examples range from trace impurities of several metals within otherwise highly pure Al_2O_3 crystals – in gemstones such as sapphires, emeralds, or rubies – to the hardening of steel by the addition of carbon. A similar development could be possible with MOFs. Consequently, the systematic investigation of defects and disorder in MOFs can reveal a third dimension in property design – besides the two dimensions of carefully choosing metal nodes and organic linkers – which can be used to tailor certain properties for highly specialized applications required to meet the rising challenges mentioned above.[4-5]

Almost any metal of the periodic system has already been used for MOF synthesis, however, the precious group metals remain mostly unexplored in this regard.[6] In this regard, this thesis could represent a very small contribution to these challenges by unveiling the defect chemistry of PGM-based MOFs.

2. State of the Art

The chemistry of metal-organic frameworks (MOFs) is at the heart of this thesis. According to the underlying multidisciplinary nature of MOFs combining inorganic, organic, macromolecular and solid-state chemistry, this thesis covers a variety of several different fields of chemistry. Superordinate relations displaying the embedding of precious group metal-based PGM-HKUST-1 analogues (Hong Kong University of Science and Technology) within the broader scientific context (top part) as well as the objectives of structural control over defects and its impact on catalytic properties are highlighted in **Scheme 1**. The aim of this introductory chapter is to provide a selection of most important state of the art insights into above-mentioned fields. Easy digestion of the subsequent results chapter is intended instead of claiming comprehensiveness.

First, structure, reactivity and synthetic accessibility of molecular transition metal complexes (some air-sensitive) of ruthenium and rhodium are discussed in **chapter 2.1**. Their utilization as preformed secondary building units (SBUs) in the synthesis of extended structures, called coordination polymers in **chapter 2.2** bridges the way to **chapter 2.3** on metal-organic frameworks in general. After introducing the most important general aspects, a special focus is set on the role of defects in MOFs within **subchapter 2.3.3**. HKUST-1 as the one exemplary MOF system and particularly its ruthenium analogue are discussed in **subchapters 2.3.5** and **2.3.6**.

Besides the merely academic interest in gaining fundamental comprehension, no doubt, precious metal-based materials are predesignated for applications in catalysis. Therefore, **chapter 2.3.4** gives a very brief overview on homogeneous and heterogeneous catalysis, some aspects of MOF-based catalysis leading to a concise overview over catalytic hydride transfer, ethene dimerization and cyclopropanation reactions relevant for the test reactions investigated in studies I (**chapter 4.1**), III (**chapter 4.3**) and IV (**chapter 4.4**) of this thesis.

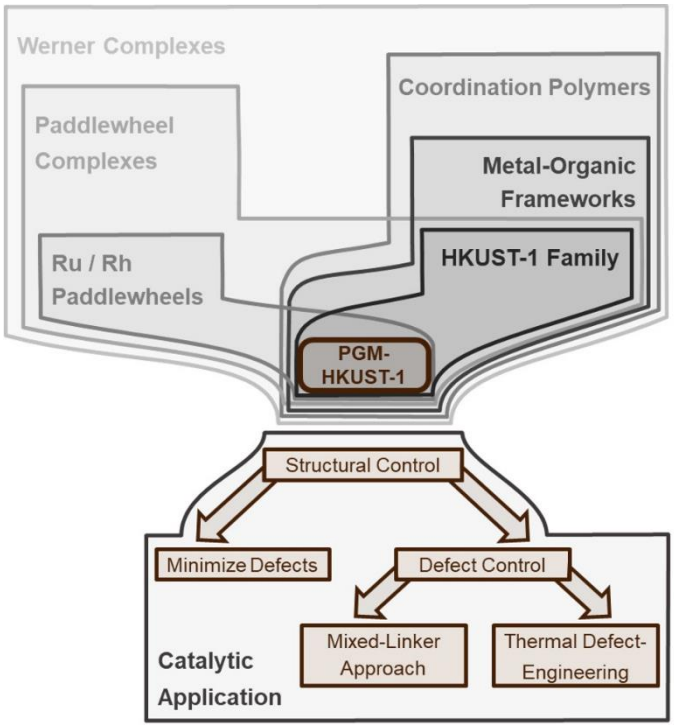

*Scheme 1: General affiliations of the most relevant topics of this thesis. The surrounding frames indicate superordinate structural motifs. The interplay between molecular **Paddlewheel Complexes** (chapter 2.1), particular the **Ru- and Rh-based PWs**, their dimensional extension into **Coordination Polymers** (chapter 2.2) and specifically **MOFs** (ch 2.3) towards Precious-Group Metal-based **PGM-MOFs** and the impact of defects (ch 2.3.3) on their catalytic properties (ch 2.4) can be seen.*

2.1 Molecular Paddlewheel Complexes of Ruthenium and Rhodium

The chemistry of ruthenium and rhodium complexes is remarkably diverse. Even for simple, mononuclear *Werner*-type complexes, the deliberate choice of the ligands allows for properties suitable for a wide range of potential applications. For instance, the optical properties of the $Ru(bipy)_3^{2+}$ motif with 2,2'-bipyridine (bipy) ligands are commonly used as visible light photosensitizers and/or photocatalysts.[7-10] Besides oxidation catalysis,[11] the flexibility of ruthenium's oxidation state has also been exploited in asymmetric hydrogenations.[12] Stereoselectivity can be achieved using chiral Ru-BINAP (BINAP = 2,2'-bis(diphenylphosphino)-1,1'-binaphthyl) but also Rh-DIPAMP (DIPAMP = ethane-1,2-diylbis[(2-methoxyphenyl)phenylphosphane] complexes found by *Noyori* and *Knowles* (Nobel Prize 2001).[13-14] Ruthenium is also applied in Fischer-Tropsch catalysis.[15-16] Most remarkably, however, the discovery of olefin metathesis as a unique feature of ruthenium complexes was one of the few fundamentally novel reactions during the last 50 years. The cleavage of an existing double bond and the subsequent transfer of the alkylidene fragments has found several applications ranging from ring closing and ring opening metathesis (RCM, ROM), its corresponding ring opening polymerization (ROMP), cross metathesis (CM) to the acyclic diene metathesis polymerization (ADMET).[17-18] The most commonly applied complexes for these reactions are ruthenium (N-heterocyclic) carbene complexes established by *Grubbs*, *Schrock*, *Herrmann* and others.[17, 19-23] For rhodium, catalytic conversion of NO_x to N_2 and O_2 applied in car combustion engines, the hydroformylation and several hydrogenation reactions (like aforementioned *Knowles* catalyst) are industrially established.[12] Besides the use of metal (nano) particles, also phosphine complexes such as the *Wilkinson* catalyst $Rh(PPh_3)_3Cl$ or phosphine-based rhodium carbonyl hydrides are widely used complexes.[13]

Besides classical, mononuclear complexes, transition metal complexes with more than one metal atom per node are known. Although tri-, tetra- or hexanuclear complexes such as the so-called "basic ruthenium acetate" $[Ru_3O(OAc)_6]^+$ are known, the binuclear complexes, particularly of the paddlewheel-type (PW), are far more investigated and easier to obtain. High thermodynamic and chemical stability and the presence of open metal sites (OMS) and potential metal-metal interactions render them interesting building blocks in academia and industry. The following subchapters will explain the structural motif of Ru- and Rh-based PW complexes, their reactivities and routes to access them synthetically.

2.1.1 Structure

Geometry

The lantern-like „paddlewheel“ structure of binuclear tetracarboxylates as shown in **Figure 1** is known for many different transition metals like Zn, Cu, Fe, Cr, Fe, Co, Ni, Cu, Zn, Mo, Ru, Rh, Pd, Re, Os and Ir. Amongst them, the Cu and Zn analogues received much attention in the field of metal-organic frameworks (MOFs) while particularly the Rh complexes found widespread catalytic applications.

In a PW complex, both metal atoms are aligned in the C_4 rotation axis of the molecule surrounded by four “equatorial” bridging carboxylate ligands each rotated by 90° representing the paddles of the metaphoric paddlewheel. Thus, a general D_{4h} symmetry is underlying. Each “axial” OMS can be occupied by a neutral (solvent) ligand for univalent M^{2+}-M^{2+} (or simplified $M^{II,II}$) as shown in **Figure 1** for water molecules coordinating the axial positions.

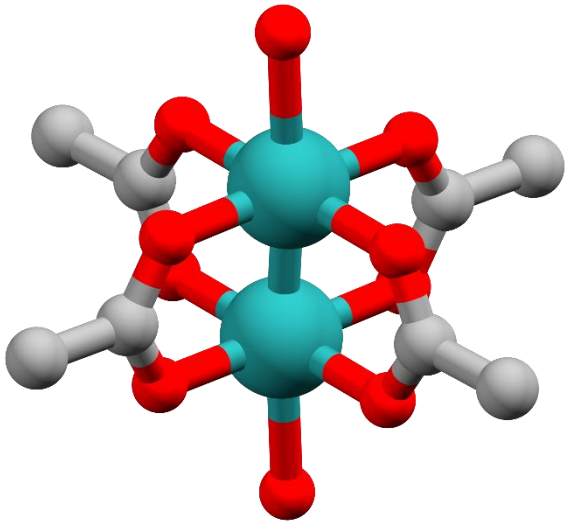

***Figure 1**: Single crystal structure representation of $[Ru_2(OAc)_4(H_2O)_2]$. Color code: Ru – cyan, O – red, C – grey. Hydrogen atoms are omitted for clarity. The dimeric ruthenium structure contains four bridging acetate ligands on equatorial positions forming the “paddlewheel” motif. Axial positions are occupied with water ligands. Hydrogen atoms are omitted for clarity.*

Generally, adducts carrying axially coordinating *Lewis* basic solvent molecules such as ketones, ethers (cyclic or acyclic), alcohols are possible. The four positive charges of the metal core are charge compensated with the four surrounding carboxylates giving overall charge neutral complexes. For most of the metals forming PW structures, the most stable oxidation state is +II/+II. However, Fe and Ru can also form mixed-valent $M^{II,III}$ PWs which represent the air-stable configurations of these metals while their univalent PWs are prone to oxidation. The additional positive charge of $M^{II,III}$ is generally compensated by one additional anionic ligand which is either bound to one of the axial positions replacing a neutral ligand (for strongly coordinating anions) or exists in proximity to the PW (for weakly coordinating ligands such as BF_4^-, PF_6^- or ClO_4^-). Depending on the localization of the odd electron and thus, the additional counterion, the electronic structure can be better described as II½,II½ or II,III.

For chloride being the additional counterion in $Ru_2(OOCR)_4X$ compounds, the PWs can be either isolated in discrete molecules $[Ru_2(OOCR)_4LCl]$ with L being a solvent ligand, or connected through axially bridging chlorides in one-dimensional (1-D) linear or zigzag chains.[24] The diruthenium tetraacetate chloride contains such zigzag chains for instance. Other isolated discrete molecular compounds with halide counterions are related to sterically bulky substituents or asymmetric equatorial ligands as observed for O,N-donor ligands such as 2-hydroxy pyridinates.[25]

Bonding Properties

An overview on PWs of most typical metals, their favoured oxidation states, related electronic configurations, metal-metal bond orders and lengths is provided in **Table 1**. For Ru complexes, the M-M bond lengths are remarkably insensitive towards variation of axial or equatorial ligands. Also the reduced bond order (BO) of 2 in $Ru^{II,II}$ complexes compared to their mixed-valent analogues (BO = 2.5) $Ru^{II,III}$ only manifests is a small lengthening of the M-M bonds.[25] For instance, the M-M bond length of 2.262 Å in $Ru_2(OAc)_4(H_2O)_2$ is just slightly longer than the 2.248 Å of the respective mixed-valent $Ru_2(OAc)_4(H_2O)_2(BF_4)$ analogue. The occupancy of the δ* orbital has only minor effects on respective bond lengths. In a similar way, the bond lengths M-L between metal and axial ligands are barely affected. For instance, the aforementioned univalent complex has a M-L distance of 2.335 Å while for its oxidised variant it is 2.310 Å respectively. Also the M-O distances between metal atoms and their equatorial oxygen donor atoms are relatively insensitive to oxidation state or type of carboxylate with only minor elongation for the reduced $Ru^{II,II}$ complexes. This slight trend is also ascribed to the occupied antibonding δ* orbital.[25]

One special feature of the dimeric nature of the PWs is their ability to comprise metal-metal interactions. Depending on metal and oxidation state, M-M bonds are present, as shown in **Table 1**. In this regard, the existence of a metal-metal quadruple bond is most remarkable. The first such compound was chromium acetate $[Cr_2(OAc)_4(H_2O)_2]$ first synthesized in 1844 by *Eugène-Melchior Péligot*. The confirming structure comprising the quadruple bond was solved in 1964 by *Frank Albert Cotton*.[26] Generally, large parts of the state of the art of molecular Ru- and Rh-based PW complexes were greatly inspired by the works of *F. A. Cotton*.

***Table 1**: Selection of different PW-forming metals, their typical oxidation states, M-M bond orders and distances. The table was created using data from Lit[27-30].*

Metal	Oxidation state	Electronic structure	Bond order	d_{M-M} [Å]
Cr	II,II	$\sigma^2\pi^4\delta^2$	4	1.8 – 2.7
Cu	II,II	$\sigma_{3d}{}^2\pi^4\delta^2\delta^{*2}\pi^{*4}\ \sigma^*_{3d}{}^2\ \sigma_{4s}{}^2$	1	≈2.6
Zn	II,II	$\sigma_{3d}{}^2\pi^4\delta^2\delta^{*2}\pi^{*4}\ \sigma^*_{3d}{}^2\ \sigma_{4s}{}^2\ \sigma^*_{4s}{}^2$	0	≈3.0
Mo	II,II	$\sigma^2\pi^4\delta^2$	4	≈2.1
W	II,II	$\sigma^2\pi^4\delta^2$	4	≈2.2
Tc	III,III	$\sigma^2\pi^4\delta^2$	4	≈2.2
	II,III	$\sigma^2\pi^4\delta^2\delta^{*1}$	3.5	≈2.1
Re	III,III	$\sigma^2\pi^4\delta^2$	4	≈2.2
Ru	II,II	$\sigma^2\pi^4\delta^2(\delta^*\pi^*)^4$	2	≈2.3
	II,III	$\sigma^2\pi^4\delta^2(\delta^*\pi^*)^3$	2.5	≈2.3
Rh	II,II	$\sigma^2\pi^4\delta^2\delta^{*2}\pi^{*4}$	1	≈2.4
Os	III,III	$\sigma^2\pi^4\delta^2(\delta^*\pi^*)^2$	3	≈2.3
Pt	III,III	$\sigma^2\pi^4\delta^2\delta^{*2}\pi^{*4}$	1	≈2.4

For an overview on literature-known univalent and mixed-valence ruthenium PW complexes and the impact of the ligands on related bond lengths and angles please refer to the **Appendix ESI Study V**.

Magnetism

The mixed-valence Ru PWs have unusually high magnetic moments of 3.6 to 4.4 BM (with one BM = $9.27 \cdot 10^{-24}$ A m²) per dimer. The strong paramagnetism is a result of the three unpaired electrons. An almost degenerate nature of π* and δ* orbitals favours the high-spin state $S = {}^{3}/_{2}$ in these complexes. The half-filled π* and δ* orbitals energetically favour the mixed-valent $Ru^{II,III}$ over their univalent $Ru^{II,II}$ counterparts. The additional electron leads to the presence of only two unpaired electrons, magnetic moments of ≈2.1 BM and $S = {}^{2}/_{2}$ in the $Ru^{II,II}$ compounds. In summary, all investigated Ru PWs show pronounced paramagnetism.[1] For the Rh dimers, the situation is different. Fully occupied δ*and π* orbitals lead to diamagnetic low-spin Rh-PW complexes, respectively.

[1] As of relevance for **Study II** of this work, the paramagnetic Ru_2 core hampers any quantitative investigation using nuclear magnetic resonance (NMR). While NMR can still give reasonably narrow signals for protons being distant to the Ru_2 core in solution, the natural signal broadening present in the solid-state undermines any meaningful MAS-NMR measurements.

2.1.2 Reactivity

Ru- and Rh-based PWs can undergo a variety of reactions that are not only relevant in the context of the self-assembly towards extended structures (i.e. MOFs) but also for their selective synthetic access and to avoid undesired side reactions during handling. At this stage, the broad reactivity should be limited to the most important aspects such as ligand exchange, solvation/desolvation and redox reactions.

Ligand Metathesis at Axial Sites

According to the different binding, a distinction between axial and equatorial ligands should be made. Compared to the much stronger bonding of bridging anionic carboxylates at the equatorial sites, the axially bound (neutral) solvent molecules (two for univalent $M^{II,II}$ systems, one for $M^{II,III}$) are more reactive. Upon synthesis, the axial sites comprise the synthetically used solvent such as acetone, tetrahydrofuran (THF), water, dimethyl sulfoxide (DMSO) or diethyl ether. Exchange of axial ligands is enthalpy driven.[31] Therefore, exchange with a more nucleophilic ligand is easy to achieve and can proceed almost quantitatively. Compared to O donors, N, S or P donor ligands usually show strong binding to axial sites due to their moderate π-acceptor properties.[32-33] While N- and S-containing axial adducts are stable compounds,[31] typically the phosphines first axially bind but then tend to migrate to equatorial positions resulting in PW disassembly. *Aquino et al.* isolated a diphosphine adduct as kinetic product and found the longest Ru-Ru bond (2.427 Å) ever reported in Ru PW complexes.[34-35] Progressive reduction of the metal bond order leads to the collapse of the PW structure into monomeric phosphine complexes.[36-39] When mixtures of potential ligands are available, statistical mixtures of complexes are expected depending on the binding affinities and the solutions' pH. *Santos et al*. investigated the axial ligand exchange with several amino acids and found the kinetics following the order cys>his>>trp≈gly according to the presence of strongly coordinating S- and N-ligator sites for cys and his.[31]

Ligand exchange towards less nucleophilic ligands (such as ketones or ethers) is technically solved through large reagent excess or withdrawal of the released former ligand. Combination of both methods in the so-called "solvent exchange" facilitates efficiently shifting the thermodynamic equilibrium towards substitution of these strongly bound ligands.

The same holds true for anionic ligands in the mixed-valent $Ru^{II,III}$ case. Strongly coordinating axial halides can be substituted elegantly by weakly coordinating anions (e.g. BF_4^-, ClO_4^-, PF_6^-) using their respective silver salts. Axial adducts comprising biologically relevant molecules such as non-steroidal antiinflammatory drugs were prepared accordingly.[40-41]

Ligand Metathesis at Equatorial Sites

Ligand exchange of equatorially bound ligands is more difficult to achieve due to the thermodynamically more stable μ-binding and the kinetically rather inert PGMs as compared to their 3d analogues. Within the PGM dimers, ligand exchange at univalent $Ru^{II,II}$ or $Rh^{II,II}$ is even slower than it is for mixed-valence $Ru^{II,III}$ PWs.[42] This might be rationalized by the higher electron density of the $Ru^{II,II}$ core resulting in stronger back bonding to equatorial ligands. These effects are also observed in **chapter 4.2** and **chapter 4.5** with univalent $Ru^{II,II}$ and $Rh^{II,II}$ MOFs featuring lower structural order compared to mixed-valence $Ru^{II,III}$ as a consequence of slower ligand exchange hampering efficient self-assembly.

Exchange of bidentate carboxylates by two monodentate ligands is entropically disfavoured. Though, exchange with other carboxylates or other bidentate ligands with similar geometry is possible and was intensively used in literature.[26, 43-49] One structurally remarkable example was the installation of carboxylate-functionalized metallocene ligands at a mixed-valent Ru-PW core reported by *Cooke et al.* in 2002 as highlighted in **Figure 2**.[50]

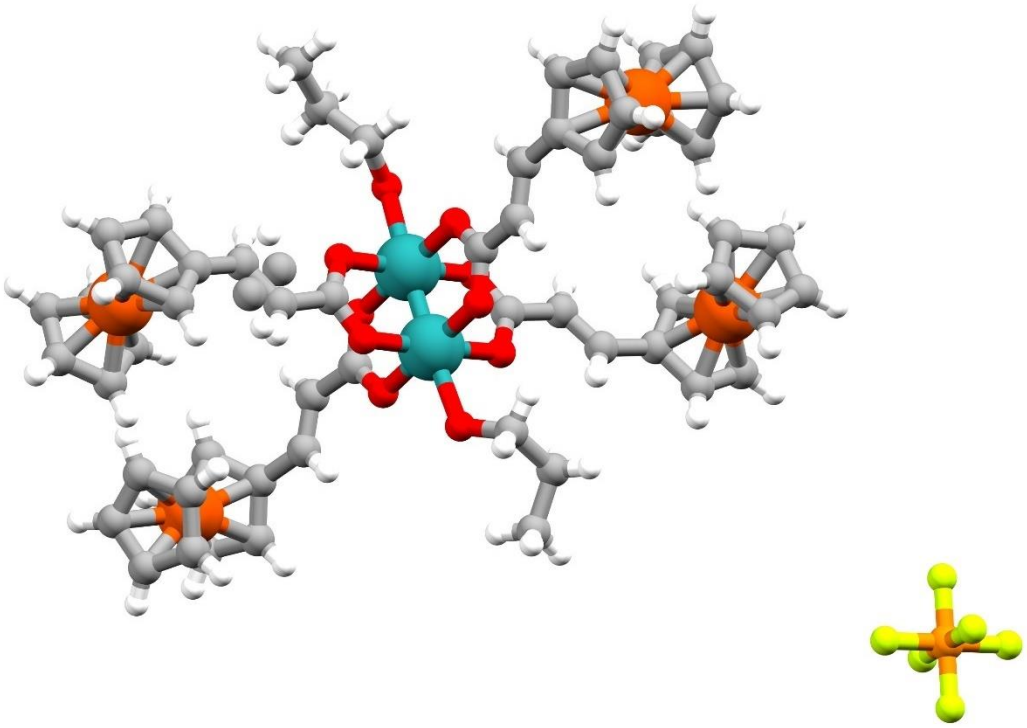

***Figure 2**: Single-crystal structure of an optically impressive example of ligand exchange reactivity: Based on $Ru_2(OAc)_4Cl$, Cooke et al. first exchanged the equatorial ligands by ferrocenyl acetate and secondly the axial chloride by hexafluorophosphate yielding the displayed compound.[50]*

Besides the O,O-donor type carboxylates, O,N- and N,N-donor ligands are known to form PW complexes. Prominent examples are 2-hydroxy pyridinates or carboxamidates (N,O-donors) and hexahydropyrimidinopyrimidine (hpp) or formamidinates (e. g. DAniF, N,N-donor).[45, 51-53] Overall, these N-containing ligands are more basic compared to the rather acidic carboxylates resulting in stronger bonds to the dimeric core.

Partial equatorial ligand exchange was reported in few studies and relied either on strong *trans* effect of electron-poor carboxylates, on stoichiometric use of strongly binding N,N ligands or on sterically demanding substituents preventing full ligand exchange on all four equatorial sites.[54-57]

Compared to transition metals of the 3d row, the 4d row elements Ru and Rh possess pronounced inertness towards ligand exchange.[42] Comparing ligand exchange kinetics of mixed-valent and univalent Ru-PWs, the latter show even lower exchange rates.

Solvation / Desolvation

A complete removal of the axially coordinated solvent can be achieved through thermal treatments in dynamic vacuum at temperatures between 60 °C and 150 °C. Consequently, highly reactive (i.e. electrophilic) *Lewis* acidic OMS are created. This process is called “desolvation” or “activation” and can proceed in both isolated molecular as well as extended PW structures. Note, the structural order of densely packed (micro)crystalline molecular PW crystals depends on the presence of the respective axial solvent molecules. During activation and the concomitant release of solvent molecules, these crystals amorphize. Note that, many generation II MOF structures can generate OMS by solvent exchange and subsequent desolvation without structural collapse as outlined in **chapter 2.3.2**.

Redox Flexibility

Starting with ruthenium, several oxidation states are synthetically accessible ranging from $Ru^{I,I}$, over $Ru^{II,II}$ and $Ru^{II,III}$ to $Ru^{III,III}$. Note, that upon metal reduction, progressive filling of antibonding orbitals π* and δ* results in lowered Ru-Ru bond orders and thus, in slightly elongated bond lengths. Only $Ru^{II,II}$ and $Ru^{II,III}$ have synthetic relevance while the other oxidation states appear rather exotic. Therefore, when referring to univalent and mixed-valent PWs in this thesis, the particular cases of $Ru^{II,II}$ and $Ru^{II,III}$ are concerned. The mixed-valence oxidation state $Ru^{II,III}$ is generally the most stable and easiest to access as can be seen in the following **chapter 2.1.3**. The synthesis of the univalent $Ru^{II,II}$-PWs is often closely associated with redox processes some involving reduction of related mixed-valent PWs. In summary, one-electron reductants like H^+/Zn, $CrCl_2$ or the Grignard-reagent Me_3SiCH_2MgCl can facilitate the conversion from mixed-valent to univalent Ru-PWs.[49, 54, 57-58] Univalent diruthenium complexes can also be obtained *via* disproportionation reaction using either mandelate or adamantylcarboxylates as discussed below.[48] The former occurs with aforementioned $Ru_2(OAc)_4Cl$, the latter requires $K_3(Ru_2(CO_3)_4)$ as precursor.[59] By employing highly charged "hard" sulphate or phosphate ligands, also the $Ru^{III,III}$ oxidation state can be stabilized.[59] Reaction of univalent diruthenium tetracarboxylates (such as acetate, propionate, benzoate or trifluoroacetate (TFA)) with NO results in diamagnetic adducts with relatively long Ru-Ru bonds which can best be described with a $Ru^{I,I}$ core and two axial NO^+ ligands.[36] In electrochemical measurements, reversible redox processes can be observed for the couples $Ru^{II,III}$-$Ru^{II,II}$, $Ru^{II,II}$-$Ru^{I,II}$, $Ru^{I,I}$-$Ru^{I,II}$, and $Ru^{II,III}$-$Ru^{III,III}$. However, with a $Ru^{I,I}$ species, any further reduction is found irreversible potentially due to collapse of the dimeric structure.

Interesting redox reactions were performed using the hydroquinone / quinone redox couple. Oxidation of the $Ru^{II,II}$-core was achieved using the electron-poor chloranil (a chlorinated quinone) which in turn was reduced to the respective tetrachlorohydroquinonate dianion bridging two Ru PW dimers with each other.[60] On the contrary, unsubstituted hydroquinone or anthraquinone can be used to reduce the $Ru^{II,III}$ core towards the univalent $Ru^{II,II}$.[61-62] It should be mentioned that such a reduction requires weakly coordinating axial anions at the mixed-valence compound.

Mixed-valence $Ru^{II,III}$ compounds have been used to catalyzed the oxidation of organic sulfides to the respective sulfoxides and sulfones mediated by *tert*-butylperoxide or hydroperoxide.[63-65]

Turning to rhodium, the redox flexibility is much more limited. The most stable and thus best investigated system is the $Rh^{II,II}$ core with a metal-metal bond order of 1. Oxidation under comparably harsh conditions (e.g. using Ce(IV), Br_2 or conc. HNO_3) results in compounds comprising mixed-valent $Rh^{II,III}$ or even $Rh^{III,III}$. Accordingly, these complexes comprise metal bond orders of 1.5 and 2. The ease of oxidation is governed by the nature of the carboxylate residue R and the axial solvent ligand L. Electron withdrawing groups (EWG) stabilize the reduced $Rh^{II,II}$ while electron donating groups promote the oxidation towards $Rh^{II,III}$ species. In contrast to Ru, one-electron reduction of the $Rh^{II,II}$ PWs is irreversible and results in the unstable $[Rh_2(OOCR)_4]^-$ anion which decomposes to mononuclear Rh^I and Rh^{II} species.[52]

Taking the overall redox flexibility of Ru and Rh PWs into account, the author of this thesis assumes that the PW structure remains intact during reduction as long as the metal bond order remains 1 or higher. Any further reduction results in a cleavage of the dimer producing monomeric species or even further to M^0. This is in line with the observations made in **Study III** (**chapter 4.3**)and IV (**chapter 4.4**) of this thesis.

2.1.3 Synthetic Access

This chapter should provide an overview on existing methods to yield carboxylate based PWs of Ru and Rh. General approaches and concepts shall be introduced briefly. However, more attention is paid to selected compounds that are most relevant in the context of this thesis. Although this thesis is to address academic and rather fundamental questions, it is embedded in the field of material science aiming for potential applications. Therefore, also practical aspects regarding the suitability of each PW complex as precursor for MOF synthesis are considered.

Inspired by their historic evolution of their use in MOF science and comparably facile synthesis, the synthetic access to mixed-valent $Ru^{II,III}$ complexes shall be discussed prior to their univalent $Ru^{II,II}$ and $Rh^{II,II}$ analogues. Strategies for the *de novo* formation of the PW motif out of simple metal halides are covered first. Other, more indirect, strategies employ already existent PWs as a platform to install more uncommon ligands. Obviously, the reactivity of the PW concerning ligand exchange reactions is important in these strategies and the additional reaction step suggests the use of easily accessible primary PW complexes. In this line of thought, the dimetal tetraacetate complexes are the most applied precursors.

$Ru^{II,III}$: Access to $Ru_2(OOCR)_4X$ via Metal (III) Chlorides

Most important in this class of substances is the diruthenium tetraacetate chloride $Ru_2(OAc)_4Cl$ with R = Me and X = Cl according to the general formula above. The synthesis is conducted using $RuCl_3 \cdot xH_2O$. Although the amount of contained water is not crystallographically defined and varies typically around three water molecules per metal atom. Reflux of this compound in a solution in acetic acid and acetic anhydride over several days results in the formation of the mixed-valent PW complex $Ru_2(OAc)_4Cl$.[33] While acetic acid is obviously both solvent and reagent, its anhydride removes water from the solution enhancing the formation and precipitation of the 1D coordination polymer with chlorides axially bridging two adjacent PWs as already outlined in **chapter 2.1.1**. The underlying reaction mechanism for the reduction from the Ru^{III} salt towards the mixed-valent $Ru^{II,III}$ is still unclear. However, a disproportionation reaction resulting in several unidentified soluble Ru^{IV} species is commonly assumed in literature.[33, 66] There is contradictory literature regarding the beneficial effect of the atmosphere which the reaction is performed in. While some references claim the reaction should be performed in oxygen,[33, 66] our group experienced positive effects on the reaction yields when flushing the reaction vessels with argon prior to the reaction.[67]

$Ru^{II,III}$: Access to $Ru_2(OOCR)_4X$ via Ligand Exchange

Variation of the carboxylate with different R groups can be achieved through ligand exchange reaction using the acetate chloride as a precursor. For instance, solid carboxylic acids might be introduced by reaction in toluene or chlorobenzene under reflux.[68-69] The released acetic acid can be withdrawn by distillation of *via* a K_2CO_3 filled Soxhlet-tube. This procedure was also applied in the synthesis of $Ru_2(chp)_4Cl$ with chp = 6-chloro hydroxypyridinate.[68] Alternatively, excessive carboxylic acid could be used, according to the synthesis of $Ru_2(OBz)_4Cl$.[70] Ru and Rh PWs with tethered dicarboxylates have been synthesized using α,α,α',α'- tetramethyl-1,3-benzenedipropionic acid (H_2esp).[69, 71] In a different concept, two adjacent alkene terminated carboxylates were linked with ring closing metathesis by *Tong Ren* and coworkers.[72]

Variation of the axial anion X can be achieved by exploiting the solubility properties of the axial chlorides. For instance, replacement by weakly coordinating anions such as NO_3^-, ClO_4^-, PF_6^-, SbF_6^-, BF_4^- is facilitated by their respective silver salts and precipitation of AgCl. Further ion exchange towards the respective bromides or iodides is facilitated using NaBr /NaI.[24, 70] Axial phenyl acetylides have been installed in N,N-bridged PW compounds accordingly.[73-74]

Diruthenium pentacarboxylates comprising linear chain alkyl carboxylates as R and X were synthesized *via* $[Ru_2(OAc)_4(H_2O)_2]BPh_4$ according to above mentioned strategy.[75] Alternatively, the pentacarboxylates can be obtained by reacting the respective chloride PWs with alkaline carboxylates in unpolar solvents. There, the driving force of the substitution is the irreversible precipitation of the resulting crystalline alkaline chloride.

$Ru^{II,II}$: Access via the Blue Solutions of Ru^{2+}

The synthesis of the oxidation sensitive $Ru^{II,II}$ PWs requires more elaborate techniques. In 1970, pioneering works were performed by Nobel prize laureate *Geoffrey Wilkinson* who reinvestigated the chemistry of the "blue solutions of Ru^{2+}" which were already described in 1804.[76-78] When exposing $RuCl_3 \cdot xH_2O$ in MeOH with catalytic amounts of PtO_2 under low hydrogen pressure, the initially black solution turns deep blue. The solution supposedly contains the cluster anion $[Ru_5Cl_{12}]^{2-}$. Although this intermediate was hypothesized already fifty years ago, a single crystal structure to support the assumptions is still lacking. In a second reaction step, this intermediate can be treated with alkaline carboxylates to yield the univalent PWs $Ru_2(OOCR)_4$. Many examples of this structure type have been synthesized comprising formate, acetate and plenty of different linear alkyl, aromatic or heterocyclic carboxylates. The workup to separate the NaCl side product typically depends on the solubility of the respective PW.

Overall, this synthetic route, though synthetically elaborate requiring the use of gaseous hydrogen, is versatile and provides access to many different diruthenium tetracarboxylates in good yields.

$Ru^{II,II}$: Access via Reduction of $Ru_2(OOCR)_4X$

According to the redox reactivity outlined in **chapter 2.1.2** , the univalent PWs can also be obtained *via* reduction of preformed mixed-valent PWs. One-electron reduction can be facilitated by H^+/Zn, $CrCl_2$ or by the *Grignard*-reagent Me_3SiCH_2MgCl.[49, 58] However, these routes suffer broad applicability and the product purification can be challenging. Therefore, the blue solution approach was used most frequently in this thesis.

In 2016, a one-pot reaction comprising equatorial ligand exchange and reduction from mixed- to univalent $Ru^{II,II}$ PWs was reported by Miyasaka and co-workers using *N,N*-dimethylaniline in a bifunctional way. It served as both solvent and reductant elegantly facilitating both reactions proceeding concomitantly.[54]

At this point, one report on the reactivity of diruthenium pentacarboxylates should be mentioned. *Rusjan et al.* used thermogravimetry and found the pentacarboxylates featuring two distinct decomposition events.[70, 79] In a first step, the axial carboxylate ligands are released while complete disintegration of the PW occurs in the second event resulting in metallic Ru.[2] Isolation of the intermediate species revealed the spectroscopic identity of the univalent tetracarboxylates. Although this study was focused on the analysis, it served an inspiration for a preparative use of thermal treatments to access univalent $Ru^{II,II}$ species as highlighted in **Study III** of this thesis.

$Ru^{II,II}$: Special Case Diruthenium Tetramandelate

A completely different strategy to access univalent $Ru^{II,II}$-PWs was found by *Frank A. Cotton* in 1989. [25, 48] During reflux of a preformed $Ru_2(OAc)_4Cl$ precursor with L-mandelic acid, two different processes occur: On the one hand, equatorial ligand metathesis provides the tetramandelate complex, with the S-configuration of the stereo center being preserved. At the same time, reduction of the mixed-valence $Ru^{II,III}$ core gives its univalent variant as confirmed by SC-XRD, magnetic and spectroscopic evidences. It was assumed that the underlying mechanism proceeds via disproportionation including a Ru^{III}-containing

[2] In contrast, the respective diruthenium tetracarboxylate chlorides showed only one large decomposition event without any intermediate product.

byproduct remaining as green solution.[48] O-, N- or S-containing α-substituted carboxylates might assist such disproportionation.[48, 80-82] In 2004, *Dikarev* and *Li* provided a structural proof for a similar reaction.[83] They obtained a single-crystal structure including both disproportionation products isolated from one mixture in a similar reaction of diruthenium tetrapropionate chloride with trifluoroacetic anhydride. From the mixed-valence $Ru_2^{II,III}$ starting material, both the oxidised mixed-valence trimer $Ru_3^{II,III,III}$ and the reduced dimer $Ru_2^{II,II}$ is formed. The latter can be isolated upon crystallisation in the aforementioned mandelate system.

Although this disproportionation route has intrinsic limitations regarding reaction yields, it is experimentally rather simple without the necessity to use gaseous hydrogen in any reaction step. For this reason, the $Ru_2(mand)_4$ complex was one candidate as precursor for the synthesis of univalent Ru-HKUST-1 samples as part of **Study V** (see page 115 ff.) presented in this thesis.

2.2 New Dimensions: From *Werner* Complexes to MOFs

It was in 1893, when *Alfred Werner* first published his coordination theory on (transition) metal complexes for which he was awarded with the Nobel prize in 1913.[84] His theory defined an isolated metal atom surrounded by a number of ligands which is usually higher than expected for the pure charge compensation. At that time, the differentiation between oxidation state and coordination number was ground-breaking and paved the way to modern metal-organic chemistry. Since that time, the definition has been expanded by multinuclear complexes with more than one central metal atom. Plenty of so-called secondary building units (SBUs) have entered the field of coordination chemistry ranging from dimeric SBUs like the PW geometry over trimeric SBUs like the "basic ruthenium acetate" to higher nuclearities for instance observed in ligated Zr_6 oxoclusters.

Over many centuries, scientists sought and still seek to find new design principles and to unveil the rationale for the directed assembly of atoms or ions into larger structures like molecules or *Werner*-type complexes. Emergence occurs when a new entity features properties its isolated constituents do not possess. Accordingly, chemistry has been driven by the curiosity to discover emergence in the molecular space for many centuries.

According to *S. Leininger*, organic synthesis routes typically comprising linear cascades of consecutive reaction steps face limitations when targeting very large structures.[85] With increasing molecular size, time-consuming isolation and purification of intermediates mean enormous synthetic efforts. Furthermore, multi-step procedures are unambiguously accompanied with progressive reaction yield deficits. Particularly for the assembly of macromolecular systems with high molecular masses comprising hundreds of atoms, other synthetic strategies ought to be selected. In this context, the self-assembly of preformed SBUs is one of the most effective and efficient strategies. Supramolecular discrete structures can be accessible within one or at least few reaction steps. In organic reactions, defects leading to side products and thus, yield deficits and are often hard to roll back. In the molecular self-assembly, all participating species are in thermodynamic equilibrium rendering the process reversible and thus structural defects become curable. Due to their kinetic lability, directorial coordinative bonds are predestined to facilitate efficient self-assembly. Freely adapted from *Leininger*, this leads to rather defect-free, self-curing assemblies of high structural integrity.[85]

Yet, the concept of self-assembly is far from being novel. In nature, this strategy is applied in all kinds of membranes and is also found in microtubules, mitochondria, chromosomes and in the capsid formation in viruses.[86-87] In general, *Whitesides* defined self-assembly as the spontaneous ordering of molecules under equilibrium conditions towards stable and structurally defined aggregates held together by non-covalent bonds.[88] Others have established their own definitions, however, the connection of individual SBUs by coordinative bonds, the selective formation of the most stable assembly and the presence of properties absent in their isolated subunits – again emergence – represents the common ground of all definitions.

Following this general introduction of self-assembly, the upstream voyage from single molecules over zero-dimensional assemblies to one- and two-dimensional coordination polymers and finally to the three-dimensional porous and structurally ordered MOFs should be briefly summarized. Selected literature examples of Ru and Rh PW-based CPs will serve for illustration at the end of the chapter. Moreover, the question why MOFs are particularly related to zero-dimensional nanoobjects should be addressed. Far from being comprehensive, this introductory chapter should merely represent an intellectual handrail to rationalize the transition from isolated molecular complexes towards structurally ordered and porous coordination networks called metal-organic frameworks. The interested reader may refer to respective review articles and book chapters provided as references.[27, 89-95]

In the 80s and 90s, mostly *Makoto Fujita* and *Peter Stang* coined the emerging field of **supramolecular assemblies** and amongst them the **zero-dimensional nanoobjects**. Their rational design principles allowed for the assembly of discrete molecular polygons (triangles, squares, rectangles, pentagons, or hexagons) and even molecular polyhedra (tetrahedra, cubes etc).

Key to these predictable structures is the directorial coordination bond of transition metals. For instance, Pd is known to form complexes with square planar geometry. If two adjacent (*cis* oriented) coordination sites are blocked by a strongly coordinating bidentate ligand, the remaining coordination sites predictably establish a ninety-degree angle. When mixed with a ditopic ligand with rigid linearly arranged functional groups such as 4,4'-bipyridine, self-assembly of the available building blocks results in the formation of a molecular square as shown in **Scheme 2** (top row). Similarly, octahedral metal sites can be modified by facial capping of three coordination sites to become the corners in a self-assembled molecular cube when reacting with the same linear linker (see **Scheme 2**, bottom row). Molecular polyhedra, or cages are porous compounds containing empty voids which can be filled with solvent molecules but can also be used for (selective) guest uptake. For instance, self-assembled Rh-PW-based cuboctahedra feature defined and accessible microporosity.[96]

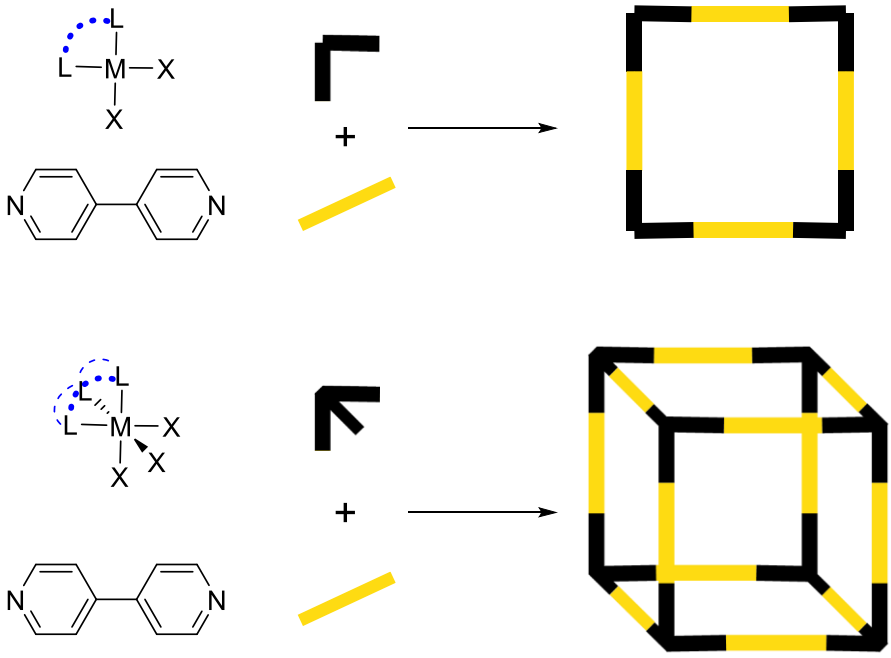

***Scheme 2**: Rational construction of zero-dimensional nanoobjects via self-assembly. Top row from left to right: A square planar metal center with two cis coordination sites being occupied by a capping ligand L and the other two sites comprising labile ligands X can represent a ninety-degrees angle (black). A ditopic ligand with linear geometry (here shown on the exemplary 4,4'-bipydridine) is represented by the yellow building block. Reaction of these two components leads to the formation of a molecular square as shown on the right. Bottom row: Similarly, an octahedral metal center with facial capping of three coordination sites represents a corner in the respective self-assembled molecular cube.*

Excitingly, it was not the geometrical beauty of such compounds that raised the scientific attention. It was the rational predictability of the product outcome by simple geometrical descriptors of the applied building units easily being transferable to almost any molecular example. The different products resulting from combination of a linker and a metal node with certain geometry are shown in **Figure 3**.

In these early days, *Fujita* and *Stang* mostly used Pd and Pt for their metal SBUs. Their ligand exchange properties represent a good compromise between dynamic ligand exchange for efficient self-assembly and at the same time sufficient stability of their coordination bonds to isolate and study the respective nanoobjects. Regarding the used bi- or trifunctional linkers, directed dative bonds are important for the predictable geometries. Therefore, pyridine derivatives are the most frequently utilized linkers of choice.

The design principle also applies for elongated SBUs or linkers which much later was termed “reticular chemistry” by *Omar Yaghi* in the field of MOFs.[95]

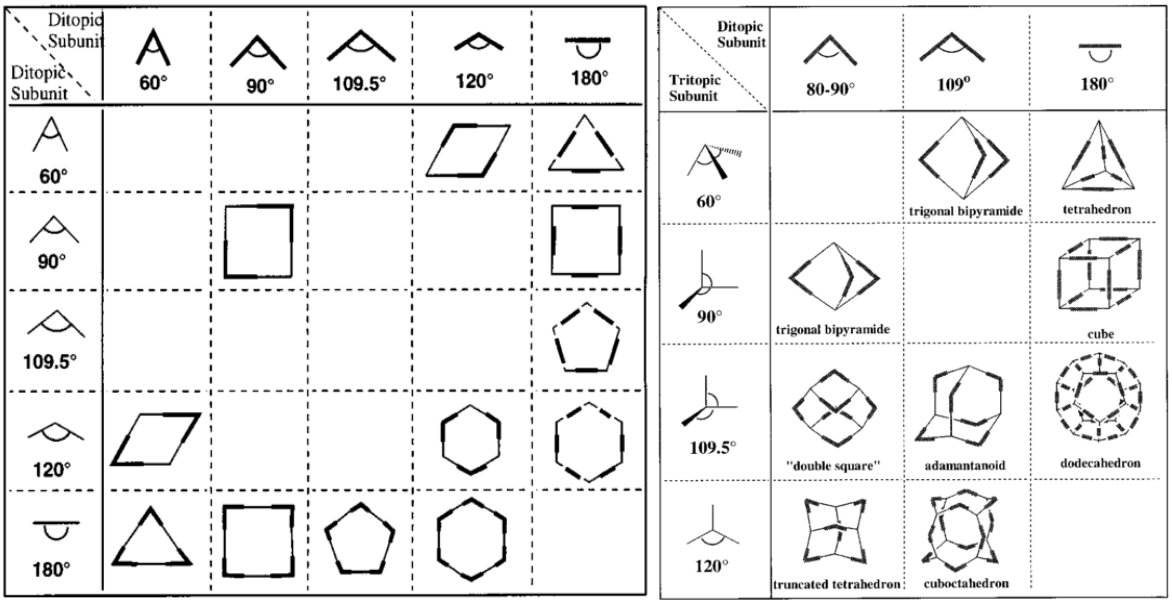

***Figure 3**: Predictable outcome of the self-assembly of certain ditopic (left) and ditopic with tritopic (right) subunits (SBUs) for the assembly of molecular polygons (left) and polyhedra (right). Reprinted with permission from Ref.[85] Copyright 2000 American Chemical Society.*

Extended structures like coordination polymers have been known much longer compared to the rather novel class of zero-dimensional nanoobjects described above. The first coordination polymer was presumably Prussian Blue, being deliberately synthesized and commercially distributed already in the early 18th century, while the term coordination polymer was first established in the 1960s.[90, 92, 97-98]

For **one-dimensional coordination polymers** (CPs), many of the design principles from the assembly of discrete structures also apply. Inorganic or metal-organic complexes and ligands are alternatingly arranged forming one-dimensional chains. More generally, both constituents, the metal center and the linker, are typically ditopic (the metal having two open metal sites (OMS), the ligand two Lewis basic groups) to facilitate the chain growth. Other coordination sites of the metal centers are occupied with terminating ligands. For PW systems, equatorial ligands are often terminating while the chain propagates one-dimensionally *via* the axial coordination sites. Generally, adjacent chains are held together by weak intermolecular forces such as *Van-der-Waals* forces or through hydrogen bonding. Often but not exclusively, 1-D coordination polymers are densely packed and do not feature any porosity.

2-D coordination polymers form 2-D sheets stacked by weak forces. Within these sheets, the building blocks often arrange in ordered patterns constructed from triangles, squares, rectangles, or hexagons. Weak interactions occur between these layers. Consequently and as for the purely inorganic graphene layers, exfoliation of 2-D coordination polymer sheets has been reported.[99] To obtain these 2-D CPs, for instance, square planar Pd or Pt centers could be interconnected using linear ditopic ligands such as aforementioned 4,4’-bipyridine to form 2-D sheets. Sticking with PW complexes, equatorial ligands also arrange in a square planar geometry. Thus, equatorial ligand exchange using any linear dicarboxylate also results in 2-D coordination polymers.

3-D coordination polymers or more suitingly termed coordination networks contain SBUs of higher connectivity leading to stable 3-D networks. For instance, tetrahedral and linear SBUs can produce diamantoid extended structures while octahedral and linear or both octahedral SBUs might result in cubic ones.

One important aspect of coordination polymers irrespective of their dimensionality is that they **do not necessarily feature structural order** and thus crystallinity. This can have several reasons: either a high density of defective connections, structural disorder due to different binding possibilities, flexibility within the linker or varying coordination angles regarding the linker orientation. However, many examples do comprise structural order and distinct reflections in X-ray diffraction. To conclude, crystalline CPs are a subgroup of the overarching group of CPs.

Another property that might be present or not is porosity. Either already originated from their underlying SBUs (for instance in aerogels with interconnected molecular polyhedra),[100] or because of a 3-D connectivity, some coordination polymers are micro-, meso- or even macro-porous materials rendering them interesting for catalysis, sorption or separation applications.[89] However, amorphous porous structures often result from solvent inclusion which collapse upon its removal. As with crystallinity, **porosity is** a property **not necessarily present** in all coordination polymers. Therefore, porous coordination polymers are another subclass within the superordinate group.

At this point, some selected literature examples should provide an overview on CPs based on Ru- and Rh PWs as SBUs. According to their structure and reactivity as introduced in **chapter 2.1.1** and **2.1.2**, examples are distinguished into either axially interconnected PWs and equatorial connection of the PWs into one-, two-, or three-dimensional CPs. Within each category, examples are sorted by increasing dimensionality of the respective CP.

Starting with **axial linkage,** the linear arrangement of both axial OMS is predestined for linear chain growth. While the ligand exchange towards 1-D CPs proceeds via the axial positions, the four bridging carboxylates are simply blocking the equatorial sites but can have an impact on chain stacking and the related weak intermolecular forces. Examples of such 1D-CPs were already introduced before: The class of $[Ru_2(OOCR)_4Cl]_n$ compounds forming 1-D chains either linearly or in zig-zag geometry. Note, that the extended structure is presented with n repeating units here, while this aspect was intentionally not highlighted in the former chapters for reasons of simplicity. Another 1-D CP based on univalent Ru and Rh PWs was reported by *Miyasaka et al.* who used a ditopic phenazine linker to axially interconnect PWs towards linear chains.[101-102] When using triazine linkers bridging the axial sites of $[Ru_2(OBz)_4]$-PWs, honeycomb (6,3) nets were obtained by *Furukawa* and coworkers.[103]

Another example is using the bifunctional ligand 1-hydroxyethylidenediphosphonic acid (H_4hedp) as phosphonate-based PW. Hydrothermal treatment under basic conditions results in the self-assembly towards $[Ru_2(hedp)_2]^{3-}$ PWs which comprise tethered ligands interconnecting two adjacent equatorial phosphonate groups at the same PW. At the same time, deprotonated hydroxy groups coordinate the axial positions of other adjacent PWs leading to the formation of 2-D layered structures interconnected by NaO_6 octahedra.[69, 71, 104-105] The same $[Ru_2(hedp)_2]^{3-}$ SBUs were also used to prepare CPs with a series of lanthanide Ln^{3+} ions. Depending on the reaction conditions, lanthanides were coordinated by the untapped oxygen atom of the phosphonate groups either in a square planar, or in a rather tetrahedral geometry. Respectively, 2-D layered structures or PtS-type 3-D porous coordination networks were formed.[106]

Miyasaka et al. reported upon an interesting series of purely inorganically connected coordination polymers / frameworks with $Ru^{II,III}$ PWs as linear SBUs. In particular, the reaction of $Ru_2(OPiv)_4(BF_4)$ with three types of polyoxometalates (POMs) $(TBA)_2[Mo_6O_{19}]$, $(TBA)_3[H_3V_{10}O_{28}]$, and $(THA)_3[PMo_{12}O_{40}]$ with TBA/THA = tetra n-butyl /n-hexyl ammonium counter ions led to the formation of 1-D, 2-D and 3-D polymeric materials in which the $Ru^{II,III}$ cationic SBUs are linearly connected *via* their axial positions with the oxo groups of the anionic POMs. Coulomb forces aided the controlled assembly of these building units.

The dimensionality of the produced CPs was governed by the match between the steric hindrance of the pivalate side groups and the size of each POM cluster.[107]

Moving to **equatorial linkage,** ligand exchange of the bridging carboxylates was used to install oligo functional carboxylates interconnecting PWs towards extended structures. Layers with square planar patterning were obtained using terephthalate (or also called benzene dicarboxylate (BDC)) or metalated TCPP [H_2TCPP = 4,4',4'',4'''-(porphine-5,10,15,20-tetrayl)tetrakis(benzoic acid)] linkers with the PWs being equatorially bound within the layers.[108-110]

Dirhodium tetraacetate was used for the construction of porous 3-D CPs using either trimesic acid (or also called 1,3,5-benzene tricarboxylate (BTC)) or extended variants thereof such as benzene 1,3,5-tribenzoate (BTB) or 4,4',4''-[1,3,5-benzenetriyltris(carbonylimino)]tristribenzoic acid (H3BTCTB).[111-112]

Not only for the respective [$Rh_3(BTC)_2$], [$Rh_3(BTB)_2$] or [$Rh_3(BTCTB)_2$] CPs, but for many other systems, permanent porosity was only accessible via special treatments with supercritical CO_2 extraction.

With this concise overview on extended PW-based structures with increasing dimensionality the theoretical background is provided for the next chapter: Metal-organic frameworks (MOFs) as one subclass of coordination polymers.

2.3 Metal-Organic Frameworks

The field of metal-organic frameworks has undergone a tremendous growth during the last two centuries and is still ongoingly fuelled. The first years of this new research discipline were dominated by the quest to explore their rational design principles, the concept of reticular chemistry and to explore new structures.[95, 113-114] Thousands of different MOF structures have been investigated since these early days. Researchers were driven by questions like: How to achieve the directed and predictable assembly of the building units into ordered porous structures? Which synthetic methods are suitable? What are the limits of porosity when using extended linkers? Dependent on their stability during solvent exchange and desolvation, MOF structures are classified into three generations. While the very early structures collapsed upon solvent exchange or removal, more rigid frameworks were discovered and investigated by the time. Their potential applicability in many fields such as catalysis, gas storage and separation, sensing and others craved the interest of science starting from day one. The exploration of flexibility in MOFs raised the 3rd generation of MOFs and inspired new developments towards stimuli-responsive materials either triggered by mechanical pressure, gas uptake, electric or magnetic fields.[3, 115-116] Such materials might be used as switchable gates which exclusively open in the presence of one specific analyte allowing selective mass transport or sorption. Optical properties and electric or ionic conductivity in MOFs render these materials interesting candidates for many applications in optics, optoelectronics, electronic devices, energy materials and related fields.[3, 117] Chiral MOFs might be obtained using chiral building blocks, but chiral pore space might also emerge from non-chiral building units. Incorporation of guest molecules offers potential in many regards. For instance, metal (oxide) nanoparticles, polyoxometalates, or enzymes and other bioactive drugs were incorporated in MOFs to investigate their enhanced stability with preserved functionality in catalysis or drug delivery and targeted release.[118-123]

It goes without saying that these diverse multidisciplinary purposes could never be possible without the unique design freedom that comes along with the enormous parameter space and the libraries of potential organic and inorganic building block that are available. In this regard, great efforts were taken to expand the scope of investigated organic ligands while metal-wise rather strong limitations exist. For many years, metals of the 3d row together with Zr, Hf and Al have dominated and still dominate the landscape of MOFs. According to the introduced concept of a vital self-assembly as prerequisite for MOF formation, the elements of the 3d row are most qualified. However, in recent years, also MOF structures relying on other metals such as alkaline, earth alkaline and earth metals, lanthanides and actinides were found.[6, 124-136] However, the availability of MOFs utilizing precious group metals is surprisingly limited despite their frequent use as catalytically active materials in chemical industry. To that end, the motivation of this thesis is to deepen the fundamental understanding of related PGM-based MOFs on the case system HKUST-1. Not only providing a general overview on MOFs, the focus of the following chapter is to clarify key aspects of MOF related to their PGM-based analogues: Which strategies are available for the synthesis of MOFs? What is the role of defects? Why is the synthesis of a “defect-free” PGM-MOF particularly challenging? How to manipulate and exploit the defect chemistry of PGM-MOFs? What is “defect-engineering” and how to achieve it? Further, the characteristics of the specific MOF system of matter, HKUST-1, are introduced and the state of the art regarding Ru-HKUST-1 is highlighted.

In short, the definition and specific terminology (**chapter 2.3.1**), general aspects (**chapter 2.3.2**) and some more unique features of MOFs such as the role of defects (**chapter 2.3.3**) as well as one of the most intensively studied structure type (HKUST-1, **chapter 2.3.5**) shall be discussed in this chapter ultimately guiding the way to the literature knowledge on the ruthenium analogue of the HKUST-1 (Hong Kong University of Science and Technology) archetype (**chapter 2.3.6**) at the core of this thesis.

2.3.1 Definition & Terminology

There are several definitions and some specific terminology in the field of MOFs to be introduced first.

Metal-organic frameworks are porous and crystalline coordination polymers, or better coordination networks. The term **metal-organic framework** (MOF) introduced by *Omar Yaghi* in the year 2000 became prevalent in the early 2000s over other terms such as porous extended frameworks, modular porous networks, hybrid open networks, functional porous coordination polymers, or crystalline porous coordination polymers.[94] Until 2020, the time this thesis was written, MOF research has grown tremendously. Nowadays, research on MOFs is one of the "hot topics" in the interdisciplinary interface of organic, inorganic, and metal-organic chemistry, material science and solid-state physics also attracting researchers in the fields of biochemistry, theoretical and analytical chemistry.

MOFs as hybrid organic inorganic materials are constructed by the assembly of inorganic metal complexes or defined clusters termed **metal nodes**. Besides isolated single-atom metal nodes, prominent examples are dimeric PWs M_2^{n+}, trimeric M_3O^{n+}, tetrameric M_4O^{n+} and hexameric $M_6O_4(OH)_4^{n+}$ clusters. Similar to previous chapters, these metal centers of different complexity are called **secondary building units** (**SBUs**). These SBUs are interconnected by di-, tri- or tetra-functional organic ligands. According to their linking purpose, these organic components are termed **linkers**. Following a procedure of self-assembly, both metal nodes and linkers are periodically arranged into these crystalline porous frameworks.

In contrast to the standardized nomenclature established for organic molecules and inorganic complexes, the **naming of MOFs is** quite **inconsistent** and not following clear rules provided by the IUPAC (international union of pure and applied chemistry). Typically, new MOF structures are named after their inventing institutions including a more or less systematic serial number for the specific structure. Some most prominent examples are the UiO-66 (Universitaet i Oslo), MIL-100 / MIL-101 (Matériaux de l'Institut Lavoisier), HKUST-1 (Hong Kong University of Science and Technology), NU-1000 (Northwestern University), NOTT-100 (Nottingham University), DUT-8 (Dresden University of Technology), MFU-1 (Metal-Organic Framework Ulm University) or TUM-1 (Technical University of Munich). The evolution of the attached serial number was again up to the inventors. For instance, MIL-100 is based on M_3O trimers interconnected with ditopic terephthalate linkers whereas MIL-101 is constructed from a tritopic trimesate linker. In the UiO case, the serial number refers to isostructural extension of the ditopic linker: UiO-66 comprises terephthalate while UiO-67 contains biphenyl dicarboxylate. Overall, some structural similarity can be deduced within a series of MOFs but there is no generally applicable systematic nomenclature.

Other MOF materials are termed according to their chemical nature, such as ZIF-8 (Zeolitic Imidazolate Framework), MOF-5 or MOF-808 (Metal-Organic Framework), IRMOF-1 (IsoReticular Metal-Organic Framework), TDC-MOF-8 (Trypticene Dicarboxylate MOF), or PCN-222 (Porous Coordination Network).

Also, for each MOF structure, different names might be established. Due to its relevance in this thesis, the HKUST-1 system should serve as an example. Besides its common name HKUST-1, it was called Cu-TMA, (TMA = trimesic acid), Cu-BTC, copper trimesate, or scientifically more precise due to the correct sum formulae: $Cu_3(TMA)_2$, $Cu_3(BTC)_2$ or by using the full sum formula $Cu_3(C_9H_3O_6)_2$. Although MOFs are extended frameworks with almost infinite periodicity, the correct indication $[Cu_3(BTC)_2]_n$ commonly applied for polymeric materials is only used in rare cases. In the course of this work and with respect to the presence of several isostructural analogues of the parent MOF, the terms, M-HKUST-1 or M-BTC will be used predominantly with M referring to the particular metal Cu, Ru, or Rh.

Similar to the BTC nomenclature instead of trimesate, terephthalate as organic linker is more frequently called BDC (benzene dicarboxylate) in the field of MOFs.

2.3.2 General Aspects

Before discussing specific MOF structures, some general aspects of MOFs shall be introduced. The concept of reticular chemistry already briefly mentioned in the context of self-assembled nanoobjects (**chapter 2.2**) will be discussed in more detail. Further, different MOF generations related to their mechanical stability are highlighted. Typical synthetic procedures to access MOF materials are introduced. Some MOF specific concepts such as the coordination modulation or the controlled SBU approach are related to the evolution of structural order will be followed by a brief introduction of mixed-metal MOFs. Ultimately, this subchapter concludes with recent developments and future opportunities in the field.

Reticular Chemistry

Although the concept of reticular chemistry was (without that name) already applied in the 80s and 90s for the controlled assembly of discrete nanoobjects, the term "reticular chemistry" was coined in the early 2000s by *Yaghi* and coworkers who demonstrated the great design freedom of MOFs on the case of the cubic MOF-5 / IRMOF series.[93-94, 137] Tetrahedral Zn_4O clusters are octahedrally coordinated by BDC linkers to form a stable and porous cubic MOF structure in MOF-5. Following the design principle of reticular chemistry, isoreticular (maintaining the same topology) variants thereof can be obtained by using variants of the BDC linker such as bromo-, amino-, alkoxy-, or fused aromatic systems (see **Figure 4**). The series of IRMOFs also comprise extended linkers with similar geometry including 2,6-naphthalene dicarboxylate (giving IRMOF-8), biphenyl dicarboxylate (leading to IRMOF-9), (hydro)-perylene dicarboxylate (IRMOF-11 &-14) and terphenyl dicarboxylate (IRMOF-16) as can be seen in **Figure 5**.[137]

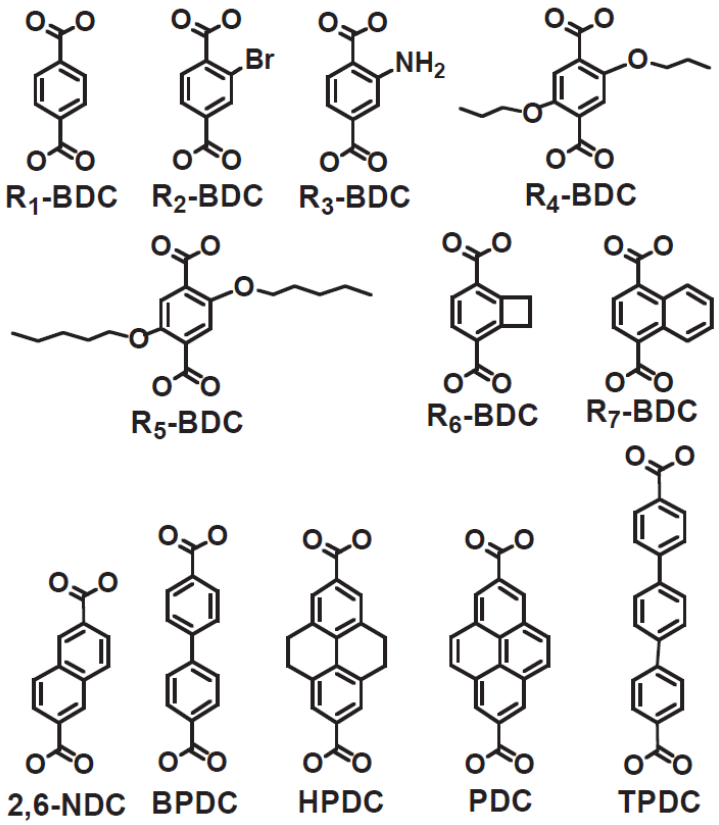

***Figure 4**: Used dicarboxylate linkers for the isoreticular MOF-5 / IRMOF series. Reprinted with permission from Ref.[137] Copyright 2002, The American Association for the Advancement of Science.*

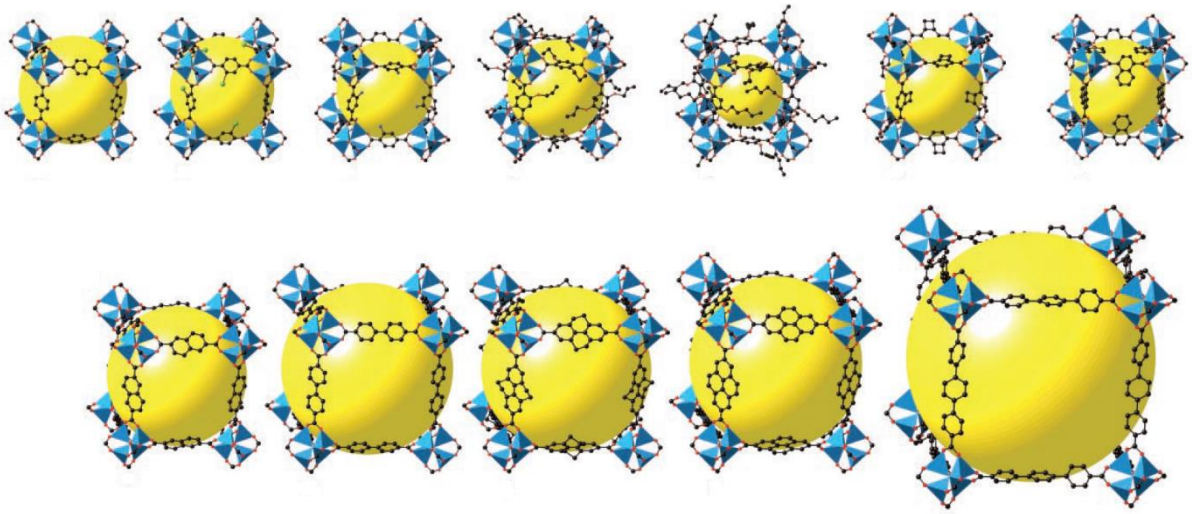

***Figure 5**: Obtained isoreticular networks: Top row: MOF-5 derivatives using pristine BDC (left structure) and substituted derivatives thereof. Bottom row: IRMOF series highlighting the concept of isoreticular expansion by linker extension. From left to right: 2,6-naphthalene dicarboxylate, biphenyl dicarboxylate, tetrahydro perylene dicarboxylate, perylene dicarboxylate, and terphenyl dicarboxylate. Reprinted with permission from Ref.[137] Copyright 2002, The American Association for the Advancement of Science.*

Isoreticular linker expansion leads to increasing pore sizes (indicated with yellow spheres) and thus higher void spaces and increased sorption capacities. Due to thermodynamics, the free surface energy correlates with the void space which renders the synthesis of MOF with larger voids more challenging. As a result, isoreticular variants with elongated linkers tend to form interpenetrated networks during synthesis. Interpenetration, however, can limit or even fully block the free and accessible porosity. Interpenetration might be avoided using more diluted reaction conditions. The concept of reticular chemistry has been expanded to many MOF systems. For instance, linker expansion was achieved from UiO-66 (BDC linker) to UiO-67 (biphenyl dicarboxylate), from NOTT-100 (biphenyl-3,3',5,5'-tetracarboxylate) over NOTT-101 and -103 to NOTT-102 (quaterphenyl-3,3''',5,5'''-tetracarboxylate) and from $Cu_3(BTC)_2$ (HKUST-1) to $Cu_3(BTB)_2$ with extended 1,3,5-benzene tribenzoate linkers.

Structural Order and Crystalline Domains

According to the general definition, MOFs are crystalline porous coordination polymers. In this regard, crystallinity or better structural order is one crucial aspect of these materials. For sure, obtaining crystalline frameworks in the laboratory might often be challenging and could peak in months or years of synthesis optimisation and parameter screening. However, structural order and the related applicability of powder- and single-crystal X-ray diffraction techniques[3] allow for unambiguous structure determination. This knowledge is of paramount importance for deriving structure-property-relations and respective conclusions on potential applications. In this line of thought, it might be the structural comprehension of MOFs that has enabled the field of MOFs to outgrow any other subclass of CPs.

New MOFs comprising novel organic ligands are preferentially realised using metals that allow their straightforward assembly such as Zn, Cu, Cd or Ni. As outlined later, often simple nitrate salts can be directly used for the MOF synthesis and the respective SBUs are readily formed under reaction conditions. These metals typically result in easy to obtain crystalline structures allowing their X-ray structure refinement. Other metals like Cr, Fe, Ti, Zr or Al are quite oxophilic forming strong and relatively stable bonds with the typical carboxylate linkers and are more difficult to use. Such oxophilic metals tend to

[3] Electron diffraction techniques could provide similar insights. However, this technique is often associated with elaborated synchrotron experiments.

immediately and irreversibly react with carboxylates under precipitation of amorphous CPs without self-assembly to occur. However, concepts to obtain crystalline frameworks utilizing these metals were established. High-temperature syntheses, coordination modulation or the concept of the controlled SBU approach can facilitate structural order.

Particularly challenging are the later transition metals of the 4d and 5d row, the precious group metals (PGMs). For them, the situation is different from the above. Rather than being very oxophilic, their slow ligand exchange reactivity renders them kinetically "inert". Therefore, the same approaches detailed below could be used. Nevertheless, the chemistry of PGM-MOFs remains complex and crystal growth is still limited to primary particles in the nano meter regime. Due to this reason, related materials hardly produce sharp and intense reflections in XRD techniques. A detailed introduction on the conundrum of particle sizes, scattering domains and the defect chemistry of PGM-MOFs can be found in **chapters 2.3.3** and **2.3.6**. It was also at the heart of **Study V** of this thesis.

Stability (Type I-III) and Activation

MOF materials can be classified into three generations according to their **stability during solvent exchange / removal**.[113-114] A schematic overview is provided in **Figure 6**.

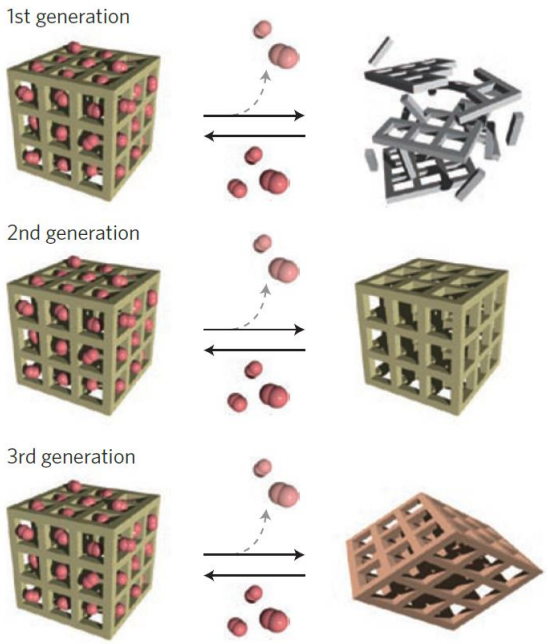

***Figure 6**: The three generations of MOFs and their behaviour during solvent exchange or removal: Top: 1st generation MOFs collapse and amorphize. Middle: 2nd generation MOFs are rigid stable frameworks with preserved structural integrity. Bottom: 3rd generation MOFs feature structural changes. Reprinted with permission from Ref.[114] Copyright 2009, Nature Publishing Group.*

The **1st generation**, Type I MOFs, collapse irreversibly whenever the stabilizing solvent is removed. This collapse is not only associated with loss of porosity but also with amorphization. In these materials, the structural order and the potential voids are dependent on the presence of the solvent used in synthesis. Many 2-D MOFs with sheet like structure and pillared-layer MOFs fall within Type I MOFs.

The **2nd generation**, Type II MOFs, are structurally stable even during solvent exchange or removal. Their porosity is typically accessible via gas sorption experiments and is determined by the rigid structure. 3-D connectivity into rigid structures prevents from amorphization. Reasonably, Type II MOFs are most interesting for applications that make use of their accessible porosity and stable ordered structures. Typical examples are gas sorption and storage but foremost catalysis. Crystalline order allows for targeted

structure-property relations, the rational design of catalysts and efficient catalyst-substrate interactions and mass transport.[120, 138-141] Due to their typically high 3-D connectivity supported by stable coordination bonds, Type II MOFs offer a certain mechanical stability. However, compared to other (even porous) inorganic or hybrid materials, MOFs are considered soft crystalline materials and mechanical pressure ultimately results in structural collapse.[114] This is one of the concerns regarding their large industrial use in heterogeneous catalysis where powders are typically pressed into pellets prior to transport and the final use. The HKUST-1 analogues studied in this thesis are all Type II MOFs.

A different behaviour can be observed for the **3rd generation**, Type III MOFs. This category of materials shows reversible flexibility upon external stimuli such as mechanical pressure, gas pressure or the presence of certain analytes. Two types of transformation are possible: The crystal-to-crystal transition is present in most Type III MOFs. One crystalline phase is directly transformed into a second also crystalline phase. In other cases, the crystalline phase converts into a second phase which has, according to *Kitagawa et al.* "imperfect crystallinity".[114] Either the second phase is amorphous, or its long-range order is weakened. However, any irreversible collapse of the framework does not occur as it would be observed in Type I MOFs. There are several modes of flexibility in MOFs such as breathing, swelling, linker rotation and subnetwork displacement. Amongst others, pillared-layer MOFs are known to exhibit said property and can switch between their open pore and their closed pore form as highlighted in **Figure 6**. The interested reader might refer to several high-quality review articles on this topic.[114, 116, 142]

Another important aspect in the context of this thesis is the **thermal stability of MOFs**. Generally, their properties are mostly affected by their underlying constituents and the stability of the coordination bond.[29, 143] Several processes can occur depending on the temperature regime. Typically, in the range between ambient temperature and 150°C, **desolvation** occurs. Within this range, first, free solvent molecules occupying the pore space are released. More reluctantly, solvent molecules coordinating OMS of the metal nodes are removed. This is in line with the axial ligand removal reactivity of PWs outlined in **chapter 2.1.2** (page 9f) before. The process of OMS creation by thermal desolvation is also termed **MOF activation** which originated from heterogeneous catalysis. When reaching higher temperatures (typically between 200 and 450 °C) progressive framework **disintegration and collapse** as result of bond cleavage and subsequent defect-introduction by removal of volatile organic fragments occur. Depending on the type of atmosphere, oxidation of all organic components in air leads to the formation of metal (oxide) nanoparticles and their subsequent sintering or agglomeration. Quantitative decomposition of MOFs in oxidising atmosphere can be utilized in thermogravimetric analysis to quantify not only thermal stabilities but also to access compositional information on the organic and metallic contents of the sample.[144-145] In inert atmosphere, decomposition occurs more retarded and the often-applied aromatic linkers of the framework pyrolyze under formation of several decomposition gases such as CO_2, CO, H_2O and diverse hydrocarbons but also non-volatile carbonaceous phases occur. If heteroaromatic linkers are present, respective nitrogen, sulphur or phosphorous oxides might emerge. So-called "**MOF derivatives**" resulting from thermally treating and thus, sacrificing MOFs have gained increasing attention in recent years. The homogeneous distribution (up to the atomic scale) of metal (oxide) particles within a potentially electrically conductive porous carbon matrix potentially doped with N, S or P atoms is an appealing motif for several electrocatalytic or photocatalytic applications.[146-155]

To utilize the porous nature of MOFs for applications in catalysis, sorption and related fields, the concepts of **solvent exchange and MOF activation** have been established. A summary of the cascade from as-synthesized materials to activated MOFs is displayed in **Figure 7**. As outlined in the next subchapter, MOF synthesis is often performed under hydro- or solvothermal conditions in high-boiling solvents. Since thermal removal of such high-boiling solvents would require relatively harsh conditions and is hard to achieve quantitatively, the apparent solvent from synthesis is exchanged by low-boiling solvents. To guarantee solubility during any step of the process, several cycles of solvent exchange are performed. In

detail, unreacted reagents from synthesis are removed by repeated washing with fresh solvent which was applied in synthesis. Then, solvent exchange with progressively lower polarity and lower boiling point is conducted and finally materials are thermally activated under reduced pressure. For instance, the PGM-HKUST-1 analogues prepared in the course of this thesis are synthesized in water / acetic acid mixtures. Solvent exchange was conducted in the following order each twice per solvent: water → ethanol → acetone → dichloromethane → drying at ambient pressure at 40 °C → activation at 150 °C in dynamic vacuum overnight. With such treatment, residual reagents and the solvents are effectively removed from the pore space and OMS are reproducibly generated. Very recently, *Omar Farha* and co-workers reviewed the historic evolution of activation and porosity of MOFs summarizing the available techniques.[156]

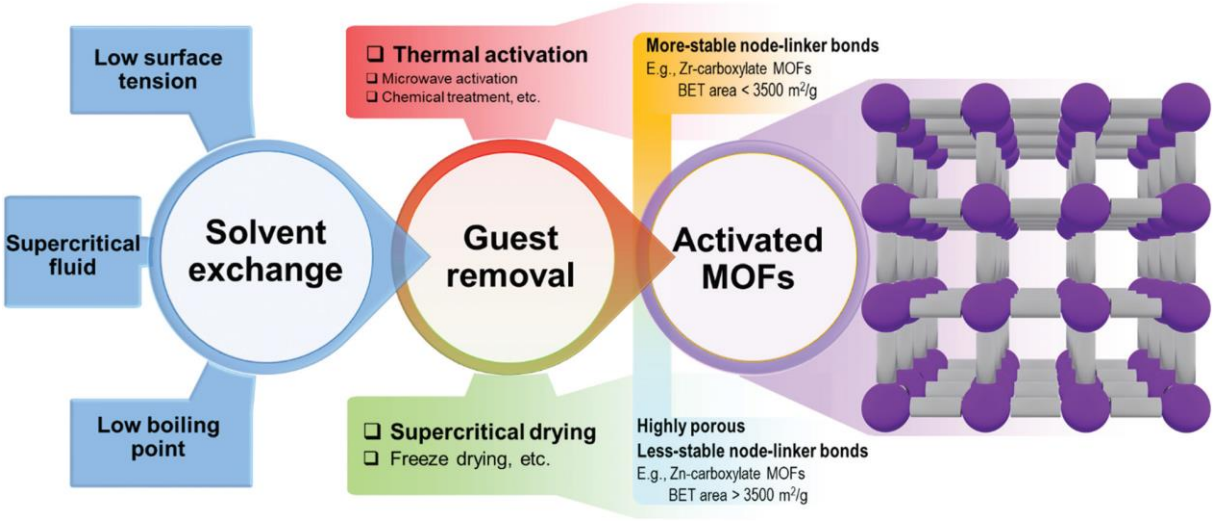

***Figure 7**: Possibilities for the process cascade from as synthesized to activated MOFs including solvent exchange and subsequent guest removal. For Type II MOFs as stable frameworks, the latter is most preferably achieved via thermal activation in dynamic vacuum. Less stable frameworks with extreme porosities up to 9000 m² per gram are more carefully treated using supercritical CO_2 extraction. Figure reprinted with permission of the Royal Society of Chemistry from Ref.[156] Copyright 2020, permission conveyed through Copyright Clearance Center, Inc.*

One important aspect of the activation of PW-based MOFs or more general CPs should be mentioned at this point. In contrast to dense crystals, the structural order of porous networks self-supported by equatorially bound linkers does not necessarily depend on the presence of axial ligands. Thus, many Type II PW-based MOFs can be activated generating OMS with preserved structural order and porosity. These OMS contain a high potential for applications such as catalysis (see **chapter 2.3.4** page 45 ff), sensing, gas storage and separation. Thus, a combination of solvent exchange and subsequent desolvation is often performed in the workup of MOFs to reveal the OMS.

Synthesis of MOFs

Crystallinity arises from structural order. Therefore, the controlled and reversible self-assembly of all building units is of crucial importance for crystalline materials. X-ray crystallography allows for unambiguous structure elucidation. Fundamental knowledge regarding the space group, the coordination environment of the metal centers, the binding modes of the organic ligands and the porous structure is key to rationalize the materials properties and thus, to find possible applications.

For all these reasons, many known MOF structures and their synthetic access result from elaborate synthesis optimizations as already outlined in the previous subchapter on structural order.

Summarizing the available literature within the field, MOFs are most commonly obtained via **hydrothermal** or more general **solvothermal synthesis**. In this method, the reaction mixture is heated in

a closed pressure-resistant vessel to temperatures higher than the respective boiling point of the mixture over prolonged times. Often the synthesis requires few days for completion. Of course, ecologically most favourable routes make use of water exclusively. However, low solubility of many organic linkers in water obstructs its exclusive use for many MOF systems. Instead, and despite its toxicity / ecological concerns, *N,N*-dimethyl formamide (**DMF**) has become the most frequently used solvent regarding the laboratory scale. Its unique physicochemical properties outperform many other less harmful solvent choices. The highly polar, high boiling organic solvent provides good solubility for both nonpolar organics as well as highly polar metal salts or precursors. Furthermore, *in-situ* thermolysis of DMF slowly produces dimethylamine. Its basicity deprotonates the used carboxylic acid groups of the linker in a controlled manner. This strongly assists the growth of MOF particles by *in-situ* limiting the available carboxylate concentration. Using the same working principle, *N,N*-diethyl formamide (**DEF**) or *N,N*-dimethyl acetamide (**DMAc**) find regular application in some MOFs. However, due to their even higher price with similar ecological concerns and identical reaction mechanisms, DEF and DMAc usually come into play, when DMF synthesis did not provide satisfying results and the targeted structures might depend either on better solubility of larger aromatic linkers or demand the slightly larger steric demand of the ethyl or acetyl groups for stabilizing the porous MOF structure. Note, that the widely applied DMF-based route is not applicable for PGM-MOFs since oxidation or reduction of the formate moiety does not allow for redox innocent synthetic conditions. Hence, the use of DMF would result in the formation of metal particles irreversibly withdrawn from the reaction equilibrium as highlighted in the introductory section of **Study II** of this thesis (see page 73ff).

Some MOFs are very easily formed, such as ZIF-8 or Cu-HKUST-1 comprising either Ni or Cu metal nodes. These MOF structures are already formed at ambient or even below ambient temperatures.[157-159] As outlined in the previous subchapter on structural order, the situation is not that easy for PGM-MOFs. Their synthesis requires temperatures of 150 to 160 °C in aqueous acetic acid for over three days. Furthermore, several additional measures were taken to assist the evolution of crystallinity as outlined below. A more detailed discussion on the dilemma of the ambivalent role of aqueous acetic acid mixture used for PGM-HKUST-1 analogues studied herein will be provided in **chapter 2.3.6** (page 55ff).

Besides the classical solvothermal routes, several **other approaches to yield MOFs** have been established. Worth mentioning are mechanochemical, electrochemical, microwave (MW)-assisted and chemical vapor deposition (CVD) approaches. **Mechanochemical synthesis** is achieved by ball milling of solid reagents (solid carboxylic acids and metal salts) which can result in crystalline porous MOFs even without any drop of solvent, although this measure could facilitate a more efficient conversion.[160] The evolution of highly porous and fragile structures by relatively rude mechanical forces is surprising since MOFs can usually collapse under mechanical pressure. **Electrochemical synthesis** of MOFs was first reported for HKUST-1 using Cu as anodic material in a H_3BTC containing solution but later many other MOFs comprising Zn, Cu, Ni, Al and other metals were obtained accordingly.[161-162] The utilization of **MW-assisted heating** is well-known from organic chemistry allowing ultra-fast reactions at temperatures lower than conventionally heated protocols. Reaction rates can be accelerated by several orders of magnitude using MW-assisted heating. Reasonably, some MOF systems that are otherwise hard to obtain have been synthesized with MW-assisted protocols such as the Cr-MIL-101.[163-164] Due to the cumulative nature of this thesis, it should be mentioned here, that we attempted the synthesis of PGM- or more specifically Ru-HKUST-1 using MW-based techniques. However, as some first trials resulted in amorphous powders only, we did not investigate this route further. Certainly, some more efforts should be made in future to develop MW-assisted protocols for the PGM-MOF synthesis since scale-up of the time-consuming conventional routes is challenging. The utilization of **CVD for MOF synthesis** is one interesting concept especially with respect to the demanding manufacturing of thin films for microelectronic applications.[117, 165-166] In this regard, the group of *Rob Ameloot* provided excellent pioneering works on the CVD synthesis of MOFs by linker

diffusion into metal layers allowing the solvent-free growth of MOFs with the general concept proved to be applicable for surfaces such as Cu, CuO, ZnO and CoO_x.[167-168]

Coordination Modulation

Coordination modulation is one concept to obtain crystalline materials from components that usually do not feature vital ligand exchange obstructing efficient self-assembly. Usually, synthesis of such compounds results in amorphous precipitates since coordination bonds do not form with the perfection required for long-range order. This mostly accounts for kinetically inert or particularly oxophilic metals such as Zr, Hf, Al but also for the PGMs Ru, Rh and others as briefly mentioned earlier. In 2007, *Roland A. Fischer* and co-workers were the first to describe the modulated synthesis of MOFs exemplified by particle size control in the growth of MOF-5 crystals.[169] The term "coordination modulation" was later introduced by *Susumu Kitagawa* who studied the influence of carboxylate-based modulators on the anisotropic growth behaviour of the pillared-layer-type MOF $[Cu_2(NDC)_2(DABCO)]_n$ (NDC = naphthalene dicarboxylate, DABCO = 1,4-diazabicyclo[2.2.2]octane).[170] The impact of modulator choice on the shape of the resulting crystals is illustrated in Figure 8.

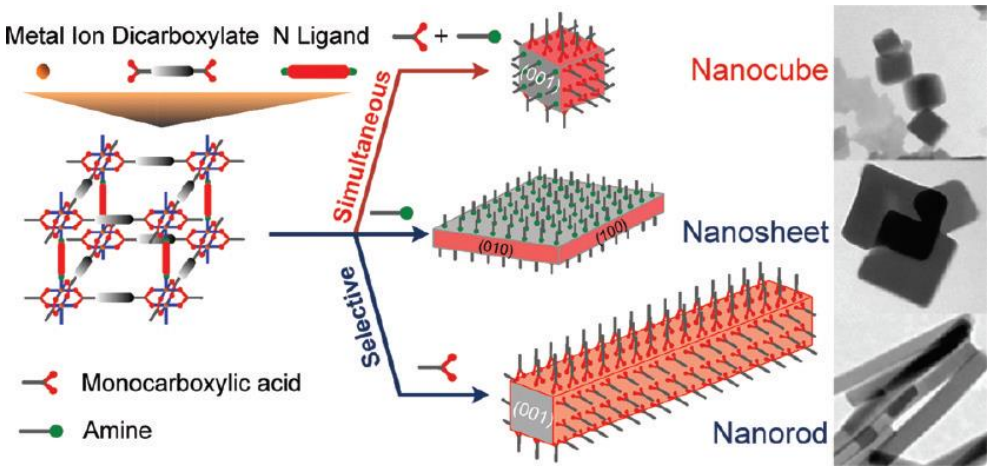

Figure 8: One of the first examples of coordination modulation as tool for the controlled growth of different crystal faces. Monocarboxylic acid modulators control the growth rates in (100) and (010) direction, whereas mono-functional amines direct the interlayer growth in (001) direction. Competition for coordination sites slows down the respective growth rates which can be utilized for selective crystal morphology. Reprinted with permission from Ref.[171] Copyright 2012, American Chemical Society.

In general, modulated synthesis, for instance of carboxylate-based MOFs, relies on the use of an additional competing monocarboxylic acid present in the synthesis solution. Fulfilling the role of a capping agent, the modulator competes with the oligo-functional linker molecules for coordination sites reducing crystal growth rates due to more "unproductive" coordination events. Since crystal growth is significantly slowed down, only correctly installed linker molecules are permanently incorporated and continue the framework extension. As a result, the obtained materials have significantly higher structural perfection since less defects are incorporated. When providing enough reaction time, highly ordered crystals suitable for single-crystal structure determination can be obtained in many cases. Furthermore, coordination modulation improves the reproducibility of MOF syntheses.

Interestingly, upon surpassing a certain threshold in modulator concentration, the inverse trend of increased defectiveness might be observed. Although required for the evolution of long-range order and thus crystallinity, high amounts of modulator can be incorporated within the materials resulting in modulator-based defects. A more detailed discussion is provided in **chapter 2.3.3** (see page 35ff) on defects in MOFs.

A general revision of the concept was recently provided by a perspective article highlighting the versatile and in part ambivalent impact on the synthetic outcome as displayed in Figure 9.

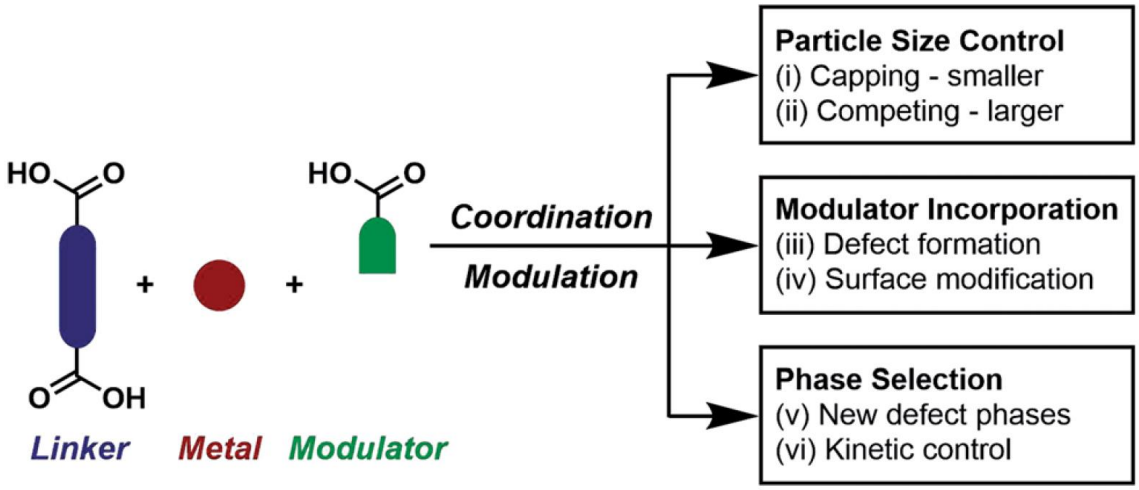

Figure 9: Schematic representation of the concept of coordination modulation with its potential impact on the synthetic outcome. According to Ross Forgan, different synthetic outcomes (displayed on the right) can occur concurrently. For instance, (i) aligns with (iv), (iii) can be accompanied with (v) and (ii) can align with (vi). Reproduced with permission from Ref.[172]

The concept of modulated synthesis received considerable attention in this thesis. In **Study II** the necessity of a modulator for the formation of crystalline PGM-based frameworks is exemplified by a mixed-metal series $[Ru_xRh_{3-x}(BTC)_2]$ peaking in the first report of a crystalline Rh-HKUST-1. In addition, the role of the precursor and modulator identity is scrutinized in **Study V** by a systematic series of substituted benzoate precursors / modulators.

Controlled Secondary Building Unit Approach

Another concept to facilitate more efficient self-assembly of the building units into structurally ordered networks is the "controlled secondary building unit approach" (CSA). For many MOF structures, the metal nodes comprise not only single metal atoms but centers of higher complexity. As introduced in **chapter 2.1** and in the general introduction of MOFs, metal nodes of higher nuclearity arise from the self-assembly of simple metal salts as thermodynamically most favoured products under given reaction conditions. Hence, during MOF formation, two individual processes of self-assembly have to occur. The formation of the metal nodes (which are PWs in the system of matter), in the first step, is a precondition prior to the assembly with the organic linkers into extended structures. Coming to kinetically inert PGMs, this second process alone is already slow enough. For this reason, the group of *Fischer* first investigated the controlled SBU approach utilizing different preformed PW-type precursors for the synthesis of the mixed-valence Ru-HKUST-1.[173-175] The exploitation of preformed PW building blocks also avoids the formation of undesired side phases or more general side products that could emerge from reactions of isolated metal ions in solution. Due to all mentioned reasons, CSA was also used for all MOF syntheses in the frame of this thesis. In particular, in **Study V,** the impact of the PW precursor and modulator choice on the resulting univalent Ru-HKUST-1 material properties is elucidated.

Mixed-Metal MOFs

Turning to a special subgroup of MOFs, mixed-metal (MM)-MOFs should be briefly introduced. Instead of constructing frameworks with one sort of metal exclusively, two or even more metals can be incorporated within a MOF. The presence of different metals can further expand the enormous parameter space of

MOFs, for incance, adding bifunctionality to catalytically active structures.[176] Here, several different strategies should be distinguished.[177]

1.) There are MOFs that comprise **metalloligands**.[178-179] The metal contained within the ligand structure is not necessarily identical to the one facilitating the self-assembly towards the self-supported stable network. Typical examples are metalated-porphyrins in Zr-based MOFs such as MOF-525, PCN-222 or PCN-224 but also metal salen complexes found application.[176, 179-180] In these structures, the homogeneous distribution of both metals is rather straightforward, since metalation of the porphyrin can be conducted prior to MOF formation and both metals fulfil different roles: The metal within the porphyrin is typically strongly bound due to the chelating effect. Amongst others, Fe, Co, Mn, Ru, Rh, Cr are frequently used for porphyrin metalation.[180-184] The Zr nodes that form under solvothermal conditions are interconnected with carboxylate groups of the porphyrin ligand motif. Both processes are isolated from each other which makes control easier. One elegant example of bimetallic Rh/Zn and Rh/Cu with 1:1 metal ratio was reported by the group of *Mori*.[185] In a first step, they prepared a Dirhodium tetraterephthalate metalloligand by equatorial ligand metathesis of $Rh_2(OAc)_4$ with mono-(2-trimethylsilyl-ethyl)-protected terephthalic acid to yield isolated complexes. After deprotection of the second carboxylates of the four BDC ligands, they used this as a metalloligand for a MOF formation with Zn or Cu salts that show high ligand exchange rates. This strategy although featuring limited reaction scope and being experimentally elaborate is an elegant detour avoiding the problematic ligand substitution kinetics of PGMs in MOF formation.

2.) There are **bimetallic hetero-structured MOFs**. For instance, in a first synthetic step, monometallic core particles are prepared that are grafted with a shell comprising a different metal in a second step. Typical **core shell particles** result from this approach.[186-188] For the efficient grafting of the second layer on top of existing particles, the structural features of both phases should match. Isostructurality, or at least identical linker functionalities should be used. Some MOF-on-MOF thin films some including structural mismatch between the two MOF layers were reported.[155, 189-190]

3.) **Heterometallic MOFs** containing two or more interchangeable metals which fulfil the same role. Ideally, both metals should be homogeneously dispersed throughout the crystal on an atomic scale instead of representing a merely physical mixture of two each monometallic sorts of crystals. Such system is classified as **solid-solution**. This kind of MM-MOFs can be synthetically obtained following different strategies.[177] a.) **Post-synthetic solvent-assisted metal exchange** (SAME) is one commonly applied strategy to exchange metal atoms within a preformed material.[191-193] Although this approach was already applied in many different cases, it appears relatively limited regarding the choice and order of exchange. Only weakly bound metals (such as Zn) can be efficiently substituted by metals that show stronger binding affinities. Moreover, highly connected nodes are inert towards metal exchange. An interesting example was reported by the group of *Natalia Shustova*.[194] PSME with Cu-HKUST-1 and Rh^{3+} salts resulted in the incorporation of purely bimetallic CuRh PW nodes with Rh^{2+} sites. b.) Another strategy to access MM-MOFs is the ***de novo* synthesis utilizing a mixture of two metal salts or precursors**.[177] It should be mentioned, that depending on the stability of the chosen precursors, metal scrambling could occur or each monometallic SBU remains intact. This strategy is experimentally convenient due to the one pot synthesis. However, the ligand exchange rates of both metals should be similar. For instance, MM-MOFs from Ni, Co, Mn or Zn can be obtained with this strategy since these metals show comparably vital ligand exchange kinetics.[195-196] PdCu-HKUST-1 was obtained by solvothermal synthesis from simple metal salts. However, concomitant Pd reduction resulted in significant amounts of Pd^0 NPs trapped within the material.[197] In another report, a NP-free PdCu-HKUST-1 was obtained via a two-step-one-pot procedure first forming PdCu- and PdPd-PWs in acetic acid and then interconnecting these nodes with H_3BTC addition under solvothermal conditions.[198] One example for a series of MM-MOFs utilizing two PGMs is presented in this thesis exemplified by the RuRh-HKUST-1 analogues as highlighted in **Study II** (see page 73ff).[145]

Attempts to obtain solid solutions of Cu and Rh HKUST-1 analogues failed. The vast differences in ligand exchange rates, however, led to heterogeneous samples with Rh-rich domains within an almost pure Cu-based matrix.[145] This issue was elegantly solved by *Guo et al.* who used a two-step procedure for the mixed-metal MOF CuPd-HKUST-1 to facilitate generation of mixed-metallic PWs prior to their interconnection to the 3-D structure.[198]

The characterization of MM-MOFs can be challenging. Combinations of different methodologies from diffraction, spectroscopy, microscopy, and elemental analysis techniques can answer the questions of global concentration, the local environment, the metals oxidation states and their distribution within the material / crystals. Thereby, correctly complying to this order of assessment is important.[177]

New Developments

During the early days of MOF research, the quest for ever increasing pore size motivated researchers exploring the limits of reticular chemistry for the last two decades. Thousands of novel MOF structures have been reported and some raise the question whether we still need new MOFs: Of course, we do! The rational design of more complex organic ligand motifs, new bimetallic variants of established systems or the utilization of still innocent metals are just a few examples that keep fuelling the exploration of new MOFs.

Some years ago, the community started to explore surface-anchored MOFs, termed SURMOFs. Design strategies like vapor-assisted conversion (VAC),[199] the aforementioned CVD-MOFs,[167-168, 200] or the layer-by-layer liquid epitaxy[201] can provide high-quality MOF thin films with controlled thickness as promising materials for plenty technological applications in energy-related fields such as solar cells, sensor materials, microelectronic devices or electro(photo)catalysis.[166]

As introduced before, MOFs are currently categorized in three generations depending on their stability. Recent developments by *Thomas Bennett* and co-workers have investigated the controlled melting of MOFs towards functional glasses and liquids.[202-208] Although these partially amorphous materials are much harder to characterize compared to their ordered cousins, liquids and glasses possess advantages and interesting potential applications. The optical isotropy of melt-quenched glasses could be used for diverse purposes. The processability into any morphology and shape could facilitate large-scale application comparable with thermoplastics that allow injection molding. The elastic moduli of metal-organic glasses could bridge a gap between brittle inorganic glasses and ductile organic plastics. Other potential field of applications might be gas sorption and separation, molecule or ion trapping or their transport or for stimuli-induced switching between crystalline MOFs and amorphous glasses similar to Type III MOFs. In any case, the growing field of MOF glasses and liquids broadens the horizon of the whole research field stimulating the creativity regarding future trends or applications.

Looking into one of the most classical applications of MOFs, there is still plenty of room for improvements regarding MOF-based catalysis. So far, most of the related studies applied the MOF materials merely for industrially irrelevant test reactions providing some pseudo applicability. Many of these catalytic test reactions are rather simple Lewis acid / base reactions. Much more relevant would be reactions involving redox processes although more difficult to control. In relation to the total number of studies involving any MOF-based catalysis, those involving redox-active metal centers are rare. To that end, **chapter 2.3.4** should provide a general overview on heterogeneous and homogeneous catalysis and particularly MOF-based catalysis of relevance for the **studies I**, **III** and **IV** of this thesis.

Computational chemistry is increasingly used in MOF research not only for assisting experimental research but establishing its own territory. For instance, the vast progress in computational capacities driven by the electronic progress allows to use DFT-based approaches for systems with ever-increasing sizes and

number of atoms.[209-213] Furthermore, databases are created comprising thousands of MOF structures automatically implemented from the Cambridge Crystallographic Data Center (CCDC) with an individual MOF subset.[214] Such libraries allow for theoretical prediction of properties. As an output, one ends up with a selection of very few structures that might perform best in the respective targeted application. This novel computer-assisted screening affords unimagined opportunities in material science and will for sure initiate future breakthroughs in various fields.[214]

MOFs are traditionally considered electronic insulators since the common coordination bonds are highly polarized obstructing efficient charge transport. Generally, charge transport and its resulting conductivity depends on both the density of charge carriers and their mobility. Most MOF structures do not contain free charge carriers in relevant amounts. In recent years, however, conductive MOFs were heavily investigated with promising progress achieved by several strategies. These developments have opened potential utilization in electronics, photonics, semiconducting materials and other energy-related fields.[165-166]

Despite the endless design possibilities of MOFs, their industrial use is still not established yet. Not to draw an over-pessimistic picture of the field, it should be mentioned that some companies have included MOFs in their portfolios and even new starups are entering the market. At this point, few of the should be mentioned, which are BASF, NovoMOF, CD Bioparticles specialized on MOF production, MOF Technologies with a focus on production and shaping, and NuMat Technologies and ACSYNAM with specialized applications. Potentially, economy of scales will cut the currently high prices for MOFs towards competitive MOF-based catalysts in industry in future.

It will be thrilling to follow the developments of MOF research in future. The tailor-made materials probably keep holding the scientific communities' attention with many more discoveries on the way. Large-scale use in industry is currently obstructed by high costs and difficult scale-up of MOF syntheses. However, the economy of scales and novel continuous flow-based MOF productions probably address some of the obstacles towards industrial applications. The best is yet to come…

2.3.3 Defects in MOFs

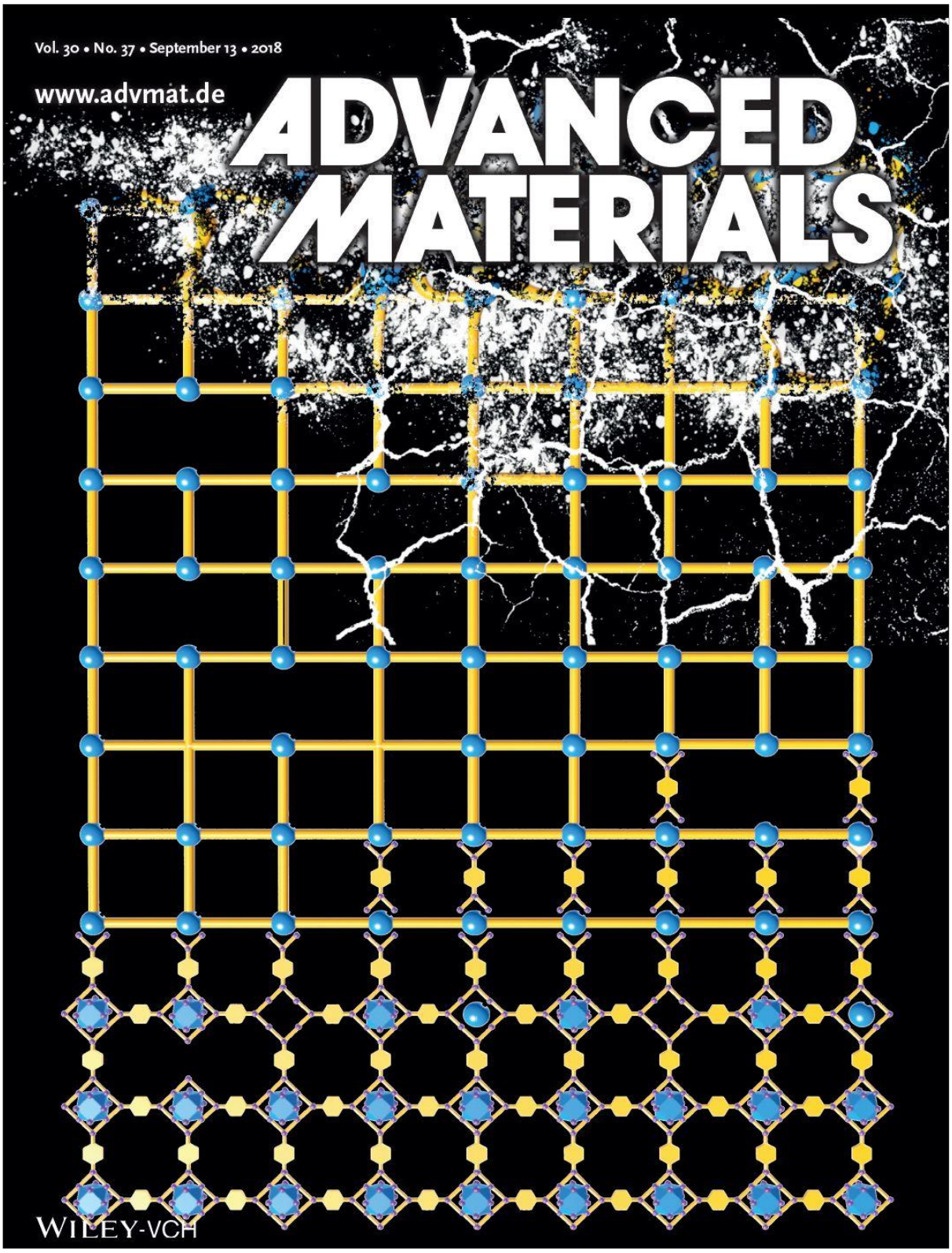

Figure 10: The review article "Defective Metal-Organic Frameworks" published in Advanced Materials and highlighted as cover page created by Stefano Dissegna, Konstantin Epp and Werner R. Heinz. The graphic illustrates a simplified 2-D representation of the UiO-66 structure comprising Zr_6 nodes and BDC linkers as the most studied platform for defective MOFs. From bottom to top, the details of linkers and nodes fade out towards more schematic representations. Point defects (missing node, missing linker defects) as well as macroscopic cracks and framework disintegration (top area) are highlighted. Reproduced with permission of John Wiley & Sons from Ref.[5] Copyright 2018, John Wiley & Sons.

Defects are present in any material. Looking at inorganic crystals, there are *Schottky*- and *Frenkel*-type defects. Defects from intentionally added impurities are key to semiconducting properties of p- and n-doped silicon single-crystals inevitable in microelectronics. In this regard, also MOFs have defects. In the early days of the field, the community only strived for structural perfection by using abovementioned approaches (see **chapter 2.3.2**). Synthesis optimization towards higher structural order in these comparably low-crystalline materials (as compared to inorganic crystals) was predominant. However, in recent years, the beneficial role of defects and disorder with respect to important applications was increasingly uncovered. For instance, a perfectly ordered crystal with ideally saturated coordination sites of all metal nodes, so a MOF without OMS, would be totally boring from a catalysis perspective. Only the presence of defects renders some MOF structures interesting candidates for certain applications. Besides catalysis, where defects can strongly impact the density and electronic properties of OMS, defective sites can be utilized for the (selective) gas sorption, the detoxification of warfare agents, the sensing of certain analytes, or the uptake and accommodation of guest molecules, nano particles or even enzymes within meso- or macroscopic voids. Defects can further modify the mechanical, optical, and magnetic properties of the framework.

For all these reasons, there was a change in paradigm concerning the perception of defects in MOFs during the last years. Formerly regarded as undesired blemish, nowadays, new research directions deliberately introducing defects to MOFs intentionally – termed defect-engineering (DE) – have emerged and received recognition throughout the whole MOF community. Beyond this general attention, the defect chemistry of PGM-based MOFs studied herein is strongly intertwined with their synthesis, characterization, and utilization as catalytically active materials. Consequently, the investigation of the defect structure of both pristine and particularly defect-engineered PGM-HKUST-1 analogues is at the core of this thesis.

This chapter should provide a sufficient overview on defects: First, different types of defects according to various classifications should set the scene including the specific terminology. Some characterization techniques useful to investigate defects qualitatively and quantitatively are highlighted. Different strategies established to intentionally introduce, control, or manipulate defects in MOFs are discussed finally peaking in a concise summary of affected material properties and respective potential applications.

During 2018, the author of this thesis together with *Konstantin Epp* and *Stefano Dissegna* equally contributed to a review article on “Defective Metal-Organic Frameworks” published in *Advanced Materials*.[5] This article represents an update to an earlier review by *Zhenlan Fang* and *Roland A. Fischer* and others written in 2014.[4] The following chapter is merely based on information from these two references unless otherwise stated.

Definition and Classification of Defects

Starting with the **definition of defects**: According to the first review article in 2014, defects are “sites that **locally** break the regular periodic arrangement of atoms or ions of the **static** crystalline parent framework because of missing or dislocated atoms or ions.” Importantly, the limitation to locally implies that any regular alteration of a parent framework for instance, the removal of solvent, is not considered as a defect. Moreover, the reference to the static framework excludes the thermal motions vibration and rotation from the definition of defects.

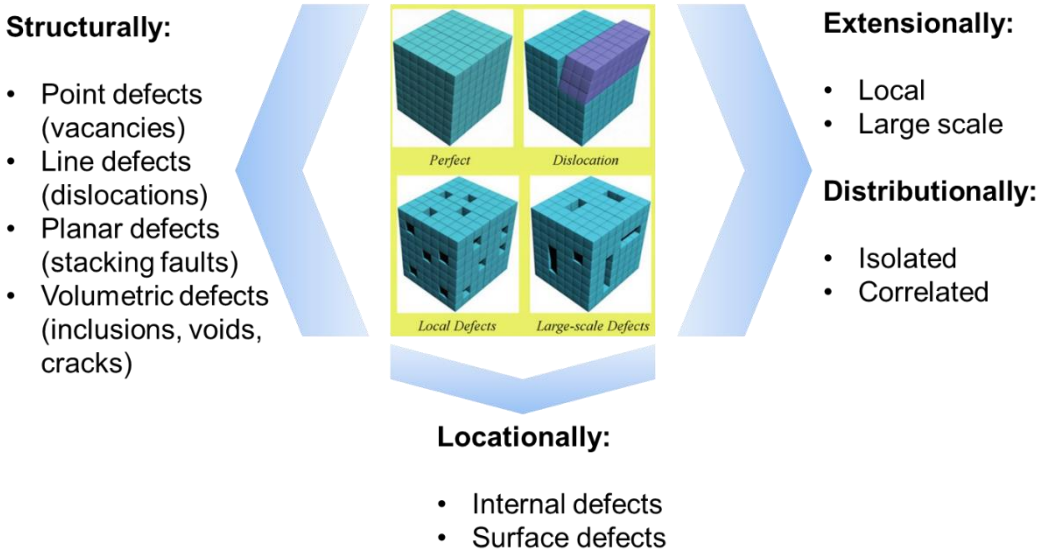

***Figure 11**: Types of defects classified by structural dimension, extension, distribution and location. Figure created by adaption of a graphic provided in Ref.[4] Reproduced with permission from Ref.[4] Copyright 2015, John Wiley & Sons.*

There are various **classifications** into which defects in MOFs can be categorized (see **Figure 11**). First to mention, there is the **structural and dimensional classification**: Defects can be zero-dimensional point defects (vacancies), 1-D line defects (dislocations), 2-D planar defects (stacking faults) and 3-D volumetric defects (inclusions, voids, cracks). Another aspect is their **extension**: Defects are either local- or large-scale variation of the pristine framework. Regarding their **distribution**, defects can be isolated or correlated. Depending on the **location**, one distinguishes between internal and surface defects. Any crystal surface represents a termination of a periodically extended materials and thus, can be regarded as a defective site. This is why, small sized MOF particles are often found to be more active in catalysis compared to larger crystallites, although porosity allows for diffusion throughout the crystal yielding theoretically full accessibility of all metal sites.

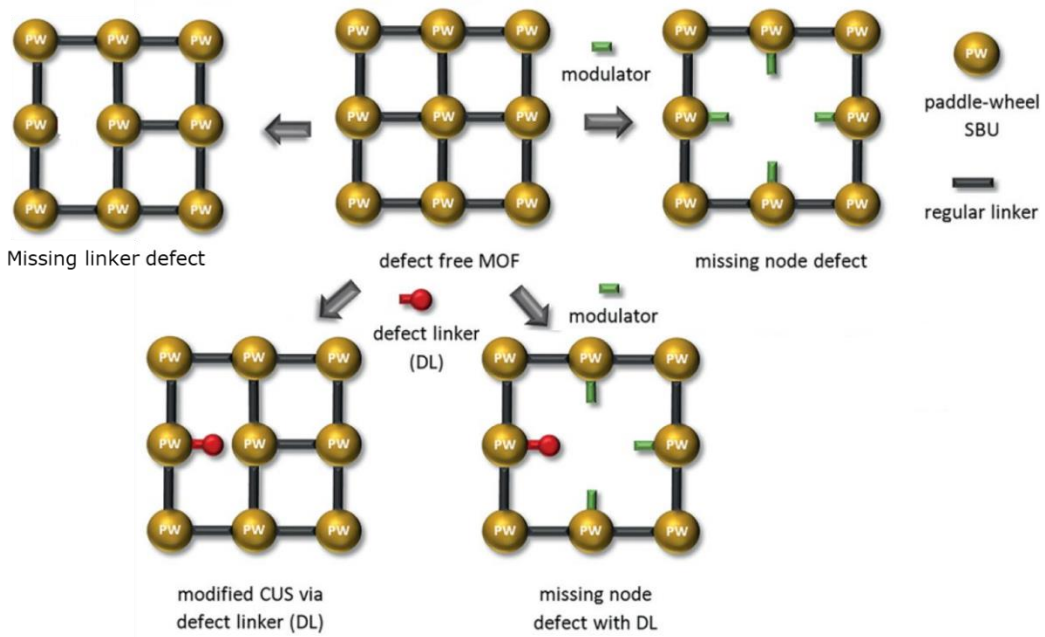

***Figure 12**: Schematic illustration of different types of point defects in PW-based MOFs with (bottom row) or without (top row) the use of a (truncated) defect linker added to the synthesis following the mixed-linker strategy as will be introduced below. Linker dislocations are omitted in this graphic. Figure partially adapted from Ref.[215] Reprinted with permission of John Wiley & Sons from Ref.[215] Copyright 2016, John Wiley & Sons.*

Both the synthetic chemical toolbox but also the availability of analytical probes to investigate defects in materials are relatively powerful when isolated metal sites are concerned. Investigation and modification of defects of higher dimensionality or of defect correlation are more challenging. Furthermore, the rather low abundance within networks of mostly perfect composition and structural order complicates their analysis dramatically. Therefore, zero-dimensional point defects have received the main attention. Focussing on point defects in MOFs, **Figure 12** provides an overview on several defect types.

As can be seen, besides an idealized "defect-free" structure, there are missing linker (linker vacancy) and missing node (metal vacancy) defects in pristine MOFs obtained from modulated synthesis. Several DE strategies have been established (see below). Some result in the incorporation of either truncated defective linkers alone (modified nodes / PWs) or in combination with modulator incorporation towards missing node or even missing cluster defects. Note, that any removal or absence of a linker would result in disbalanced charge of the framework. Therefore, different possibilities for charge compensation are plausible. Either the missing negative charge from the linker is countered by the affected metal node featuring reduced oxidation states. For instance, a perfect Cu^{2+}-Cu^{2+} PW could be reduced to a mixed-valent Cu^{+}-Cu^{2+} defective PW compensating the absence of a $RCOO^{-}$ ligand. Alternatively, another anion either coordinating (for instance hydroxid, oxide, or halides) or weakly coordinating (nitrate, tetrafluoroborate, hexafluorophosphate etc.) accounts for charge compensation. A third possibility is the formation of a positively charged defective PW while charge compensation is achieved through the presence of a negatively charged PW (containing surplus axial anionic ligands) elsewhere in the lattice. The latter is in analogy to *Frenkel*-type defects known from other solid-state materials.

Other point defects in MOFs are dangling linkers. The either result from uncoordinated metal centers with charge compensation possible *via* additional anions or through partial metal reduction as explained above, or result from added defect linkers which are of higher functionality compared to the pristine linker. Their additional binding sites do not match with the crystal lattice of the pristine framework and thus, are uncoordinated.

Characterization Techniques to Analyse Defects

The analytical investigation meaning the detection, characterization, and quantification of defects in MOFs is one challenging objective. First of all, their relatively low abundance in extended structures requires sensitive techniques searching for small variations from the perfect lattice. In addition, defects such as dislocations like dangling linkers (often) feature the perfect composition but subtle differences in their connectivity. Highly reactive reduced modified PWs can undergo deactivation during measurements that include at least one factor from high temperatures, interaction with guest molecules (for sorption, spectroscopy using probe molecules, or during catalysis), or chemical dissolution to access the elemental or molecular content of each sample. PXRD – usually one of the most powerful techniques in crystalline solid-state chemistry – relies on the long-range order of the microcrystalline materials and is usually insensitive towards isolated point defects. Even if defective linkers might cause rather periodic modification of the lattice, typically the observed changes in XRD patterns are subtle and require careful investigation. Microscopic techniques such as scanning electron microscopy (SEM) or transmission electron microscopy (TEM) do not reach the resolution required to image these sub nanoscale variations. Although recent advances revised their applicability for many cases, the fragile structure of MOFs tends to disintegrate under the focused high-energy beam of these techniques and if low acceleration potentials are used, typically the accessible resolution drops in turn.

In summary, there is no all-in-one solution to scrutinize the defect structure in MOFs. Rather a multitude of several techniques and clever combination of the respective results are required to obtain a comprehensive picture. In this subchapter, the most relevant methods and their respective contributions

to the entire picture - similar to a puzzle being compiled by many pieces – should be briefly introduced (see **Figure 13**). Although, there are more advanced highly sophisticated methods, a special focus is put on the ease of access instead of relying on highly restricted synchrotron-based techniques. For reasons of comprehensiveness, however, some of the techniques of such kind shall be briefly mentioned at the end of the chapter. As highlighted in **Figure 13**, different **aspects** (shown on the left) of defective MOFs need to be studied. Many **analytical techniques** can provide insights ranging from elemental analysis, diffraction, spectroscopy, microscopy to several indirect methods.

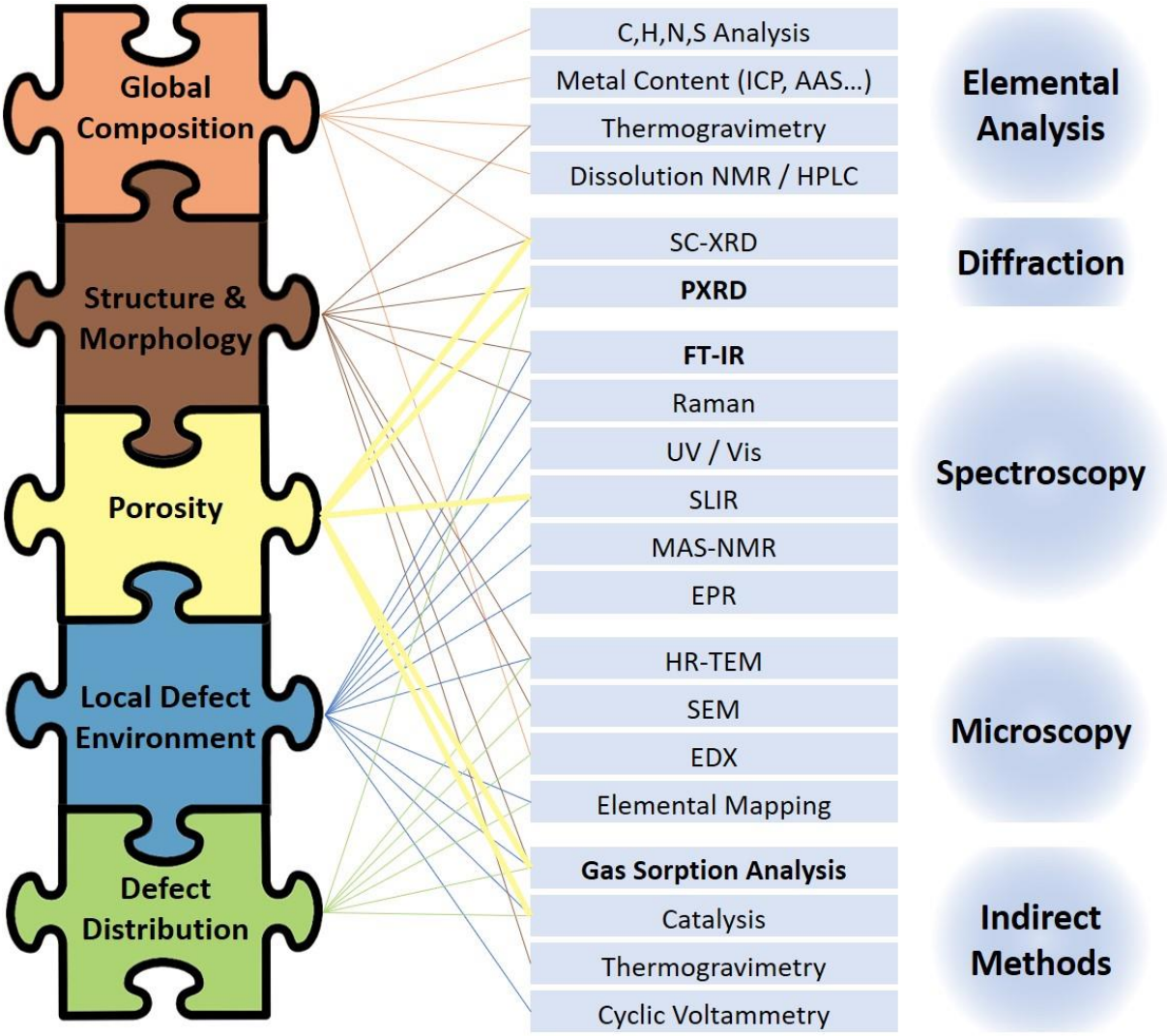

***Figure 13**: In-depth characterization of defective MOFs requires a multitude of different techniques. Left: The puzzle revealing the entire picture of the material contains several pieces: First, an overview on the global composition and structure and morphology should be gained. An important aspect is porosity, which should be followed by detailed investigation of the local defect environment. The most specialized piece is the spatial defect distribution. Lines indicate the connection of individual analytical techniques grouped into five categories and their delivered insights. Basic characterization techniques that usually appear in MOF reports are displayed in **bold** letters.*

The **global composition** is accessible via C,H,N,S elemental analysis, while several techniques such as atom absorption spectroscopy (AAS), inductively coupled plasma – optical emission spectroscopy or coupled with mass spectrometry (ICP-OES /-MS), X-ray photoelectron spectroscopy (XPS), energy dispersive X-ray spectroscopy (EDX), thermogravimetric analysis (TGA) or X-ray fluorescence (XRF, not shown) reveal the metal contents. NMR-based techniques either in solid-state or upon acid digestion allow for identification and quantification of molecular entities such as solvent, modulator, linker or organic counterions. One interesting approach to quantify Bronsted acid or basic sites recently gained attention. The potentiometric

acid/base titration can reveal the presence and quantity of acidic or basic sites that might arise from dangling linkers or free hydroxy groups. The unambiguous detection of low amounts of protons, hydroxides or oxides within extended frameworks is generally difficult. Therefore, this technique has a lot of potential. However, it is strongly limited to highly stable acid or base resistant MOFs and data evaluation for complex systems might be challenging.[144, 216-217]

Structure and morphology can be investigated merely with X-ray diffraction techniques. Alternatives would be neutron or electron diffraction. Imaging techniques such forms of microscopy (like SEM, TEM, STM or AFM, not shown) reveal the morphology. Insights into the connectivity of the structure are also obtained by indirect TGA measurements since defective structures typically feature lower decomposition temperatures as compared to their more prefect analogues.

Gas sorption analysis including a pore size distribution analysis elucidate the **porosity** of the framework as one aspect of structure and morphology. One interesting alternative that is particularly useful for non-accessible porosity has entered the field of MOFs in recent years: The positron annihilation lifetime spectroscopy (PALS).[202, 218] Positrons, the antimatter of electrons annihilate upon collision with electrons resulting in high-energy photons that are subsequently detected. Due to the electron density differences between pores and pore walls, PALS can be used to scrutinize the porous structure of materials and can also be used during synthesis to monitor its evolution. Especially those materials that suffer from structural collapse at the particle surfaces and thus, avoiding entry of guests such as N_2, Ar, or Kr typically used in gas sorption measurements are predestined for PALS. Other indirect means to access the porosity of materials are the surface-ligated IR spectroscopy (SLIR) often using pyridine, CO or CO_2 as probe molecules, but also selected (catalytic) test reactions that exploit the steric differences of various substrates and their uptake / conversion in materials of certain porosity. In this regard, the uptake of large-sized coomassie brilliant blue R250 dye into hierarchically porous defective UiO-66 is one prime example.[219]

The investigation of the **local defect environment** is probably the most outstanding aspect of defective MOFs. Apparent in **Figure 13**, amongst others, mostly spectroscopy is associated with this aspect. It should be further distinguished between the geometric and the electronic environment of the defective metal nodes. XPS, UV/VIS, extended X-ray absorption fine structure (EXAFS), X-ray absorption near edge spectroscopy (XANES, both synchrotron-based and not shown in **Figure 13**) and cyclic voltammetry (CV) can elucidate the metals oxidation states. One interesting alternative is the SLIR using CO as a probe molecule. The intense IR vibrations of the highly polar CO bond are very sensitive towards its strong binding to transition metal centers via OMS. Not only oxidation states, but also indications for the abundance and accessibility of OMS are obtained. The hydrophilic / hydrophobic environment of MOFs can be probe by water adsorption measurements. The affinity for water adsorption results in the Henry constant which is one indicator for the increasing hydrophilicity of a MOF containing missing linker defects as has been shown by *Dissegna* and others.[220-222] Another synchrotron-based technique is the pair-distribution function analysis (PDF) which provides information on the interatomic distances present in materials without the necessity of crystallinity. More abundant techniques to study the geometric environment of defects are MAS-NMR, EPR, HR-TEM-based elemental mapping but also the pore size distribution (PSD) derived from gas sorption analysis. The exploitation of catalytic parameters such as activity, chemo-, and diastereoselectivity as analytical probe to investigate complex heterogeneous materials is a novel concept demonstrated based on the catalytic cyclopropanation within **Study IV** of this thesis.

Information on the **spatial distribution** of defects are rather hard to derive. Tailor-made catalytic test reaction could be utilized to investigate defect correlation through adjacent metal nodes. PSD analysis from gas sorption can reveal the fusion of several micropores into larger mesopores indicating a

correlation of defects. Besides these rather rare cases, the main techniques to investigate distribution of defects are microscopy related. Elemental mapping could give valuable information in heterogeneous distribution of contributing elements. In recent developments, IR micro-spectroscopy was used to study the spatial distribution of missing linker / modified PW defects in HKUST-1.[223-224] Few theoretical studies revealed the significant impact of isolated or correlated defects on the mechanical stability of MOFs.[215, 225-228] Although there are only few experimental studies on the mechanical stability of MOFs, the obtained results can be correlated with the materials defectiveness.[229] Again a shift in paradigm might take place in future. Instead of focusing on the drawbacks of the weakened rigid structure, the potential of emerging flexibility could find its appreciation.[5]

Defect-Engineering

As introduced before, the perception of defects has changed within recent years and scientists are increasingly interested in concepts to intentionally introduce and manipulate defects in MOFs which was termed "defect-engineering" by *Roland A. Fischer*.[4, 230-231] Consequently, several approaches were developed which can be grouped in two main categories: The ***de novo* synthesis of defects**, and the **post synthetic defect introduction**. An overview on existing methods is provided in **Figure 14**.

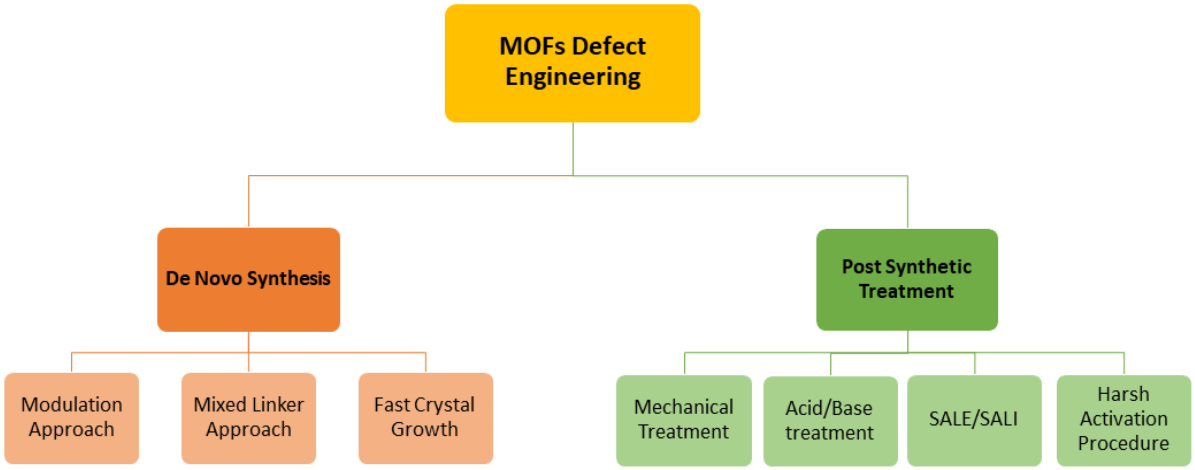

***Figure 14**: Strategies for MOF defect-engineering. Within the de novo synthesis approaches, there are modulated synthesis, the mixed linker approach and fast crystal growth that produce defective MOFs. Some post synthetic treatments can introduce defects into already existing relatively defect-free MOFs: Mechanical treatment, acid / base etching, the solvent-assisted linker exchange or incorporation (SALE/SALI) and harsh activation procedures. The latter was recently refined towards "thermal defect-engineering" as highlighted in Study III of this thesis. Reproduced with permission of John Wiley & Sons from Ref.[5] Copyright 2018, John Wiley & Sons.*

Starting with the *de novo* synthesis of defective MOFs: As already introduced in **chapter 2.3.2**, excessive modulator can be used to incorporate modulator-based defects at metal nodes. This so-called "**modulation approach**" is a frequently used DE strategy due to its high synthetic control and simple realisation. Although a PW comprising modulator-derived monocarboxylates is not defective from a coordination environments perspective, it is from the connectivity's perspective. Lowered overall PW connectivity and thus, hampered mechanical stability and reduced crystal sizes are typically observed. Depending on the chemical nature of the monocarboxylate modulator, it might be easily thermally removed to generate OMSs postsynthetically.[232-234]

The **mixed-linker approach** received considerable attention for MOF systems comprising linkers with topicities greater than two. During synthesis, a second, **defective linker** (DL) with similar geometry compared to the pristine is added and subsequently incorporated. One can distinguish between **truncated** and **extended mixed-linker** approach. Truncated linkers have generally lower topicity than the pristine

linker. For instance, isophthalic acid, its derivatives and 3,5-pyridine dicarboxylic acid have been used as defective truncated linker in the synthesis of 1,3,5-benzene tricarboxylate-based Cu- and Ru-HKUST-1 analogues.[67, 230, 235-237] DL incorporation results in the formation of reduced modified PWs as highlighted in **Figure 15**.[236]

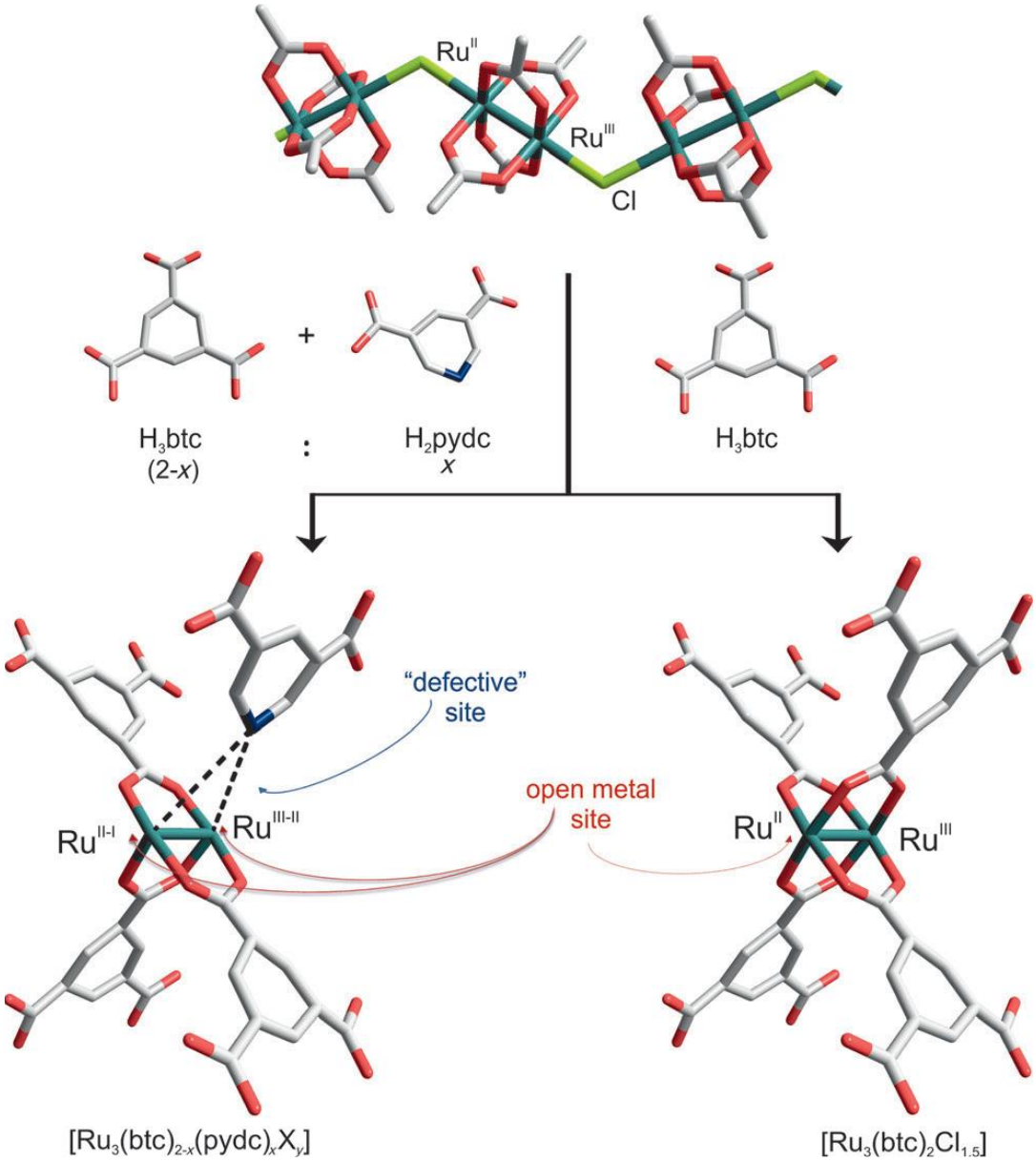

***Figure 15**: Representation of the truncated mixed-linker approach resulting in modified PW defects exemplified by the mixed-valence Ru-HKUST-1. Synthesis doping with 3,5-pyridine dicarboxylic acid (H_2pydc) yields partially reduced metal nodes with higher catalytic reactivity in several test reactions. Figure reproduced with permission of John Wiley & Sons from Ref.[231] Copyright 2014, John Wiley & Sons.*

The use of extended linkers for defect creation is much less common since linkers of larger size and/or higher topicity tend to form additional crystalline phases instead of homogeneous solid-solutions.[4]

Fast crystal growth either achieved by conventional techniques or through MW-assisted protocols is another DE strategy. The reason for the pronounced defectiveness lies in the absence of sufficient time for self-assembly. Although, there are studies investigating this DE approach, its synthetic control is rather limited and so is its utility.[218, 238-240]

There are numerous reports of **post synthetic treatments** (PST) of MOFs including linker side group functionalizations, post-synthetic metalation, metal or linker exchange and others. PSTs being closely associated with DE are: Mechanical, chemical and thermal treatments. Starting with a **mechanical treatment**, mostly ball milling having strong mechanical impact on the MOF particles was used by *Bennett* and co-workers to create defective / disordered materials. Interestingly, in UiO-66, the Zr_6 nodes remained intact, while ZnO-based MIL-140 and MIL-140b suffered from severe distortion.[241] Both approaches, the acid / base treatment as well as SALE/SALI belong to chemical treatments of pristine MOF materials. In both cases, a reagent is utilized to initiate the substitution of framework inherent components. For the **acid / base treatment**, usually strong mineral acids or either inorganic or organic bases were used for etching. Acids can protonate incorporated linkers, facilitate their removal or at least (partial) disconnection and substitute them by their own respective acid anions such as F_3CCOO^- (TFA) or ClO_4^-. *Bronsted* and *Lewis* acidic sites were observed in MIL-100 (Fe) upon such treatments. [232] Bases compete with coordination sites directly and can facilitate linker replacement, too.[242] The **SALE / SALI** approach can be regarded as form of ligand metathesis since the pristine linkers of a MOF are subsequently exchanged by structurally similar but functionalized, elongated or metalated (metalloligand) variants thereof.[243-244] The exchange by solvent alone as some kind of solvolylsis is also possible.[245-246] This partial linker replacement is in accord with the definition of defects stated above. Some MOFs although being inaccessible *via* direct synthesis or mixed-linker strategies are accessible through SALE.[244, 247]

Harsh thermal activation protocols can be used for defect introduction as well. Some reports highlighted an increasing thermal stress having beneficial impact on materials performance in several catalytic test reactions. Particularly carboxylate-based MOFs, such as MOF-5,[248] HKUST-1,[249] MIL-101,[250] MUF-32 (Massey University Framework,[245] and UHM-3,[251] were thermally treated. Interestingly, in inert atmosphere, decarboxylation occurs giving partially reduced metal sites accompanied with the release of CO_2.

One study of highest relevance for **chapter IV** of this thesis was the work by *Agirrezabal-Telleria* and co-workers who investigated different DE strategies on the system Ru-HKUST-1.[252] Interestingly, the mixed-linker approach using PYDC defect linker gave comparable impacts on material properties as a thermal annealing of the material. The performance of all samples was compared in the catalytic dimerization of ethene under intrapore condensation conditions facilitated through the pore confinement of the HKUST-1 lattice. This report is a rare case applying and comparing different DE strategies with each other. Further, the gained insights strongly inspired us to investigate, reinvent and apply the concept of thermal annealing in our PGM-MOFs. Therefore, it received attention within **chapter 2.3.6** (page 55ff), **Study III** (page 87ff) and **Study IV** (page 103).

Impact on Material Properties

The beneficial impact of DE on materials properties should be briefly mentioned here. However, not to go beyond the scope of this thesis, exemplary applications are limited to general concepts rather than specific reports. Please, consider the given references for further reading. Potential applications of defective MOFs cover catalysis, gas sorption, decontamination, dye uptake and degradation, hydrophobicity, conductivity and many more yet unexplored fields of application.

For **catalytic purposes**, the role of defects is rather apparent. The generation and/or modification of OMS highly enhances metal-based catalysis. Further, the formation of mesoporous or hierarchically porous MOFs assists the efficient mass transport throughout the catalyst particles or could be used for uptake, accommodation and stabilization of larger catalysts species such as nanoparticles, polyoxometalates, or

enzymes.[120-122, 138-139, 253] MOF melting to liquids or melt-quenched glasses could provide novel ways of particle shaping highly relevant for industrial catalysis.[205-206]

Gas sorption can benefit from both newly created void space induced by defect formation or incorporation but also from the tailor-made functionalization of the respective pore walls to guide the (selective) sorption. To that end, N_2, CH_4 and CO_2 sorption was enhanced while SO_2 sorption was even facilitated by DE techniques.[239, 245, 254-255]

Using MOFs for **decontamination purposes**, for instance, of chemical warfare agents or simulants thereof was largely investigated by *Joseph Hupp* and co-workers.[256-258] Several concepts some involving metal-substitution, MOF/polymer composite materials, or even enzyme immobilization were investigated. Decontamination and detoxification can proceed via catalysis or photocatalysis. Often missing-linker defects created by various abovementioned approaches provide sufficient *Lewis* acidity for the sorption and conversion of warfare agent simulants towards degradation products with low toxicity. [256-259] Patents for the use of defective MOFs such as UiO-66 and others have been filed.

Hierarchically porous MOFs have been investigated with respect to their **dye uptake** properties arising from defect-induced mesopore formation. [219] **Hydrophobic MOFs** can be obtained *via* pore wall decoration with either fluorinated or non-fluorinated long-chain alkly carboxylates. The respective materials revealed improved hydrolytic stability under various conditions.[260] [261] Several reviews have summarized this emerging field recently.[260, 262-263]

Electronic conductivity can be added to MOFs *via* PSTs incorporating redox-active guests that either create free charge carriers and/or establish new charge transport pathways.[264-272] **Ionic conductivity** and most importantly proton and hydroxide conduction was studied in several MOFs upon PST.[242, 273-277]

2.3.4 Catalysis in MOFs

Catalysis is one of the most important disciplines in chemistry when it comes to large-scale relevance. The field can be divided into homogeneous and heterogeneous catalysis depending on the phase both catalyst and substrates are located in. Typically, sophisticated molecular complexes as homogeneous catalysts are tailor-made, highly active, and thus, allowing minimum catalyst loadings, and can possess high selectivities. In this regard, also strong diastereo- and enantioselectivities can be achieved relevant for biochemical, pharmaceutical and drug industries. The major drawback of homogeneous catalysis, however, is the challenging catalyst separation and recycling. While extremely active polymerization catalysts often simply remain in ppb to ppm concentrations within the formed technical products, such an approach is obviously not approved in pharmaceutical products ingested into the human body. Consequently, elaborate purification steps are mandatory. This aspect is better solved in heterogeneous catalysis. Often, solid-state catalysts dispersed on high-surface geometries packed within a flow reactor (such as fluidized bed reactors) allow for the conversion of substrates on the catalyst surface towards the desired products and them being easily transported away. In industry, such heterogeneous catalysts offer long lifetimes, simple product purifications and a continuous operation. Most importantly these processes are highly scalable towards a cost-effective operation to reimburse the enormous initial investments associated with large-scale industrial production plants.

Having the pros and cons of both types of catalysis in mind, reasonable efforts are made to find ways combining the best of both worlds. In this regard, the immobilization of essentially homogeneous catalysts such as nanoparticles or isolated molecular complexes is one promising strategy. Physisorption or chemical anchoring to dense solid-support materials such as silica or alumina is an often-applied approach. However, MOFs can make versatile contributions as well which should be outlined in the following.

While the next subchapter shall provide a more general overview on aspects of MOF-based catalysis, the subsequent chapters will provide detailed insights into some specific reactions that were studied in the course of this thesis. These are hydride transfer reactions (the isomerization of allylic alcohols to saturated ketones and the *Meerwein-Ponndorf-Verley* (MPV) reaction), the dimerization of ethene and the cyclopropanation reaction. Important mechanistic aspects are given allowing easy digestion and comprehension of the conclusions drawn within the results section.

General Aspects – From Innocent Hosts and Supporting Frames to Active MOF Catalysts

As the heading of this subchapter already implies, three different aspects of MOFs in catalysis should be briefly introduced. Probably the most trivial function of a MOF in a catalytic process is its role as innocent host for other active species. These species could be attached in the pore space of the framework by simple physisorption or anchored *via* chemical means. Postsynthetic functionalization *via* reactive side groups represents one possibility.[191, 250, 254, 278] In this regard, the MOF can provide permanent porosity, a stable and rather rigid frame to protect the active species. For instance, metal nanoparticles, polyoxometalates but even enzymes were stabilized in MOFs.[120, 122, 139-141, 219, 279-280] Stabilization in this context means the prevention from particle agglomeration but also the avoidance of deactivation of fragile active species induced by harsh conditions (such as acids or bases denaturate enzymes). The second use of MOFs in catalysis can be related to the role as functional host. For instance, substrate specificity by size-exclusion phenomena can be facilitated. Key factor is the pore aperture allowing substrate entry to approach the active species located within the framework. Other strategies rely on the hydrophilic / hydrophobic properties of a MOF potentially manifested through side group decoration inducing preferred substrate entrance or product repulsion. The third aspect of MOF-based catalysis and probably the most sophisticated one is its use as active, self-supported catalyst. In this regard, the MOF

must fulfil multiple functions. On the one hand, its defined porosity should facilitate efficient and ideally also selective mass transport through the pores. Secondly, the active sites should possess high activity, selectivity and good stability for high turn-over numbers and frequencies (TON /TOF). The entire framework should tolerate the applied reaction conditions with respect to pH, present species and both thermal and mechanical stress. For industrial purposes, catalyst shaping such as pressing pellets should be possible without framework disruption / amorphization. Irrespective from the role of the MOF, its inherent porosity, structural order and large tuneability of the pore space can be used to achieve size- and shape-specificity and at the same time selectivity by pore confinement effects. An overview on the different possibilities to use MOFs in catalysis is shown in **Figure 16**.

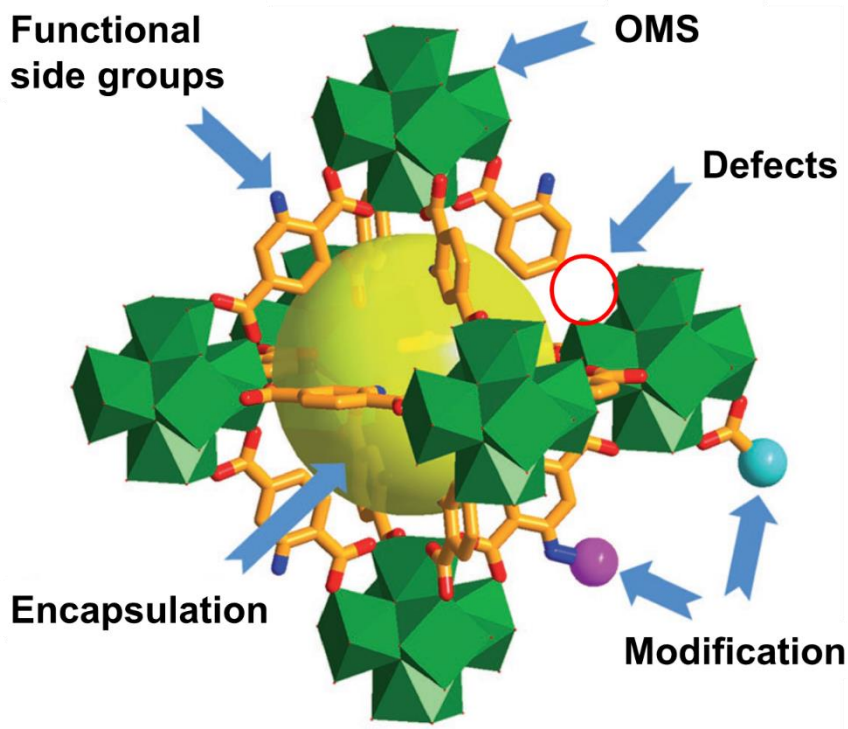

***Figure 16**: Schematic representation of possible catalytically active species. Besides encapsulation of active species, the MOF itself can provide naturally present functional side groups, open metal sites (OMS) and defects. Postsynthetic modification can be applied to intentionally create these active sites as well. Figure adapted with permission of John Wiley & Sons from Ref.[141] Copyright 2017, John Wiley & Sons.*

Turning to the supreme discipline, MOFs being catalytically active themselves, one can distinguish between linker- and metal-based activity. Some reactions are merely catalyzed by *Bronsted* or *Lewis* basic sites provided by functional linker side groups such as amines, hydroxides, or others. Active metalloligands also belong to the category of linker-based catalysis although their active sites are metal-based. In contrast, catalytic reactions facilitated by the framework constructing metal nodes often rely on their *Lewis* acidity. Consequently, MOF systems with regularly occurring OMS such as HKUST-1, MIL-100 /-101 or the NOTT family are predestined for metal-based catalysis. Oxides or hydroxides at the metal nodes can also provide *Bronsted* acid / base catalytic activity. In this context, defects can play a decisive role in the catalytic activity of many MOF structures since missing linker defects occurring naturally or artificially via DE strategies can significantly enhance the number of OMS.

Summarizing the field of MOF-based catalysis during the last two centuries, there are endless possibilities to utilize the great design freedom and large tailor ability of MOFs for catalytic purposes. However, to the impression of the author of this thesis, the vast majority of studies investigated rather straight-forward (and subjectively perceived maybe boring) *Lewis* acid/base catalyzed reactions. Reactions that involve changes in oxidation states are relatively rare. In this context, the potential of redox-active metals such

as Mn, Cr, Fe, and others is far from being maxed out. In particular, the precious group metals (PGMs) industrially widely applied have only found little attention in the field of MOFs. For instance, Ru is the prime element for olefin metathesis, asymmetric hydrogenations or the *Fischer-Tropsch* synthesis. Rh is known for its activity in the hydroformylation and in diverse hydrogenation reactions, while Pd is the first choice in cross-coupling reactions and in the Wacker process. The even heavier Ir and Pt are used, for instance, in the *Cativa* process, in hydrogenations and in the *Ostwald* process. In contrast to these large-scale industrial applications, MOF-based catalysis is far from being industrially relevant. In academic publications, catalysis is still often simply used as test reaction to improve the value of the study pretending the materials applicability. The challenging industrially relevant reactions are still rarely covered. Few exemptions from this overall impression might be the fields of electro (photo) catalysis and CO_2 capture and conversion which have received much attention in recent years.

From this more general perspective on MOFs and catalysis, the next chapters should provide a closer look on some particular reactions of special relevance in this thesis.

Hydride Transfer Catalysis

In **Study I**, two different types of hydride transfer reactions are investigated. The isomerization of allylic alcohols and the *Meerwein-Ponndorf-Verley* (MPV) reaction. The latter involves an intermolecular transfer hydrogenation from ketones to secondary alcohols while another "sacrificial" secondary alcohol present in the reaction solution is oxidized to its corresponding ketone. In particular, the reaction of cyclohexanone to cyclohexanol with the concomitant oxidation of 2-butanol to 2-butanone was investigated. The respective reaction mechanism is highlighted in **Scheme 3**. As can be seen, the catalytic cycle can be initiated by two ways: Either through coordination and subsequent deprotonation of an alcohol, or by the presence of a ruthenium hydride species directly enabling the cyclohexanone reduction.

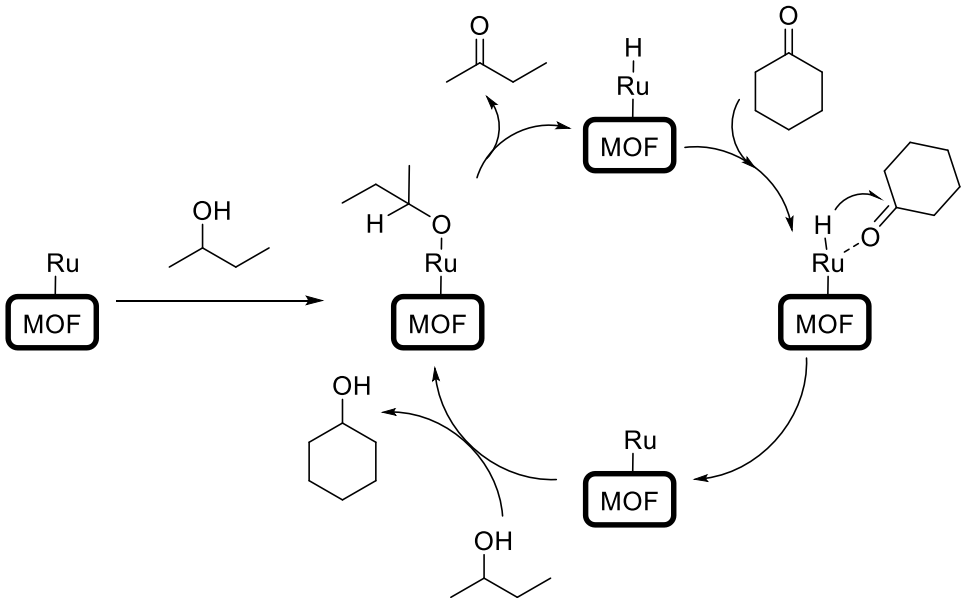

***Scheme 3**: Reaction mechanism of the MPV reaction of cyclohexanone to cyclohexanol with the concomitant oxidation of 2-butanol to 2-butanone. The reaction can either be initiated by coordination and deprotonation of an alcohol to an OMS of the Ru-MOF, or by the presence of an active metal hydride.*

Turning to the isomerization of allylic alcohols, in **Study I**, the isomerization of 1-octene-3-ol to 3-octanone catalyzed by Ru-HKUST-1 and its defective variants. In general, the isomerization of allylic alcohols represents a transfer of the C=C double bond to the C-O bond. In the reverse perspective, hydrogen is transferred from the CH-OH fragment to the $CH=CH_2$ fragment. Typically, this transfer hydrogenation is

conducted in the presence of additives providing a hydrogen storage. During this stepwise procedure, a proton and a hydride must be trapped at the same time. For this reaction to occur, often *Lewis* basic sites accommodating the proton capture in close proximity to *Lewis* acidic metal centers representing the host for hydrides are present. Various metals are known to catalyze this reaction.[281-284] In the studied Ru-DE-MOF system, it is the presence of PYDC in proximity to the redox-active Ru dimers presumably forming a pyridinium ion and a ruthenium hydride couple. A comparison between two strategies of this reaction namely the two-step and the one-step isomerization is shown in **Scheme 4**.

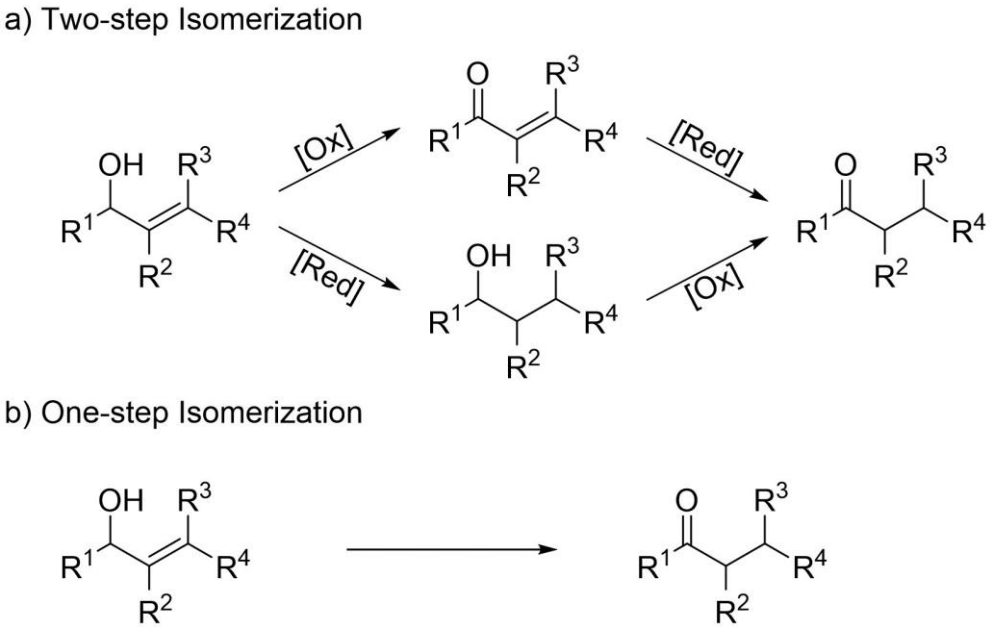

***Scheme 4**: Possibilities for the isomerization of allylic alcohols towards saturated ketones. The two-step isomerization involves two consecutive steps of oxidation and reduction respectively, while the one-step isomerization proceeds in a concerted fashion as alkene isomerization.*

Ethene Dimerization Catalysis

The dimerization of ethene *via* transition metal catalysts is also associated with metal hydrides. Formation of these either in terms of a hydrogen pretreatment, or during an initiation period under catalysis conditions is a prerequisite for the catalytic activity. In contrast to the PGM-MOFs studied herein (see **Study III**), most of the reported reference systems rely on an additional chemical activators such as Et_2AlCl or methyl aluminoxane (MAO) generating active metal alkyl or hydride species.[285-291] Regarding the reaction mechanism, the active metal hydride undergoes two subsequent cycles of ethene coordination and migratory insertion firstly into the M-H bond generating a metal ethyl species and secondly into the formed M-C bond of such metal ethyl for chain elongation. Subsequent β-H elimination results in release of the 1-butene product and regeneration of the M-H species. The whole catalytic cycle is displayed in **Scheme 5**.

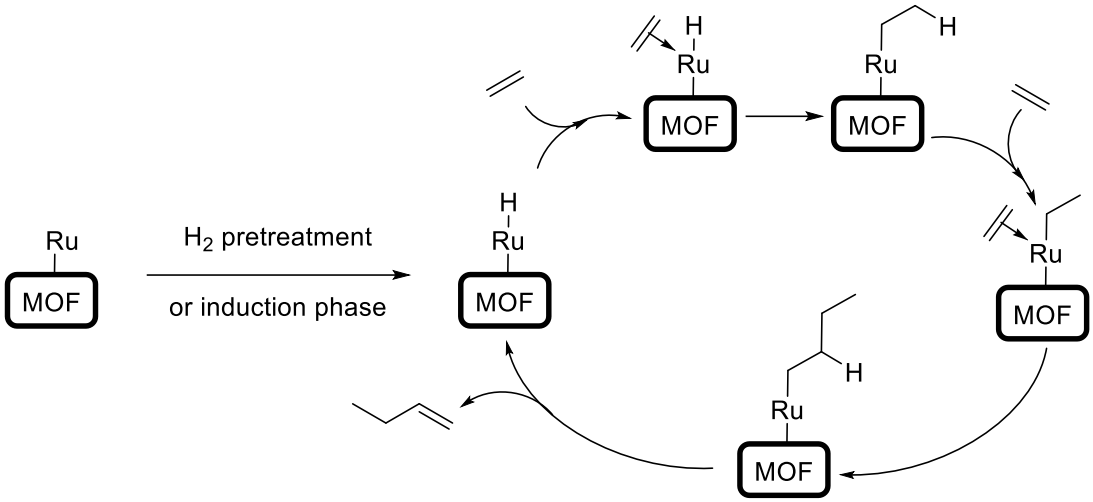

***Scheme 5**: Reaction mechanism of the dimerization of ethene catalyzed by ruthenium hydride species. Upon initial ethene coordination, a migratory insertion yields the intermediate metal alkyl species. Coordination and subsequent repeated insertion of a second ethene yield the metal butyl species. The β-H elimination terminates the chain growth to yield the targeted 1-butene under recreation of the ruthenium hydride closing the catalytic cycle.*

Cyclopropanation Catalysis

The third type of catalytic reaction investigated in this thesis is the cyclopropanation reaction. Due to the strained geometry of the three membered ring, cyclopropanes are interesting structural motifs present in many natural products.[292-294] Note that, real application in natural product synthesis requires strong diastereo- and even enantioselectivities (DS, ES) to yield the specific enantiomer selectively. Enormous efforts have been made in molecular catalysis to create libraries of designed molecular complexes on the quest to increase DS and ES. For non-chiral MOFs, ES is intrinsically hard to achieve. In general, the use and denitrification of diazo compounds forms metal carbenoid species which are subsequently transferred to the respective alkene in a concerted fashion under ring-closure towards the highly strained three membered ring. The CP reaction has been subject to previous MOF-based publications.[295-296]

The following paragraphs are adopted from the electronic supporting information of **Study III** of this thesis and provide a concise overview on the mechanistic background of the cyclopropanation reaction and the key parameters when using PW-based metal complexes as catalyst:[297]

It is general knowledge that transition metal carbenoids play an important role as active species or intermediates in many catalytic reactions, such as olefin metathesis, O-H, N-H and C-H bond activation just to name a few.[53, 298] For PW complexes, the CP is probably the most investigated reaction. Almost any imaginary combination (both inter- and intramolecularly) of Rh-PW catalyst, diazo compound, and olefin was screened to achieve deeper mechanistic comprehension of important parameters.[292-293, 299-300]

The first, rate-determining step (r.d.s.) of transition metal-catalyzed CP is the denitrification of diazo compounds and formation of a metal-carbene, which then transfers the carbene to the olefin in an outer-sphere fashion, which is fast, since the carbenes are highly reactive. For the r.d.s. and the catalytic activity, respectively, the availability of open metal sites (OMS) is thus most decisive. For styrene and EDA as reactants, the nature of the equatorial PW ligands was found to guide the diastereoselectivity. While strongly binding electron-rich carboxylates or carbamates at the PW give 64-68% *trans* selectivity, electron-poor fluorinated carboxylates lack any preference with 50% *trans* selectivity.[301] Labile ligands temporarily dissociate yielding defective PWs. At those defective or modified PWs, more trajectories for styrene to approach the carbene are possible obstructing higher diastereoselectivities.[53, 301] In contrast, the steric demand of the carboxylates (like acetate, pivalate or benzoate) has only minor impact on

diastereoselectivities since the PW-inherent square planar geometry spanned by the metal atom and its four adjacent O ligator atoms governs the diastereomeric preference and more distant side groups perpendicular to the axially bound carbene do not play a decisive role. Unwanted side-products resulting from homocoupling of two carbenes or from C–H activation are known to occur.[298] Homocoupling is usually suppressed by process control *via* slow addition of a diluted EDA solution over time and the excessive use of olefin.[180] Other side products can emerge from C-H activation of styrene.[298] Such a carbene-transfer results in linear allyl species which are further denoted as linear products. Other, non-PW complexes are known to produce cyclopropanes and linear products in different ratios.[22, 302-304] In contrast to the CP formation, these linear products could emerge via metallacyclobutane intermediates requiring additional OMS at the metal centre.[22, 298] From this fact, we conclude that their formation (which is not observed in perfect PW systems like $Rh_2(OAc)_4$ or $Cu_3(BTC)_2$) is indicative for the presence of modified PWs in PGM-MOFs as presented earlier by several other analytical techniques.[305]

2.3.5 The HKUST-1 Family

Previous chapters were dedicated to introducing concepts of general relevance. In contrast, this chapter should summarize the properties of the whole isostructural series of HKUST-1 analogues. Although covering the other analogues, the pristine and most famous Cu-HKUST-1 is the most intensively studied material. Therefore, the parent structure has a special role within the series and its properties are discussed first within this chapter. At the end of the chapter, the other analogues shall receive some attention before the special case of the Ru-based analogue will be subject of the following **chapter 2.3.6** (page 55ff).

Discovery of Cu_3BTC_2

In 1999, *Chui et al.* reported upon a new crystalline and porous coordination network comprising Cu-based PW units interconnected with tritopic trimesate linkers.[28] This MOF – at that time, the term not yet being established – has evolved into one of the best investigated and most used materials in the field. Although many different synthetic protocols were developed, its synthesis is nonetheless very simple. The high driving force to assemble into the crystalline 3-D porous material even allows for rapid room temperature syntheses.[157]

Structure & Properties

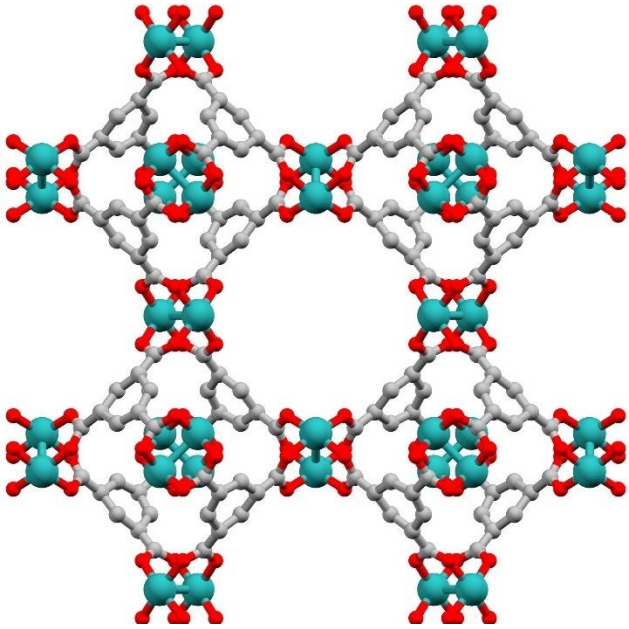

***Figure 17**: The cubic crystal structure of HKUST-1 viewed along a direction. The space group is $Fm\bar{3}m$, three different pores are present, one small pore and two degenerate large pores of 8 and 10 Å pore widths, respectively. Dimeric copper PWs are interconnected with four tritopic BTC linkers each resulting in high connectivity and mechanical stability. Color code: Cu – cyan, O – red, C – grey.*

The combination of PW-type SBUs being represented by square planar connected subunits with BTC linkers of triangular geometry results in a cubic 3-D connected framework as highlighted in **Figure 17**. The cubic nano porous structure has the space group $Fm\bar{3}m$ (a = 26.4 Å). Note, that the size of the unit cell is subject to the nature of the metal and can vary for the other analogues according to their atomic van-der-Waals radii. The combination of tetratopic M_2 PWs with tritopic BTC linkers gives rise to a total sum formula of $[Cu_3(BTC)_2]_n$. Upon synthesis, axial OMSs are typically solvent coordinated which can be

removed by thermal activation as outlined in **chapter 2.1.2** (page 9ff) for molecular systems and in **chapter 2.3.2** (page 23ff) for MOFs in general. The structure contains three different pores. For a better visualization, the three cages confining these pores are displayed in **Figure 18**.

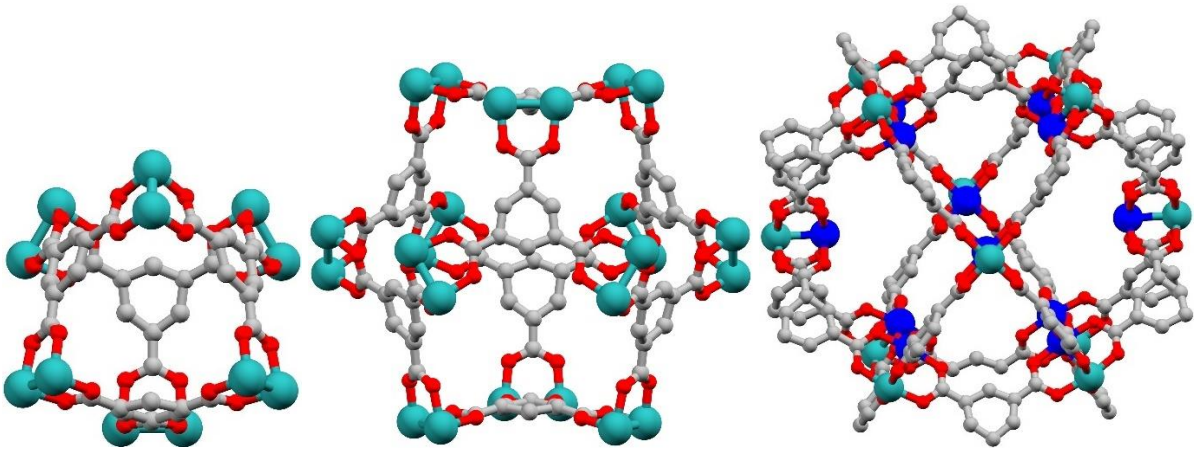

***Figure 18**: The three different cages of HKUST-1. Left: Small pore with its cage of six surrounding PWs which represents a trigonal antiprismatic structure. None of the axial coordination sites of the PWs is directed towards the small pore. Middle: Large pore without OMS pointing inside. The pore is surrounded by a cuboctahedral cage of twelve PWs which could be distributed in a 3-6-3 fashion with the two bottom and top triagonals being antiprismatically arranged. Right: Second large pore constructed by a cuboctahedral cage of twelve PWs organized in a 4-4-4 fashion with OMS pointing inside the cage. For visualization, the intrapore metal-atoms of each PW are highlighted in dark blue. Color code: M – cyan/dark blue, O – red, C – grey.*

The small pore (SP) has ≈8 Å pore width while two degenerate large pores (LP) are ≈10 Å wide. At this point it should be noted, that though degenerate in size, both large pores feature a different pore environment. While there are axial sites of the PWs pointing into one of the LPs (see the right cage in **Figure 18**, inner cage metal atoms are highlighted in dark blue), the other one is not decorated with axial sites (see middle cage). This information becomes relevant once axial ligands such as solvent ligands or charged anions in the case of mixed-valence $M^{II,III}$-HKUST-1 derivatives are present. These axial ligands abrogate the degeneracy since they reduce the size of one LP selectively. This topic will be revisited in **Study III** (page 87ff) of this thesis.

Due to its high connectivity and its crosslinking nodes and linkers, HKUST-1 is one of the most stable porous frameworks. To the best knowledge of the author, the bulk modulus of 30.7 GPa of Cu-HKUST-1 is the highest record for MOF structures known so far.[142, 226, 229] The material features also rather high thermal robustness with single-crystals being stable up to 240 °C.[28] Despite its high thermal and mechanical robustness, the chemical stability of the pristine copper-based analogue is relatively poor. Although synthesized in aqueous solvents, upon thermal activation the structure becomes water sensitive. Exposition to moist atmosphere or even water results in structural collapse due to hydrolysis of the labile Cu-O coordination bonds. Similar issues are observed for the Zn-derivative. Much greater chemical stability is observed for the Ru- and Rh-based PGM-derivatives studied herein. A more detailed discussion will be provided within the respective **chapter 2.3.6** particularly focusing on Ru-HKUST-1.

The parent Cu-HKUST-1 was intensively studied regarding its properties and potential for gas sorption,[306-309] separation,[310] mechanical and thermal stability,[29, 142, 215, 311-312] magnetism,[313] particle growth,[224, 314] conductivity enhancement by retrofitting,[315-319] defect-chemistry and defect-engineering.[215, 230, 237, 312, 319-324] Many studies further used this material and its DE-analogues for catalytic applications.[138-141, 253, 295-296, 322, 325]

From Cu to other members of the family

The concept of reticular chemistry does not only allow for linker variations and modifications similar to those shown in **Figure 5** on page 24 but includes variation of the metal nodes, too. Theoretically, the HKUST-1 structure should be accessible for any metal forming PW structures. However, several practical issues such as low oxidative or hydrolytic stability of other PWs hamper their straight-forward use for the construction of the extended structure. Moreover, their different ligand exchange properties can strongly undermine the inevitable self-assembly.

After the milestone discovery of **Cu-HKUST-1** in 1999, the second analogue being discovered in 2004 was **Zn**.[326] Two years later, the Mo-based analogues comprising a metal-metal quadruple bond was reported by the group of *Stefan Kaskel*.[327] In 2007, the respective iron (**Fe**) analogue was first synthesized.[328] This was the first structure comprising mixed-valence metal centers $Fe^{II,III}$ of this series. *Mircea Dinca*, *Jeffrey Long* and co-workers reported upon the **Cr**-HKUST-1 in 2010.[329] Both, **Ni**- and **Ru**-based structures were first reported in 2011 by *Norbert Stock* (Ni) and *Roland Fischer* (Ru).[175, 330] Similar to iron, ruthenium showed mixed-valency with $Ru^{II,III}$ metal nodes in line with its air-stability as already highlighted for isolated PW-complexes in **chapter 2.1.2**. The same group prepared a univalent analogue $Ru^{II,II}$-HKUST-1 in 2016.[331] The group of *Dirk De Vos* reported upon the first main group HKUST-1s using the alkaline earth metals Ba and Sr.[332] Although, a first **Rh**-BTC coordination polymer was described by *Kaskel* in 2013,[112] it took six more years until a crystalline monometallic Rh-BTC was described in the frame of this thesis (see **Study II**, page 73ff) for the first time.

A range of bimetallic analogues has been synthesized during the last years. Amongst others, there are Co-Ni, Co-Zn, Mn-Ni, Cu-Rh, Zn-Rh, Cu-Pd and Ru-Rh (this work).[145, 185, 194-195, 198] Mixed-metal MOFs were obtained according to the concepts previously described in **chapter 2.3.2**.

HKUST-1 analogues of metals of the 5d row, such as W, Re, Os and Ir, are yet unexplored but their discovery is expected by the author of this thesis. All of those metals are known to form PW structures. Following the trend of progressively reduced kinetic reactivity regarding the ligand exchange kinetics, their self-assembly towards structurally ordered frameworks might be an even greater challenge than the Ru- and Rh-analogues studied herein. However, the results presented in **Study V** on the right choice of PW precursor might be applicable to these even heavier elements as well.

2.3.6 The Ru-HKUST-1 Analogues

The Ru-HKUST-1 analogues are the central motif of this thesis. Therefore, this chapter should provide a concise overview on the structural peculiarities, the challenging synthesis, the special role of defects in this MOF system and their resultant characterization, modification *via* defect-engineering and exploitation exemplified on several catalytic test reactions. The topics of molecular PW complexes, their interconnection into assemblies of higher dimensionality, the chemistry of metal-organic frameworks including synthesis approaches, the role of defects, and the HKUST-1 system were already introduced in the last chapters. To reduce redundancy, this chapter will just briefly return to those aspects giving reference to earlier chapters. The chemical background of some of the test reactions was issued in **chapter 2.3.4** (page 45 ff). Note, that this literature chapter on Ru is also on behalf of the Rh analogue since the latter has not been described in literature prior to the works performed herein. However, significant attention was paid to the similarities and differences between Ru and Rh in **Study II, III and IV** within this thesis.

Mixed-Valent Ru-HKUST-1

In contrast to most of the other HKUST-1 analogues, for instance comprising metals like Zn, Cu, Mo or Sr and Ba, there are two different isostructural analogues of Ru-HKUST-1 depending on the oxidation state. As introduced for molecular PWs (see **chapter 2.1.1**, page 6ff), mainly two stable oxidation states are synthetically relevant. The same holds true for the MOF systems: The mixed-valence $Ru^{II,III}$-HKUST-1 and the univalent $Ru^{II,II}$-HKUST-1. In the air-stable mixed-valence system, there are 50% of the available axial OMS occupied by the additional counter ions acetate or chloride. A mixture of both anions is present in the material resulting from modulated synthesis and from the chosen diruthenium tetraacetate chloride precursor which was used following the CSA. The synthesis of both MOF systems will be described in the next paragraph but one. In literature, the mixed-valence Ru-HKUST-1 was intensively studied while the univalent system did not draw much attention yet.

In 2011, a ruthenium-based MOF of the HKUST-1 structure type was first described by *Olesia Kozachuk*, *Roland Fischer* and co-workers.[175] This first report investigated the solvothermal growth of the Ru-MOF as thin films on alumina or silica supports. Since the synthesis was conducted using simple $RuCl_3$ in an autoclave with the support being present, neither the CSA was applied nor any control on thin film growth was present at that time. However, crystalline phases of HKUST-1 type deposited on the supporting surfaces with accessible porosity. PXRD, XPS and magnetic susceptibility measurements served for a first structural and electronic assessment of the mixed-valency within the Ru-HKUST-1. In 2013, the CSA and the solvothermal method were utilized to grow the bulk MOF without any support. A combination of experimental and theoretical methods was used for a more detailed characterization of the material. In this regard, PXRD, XPS and (mid and far) FT-IR measurements were supplemented by the CO probe IR-spectroscopy (surface-ligated IR: SLIR) to assess the oxidation states and presence of OMS within the materials more sophisticatedly. The identity of two emerging CO species bound to the framework was investigated with the assist of theoretical DFT calculations on model compounds revealing a rather complex picture of the materials.

In 2014, an elaborated study on defect-engineering was reported and the respective pristine and DE-materials were investigated in terms of sorption and catalytic properties.[235] The utilization of the (truncated) mixed-linker approach doping the synthesis with 3,5-pyridine dicarboxylic acid (H_2PYDC) resulted in DE-Ru-MOF samples. The authors found that PYDC was equally incorporated as BTC giving mixed-linker solid-solutions. The absence of the third carboxylate resulted in both the creation of additional OMS and partially reduced $Ru^{\delta+}$ sites. These modified PWs were found responsible for enhanced CO sorption, improved hydride generating ability (HGA, the term was coined in **Study III** of this

thesis), and catalytic alkene hydrogenation activity. Further, there were indications for a dissociative chemisorption reactivity of CO_2 based on the release of CO and FT-IR-based pyridine *N*-oxide bands.[235]

In 2015, the impact of the CSA including the specific PW precursor was studied by *Wenhua Zhang*, the successor of *Olesia Kozachuk* (also appearing as *Olesia Halbherr*) within the *Fischer* group.[173] There was not only variation of the equatorial precursor carboxylates comparing acetate with the sterically bulkier pivalate (2,2-dimethyl propionate), but also variation of the axial counterion. In this regard, the strongly coordinating Cl^- was compared with weakly coordinating BF_4^- or BPh_4^- counterions. Interestingly, the use of both sterically more demanding carboxylates as well as weakly or even non-coordinating axial counterions was found beneficial for the Ru-MOF formation with higher structural order. However, exclusive assignment to the sterics or coordinating nature of the anions is not possible from this study since the availability of the PW precursor during synthesis has an additional impact on the MOF formation. In contrast to the badly soluble 1-D coordination polymer of $Ru_2(OAc)_4Cl$ comprising both ligand types acetate and chloride, the other investigated precursors namely $[Ru_2(OPiv)_4(H_2O)Cl](MeOH)$, $[Ru_2(OAc)_4(THF)_2](BF_4)$, $[Ru_2(OAc)_4(H_2O)_2](BPh_4)$ consist of isolated, well-soluble PWs. Thus, the impact of the precursors' solubility might outweigh the influence of carboxylate or counterion.[173]

In 2016, a more detailed investigation on the mixed-linker DE strategy was reported.[236] In this follow-up study, an expanded series of isophthalic acid (IPA) derivatives with different substituents in 5-position was used. Parent isophthalic acid, the 5-bromo, 5-amino and 5-hydroxy isophthalic acids were used. A sophisticated set of analytical techniques was applied to study the related materials. Besides standard techniques such as PXRD, FT-IR, BET nitrogen sorption experiments, acid-digested dissolution ^{1}H-NMR and TGA, more advanced measurements like XANES, XPS and CO probe FT-IR spectroscopy in ultra-high vacuum (UHV) served for an in-depth understanding. The findings support the presence of two types of defects being formed within the materials: Modified PWs and missing-node defects. Modified PWs are predominantly formed for low DL doping amounts and with DLs that contain *Lewis* basic functional groups in 5-position (such as PYDC or 5-OH-IPA, 5-NH_2-IPA). A change in preference is observed for higher DL amounts and non-coordinating DLs such as pristine unfunctionalized IPA where preferably missing-node defects occur. In any case, both defect types can occur concomitantly giving a rather complicated overall picture of the materials. The usability of DE-Ru-HKUST-1 samples was further examined in two catalytic test reactions: the dimerization of ethylene and the *Lewis* acid catalysed *Paal-Knorr* pyrrole synthesis with DE-MOFs having superior activity compared to the pristine "defect-free" Ru-HKUST-1.[236]

Moreover, the first report of the univalent Ru-HKUST-1 featuring a +II / +II oxidation state was published in the same year and shall be described in the next subchapter.[331]

Univalent Ru-HKUST-1

Again, following the concepts of CSA and modulated synthesis, a novel, univalent Ru-HKUST-1 was first described in 2016.[331] Diruthenium tetraacetate was used as preformed PW precursor already providing the targeted $Ru^{II,II}$ oxidation state. All reaction steps, materials manipulations, and storage had to be conducted under inert atmosphere, consequently. Despite these increased synthetic efforts, the univalent MOF is structurally very promising as it does not comprise additional counter ions for charge compensation. Both OMSs per PW are available upon MOF activation and can be used for diverse applications. In addition, the BET surface area of 1371 m^2g^{-1} was considerably higher compared to the mixed-valence analogue (704-1180 m^2g^{-1}).[331] Interestingly, already this earlier report recognized the significant amounts of acetate incorporated within the material. Usual solvent exchange and MOF activation did not facilitate its removal and thus, acetate must have been present as framework-inherent component. It was assumed that it is trapped in the form of modulator-induced defects equatorially bound to the PWs resulting from incomplete ligand substitution by BTC. This open question was later

addressed and solved by **Study II** of this thesis. Because of these vast acetate amounts residing at equatorial sites, the respective materials are of poor crystallinity. This is even more dramatic for the univalent Ru-MOF although the mixed-valence Ru-MOF already has just moderate structural order. The improvement of structural order in the univalent $Ru^{II,II}$-HKUST-1 was subject of **Study V** of this thesis investigating the role of several PW precursors (mainly benzoate derivatives) on the evolution of structurally ordered materials.

Synthesis of the Ru-HKUST-1 Analogues

Both Ru-HKUST-1 analogues, the mixed-valent and the univalent one, are synthetically accessible via the same procedure. The PGM-MOFs require rather harsh conditions for the self-assembly to proceed. However, their precious metallic nature comes along with the tendency for reduction to M^0 species withdrawing active metal from the synthesis. Thus, reduction should be avoided by any means. The synthesis is conducted in steel-autoclaves with 20mL PTFE inliners at 150-160 °C for 3 d reaction time. Following the CSA, either $[Ru_2(OAc)_4Cl]$ or $[Ru_2(OAc)_4]$ are used in 0.36 mmol reaction scale. The ideal molar ratio of 2:3 was used for the addition of trimesic acid. Both reagents were dissolved in 0.7 mL acetic acid and 4 mL water, assisted by a short ultrasound treatment. Note, that dissolution of the polymeric $[Ru_2(OAc)_4Cl]$ was incomplete prior to the reaction. The PTFE inliner and steel autoclave are tightly closed, and the mixtures are exposed to the abovementioned reaction conditions. Note, that all preparations related with the synthesis of the air-sensitive $Ru^{II,II}$-MOF are carried out under exclusion from oxygen. To do so, Ar-filled gloveboxes (either dry, or under moist atmosphere) and standard *Schlenk* techniques were applied. In the course of this thesis, these syntheses were upscaled by a factor of two. To avoid metal formation occurring as side reaction, the reaction temperature was set to 150 °C. To account for the higher reagent amounts, the reaction time was increased to 4 d consequently.

The incorporation of high acetate amounts as stated above initiated two independent developments within this thesis. On the one hand, control on the defect formation on the other hand exploitation of these defects was the goal. A reduced defectiveness was targeted by variation of the PW precursor for the univalent diruthenium tetracarboxylate precursors. This strategy is outlined in **Study V**. The second strategy, the utilization of the modulator-based defects, present in the materials, inspired us to establish a method for the controlled thermal defect-engineering (TDE) to (selectively) remove these acetate defects. The generation of additional OMS having reduced metal oxidation states was resulting therefrom. TDE-MOFs were subject in **Study III** and **IV**, respectively.

3 Objective

The high mechanical, chemical and thermal stability arising from 3-D crosslinked SBUs and their kinetically inert and thus, robust coordination bonds fosters the PGM analogues of the iconic HKUST-1 structure promising candidates for catalytic purposes. As heterogeneous catalysts, they offer high permanent porosity, defined single active sites with regular OMSs and the general PGM-inherent catalytic properties. The previous works on this system have achieved progress regarding synthetic access, basic characterization and defect-engineering following the mixed-linker strategy to explore the potential of further manipulating their properties. Some catalytic test reactions served to underline their utility. Despite these achievements and advances on this system, many questions remained unsolved: Regarding the naturally high acetate content of Ru-HKUST-1s:

Where is the acetate located? Is it merely physisorbed within the pores or does it rather represent a framework inherent component strongly bound to the metal sites? How can these acetate defects be avoided, or can we utilize them?

Until the time these PhD works were started, ruthenium was the first and only PGM of the HKUST-1 series to be reported upon. However, other PGMs form PW complexes, too. Hence, questions arose like:

Can we expand the HKUST-1 family to other members of the PGMs, for instance rhodium? Which synthetic adoptions must be made for their synthesis? Are the concepts of modulated synthesis and CSA transferrable? Is the pronounced defectiveness of Ru-HKUST-1 element specific or is it rather a common symptom of PGM complex chemistry in general? Can we deduce more general insights to PGM-based MOFs regarding redox-flexibility, defect-incorporation, or catalytic potential without the limitation to one particular metal or structure type?

When turning to defective MOFs, of course, the applicability of defect-engineering kept attracting our attention. Low reproducibility and fluctuating sample quality from batch to batch complicated the synthesis and comparability of pristine and DE-MOFs obtained by *de novo* methods. In this regard, a recent report on the thermal annealing of Ru-HKUST-1 for defect creation caught our attention.[252] In this report, the *de novo* mixed-linker approach and postsynthetic thermal defect-creation were largely comparable both enhancing the performance in ethylene dimerization catalysis. Although representing a strong inspiration for this thesis, the reported procedure was hardly reproducible and suffered from technical limitations with respect to process control. Driving questions were:

How can we design a process for a controlled thermal defect-engineering (TDE) to precisely obtain samples with predefined defectiveness? Can we trap metastable modified PWs within an exothermal decomposition process without running into complete structural collapse as final destination of the thermal treatment? How do structural order, porosity and sample homogeneity evolve during such treatment? What are the specific decomposition events? What is the impact of the specific metal? Does Rh allow for a similarly versatile defect-tolerance upon DE?

The research performed in this thesis is driven to provide solutions for these questions and the obtained results are presented in the following chapter.

4 Results

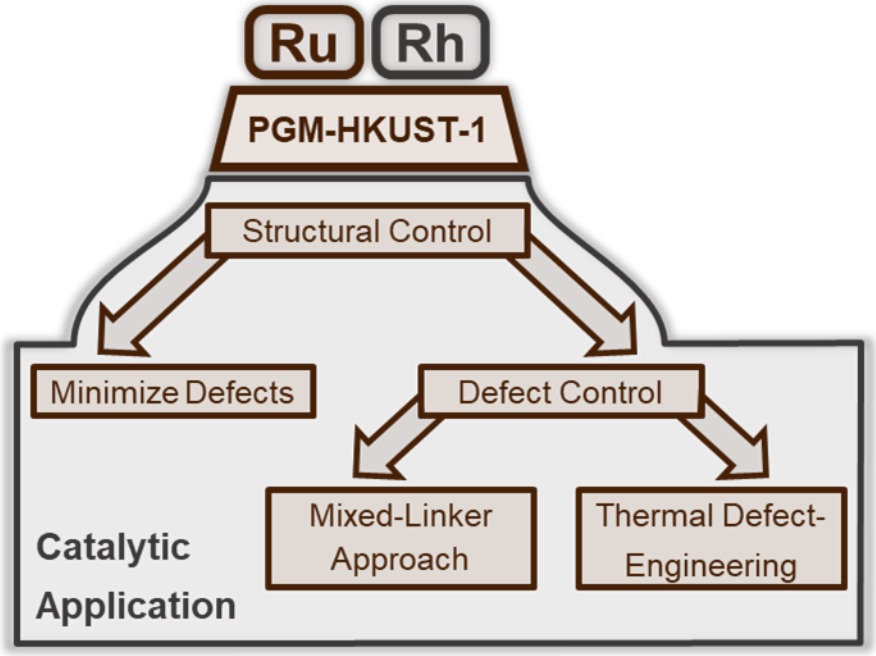

*Figure 19: Summary of the results presented in this thesis. The PGM-HKUST-1 analogues of Ru and Rh were studied. After their successful synthesis and characterization (**Study II**), a clear focus was set on structural control and its implications on catalysis. This is manifested in defect minimization (**Study V**), and defect control. The latter was achieved through the defect engineering strategies of the mixed-linker approach (**Study I**) or through a novel thermal defect-engineering (**Study III & IV**).*

4.1 Study I

Defect-Engineered Ruthenium MOFs as Versatile Heterogeneous Hydrogenation Catalysts

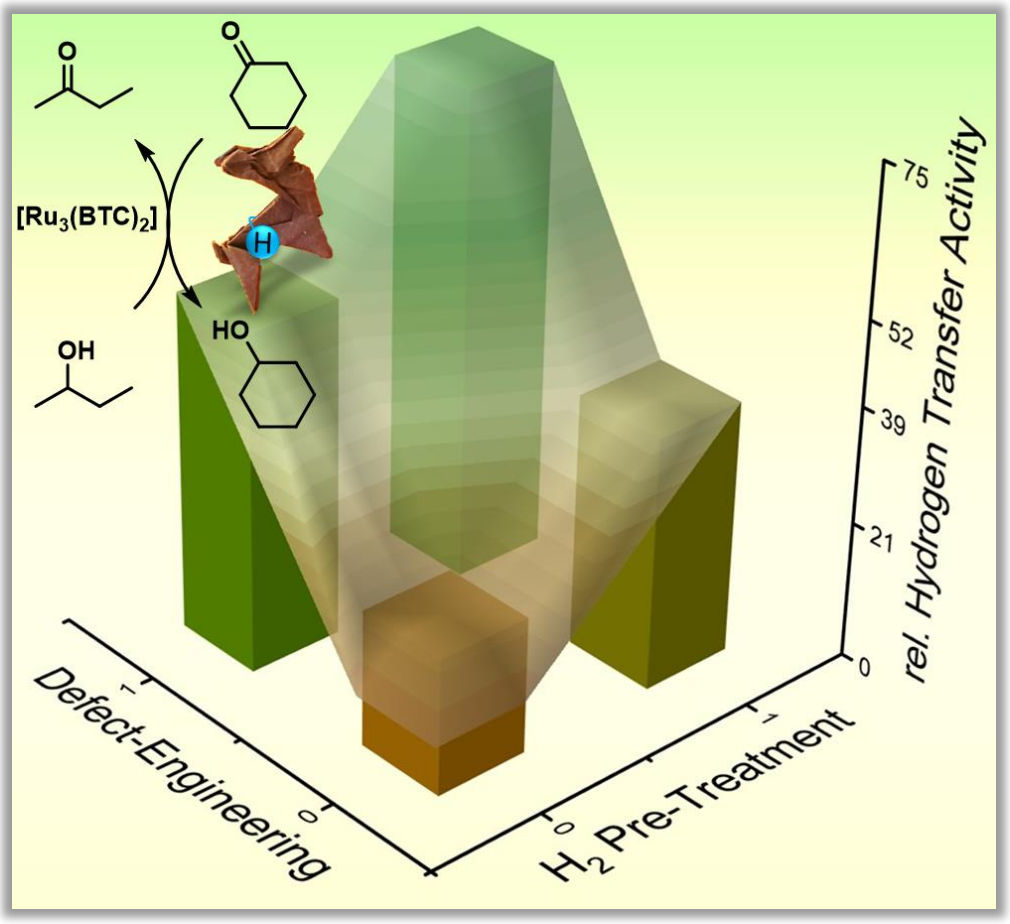

Defect-Engineered Ruthenium MOFs as Versatile Heterogeneous Hydrogenation Catalysts

Konstantin Epp, Ignacio Luz, Olesia Kozachuk, Wenhua Zhang, Werner R. Heinz, Anastasia Rapeyko, Francesc X. Llabrés i Xamena and Roland A. Fischer

ChemCatChem **2020**, 12, 1720 – 1725.

In this study, defect-engineering of mixed-valent $Ru^{II,III}$-HKUST-1 was performed according to previous reports and the impact on two different catalytic hydrogenation reactions was investigated. Based on the former works of the group, the mixed-linker approach using PYDC as defective linker for *de novo* defect-engineering was applied. Besides this, a postsynthetic hydrogen treatment at elevated temperatures was applied. In summary, both measures increased the catalytic performance of the isomerization of allylic alcohols to saturated ketones and in the MPV reaction. The highest catalytic activity was found for the DE-MOF with additional hydrogen pretreatment. Our results underline the beneficial impact of DE and indicate yet unresolved metal hydride species being responsible for the catalytic hydrogenation activity.

ChemPubSoc Europe

DOI: 10.1002/cctc.201902079

CHEMCATCHEM Full Papers

Defect-Engineered Ruthenium MOFs as Versatile Heterogeneous Hydrogenation Catalysts

Konstantin Epp,[a] Ignacio Luz,[b, c] Werner R. Heinz,[a] Anastasia Rapeyko,[b] Francesc X. Llabrés i Xamena,*[b] and Roland A. Fischer*[a]

Ruthenium MOF $[Ru_3(BTC)_2Y_y]\cdot G_g$ (BTC = benzene-1,3,5-tricarboxylate; Y = counter ions = Cl^-, OH^-, OAc^-; G = guest molecules = HOAc, H_2O) is modified *via* a mixed-linker approach, using mixtures of BTC and pyridine-3,5-dicarboxylate (PYDC) linkers, triggering structural defects at the distinct Ru_2 paddlewheel (PW) nodes. This defect-engineering leads to enhanced catalytic properties due to the formation of partially reduced Ru_2-nodes. Application of a hydrogen pre-treatment protocol to the Ru–MOFs, leads to a further boost in catalytic activity. We study the benefits of (1) defect engineering and (2) hydrogen pre-treatment on the catalytic activity of Ru–MOFs in the *Meerwein-Ponndorf-Verley* reaction and the isomerization of allylic alcohols to saturated ketones. Simple solvent washing could not avoid catalyst deactivation during recycling for the latter reaction, while hydrogen treatment prior to each catalytic run proved to facilitate materials recyclability with constant activity over five runs.

Introduction

Modifications at the organic linker in metal-organic frameworks (MOFs) allows for both changes in structure, physical properties and chemical reactivity of the materials.[1] Concerning the reactivity of MOFs in catalysis, changes of the coordination environment of the secondary building unit (SBU), i.e. free coordination sites at the metal, may drastically influence their catalytic properties.[2] A common strategy in creating defective MOFs is to use mixed-linkers in the *de-novo* solvothermal synthesis,[3,4] whereby in parallel to the introduction of the regular linker, stoichiometric amounts of a "defect-generating linker" featuring reduced connectivity can be incorporated into the framework by means of a co-polymerization process.[3] Thus, unsaturated metal sites are generated, exhibiting diverse catalytic properties which are not present in the parent frameworks. In our previous work, pyridine-3,5-dicarboxylic acid (PYDC) was incorporated into the Ru analogue of HKUST-1, $[Ru_3(BTC)_2Y_y]\cdot G_g$ (**1**) (BTC = benzene-1,3,5-tricarboxylate ; Y = counter ions = Cl^-, OH^-, OAc^-; G = guest molecules = AcOH, H_2O) resulting in material $[Ru_3(BTC)_{2-x}(PYDC)_xY_y]\cdot G_g$ (**D**).[5,6] Therein, the catalytic properties of defect-engineered Ru–MOFs were evaluated in the hydrogenation of olefins, whereas **D** outperformed their untreated parent counterpart **1**. This was explained by the formation of partially reduced Ru-centers (modified PWs) which are undercoordinated due to the incorporation of ditopic carboxylate PYDC linkers (instead of tritopic carboxylates as in the case of BTC) and thus, better accessible showing enhanced catalytic activity when compared to fully coordinated Ru-centers present in the "defect-free" Ru–MOFs (see Figure 1). Interestingly, a pre-treatment protocol involving the exposure of **1** and **D** to hydrogen atmosphere at ~150 °C leads to superior catalytic activity compared to their non-treated analogues.[7] *In-situ* UHV-FTIR studies (ultra-high vacuum *Fourier* transformed infrared spectroscopy), identified Ru–H species at the mixed-valent $Ru_2^{II,III}$ paddlewheels as a key-intermediate, which formation is favored by the defectiveness of the structure present in defect-engineered Ru–MOF. These results broadened our understanding on how defective structure, hydrogen pre-treatment and catalytic reactivity are interlinked and motivated us to study the particular catalytic reactivity of defect-engineered PYDC-containing Ru–MOFs in more detail. Thus, we herein present our investigations regarding the effects of PYDC incorporation into Ru–MOFs on the catalytic activity demonstrated in both the MPV (*Meerwein-Ponndorf-Verley*) reaction and the isomerization of allylic alcohols.

[a] Dr. K. Epp, W. R. Heinz, Prof. R. A. Fischer
Inorganic and Metal-Organic Chemistry
Catalysis Research Center and Department of Chemistry
Technical University of Munich
Ernst-Otto-Fischer-Straße 1
D-85748 Garching bei München (Germany)
E-mail: roland.fischer@tum.de

[b] Dr. I. Luz, A. Rapeyko, Dr. F. X. Llabrés i Xamena
Instituto de Tecnología Química
Consejo Superior de Investigaciones Científicas
Universitat Politècnica de València
Camí de Vera s/n
46022 Valenncia (Spain)
E-mail: fllabres@itq.upv.es

[c] Dr. I. Luz
Current address: RTI International
Research Triangle Park
Durham NC-27709-2194 (USA)

Supporting information for this article is available on the WWW under https://doi.org/10.1002/cctc.201902079

ChemPubSoc Europe

CHEMCATCHEM Full Papers

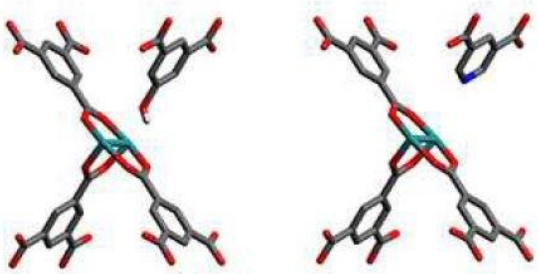

Figure 1. Illustration of an ideal Ru paddlewheel (left) ligated by trimesate molecules, compared to a defect-engineered Ru paddlewheel (modified PW) with incorporated PYDC as defect-generating linker (Ru: teal, O: red, N: blue, C: grey, H was omitted for clarity).

Results and Discussion

Synthesis and Characterization

In accordance to our previous synthetic protocols, in this study we synthesized defect-engineered Ru–MOF **D30** with a 30% PYDC feeding ratio.[6] The incorporation of PYDC was verified by ^{1}H NMR of acid digested samples (supporting information, S1) in combination with elemental analysis (supporting information, S2).

Due to the fact that no *N*-containing solvent or reagents were used in the synthesis, the *N*-content found in the samples can be associated with the incorporated PYDC. Both data are in good agreement to the suggested sum formula of **D30** $[Ru_3(BTC)_{1.4}(pydc)_{0.6}Cl_x]\cdot AcOH_{2.65}$, showing that slightly less PYDC than the feeding ratio was incorporated in the final solid. **D30** sample is isoreticular to parent Ru–MOF, as it is indicated by powder X-ray diffraction (PXRD) (see supporting information, S3). Moreover, the structural integrity is not significantly affected by the doping, showing the tolerance of the framework to the incorporation of PYDC. Microporous **D30** sample shows a type I isotherm (see supporting information, S4) with BET (*Brunauer, Emmett, Teller*) surface area of 647 m^2/g. The thermal stability was investigated by thermal gravimetric analysis (TGA), indicating moderate thermal stability of the defect-engineered sample up to ~220 °C, which is in the same region as their "defect free" parent analogue **1** (see supporting information, S5). **D30** reveals an additional decomposition event which is close to the decomposition temperature of BTC (~220 °C). Most likely, this decomposition step can be associated with the decomposition of PYDC, since both compounds have similar decomposition temperatures. Based on the data obtained by TGA, a BTC to PYDC ratio of 3:1 can be calculated which is in good agreement with the feeding ratios and elemental analysis, giving evidence of the successful incorporation of PYDC. As a crucial procedure to trigger the hydrogenation reactivity of **D30**, the sample was treated with molecular H_2 at elevated temperatures (150 °C), which leads to the desired formation of Ru–H, as previously reported by our group.[6] Following on from this interesting catalytic behavior, we tested parent and defect-engineered Ru–MOFs in two kinds of heterogeneously transition-metal-catalyzed hydrogen-transfer reactions, namely the reduction of carbonyl compounds to alcohols with secondary alcohols as the hydrogen donor (MPV, *Meerwein-Ponndorf-Verley* reaction) and the isomerization of allylic alcohols to saturated ketones. Herein, we want to highlight the H_2 pre-treatment as a key tool of post-synthetic modification of the underlying Ru–MOFs/PYDC-DEMOFs and that the reactivity of PYDC-DEMOFs can be transferred also to other reactions types.

Catalytic tests

Hydrogen transfer reactions

Firstly, we investigated Ru–MOFs in the MPV reaction of cyclohexanone to give cyclohexanol, whereby 2-butanol acts as a hydrogen donor source which formally transfers hydrogen to the unsaturated substrate (ketone). In a typical reaction 10 mg of ketone (0.1 mmol), 5 mg of Ru–MOF catalyst (17 mol% of Ru), and 1 mL of alcohol (ca. 11 eq) were placed into a closed pressured reactor under 2 bar of N_2 at 120 °C. In all the reactions described below, cyclohexanol was the only product detected. Therefore, full selectivity was observed in all cases. Figure 2 shows the time-yield plots obtained for **D30** (30% PYDC) and "defect free" **1** Ru–MOF compounds, both before and after H_2 pre-treatment at 150 °C. The resulting data reveal the higher catalytic activity for **D30** (30% PYDC) compared to **1** the "defect free" Ru–MOF counterpart, providing evidence of the beneficial contribution of the incorporated PYDC defects on the catalytic activity of the system. In particular, the yield when **D30** is used as a catalyst increases from 16 to 43% compared to parent MOF **1** after 2.5 h reaction time.

H_2 pre-treatment causes a further positive impact on the catalytic activity of parent as well as defective Ru–MOFs. The

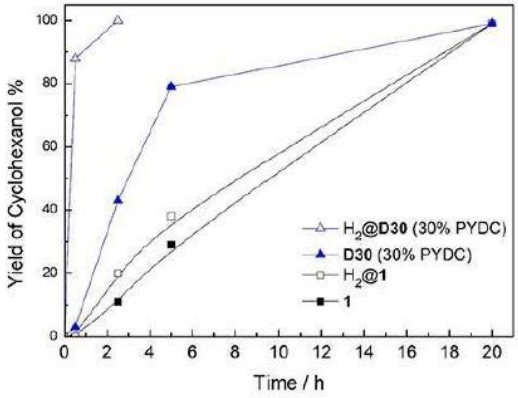

Figure 2. Time-yield plot of MPV reaction. Comparison of the reactivity of Ru–MOF/PYDC DEMOF (closed symbols) and their H_2 pre-treated analogues (open symbols). The number in the brackets indicate the feeding ratios of PYDC into parent Ru–MOF.

ChemPubSoc Europe

CHEMCATCHEM Full Papers

boost in catalytic activity is much more pronounced in H_2@D30 (hydrogen pre-treated D30) reaching 99% yield after 2.5 hthe non-treated analog D30. Due to introduced point defects like "missing linker", "missing node" and modified PW" within the framework of D30, the probability of H_2 to access Ru_2-nodes should be higher than for "defect free" Ru–MOFs, where only modulator-induced defects are present.[8] Therefore, the formation of Ru-H species is supposed to be more likely. Based on the drastic improvement of the activity of the H_2 pre-treated samples, the reaction mechanism shown in Scheme 1 can be assumed, usually referred to as "hydridic route".[9] Unlike classical MPV reactions promoted by aluminum and other non-transition metals involving a direct hydrogen transfer from the alcohol to the ketone *via* a cyclic transition state, the hydridic route implies the active participation of Ru–H species similar to other hydride-catalyzed reactions like the dimerization of olefins.[7] According to this reaction mechanism, a catalytically active ruthenium hydride species, Ru–H, is initially formed by the abstraction of the α-hydrogen of 2-butanol, followed by the MPV-type reduction of cyclohexanone to cyclohexanol. It is thus evident that H_2-pretreated Ru–MOFs will show a higher catalytic activity as compared to the corresponding non-treated compounds, since we already demonstrated that Ru–H species are indeed formed during H_2 pretreatment.[6]

A number of ruthenium complexes are well known to catalyze hydrogen transfer reactions,[9] and their activity can be significantly boosted by the addition of a small amount of base.[10] Note in this sense that the PYDC linkers present in D30 offer a basic pyridyl-N atom in the proximity of the reactive Ru centers which may have a similar enhancing effect as an added external base. This would easily explain the large difference in catalytic activity observed for compounds 1 and D30 (see Figure 2). Secondly, it was investigated if the presented Ru–H chemistry of PYDC-DEMOFs is transferable to other related reactions, namely the transfer hydrogenation of allylic alcohols to the corresponding saturated ketones. Conversion of allylic alcohols into saturated ketones is usually carried out in two steps: hydrogenation of the C=C bonds followed by dehydrogenation of the alcohol, which usually requires further protection and deprotection steps. Thus, the one-pot redox isomerization evaluated here represents an attractive alternative (see Scheme 2).[11]

This reaction can be considered as an intramolecular hydrogen transfer reaction, in which hydrogen is transferred from the alcohol to the C=C bond. Isomerization of allylic alcohols is usually carried out in the presence of additives, such as bases or hydrogen acceptors, to promote the reaction. Various metals from groups 8, 9, and 10 (including Ru) are known to catalyze this reaction.[12] As a model reaction to evaluate the activity of Ru–MOFs, we studied the isomerization of 1-octene-3-ol to octane-3-one in the presence of 2-propanol acting as a solvent as well as a hydrogen donor. In a typical reaction, 40 mg of the allylic alcohol (1-octene-3-ol, *ca.* 0.3 mmol) 2 mg of Ru–MOF catalyst (2 mol% of Ru), and 1 mL of *i*-PrOH (ca. 13 eq) were placed into a closed pressured reactor under 2 bar of N_2 at 120 °C. The results obtained are shown in Figure 3.

Similar to what was observed in the MPV reaction, both, the introduction of defect-generating PYDC linkers as well as the H_2 pre-treatment result in superior catalytic activity compared to defect-free and non-treated parent Ru–MOFs (Figure 3). Defect-

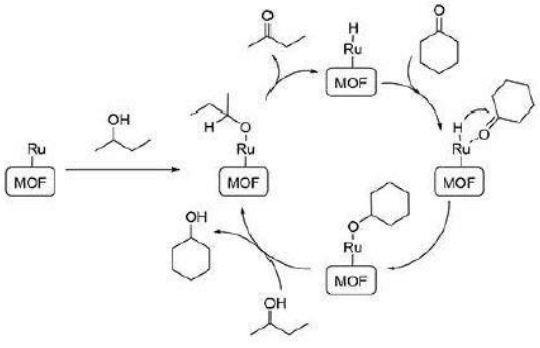

Scheme 1. Proposed reaction mechanism for the MPV reduction of cyclohexanone through a "hydridic route".

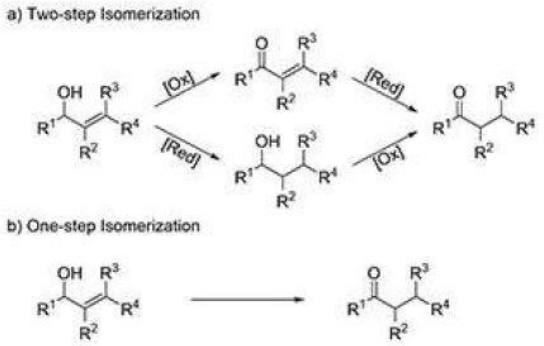

Scheme 2. a) Two step and b) one step isomerization of allylic alcohols.

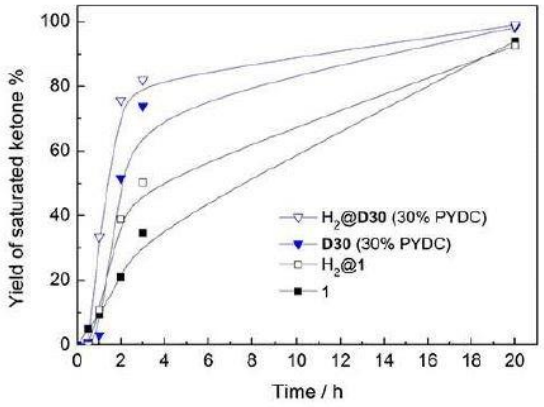

Figure 3. Yield-time plot of catalytic transfer hydrogenation of 1-octene-3-ol to octane-3-one using different Ru catalysts. Comparison between the reactivity of Ru–MOF/PYDC DEMOF (closed symbols) and their H_2 pre-treated analogues (open symbols).

ChemPubSoc Europe

CHEMCATCHEM Full Papers

engineering boosted the catalytic activity of parent Ru–MOF **1** by a factor of about 2.5, namely, from 21 to 52% (**D30**) after 2 h reaction time. Upon H_2 pre-treatment, we observed a 1.9-fold increase in yield (after 2 h reaction time) for **1** (yield increased from 21% to 39%) and by a factor of 1.4 for **D30** (yield from 52% to 75%), respectively. Hence, both strategies for catalyst optimization exhibit a cumulative increase by a factor of roughly 3.6. As it was discussed in the MPV reaction, the higher catalytic activity of the H_2 pre-treated samples and DEMOFs can possibly be explained by the higher amount of incorporated structural point defects resulting in a preferential formation of Ru–H species reasoned by the lower coordination number at the Ru-nodes. As already mentioned above for the MPV reaction, the formation of ruthenium hydride species is a key step in the transfer hydrogenation reaction leading to the isomerization of allylic alcohols to the corresponding saturated ketone. In analogy to the previous report by *Yamaguchi et al.* using $Ru(OH)_x/Al_2O_3$ as a heterogeneous catalyst,[13] the overall mechanism for the allylic alcohol isomerization is depicted in Scheme 3. According to the above mechanism, adsorption of the allylic alcohol onto the Ru sites first gives rise to the corresponding alcoholate, followed by the formation of the Ru–H hydride key species and α,β-unsaturated ketone. Then, hydride transfer to the unsaturated ketone gives rise to the corresponding enolate, which is finally desorbed as the saturated ketone upon adsorption of a new allylic alcohol molecule. In order to verify the heterogeneous nature of the catalyst, and to exclude leaching of Ru-species, a hot filtration test has been conducted at low conversion rates showing no further reaction progress as soon as the catalyst was filtered off (see supporting information, S6).

Recyclability

We selected the isomerization of the allylic alcohol 1-octene-3-ol as a test reaction to evaluate the stability and reusability of the catalysts. To this end, the reaction was first carried out for 2 h following the same procedure as described above. At this point, the catalysts were recovered by filtration, thoroughly washed with 2-butanol and dried at room temperature. Catalysts **1** and **D30** were directly used on consecutive catalytic cycles, while H_2 pre-treated catalysts H_2@**1** and H_2@**D30** were submitted again to a hydrogenation treatment with H_2 at 150°C prior to use. The results obtained for five consecutive catalytic cycles are shown in Figure 4. As can be seen, the catalytic activity (*viz.*, yield of saturated ketone obtained after 2 h of reaction) decreases progressively with the use in the case of catalysts **1** and **D30**. This is most likely due to the progressive accumulation of adsorbed species on the solid catalyst like products from previous runs that are not completely removed during washing. This results in an increasing poisoning of the catalytically active sites. Thus, an almost complete loss of activity of the catalysts is observed after already three catalytic cycles. Conversely, catalysts deactivation is not observed for the H_2 pre-treated catalysts H_2@**1** and H_2@**D30**. This H_2 pre-treatment of the catalyst between two consecutive catalytic cycles proves to be more effective to remove adsorbed species than solvent washing alone, which most likely explains the preservation of the catalytic activity of these catalysts for at least five consecutive catalytic cycles. Powder X-ray diffraction measurements and TEM images of the collected solids indicate preserved crystallinity (see supporting information Figure S8–9) and particle morphology and size.

Conclusions

In summary, we demonstrate defect-engineering as an effective synthetic tool for the introduction of structural point defects into ruthenium MOFs and highlight their superior catalytic activity compared to their parent analogues. Additionally, we show that a hydrogen pre-treatment procedure has a strong impact to further boost the catalytic activity of Ru–MOFs which we demonstrated in the MPV reaction (*Meerwein-Ponndorf-*

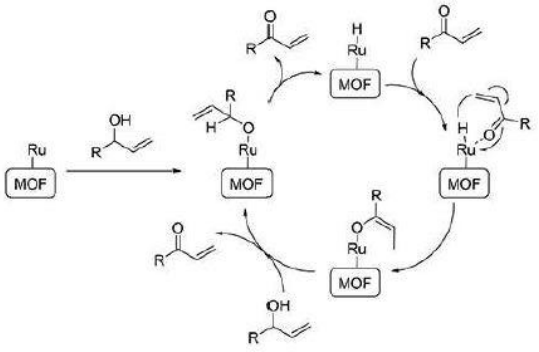

Scheme 3. Reaction mechanism for the isomerization of allylic alcohols to saturated ketones over Ru–MOFs.

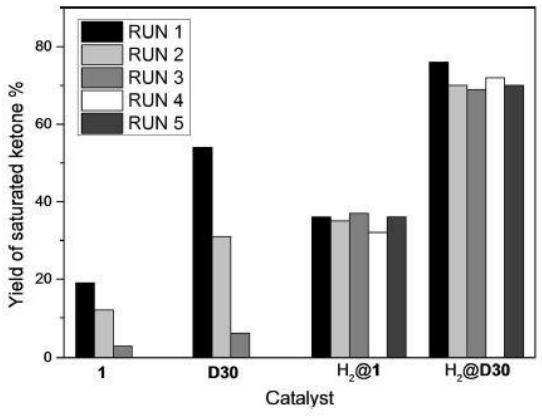

Figure 4. Recyclability tests of the Ru-BTC catalysts, showing the yield of saturated ketone obtained after 2 h of reaction with solvent wash (**1** and **D30**) or repeated activation *via* H_2 pre-treatment (H_2@**1** and H_2@**D30**).

ChemPubSoc Europe

CHEMCATCHEM Full Papers

Verley) and the isomerization of allylic alcohols. A similar beneficial effect of the hydrogen pretreatment of the Ru–MOFs was already described for the dimerization of ethylene by *Agirrezabal-Telleria et al.* and the hydrogenation of olefins in our previous report.[5,7] Moreover, the presence of a basic pyridyl-N atom in the PYDC linkers allowed us to carry out the hydrogen transfer reactions under base free conditions with excellent results and given recyclability.

Experimental Section

Materials and Synthesis

$RuCl_3 \cdot xH_2O$, LiCl, benzene-1,3,5-tricarboxylic acid (H_3BTC), and pyridine-3,5-dicarboxylic acid (PYDC) and all solvents [CH_3COOH, H_2O, CH_3OH, acetic anhydride, acetone, hexane, tetrahydrofuran, toluene, EtOH, acetonitrile and MeOH] were used as commercially received unless otherwise noted.

Synthesis

$[Ru_2(OOCCH_3)_4Cl]$

Tetraaceto-diruthenium (+II, +III) chloride was synthesized following a slightly modified synthesis description which was introduced by *Mitchel et al.*[14] 0.5 g $RuCl_3 \cdot xH_2O$ (~2.4 mmol), 0.5 g LiCl (12 mmol) and 3.5 mL acetic anhydride was mixed with 17.5 mL acetic acid (99.5 %) in a 50 mL preheated Schlenk flask. The reaction mixture was stirred and refluxed for 24 h at 140 °C in argon atmosphere. The black suspension turns brown/red after a few hours. Afterwards, it was allowed to cool down to room temperature and the precipitated brown/red solid was filtered (membrane filter) and washed manually using 3×acetone (≥ 99.8 %). Yield: 0.35 g (62 %). ^{1}H NMR δ (298 K, 200 MHz, DMSO-d_6) 1.9 (s, 3H, $-CH_3$) ppm.

RuMOF, $[Ru_3(BTC)_2Y_y] \cdot G_g$ (1)

0.17 g $Ru_2(OOCCH_3)_4Cl$ (1.5 eq.; 0.36 mmol) and 0.1 g H_3BTC (benzene-1,3,5-tricarboxylic acid) (2 eq.; 0.48 mmol) were dispersed in 4 mL H_2O (HPLC grade) and 0.7 mL glacial acetic acid, transferred to a PTFE vessel, which was sealed with a stainless steel autoclave and placed in a preheated oven at 150 °C for 72 h. No temperature-controlled program was applied. The reaction mixture was allowed to cool down to r.t. and the liquid was separated from the solid by centrifugation (7830 rpm, 15–20 min). The suspension was decanted and sonicated for 10 min and washed twice with ~20 mL H_2O (HPLC grade) and acetone with subsequent centrifugation (7830 rpm, 15–20 min). The dark brown solid was dried in vacuum (~10^{-3} mbar) and was digested in 4 droplets DCl and around 0.5 ml DMSO-d_6 for ^{1}H NMR measurement. ^{1}H NMR δ (298 K, 200 MHz, DMSO-d_6) 8.6 (s, 3H, C–H_{Ar}) ppm, 1.9 (s, 3H, $-CH_3$).

$[Ru_3(BTC)_{2-x}(PYDC)_xY_y] \cdot G_g$, (D30)

The defect-engineered Ru–MOF was synthesized in accordance to the synthesis for the parent Ru–MOF, besides adding specific amounts of pydrine-3,5-dicarboxylic acid (PYDC) into the reaction solution. In the synthesis of **D30**, 1.4 eq. of H_3BTC (71 mg, 0.34 mmol) and 0.6 eq. PYDC (24 mg, 0.14 mmol) were dispersed in 4 mL H_2O (HPLC grade) and 0.7 mL glacial acetic acid. Afterwards, the mixture was transferred to a PTFE vessel, which was sealed with a stainless steel autoclave and placed in a preheated oven at 150 °C for 72 h. No temperature-controlled program was applied. The reaction mixture was allowed to cool down to r.t. and the liquid was separated from the solid by centrifugation (7830 rpm, 15–20 min). The suspension was decanted and sonicated for 10 min and washed twice with ~20 mL H_2O (HPLC grade) and acetone with subsequently centrifugation (7830 rpm, 15–20 min). The black solid was dried in vacuum (~10^{-3} mbar) and was digested in 4 droplets DCl and around 0.5 ml DMSO-d_6 for ^{1}H NMR measurement ^{1}H NMR δ (298 K, 200 MHz, DMSO-d_6) 8.6 (s, 3H, C–H_{Ar}) ppm, 1.9 (s, 3H, $-CH_3$).[6]

Thermogravimetric analysis (TGA)

Thermogravimetric studies were conducted using a Mettler Toledo TGA/SDTA851e apparatus with an applied heating ramp of 10 °K/min under oxidizing conditions in a N_2/O_2 (80/20 %) flow in Al_2O_3 crucibles.

Powder X-ray diffraction (PXRD)

Measurements were performed using *Bragg-Brentano* geometry on a PANalytical CUBIX diffractometer equipped with a PANalytical X'Celerator detector. X-ray Cu Kα radiation ($\lambda1 = 1.5406$ Å, $\lambda2 = 1.5444$ Å, I2/I1 = 0.5) was used for the measurements. Voltage and intensity were 45 kV and 40 mA, respectively. The arm goniometer length was 200 mm, and a variable divergence slit (irradiated area = 2.5 mm) was employed. The measurement range was from 2.0° to 90.0° (2θ), with a step size of 0.040° (2θ) and an acquisition time of 35 seconds per step. The measurement was performed at 298 K, and the sample was rotated during the measurement at 0.5 rps.

N_2-physisorption (BET)

N_2-physisorption measurements were performed on a Micromeritics ASAP 20120 device using N_2 at 77 K. Before the measurement the samples (~100 mg) were degassed for 12 h at 120 °C under dynamic vacuum.

Gas Chromatography (GC)

Gas chromatography measurements were performed on a Agilent Technologies 7890 A with FID (flame ionization detector) using a capillary column HP-5 (5 % phenylmethylpolysiloxane) of 30 m length and 0.32 mm internal diameter as well as BP20(WAX) of 15 m length and 0.32 mm internal diameter as another column. Thereby, the samples were measured in high dilution using volatile organic solvents (usually ethanol or acetone).

Nuclear magnetic resonance (NMR)

Liquid phase ^{1}H-NMR measurements were performed using a Bruker RMN AVANCE (AVANCE III) 300 MHz at 298 K and Bruker Avance DPX-200 spectrometer at 293 K in DCl/DMSO-d_6 for the digested activated MOF samples. Thereby, approximately 5 mg samples were digested in 4 droplets of DCl, placed in an ultrasonic bath for at least 30 min, and 0.7 mL DMSO-d_6 were added. For better digestion, the samples were carefully heated until the solution became clear.

ChemPubSoc Europe

CHEMCATCHEM Full Papers

Acknowledgements

Funding by the Spanish Government is acknowledged through projects MAT2017-82288-C2-1-P and Severo Ochoa (SEV-2016-0683). This project is further funded by the Deutsche Forschungsgemeinschaft grant no. FI-502/32-1 ("DEMOFs"). KE and WRH would like to thank TUM Graduate School and the Gesellschaft Deutscher Chemiker (GDCh) for financial support. KE gratefully acknowledges support from the colleagues Olesia Halbherr (neé Kozachuk) and Wenhua Zhang.

Conflict of Interest

The authors declare no conflict of interest.

Keywords: Metal-Organic Frameworks · defects · ruthenium · Ru-BTC · Ru–MOF · HKUST-1 · Defect-Engineering · MOF catalysis · DEMOF

[1] a) J. Gascon, A. Corma, F. Kapteijn, F. X. Llabres i Xamena, *ACS Catal.* **2014**, *4*, 361–378; b) S. Hasegawa, S. Horike, R. Matsuda, S. Furukawa, K. Mochizuki, Y. Kinoshit, S. Kitagawa, *J. Am. Chem. Soc.* **2007**, *129*, 2607–2614; c) Z. Wang, S. M. Cohen, *Chem. Soc. Rev.* **2009**, *38*, 1315–1329.

[2] a) F. Vermoortele, B. Bueken, G. Le Bars, B. Van de Voorde, M. Vandichel, K. Houthoofd, A. Vimont, M. Daturi, M. Waroquier, V. Van Speybroeck, C. Kirschhock, D. E. De Vos, *J. Am. Chem. Soc.* **2013**, *135*, 11465–11468; b) J. Zheng, J. Ye, M. A. Ortuño, J. L. Fulton, O. Y. Gutiérrez, D. M. Camaioni, R. K. Motkuri, Z. Li, T. E. Webber, B. L. Mehdi, N. D. Browning, R. L. Penn, O. K. Farha, J. T. Hupp, D. G. Truhlar, C. J. Cramer, J. A. Lercher, *J. Am. Chem. Soc.* **2019**, *141*, 9292–9304; c) S. M. J. Rogge, A. Bavykina, J. Hajek, H. Garcia, A. I. Olivos-Suarez, A. Sepúlveda-Escribano, A. Vimont, G. Clet, P. Bazin, F. Kapteijn, M. Daturi, E. V. Ramos-Fernandez, F. X. Llabrés i Xamena, V. Van Speybroeck, J. Gascon, *Chem. Soc. Rev.* **2017**, *46*, 3134–3184; d) D. Farrusseng, S. Aguado, C. Pinel, *Angew. Chem. Int. Ed.* **2009**, *48*, 7502–7513; e) P. Valvekens, F. Vermoortele, D. De Vos, *Catal. Sci. Technol.* **2013**, *3*, 1435–1445; f) C. J. Doonan, C. J. Sumby, *CrystEngComm* **2017**, *19*, 4044–4048; g) A. Dhakshinamoorthy, Z. Li, H. Garcia, *Chem. Soc. Rev.* **2018**, *47*, 8134–8172; h) Y. Wang, C. Wöll, *Catal. Lett.* **2018**, *148*, 2201–2222; i) D. T. Genna, L. Y. Pfund, D. C. Samblanet, A. G. Wong-Foy, A. J. Matzger, M. S. Sanford, *ACS Catal.* **2016**, *6*, 3569–3574; j) H. Chen, Y. He, L. D. Pfefferle, W. H. Pu, Y. L. Wu, S. T. Qi, *ChemCatChem* **2018**, *10*, 2558–2570.

[3] S. Marx, W. Kleist, J. Huang, M. Maciejewski, A. Baiker, *Dalton Trans.* **2010**, *39*, 3795–3798.

[4] a) Z. Fang, B. Bueken, D. E. De Vos, R. A. Fischer, *Angew. Chem. Int. Ed.* **2015**, *54*, 7234–7254; b) S. Dissegna, K. Epp, W. R. Heinz, G. Kieslich, R. A. Fischer, *Adv. Mater.* **2018**, *30*, 1704501; c) Y.-B. Zhang, H. Furukawa, N. Ko, W. Nie, H. J. Park, S. Okajima, K. E. Cordova, H. Deng, J. Kim, O. M. Yaghi, *J. Am. Chem. Soc.* **2015**, *137*, 2641–2650; d) F. Drache, F. G. Cirujano, K. D. Nguyen, V. Bon, I. Senkovska, F. X. L. i Xamena, S. Kaskel, *Cryst. Growth Des.* **2018**, *18*, 5492–5500; e) W. Zhang, M. Kauer, O. Halbherr, K. Epp, P. H. Guo, M. I. Gonzalez, D. J. Xiao, C. Wiktor, F. Xamena, C. Woll, Y. M. Wang, M. Muhler, R. A. Fischer, *Chem. Eur. J.* **2016**, *22*, 14297–14307.

[5] O. Kozachuk, K. Yusenko, H. Noei, Y. Wang, S. Walleck, T. Glaser, R. A. Fischer, *Chem. Commun.* **2011**, *47*, 8509–8511.

[6] O. Kozachuk, I. Luz, F. X. L. i Xamena, H. Noei, M. Kauer, H. B. Albada, E. D. Bloch, B. Marler, Y. Wang, M. Muhler, R. A. Fischer, *Angew. Chem. Int. Ed.* **2014**, *53*, 7058–7062.

[7] I. Agirrezabal-Telleria, I. Luz, M. A. Ortuño, M. A. Ortuno, M. Oregui-Bengoechea, I. Gandarias, N. Lopez, M. A. Lail, M. Soukri, *Nat. Commun.* **2019**, *10*, 2076.

[8] a) W. Zhang, O. Kozachuk, R. Medishetty, A. Schneemann, R. Wagner, K. Khaletskaya, K. Epp, R. A. Fischer, *Eur. J. Inorg. Chem.* **2015**, 3913–3920; b) W. R. Heinz, T. Kratky, M. Drees, A. Wimmer, O. Tomanec, S. Gunther, M. Schuster, R. A. Fischer, *Dalton Trans.* **2019**, *48*, 12031–12039.

[9] J.-E. Bäckvall, *J. Organomet. Chem.* **2002**, *652*, 105–111.

[10] R. L. Chowdhury, J.-E. Bäckvall, *J. Chem. Soc. Chem. Commun.* **1991**, 1063–1064.

[11] N. Ahlsten, A. Bartoszewicz, B. Martín-Matute, *Dalton Trans.* **2012**, *41*, 1660–1670.

[12] a) N. Ahlsten, H. Lundberg, B. Martín-Matute, *Green Chem.* **2010**, *12*, 1628–1633; b) D. Cahard, S. Gaillard, J.-L. Renaud, *Tetrahedron Lett.* **2015**, *56*, 6159–6169; c) T. Xia, Z. Wei, B. Spiegelberg, H. J. Jiao, S. Hinze, J. G. de Vries, *Chem. Eur. J.* **2018**, *24*, 4043–4049; d) F. Scalambra, P. Lorenzo-Luis, I. de los Rios, A. Romerosa, *Coord. Chem. Rev.* **2019**, *393*, 118–148.

[13] K. Yamaguchi, T. Koike, M. Kotani, M. Matsushita, S. Shinachi, N. Mizuno, *Chem. Eur. J.* **2005**, *11*, 6574–6582.

[14] R. W. Mitchell, A. Spencer, G. Wilkinson, *J. Chem. Soc. Dalton Trans.* **1973**, 846–854.

Manuscript received: November 2, 2019
Revised manuscript received: January 19, 2020
Accepted manuscript online: January 23, 2020
Version of record online: February 19, 2020

4.2 Study II

Volume 48 | Number 32 | 28 August 2019 | Pages 11987–12350

Dalton Transactions

An international journal of inorganic chemistry

rsc.li/dalton

ISSN 1477-9226

ROYAL SOCIETY OF CHEMISTRY | Celebrating IYPT 2019

PAPER

Roland A. Fischer *et al.*

Mixed precious-group metal–organic frameworks: a case study of the HKUST-1 analogue $[Ru_xRh_{3-x}(BTC)_2]$

Mixed Precious-Group Metal-Organic Frameworks: Case Study of the HKUST-1 Analogue $[Ru_xRh_{3-X}(BTC)_2]$

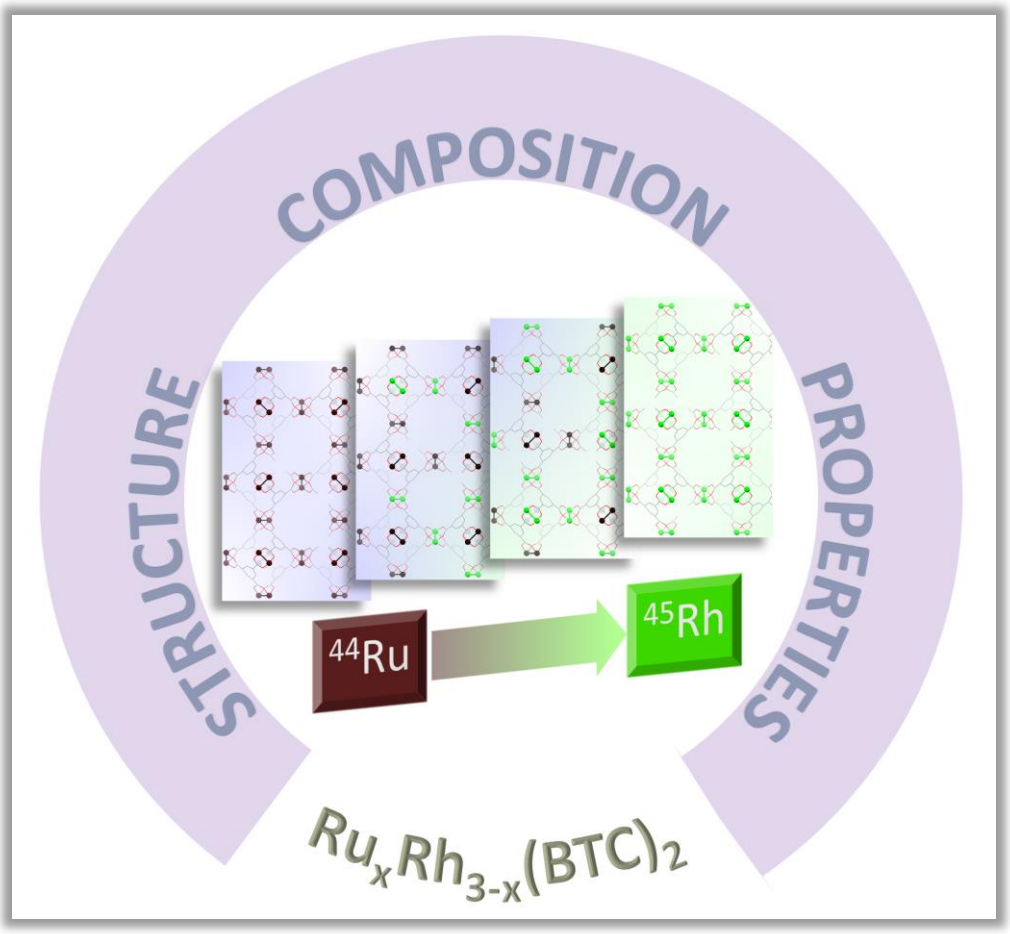

Mixed Precious-Group Metal-Organic Frameworks: Case Study of the HKUST-1 Analogue $[Ru_xRh_{3-X}(BTC)_2]$

Werner R. Heinz, Tim Kratky, Markus Drees, Andreas Wimmer, Ondřej Tomanec, Sebastian Günther, Michael Schuster, and Roland A. Fischer

Dalton Transactions **2019**, 48, 12031 – 12039.

This work expands the HKUST-1 family and presents the first series of mixed precious-group metal-organic frameworks (MPG-MOFs) from ruthenium and rhodium and the first monometallic $[Rh_3(BTC)_2]$. The crystalline, highly porous and thermally robust materials are analysed by means of powder X-ray diffraction, N_2 / CO_2 sorption, thermogravimetry, spectroscopic methods (IR, Raman, UV/VIS-, NMR and XPS) as well as HR-TEM with elemental mapping. Additionally, experimental findings are supported by computational (time dependent) density functional theory methods. This study provides insights in understanding MPG-MOFs as a foundation for future (catalytic) applications. Previously established methods like the modulated solvothermal synthesis and the controlled secondary building-unit approach (CSA) are utilized to obtain a mixed-metal series of RuRh-HKUST-1 analogues.

Dalton Transactions

PAPER

View Article Online
View Journal | View Issue

Cite this: *Dalton Trans.*, 2019, **48**, 12031

Mixed precious-group metal–organic frameworks: a case study of the HKUST-1 analogue $[Ru_xRh_{3-x}(BTC)_2]$†

Werner R. Heinz,[a] Tim Kratky,[b] Markus Drees,[a] Andreas Wimmer,[c] Ondřej Tomanec,[d] Sebastian Günther,[b] Michael Schuster[c] and Roland A. Fischer*[a]

Received 20th March 2019,
Accepted 13th June 2019

DOI: 10.1039/c9dt01198f

rsc.li/dalton

This work presents the first full series of mixed precious-group metal–organic frameworks (MPG-MOFs) using ruthenium and rhodium. The obtained crystalline, highly porous and thermally robust materials were characterized by means of powder X-ray diffraction, N_2/CO_2 sorption isotherms, thermogravimetry, spectroscopy methods (IR, Raman, UV/VIS-, NMR and XPS) and as well by high resolution transmission electron microscopy (HR-TEM) with elemental mapping (HAADF-EDS). Additionally, the assignment of spectroscopic data is supported by computational (time dependent)-density functional theory methods. The materials turned out to consist of homogeneously dispersed Ru_2 and Rh_2 paddlewheel units being linked by benzenetricarboxylate (BTC) to yield a framework that is isoreticular to $[Cu_3(BTC)_2]$ (HKUST-1, Hong Kong University of Science and Technology). However, acetate (OAc) is incorporated as an intrinsic component which compensates for missing BTC-linker defects and some Cl is coordinated to the Ru centre at an apical position. The exact empirical formula of the MPG-MOFs is derived as $[Ru_xRh_{3-x}(BTC)_{2-a}(OAc)_b(Cl)_c]$.

Introduction

Although there has been tremendous growth in the field of metal–organic frameworks (MOFs) over the last twenty years and vast arrays of organic linkers have been used, only a limited number of metals is utilized for the construction of these materials with preference to first row (3d) transition metals or lanthanoids (4f).[1] MOFs based on precious group metals (PGMs) (Ru, Rh, Pd, Os, Ir, Pt) are rare. In 2011, we first reported powder and thin films of crystalline Ru-BTC (1,3,5-benzene tricarboxylate) as an isostructural analogue of the iconic paddlewheel-based copper HKUST-1 (Hong Kong University of Science and Technology).[2] We continued these investigations including optimized synthesis protocols based on the controlled secondary building unit (SBU) approach (CSA),[3] detailed material characterisation studies[4] as well as the preparation of mixed-valence $Ru^{II,III}$ and univalent $Ru^{II,II}$ systems.[5] In addition, we investigated the effects of an intentional introduction of defects (the so-called defect-engineering) by framework implementation of defect generating linkers to further design material properties.[6–8] Agirrezabal-Telleria *et al.* recently expanded this strategy by thermal defect generation and found the resulting Ru-BTC derivatives to be efficient catalysts in ethylene dimerization under intrapore condensation conditions.[9] Accompanying the synthesis approach, which allowed high yields and phase purity and good crystallinity, acetate was always found to be a substantial component in Ru-BTC. However, the exact role of acetate within the frameworks has not unambiguously been assigned yet. At this point, it should be emphasized that all our attempts to avoid the incorporation of acetate by using acetate-free metal precursors and solvent mixtures without acetic acid as a modulator were not successful.

Although, there are reports on mixed-metallic systems including PGMs (Cu–Rh, Cu–Pd)[10–13] and a high number of mono PGM amorphous coordination networks and as well some crystalline metal–organic polyhedra (MOPs),[14–25] to date, ruthenium and very recently palladium remain the only PGMs

[a]*Chair of Inorganic and Metal-Organic Chemistry, Department of Chemistry, Technical University of Munich, Lichtenbergstraße 4, 85748 Garching, Germany. E-mail: roland.fischer@tum.de*
[b]*Chair of Physical Chemistry with Focus on Catalysis, Department of Chemistry, Technical University of Munich, Lichtenbergstraße 4, 85748 Garching, Germany. E-mail: sebastian.guenther@tum.de*
[c]*Chair of Analytical Chemistry, Department of Chemistry, Technical University of Munich, Lichtenbergstraße 4, 85748 Garching, Germany. E-mail: michael.schuster@ch.tum.de*
[d]*Group of Carbon nanostructures and biomacromolecules, Regional Centre of Advanced Technology and Materials, Šlechtitelů 27, 78371 Olomouc, Czech Republic. E-mail: ondrej.tomanec@upol.cz*
†Electronic supplementary information (ESI) available. See DOI: 10.1039/c9dt01198f

View Article Online
Paper Dalton Transactions

with reported crystalline monometallic MOF structures.[13] For instance, in 2013, Nickerl *et al.* have reported the synthesis of self-supported coordination polymers (CPs) based on rhodium paddle-wheel (PW) building blocks connected with BTC or BTB (benzene tribenzoate) linkers.[26] However, the obtained BTC-based CP has been found to be amorphous, and its pores could only be made accessible with the help of supercritical CO_2 extraction. Still, nitrogen physisorption data of the activated sample revealed relatively low surface areas of these materials. Thermal activation alone led to non-porous phases. To the best of our knowledge, there are no reports of crystalline Pd-BTC, Rh-BTC or any mixed-precious group metal–organic frameworks (MPG-MOF). Obviously, the incorporation of PGMs in MOFs as structure-determining components remains challenging despite the very rich molecular coordination chemistry of these metals.[12,15,27] Several reasons for that can be identified: first, precious metal salts are easily reduced to metal nanoparticles by non-redox innocent solvents, modulators, organic linkers or the presence of base metals. The metal or metal oxide particles formed are usually difficult to re-dissolve under the MOF synthesis conditions, thus precipitation needs to be avoided. Due to the well-known substitutional kinetic inertness of PGM complexes, the required self-assembly process for MOF synthesis is dramatically slowed down and long reaction times and high temperatures are required. In contrast, fast ligand substitution kinetics favours the nucleation and growth of MOF crystallites. In addition, for mixed-metallic systems, both metal SBUs (secondary building-units) should exhibit similar substitution kinetics to avoid both the formation of two different kinds of mostly monometallic particles and incomplete (non-quantitative) incorporation of the more inert metal. In this work, we present the synthesis of the first full series of MPG-MOFs with $[Ru_xRh_{3-x}(BTC)_2]$ ($0 < x < 3$) as the example, including the pure Rh-BTC phase ($x = 0$) with decent crystallinity. Characterization of the materials is elaborated with different analytical techniques. Experimental and computational results are compared and conclusions for the mechanism of formation and defect incorporation are drawn.[28]

Results and discussion

The synthesis of the mixed-metal Ru/Rh-BTC series was conducted with $Ru_2(OAc)_4Cl$ and $Rh_2(OAc)_4$ as metal precursors following the CSA concept. The complexes were mixed with trimesic acid in the stoichiometrically required ratio of 3 : 4 and the resulting reaction mixture was exposed to hydrothermal conditions at 150 °C for four days in the presence of a huge excess of acetic acid as both the modulator and cosolvent. In a series of experiments, the $Ru_2(OAc)_4Cl$ component was then gradually substituted by $Rh_2(OAc)_4$ for the synthesis of MPG-MOFs. In the following, the thus synthesized materials are denoted with the intended atom percentage of Rh based on the metal feed during synthesis. Thus, materials with 0%, 5%, 10%, 20%, 50%, 75%, 95% and 100% Rh have been successfully synthesized and characterized. In this series, the 0% and 100% samples refer to pure mono-metallic Ru-BTC and Rh-BTC, respectively. While the pure Ru-BTC (0%) sample appears dark brown to almost black in colour, pure Rh-BTC (100%) is a bright green solid, in line with the colour of the metal ion precursors. This indicates that the PW structure is still present in the framework. Below, the structure and composition of the materials are presented, complemented subsequently by the discussion of analytical techniques elucidating the distribution and properties of metals and organic constituents within the frameworks.

Characterisation

Topology and structure. PXRD studies have been performed in order to analyse the structure and topology of the series depending on the rhodium content. All patterns are depicted in Fig. 1.[29] Similar to the parent Cu-HKUST-1, the mixed-metal Ru/Rh analogues crystallize in the cubic space group $Fm\bar{3}m$. With increasing Rh content, all reflections are broadened and slightly shifted to lower angles. This indicates lower crystallite size/crystallinity (crystallite coherence length) and a slightly increased size of the unit cell. Lower oxidation states ($Rh^{II,II}$ compared to $Ru^{II,III}$), *i.e.* larger metal cation radii and a slightly weaker coordination bonding might serve as an explanation. The diffraction data strongly indicate the whole series to be isostructural. At this point, it should be noted, that in the 10% Rh sample small amounts of the Ru precursor are present (12.7° and 13.1° 2θ), which obviously has not been removed by the routine washing procedures applied to all samples. However, the very small reflection intensities of the usually highly crystalline $Ru_2(OAc)_4Cl$ precursor suggest only trace amounts of this impurity being present in the samples (Fig. 2).

Composition. Elemental analysis for C, H, and Cl and ICP-MS analysis of the metal content (Ru,Rh) were applied.

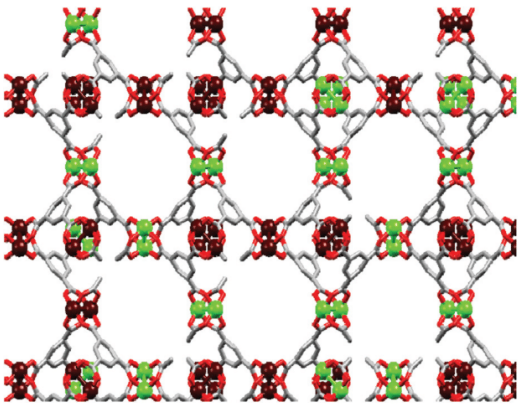

Fig. 1 Simplified representation of the microstructure of RuRh-MPG-MOFs. The materials contain randomly distributed intact assumingly monometallic PWs from Ru (brown) and Rh (green) and incorporate high amounts of acetate modulator-based defects. Additional axial ligands (Cl^- or OAc^-) for charge compensation of $Ru^{II,III}$-PWs and hydrogen atoms are omitted for clarity.

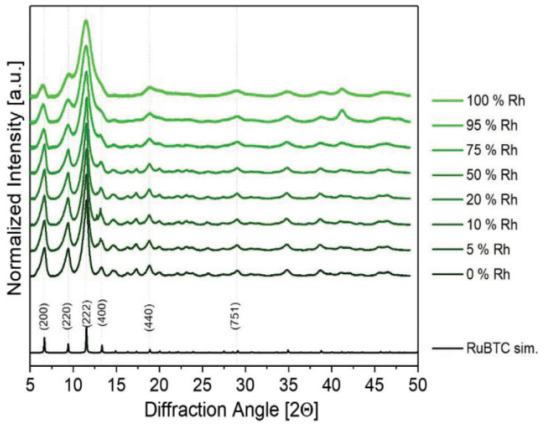

Fig. 2 Background corrected powder XRD patterns of Ru/Rh-MOFs (green) indicate isostructural materials. A simulated reference pattern of Ru-BTC (black, based on literature refinements) is added and reflections are assigned to lattice planes.

The oxygen content in each sample is assumed to be the missing residue, since no other element should be present in the samples. With the thus obtained values for C, H and O, the OAc/BTC ratio for each sample could be calculated resulting in a tentative composition of the unit cell in each case (Table 1). Details of the compositional analysis and the calculation of framework components are described in the ESI.†

Most importantly, all Ru : Rh ratios match well with the feed ratios applied in the synthesis, suggesting comparable framework incorporation for both metals (see Table 1).

With increasing rhodium feeds in syntheses, the total metal contents of the synthesized materials are progressively higher than expected which may be attributed to both the decreasing amount of additional axial counter ions as well as a higher number of modulator-induced defects.

A high acetate incorporation, particularly for 95% and 100% Rh samples, is observed throughout the whole series. However, the chemical role of the acetate within the framework cannot be attributed to by elemental analysis only. Besides simple in-pore adsorption, acetate can coordinate at the axial position of the PW nodes or also substitute BTC as a bridging ligand thus causing missing linker defects within the framework. Indeed, this might be the cause for the reflection broadening observed in the PXRDs (*vide supra*).

In order to determine the reliability of the acetate content determined by elemental analysis, ^{1}H-MAS-NMR of the 0%, 50% and 100% Rh samples was recorded. However, due to the paramagnetic nature of the Ru PW, only pure Rh-BTC allowed interpretation of the spectra. Indeed, the acetate amount found by EA (BTC : OAc ≈ 1.3) is confirmed by ^{13}C-MAS-NMR (BTC : OAc ≈ 1.4) validating the fitting approach with an independent technique. Further information on MAS-NMR measurements, spectra (Fig. S1–3†) and signal interpretation can be found in the ESI.†

In the following, further characterisation methods will primarily address two main points of discussion: bimetallic incorporation together with its distribution and secondly, the nature of acetate incorporation together with its location and bonding situation within the framework.

Elemental distribution. In order to investigate the homogeneity and elemental distribution within the samples, we performed high resolution scanning transmission electron microscopy (HR-STEM) together with the high angle annular dark-field (HAADF) technique and energy dispersive X-ray spectroscopy (EDS) for elemental mapping. The question is: do the synthesized RuRh-MPG-MOFs consist of bimetallic primary particles (as true solid-solutions) or is the obtained bulk material a physical mixture of two mono metallic primary particles? The 50% and 75% Rh samples were chosen as representative samples of the MPG-MOF series. As shown in Fig. 3 (images of the 75% Rh sample are shown in the ESI, see Fig. S4–8†), the primary particles of both samples have a homogeneous elemental distribution for C, O, Ru and Rh. Indeed, increasing rhodium counts are visible in the maps of the 75% Rh sample. Additional HR-TEM images (ESI) further show uniform electron absorption. As a conclusion, we can assume a statistical, homogeneous incorporation of both Ru- and Rh-PWs without the formation of metal (oxide) nanoparticles. This is in accordance with the aforementioned constant total metal contents found in elemental analysis.

Table 1 Elemental contents, metal ratios, calculated sum formulas and found surface areas for nitrogen and carbon dioxide sorptives determined according to the BET theory

Sample	Found C/H/Cl/Ru/Rh [%]	Found M_{total}	Found Rh : M_{total}	Calculated repeating unit[a]	N_2 surface area		CO_2 surface area	
					[m^2 g^{-1}]	[m^2 mmol^{-1}]	[m^2 g^{-1}]	[m^2 mmol^{-1}]
0% Rh	29.81/1.34/2/38.9/0	38.9%	0%	$[Ru_3(BTC)_{1.89}(OAc)_{1.19}Cl_{0.44}]$	960	848	848	749
5% Rh	30.62/1.35/2.2/35.5/2.0	37.5%	5.3%	$[Ru_{2.84}Rh_{0.16}(BTC)_{2.06}(OAc)_{1.04}Cl_{0.50}]$	944	764	n.d.	n.d.
10% Rh	30.50/1.32/1.2/34.0/4.2	38.2%	11.0%	$[Ru_{2.67}Rh_{0.33}(BTC)_{1.95}(OAc)_{1.34}Cl_{0.27}]$	939	748	n.d.	n.d.
20% Rh	31.11/1.37/1.8/28.0/7.6	35.7%	21.4%	$[Ru_{2.37}Rh_{0.63}(BTC)_{2.04}(OAc)_{1.88}Cl_{0.43}]$	1009	865	n.d.	n.d.
50% Rh	28.73/1.79/1.7/18.8/20.8	39.6%	52.6%	$[Ru_{1.44}Rh_{1.56}(BTC)_{1.70}(OAc)_{1.69}Cl_{0.41}]$	1211	935	928	717
75% Rh	30.01/1.35/0.7/9.8/30.4	40.2%	75.6%	$[Ru_{0.74}Rh_{2.26}(BTC)_{1.92}(OAc)_{0.93}Cl_{0.15}]$	1178	901	872	667
95% Rh	29.30/1.22/0.24/1.2/39.8	41.0%	97.1%	$[Ru_{0.09}Rh_{2.91}(BTC)_{1.72}(OAc)_{1.46}Cl_{0.05}]$	1240	933	918	691
100% Rh	29.82/1.40/0/0/40.4	40.5%	100%	$[Rh_3(BTC)_{1.79}(OAc)_{1.40}]$	1248	946	890	675

[a] Inaccessible metal oxidation states obstructed proton-based charge balancing.

View Article Online
Paper Dalton Transactions

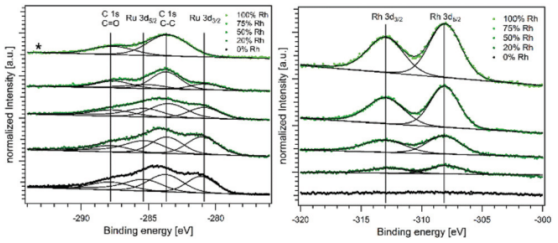

Fig. 3 XP spectra of the Ru 3d/C 1s region (left) exhibiting overlapping signals (C 1s (C═O), Ru 3d3/2, C 1s (C–C) and Ru 3d5/2 components from left to right) as well as isolated Rh 3d signals (right). The spectrum marked with an asterisk was acquired with different analyser settings leading to a broader line shape (see the ESI†).

X-ray photoelectron spectroscopy (XPS). In order to gain insight into the complex materials on an atomistic level, we performed XPS measurements with most of the samples (0%, 20%, 50%, 75% and 100% Rh). The results were interpreted in comparison with the three reference compounds $Rh_2(OAc)_4$, $Ru_2(OBz)_4$ and $Ru_2(OAc)_4Cl$, which exhibit defined oxidation states in different carbon environments. This is particularly beneficial for the interpretation of the Ru 3d and C 1s signal overlapping. Three major questions have been addressed by XPS: metal oxidation states, the Ru : Rh ratio on the particle surface as well as the depth-profile of the metal ratio.

The Ru 3d signal overlap with the C 1s components (see Fig. 4, left spectra), hampers reliable quantification and oxidation state assignment. For metal ratio determinations, the Ru $3p_{3/2}$ signal was used instead. In addition, highly insulating MOF structures cause strong differential charging, which gives rise to prominent peak broadening.

The obtained XP spectra confirm the similarity of the organic matrix throughout the whole series of materials as the ratio of the two carbon components is identical in all samples. The varying metal ratios can clearly be spotted in their spectra and are quantitatively matched to the metal ratios as determined by ICP-MS (*vide supra*; also see the ESI† for details). The presence of Ru metal nanoparticles in the samples is unlikely. This is deduced from the absence of a signal around ≈−280 eV characteristic for Ru(0). Unfortunately, a distinction between +I, +II and +III metal oxidation states is not possible based on the present data. Interestingly, deconvolution of the Ru 3d/C 1s spectra using only one Ru component (meaning one oxidation state) leads to a reasonable fit of the experimental XPS spectra. Since this is also true for the (clearly mixed-valent) reference compound $Ru_2(OAc)_4Cl$ as well as pure Ru-BTC (different oxidation states have been confirmed with CO probed FT-IR spectroscopy in the literature),[4,30,31] a differentiation of oxidation states by XPS in this class of compounds is obviously difficult. The same takes effect for rhodium signals at ≈−308 eV and ≈−313 eV which can be seen in Fig. 4 (right).

Depth profiling. Depth profiling including repeated argon ion sputtering and subsequent XPS measurements was conducted with the 20% Rh and the 75% Rh samples to shed light on the nucleation and growth process during the MPG-MOF synthesis.

As shown in Fig. 6, the Ru to Rh ratio of both samples does not change with increasing depth throughout the bulk of the specimen. This finding suggests similar metal ratios in feed, surface and bulk and it goes hand in hand with results from EA and elemental mapping as discussed above. However, Ar^+

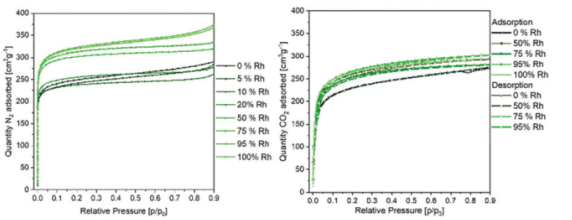

Fig. 5 Left: adsorption branches of N_2 sorption isotherms; right: CO_2 sorption isotherms containing adsorption and desorption branches. All materials show similar sorption capacities with a rise upon higher Rh contents. Full N_2 isotherms are shown in Fig. S12 (ESI†).

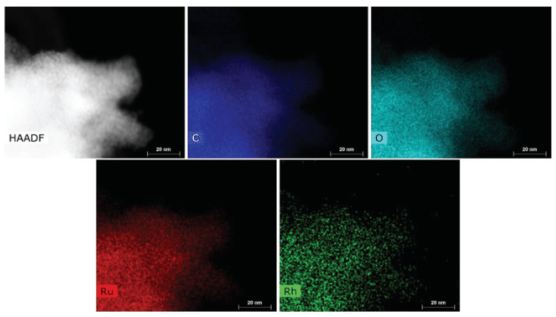

Fig. 4 HR-STEM images of representative particles of the 50% Rh sample: from left to right: HAADF image and elemental mapping for C, O, Ru and Rh of the same primary particle show uniform elemental distribution and indeed mixed-metal particles.

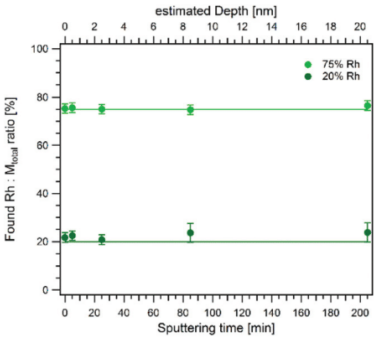

Fig. 6 Depth profiling for 20% and 75% Rh samples: depth dependent evolution of Rh : M_{total} ratios indicate homogeneous metal contents and distribution within the samples.

View Article Online
Dalton Transactions Paper

sputtering does not only remove the top layers from the sample surface, but also induces stimulated reduction of the metal species and, thus, changes their oxidation states. This process has been reported for both involved metals.[32,33] As a consequence, metalation of the samples occurs which is indicated by an emerging Ru(0) peak at −279 eV. Although a precise prediction for the number of removed atomic layers for each sputter cycle is difficult, ablation rates in the range of 1 Å min^{-1} are reasonable for such powder samples based on our experience. Thus, the order of magnitude for ablation is assumed to be about 20 nm. Taking the mean primary particle size based on HR-TEM images into account, these ablation depths are considered to be sufficiently sensitive for changes in the sample composition.

Porosity investigations. In order to investigate porosity and gas sorption abilities of the synthesized materials, N_2 and CO_2 sorption studies were performed. On the basis of the calculated compositions, weight-based BET surface areas are converted to molar based values accounting for the higher molar weight of the used metals compared to Cu-HKUST-1. Table 1 contains the thus determined experimental surface areas for both adsorbed gases. All sorption isotherms are displayed in Fig. 5 (N_2: left, CO_2: right).

All samples show type I isotherms typical of microporous materials. Surface areas of all samples are well comparable, indicating both isostructurality and similar pore accessibility. At the same time, the range of surface areas is in good agreement with reported literature values on Ru-BTC and Cu-BTC.[5,7,34–40] Moreover, there is a trend towards higher sorption capacities upon Rh increase. Interestingly, CO_2-based surface areas nicely reflect the same trend. This indicates similar affinities towards quadrupolar CO_2 for both metals and complements previous literature results on CO_2 uptake of HKUST-1 derivatives.[34]

We assume two factors potentially accounting for the increasing porosity with increasing rhodium content: a higher number of coordinatively unsaturated sites (CUS) due to a lower average oxidation state ($Rh^{II,II}$ instead of $Ru^{II,III}$) as well as more modulator induced missing linker defects. This assumption is based on both the previously described compositions as well as results from vibrational spectroscopy (*vide infra*). An overview on weight- and molar-based BET surface areas of materials from different batches is provided in the ESI (see Fig. S13†). DFT-based pore size analyses indicate unaffected mean sizes of both small and large pores. However, broadened distributions and slight mesoporosity (≈1.9 nm width) arising upon Rh increase confirm the increased defectiveness of these materials (see Fig. S14†).

Vibrational spectroscopy

In order to access information on the binding situation of the RuRh-MPG-MOFs, we performed Fourier transformed infrared (FTIR) as well as Raman spectroscopy studies on all samples. In addition to the experimental results we performed density functional theory (DFT) calculations on isolated model molecules. Thus, the specific influence of axial [$(H_2O)_2$, Cl, Cl_2 or non-coordinated] and equatorial ([$(OAc)_x(OBz)_{4-x}$] with $0 < x < 4$; [$(H_2BTC)_4$]) substitution of a $Rh_2^{II,II}$-paddle-wheel was modelled. An overview of the most prominent vibrational frequencies from both IR and Raman in experiment and theory with an assignment of vibrational modes as well as all experimental spectra and calculated vibrational modes is summarized in Table S4 (ESI†). Selected modes are displayed in Fig. S17–25.†

Infrared spectroscopy. In Fig. 8 the experimental IR spectra assignment of vibrational modes has been done on the basis of computational DFT calculations on representative model molecules as well as literature data on HKUST-1(Cu).[41–46] Most importantly, all spectra do not contain significant signals between 4000 cm^{-1} and 2000 cm^{-1}. This contrasts with computational findings and may result from experimental sensitivity issues. Thus, all spectra in Fig. 8 are displayed from 2000 cm^{-1} to 400 cm^{-1}. The most intense bands can be

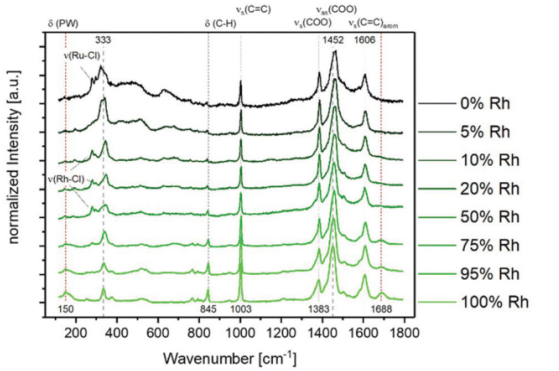

Fig. 7 Raman spectra of RuRh-BTC series show similar bonding situation in general but emerging Rh–Cl vibration for intermediate metal ratios (10–75% Rh samples) and a vibration from axially uncoordinated PWs for pure Rh-BTC (150 cm^{-1}).

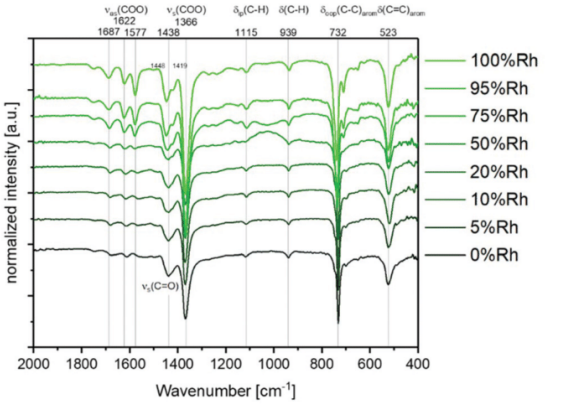

Fig. 8 FT-IR spectra with assignment of the most intense vibrations generally show an equal binding situation but increasing acetate contents and terminal binding of those.

assigned to ν_s(CO), ν_s(COO), δ_{oop}(C–H_{arom}) and δ_{ip}(C=C) modes. Interestingly, a metal-independent combinational deformation vibration is found for all samples at 523 cm^{-1} which is in accordance with our DFT calculations.

Absorption bands between 1570 cm^{-1} and 1687 cm^{-1} exhibit increasing intensity with increasing Rh content. According to the findings of Delen *et al.* the observed bands at 1622 cm^{-1} and 1577 cm^{-1} can be assigned to (partially) acetate-coordinated rhodium PW structures.[41] This is well in line with the higher acetate contents of those samples as determined by elemental analysis. A reference spectrum of $Rh_2(OAc)_4$ is given in Fig. S15 (ESI†). The broad band at 1687 cm^{-1} (also observed and discussed in the Raman section, *vide infra*) is assigned to terminal acetates.[47] In contrast, most of the absorption bands just shift slightly when comparing the 0% Rh and 100% Rh samples, *e.g.* δ_{oop}(C–H_{arom}) (732 cm^{-1} *vs.* 738 cm^{-1}), ν_{as}(COO) (1368 cm^{-1} *vs.* 1366 cm^{-1}) and ν_s(COO) (1611 cm^{-1} *vs.* 1622 cm^{-1}). The increasing $\Delta\nu$ of the symmetric and asymmetric modes is attributed to the increasing metal–metal distance in Rh_2 *vs.* Ru_2 PWs resulting in a higher O–C–O angle.[47] Due to the upshift of ν_{as}, a shoulder at 1419 cm^{-1} becomes more prominent for rhodium-rich samples.

Raman spectroscopy. Raman spectra for all materials are shown in Fig. 7 and were recorded from 100 cm^{-1} to 2000 cm^{-1}. It should be mentioned, that no peaks appeared in the spectral range between 2000 cm^{-1} and 4000 cm^{-1}. Again, the most intense vibration modes have been assigned to ν_{as}(COO), ν_s(COO) and ν_s(C=C_{arom}) modes. Emerging signals at 845 cm^{-1} (C–H deformation) and 1688 cm^{-1} (ν (COO) of terminal acetate) indicate increasing defects in Rh-rich samples which is in accordance with the increasing acetate content of Rh rich samples as determined by elemental analysis (*vide supra*). Both signals are not present in Ru-rich samples, which points to the presence of two different defect types: (i) acetate incorporation as a defect-linker (truncated linker) which is observed throughout the whole series of MPG-MOFs, and (ii) misconnected carboxylates (monodentate), which are present in Rh rich samples (1688 cm^{-1}).[28] With the help of computational simulations, the origin of the signal at 150 cm^{-1} could be identified as a unique PW deformation mode which is only visible when axial coordination sites are unoccupied. This vibration is also rather insensitive towards the type of the equatorial carboxylates. This is well in line with the experimental spectra which show a strong increase in the intensity of this signal with increasing rhodium content. Thus, in Ru_2 PW structures the axial positions are more likely to be occupied by at least one anionic ligand suppressing this deformation mode. Based on this, an univalent $Rh_2^{II,II}$ oxidation state is obviously predominant in pure Rh-BTC. With these Raman findings, it is reasonable to assume that acetate mainly serves as a defect-linker replacing BTC linkers at equatorial PW positions instead of axial PW coordination, at least in rhodium rich samples.

Solid-state UV/Vis spectroscopy. Solid-state UV/Vis spectroscopy was performed in order to investigate the electronic transitions in the strongly colored samples (Fig. 9). Ru-BTC

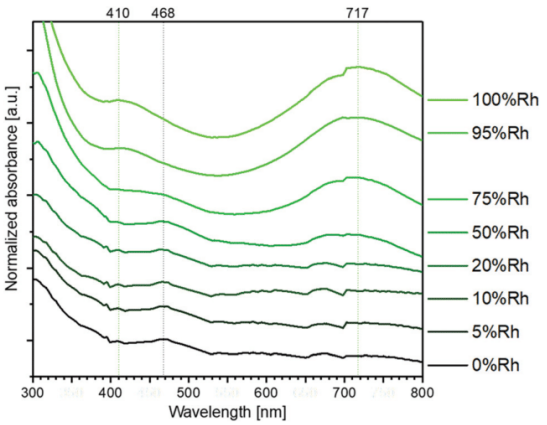

Fig. 9 Solid-state UV/vis spectra of RuRh MPG-MOFs. Spectra are stacked for clarity and indicate the presence of isolated Ru_2 and Rh_2 PWs. Detector changes at 400 and 700 nm account for signal discontinuities.

appears dark brown in colour due to broad absorptions over the full UV and visible spectral region with only one defined absorption band centred at 468 nm. This is also the predominant feature in Ru-rich MPG-MOFs in this work (0–50% Rh samples). With increasing Rh contents, defined electronic transitions emerge in the form of two absorptions at 410 nm (band **I**) from π*(Rh–Rh) → σ*(Rh–O)[48–50] or π(Rh–O) → σ*(Rh–O) and 717 nm (band **II**) from a π*(Rh–Rh) → σ*(Rh–Rh) transition, respectively.[51] According to the literature on rhodium acetate coordination compounds, the location and presence of two clear absorption bands of Rh-BTC indicate that intact PW SBUs are still present in the MOF.[52] As shown in Fig. S16 (ESI†), rehydration of Rh-BTC induces both a bathochromic shift of the 410 nm absorption (to 445 nm) and a hypsochromic shift of the low energy transition from 717 nm to 595 nm. Axial coordination to the PW destabilizes the σ*(Rh–Rh) orbital much more than the π*(Rh–Rh) orbital which explains the blue shift of band **II**. As σ*(Rh–O) is almost unaffected, a red shift occurs for band **I**. A comparison of absorption wavelengths of different dirhodium tetracarboxylates (experimental and theoretical from this work and from the literature.[52]) is presented in Table S5 in the ESI† as well. Based on this comparison, one can draw two conclusions: substitution of acetate ligands by aromatic benzoate ligands results in strong bathochromic shifts of band **II** (destabilisation of π*(Rh–Rh) orbital) while hydration of the axially unsaturated sites results in strong hypsochromic shifts of the same band. Interestingly, mixed-metallic samples do not show additional absorption bands stemming from mixed-metallic chromophores ($Ru^{II}Rh$ or $Ru^{III}Rh$ dimers). Thus, the formation of mixed-metallic PWs is also not substantiated by UV/VIS spectroscopy. In general, metal exchange in PW-based MOFs is literature-known.[13,53] However, in the present system metal–metal bonding, strong ligand coordination and PW stabilization *via* ligand excess during synthesis might contradict the formation of mixed-

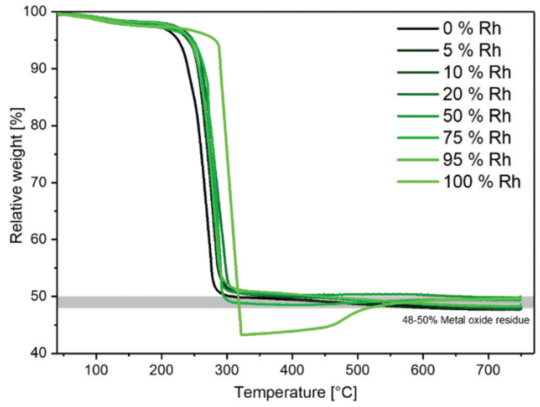

Fig. 10 Thermal decomposition curves from RuRh-BTC samples measured in synthetic air (20 mL min^{-1}; 10 K min^{-1} ramp). All samples show similar thermal robustness with a slight increase for Rh rich materials.

metallic PWs. Only highly sophisticated synchrotron-based methods like XANES could provide clear insights into the presence of mono- or mixed-metallic PWs in the future.

Thermal properties. Thermogravimetry was used for the assessment of the thermal stability of the MPG-MOFs. Furthermore, it provides verification for the total metal content and validates quantitative sample activation. Fig. 10 displays the thermal decomposition graphs as recorded in an atmosphere of synthetic air. All samples show similar decomposition behaviour and thermal stability. In detail, the main decomposition (linker fragmentation) occurs in one clear step for all samples between 250 and 300 °C with a correlation of higher thermal robustness with increasing Rh content. The relative weight of the residues after decomposition corresponds well with the calculated weight of the respective oxides (RuO_2/Rh_2O_3) and is therefore in line with the elemental analyses data.[54–56] Table S1† summarizing the quantitative results obtained by ICP-MS, TGA and XPS is provided in the ESI.† The absence of a pronounced weight loss between the ambient temperature and 150 °C indicates the almost complete sample activation of all materials.

Interestingly, pure Rh-BTC shows a unique decomposition behaviour. After a strong weight loss in the main decomposition step, a regain in weight can be observed with higher temperatures. PXRD measurements and the corresponding weight change confirm the initial formation of Rh(0) and subsequent reoxidation to Rh_2O_3 at higher temperatures. A similar behaviour has been described for rhodium acetate earlier.[52,57] Interestingly, this process does not occur, even if only small amounts of ruthenium are present within the framework.

Conclusion and outlook

This work presents the synthesis of the mixed-metal MOFs $[Ru_xRh_{3-x}(BTC)_2]$ $(0 < x < 3)$ including pure Rh-BTC by the reaction of the respective mixture of metal acetates with BTC. With the preparation of eight different metal ratios, we show that every Ru : Rh ratio results in a crystalline, highly porous, homogeneous mixed-metallic framework which is isostructural to HKUST-1 without the formation of metal (oxide) side products. To the best of our knowledge, this work is the first entire series of bimetallic precious metal containing MOFs. Our synthesis approach also gives access to crystalline Rh-BTC. Based on various characterisation methods including both experimental and computational techniques, the complex microstructure including the role of acetate as a framework component was elucidated. Thus, with high rhodium contents, increasing amounts of modulator-induced missing-linker defects are incorporated, which manifest by pronounced acetate incorporation forming mixed-component MOFs. As acetate results from modulated synthesis, PGM-MOFs might be regarded as modulator-induced defect compensated materials containing mixtures of intact monometallic PWs. A multimethodical approach based on three independent analytical techniques (EA, TGA, and XPS) provides highly consistent information on composition and particularly the metal ratios. N_2 and CO_2 sorption studies as well as thermal experiments indicate thermally robust materials with high and easily accessible permanent porosity. (TD)-DFT calculations on model compounds confirm vibrational mode assignments and experimental findings from SS-UV/Vis spectroscopy. Additionally, particle homogeneity was confirmed by both elemental mapping (HR-TEM) and depth profiling (XPS). Intriguingly, up to now, the formation of decent crystallinity in PGM-MOFs requires distinct modulator amounts. MPG-MOFs with incorporated acetate could potentially be used for the decarboxylative, post-synthetic generation of CUS (defect-engineering) similarly found in defective/mixed-component UiO-66.[58] On the contrary, to obtain less defective MPG-MOFs, modulator incorporation could potentially be reduced utilizing sterically or electronically different precursor ligands and modulators. These considerations and further studies regarding properties, functions and applications of (mixed-) PGM-MOFs are currently under investigation.

Table 2 Used reagent amounts for the synthesis of mixed-metal Ru/Rh-BTC samples resulting in the stoichiometrically required ratio of 3 : 4 metal acetate to linker

Sample	0% Rh	5% Rh	10% Rh	20% Rh	50% Rh	75% Rh	95% Rh	100% Rh
X mg $Ru_2(OAc)_4Cl$	340	324	308	276	170	85	9	0
Y mg $Rh_2(OAc)_4$	0	16	32	64	159.6	238	301.3	317.2
Z mg H_3BTC	202	202	202	202	202	202	202	202

Experimental

General considerations about working procedures, used chemicals and solvents as well as instrumental details are listed in the ESI.†

Synthesis

The synthesis of MPG-MOFs was conducted in analogy to the literature procedure for Ru-MOF with slight modifications.[4] $Ru_2(OAc)_4Cl$ was synthesized according to literature procedures.[35] According to Table 2, for each reaction X mg $Ru_2(OAc)_4Cl$ and Y mg $Rh_2(OAc)_4$ together with Z mg trimesic acid (H_3BTC) were dispersed in 8.0 mL water and 1.4 mL acetic acid in a PTFE inliner. After careful dispersion using an ultrasonic bath the inliner was closed and sealed in a steel autoclave. These autoclaves were heated for four days at 150 °C in a preheated drying oven. After cooling, the supernatant was removed with a syringe and the solvent was exchanged with water, ethanol, acetone and dichloromethane (each 2 × 8 mL) consecutively. The samples were allowed to soak in each solvent for at least one day. After the last washing step, the powder was dried in an oven at 70 °C and desolvated at 150 °C in a dynamic vacuum ($<5 \times 10^{-2}$ mbar) for at least 24 h.

Conflicts of interest

The authors declare no competing financial interests.

Acknowledgements

This work was funded by the Deutsche Forschungsgemeinschaft grant no. FI-502/32-1 ("DEMOFs"). The authors thank Christian Schneider for help with Raman spectroscopy measurements and for his and Miguel Rivera-Torrente's help with the data interpretation, Pia Vervoorts and Dardan Ukai for conducting gas sorption measurement, Gabriele Raudaschl-Sieber for performing MAS-NMR measurements and Christian Gemel for strong support with the preparation of the manuscript. Markus Drees thanks the LRZ computing centre for the provision of computing time on their Linux Cluster. WRH would like to thank TUM Graduate School for support.

References

1 T. Devic and C. Serre, *Chem. Soc. Rev.*, 2014, **43**, 6097–6115.
2 O. Kozachuk, K. Yusenko, H. Noei, Y. Wang, S. Walleck, T. Glaser and R. A. Fischer, *Chem. Commun.*, 2011, **47**, 8509–8511.
3 W. Zhang, O. Kozachuk, R. Medishetty, A. Schneemann, R. Wagner, K. Khaletskaya, K. Epp and R. A. Fischer, *Eur. J. Inorg. Chem.*, 2015, **2015**, 3913–3920.
4 H. Noei, O. Kozachuk, S. Amirjalayer, S. Bureekaew, M. Kauer, R. Schmid, B. Marler, M. Muhler, R. A. Fischer and Y. Wang, *J. Phys. Chem. C*, 2013, **117**, 5658–5666.
5 W. Zhang, K. Freitag, S. Wannapaiboon, C. Schneider, K. Epp, G. Kieslich and R. A. Fischer, *Inorg. Chem.*, 2016, **55**, 12492–12495.
6 W. Zhang, M. Kauer, O. Halbherr, K. Epp, P. Guo, M. I. Gonzalez, D. J. Xiao, C. Wiktor, F. X. L. i. Xamena, C. Wöll, Y. Wang, M. Muhler and R. A. Fischer, *Chem. – Eur. J.*, 2016, **22**, 14297–14307.
7 O. Kozachuk, I. Luz, F. X. L. i. Xamena, H. Noei, M. Kauer, H. B. Albada, E. D. Bloch, B. Marler, Y. Wang, M. Muhler and R. A. Fischer, *Angew. Chem., Int. Ed.*, 2014, **53**, 7058–7062.
8 W. Zhang, M. Kauer, P. Guo, S. Kunze, S. Cwik, M. Muhler, Y. Wang, K. Epp, G. Kieslich and R. A. Fischer, *Eur. J. Inorg. Chem.*, 2017, **2017**, 925–931.
9 I. Agirrezabal-Telleria, I. Luz, M. A. Ortuño, M. Oregui-Bengoechea, I. Gandarias, N. López, M. A. Lail and M. Soukri, *Nat. Commun.*, 2019, **10**, 2076.
10 W. Zhang, Z. Chen, M. Al-Naji, P. Guo, S. Cwik, O. Halbherr, Y. Wang, M. Muhler, N. Wilde, R. Glaser and R. A. Fischer, *Dalton Trans.*, 2016, **45**, 14883–14887.
11 S. Matsunaga, K.-i. Hasada, K. Sugiura, N. Kitamura, Y. Kudo, N. Endo and W. Mori, *Bull. Chem. Soc. Jpn.*, 2012, **85**, 433–438.
12 P. Guo, C. Froese, Q. Fu, Y.-T. Chen, B. Peng, W. Kleist, R. A. Fischer, M. Muhler and Y. Wang, *J. Phys. Chem. C*, 2018, **122**, 21433–21440.
13 C.-H. Wang, W.-Y. Gao, Q. Ma and D. C. Powers, *Chem. Sci.*, 2019, **10**, 1823–1830.
14 W. Mori, S. Takamizawa, C. N. Kato, T. Ohmura and T. Sato, *Microporous Mesoporous Mater.*, 2004, **73**, 31–46.
15 J. A. R. Navarro, E. Barea, J. M. Salas, N. Masciocchi, S. Galli, A. Sironi, C. O. Ania and J. B. Parra, *Inorg. Chem.*, 2006, **45**, 2397–2399.
16 T. Sato, W. Mori, C. N. Kato, E. Yanaoka, T. Kuribayashi, R. Ohtera and Y. Shiraishi, *J. Catal.*, 2005, **232**, 186–198.
17 Y. Kataoka, K. Sato, Y. Miyazaki, Y. Suzuki, H. Tanaka, Y. Kitagawa, T. Kawakami, M. Okumura and W. Mori, *Chem. Lett.*, 2010, **39**, 358–359.
18 A. Carné-Sánchez, G. A. Craig, P. Larpent, T. Hirose, M. Higuchi, S. Kitagawa, K. Matsuda, K. Urayama and S. Furukawa, *Nat. Commun.*, 2018, **9**, 2506.
19 S. Furukawa, N. Horike, M. Kondo, Y. Hijikata, A. Carné-Sánchez, P. Larpent, N. Louvain, S. Diring, H. Sato, R. Matsuda, R. Kawano and S. Kitagawa, *Inorg. Chem.*, 2016, **55**, 10843–10846.
20 Z. Ren, Y. Lyu, S. Feng, X. Song and Y. Ding, *Mol. Catal.*, 2017, **442**, 83–88.
21 T. Itoh, M. Kondo, H. Sakamoto, K. Wakabayashi, M. Kanaike, K. Itami and S. Masaoka, *Dalton Trans.*, 2015, **44**, 15334–15342.
22 W. Kosaka, K. Yamagishi, J. Zhang and H. Miyasaka, *J. Am. Chem. Soc.*, 2014, **136**, 12304–12313.

23 D. K. Kumar, A. S. Filatov, M. Napier, J. Sun, E. V. Dikarev and M. A. Petrukhina, *Inorg. Chem.*, 2012, **51**, 4855–4861.
24 W. Mori, S. Takamizawa, C. N. Kato, T. Ohmura and T. Sato, *Microporous Mesoporous Mater.*, 2004, **73**, 31–46.
25 W. Kosaka, K. Yamagishi, A. Hori, H. Sato, R. Matsuda, S. Kitagawa, M. Takata and H. Miyasaka, *J. Am. Chem. Soc.*, 2013, **135**, 18469–18480.
26 G. Nickerl, U. Stoeck, U. Burkhardt, I. Senkovska and S. Kaskel, *J. Mater. Chem. A*, 2013, **2**, 144.
27 J. M. Teo, C. J. Coghlan, J. D. Evans, E. Tsivion, M. Head-Gordon, C. J. Sumby and C. J. Doonan, *Chem. Commun.*, 2016, **52**, 276–279.
28 S. Dissegna, K. Epp, W. R. Heinz, G. Kieslich and R. A. Fischer, *Adv. Mater.*, 2018, **30**, 1704501.
29 N. Al-Janabi, P. Hill, L. Torrente-Murciano, A. Garforth, P. Gorgojo, F. Siperstein and X. Fan, *Chem. Eng. J.*, 2015, **281**, 669–677.
30 O. Kozachuk, I. Luz, F. X. Llabrés i Xamena, H. Noei, M. Kauer, H. B. Albada, E. D. Bloch, B. Marler, Y. Wang, M. Muhler and R. A. Fischer, *Angew. Chem., Int. Ed.*, 2014, **53**, 7058–7062.
31 W. Zhang, M. Kauer, O. Halbherr, K. Epp, P. Guo, M. I. Gonzalez, D. J. Xiao, C. Wiktor, F. X. Llabrés i Xamena, C. Wöll, Y. Wang, M. Muhler and R. A. Fischer, *Chem. – Eur. J.*, 2016, **22**, 14297–14307.
32 K. S. Kim, W. E. Baitinger, J. W. Amy and N. Winograd, *J. Electron Spectrosc. Relat. Phenom.*, 1974, **5**, 351–367.
33 P. Froment, M. J. Genet and M. Devillers, *J. Electron Spectrosc. Relat. Phenom.*, 1999, **104**, 119–126.
34 C. R. Wade and M. Dinca, *Dalton Trans.*, 2012, **41**, 7931–7938.
35 W. Zhang, O. Kozachuk, R. Medishetty, A. Schneemann, R. Wagner, K. Khaletskaya, K. Epp and R. A. Fischer, *Eur. J. Inorg. Chem.*, 2015, **2015**, 3913–3920.
36 M. K. Bhunia, J. T. Hughes, J. C. Fettinger and A. Navrotsky, *Langmuir*, 2013, **29**, 8140–8145.
37 A. G. Wong-Foy, A. J. Matzger and O. M. Yaghi, *J. Am. Chem. Soc.*, 2006, **128**, 3494–3495.
38 J. Liu, J. T. Culp, S. Natesakhawat, B. C. Bockrath, B. Zande, S. G. Sankar, G. Garberoglio and J. K. Johnson, *J. Phys. Chem. C*, 2007, **111**, 9305–9313.
39 M. Hartmann, S. Kunz, D. Himsl, O. Tangermann, S. Ernst and A. Wagener, *Langmuir*, 2008, **24**, 8634–8642.
40 A. Ö. Yazaydın, A. I. Benin, S. A. Faheem, P. Jakubczak, J. J. Low, R. R. Willis and R. Q. Snurr, *Chem. Mater.*, 2009, **21**, 1425–1430.
41 G. Delen, Z. Ristanović, L. D. B. Mandemaker and B. M. Weckhuysen, *Chem. – Eur. J.*, 2018, **24**, 187–195.
42 C. Prestipino, L. Regli, J. G. Vitillo, F. Bonino, A. Damin, C. Lamberti, A. Zecchina, P. L. Solari, K. O. Kongshaug and S. Bordiga, *Chem. Mater.*, 2006, **18**, 1337–1346.
43 G. Mahalakshmi and V. Balachandran, *Spectrochim. Acta, Part A*, 2014, **124**, 535–547.
44 N. R. Dhumal, M. P. Singh, J. A. Anderson, J. Kiefer and H. J. Kim, *J. Phys. Chem. C*, 2016, **120**, 3295–3304.
45 M. Todaro, A. Alessi, L. Sciortino, S. Agnello, M. Cannas, F. M. Gelardi and G. Buscarino, *J. Spectrosc.*, 2016, **2016**, 7.
46 G. Socrates, *Infrared and Raman Characteristic Group Frequencies: Tables and Charts*, Wiley, 2004.
47 E. G. Palacios, G. Juárez-López and A. J. Monhemius, *Hydrometallurgy*, 2004, **72**, 139–148.
48 H. Kitamura, T. Ozawa, K. Jitsukawa, H. Masuda, Y. Aoyama and H. Einaga, *Inorg. Chem.*, 2000, **39**, 3294–3300.
49 T. Kawamura, H. Katayama, H. Nishikawa and T. Yamabe, *J. Am. Chem. Soc.*, 1989, **111**, 8156–8160.
50 E. B. Boyar and S. D. Robinson, *Coord. Chem. Rev.*, 1983, **50**, 109–208.
51 A. L. Abuhijleh, H. A. Ali and A.-H. Emwas, *J. Organomet. Chem.*, 2009, **694**, 3590–3596.
52 J. Kitchens and J. L. Bear, *Thermochim. Acta*, 1970, **1**, 537–544.
53 C. K. Brozek and M. Dincă, *Chem. Soc. Rev.*, 2014, **43**, 5456–5467.
54 H. Liu, W. P. Gan, F. Zheng, G. Q. Guo, H. R. Ma and J. Luo, *Synth. React. Inorg., Met.-Org., Nano-Met. Chem.*, 2010, **40**, 499–502.
55 M. Rusjan, E. E. Sileo and F. D. Cukiernik, *Solid State Ionics*, 2003, **159**, 389–396.
56 M. C. Rusjan, E. E. Sileo and F. D. Cukiernik, *Solid State Ionics*, 1999, **124**, 143–147.
57 J. Kitchens and J. L. Bear, *J. Inorg. Nucl. Chem.*, 1970, **32**, 49–58.
58 B. Bueken, N. Van Velthoven, A. Krajnc, S. Smolders, F. Taulelle, C. Mellot-Draznieks, G. Mali, T. D. Bennett and D. De Vos, *Chem. Mater.*, 2017, **29**, 10478–10486.

4.3 Study III

Thermal Defect-Engineering of Precious Group Metal-Organic Frameworks:

A Case Study on Ru/Rh-HKUST-1 Analogues

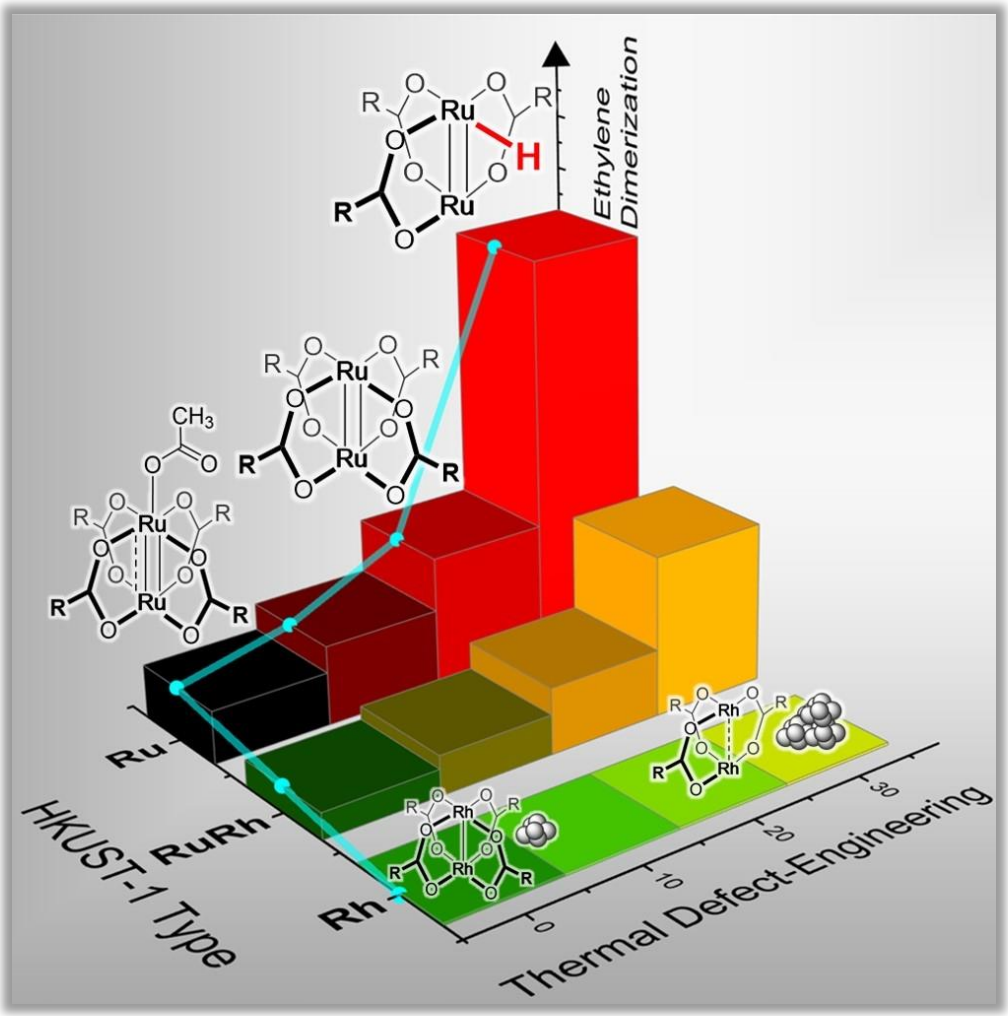

Thermal Defect-Engineering of Precious Group Metal-Organic Frameworks:

A Case Study on Ru/Rh-HKUST-1 Analogues

Werner R. Heinz, Iker Agirrezabal-Telleria, Raphael Junk, Jan Berger, Junjun Wang, Dmitry I. Sharapa, Miryam Gil-Calvo, Ignacio Luz, Mustapha Soukri, Felix Studt, Yuemin Wang, Christof Wöll, Hana Bunzen, Markus Drees and Roland A. Fischer

ACS Applied Materials & Interfaces **2020**, 12, 40635 – 40647.

Inspired by the works of *Agirrezabal-Telleria*,[252] this study widens the toolbox of defect-engineering strategies. A new methodology is introduced for controlled post-synthetic **thermal defect-engineering** (TDE) of the PGM-MOFs Ru- RuRh- and Rh-HKUST-1. Online quantitative monitoring the TDE process allowed for predefined levels of defectiveness within the produced materials. Characterization of the samples employing a complementary set of analytical, spectroscopic, and computational techniques reveals that the compositionally complex TDE-MOF materials result from elimination and/or fragmentation of ancillary ligands and/or linkers. TDE involves the preferential secession of acetate ligands, intrinsically introduced via coordination modulation during synthesis, and the gradual decarboxylation of ligator sites of the framework linker BTC. Both processes lead to modified Ru/Rh PW nodes. These nodes exhibit a lowered average oxidation state and more accessible OMS, as deduced from SLIR using CO as probe and supported by DFT-based computations. The monometallic and the mixed metal PGM-MOFs systematically differ in their TDE properties and, in particular, in the hydride generation ability (HGA) demonstrated on the basis of ethene dimerization activity. Eventually, this work provides answers to the origin of the increased hydrogen transfer activity as observed in **Study I**.

ACS APPLIED MATERIALS & INTERFACES

www.acsami.org Research Article

Thermal Defect Engineering of Precious Group Metal–Organic Frameworks: A Case Study on Ru/Rh-HKUST-1 Analogues

Werner R. Heinz, Iker Agirrezabal-Telleria, Raphael Junk, Jan Berger, Junjun Wang, Dmitry I. Sharapa, Miryam Gil-Calvo, Ignacio Luz, Mustapha Soukri, Felix Studt, Yuemin Wang, Christof Wöll, Hana Bunzen, Markus Drees, and Roland A. Fischer*

Cite This: *ACS Appl. Mater. Interfaces* 2020, 12, 40635–40647 Read Online

ACCESS | Metrics & More | Article Recommendations | Supporting Information

ABSTRACT: A methodology is introduced for controlled postsynthetic thermal defect engineering (TDE) of precious group metal–organic frameworks (PGM-MOFs). The case study is based on the Ru/Rh analogues of the archetypical structure $[Cu_3(BTC)_2]$ (HKUST-1; BTC = 1,3,5-benzenetricarboxylate). Quantitative monitoring of the TDE process and extensive characterization of the samples employing a complementary set of analytical and spectroscopic techniques reveal that the compositionally very complex TDE-MOF materials result from the elimination and/or fragmentation of ancillary ligands and/or linkers. TDE involves the preferential secession of acetate ligands, intrinsically introduced via coordination modulation during synthesis, and the gradual decarboxylation of ligator sites of the framework linker BTC. Both processes lead to modified Ru/Rh paddlewheel nodes. These nodes exhibit a lowered average oxidation state and more accessible open metal centers, as deduced from surface-ligand IR spectroscopy using CO as a probe and supported by density functional theory (DFT)-based computations. The monometallic and the mixed-metal PGM-MOFs systematically differ in their TDE properties and, in particular in the hydride generation ability (HGA). This latter property is an important indicator for the catalytic activity of PGM-MOFs, as demonstrated by the ethylene dimerization reaction to 1-butene.

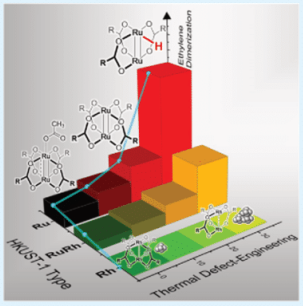

KEYWORDS: *metal–organic framework, HKUST-1, Ru-BTC, Rh-BTC, precious metal, thermal defect engineering, ethylene dimerization, solid–gas interactions*

INTRODUCTION

Metal–organic frameworks (MOFs) are unique among solid-state materials in structural design and precise molecular tunability[1−3] and, thus, offer fascinating dimensions for potential applications.[4−6] The very high abundance of exposed and accessible reaction centers of defined nature as well as the chemically programmable and confined coordination space of the pore structure render MOFs highly interesting for catalysis.[7−11] Although reticular chemistry naturally strived for perfect compositional definition, highest crystallinity of samples, and thus maximizing framework structural perfection, this paradigm is hence shifting toward also acknowledging the new opportunities that arise from defective structures, a characteristic feature of any solid-state material,[12] and thus to compositionally much more complex MOFs.[13−16]

The controlled introduction of defects—termed defect engineering (DE)—has been recognized as a valuable tool of tailoring MOF properties beyond the choice of nodes, linkers, and topology.[17−20] DEMOF design strategies can be grouped into two categories: de novo synthesis, for example, by implementing defect generating (truncated) linkers during synthesis[21−24] and postsynthetic modifications (PSM) of pristine MOFs.[18,25] For example, PSM by thermal annealing (TA) beyond activation is widely used to remove chemisorbed coordination modulators to yield open metal sites (OMS) at the nodes. UiO-66 has been the prime model case for this concept and as well as HKUST-1 (Cu, Ru) and UHM-3 for exploiting related linker fragmentation processes (e.g., decarboxylation).[13,26−28]

The thermal annealing (TA) could thus become a very attractive and general method for DEMOF synthesis. TA targets the more or less narrow temperature window between activation (desorption of physisorbed guests)[29] and decomposition (collapse of the framework; carbonizing to MOF-derived materials).[30−32] However, moving from the more qualitative TA toward a truly quantitative thermal defect engineering (TDE) requires quite a conceptual step ahead in process design and the precise control of thermal PSM of MOFs.

Received: June 12, 2020
Accepted: August 14, 2020
Published: August 14, 2020

https://dx.doi.org/10.1021/acsami.0c10721
ACS Appl. Mater. Interfaces 2020, 12, 40635–40647

Herein, we want to present our results on TDE of the precious group metal (PGM)-based HKUST-1 (Ru, Rh) analogues as the materials of choice for our proof-of-concept study. The selection is based on the combination of high chemical, thermal, and mechanical stability with defect tolerance and redox flexibility. In addition, our choice is motivated by the importance of PGMs for catalysis on an industrial scale and the lack of fundamental and systematic research on PGM-based MOFs. Among the first PGM-MOFs to be investigated in some detail were the mixed valent $Ru^{II,III}$ and the univalent $Ru^{II,II}$ analogues of the archetypical $[Cu_3(BTC)_2]$ (HKUST-1; BTC = 1,3,5-benzenedicarboxylate).[33−35] Like the parent structure, the Ru-HKUST-1 features tetra-connected, dinuclear Ru-paddlewheel (PW) nodes. In the mixed-valence $Ru^{II,III}$ case, additional chloride (Cl) and acetate (OAc) ligands axially coordinate to the PWs and compensate for the higher oxidation state.[36] The synthesis of Ru-HKUST-1 is based on the so-called controlled secondary building unit approach (CSA) employing precursors with preformed $M_2(OAc)_2$ PW units. A range of PGM-HKUST-1 analogues have been obtained accordingly (M = Ru, Rh[34−40]), including mixed-metal congeners with homometallic $Ru^{II,III}$ and $Rh^{II,II}$ nodes in varying molar ratios and doped (Cu, PGM)-HKUST-1 derivatives.[41−43] For Ru/Rh-HKUST-1, it was found that the preparation of phase pure, crystalline, and highly porous products is strongly reliant on high amounts of acetic acid (HOAc) as the cosolvent.[21,23,44] It acts as a coordination modulator and is retained (chemisorbed) in the final material due to very slow substitution kinetics at the PGM nodes.[18,19] The development of an acetate-free synthesis for perfect, i.e., "defect-free", compositionally simple PGM-HKUST-1 (exactly matching the empirical formula $[M_3(BTC)_2]$) has proved to be highly demanding, and this problem is still not solved.

Herein, we present a comprehensive report on TDE of Ru/Rh-HKUST-1 by comparing the univalent $Rh^{II,II}$ and mixed-valence $Ru^{II,III}$ with their mixed-metal RuRh derivatives together with the univalent $Ru^{II,II}$ based on a complementary set of analytical techniques. We present structure−property relationships on the solid−gas interactions (N_2, CO, H_2, D_2, C_2H_6, C_2H_4) and on the catalytic ethylene dimerization to 1-butene as a test reaction as highlighted in Figure 1.

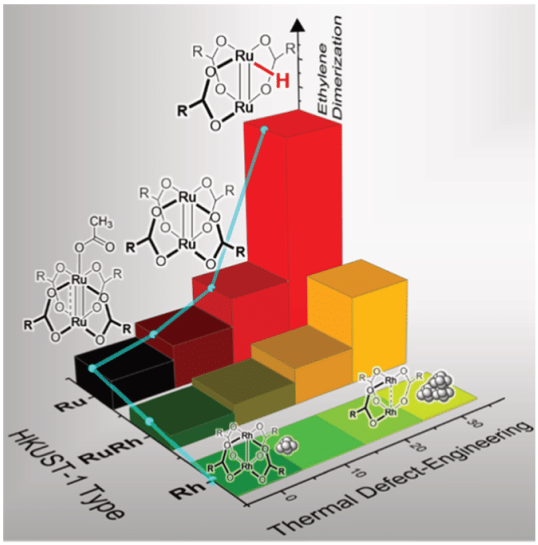

Figure 1. Presented in this work, thermal defect engineering (TDE) of Ru/Rh-HKUST-1 activates the materials for efficient ethylene dimerization by creating modified node defects featuring a lower average oxidation state, more accessible metal centers, and M-H species as a function of the Ru/Rh composition.

EXPERIMENTAL SECTION

General Information. Full experimental details regarding utilized reagents, solvents, analytical techniques (instruments), and methods are provided in the Supporting Information (SI). For all prepared samples, an (X/Y) nomenclature will be used, referring to X % Rh feed fraction (incorporation confirmed by inductively coupled plasma mass spectrometry (ICP-MS))[40] of the respective parental M-MOF (M-HKUST-1) and Y % postsynthetically induced defects. Note, the value Y % refers basically to the amount of removed carboxylate ligator sites (CO_2) coordinating to the paddlewheel units of the framework. However, the details are complicated and will be discussed in the main text. An elaborate description of how this empirical parameter was derived based on the analytical data is given in the Supporting Information.

Thermal defect engineering (TDE) was performed using a thermogravimetric analysis (TGA)-MS setup operated within an argon-filled glovebox. Volatiles were analyzed on-line with mass spectrometry (TG-MS coupling), and powder X-ray diffraction (PXRD) was conducted with Cu $K\alpha$ radiation in a range of 5−50° 2θ using a Panalytical Empyrean. Analytical C and H contents were determined using a Hekatech EuroEA elemental analyzer, and metal contents (Ru, Rh) were derived from TGA-based metal oxide residues (assuming M_2O_3 as confirmed by PXRD) in synthetic air in accordance with ICP-MS as reported earlier.[40] Repeating units for deriving the empirical formulae were calculated using elemental contents (C, H, M) and a solver-based approach using Microsoft Excel (for details, see the SI). Variable temperature PXRD and Fourier transform infrared (FT-IR) measurements were conducted with pristine Ru-, RuRh-, and Rh-MOFs (0/0), (50/0), and (100/0). The sorption properties of pristine and defective samples were studied using nitrogen (N_2, 77 K), ethane (C_2H_6), and ethene (C_2H_4), each 278, 288, and 298 K. Density functional theory (DFT)-based pore size distributions were determined using N_2 sorption isotherms, and isosteric energies of adsorption for ethane and ethene sorption were determined using Clausius−Clapeyron and Langmuir−Freundlich equations for gas loadings in the range of 10−50 $cm^3\ g^{-1}$. FT-IR spectra were recorded from 4000 to 400 cm^{-1} using an attenuated total reflection (ATR) unit, and Raman spectra were recorded from 20 to 2000 cm^{-1} with 532 nm laser wavelength excitation. Variable temperature FT-IR was conducted using (0/0), (50/0), (100/0), and $Ru^{II,II}$ samples with N_2, H_2, or D_2 gas flow. High-resolution CO probe FT-IR spectroscopy was conducted in UHV at low temperatures after treatments at different annealing temperatures for defect creation. All density functional theory (DFT) calculations were performed in ORCA 4.2.0. Minnesota DFT functionals (M06 and M06L) were used with a def2-TZVP basis set and RIJCOSX approximation (see the Supporting information for details).

TDE-MOF Synthesis Method. Pristine samples of Ru-MOF (0% Rh), RuRh- (50%Rh), and Rh-MOF (100%Rh) and a $Ru^{II,II}$-MOF reference sample were prepared in solvothermal reactions following the controlled secondary building unit approach (CSA) as reported earlier.[35,40] After stepwise solvent exchange (H_2O, EtOH, Me_2CO, CH_2Cl_2, each twice), subsequent desolvation (activation in dynamic vacuum at 150 °C, ≈10^{-2} mbar) and basic characterization (PXRD, FT-IR, N_2 adsorption), thus obtained pristine, clean MOF samples were further processed using a thermogravimetry instrument (TG) coupled with a mass spectrometer (MS). This led to the definition of thermal defect-engineering protocols (TDE) and the reproducible synthesis of samples with defined defectiveness on a preparative microscale (~30 mg). TDE of the samples was performed using a TG-MS setup within a glovebox. This allowed accessibility of both

https://dx.doi.org/10.1021/acsami.0c10721
ACS Appl. Mater. Interfaces 2020, 12, 40635−40647

predefined weight losses and the protection of the obtained highly reactive samples from undesired deactivation in air (e.g., uncontrolled guest sorption or oxidation). TDE-MOF sample homogeneity is ensured through a multistep temperature program design (Figure 2)

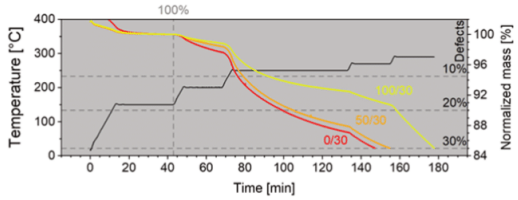

Figure 2. Weight loss profiles and the temperature program for PGM-MOF thermal defect engineering (TDE). The plateau at 150 °C between 20 and 40 min (vertical reference line) indicates complete removal of weakly physisorbed species and guests (solvents). The dashed vertical line indicates the point of weight referencing (activated, "clean" sample). The dashed horizontal lines indicate the targeted weight loss for 10, 20, and 30% defectiveness. For experimental details, see the SI.

utilizing successive isothermal steps as a combination of isothermal parts and ramps with constant heating rates.[45] Weight loss monitoring allowed for a controlled TDE between 150 °C (423 K) and 300 °C (573 K) to reproducibly yield samples of specified (Y%) defectiveness. Specifically, predefined analytical mass losses of 5.5, 10, and 15% (due to small molecular mass species $C_xH_yO_z$, e.g., H_2O, CO, CO_2, $H_2C{=}C{=}O$) were targeted to yield three series of samples for each pristine MOF of the study. On the basis of elemental analysis and thereof derived sum formulae, different quantitative defect descriptors (%) were calculated depending on the whole organic fraction, removed carboxylate ligator sites (CO_2), and finally including Cl ligands. An overview is provided in Table S3. Using the above-mentioned nomenclature, the samples are denoted 10, 20, and 30% defectiveness in the following. However, note that this descriptor is simplified to facilitate sample denomination. Details are discussed in the main text and the SI.

RESULTS AND DISCUSSION

Concept of Study and Leading Questions. Previous work on various kinds of defect-engineered and/or hydrogen-pretreated Ru-HKUST-1[46] revealed a characteristic boost of the catalytic activity in several test reactions such as the Meerwein–Ponndorf–Verley hydride transfer, in the isomerization of allylic alcohols to saturated ketones and in selective ethene dimerization to 1-butene.[23,47] These studies raised a number of questions: What is the role of the high amount of residual (chemisorbed) acetate and chloride ligands in the pristine Ru-MOF samples and the fate of these species during activation and defect engineering? How are Ru-H species formed? How is the metal oxidation state affected during TDE, and how does this correlate with the catalytic activity? To which extent a transfer of findings is possible from Ru to Rh? Can we draw more general conclusions on TDE of MOFs using the above-defined model systems as a study case? Previous works on thermal treatments of MOFs typically lack precise analytical monitoring of the process and have mainly been limited to MOF-5 and UiO-66 (and related systems), the investigation of the activation parameters,[29] and removing loosely bound framework components, including coordination modulators.[13,26,48] Our study goes beyond this previous work. It is guided by the idea of targeting controlled linker fragmentation (e.g., decarboxylation) at the temperature window between activation and framework collapse. Since PGM-HKUST-1 analogues are thermally very robust and at the same time contain catalytically very versatile and redox-active metal centers, we selected them for this detailed case study.

Sample Synthesis: TDE Based on TG-MS Data. Based on the previous report on thermal treatment of Ru-HKUST-1,[62] we developed a procedure to reproducibly access different stages of defectiveness in the MOF samples (experimental part, see also the SI). From the TG-MS data of the carefully activated samples in the temperature window between 150 and 300 °C, the following information is obtained. For all samples, H_2O, CO, and CO_2 are observed as major elimination species peaking on each temperature increase (Figures S1 and S2). Additional species, in particular ketene ($H_2C{=}C{=}O$) and other small $C_xH_yO_z$ fragments (C_3H, $C_2H_4O_2$, $C_2H_2O_3$) are detected. The comparison with literature data on the thermal properties of densely packed (stacked metal sites) metal carboxylates suggests similar decomposition mechanisms taking place in open, highly porous frameworks (isolated metal sites), i.e., MOFs studied herein.[49] In contrast to these species, acetate elimination (m/z = 60) takes place at 250 °C almost quantitatively without detectable peaks at lower or higher temperatures. This suggests a preferred removal of

Table 1. Elemental Contents, Calculated Sum Formulae, Derived Metal Charges, and Related N_2 Surface Areas

sample		found C/H/Cl/M_{tot} content (wt %)	ascertained sum formula	mean metal charge	BET surface area ($m^2\ g^{-1}$)	BET surface area ($m^2\ mmol^{-1}$)
Rh-BTC	(100/0)	29.1/1.56/0/41.0	$[Rh_3(BTC)_{1.61}(OAc)_{1.89}]$	+2.24	1360	1025
	(100/10)	28.1/1.30/0/43.1	$[Rh_3(BTC)_{1.22}(IPA)_{0.39}(OAc)_{1.34}]$	+1.92	1340	943
	(100/20)	27.9/1.28/0/45.5	$[Rh_3(BTC)_{0.86}(IPA)_{0.74}(OAc)_{1.01}]$	+1.70	1424	954
	(100/30)	27.6/1.22/0/48.0	$[Rh_3(BTC)_{0.61}(IPA)_{0.99}(OAc)_{0.64}]$	+1.49	1274	812
RuRh-BTC	(50/0)	30.4/1.66/1.5/39.2	$[Ru_{1.44}Rh_{1.56}(BTC)_{1.52}(OAc)_{2.69}Cl_{0.3}]$	+2.53	1211	958
	(50/10)	30.0/1.26/1.5/40.4	$[Ru_{1.44}Rh_{1.56}(BTC)_{1.36}(IPA)_{0.57}(OAc)_{1.03}Cl_{0.3}]$	+2.19	n.d.	n.d.
	(50/20)	28.9/1.26/1.5/42.8	$[Ru_{1.44}Rh_{1.56}(BTC)_{0.64}(IPA)_{1.27}(OAc)_{0.64}Cl_{0.3}]$	+1.80	n.d.	n.d.
	(50/30)	28.3/1.22/1.45/44.8	$[Ru_{1.44}Rh_{1.56}(BTC)_{0.54}(IPA)_{1.27}(OAc)_{0.52}Cl_{0.3}]$	+1.66	n.d.	n.d.
Ru-BTC	(0/0)	29.8/1.34/3.0/37.4	$[Ru_3(BTC)_{1.89}(OAc)_{1.55}Cl_{0.7}]$	+2.64	1018	825
	(0/10)	29.1/1.67/3.0/39.1	$[Ru_3(BTC)_{0.56}(IPA)_{1.32}(OAc)_{1.55}Cl_{0.65}]$	+2.18	1065	801
	(0/20)	30.8/0.93/2.9/41.2	$[Ru_3(BTC)_{0.82}(IPA)_{1.44}(OAc)_0Cl_{0.61}]$	+1.97	1034	755
	(0/30)	28.8/1.04/2.9/43.6	$[Ru_3(BTC)_{1.12}(IPA)_{0.76}(OAc)_{0.24}Cl_{0.57}]$	+1.90	1173	816
	$Ru^{II,II}$	27.4/1.50/0/42.5	$[Ru_3(BTC)_{1.32}(OAc)_{2.22}]$	+2.06	1493	1056

https://dx.doi.org/10.1021/acsami.0c10721
ACS Appl. Mater. Interfaces 2020, 12, 40635−40647

acetate (both monodentate and bridging) over complete BTC elimination or partial BTC ligator site decarboxylation, which takes place mostly at higher temperatures. A differentiation between eliminated monodentate (axial) and bridging (equatorial) acetates is not substantiated on a quantitative basis (for qualitative assignments, CO-SLIR and Raman data are discussed below and in Table S2). However, chemical intuition suggests the removal of $OAc_{(axial)}$ > $OAc_{(eq)}$ > $BTC_{(fragmentation)}$ according to hapticity (monodentate vs bridging) and binding properties (with or without framework incorporation/dative or covalent bond). Upon temperature increase to 250 °C, the detection of trace amounts of ^{35}Cl in Ru-containing samples indicates the removal of Cl-species from the mixed-valent $Ru^{II,III}$ nodes. However, as discussed later, elemental analysis revealed the Cl content to be mostly unaffected. Traces of Cl are potentially released in the form of HCl. From a TGA-MS experiment with consecutive treatment in N_2 and H_2 atmosphere (Figure S3), we conclude that Cl—although more difficult to be removed in an inert atmosphere (N_2)—readily forms HCl (m/z = 35) when TDE is conducted in a H_2 atmosphere and thereby generates M-H species (detected by FT-IR, vide infra). Upon TDE, the samples darkened, especially the bright green 100% Rh sample. This can indicate the formation of modified PWs and/or of metal nanoparticles. Rh-MOF appears to have a slightly higher thermal stability as defect generation requires more time or higher temperatures as compared to Ru-MOF.

Composition and Definition of Defectiveness. TGA allows for the quantification of the metal oxide residues (according to ref 40) and, thus, the determination of the total metal content (M_{tot}) of each sample. With the increasing loss of small $C_xH_yO_z$ components (as described above), the "defectiveness" is rising and, consequently, all samples exhibit rising M_{tot} as well (Table 1). This empirical parameter defectiveness can be quantitatively defined in various ways depending on the removed fraction of (a) the nonmetallic content ($C_wH_xO_yCl_z$), (b) the total removed ligands (CH_3CO_2, CO_2, and Cl), or (c) particularly referring to the removed carboxylate ligator sites (CO_2). For reasons of simplicity and to level the slight differences between these different viewpoints, the TDE samples are thus denoted as 10, 20, and 30% defectiveness, respectively. Detailed definitions for defectiveness and related quantitative defect amounts (Table S3) are provided in the SI. The derived M_{tot} were complemented by analytical C, H, and Cl elemental analyses (EA), providing the basis for nonlinear solver-assisted empirical sum formulae calculations. As shown previously, C, H, and M contents serve a sufficient basis for a reliable sum formulae calculation utilizing a tailored solver approach.[40] Note that, however, unfortunately, quantitative acid digestion (even in aqua regia) is not possible with these samples. Thus, a reliable quantitative determination of organic components, e.g., BTC, IPA, and OAc proved to be not sufficiently reliable by high-performance liquid chromatography (HPLC) or NMR analysis.[40] Defining OAc and BTC as the exclusive organic framework components, the applied solver provides good and reproducible fitting results for the pristine PGM-MOFs. For the TDE-MOF samples, we nevertheless have to make assumptions for the composition based on the combined analytical and spectroscopic evidence. Thus, the scope of plausible framework components is complemented by isophthalate (IPA) as the decarboxylation product from BTC. Benzoic acid resulting from potential double decarboxylation was without regard since BTC is still present in most defective samples. This reasoning is in line with the existing literature.[50,51] Both the experimentally found hydrogen content as well as the derived (formal) mean metal charges correlate well with increasing sample defectiveness defined by TGA, as can be seen in Figure 3. Taking into account that pristine Ru- and Rh-MOFs should have mean (formal) metal charges of 2.5 and 2.0, the herein obtained values are in good agreement with the expected outcome. A differentiation between axially and equatorially (bridging) bound acetates is shown for pristine MOFs in Table S2. Neither hydrides nor hydroxides nor acidic protons were considered (due to the absence of quantification methods) in the calculation of the formal mean metal charges. Thus, there is some intrinsic uncertainty of the assumed sum formulae. As reported earlier, X-ray photoemission spectroscopy (XPS) does not allow unambiguous quantification and assignments of metal oxidation states in these PGM-MOFs.[40] Alternatives to the herein chosen approach (EA-based solver and CO probe FT-IR spectroscopy as discussed below) to access metal oxidation states are sophisticated synchrotron techniques like the X-ray absorption near-edge structure spectroscopy (XANES). Since the high energy X-rays particularly required for Ru and Rh are limited to just a few facilities worldwide, such synchrotron-based techniques were not available for this study.[40]

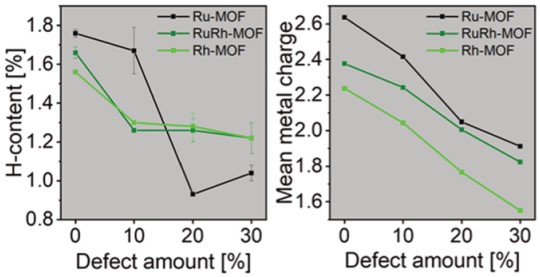

Figure 3. Correlation of the hydrogen content (left) and calculated mean metal charge (right) with sample defectiveness (see definition 1 in the SI). Calculation assuming quantitatively deprotonated carboxylates (OAc, IPA, BTC).

All of the obtained TDE-MOF samples were then characterized by standard TGA. The resulting graphs are depicted in Figures S10–S12. A correlation between defectiveness and thermal stability can be deduced. The slightly decreasing characteristic decomposition temperatures (above 250 °C) are perfectly aligned with the materials' rising defectiveness. Intuitively, any removal of stabilizing linkers creates an ever more destabilized structure. However, we emphasize that the decrease of thermal stability in DE-Cu-HKUST-1 (de novo synthesis by defect generating linkers) is much more pronounced with rising defectiveness as compared to TDE-PGM-HKUST-1 studied herein.[24]

TDE-MOFs: Structure and Stability. Variable temperature-programmed XRD data (VT-XRD) of the three pristine Ru/Rh-MOF samples 100%Rh, 50%Rh, and 0%Rh are displayed in Figure 4. All three samples preserve their structure until amorphization between 350 and 400 °C, with Ru-MOF (0%Rh) showing the highest thermal stability. Amorphization occurs without any intermediate phase transformation for all samples. On first glance, this is inconsistent with TGA-based

https://dx.doi.org/10.1021/acsami.0c10721
ACS Appl. Mater. Interfaces 2020, 12, 40635–40647

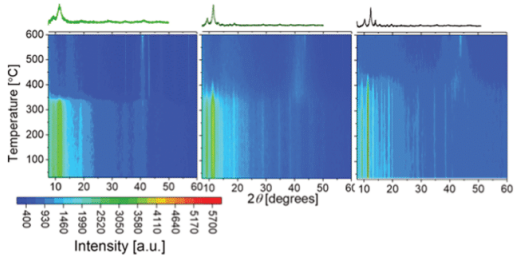

Figure 4. VT-XRD pattern contour plots of PGM-MOFs. Left: 100% Rh-, middle: 50%Rh-, and right: 0%Rh sample. Upon higher temperatures, new reflections indicate NP formation. PXRD patterns of pristine MOFs at ambient temperature are shown on top. Note: Additional lines from the Al sample holder become visible.

results, from which Rh-BTC seems slightly more stable. As amorphization in general depends on the thermal stability, we primarily attribute these findings to differences in the pristine defect content and crystallite sizes.[52,53] The individual PXRD measurements of all synthesized, still crystalline TDE-MOFs indicate retention of the HKUST-1 analogous structure, as can be seen in Figures S4−S6. The 100%Rh sample treated up to 250 °C features broad reflections and, in this case, Rh-NP formation (41.1° 2θ) correlates with the defect amount, which is already visible in the (100/10) sample. Additional high-resolution transmission electron microscopy (HR-TEM) images confirm the formation of metal NPs in Rh-containing samples as displayed in Figures S47−S48.

Sorption Properties. *Nitrogen Sorption.* For all samples, nitrogen ad- and desorption follows a reversible type I (b) isotherm. Generally, TDE can enhance the gravimetric N_2 surface areas with respect to the pristine MOFs, as shown in Table 1 and Figure 5. The increase in the gravimetric surface area is more pronounced in Ru-based materials. Transformed

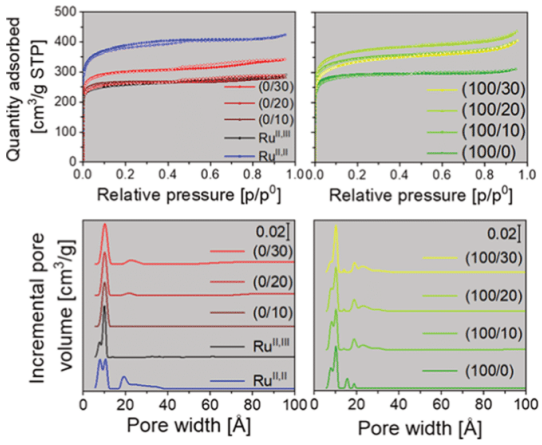

Figure 5. Top: Nitrogen sorption isotherms recorded at 77 K. Closed symbols represent adsorption and open symbols represent desorption branches. Bottom: Incremental pore volumes displaying the DFT-derived pore size distribution assuming cylindrical pores on oxide surfaces. Left: 0%Rh series; right: 100%Rh series. TDE leads to an increase in gas uptake and merging of small pores into larger mesopores (see pores > 15 Å).

into molar values, a decrease can be observed, which is attributed to the removal of framework components during TDE and, thus, the lower typical molar mass of the respective repeating units. The still high and preserved porosity is in accordance with predominantly preserved framework structures as found through crystallographic and spectroscopic means. All TDE-MOFs exhibit a successively reduced number of micropores of ∼7−8 Å to the benefit of larger (meso) pores (>15 Å) (see the emerging hysteresis in the plateaus of the TDE isotherms and their PSD plots in Figure 5 and also Figures S17−S20), which is assigned to linker fragmentation via decarboxylation (BTC → IPA) upon TDE. Pristine mixed-valence $Ru^{II,III}$-MOF, comprising axial ligands (Cl, OAc), features additional pores. A medium-sized micropore of ∼9 Å is present. In HKUST-1-type frameworks, three different pores occur: a small one (further called pore A) with ∼8 Å and two degenerate pores with ∼10 Å size (further called pores B and C). However, the axial positions of the PWs point only into one (pore B) of these degenerate pores. Thus, the presence of axial ligands in mixed-valent $Ru^{II,III}$-HKUST-1 causes this pore B to be reduced to ∼9 Å, abolishing the degeneration. Upon TDE, axial acetate ligands seem to be removed preferentially as the aforementioned medium-sized micropore cannot be observed in TDE-Ru-MOFs anymore. As reported earlier, the synthesis procedure for the $Ru^{II,II}$-MOF provides a rather defective material also featuring mesopores (see Figure 5).[35]

Ethane and Ethene Sorption. Ethane (C_2H_6) and ethene (C_2H_4) sorption experiments were performed, aiming for correlations with the observed differences of the TDE-MOFs in ethene dimerization activity (see below). For ideal, reversible sorption on innocent hosts, adsorbed gas amounts should decrease with higher sorption temperatures. With isotherms recorded at different temperatures (here, 278, 288, and 298 K), the isosteric enthalpy of adsorption (EoA) can be determined. For the saturated hydrocarbon ethane, the trends appear as expected, and (gravimetric) sorption capacities increase with defectiveness (Figures S21−S28, Table S4). In line with the N_2-based results, the sample (100/20) has the highest ethane uptake within the Rh series. Within the Ru series, the uptake also increases with defectiveness and the $Ru^{II,II}$ sample allows the highest uptake. The desorption of ethane is quantitative for all samples, suggesting fully reversible sorption processes. The derived EoAs for ethane can be seen in Figure 6. Ru-based TDE-MOFs have only subtle differences in ethane sorption enthalpies, which decrease with higher loadings (left graph), suggesting preferred adsorption sites as also observed for Cu-HKSUT-1.[54] Interestingly, the univalent Ru-MOF features lower EoA (≈25 kJ mol^{-1}) than the mixed-valent Ru-MOF (≈30 kJ mol^{-1}). Temperature-induced removal of axially bound OAc seems to render the pore environment less lipophilic. In contrast, on Rh samples, ethane EoAs are independent of the loading but generally increase upon TDE from ≈30 kJ mol^{-1} in pristine Rh-MOF up to ≈40 kJ mol^{-1} in the (100/20) sample (right graph).

The ethene (C_2H_4) sorption isotherms are depicted in Figures S29 and S30. Strong hysteresis between adsorption and desorption branches as well as significant amounts of irreversibly adsorbed species (further called residues) are observed most predominantly for TDE-MOFs. Such behavior of inversed temperature trends to what was anticipated has been rarely reported in the MOF literature so far.[55,56] These other data were assigned to pore window blocking at low temperatures. Herein, however, we assign our data to a partial

https://dx.doi.org/10.1021/acsami.0c10721
ACS Appl. Mater. Interfaces 2020, 12, 40635−40647

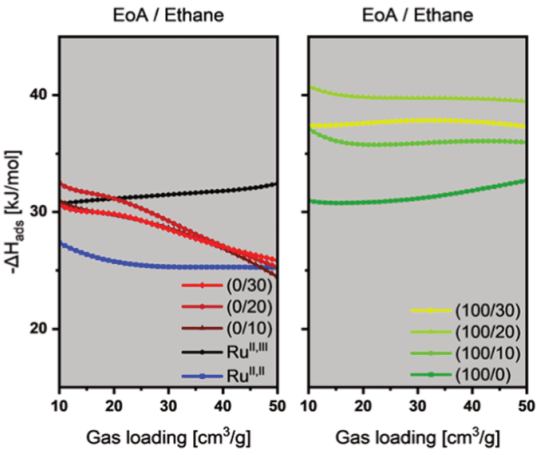

Figure 6. Isosteric enthalpy of adsorption for ethane derived from sorption isotherms. Left: Ru-based MOFs; right: Rh-based MOFs. No energetic differences can be observed for TDE-MOFs. Energies of adsorption slightly decrease upon higher loadings. For Rh-TDE-MOFs, EoA increases upon TDE peaking in (100/20).

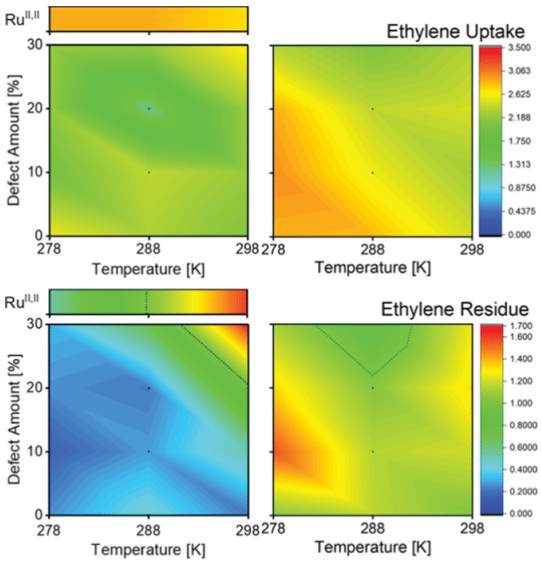

Figure 7. Contour plots of ethylene sorption: Left side: Ru-; right side: Rh-MOFs. Top row: uptake in molecules per PW. Bottom row: residue in molecules per PW. The dashed isoline represents the threshold of one molecule per PW. A different visualization is shown in Figures S31 and S32.

chemisorption of ethene (e.g., to some chemical reactivity at the nodes). This correlates with temperature dependence and counteracts the anticipated physisorption behavior inverting the expected trend. Unfortunately, this effect prevents meaningful EoA calculations for comparison. Nevertheless, some additional conclusions can be drawn from ethene sorption isotherms. Based on the molar uptake and amounts of residues (mmol g_{MOF}^{-1}), we estimated the number of adsorbed ethene molecules per paddlewheel unit. Correlation of ethene uptakes and residues with sorption temperature and sample defectiveness was visualized in contour plots displayed in Figure 7. Strong chemisorption of ethene occurs on Ru-MOF and on Rh-MOF (most certainly at OMS: see Figures S21 and S22 for N_2 isotherms and PSDs after repeated ethene sorption according to literature reports[57,58]). However, some additional reactivity seems to be exclusive for Ru-based MOFs. This can be concluded from the significantly increased amounts of residues at the highest sorption temperature (see Tables S5 and S6). Drastically increased uptake and residues for the most defective (0/30) Ru-MOF sample suggest the highest reactivity toward ethene in this series. In line with the postulated TDE-induced metal reduction to $Ru^{\delta+}$ species (see below), the $Ru^{II,II}$ reference sample (see the band on top of the Ru residue contour map in Figure 7) perfectly follows the same temperature dependence. This is in line with the hydride generating ability (HGA) of Ru-MOF discussed later (see IR spectra in Figure 8, bottom left graph) being a prerequisite for ethene dimerization (or oligomerization) reactivity.

To summarize sorption properties, TDE does not critically affect the porous structure of the pristine MOFs, but partial linker fragmentation (decarboxylation BTC → IPA + CO_2) and/or removal (OAc → $CO/CO_2/C_xH_yO_z$) supports a mesopore formation in all materials. For ethane, enthalpy of adsorption is ≈30 kJ mol^{-1} for Ru-MOFs irrespective of their defectiveness, while defects in Rh-MOFs clearly increase EoAs up to ≈40 kJ mol^{-1}. Typical for nonreactive sorbents, lower sorption temperatures allow higher gas uptakes for ethane.

There is strong ethene uptake for Ru-MOF and Rh-MOF, rather irrespective of both the temperature and defectiveness peaking at the $Ru^{II,II}$ sample. Both metals obviously bind ethene strongly. Thus, ethene residues remain bound in the materials after desorption. In Rh-MOFs, roughly one molecule of ethene per PW remains bound, rather independent of sorption temperature and sample defectiveness. Opposingly, defective Ru-MOFs and particularly their univalent $Ru^{II,II}$ analogue trap increasing amounts of ethene at higher temperatures, indicating a reactive sorption (chemisorption). Residues exceeding one molecule ethene bound per PW support the postulated reduction and generation of more OMS upon TDE.

Vibrational Spectroscopy. To gain comprehensive insights into the bonding situation, both FT-IR and Raman spectroscopy were applied (including CO as a probe molecule) and further supported by computational calculations on model molecules allowing assignment of individual vibration modes (see Table S7).

Almost identical FT-IR spectra support the overall isostructurality of all samples as shown in Figure 8 (top graph) and Figures S33−S35. Significant changes, however, occur upon TDE, particularly with Ru-MOF (0%Rh samples). Generally, in carboxylate-based coordination compounds, the valence modes of COO are very sensitive toward changes at the metal center due to their direct bonds and close vicinities.[59] Here, a hypochromic shift of ν_{as}(COO) of mixed-valent $Ru^{II,III}$-MOF results in a band shape and position identical to the univalent 100%Rh and the $Ru^{II,II}$ reference sample as displayed in the bottom right graph in Figure 8. This is explained by the hypothesis of a thermally induced metal reduction of the mixed-valence $Ru^{II,III}$ to the univalent $Ru^{II,II}$, as a consequence of axial ligand removal. As the chloride content of the Ru-containing samples does not change significantly,

https://dx.doi.org/10.1021/acsami.0c10721
ACS Appl. Mater. Interfaces 2020, 12, 40635−40647

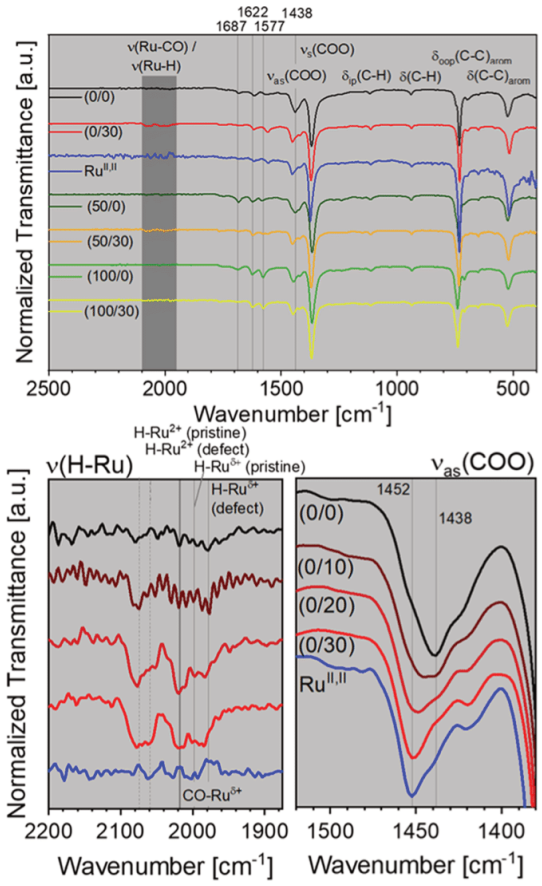

Figure 8. Top: FT-IR spectra of selected TDE-MOF and Ru^{II,II} samples revealing the general bonding similarity. Bottom: zoom-ins of highlighted regions for Ru-MOF samples. Left: emerging Ru-H (dashed lines: Ru^{2+}-H, compact lines: Ru$^{\delta+}$-H and Ru-CO (bold line) bands upon TDE). Intensities are scaled by a factor of 3. Right: blue shift of ν_{as}(COO) suggests axial acetate removal and reduction toward Ru^{II,II} nodes upon TDE.

axial acetate must be preferentially removed. This is in accordance with the existing literature on isolated dimeric Ru tetra- and pentacarboxylate complexes.[60,61] Low-intensity signals resulting from weakly bound carboxylates (≈1687 cm^{-1}) mainly occur in the (50/0) and (100/0) samples and disappear upon TDE.[62−65]

In line with the FT-IR spectra of the whole series, recorded Raman spectra support the removal of axial ligands and decarboxylation (see Figures S36−S38 and Table S7). The spectra coincide with most of the signals throughout the series of samples. Nevertheless, three characteristic effects can be observed: (1) Vibration modes attributed to axial ligands present in Ru-containing samples mainly disappear in the course of TDE. The ν(Ru-Cl) bands at 276 cm^{-1} exhibit only slightly decreased intensity, while ν(Ru-OAc$_{axial}$) at 324 cm^{-1} almost completely disappears. (2) Weakly bound or free carboxylates are readily removed by TDE from 100% Rh sample, as indicated by the disappearing signal at 1688 cm^{-1}. The broadening of the band attributed to ν_s(C═C)$_{arom}$ (at 1606 cm^{-1}) suggests a modification of the aromatic scaffold, which might be caused by the assumed linker decarboxylation, thus representing the increasing abundance of IPA with respect to the parent BTC linker. This supports the validity of the applied solver approach, including IPA, as a potential framework constituent.

Hydride Generating Ability (HGA). Upon TDE, H-Ru (hydride) species can be identified according to the emerging bands ranging from 2100 to 1950 cm^{-1}.[66] As indicated in the bottom left graph in Figure 8, H-Ru^{2+} (dashed lines at 2074 and 2059 cm^{-1}) emerge at an early stage of defect formation (samples (0/10) and (0/20)), while reduced site H-Ru$^{\delta+}$ preferentially emerge in highly defective samples. The signal assignment is based on literature information.[23,47] The observation of hydrides is remarkable since TDE is performed in an inert atmosphere without any supply of H_2 gas. However, in line with the literature, an alternative thermal treatment at 150 °C in a H_2 atmosphere yields identical Ru-H species. As demonstrated previously, the formation of these metal hydrides appears to be a key requisite for ethene dimerization reactivity and can enhance hydride transfer reactions.[46,47,67] It remains unclear at this level of our study how the mechanism for metal hydride formation proceeds under otherwise inert conditions. We assume the decomposition of hydrogen-containing framework components (OAc, BTC) by radical mechanisms and/or by concerted C−H activation and potential H-transfer to the metal nodes. Interestingly, such species are barely visible in Rh-based TDE-MOFs, revealing significant differences in the metal-based HGA (see Figures S33−S35). This is supported by very weak rhodium hydride signals even after H_2 or D_2 treatment (see Figures S39 and S40) and a neglectable ethene dimerization activity, as will be discussed later.

To gain deeper insights into the differences of the applied materials, we utilized more elaborate IR studies using variable temperatures and CO probing at low temperatures under UHV conditions, which are part of the discussion in the next chapter.

CO Probe FT-IR Spectroscopy. The controlled introduction of defects in the MOFs via TDE was monitored by the CO-SLIR (surface-ligand IR spectroscopy) approach,[68] highly sensitive to the oxidation states and coordination environments of metal atoms. Figure 9 shows the corresponding IR results for different TDE-MOFs after exposure to CO recorded at 105 K. Clearly, a number of distinctly different bands are observed. On the basis of previous work[21] and the present new findings, these characteristic bands are assigned in Table 2.

The mixed-valent, pristine (activated) Ru-MOF is dominated by two characteristic CO bands at 2171 cm^{-1} (OC-Ru^{3+}) and 2135 cm^{-1} (OC-Ru^{2+}), which have been reported previously.[21] The TDE of Ru-MOF at elevated temperatures leads to the appearance of two new low-frequency peaks at 2040 and 1996 cm^{-1}, which are assigned to OC-Ru$^{\delta+}$ species (CO bound to reduced electron-rich Ru centers) with lower Ru coordination numbers. This conclusion is in line with the observation of similar frequencies reported for Ru-OMS of DE-Ru-HKUST-1 prepared by the mixed-linker approach.[22,23,44] The formation of Ru$^{\delta+}$ defects in TDE-Ru-MOF samples is further accompanied by a slight red-shift of the OC-Ru^{2+} bands from 2135 to 2122 cm^{-1}. This feature is assigned to the structural and electronic modifications of Ru-dimer nodes caused by thermal decarboxylation.

This is in line with the spectrum of the univalent Ru^{II,II} sample, which already in its pristine state seems to be

https://dx.doi.org/10.1021/acsami.0c10721
ACS Appl. Mater. Interfaces 2020, 12, 40635−40647

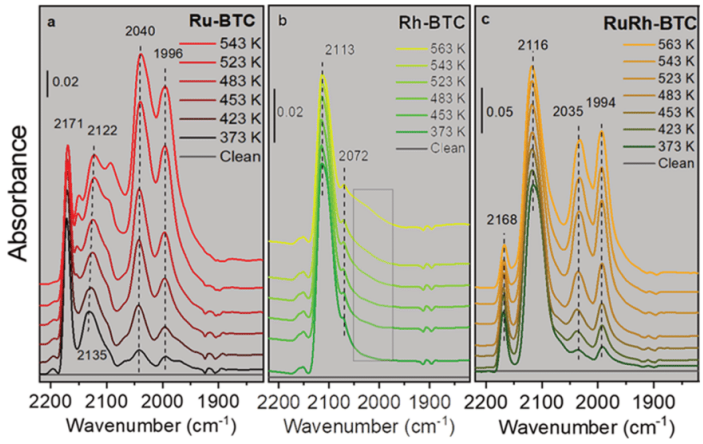

Figure 9. UHV-FTIRS data obtained after CO adsorption (0.01 mbar) on different pristine and TDE-PGM-MOFs at 105 K. Before CO adsorption, the samples were preheated at the indicated temperatures (373−563 K) for in situ defect generation: (a) Ru-MOF (0% Rh); (b) Rh-MOF (100% Rh); and (c) Ru/Rh-MOF (50% Rh).

Table 2. CO FT-IR Probe Spectroscopy[a]

sample	band (cm^{-1})	assignment
Ru-MOF	2171	Ru^{3+}-CO
	2135−2122	Ru^{2+}-CO
	2040, 1996	$Ru^{\delta+}$-CO
Rh-MOF	2113	Rh^{2+}-CO
	2072	Rh^{1+}-CO
RuRh-MOF	2168	Ru^{3+}-CO
	2116	Rh^{2+}-CO
	2035,1994	$Ru^{\delta+}$-CO
Cu-HKUST-1[27]	2179	Cu^{2+}-CO
	2156[b]	Cu^{+}-$(CO)_2$
	2121	Cu^{+}-CO
UHM-3[28]	2175	Cu^{2+}-CO
	2153	unclear[c]
	2118	Cu^{+}-CO

[a]Assignment of bands for PGM-MOF samples, including Cu-HKUST-1 and UHM-3 literature values. [b]Putative assignment. [c]We assume $Cu^{+}(CO)_2$ similar to the Literature.[27]

dominated by a related and rather defective structure (see sorption data in Figures 5 and S46). As shown in Figure 9a, the defect-related CO bands gain substantial intensity only after annealing the sample to temperatures at or higher than 480 K. The situation is thus similar to Cu-based UHM-3[28] and HKUST-1.[27,69] However, in these different MOFs, TDE was found to occur at lower temperatures (370−420 K). Thus, $Ru^{II,III}$-HKUST-1 reveals a higher thermal stability as compared to the Cu-PW based analogues.[27,28] The CO-SLIR data for the pristine Rh-HKUST-1 exhibits one intense IR band at 2113 cm^{-1} (Figure 9b), which is attributed to an OC-Rh^{2+} species. We assign the weak shoulder at 2072 cm^{-1} to a small amount of reduced OC-Rh^{1+} defect sites. The spectral evolution along with the annealing to higher temperatures reveals that the $Rh^{II,II}$-MOF is slightly more stable (a significant decrease of the OC-Rh^{2+} band occurs at T > 540 K) than the $Ru^{II,III}$-MOF, which is in excellent agreement with the TGA-based data (see Figures 2 and S9−S11). Furthermore, the IR signal at 2153 cm^{-1} indicates the presence of a geminal dicarbonyl species $(OC)_2Rh^{1+}$, indicating a reduced Rh^{1+} site being 2-fold coordinatively unsaturated.[24]

Upon further heating and annealing above 560 K, a broad feature appears at about 2000−2060 cm^{-1}. Such low vibrational frequencies suggest the presence of (uncharged) metal Rh nanoparticles, resulting from a progressive thermal decomposition of the MOF framework. This is in line with PXRD data (Figures S4−S9).

The pristine RuRh-MOF (50%Rh) is characterized by two dominating IR bands at 2168 and 2116 cm^{-1} originating from OC-Ru^{3+} and OC-Rh^{2+} species, respectively (Figure 9c). As observed and discussed earlier, the mixed-metal sample presumably comprises a statistic mixture of monometallic PWs rather than mixed-metal PWs.[40] The band assignment is further supported by temperature-dependent CO-SLIR. As shown in Figure S45, CO desorbs from Ru^{3+} sites already at about 130 K, while for Rh^{2+} and Rh^{1+} sites, substantially higher desorption temperatures (above 320 K) are observed. We explain this by stronger bonds, resulting from additional charge available for π-backdonation in relation to OC-Ru^{3+}, as confirmed by DFT calculations (see Table 3). For the TDE-MOFs heated to elevated temperatures (c), we clearly see two additional vibrations at 2035 and 1994 cm^{-1}, demonstrating the creation of reduced $Ru^{\delta+}$ defects. These peaks dominate only after heating to T > 520 K, revealing a higher thermal stability of bimetallic RuRh-MOFs relative to the monometallic $Ru^{II,III}$ analogue.

Table 3. Computed binding energies (E_{ads}) and vibrational frequencies (ν_{CO}) of CO adsorbed on Rh-PWs

system	E_{ads} (kJ mol^{-1})	ν_{CO} (cm^{-1})[a] (shift from gas CO)
Gas CO		2143
Pristine-CO	97	2096 (−47)
Pristine-2CO	63	2097 (−46)
Defect-CO	224	2044 (−99)
Defect-2CO	203	2065 (−78)

[a]Scaled with respect to gas CO.

https://dx.doi.org/10.1021/acsami.0c10721
ACS Appl. Mater. Interfaces 2020, 12, 40635−40647

We have further carried out DFT calculations to gain deeper insights into the interaction of CO with pristine and TDE-Rh-MOFs. Figure 10 shows the DFT-optimized atomic structures

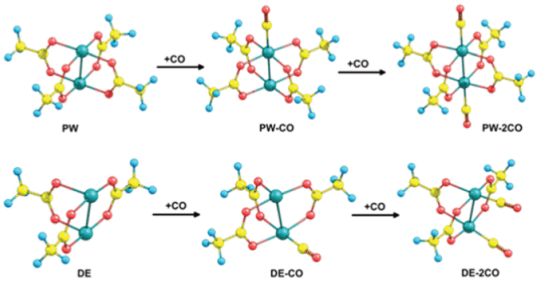

Figure 10. DFT-optimized atomic structures of CO adsorption on pristine and defect-engineered Rh-PWs. Carbon, yellow; oxygen, pink; hydrogen, blue; and rhodium, turquoise.

of various CO species bound to intact Rh^{2+}/Rh^{2+} as well as reduced Rh^{+}/Rh^{2+} dimers. The corresponding CO stretching frequencies and binding energies are summarized in Table 3 (see the SI, Tables S8 and S19 and Figures S49–S59 for details). Overall, there is good agreement between the computed and experimental results (see Table 2). We note that in the case of reduced Rh^{+}/Rh^{2+} paddlewheels, the adsorption of two CO molecules (one CO at each of the two Rh cations) leads to a blue-shift in frequency (21 cm^{-1}) compared to that of the one CO structure (Figure 10). This is attributed to the electronic redistribution of the reduced Rh dimers along with the second CO adsorption. Furthermore, computations reveal that the adsorption of CO on Rh^{+}/Rh^{2+} defects can stabilize the low-spin state of the system. Accordingly, CO binds stronger to Rh^{+}/Rh^{2+} than to pristine paddlewheels (Table 3), in line with the temperature-dependent IR observation (Figures S41–S45). In addition, CO sorption experiments were conducted at higher temperatures and at ambient pressure (see desorption graphs in Figure 11). The binding of CO at OMS was examined after

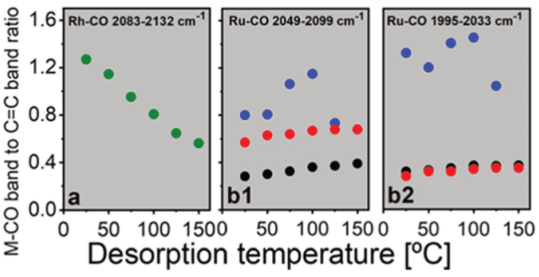

Figure 11. Ratio of the integrated band areas for Rh-CO (a) and the two bands for Ru-CO (b1, b2) to $\nu(C{=}C)_{arom}$ as a function of desorption temperature in N_2. MOF catalysts were pretreated at 150 °C in N_2 and CO adsorbed at 30 °C. The mixed-valent Ru-BTC is indicated with black (150 °C N_2 pretreatment) and red (300 °C N_2 pretreatment simulating the (0/30) sample), and univalent $Ru^{II,II}$ with blue data points. The data indicates labile CO binding to Rh but strong interactions with Ru sites and increasing OMS. The increase in b1 (red data points) suggests a preferred removal of axial over equatorial acetate.

CO adsorption at room temperature and its controlled desorption up to 150 °C. Thus, Figure 11 shows the ratios of the integrated band areas for Rh (a: 2083–2132 cm^{-1}) and for Ru (b1: 2049–2099 cm^{-1} and b2: 1995–2033 cm^{-1}) as a function of the area of the samples' C=C band (~1390 cm^{-1}). All individual FT-IR spectra are provided in the SI (Figures S41–S44). The strong binding of CO onto Ru sites, either in $Ru^{II,III}$ or $Ru^{II,II}$, as compared to Rh sites, becomes evident with the slope for increasing desorption temperatures.

Compared to the pristine Ru-MOF (treated at 150 °C, 10 min, black data points), a short pretreatment at 300 °C (10 min, red data points) roughly doubles the intensity of CO band b1, which is in accordance with the observation that the number of OMS also roughly doubles (see TGA-based CO titration experiment displayed in Figures S13–S16 and Table S1). Interestingly, the CO band b2, which can be assigned to partially reduced, defective $Ru^{\delta+}$ sites, does not increase with the (short-time) thermal treatment of mixed-valent Ru-MOF but merely shows a strong increase for the univalent $Ru^{II,II}$ sample. With respect to the band assignments discussed before, we conclude a preferred removal of axial over equatorial (bridging) acetates first, giving more Ru^{2+} sites prior to the formation of defective $Ru^{\delta+}$ sites. Thus, we assume the aforementioned order of ligand removal/fragmentation $OAc_{(axial)} > OAc_{(eq)} > BTC_{(fragmentation)}$, which is also consistent with the trends observed for $\nu_{as}(COO)$ as highlighted in Figure 8 (IR, bottom right graph). The different material properties with respect to metal, oxidation state, and their manipulation using the controlled TDE render these materials interesting for catalysis, as detailed below.

Catalytic Ethene Dimerization. As outlined in the previous subchapter, the HGA in the TDE-MOFs and their relevance in catalysis was placed under scrutiny using ethene dimerization to 1-butene as a probe reaction. The samples were thermally treated in N_2 for defect generation and in situ metal hydride formation prior to ethene dimerization. Ru-based MOF samples were treated at 300 °C (N_2), and intrinsic Ru-H formation takes place at this condition; however, the HGA at Rh sites required additional treatment under hydrogen. We used D_2 for unambiguous detection of such hydride formation and indeed observed a second band assigned to Rh-D. Figure 12 shows ethene dimerization turnover frequencies (TOF, per total metal, M_{tot}) as a function of the Ru content in the TDE-

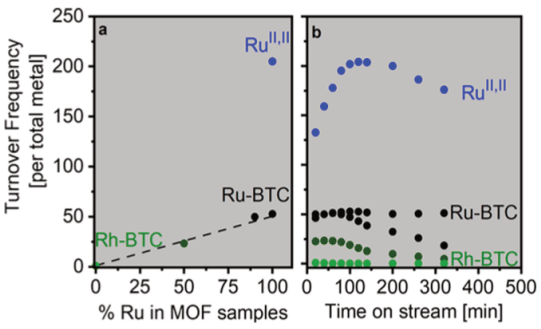

Figure 12. (a) Ethene dimerization turnover frequency (TOF) per total metal per hour as a function of the Ru content at 5 bar and 50 °C; (b) TOF as a function of time-on-stream. Besides Rh-BTC, Ru-BTC, $Ru^{II,II}$-BTC, and the 50% Rh sample, a RuRh (90:10)-BTC sample (10% Rh) was investigated.

https://dx.doi.org/10.1021/acsami.0c10721
ACS Appl. Mater. Interfaces 2020, 12, 40635–40647

MOF samples at 50 °C and 5 bar ethene. Such conditions enable a correct catalyst comparison under gaseous conditions and avoid different solvation phenomena in catalysis via intrapore condensation.[47] As observed in the linear trend of TOF values, the 100%Rh-MOF shows much less activity for C−C coupling reactions into ethene dimers even after the additional hydride formation with H_2/D_2. This is despite the more accessible univalent Rh nodes as a consequence of the absence of axial chloride or acetates compared to the mixed-valent Ru nodes. With the increasing Ru content, the PGM-MOFs are much more catalytically active. This is in accordance with the trends seen in the hydride generating ability (HGA) upon TDE.

Such differences between Ru-MOF and Rh-MOF also become evident when the Ru oxidations states are modified by TDE. After thermal treatment at 300 °C in N_2, the TDE-$Ru^{II,II}$-MOF catalyst shows about four times higher activity in ethene dimerization than the mixed-valent pristine $Ru^{II,III}$-MOF and is thus superior to the previously reported Ru-based MOF catalysts under the same reaction conditions.[47] These results confirm the relevance of the metal choice, its hydride generating ability (HGA) upon TDE, and the oxidation state. TDE yields lower average Ru oxidation states if starting out with the univalent $Ru^{II,II}$-MOF as compared to the mixed-valence $Ru^{II,III}$-MOF. In addition, the TOF values as a function of time-on-stream (Figure 12b) show a pronounced induction period for $Ru^{II,II}$, in contact with ethylene at 5 bar (which has been reported for Ru-MOF earlier[47]). This can be attributed to the enhanced HGA in the ethene stream even at 50 °C. Once at maximum TOF values, however, the activity for $Ru^{II,II}$ shows a steady decay, attributed to the progressive deposition of larger oligomers. However, since all MOF catalysts show a 100% selectivity to 1-butene (within the detection limits), these oligomers must be formed in trace amounts. As reported earlier,[47] higher ethene pressures leading to intrapore solvation phenomena can inhibit these oligomers and, thus, should avoid such a progressive deactivation. A comparison between the catalytic performance of this and previous works is provided in Table S20.

CONCLUSIONS

In summary, the present study demonstrates a methodology for postsynthetic thermal defect engineering (TDE) used to systematically access well-defined precious group metal (PGM) TDE-MOFs (Ru/Rh-HKUST-1 analogues). Characterization with a complementary set of analytical techniques (VT-PXRD, FT-IR, Raman, HR-TEM, TGA, EA, N_2, C_2H_6, and C_2H_4 physisorption and CO probe FT-IR spectroscopy in UHV) shows that these compositionally very complex materials undergo a successive reduction of the PGM centers at the dimeric metal nodes by ligand/linker removal or fragmentation upon TDE (a set of the putative defective (modified) PW structures is provided in Schemes S1 and S2). This can occur via complete removal of modulator-based acetate ligands or through decarboxylation of framework linkers (BTC → IPA). Both processes generate more open and partially reduced metal sites; thus, the average oxidation state of the PGM paddlewheel nodes is lowered as seen by CO-SLIR analysis and related DFT-based computations. In the mixed-valent $Ru^{II,III}$-HKUST-1 case, the additional axial acetate or chloride ligand accounting for the higher charge strongly impacts the occurring reduction process. While axial acetates are readily removed, the reduction of metal nodes comprising chloride counterions requires harsher conditions. A remarkable hydride generating ability (HGA) and redox flexibility during TDE are observed for Ru-MOFs, while with increasing Rh content reduction toward Rh^0 (nanoparticle formation) becomes relevant.

Investigation of the catalytic ethene dimerization as the test reaction peaked in a four-fold activity increase of TDE-$Ru^{II,II}$-HKUST-1 compared to the best result previously reported for TDE-$Ru^{II,III}$-HKUST-1 as schematically displayed in Figure 1.[47]

From our data, we deduce the suggestion to take advantage of the comparably high kinetic and, in particular thermal stability of PGM-MOFs. We highlight careful in situ monitored thermal defect engineering as a tool to tailor the defect structure quantitatively and reproducibly and thus to modulate the catalytic properties of the materials. There should be much room for design and tailoring PGM-MOFs and their TDE derivatives much beyond the scope of this conceptual study.

ASSOCIATED CONTENT

Supporting Information

The Supporting Information is available free of charge at https://pubs.acs.org/doi/10.1021/acsami.0c10721.

Experimental details, syntheses and utilized analytic devices and tools, additional XRD, sorption, EA, TGA-MS, FT-IR, Raman, computational results and catalytic data (PDF)

AUTHOR INFORMATION

Corresponding Author

Roland A. Fischer − *Department of Chemistry, Chair of Inorganic and Metal-Organic Chemistry, Technical University of Munich (TUM), 85748 Garching, Germany;* orcid.org/0000-0002-7532-5286; Email: roland.fischer@tum.de

Authors

Werner R. Heinz − *Department of Chemistry, Chair of Inorganic and Metal-Organic Chemistry, Technical University of Munich (TUM), 85748 Garching, Germany*

Iker Agirrezabal-Telleria − *Department of Chemical and Environmental Engineering, Engineering School of the University of the Basque Country (UPV/EHU), 48013 Bilbao, Spain*

Raphael Junk − *Department of Chemistry, Chair of Inorganic and Metal-Organic Chemistry, Technical University of Munich (TUM), 85748 Garching, Germany*

Jan Berger − *Department of Chemistry, Chair of Inorganic and Metal-Organic Chemistry, Technical University of Munich (TUM), 85748 Garching, Germany;* orcid.org/0000-0002-9230-0398

Junjun Wang − *Institute of Functional Interfaces (IFG), Karlsruhe Institute of Technology (KIT), 76344 Eggenstein-Leopoldshafen, Germany*

Dmitry I. Sharapa − *Institute of Catalysis Research and Technology (IKFT), Karlsruhe Institute of Technology (KIT), 76344 Eggenstein-Leopoldshafen, Germany;* orcid.org/0000-0001-9510-9081

Miryam Gil-Calvo − *Department of Chemical and Environmental Engineering, Engineering School of the University of the Basque Country (UPV/EHU), 48013 Bilbao, Spain*

Ignacio Luz − *RTI International, Durham, North Carolina 27709, United States;* orcid.org/0000-0002-5020-9211

https://dx.doi.org/10.1021/acsami.0c10721
ACS Appl. Mater. Interfaces 2020, 12, 40635−40647

Mustapha Soukri − *RTI International, Durham, North Carolina 27709, United States;* orcid.org/0000-0002-8512-8067
Felix Studt − *Institute of Catalysis Research and Technology (IKFT), Karlsruhe Institute of Technology (KIT), 76344 Eggenstein-Leopoldshafen, Germany;* orcid.org/0000-0001-6841-4232
Yuemin Wang − *Institute of Functional Interfaces (IFG), Karlsruhe Institute of Technology (KIT), 76344 Eggenstein-Leopoldshafen, Germany;* orcid.org/0000-0002-9963-5473
Christof Wöll − *Institute of Functional Interfaces (IFG), Karlsruhe Institute of Technology (KIT), 76344 Eggenstein-Leopoldshafen, Germany;* orcid.org/0000-0003-1078-3304
Hana Bunzen − *Chair of Solid-State and Materials Chemistry, Institute of Physics, University of Augsburg, 86159 Augsburg, Germany*
Markus Drees − *Department of Chemistry, Chair of Inorganic and Metal-Organic Chemistry, Technical University of Munich (TUM), 85748 Garching, Germany*

Complete contact information is available at: https://pubs.acs.org/10.1021/acsami.0c10721

Author Contributions

This manuscript was written through contributions of all authors.

Funding

This work was funded by the Deutsche Forschungsgemeinschaft grant no. FI-502/32-1 ("DEMOFs"). WRH would like to thank TUM Graduate School and the Gesellschaft Deutscher Chemiker (GDCh) for travel support. J.B. would like to acknowledge the DFG project FOR2433 on MOF-Switches for funding.

Notes

The authors declare no competing financial interest.

■ ACKNOWLEDGMENTS

The authors thank Pia Vervoorts and Dardan Ukaj for their support with sorption measurements and Matthias Nobis for the access to the glovebox TGA-MS setup. M.D. thanks the LRZ computing center for the provision of computing time on their Linux Cluster.

■ ABBREVIATIONS

BDC, benzene dicarboxylate
BET, Brunauer−Emmett−Teller
BTC, benzene tricarboxylate
CSA, controlled secondary building unit approach
DE, defect engineering
DFT, density functional theory
EA, elemental analysis
EDX, energy-dispersive X-ray spectroscopy
EoA, enthalpy of adsorption
SI, supporting information
FT-IR, Fourier transform infrared (spectroscopy)
HGA, hydride generating ability
HKUST, Hong-Kong University of Science and Technology
MOF, metal−organic framework
MS, mass spectrometry
NP, nanoparticle
PSD, pore size distribution
PW, paddlewheel
PXRD, powder X-ray diffraction
SLIR, surface-ligand IR spectroscopy
TA, thermal annealing
TDE, thermal defect engineering
TGA, thermogravimetric analysis
TOF, turnover frequency
UHV, ultrahigh vacuum
VT, variable temperature

■ REFERENCES

(1) Zhou, H.-C.; Long, J. R.; Yaghi, O. M. Introduction to Metal−Organic Frameworks. *Chem. Rev.* **2012**, *112*, 673−674.
(2) Zhou, H.-C. J.; Kitagawa, S. Metal−Organic Frameworks (MOFs). *Chem. Soc. Rev.* **2014**, *43*, 5415−5418.
(3) Yaghi, O. M.; O'Keeffe, M.; Ockwig, N. W.; Chae, H. K.; Eddaoudi, M.; Kim, J. Reticular Synthesis and the Design of New Materials. *Nature* **2003**, *423*, 705−714.
(4) Furukawa, H.; Cordova, K. E.; O'Keeffe, M.; Yaghi, O. M. The Chemistry and Applications of Metal-Organic Frameworks. *Science* **2013**, *341*, No. 1230444.
(5) Medishetty, R.; Zaręba, J. K.; Mayer, D.; Samoć, M.; Fischer, R. A. Nonlinear Optical Properties, Upconversion and Lasing in Metal−Organic Frameworks. *Chem. Soc. Rev.* **2017**, *46*, 4976−5004.
(6) Wang, H.; Vagin, S. I.; Lane, S.; Lin, W.; Shyta, V.; Heinz, W. R.; Van Dyck, C.; Bergren, A. J.; Gardner, K.; Rieger, B.; Meldrum, A. Metal−Organic Framework with Color-Switching and Strongly Polarized Emission. *Chem. Mater.* **2019**, *31*, 5816−5823.
(7) Dhakshinamoorthy, A.; Li, Z.; Garcia, H. Catalysis and Photocatalysis by Metal-Organic Frameworks. *Chem. Soc. Rev.* **2018**, *47*, 8134−8172.
(8) Jiao, L.; Wang, Y.; Jiang, H.-L.; Xu, Q. Metal−Organic Frameworks as Platforms for Catalytic Applications. *Adv. Mater.* **2018**, *30*, No. 1703663.
(9) Valvekens, P.; Vermoortele, F.; De Vos, D. Metal-Organic Frameworks as Catalysts: The Role of Metal Active Sites. *Catal. Sci. Technol.* **2013**, *3*, 1435−1445.
(10) Vermoortele, F.; Ameloot, R.; Alaerts, L.; Matthessen, R.; Carlier, B.; Fernandez, E. V. R.; Gascon, J.; Kapteijn, F.; De Vos, D. E. Tuning the Catalytic Performance of Metal-Organic Frameworks in Fine Chemistry by Active Site Engineering. *J. Mater. Chem.* **2012**, *22*, 10313−10321.
(11) Wang, Y.; Wöll, C. Chemical Reactions at Isolated Single-Sites Inside Metal−Organic Frameworks. *Catal. Lett.* **2018**, *148*, 2201−2222.
(12) Tilley, R. J. D. Defects in Solids. *Encyclopedia of Inorganic Chemistry*; John Wiley & Sons, Ltd., 2006.
(13) Vermoortele, F.; Bueken, B.; Le Bars, G.; Van de Voorde, B.; Vandichel, M.; Houthoofd, K.; Vimont, A.; Daturi, M.; Waroquier, M.; Van Speybroeck, V.; Kirschhock, C.; De Vos, D. E. Synthesis Modulation as a Tool To Increase the Catalytic Activity of Metal−Organic Frameworks: The Unique Case of UiO-66(Zr). *J. Am. Chem. Soc.* **2013**, *135*, 11465−11468.
(14) Tu, B.; Pang, Q.; Wu, D.; Song, Y.; Weng, L.; Li, Q. Ordered Vacancies and Their Chemistry in Metal−Organic Frameworks. *J. Am. Chem. Soc.* **2014**, *136*, 14465−14471.
(15) Canivet, J.; Vandichel, M.; Farrusseng, D. Origin of Highly Active Metal-Organic Framework Catalysts: Defects? Defects! *Dalton Trans.* **2016**, *45*, 4090−4099.
(16) Cheetham, A. K.; Bennett, T. D.; Coudert, F.-X.; Goodwin, A. L. Defects and Disorder in Metal-Organic Frameworks. *Dalton Trans.* **2016**, *45*, 4113−4126.
(17) Shearer, G. C.; Chavan, S.; Bordiga, S.; Svelle, S.; Olsbye, U.; Lillerud, K. P. Defect Engineering: Tuning the Porosity and Composition of the Metal−Organic Framework UiO-66 via Modulated Synthesis. *Chem. Mater.* **2016**, *28*, 3749−3761.
(18) Dissegna, S.; Epp, K.; Heinz, W. R.; Kieslich, G.; Fischer, R. A. Defective Metal-Organic Frameworks. *Adv. Mater.* **2018**, *30*, No. 1704501.

https://dx.doi.org/10.1021/acsami.0c10721
ACS Appl. Mater. Interfaces 2020, 12, 40635−40647

(19) Fang, Z.; Bueken, B.; De Vos, D. E.; Fischer, R. A. Defect-Engineered Metal−Organic Frameworks. *Angew. Chem., Int. Ed.* **2015**, *54*, 7234−7254.
(20) Taddei, M. When Defects Turn into Virtues: The Curious Case of Zirconium-Based Metal-Organic Frameworks. *Coord. Chem. Rev.* **2017**, *343*, 1−24.
(21) Noei, H.; Kozachuk, O.; Amirjalayer, S.; Bureekaew, S.; Kauer, M.; Schmid, R.; Marler, B.; Muhler, M.; Fischer, R. A.; Wang, Y. CO Adsorption on a Mixed-Valence Ruthenium Metal−Organic Framework Studied by UHV-FTIR Spectroscopy and DFT Calculations. *J. Phys. Chem. C* **2013**, *117*, 5658−5666.
(22) Kozachuk, O.; Luz, I.; Llabrés i Xamena, F. X.; Noei, H.; Kauer, M.; Albada, H. B.; Bloch, E. D.; Marler, B.; Wang, Y.; Muhler, M.; Fischer, R. A. Multifunctional, Defect-Engineered Metal−Organic Frameworks with Ruthenium Centers: Sorption and Catalytic Properties. *Angew. Chem., Int. Ed.* **2014**, *53*, 7058−7062.
(23) Zhang, W.; Kauer, M.; Halbherr, O.; Epp, K.; Guo, P.; Gonzalez, M. I.; Xiao, D. J.; Wiktor, C.; Xamena, F. X. L. i.; Wöll, C.; Wang, Y.; Muhler, M.; Fischer, R. A. Ruthenium Metal−Organic Frameworks with Different Defect Types: Influence on Porosity, Sorption, and Catalytic Properties. *Chem. - Eur. J.* **2016**, *22*, 14297−14307.
(24) Fang, Z.; Dürholt, J. P.; Kauer, M.; Zhang, W.; Lochenie, C.; Jee, B.; Albada, B.; Metzler-Nolte, N.; Pöppl, A.; Weber, B.; Muhler, M.; Wang, Y.; Schmid, R.; Fischer, R. A. Structural Complexity in Metal−Organic Frameworks: Simultaneous Modification of Open Metal Sites and Hierarchical Porosity by Systematic Doping with Defective Linkers. *J. Am. Chem. Soc.* **2014**, *136*, 9627−9636.
(25) Taddei, M.; Wakeham, R. J.; Koutsianos, A.; Andreoli, E.; Barron, A. R. Post-Synthetic Ligand Exchange in Zirconium-Based Metal−Organic Frameworks: Beware of The Defects! *Angew. Chem., Int. Ed.* **2018**, *57*, 11706−11710.
(26) Chun, H.; Bak, W.; Hong, K.; Moon, D. A Simple and Rational Approach for Binodal Metal−Organic Frameworks with Tetrahedral Nodes and Unexpected Multimodal Porosities from Nonstoichiometric Defects. *Cryst. Growth Des.* **2014**, *14*, 1998−2002.
(27) St. Petkov, P.; Vayssilov, G. N.; Liu, J.; Shekhah, O.; Wang, Y.; Wöll, C.; Heine, T. Defects in MOFs: A Thorough Characterization. *ChemPhysChem* **2012**, *13*, 2025−2029.
(28) Wang, Z.; Sezen, H.; Liu, J.; Yang, C.; Roggenbuck, S. E.; Peikert, K.; Fröba, M.; Mavrandonakis, A.; Supronowicz, B.; Heine, T.; Gliemann, H.; Wöll, C. Tunable Coordinative Defects in UHM-3 Surface-Mounted MOFs for Gas Adsorption and Separation: A Combined Experimental and Theoretical Study. *Microporous Mesoporous Mater.* **2015**, *207*, 53−60.
(29) Bentley, J.; Foo, G. S.; Rungta, M.; Sangar, N.; Sievers, C.; Sholl, D. S.; Nair, S. Effects of Open Metal Site Availability on Adsorption Capacity and Olefin/Paraffin Selectivity in the Metal−Organic Framework Cu3(BTC)2. *Ind. Eng. Chem. Res.* **2016**, *55*, 5043−5053.
(30) Dang, S.; Zhu, Q.-L.; Xu, Q. Nanomaterials Derived from Metal−Organic Frameworks. *Nat. Rev. Mater.* **2018**, *3*, No. 17075.
(31) Hussain, M. Z.; Schneemann, A.; Fischer, R. A.; Zhu, Y.; Xia, Y. MOF Derived Porous ZnO/C Nanocomposites for Efficient Dye Photodegradation. *ACS Appl. Energy Mater.* **2018**, *1*, 4695−4707.
(32) Yang, Y.; Dong, H.; Wang, Y.; He, C.; Wang, Y.; Zhang, X. Synthesis of Octahedral Like Cu-BTC Derivatives Derived from MOF Calcined under Different Atmosphere for Application in CO Oxidation. *J. Solid State Chem.* **2018**, *258*, 582−587.
(33) Chui, S.-Y.C.; Lo, S. M.-F.; Charmant, J. P. H.; Orpen, A. G.; Williams, I. D. A Chemically Functionalizable Nanoporous Material [Cu3(TMA)2(H2O)3]n. *Science* **1999**, *283*, 1148−1150.
(34) Kozachuk, O.; Yusenko, K.; Noei, H.; Wang, Y.; Walleck, S.; Glaser, T.; Fischer, R. A. Solvothermal Growth of a Ruthenium Metal−Organic Framework Featuring HKUST-1 Structure Type as Thin Films on Oxide Surfaces. *Chem. Commun.* **2011**, *47*, 8509−8511.
(35) Zhang, W.; Freitag, K.; Wannapaiboon, S.; Schneider, C.; Epp, K.; Kieslich, G.; Fischer, R. A. Elaboration of a Highly Porous RuII,II Analogue of HKUST-1. *Inorg. Chem.* **2016**, *55*, 12492−12495.
(36) Zhang, W.; Kozachuk, O.; Medishetty, R.; Schneemann, A.; Wagner, R.; Khaletskaya, K.; Epp, K.; Fischer, R. A. Controlled SBU Approaches to Isoreticular Metal-Organic Framework Ruthenium-Analogues of HKUST-1. *Eur. J. Inorg. Chem.* **2015**, *2015*, 3913−3920.
(37) Kumar, D. K.; Filatov, A. S.; Napier, M.; Sun, J.; Dikarev, E. V.; Petrukhina, M. A. Dirhodium Paddlewheel with Functionalized Carboxylate Bridges: New Building Block for Self-Assembly and Immobilization on Solid Support. *Inorg. Chem.* **2012**, *51*, 4855−4861.
(38) Kitamura, H.; Ozawa, T.; Jitsukawa, K.; Masuda, H.; Aoyama, Y.; Einaga, H. Syntheses, Structures, and Properties of Tetrakis(mu-acetato)dirhodium(II) Complexes with Axial Pyridine Nitrogen Donor Ligands with or without Assistance of Hydrogen Bonds. *Inorg. Chem.* **2000**, *39*, 3294−300.
(39) Nickerl, G.; Stoeck, U.; Burkhardt, U.; Senkovska, I.; Kaskel, S. A Catalytically Active Porous Coordination Polymer Based on a Dinuclear Rhodium Paddle-Wheel Unit. *J. Mater. Chem. A* **2014**, *2*, 144−148.
(40) Heinz, W. R.; Kratky, T.; Drees, M.; Wimmer, A.; Tomanec, O.; Günther, S.; Schuster, M.; Fischer, R. A. Mixed Precious-Group Metal−Organic Frameworks: A Case Study of the HKUST-1 Analogue [RuxRh3−x(BTC)2]. *Dalton Trans.* **2019**, *48*, 12031−12039.
(41) Zhang, W.; Chen, Z.; Al-Naji, M.; Guo, P.; Cwik, S.; Halbherr, O.; Wang, Y.; Muhler, M.; Wilde, N.; Glaser, R.; Fischer, R. A. Simultaneous Introduction of Various Palladium Active Sites into MOF via One-Pot Synthesis: Pd@[Cu3-xPdx(BTC)2]n. *Dalton Trans.* **2016**, *45*, 14883−14887.
(42) Guo, P.; Froese, C.; Fu, Q.; Chen, Y.-T.; Peng, B.; Kleist, W.; Fischer, R. A.; Muhler, M.; Wang, Y. CuPd Mixed-Metal HKUST-1 as a Catalyst for Aerobic Alcohol Oxidation. *J. Phys. Chem. C* **2018**, *122*, 21433−21440.
(43) Shakya, D. M.; Ejegbavwo, O. A.; Rajeshkumar, T.; Senanayake, S. D.; Brandt, A. J.; Farzandh, S.; Acharya, N.; Ebrahim, A. M.; Frenkel, A. I.; Rui, N.; Tate, G. L.; Monnier, J. R.; Vogiatzis, K. D.; Shustova, N. B.; Chen, D. A. Selective Catalytic Chemistry at Rhodium(II) Nodes in Bimetallic Metal−Organic Frameworks. *Angew. Chem., Int. Ed.* **2019**, *58*, 16533−16537.
(44) Zhang, W.; Kozachuk, O.; Medishetty, R.; Schneemann, A.; Wagner, R.; Khaletskaya, K.; Epp, K.; Fischer, R. A. Controlled SBU Approaches to Isoreticular Metal-Organic Framework Ruthenium-Analogues of HKUST-1. *Eur. J. Inorg. Chem.* **2015**, *2015*, 3913−3920.
(45) Picheau, E.; Hof, F.; Derré, A.; Daffos, B.; Pénicaud, A. Thermal Oxidation of Carbonaceous Nanomaterials Revisited: Evidence of Mechanism Changes. *Angew. Chem., Int. Ed.* **2019**, *58*, 16013−16017.
(46) Epp, K.; Luz, I.; Heinz, W. R.; Rapeyko, A.; Llabres i Xamena, F. X.; Fischer, R. A. Defect Engineered Ruthenium MOFs as Versatile Hydrogenation Catalysts. *ChemCatChem* **2020**, *12*, 1720−1725.
(47) Aguirrezabal-Telleria, I.; Luz, I.; Ortuño, M. A.; Oregui-Bengoechea, M.; Gandarias, I.; López, N.; Lail, M. A.; Soukri, M. Gas Reactions Under Intrapore Condensation Regime within Tailored Metal−Organic Framework Catalysts. *Nat. Commun.* **2019**, *10*, No. 2076.
(48) Lee, S. J.; Doussot, C.; Baux, A.; Liu, L.; Jameson, G. B.; Richardson, C.; Pak, J. J.; Trousselet, F.; Coudert, F.-X.; Telfer, S. G. Multicomponent Metal−Organic Frameworks as Defect-Tolerant Materials. *Chem. Mater.* **2016**, *28*, 368−375.
(49) De Jesus, J. C.; González, I.; Quevedo, A.; Puerta, T. Thermal Decomposition of Nickel Acetate Tetrahydrate: An Integrated Study by TGA, QMS and XPS Techniques. *J. Mol. Catal. A: Chem.* **2005**, *228*, 283−291.
(50) Hayes, J. C.; Guan, H.; Collias, D. I. Production of Terephthalic Acid via Reductive Coupling of Propiolic Acid or Propiolic Acid Derivatives. U.S. Patent WO2016149091(A, 2016.
(51) Friedman, S.; Kaufman, M. L.; Wender, I. The Metal Carbonyl Catalyzed Decarboxylation of Aromatic Anhydrides and Acids. *Ann. N.Y. Acad. Sci.* **1967**, *145*, 141−149.
(52) Shearer, G. C.; Chavan, S.; Ethiraj, J.; Vitillo, J. G.; Svelle, S.; Olsbye, U.; Lamberti, C.; Bordiga, S.; Lillerud, K. P. Tuned to

https://dx.doi.org/10.1021/acsami.0c10721
ACS Appl. Mater. Interfaces 2020, 12, 40635−40647

Perfection: Ironing Out the Defects in Metal−Organic Framework UiO-66. *Chem. Mater.* **2014**, *26*, 4068−4071.
(53) Howarth, A. J.; Liu, Y.; Li, P.; Li, Z.; Wang, T. C.; Hupp, J. T.; Farha, O. K. Chemical, Thermal and Mechanical Stabilities of Metal−Organic Frameworks. *Nat. Rev. Mater.* **2016**, *1*, No. 15018.
(54) Farrusseng, D.; Daniel, C.; Gaudillère, C.; Ravon, U.; Schuurman, Y.; Mirodatos, C.; Dubbeldam, D.; Frost, H.; Snurr, R. Q. Heats of Adsorption for Seven Gases in Three Metal−Organic Frameworks: Systematic Comparison of Experiment and Simulation. *Langmuir* **2009**, *25*, 7383−7388.
(55) Kanoo, P.; Reddy, S. K.; Kumari, G.; Haldar, R.; Narayana, C.; Balasubramanian, S.; Maji, T. K. Unusual Room Temperature CO2 Uptake in a Fluoro-Functionalized MOF: Insight from Raman Spectroscopy and Theoretical Studies. *Chem. Commun.* **2012**, *48*, 8487−8489.
(56) Gao, Q.; Xu, J.; Cao, D.; Chang, Z.; Bu, X.-H. A Rigid Nested Metal−Organic Framework Featuring a Thermoresponsive Gating Effect Dominated by Counterions. *Angew. Chem., Int. Ed.* **2016**, *55*, 15027−15030.
(57) Cai, G.; Jiang, H.-L. A Modulator-Induced Defect-Formation Strategy to Hierarchically Porous Metal−Organic Frameworks with High Stability. *Angew. Chem., Int. Ed.* **2017**, *56*, 563−567.
(58) Hu, Z.; Peng, Y.; Gao, Y.; Qian, Y.; Ying, S.; Yuan, D.; Horike, S.; Ogiwara, N.; Babarao, R.; Wang, Y.; Yan, N.; Zhao, D. Direct Synthesis of Hierarchically Porous Metal−Organic Frameworks with High Stability and Strong Brønsted Acidity: The Decisive Role of Hafnium in Efficient and Selective Fructose Dehydration. *Chem. Mater.* **2016**, *28*, 2659−2667.
(59) Aquino, M. A. S. Diruthenium and Diosmium Tetracarboxylates: Synthesis, Physical Properties and Applications. *Coord. Chem. Rev.* **1998**, *170*, 141−202.
(60) Rusjan, M.; Sileo, E. E.; Cukiernik, F. D. Thermal Stability of Mixed-Valent Diruthenium (II,III) Carboxylates. *Solid State Ion.* **2003**, *159*, 389−396.
(61) Rusjan, M. C.; Sileo, E. E.; Cukiernik, F. D. Thermal Decomposition of Mixed-Valent Diruthenium Pentakis(alkanoates) Enhanced by Their Liquid Crystalline State. *Solid State Ion.* **1999**, *124*, 143−147.
(62) Delen, G.; Ristanović, Z.; Mandemaker, L. D. B.; Weckhuysen, B. M. Mechanistic Insights into Growth of Surface-Mounted Metal-Organic Framework Films Resolved by Infrared (Nano-) Spectroscopy. *Chem. - Eur. J.* **2018**, *24*, 187−195.
(63) Mahalakshmi, G.; Balachandran, V. FT-IR and FT-Raman Spectra, Normal Coordinate Analysis and Ab Initio Computations of Trimesic Acid. *Spectrochim. Acta, Part A* **2014**, *124*, 535−547.
(64) Prestipino, C.; Regli, L.; Vitillo, J. G.; Bonino, F.; Damin, A.; Lamberti, C.; Zecchina, A.; Solari, P. L.; Kongshaug, K. O.; Bordiga, S. Local Structure of Framework Cu(II) in HKUST-1 Metallorganic Framework: Spectroscopic Characterization upon Activation and Interaction with Adsorbates. *Chem. Mater.* **2006**, *18*, 1337−1346.
(65) Palacios, E. G.; Juárez-López, G.; Monhemius, A. J. Infrared Sectroscopy of Metal Carboxylates: II. Analysis of Fe(III), Ni and Zn Carboxylate Solutions. *Hydrometallurgy* **2004**, *72*, 139−148.
(66) Socrates, G. *Infrared and Raman Characteristic Group Frequencies: Tables and Charts*; Wiley, 2004.
(67) Zhang, W.; Kauer, M.; Halbherr, O.; Epp, K.; Guo, P.; Gonzalez, M. I.; Xiao, D. J.; Wiktor, C.; Liabrés i Xamena, F. X.; Wöll, C.; Wang, Y.; Muhler, M.; Fischer, R. A. Ruthenium Metal−Organic Frameworks with Different Defect Types: Influence on Porosity, Sorption, and Catalytic Properties. *Chem. - Eur. J.* **2016**, *22*, 14297−14307.
(68) Wöll, C. Structure and Chemical Properties of Oxide Nanoparticles Determined by Surface-Ligand IR Spectroscopy. *ACS Catal.* **2020**, *10*, 168−176.
(69) Wang, W.; Sharapa, D. I.; Chandresh, A.; Nefedov, A.; Heißler, S.; Heinke, L.; Studt, F.; Wang, Y.; Wöll, C. Interplay of Electronic and Steric Effects to Yield Low-Temperature CO Oxidation at Metal Single Sites in Defect-Engineered HKUST-1. *Angew. Chem., Int. Ed.* **2020**, *59*, 10514−10518.

https://dx.doi.org/10.1021/acsami.0c10721
ACS Appl. Mater. Interfaces 2020, 12, 40635−40647

4.4 Study IV

Thermal Defect-Engineering of Precious Group Metal-Organic Frameworks:

Impact on the Catalytic Cyclopropanation Reaction

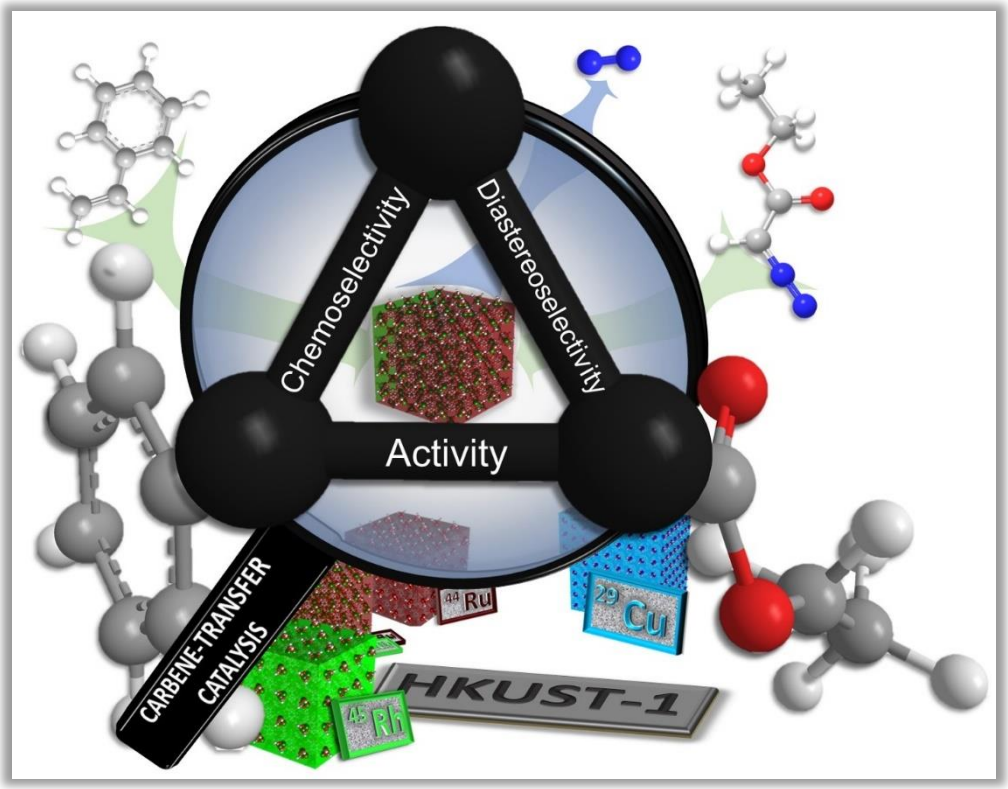

Thermal Defect-Engineering of Precious Group Metal-Organic Frameworks:

Impact on the Catalytic Cyclopropanation Reaction

Werner R. Heinz, Raphael Junk, Iker Agirrezabal-Telleria, Bart Bueken, Hana Bunzen, Thorsten Gölz, Mirza Cokoja, Dirk De Vos, and Roland A. Fischer

Catalysis Science & Technology **2020**, 10, 8077 – 8085.

Having the TDE-PGM-MOFs characterized in **Study II** and **Study III** of this thesis, we were motivated to further explore the catalytic potential of these materials. In the molecular regime, the PW-type dirhodium tetracarboxylate motif is the benchmark catalyst system when it comes to the catalytic cyclopropanation. All PGM-MOFs of this thesis were studied in the reaction of ethyl diazoacetate with styrene and compared with their TDE analogues as well as several reference catalysts. Interestingly, the reaction parameters such as activity, chemoselectivity as well as diastereoselectivity correlate with the degree of defectiveness within the materials. These correlations serve the rational basis for this proof-of-concept study: In contrast to other reports on this reaction, here, the catalytic cyclopropanation is demonstrated to be a feasible and sensitive analytical probe to investigate compositionally complex defective MOFs. While the observed catalytic activity is a measure for the number, density and accessibility of OMS, the chemo- and diastereoselectivities can be used to deduce valuable information on the nature of the metal node (perfect or modified PW) and the presence of axial ligands.

Catalysis Science & Technology

ROYAL SOCIETY OF CHEMISTRY

PAPER

View Article Online
View Journal | View Issue

Cite this: *Catal. Sci. Technol.*, 2020, **10**, 8077

Thermal defect engineering of precious group metal–organic frameworks: impact on the catalytic cyclopropanation reaction†

Werner R. Heinz,[a] Raphael Junk,[a] Iker Agirrezabal-Telleria,[b] Bart Bueken,[c] Hana Bunzen,[d] Thorsten Gölz,[a] Mirza Cokoja,[a] Dirk De Vos[c] and Roland A. Fischer*[a]

Received 23rd July 2020,
Accepted 29th September 2020

DOI: 10.1039/d0cy01479f

rsc.li/catalysis

We report on the engineering of defects in precious group metal (PGM)-based HKUST-1 (Hong Kong University of Science and Technology) analogues ($Rh^{II,II}$, $Ru^{II,II}$, $Ru^{II,III}$) and the ramification on the catalytic activity by using the cyclopropanation of styrene with ethyl diazoacetate (EDA) as an analytical probe to investigate complex metal–organic framework (MOF) structures. We have characterized the active sites within the extended frameworks by their activity, product distribution and stereoselectivity. The role of the metal, its oxidation state and the availability of open metal sites is elucidated. With a set of 17 samples including reference to Cu-HKUST-1, metal nanoparticles and existing literature, conclusions on the tuneability of paddlewheel complexes within self-supported porous and crystalline frameworks are presented. In particular, additional axial ligands (OAc^-/Cl^-) accounting for charge compensation at the mixed-valent $Ru^{II,III}$ nodes seem responsible for side-product formation during catalysis. Thermal defect-engineering allows for controlled and preferential removal of those axial ligands accompanied by reduction of the average metal oxidation state. This enhances the number of open metal sites (OMS) and the catalytic activity as well as improving the chemoselectivity towards cyclopropanes. The preference towards formation of *trans*-cyclopropane is assigned to the steric crowding of the paddlewheel moiety. This diastereoselectivity gradually diminishes with rising defectiveness of the PGM-HKUST-1 analogues featuring modified paddlewheel nodes.

Introduction

The transition metal catalyzed cyclopropanation (CP) of olefins is a well-established reaction in molecular catalysis. From the first report of $Rh_2(OAc)_4$ almost fifty years ago, its underlying lantern-like binuclear "paddlewheel" structure (PW, see Fig. 1) has ascended and now represents the benchmark catalyst system for this reaction.[1–3] Many efforts have been made and libraries of new ligands (all kinds of carboxylates, carboxamidates, phosphonates and others) were created to achieve higher activities but also to access chemo-, diastereo- and even enantioselectivity.[4] Consequently, deepest mechanistic comprehension of important parameters for this and other related reactions involving transition metal carbenoid species is available in the literature.[2,5–9] Side-products resulting from homocoupling of two carbenes or from C–H activation are known to occur.[10–15] The latter reaction requires two open metal sites (OMS) at the metal center and yields linear allyl species which are further denoted as linear products. A mechanistic summary assisting the conclusions from this paper is provided in the ESI.†

One possible strategy to overcome the limitations of isolated complexes in homogeneous catalysis (*e.g.* catalyst separation, recycling) is their immobilization in solid materials.[16–21] Consequently, the performance of some related materials has been studied in the cyclopropanation of styrene with ethyl diazoacetate (EDA) as test reaction.[12,22–25] Many of these reports focused on the influence of tuning the local structure of the catalytically active centers on the catalytic activity. For instance, Buntkowsky *et al.* studied rhodium-based coordination polymers with 2D sheet

[a] *Chair of Inorganic and Metal-Organic Chemistry, Department of Chemistry and Catalysis Research Center, Technical University of Munich, Ernst-Otto-Fischer-Straße 1, D-85747 Garching bei München, Germany. E-mail: roland.fischer@tum.de*
[b] *Department of Chemical and Environmental Engineering, Engineering School of the University of the Basque Country (UPV/EHU), Plaza Torres Quevedo 1, 48013 Bilbao, Spain*
[c] *Centre for Membrane Separations, Adsorption, Catalysis and Spectroscopy for Sustainable Solutions, Department of Microbial and Molecular Systems (M2S), KU Leuven, Celestijnenlaan 200F p.o. box 2461, 3001 Leuven, Belgium*
[d] *Chair of Solid State and Materials Chemistry, Institute of Physics, University of Augsburg, Universitätsstraße 1, D-86159 Augsburg, Germany*
† Electronic supplementary information (ESI) available. See DOI: 10.1039/d0cy01479f

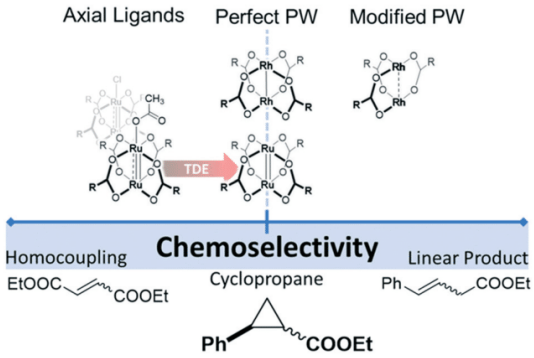

Fig. 1 Concept of this work: the carbene-transfer catalysis and its catalytic characteristics such as activity, chemo- and diastereoselectivity can be exploited as analytical tools to investigate compositionally complex porous catalyst materials (here precious metal-based HKUST-1 analogues) comprising different kinds of paddlewheel structures. Putative assignment of the PW-types (mixed-valent with axial ligands, perfect or modified) with their catalytic chemoselectivity: middle: cyclopropanes; left: tendency to form homocoupling products; right: tendency to form linear products. During TDE, the mixed-valent Ru-PWs undergo axial ligand removal and reduction towards univalent PWs leading to improved CP selectivity. In contrast, Rh-HKUST-1 comprises mixtures of perfect and defective PWs being mostly unaffected by TDE. The organic residue R can be either CH_3 as modulator derived acetate defect or $C_8H_3O_4$ as trimesate linker. The full structural complexity is highlighted in Schemes S1 and S2.†

structure comprising Rh_2-PWs interconnected with terephthalate linkers regarding the impact of linker side chains in this reaction.[23–25] Corma *et al.* reported $Cu_3(BTC)_2$ (BTC = 1,3,5-benzene tricarboxylate; aka HKUST-1, Hong Kong University of Science and Technology), to exhibit good activity and stability in this CP.[26] More recently, we have found unexpectedly high diastereomeric selectivity for the cyclopropanation of substituted styrenes catalyzed by metalated porphyrin-based MOFs as a result of pore confinement and directing effects by adjacent metal nodes.[12] The CP-enantioselectivity is intrinsically more difficult to control with MOF catalysts.

In recent years, the perception of defects in MOFs has changed significantly as defective sites often dominate material properties relevant for manifold applications such as catalysis, gas sorption and separation or electric and ionic conductivity.[27–30] Thus, ways to control the defect formation or even to intentionally introduce defects into MOFs either *de novo* during synthesis or postsynthetically have been developed. Recently, we established a process for thermal defect-engineering (TDE) of MOFs as novel way to postsynthetically introduce defects into precious-group metal (PGM)-based analogues of the archetypical PW-based HKUST-1 structure.[31] In contrast to their structural parent (Cu-HKUST-1), the PGM analogues (Ru, Rh and mixed-metal RuRh) feature high compositional complexity due to their pronounced defectiveness and are challenging to characterize on the atomic scale. Many common techniques such as single-crystal X-ray diffraction (SC-XRD), compositional analysis after acid digestion, X-ray photoelectron (XPS) and energy-dispersive X-ray spectroscopy (EDX) are not applicable or do not fulfil their typical potential in these microcrystalline, highly stable PGM-based materials.

In contrast to previous studies on the catalytic CP seeking for ever increasing catalyst performance, and in the light of our previous reports on the influence of macroscopic structural modifications of MOFs,[31] we intend to demonstrate an opposite strategy herein. In this proof-of-concept study, we aspire to probe the local catalyst structure (and its changes) for a better structural comprehension by the CP reaction and its characteristics (such as activity and selectivity as highlighted in Fig. 1). In other words, we were motivated to exploit the well-established comprehension of the manifold reaction characteristics as analytical probe to access the complex defect chemistry of isostructural TDE-PGM-HKUST-1 analogues. The specific impact of the metal choice, its oxidation state and defectiveness (as modified by TDE) are investigated and conclusions on the tuneability are drawn.

Experimental

General considerations about working procedures, used chemicals and solvents as well as instrumental details are listed in the ESI.† Spectra and analytical data regarding MOF characterization are also provided.

Synthesis of MOF samples

The synthesis of the pristine precious-metal MOFs was conducted in analogy to the literature procedures for $Ru_3(BTC)_2$ (univalent), $Ru_3(BTC)_2Y_{1.5}$ (Y = Cl^-/OAc^-; mixed-valent) and $Ru_xRh_{3-x}(BTC)_2Y_{x/2}$ (mixed-metal).[32–35] $Cu_3(BTC)_2$ was synthesized according to a room temperature literature procedure.[36] Defective samples were produced from pristine materials by means of a TGA-based thermal treatment within an argon-filled glovebox allowing access to predefined and reproducible degrees of additional defectiveness within the samples. Weight-losses of 5.5%, 10% and 15% were chosen to obtain samples denoted 10%*D*, 20%*D* and 30%*D* (*D* = defects) according to their rough defect amounts. For defective samples, a (*XX*/*YY*) nomenclature was used, referring to *XX*% rhodium fraction within the bimetallic MOF samples of Ru and Rh. *YY*% refers to the post-synthetically introduced defect amount (0% for the pristine and ≈10%, 20% and 30% for defective samples). Metal nanoparticles were produced through complete thermal decomposition of respective MOF samples.

Basic characterization data (PXRD, TGA, EA, N_2 physisorption, IR and Raman spectroscopy) of all MOF samples is given in the ESI.†

HR-TEM and elemental mapping

HR-TEM, STEM micrographs and EDS elemental mappings were recorded with a JEM NEOARM microscope (JEOL) with a cold FEG electron source operated at 200 kV. Samples were prepared by depositing a drop of the crystalline products

dispersed in ethanol onto carbon-coated copper grids (200 mesh) and dried in air. Images of all samples are displayed in Fig. 2 and S21–S23.† Elemental maps are displayed in Fig. 2 and S24 and S25.†

CO titration of OMS

TGA-based OMS titration experiments using CO were conducted in the following manner: in a stream of Ar (40 mL min^{-1}), the MOF sample was heated to either 150 or 300 °C in Ar and successively to 150 °C in H_2 for activation or defect generation. After cool-down to ambient temperature, the residual weight was taken as reference and further monitored during additional CO dosage with increasing flow rates (5, 10 and 15 mL min^{-1}). Calculated CO uptakes (Table S3†) refer to mass peak values during CO dosage. All related graphs, temperature programs and respective weight curves are displayed in Fig. S16–S20.†

Catalysis experiments

Cyclopropanation reactions were carried out with an optimized procedure. Either each 5 mg ("same weight") or 1.32 mol% (with respect to EDA; "same equivalents") of finely ground activated MOF samples was weighed in screw-capped vials with septa within a solvent-free argon-filled glovebox. A cross-shaped stirring bar was added, and the vials were tightly closed prior to the transfer out of the glovebox. A solution of 0.5 mL styrene in 0.5 mL dichloromethane was added and the mixture was vigorously stirred to obtain a homogeneous dispersion. For the entire reaction, a stirring rate of 150 min^{-1} was set. Utilizing a syringe pump, a solution comprising 2.4 mL dichloromethane, 2.4 mL styrene, 0.2 mL toluene and 0.2 mL EDA was added with a rate of 0.087 mL s^{-1} to achieve a total addition time of one hour. An additional cannula accounted for pressure release upon nitrogen formation. Samples of 0.1 mL were taken at the respective reaction time (t = 0 at the end of the addition time), diluted in 0.7 mL dichloromethane and syringe filtered (0.2 μm pores). Reaction conversions and selectivities were determined by GC (HP-5 column) with flame ionization detection. Product identification was performed according to earlier reports.[12,15]

For the hot filtration test, the catalytic procedure was conducted accordingly with separation of a sample of 1 mL and successive syringe filtration into a similarly stirred reaction vial including continuous sampling. Reusability was verified by repeated use of MOF material in five consecutive runs with sampling after 4 h each. The catalyst was centrifuged afterwards, and a fresh EDA dose was added according to the general procedure. The small residual amount was used for PXRD after the fifth run. Formulae for TOF and selectivity calculations are provided in the ESI.†

Results and discussion

Synthesis & characterization of thermal defect-engineered MOFs

Modulated hydrothermal synthesis utilizing the concept of the controlled secondary building unit approach was chosen to produce precious metal-based HKUST-1 derivatives of ruthenium, rhodium, and a bimetallic variant. Therein, the ruthenium dimers in paddlewheel (PW) structures possess a

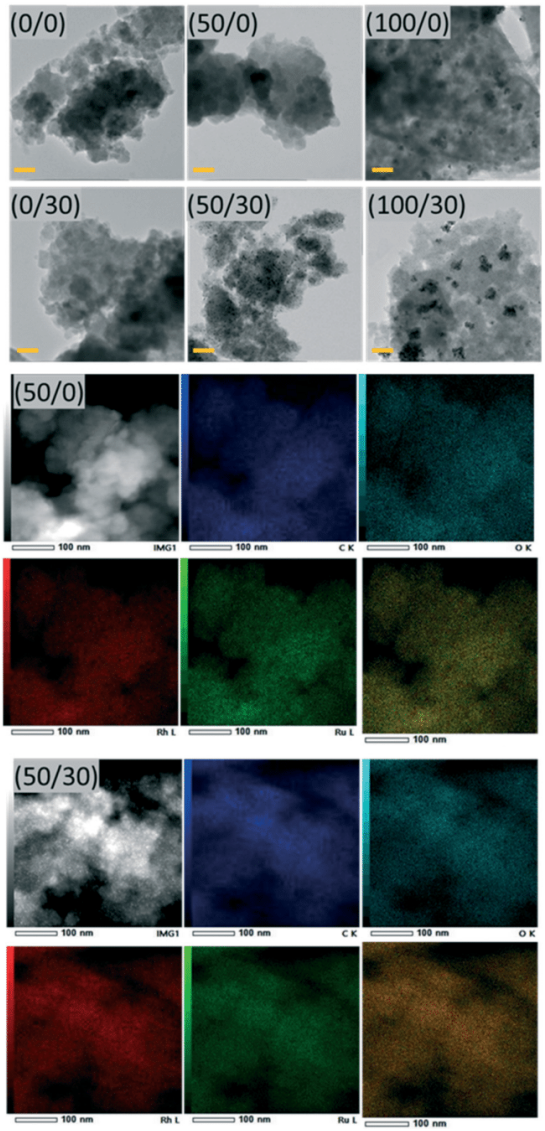

Fig. 2 Top block: HR-TEM images of representative samples: left: pristine (0/0) and most defective Ru-MOF (0/30), middle: pristine (50/0) and most defective RuRh-MOF (50/30), right: pristine (100/0) and most defective Rh-MOF (100/30). Yellow scale bars represent 50 nm. TDE does not impose topological changes or NP formation in Ru-MOF. In contrast, Rh-containing MOFs exhibit increasing NP formation. Note: the (100/0) pristine sample already contains NPs from synthesis. Middle and bottom blocks: Selected dark field STEM images of representative particles of (50/0) (middle) and (50/30) (bottom) and the corresponding EDS elemental mapping for C, O, Rh, Ru and the overlayed Ru/Rh signals. White scale bars represent 100 nm. The maps support the bimetallic nature of the mixed-metal particles even upon NP formation during TDE. Maps for pure Rh-based samples are provided in Fig. S23 and S24.†

mixed valency (II, III) while rhodium PWs are univalent (II, II). In the mixed-valent Ru case, one additional axially bound ligand (acetate or chloride) per PW accounts for charge compensation. The selected oxidation states represent the air-stable configurations and accord to the chosen precursors $Ru_2(OAc)_4Cl$ and $Rh_2(OAc)_4$. In the following, an (*X*/*Y*) notation is used to describe the samples with *X* referring to the fraction of rhodium within the metal nodes (0, 50, 100% with respect to the $Rh^{II,II}$ to $Ru^{II,III}$ ratio) and *Y* describing the defectiveness (0, 10, 20, 30%) introduced postsynthetically *via* TDE. Note that *Y* merely qualitatively describes the postsynthetically introduced defect amounts and should simplify the exact results derived from various experimental data, calculation approaches and different pristine MOF samples. A detailed description of definitions and precise calculations of the defectiveness is given in the ESI† (see Table S2). As introduced in our earlier report,[31] the controlled thermal defect-engineering (TDE) with successive isothermal steps (see Fig. S1†) was performed with a TGA-MS setup within a glovebox. This allows to produce and handle TDE-MOF samples with unique gravimetric process control over the progress of thermal annealing and to prevent these highly reactive samples from undesired (and uncontrolled) deactivation in air or moisture. For TDE-MOF sample synthesis, precise weight losses of 5.5, 10 and 15 wt% with respect to the activated pristine PGM-MOFs were targeted. To ensure high reproducibility, initial sample weights (100 wt%) were referenced to the stable weights at 150 °C isothermal treatment.

All samples – pristine and TDE-MOFs – were characterized with PXRD, elemental analysis, FT-IR, Raman, nitrogen physisorption (including pore size analysis) and thermogravimetry. All related patterns, spectra and isotherms are displayed in the ESI† (see the Fig. S2–S15 and Table S1). The performed analyses suggest that TDE does not negatively affect the crystallinity of the isostructural samples. In Rh-based MOFs, however, upon TDE, increasing nanoparticle (NP) formation can be observed in the XRD patterns. Information derived from vibrational spectroscopy suggests decarboxylation of BTC linkers forming isophthalate and the removal of axial and equatorial acetate (modulator) ligands. Pristine mixed-valent ruthenium PWs typically possess one additional axial ligand for charge compensation being either acetate or chloride. During TDE, the axial acetates are readily removed providing access to univalent $Ru^{II,II}$ sites with two open metal sites (OMS) per PW. In contrast, the axial chloride ligands mostly remain strongly bound. Regarding the porous structure, all samples exhibit and retain their high porosity during TDE with slight shifts towards larger pore sizes because of partial pore wall removal during TDE. Elemental analysis data, with some assumptions, allow for the determination of empirical sum formulae. These also support the removal of organic constituents during TDE with a preference towards acetate removal. As a result, the mean metal valences decrease due to the formation of modified PWs. PXRD, EA, IR, Raman and BET data are provided in the ESI.†

To visualize the morphology and crystallite sizes of the produced MOF samples, high-resolution transmission electron microscopy (HR-TEM) with elemental mapping was performed. Representative images of selected samples are displayed in Fig. 2. NPs can be identified neither in the pristine Ru-MOF (0/0) nor in the respective TDE-MOFs (0/30) (top block, left images). In contrast, clusters of NPs are already present in the pristine Rh-MOF (100/0) sample migrating and agglomerating into larger NPs upon TDE (100/30). The pristine mixed-metal MOF sample (50/0) does not contain NPs but small NPs emerge from 20% defects on. These findings are supported by the PXRD data mentioned earlier (see the ESI,† Fig. S2 and S3). The elemental maps displayed in Fig. 2 indicate the bimetallic nature of both the pristine (50/0) and the TDE-RuRh-MOF (50/30) and support the absence of demixing phenomena and overall preserved structural integrity (confirmed by PXRD) during TDE.

To quantify the catalytically relevant number of OMS, we designed a TGA-based titration experiment utilizing carbon monoxide as a probe molecule (for selected samples, see Fig. S16†). First, each pristine MOF sample was treated at higher temperatures to fully desolvate the axial coordination sites or to thermally induce defects into the materials. At ambient temperature, a diluted stream of CO was dosed through the chamber and the respective weight gain was monitored (see Table S3†). Gravimetric numbers were converted into molecules CO per PW assuming stoichiometric sorption of 1 CO per metal site as concluded from earlier reports.[31] For instance, thermal treatment leads to an increase from 0.72 CO per PW (after 150 °C) to 1.86 CO per PW (after 300 °C treatment) of the $Ru^{II,II}$ sample. Pretreated at 300 °C, 0.59 CO adsorb at each Rh PW, while it is 0.97 CO per $Ru^{II,III}$-PW after the identical defect creating treatment. The respective thermogram and all values are given in the ESI† confirming the redox flexibility of ruthenium samples with increasing number of OMS upon thermal treatments.

TDE-MOFs as catalysts for the cyclopropanation of styrene

As introduced above, the CP of styrene with ethyl diazoacetate (EDA) was studied intensively in molecular catalysis. Related reaction characteristics such as activity, chemoselectivity and diastereoselectivity predictably correlate with the number (and reactivity) of OMS, the electronic environment of the PW (oxidation state, presence/absence of axial counterions) and its steric properties (ideal/defective PW). With this solid literature basis, we wanted to use the reaction as a probe to obtain deeper insights into the complex structure of PGM-MOFs and their thermally defect-engineered derivatives (TDE-MOFs), and to investigate the possibilities of catalyst improvement for this reaction. Previous analysis of the related materials was used to validate the results of this novel approach.

First, a general procedure for the CP was developed using a low catalyst loading of only 1.3 mol% related to the limiting EDA amount. Similar to earlier reports, a large excess of olefin was used and slow addition of the EDA solution used to suppress a homocoupling reaction between the formed carbene

species and a second EDA molecule, which then results in diethyl fumarate or maleate as side products.[12,37,38] The reaction was performed by suspending the solid MOF catalyst in dichloromethane at ambient temperature for reasons of experimental convenience and comparability with previous works. Within this study, three different groups of products were observed (see Fig. 1 and Scheme 1). The desired *cis* and *trans*-cyclopropanes ethyl 2-phenylcyclopropane-1-carboxylate are the main reaction products. As side products, the aforementioned homocoupling products but also a couple of linear allyl species resulting from carbene C–H insertion are observed in some reactions (see Fig. 1). Note, that the selectivity of this reaction is generally unaffected by conversion, temperature, solvent or catalyst loading. Therefore, chemoselectivities after 24 h are compared in Fig. 4.

Investigation of the pristine MOF catalysts. All investigated PGM-MOFs exhibit catalytic activity for the cyclopropanation of styrene with EDA. Turnover frequencies (TOFs) representing the activity of the materials are displayed in Fig. 3 for all PGM-MOFs (time–conversion graphs for early data points are provided in Fig. S26†). At first, we compared results obtained with identical MOF catalyst loadings of 5 mg each (metal contents range between 37 and 48%, detailed values are given in the ESI†). While the activity of the pristine Ru-MOF is comparably low with 40% conversion after 4 h, the mixed-metal RuRh (50/0) sample reaches 92% after 4 h. An even greater activity can be observed for the pure Rh-MOF reaching quantitative conversion of EDA already after 1 h. Normalized to the metal content, the initial activities are rather comparable for both pristine RuRh- and Rh-MOF (see Fig. 3, bottom graph). Note, that a reference experiment with molecular $Rh_2(OAc)_4$ gave full conversion already at the first sampling (0 min) at the end of the EDA addition. Thus, the experimental procedure applied herein limits the calculated TOF for $Rh_2(OAc)_4$ to 145 h^{-1}.

Looking at the product distribution, significant differences can be observed within the used metals as can be seen in Fig. 4. A schematic overview of the different PW-types (mixed-valent, univalent, modified) and their associated selectivity is given in Fig. 1. Interestingly, Ru-MOF forms

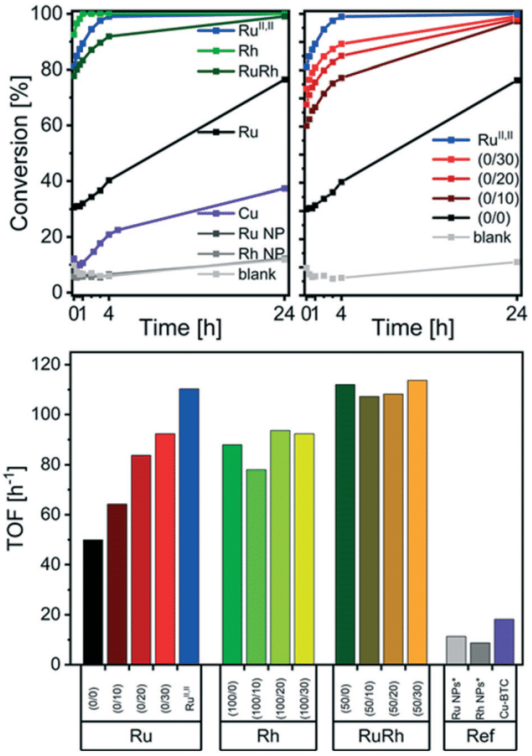

Fig. 3 Activity in the cyclopropanation reaction of styrene with EDA. Top left: Time–conversion plots comparing different pristine HKUST-1 analogues of Cu (purple), Ru (mixed-valent (black) and univalent (blue)) and Rh (green) with respective NPs (grey) as catalysts. Top right: Activity comparison of different ruthenium-based MOFs: the moderate activity of the mixed-valent $Ru^{II,III}$-MOF (0/0) is strongly enhanced by TDE (0/10 → 30) (brown to red curves). Bottom: Overview on turnover frequencies (TOFs) derived from initial conversions and 30 min average reaction time within 1 h for the controlled EDA addition. As can be seen, compared to the reference materials, all PGM-MOFs exhibit high activities and the beneficial effect of TDE to enhance the activity of Ru-MOF by OMS generation can be seen. *Observed conversions are in the range of the uncatalyzed background reaction. The molecular $Rh_2(OAc)_4$ (not displayed) reached full conversion already at 0 min, thus its TOF is experimentally limited to 145 h^{-1}.

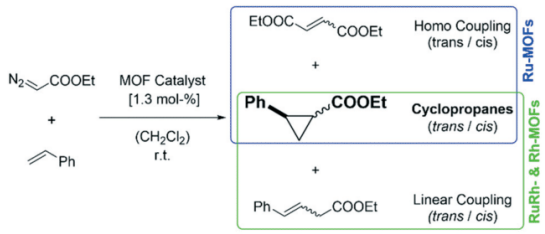

Scheme 1 Overview of the reaction products from the reaction of styrene with EDA catalyzed by MOF catalysts. A molar ratio of 0.013 : 1 : 15.66 with respect to metal, EDA and styrene was applied. The catalyst was suspended in a mixture of 0.5 mL styrene and 0.5 mL dichloromethane for 15 min until a solution of 2.1 mL styrene, 2.1 mL dichloromethane, 0.1 mL toluene and 0.1 mL EDA was added *via* a syringe pump over one hour. Sampling was started at the end of addition.

large amounts of homocoupling products (≈30%) with CP selectivities of ≈64–68%. Rh-Containing MOFs do not induce the formation of the homocoupling product. However, besides the cyclopropanes, different products that stem from the coupling of styrene with EDA are observed instead. Linear allyl species (15–18% selectivity) are formed. These could potentially arise from a C–H insertion reaction of the carbene species into olefinic C–H bonds or result from ring opening reactions. The former reaction, often termed "C–H insertion" or "homologation reaction", has rarely been reported for PW-type catalysts.[11,37,39,40] Predominantly, isolated ruthenium complexes were found to yield these linear side products also using excessive styrene concentrations.[11,13,15,41] The molecular $Rh_2(OAc)_4$ reference did not produce such linear

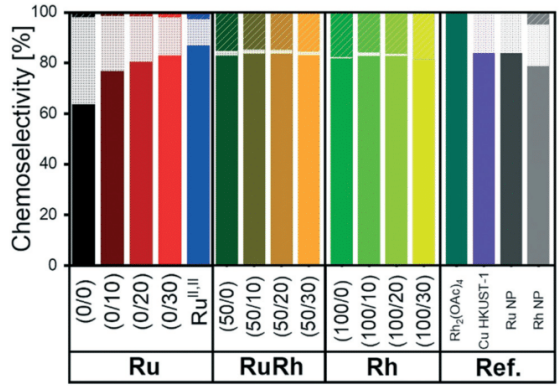

Fig. 4 Chemoselectivities for all samples after 24 h. The three groups of products are displayed in stacked columns. The bottom bars represent the cyclopropanes (strongly colored), the fractions in the middle (pale) represent the observed homocoupling products. Top bars (cross-shaded) represent the fractions of linear products. Left group: Ru-MOF samples indicate improved chemoselectivity towards CPs and decreasing homocoupling upon TDE indicating the axial ligand removal. Middle left (mixed-metal RuRh-MOFs) and middle right (Rh-MOFs) group: linear products as side products emerge. TDE has no effect on the chemoselectivity for RuRh- and Rh-based samples. Right group: Reference samples. Note that, the conversion of metal NPs is very low, thus represents merely the uncatalyzed background reaction.

products in detectable amounts under our reaction conditions. In general, for CP to occur, only one available OMS is required for the carbene formation/coordination. The axial position of PW complexes serves this purpose well. All literature reports have in common that the C–H activation requires more space at the metal site allowing for the coordination of both the carbene species and the olefin simultaneously.[11] Therefore, we conclude that the formation of the linear allyl species might be catalyzed by modified PWs (present in missing linker defects, see Fig. 1 and Scheme S3†).[35] In principle, styrene should be capable to coordinate to all types of OMS. At a defective PW, this is one free equatorial position and the two adjacent axial positions. All of them may be coordinated by styrene molecules at the beginning of the reaction. Upon EDA dosing, one axial styrene can be substituted by EDA accompanied by N_2 release and formation of the proposed metal carbenoid species. The adjacent coordination (*cis*) of both styrene and the carbene species at one metal center (such a potential intermediate is displayed in Scheme S3†) meets the conditions for the C–H insertion as proposed in the literature.[11] Turning to the mixed-metal RuRh-MOF, an almost identical product distribution as for the Rh-MOF can be observed (≈15% linear products; no homocoupling products). Together with the similar activity of both catalyst materials, its catalytic properties seem to be dominated by the rhodium sites.

Focusing on the stereoselectivity, the *trans*-isomer is slightly favoured (≈64–68%) when using "perfect" PWs like $Rh_2(OAc)_4$ or heterogenized PWs as they are present in Cu-HKUST-1.[22,26,38] As explained in the ESI† in detail, the reaction is controlled through the geometry of the PW. As displayed in Fig. 5, the resulting diastereoselectivity in HKUST-1 analogues is decreasing in the order Cu ≫ Ru > RuRh > Rh. This order is also representing the intrinsic defectiveness of pristine samples resulting from modulated synthesis. Defective PWs presumably miss the directing effects of the steric "wall" formed by the metal and its four equatorial oxygen atom ligators. This is in line with earlier reports on Ru- and Rh-based HKUST-1 analogues featuring increasing amounts of defects.[34,35,42]

Investigation of the TDE-MOF catalysts. Proceeding from the pristine PGM-MOFs towards their thermally treated defective analogues, we performed identical catalytic reactions with all TDE-MOFs and an additional univalent $Ru^{II,II}$ reference sample. In the ruthenium case, TDE clearly increases the catalytic performance as can be seen in both Fig. 3 and in the time–conversion plots for the whole series (see Fig. S26–S29†). The strong increase in activity is also visible in more than doubled TOFs (from ≈50 h^{-1} for pristine Ru-MOF over ≈92 h^{-1} for the (0/30) sample towards ≈110 h^{-1} for the $Ru^{II,II}$-MOF) presented in Fig. 3. This activity improvement can be attributed to the removal of the axial acetate ligands providing a higher number of OMS per PW as outlined above. Beyond the observed increase in activity, TDE of Ru-MOF also enhances the chemoselectivity as highlighted in Fig. 1 and 4. Starting from 67% selectivity with respect to the CP products observed for pristine Ru-MOF, the number gradually increases to 85% in the (0/30) sample almost matching the 87% from the $Ru^{II,II}$-MOF. This observation led us to conclude that axial acetate ligands on mixed-valent Ru-PWs are the main source for the undesired homocoupling side products as they are successively removed during TDE. In other words, thermally induced axial ligand removal and

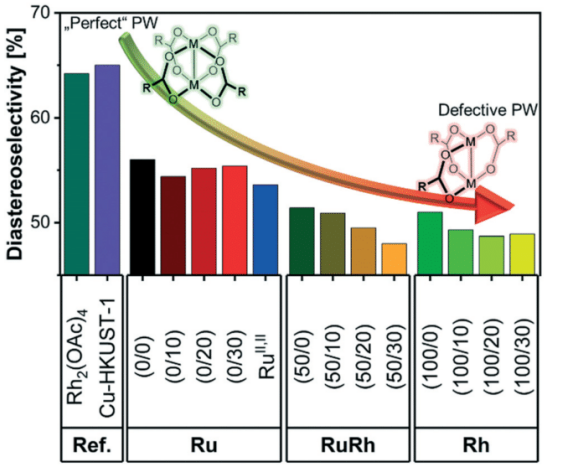

Fig. 5 Diastereoselectivities of PW systems studied herein after 4 h. The progressive decrease in diastereoselectivity can be correlated with the assumed structural changes with increasing defectiveness of the PWs as indicated schematically. The trend is visible in the order Cu ≫ Ru > RuRh > Rh as well as upon increasing TDE.

View Article Online
Catalysis Science & Technology Paper

the subsequent metal reduction correspond with improved selectivities towards the desired cyclic products for Ru-BTC.

In contrast, both Rh- and RuRh-MOF samples exhibit rather constant activities irrespective of the postsynthetic defect generation. Although, the obtained data suggest a slight drop of activity for low defect amounts (samples (50/10) and (100/10) as shown in Fig. 3), the values observed for higher amounts rise again. This intermediate drop could potentially arise from particle agglomeration during TDE responsible for a first drop. Further thermal treatment, however, recreates the catalytic performance as more OMS are generated. No impact on the chemoselectivity of Rh- and RuRh-MOF is observed. This suggests that the nature and the environment of the active Rh sites are apparently not affected by the thermal treatment. Interestingly, any increase in the linear side products that would be expected for a higher number of defective PWs is not substantiated. This is in line with results from CO probe FT-IR measurements that do not suggest large amounts of partially reduced Rh nodes while strong bands for reduced Ru-sites can be observed.[31]

Focusing on the diastereoselectivities of all TDE-MOFs, the slight preference of the *trans*-CP observed for Ru-MOF (≈57 : 43) is reduced to 53 : 47 (±1%) for $Ru^{II,II}$-MOF. Similar trends of equality of diastereoisomers can be observed for the mixed-metal RuRh – as well as the pure Rh-MOF. Respective graphs are displayed in Fig. 5 for 4 h reaction time. TDE-MOF samples follow the trend of reduced stereo control as described for the pristine MOFs. From these data we conclude the progressive formation of defective, modified PWs during TDE.

Reference experiments have been performed with Cu-BTC, nanoparticles of Ru and Rh and molecular $Rh_2(OAc)_4$. As can be seen in Fig. 3 (bottom graph) and S30–S32,† Cu-BTC exhibits low activity with a TOF of ≈18 h^{-1}. Furthermore, its conversion contained a strong induction period. Expanded investigations with hot filtration (performed after 20 min of stirring the suspensions) revealed the activity of Cu-BTC to mainly rely on leaching which is in contrast to findings in a previous report.[26] Compared with the well-known copper analogue, precious group metal-based HKUST-1 derivatives studied herein, though more demanding to synthesize, have significantly higher stability towards water and solvents.[32,33,35] A hot filtration experiment with the most active $Ru^{II,II}$-MOF confirms catalyst heterogeneity as can be seen in Fig. S30.† Further, emerging nanoparticles being responsible for the increase in activity upon TDE are clearly ruled out (see Fig. 3 and S32†) as their activity is in the range of the uncatalyzed background reaction. Note, that the presence and potential catalytic impact of ultra-small NPs/single metal atoms is hard to evaluate due to absence of suitable characterization techniques and is thus without consideration. The $Rh_2(OAc)_4$ reference sample reaches quantitative conversion already after the addition time (0 min), thus its TOF is experimentally limited to 145 h^{-1} with a chemoselectivity of 100% towards cyclopropanes in a diastereomeric ratio of ≈64 : 36. This is in accordance with existing literature.[43] Confinement effects accounting for the diastereoselectivity trends or the formation of the linear products might be ruled out, since both molecular $Rh_2(OAc)_4$ and Cu-HKUST-1 produce equally high diastereoselectivities. While any confinement is absent in the former, the latter is isostructural to the PGM-MOFs studied herein.

Reusability (catalyst cycling) experiments were performed using $Ru^{II,II}$- and $Rh^{II,II}$-BTC samples. For both activated materials, reduced activities are observed within consecutive runs as no additional catalyst sample activation was performed between two different runs (see Fig. S33 and S34†). For the Rh-MOF, the chemoselectivity towards linear products is reduced with progressive cycling which we attribute to increasing saturation of modified PWs. The univalent $Ru^{II,II}$ sample follows the chemoselectivity trends observed during TDE in the opposite direction. This clearly suggests a progressive reoxidation and axial ligation back to mixed-valent $Ru^{II,III}$ species featuring lower activity and chemoselectivity with homocoupling side products being formed again. With respect to the low sample amounts, the structural order is mostly preserved after five consecutive cycles (see Fig. S35†).

Conclusions

Overall, thirteen different samples of precious group metal (PGM)-based HKUST-1 derivatives including thermal defect-engineered variants thereof have been synthesized, characterized, and applied in the cyclopropanation of styrene with ethyl diazoacetate. All PGM-HKUST-1 analogues ($Ru^{II,II}$, $Ru^{II,III}$, $Rh^{II,II}$ and mixed-metal $Ru^{II,III}Rh^{II,II}$) are good CP catalysts with the pristine $Ru^{II,III}$ being less active compared to $Ru^{II,II}$ or $Rh^{II,II}$ but much more tuneable by thermal defect-engineering (TDE). A doubling of the activity and at the same time diminished formation of homocoupling side products (fumarate and maleate) by 67% are observed. This improvement is rationalized by the successive metal reduction (creation of more OMS) upon TDE. For both Rh- and RuRh-HKUST-1, TDE did not affect the activity or the chemoselectivity but reduced diastereomeric preference suggests progressive formation of modified PWs. The studied PGM-MOFs have good chemical stability and exhibit no leaching as it is observed for Cu-HKUST-1. Nanoparticles or metal leaching contributing to the catalytic activity are ruled out for the PGM-MOFs studied herein, while the moderate activity of Cu-BTC seems to be governed by leaching species. In light of our findings in the CP reaction (presented herein) and in the dimerization of ethene (studied earlier),[31] we highlight the potential of TDE for the controlled post-synthetic defect incorporation in MOFs and recommend this process over other DE strategies.

The key message of this conceptual study, however, is to make use of the catalytic CP reaction and its corresponding characteristics (activity, chemo- and diastereoselectivity) as novel analytical probe to study MOFs. The PGM-HKUST-1 analogues investigated herein are promising materials for

catalytic applications, but their intrinsically pronounced defectiveness is just one factor contributing to their high compositional and structural complexity. Their characterization is challenging and usually requires a multitude of analytical techniques which often just provide fragmented insights that need to be compiled carefully. In this regard, the well-investigated CP reaction is experimentally easy to conduct and could furnish several analytical indications: the relative number and density of OMS, their chemical nature (perfect *vs.* modified PW), whether axially bound anions are present and consequently the metals' oxidation state and its stability under catalysis conditions. Computational ways to describe the observed phenomena to support the findings presented herein are currently under investigation.

Conflicts of interest

There are no conflicts to declare.

Acknowledgements

This project was funded by Deutsche Forschungsgemeinschaft grant no. FI-502/32-1 ("DEMOFs"). WRH would like to thank TUM Graduate School and GDCh for travel funding. All authors thank Jan Berger, Pia Vervoorts and Dardan Ukaj for experimental support with physisorption measurements and Miryam Gil-Calvo for help with CO titration experiments. WRH thanks Simon Smolders for experimental assistance.

References

1 R. Paulissen, H. Reimlinger, E. Hayez, A. J. Hubert and P. Teyssié, *Tetrahedron Lett.*, 1973, **14**, 2233–2236.
2 A. J. Anciaux, A. J. Hubert, A. F. Noels, N. Petiniot and P. Teyssie, *J. Org. Chem.*, 1980, **45**, 695–702.
3 C. Ebner and E. M. Carreira, *Chem. Rev.*, 2017, **117**, 11651–11679.
4 H. Lebel, J.-F. Marcoux, C. Molinaro and A. B. Charette, *Chem. Rev.*, 2003, **103**, 977–1050.
5 M. Brookhart and W. B. Studabaker, *Chem. Rev.*, 1987, **87**, 411–432.
6 A. Padwa, D. J. Austin, S. F. Hornbuckle, M. A. Semones, M. P. Doyle and M. N. Protopopova, *J. Am. Chem. Soc.*, 1992, **114**, 1874–1876.
7 M. P. Doyle, L. J. Westrum, W. N. E. Wolthuis, M. M. See, W. P. Boone, V. Bagheri and M. M. Pearson, *J. Am. Chem. Soc.*, 1993, **115**, 958–964.
8 M. P. Doyle and D. C. Forbes, *Chem. Rev.*, 1998, **98**, 911–936.
9 M. P. Doyle, *J. Org. Chem.*, 2006, **71**, 9253–9260.
10 M. P. Doyle and D. Ren, in *Prog. Inorg. Chem.*, 2007, pp. 113–168, DOI: 10.1002/9780470166512.ch2.
11 A. F. Noels and A. Demonceau, *J. Phys. Org. Chem.*, 1998, **11**, 602–609.
12 K. Epp, B. Bueken, B. Hofmann, M. Cokoja, K. Hemmer, D. E. De Vos and R. A. Fischer, *Catal. Sci. Technol.*, 2019, **9**, 6452–6459.
13 G. Maas, *Chem. Soc. Rev.*, 2004, **33**, 183–190.
14 F. A. Cotton, K. R. Dunbar and M. G. Verbruggen, *J. Am. Chem. Soc.*, 1987, **109**, 5498–5506.
15 F. Simal, A. Demonceau, A. F. Noels, D. R. T. Knowles, S. O'Leary, P. M. Maitlis and O. Gusev, *J. Organomet. Chem.*, 1998, **558**, 163–170.
16 R. Ye, J. Zhao, B. B. Wickemeyer, F. D. Toste and G. A. Somorjai, *Nat. Catal.*, 2018, **1**, 318–325.
17 X. Cui, W. Li, P. Ryabchuk, K. Junge and M. Beller, *Nat. Catal.*, 2018, **1**, 385–397.
18 Z. Liu, X. Yuan, S. Zhang, J. Wang, Q. Huang, N. Yu, Y. Zhu, L. Fu, F. Wang, Y. Chen and Y. Wu, *NPG Asia Mater.*, 2019, **11**, 12.
19 D.-H. Nam, P. De Luna, A. Rosas-Hernández, A. Thevenon, F. Li, T. Agapie, J. C. Peters, O. Shekhah, M. Eddaoudi and E. H. Sargent, *Nat. Mater.*, 2020, **19**, 266–276.
20 B. C. Hodges, E. L. Cates and J.-H. Kim, *Nat. Nanotechnol.*, 2018, **13**, 642–650.
21 D. Farrusseng, S. Aguado and C. Pinel, *Angew. Chem., Int. Ed.*, 2009, **48**, 7502–7513.
22 J. Kim, H.-Y. Cho and W.-S. Ahn, *Catal. Surv. Asia*, 2012, **16**, 106–119.
23 J. Liu, C. Fasel, P. Braga-Groszewicz, N. Rothermel, A. S. Lilly Thankamony, G. Sauer, Y. Xu, T. Gutmann and G. Buntkowsky, *Catal. Sci. Technol.*, 2016, **6**, 7830–7840.
24 J. Liu, Y. Xu, P. B. Groszewicz, M. Brodrecht, C. Fasel, K. Hofmann, X. Tan, T. Gutmann and G. Buntkowsky, *Catal. Sci. Technol.*, 2018, **8**, 5190–5200.
25 J. Liu, P. B. Groszewicz, Q. Wen, A. S. L. Thankamony, B. Zhang, U. Kunz, G. Sauer, Y. Xu, T. Gutmann and G. Buntkowsky, *J. Phys. Chem. C*, 2017, **121**, 17409–17416.
26 A. Corma, M. Iglesias, F. X. Llabrés i Xamena and F. Sánchez, *Chem. – Eur. J.*, 2010, **16**, 9789–9795.
27 J. Canivet, M. Vandichel and D. Farrusseng, *Dalton Trans.*, 2016, **45**, 4090–4099.
28 A. K. Cheetham, T. D. Bennett, F.-X. Coudert and A. L. Goodwin, *Dalton Trans.*, 2016, **45**, 4113–4126.
29 S. Dissegna, K. Epp, W. R. Heinz, G. Kieslich and R. A. Fischer, *Adv. Mater.*, 2018, **30**, 1704501.
30 Z. Fang, B. Bueken, D. E. De Vos and R. A. Fischer, *Angew. Chem., Int. Ed.*, 2015, **54**, 7234–7254.
31 W. R. Heinz, I. Agirrezabal-Telleria, R. Junk, J. Berger, J. Wang, D. I. Sharapa, M. Gil-Calvo, I. Luz, M. Soukri, F. Studt, Y. Wang, C. Wöll, H. Bunzen, M. Drees and R. A. Fischer, *ACS Appl. Mater. Interfaces*, 2020, **12**(36), 40635–40647.
32 O. Kozachuk, K. Yusenko, H. Noei, Y. Wang, S. Walleck, T. Glaser and R. A. Fischer, *Chem. Commun.*, 2011, **47**, 8509–8511.
33 W. Zhang, O. Kozachuk, R. Medishetty, A. Schneemann, R. Wagner, K. Khaletskaya, K. Epp and R. A. Fischer, *Eur. J. Inorg. Chem.*, 2015, **2015**, 3913–3920.
34 W. Zhang, K. Freitag, S. Wannapaiboon, C. Schneider, K. Epp, G. Kieslich and R. A. Fischer, *Inorg. Chem.*, 2016, **55**, 12492–12495.

35 W. R. Heinz, T. Kratky, M. Drees, A. Wimmer, O. Tomanec, S. Günther, M. Schuster and R. A. Fischer, *Dalton Trans.*, 2019, **48**, 12031–12039.
36 J.-L. Zhuang, D. Ceglarek, S. Pethuraj and A. Terfort, *Adv. Funct. Mater.*, 2011, **21**, 1442–1447.
37 J. Adams and D. M. Spero, *Tetrahedron*, 1991, **47**, 1765–1808.
38 A. Caballero, A. Prieto, M. M. Díaz-Requejo and P. J. Pérez, *Eur. J. Inorg. Chem.*, 2009, **2009**, 1137–1144.
39 C. G. Espino and J. Du Bois, *Angew. Chem., Int. Ed.*, 2001, **40**, 598–600.
40 M. C. Pirrung and A. T. Morehead, *J. Am. Chem. Soc.*, 1994, **116**, 8991–9000.
41 A. Tudose, A. Demonceau and L. Delaude, *J. Organomet. Chem.*, 2006, **691**, 5356–5365.
42 W. Zhang, O. Kozachuk, R. Medishetty, A. Schneemann, R. Wagner, K. Khaletskaya, K. Epp and R. A. Fischer, *Eur. J. Inorg. Chem.*, 2015, **2015**, 3913–3920.
43 H. M. L. Davies and S. A. Panaro, *Tetrahedron*, 2000, **56**, 4871–4880.

4.5 Study V

Scrutinizing Ligand Exchange Reactions in the Formation of the Precious Group MOF $Ru^{II,II}$-HKUST-1:

The Impact of Diruthenium Tetracarboxylate Precursor and Modulator Choice

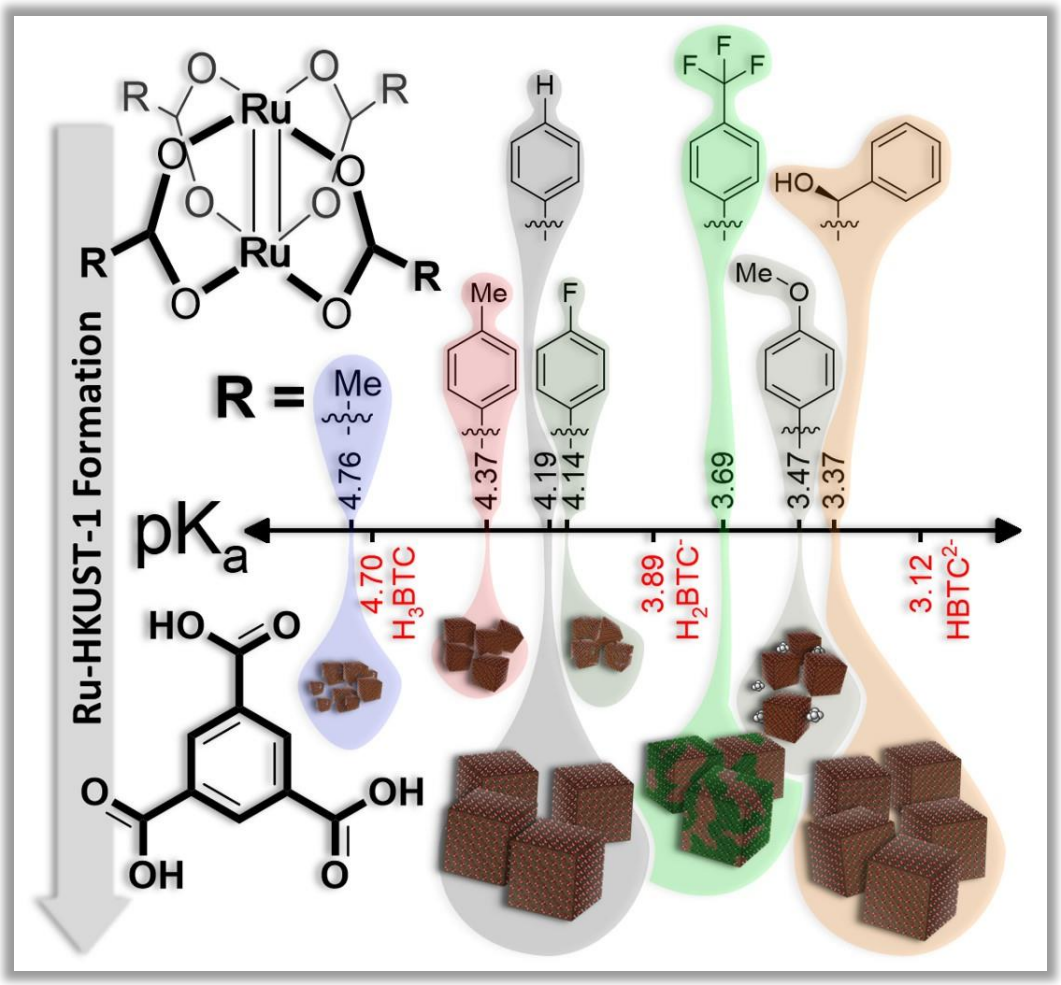

Scrutinizing Ligand Exchange Reactions in the Formation of the Precious Group MOF $Ru^{II,II}$-HKUST-1:

The Impact of Diruthenium Tetracarboxylate Precursor and Modulator Choice

Werner R. Heinz, Dominik Staude, David Mayer, Hana Bunzen, and Roland A. Fischer

Dalton Transactions **2021**, accepted manuscript.

https://doi.org/10.1039/D1DT00118C

In the studies presented above, the remarkable tuneability of the Ru-HKUST-1 in particular and of the high catalytic functionality of PGM-HKUST-1 analogues in general was demonstrated. In this regard, the utilization of either *de novo* DE or postsynthetic TDE has a beneficial effect on materials properties due to partial reduction and the subsequent creation of more OMS. Remarkably, the univalent $Ru^{II,II}$ analogue already features superior properties compared to its oxidized mixed-valence counterpart $Ru^{II,III}$. Despite all these convincing results, the synthesis of a rather defect-free PGM-MOF was still unachieved. In terms of particle size and structural order, the univalent $Ru^{II,II}$ as well as $Rh^{II,II}$ MOF samples are even worse than the mixed-valence $Ru^{II,III}$-HKUST-1 analogue.

For this reason, the challenging case of the air-sensitive $Ru^{II,II}$ was selected to systematically investigate ligand exchange reactions as prerequisite for any MOF formation. All efforts of variation of synthetic conditions utilizing the established $[Ru_2(OAc)_4]$ precursor and acetic acid modulation did not result in improved structural order or domain sizes. Therefore, a series of new diruthenium tetracarboxylate precursor complexes was synthesized, characterized, and subsequently utilized for MOF syntheses under standardized conditions. A careful selection of *para*-substituted benzoate derivatives as well as L-mandelate served as both precursor ligand and (in form of their respective acids) as coordination modulator allowing for the systematic variation of the ligands pK_a and its impact on the formed MOF material. Our results underline the importance of a careful precursor selection and provide solutions for optimized particle sizes, improved structural order and Ru-HKUST-1 materials with an unprecedented porosity close to the computed values of a perfect structure.

Dalton Transactions

Scrutinizing Ligand Exchange Reactions in the Formation of the Precious Group Metal-Organic Framework $Ru^{II,II}$-HKUST-1: The Impact of Diruthenium Tetracarboxylate Precursor and Modulator Choice

Received 00th January 20xx,
Accepted 00th January 20xx

DOI: 10.1039/x0xx00000x

www.rsc.org/

Werner R. Heinz,[a] Dominik Staude,[a] David Mayer,[a] Hana Bunzen,[b] and Roland A. Fischer[a,*]

The precious group metal (PGM) analogues of the iconic metal-organic framework $[Cu_3BTC)_2]$ (HKUST-1; BTC = 1,3,5 benzenetricarboxylate) still represent a synthetic challenge, especially if targeting the univalent and ideally defect-free $Ru^{II,II}$ variant. Herein we present a systematic study employing the controlled secondary building unit approach (CSA) by using a variety of diruthenium tetracarboxylate complexes $[Ru_2(RCO_2)_4]$ as precursors in the synthesis of univalent Ru-HKUST-1 samples. Carboxylate ligand exchange test reactions suggest the importance of a pK_a match between precursor ligand and BTC linker. For example, L-mandelate substituted precursors resulted in the most "perfect" samples of the investigated series with a fourfold increase in crystalline domain sizes compared to the established acetate route (according to PXRD and HR-TEM), high compositional purity (FT-IR, Raman, TGA and elemental analysis) and feature a so far unprecedentedly high BET surface area of 1789 m^2g^{-1} with the expected pore size distribution and total pore volume all similar to the ideal HKUST-1 parent structure.

Introduction

Precious group metal (PGM)-based metal-organic frameworks (MOFs) have received attention as they represent heterogenized variants of homogeneous transition metal complexes as catalysts.[1-6] The synergy of high permanent porosity for efficient mass transport, structurally ordered and defined PGM nodes interconnected into stable three-dimensional scaffolds with open metal sites (OMS) and more diverse redox chemistry predestines $[(PGM)_3BTC_2]$ (PGM = Ru, Rh, etc.; isostructural to $[Cu_3BTC_2]$ = HKUST-1) as promising materials for application as heterogeneous catalysts.[8] The dimeric lantern-like paddlewheel (PW) node attain charge neutrality with the ideal formula $[Cu_3(BTC)_2]$ having every copper dimer coordinated by four anionic carboxylate linkers (1,3,5-benzene tricarboxylate; BTC). Targeting the rhodium analogue, the univalent oxidation state $Rh^{II,II}$ appears relatively inert to redox chemistry and $Rh^{II/III}$ mixed valence states are less accessible.[6, 7] In contrast, ruthenium is more redox flexible and thus offers two different situations namely the univalent $Ru^{II,II}$ (air-sensitive) and the mixed-valent $Ru^{II,III}$ (air stable) analogue of HUKST-1.[9, 10] While the univalent system more directly allows for approaching the ideal empirical formula $[Ru_3(BTC)_2]$, the mixed-valent system requires additional anions for charge compensation giving rise to more complex compositions $[Ru_3(BTC)_2Y_{1.5}]$ (with Y = Cl^- or OAc^-). These additional counterions occupy 50% of the OMS significantly lowering the catalytic potential of the mixed-valent Ru-HKUST-1. Although defect-engineering strategies[11, 12] (either *de novo* via mixed-linker approach[4, 13, 14] or postsynthetically via thermal defect-engineering[1, 7]) have been developed to access reduced metal centres creating more OMS and higher performances in several catalytic test reactions,[1, 4, 7, 13, 15] the synthesis of relatively "defect-free" PGM-HKUST-1 is still far from being optimized.

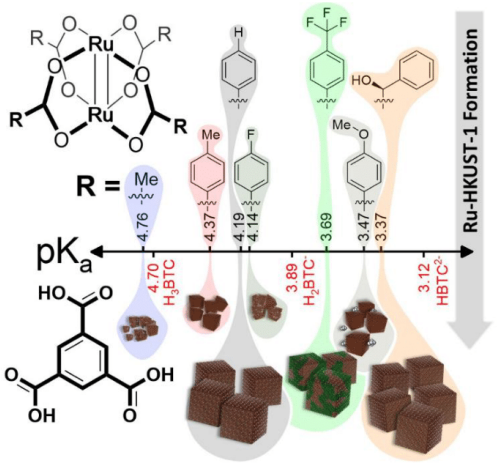

Scheme 1: Schematic representation of this work: Careful pK_a tuning of the precursor ligand / modulator has a major impact on the efficiency and reversibility of the self-assembly into Ru-HKUST-1 derivatives. While the established acetate route (blue marker) yields small crystallites with high acetate defect incorporation, the intermediate acidity of benzoate (grey marker) and of L-mandelate (orange) gives four times larger crystallites and a comparably defect-free MOF material matching the expected composition close to the ideal stoichiometry of $[Ru_3BTC_2]$. The 4-trifluoromethyl benzoate precursor (bright green) yields samples with pronounced modulator incorporation preferentially located at the particle surface. The 4-methyl benzoate (red) and 4-fluoro benzoate (green) precursors result in small and, in the fluoro case rather defective particles. A 4-methoxy benzoate precursor (olive) results in pronounced nanoparticle formation.

[a] *Chair of Inorganic and Metal-Organic Chemistry, Department of Chemistry and Catalysis Research Center, Technical University of Munich, Lichtenbergstraße 4, 85748 Garching, Germany. E-mail: roland.fischer@tum.de.*
[b] *Chair of Solid-State and Materials Chemistry, Institute of Physics, University of Augsburg, Universitätsstraße 1, 86159 Augsburg, Germany.*
Electronic Supplementary Information (ESI) available: [details of any supplementary information available should be included here]. See DOI: 10.1039/x0xx00000x

Such a "defect-free" material would not only allow investigating its native properties without defects obstructing the comparability within the isostructural series of HKUST-1 analogues. Larger, less defective particles resulting from optimized synthesis protocols would also enhance the materials mechanical stability, processability and yields during workup. Although the mixed-valent $Ru^{II,III}$-HKUST-1 is accessible with moderate crystallinity, the univalent $Ru^{II,II}$- and $Rh^{II,II}$-HKUST-1 samples obtained so far are reported as poorly crystalline and comprise significant amounts of modulator-induced acetate defects. The latter is a main complication in the synthesis of PGM-MOFs in general and is related to the intrinsic kinetic inertness of these PGM ions in ligand substitution reactions. High compositional and structural perfection of MOF samples correlate with fast ligand exchange reactions which corresponds to facile self-assembly of the building blocks and rapid establishment of the coordination and crystallite growth equilibrium. Besides high temperatures and long reaction times, both, the "controlled SBU approach" (CSA) employing preformed PW complexes (instead of simple metal salts) and the selection of coordination modulators has been shown to be efficient for PGM-HKUST-1 synthesis. Although the use of a modulator (typically acetic acid) is imperative, its role is Janus-faced. On the one hand, acetic acid modulation turned out to be essential for a reversible self-assembly as prerequisite for structural order and crystallinity (see lit.[6, 9, 16-18] and ESI Table S7 and Figure S13). On the other hand, application of large amounts of acetic acid modulator (e.g., even used as solvent) favours its incorporation as framework inherent component resulting in missing linker (BTC) defects and missing node defects. The respective framework connectivity defects interfere with the crystallite growth and limit the crystallite domain size and thus the overall long-range structural order. Nevertheless, the solvothermal synthesis with $[PGM_2(OAc)_4]$ (PGM = Ru, Rh; OAc = CH_3CO_2) in water and acetic acid (CH_3COOH) acting as modulator and cosolvent is still the state-of-the-art procedure to obtain PGM-HKUST-1.[10] This work provides a study of synthesis conditions towards improved univalent $Ru^{II,II}$-HKUST-1 material properties (see Scheme 1), including structural order and crystallite particle size, porosity and pore size distribution, and compositional purity by systematically scrutinizing the impact of precursor and modulator choice.

Results and discussion

Concept of study

For PGM-HKUST-1 formation to occur effectively, the free acid H_3BTC must undergo three deprotonation steps and facilitating BTC coordination to the Ru dimer $[Ru_2(RCO_2)_4]$ via substitution of the introduced monodentate carboxylate ligand in competition with the chosen carboxylate modulator. Only if all three carboxylate groups of the BTC coordinate to the metal centres at the dimetallic node in a bridging fashion, a defect free three-dimensional network is being formed with perfect stoichiometry of $[PGM_3(BTC)_2]$. The kinetics of such competitive ligand exchange reactions and the parameters of the coordination equilibrium (thermodynamics) control this self-assembly process. The relation between acidities (pK_a) of the precursor ligand/modulator and of the BTC-linker is probably the most decisive parameter to render each of the substitutions reversible and efficient. All our attempts to further optimize the synthesis of univalent Ru-HKUST-1 with the established tetraacetate precursor $[Ru_2(OAc)_4]$ by solvent, temperature or concentration variation were unsuccessful. Still, only the water / acetic acid mixture resulted in nano- to micro-crystalline powder samples of at least certain structural quality.[9,10]

To elucidate the impact of the properties of the chosen carboxylate ligands at the Ru-PW precursor, we now selected a series of *para*-substituted benzoate derivatives with merely identical steric bulk but covering a range of pK_a values. A set of carboxylate-based, molecular $Ru^{II,II}$-PW complexes $[Ru_2(RCO_2)_4]$ including the established acetate (OAc = CH_3CO_2; R = CH_3) but also L-mandelate (R = $C_6H_5CH(OH)$) and some 4-substituted benzoate complexes (OBz-X = RCO_2 with R = XC_6H_4; X = -H, -F, -CF_3, -Me, -OMe) was synthesized and employed as precursors (together with their corresponding free acids as modulators) in univalent Ru-HKUST-1 MOF syntheses according to the concepts of controlled SBU approach and coordination modulation. At this point, the special ease of synthesis of the L-mandelate precursor should be highlighted following a two-step synthesis via ruthenium acetate chloride (air stable) without the necessity of using gaseous hydrogen rendering this complex a particularly interesting candidate as MOF precursor for this study and beyond.

To simplify sample denomination, all MOF samples were named according to the respective precursor ligands/modulators used for their synthesis e.g. OBz-X for all 4-substituted benzoates with X other than H. Note, that the unfunctionalized benzoate will be termed OBz only. All precursors applied in this study have larger steric demand than the established acetate. With acetate modulation, much of the defectiveness of previous materials might be rationalized by a possible formal exchange of one BTC linker by three acetate ligands, thus reducing the network connectivity if a BTC anchoring position at a given node is occupied by acetate. With the chosen aromatic ligands instead of acetate at the Ru-PW for CSA, this kind of modulator-induced defect formation should be less favourable within the confined pore space of the growing framework.

Comprehensive analysis of all MOF materials allowed us to characterize the resulting MOF sample quality (structural order, crystallite & particle size, purity and porosity with defined pore sizes) as a function of the chosen precursor and ligand/modulator situation. Note, that, describing structural quality of samples as more/less "perfect" or "defect-free" refers to a relative comparison within this set of materials rather than claiming absolute perfection. In the following, the synthesized molecular PW precursors will be characterized first. Finally, the developed procedure for the univalent Ru-HKUST-1 synthesis is described and the analysis of the obtained MOF materials is presented and used to draw conclusions on how to control and reduce the defect incorporation in the univalent Ru-HKUST-1 analogue.

Synthesis & Characterization of Precursors

The benzoate- and the acetate-based diruthenium tetra carboxylates of this study were obtained *via* the "blue solutions of Ru(II)".[19] The systematic series of benzoate derivatives is complemented by an L-mandelate complex following an alternative synthetic route.[20] Instead of the experimentally more sophisticated "blue solutions" route, the L-mandelate complex is obtained by a two-step procedure via the air-stable mixed-valence PW compound $[Ru_2(OAc)_4Cl]$ and successive reaction with L-mandelic acid. Although the occurring disproportionation reaction limits the yield, this synthesis appeals through its experimental ease rendering the L-mandelate complex an interesting alternative for Ru-MOF synthesis. The as-synthesized PW structures typically comprise two coordinated solvent molecules ligating both axial PW positions $[Ru_2(RCO_2)_4(L)_2]$ (L = solvent, e.g. THF, Acetone). These crystalline adducts can be desolvated in vacuo at higher temperatures to obtain "activated" PWs with two Ru-OMS. All isolated PW complexes were characterized with ^{1}H-NMR, elemental analysis, LIFDI mass spectrometry and FT-IR spectra. All data are provided in the electronic supporting information (ESI). The synthesis of a trifluoro acetate complex was attempted according to a ligand exchange approach described in literature.[21] However, very low synthetic yields obstructed its applicability in this study. In addition, a 3,5-dimethoxy benzoate complex was synthesized. Purification of this compound turned out to be challenging, thus preventing its use for MOF syntheses in this study. So far not documented structures were obtained for the compounds $[Ru_2(OBz\text{-}F)_4(Me_2CO)_2]$, $[Ru_2(OBz\text{-}Me)_4(Me_2CO)_2]$, $[Ru_2(OBz\text{-}OMe)_4(Me_2CO)_2]$ and $[Ru_2(OBz\text{-}(OMe)_2)_4(Me_2CO)_2]$, which could be characterized by single-crystal X-ray diffraction (SCXRD) analysis. Details of the respective structures are given in the ESI (see Tables S1-5 and Figures S4-8). Typical for these compounds, the tetra-μ-carboxylato diruthenium(II,II) complexes show a binuclear paddlewheel structure $Ru_2(O_2CR)_4$, with the Ru(II) atoms being bridged by benzoate ions. All binuclear complexes $[Ru_2(OBz\text{-}X)_4]$ (X = Me, F, OMe) and $[Ru_2(OBz\text{-}(OMe)_2)_4]$ comply well with D_{4h} symmetry, where the centre of gravity of the complexes corresponds with a centre of inversion of their respective space groups. The $Ru_2(O_2CR)_4$ complexes are coordinated by Me_2CO, ligating the free axial positions with the carbonyl oxygen atoms. $[Ru_2(OBz\text{-}Me)_4(Me_2CO)_2]$ and $[Ru_2(OBz\text{-}(OMe)_2)_4(Me_2CO)_2]$ both crystallize in the triclinic space group $P\bar{1}$, with one symmetry independent binuclear complex in the unit cell. $[Ru_2(OBz\text{-}F)_4(Me_2CO)_2]$ and $[Ru_2(OBz\text{-}OMe)_4(Me_2CO)_2]$ both crystallize in the monoclinic space group $C2/c$, where $[Ru_2(OBz\text{-}OMe)_4(Me_2CO)_2]$ shows one symmetry independent binuclear complex in the unit cell, and $[Ru_2(OBz\text{-}F)_4(Me_2CO)_2]$ shows two symmetry independent paddlewheel complexes in its unit cell (indistinguishable within the error tolerance). The Ru-O distances between the bridging benzoate ions and the Ru(II) centres lay in the expected ranges of comparable compounds (~ 206 pm). O-Ru-O angles deviate only minimal from the expected angles of D_{4h} symmetry. The Ru(II) atoms are coordinated in a square planar fashion by the benzoate oxygen atoms, with minimal lateral deviation of the Ru(II) centres. The Ru-Ru distances show expected values (~ 226 pm) and are comparable with e.g. $Ru_2(CH_3COO)_4(THF)$. In all cases, the Ru-O distances of the axial coordinating Me_2CO are longer than Ru-O distances of the benzoate ions, the former ranging from 230 to 235 pm. Interestingly, the bond lengths and angles appear to be rather insensitive in variation of the carboxylate ligand (Table S6 provides an overview as well as categorisation with respect to known compounds).

We conducted a series of NMR-based carboxylate ligand exchange reactions to investigate the properties of all studied precursors in a simplified test reaction mimicking a key aspect of the MOF self-assembly process. For this purpose, 3,5-bis(trifluoromethyl) benzoic acid was selected as co-ligand featuring steric and electronic properties similar to the BTC linker but being monofunctional. This avoids undesired formation of extended structures. Details of this test reaction are outlined in the ESI (see Figures S9-12 &explaining paragraphs). The equilibrium constant K is defined the ratio of free carboxylic acid of the precursor ligand to the free co-ligand representing the equilibrated exchange efficiency. In theory, more acidic (low pK_a) modulators are more likely deprotonated and remain competitive in metal coordination. An ideal self-assembly could be assumed for equal competition ($K \approx 1$) of modulator and linker. The experiments show equilibrium constants K decreasing with higher acidity (see Figure S9) as general trend but not strictly following a perfect order. OBz, OBz-F and mandelate have K in the range of 1. A high exchange rate as found for OAc, OBz and mandelate is another prerequisite for vital self-assembly and efficient MOF formation. Based on the kinetic data of these simplified exchange experiments, OBz and mandelate appear to be promising candidates as precursors for the univalent Ru-HKUST-1 of high structural quality. However, the processes under real MOF formation conditions are more complex with more interrelated kinetics and chemical equilibria, at least three different pK_a values of H_3BTC need to be considered.

MOF synthesis & characterization – Impact of precursor

Modified synthesis procedure accounting for solubility of precursor/modulator &extensive washing procedure

The MOF synthesis procedure should be generally applicable allowing equal reaction conditions for all precursors under investigation. However, the established literature procedure using water and acetic acid is not transferable to other precursor ligand/modulator systems. The acetic acid has a dual function and acts as modulator but also as cosolvent enhancing BTC dissolution. For the solid benzoic acid derivatives such solubilizing effect is absent and for some, the solubility in water is not sufficient. Therefore, we developed a more generally applicable solvent concept and synthesis procedure using 4 mL water, 4 mL acetone and 12.2 mmol modulator for each PW precursor (0.36 mmol with respect to PWs + 0.48 mmol H_3BTC). Details of the parameter optimization and all used reagent amounts are summarized in the supporting information (see Table S7-8, Figure S13). According to previous reports, samples were synthesized in steel autoclaves with PTFE insets at 150 °C

Table 1: Summary of MOF samples obtained using different precursors. *R refers to the used $Ru_2(OOCR)_4$ precursor and HOOCR modulator, respectively. Domain sizes are mean values obtained by the Scherrer equation and full width at half maximum (FWHM) values of the three most intense reflections (220), (222) and (400). The Ru content is based on TGA-related metal oxide residues. Comments refer to conclusions from all available analytical techniques. The sample OAc (x2 Mod) was synthesized with the twofold amount of modulator. *Higher yield due to less extensive washing procedure. **Traces of benzoate are present.

Sample Notation	R* =	pK_a	Isolated Yield [mg]	Domain Size [nm]	BET surface area [m^2g^{-1}]	Ru content [wt-%]	Comment / Purity
OAc	$-CH_3$	4.76	200*	11.3	1493	40.4	Acetate defects
OAc (x2 Mod)	$-CH_3$	4.76	198*	15.2	n.d.	41.2	Acetate defects
OBz	$-C_6H_5$	4.19	101	40.1	1432	41.9	Rather pure**
OBz-F	$-C_6H_4F$	4.14	93	16.0	1516	41.8	Pure, large mesopores
OBz-CF_3	$-C_7H_4F_3$	3.69	104	37.2	987	32.6	HOBz-CF_3 impurity
OBz-Me	$-C_7H_7$	4.37	107	14.5	1401	29.2	Low Ru content
OBz-OMe	$-C_7H_7O$	3.47	139	26.5	1505	50.4	Ru NPs impurity
Mandelate	$-C_7H_7O$	3.37	120	28.4	1789	41.7	Pure

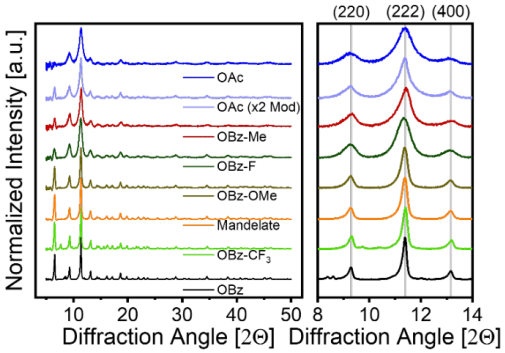

Figure 1: PXRD patterns of the whole series of Ru-HKUST-1 samples ordered according to their full width at half maximum (FWHM) values of the three most dominant reflections (220), (222) and (400). Left: Whole diffraction patterns, right: zoom-in of the three low angle reflections used for the crystallite size calculations. Note, that instrument-related factors and baseline correction led to lower relative signal intensities of the (200) reflection (6.5° 2Θ) for the low crystalline samples.

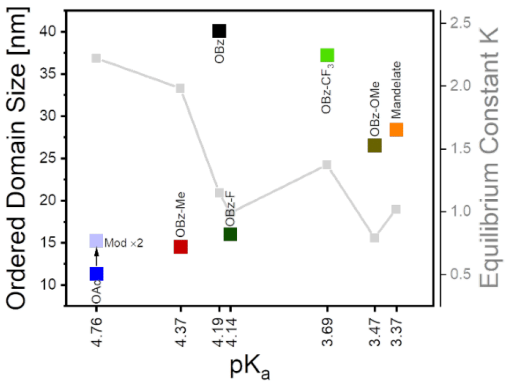

Figure 2: The derived MOF domain sizes as a function of the precursor ligand/modulators acidity (pK_a). Additional equilibrium constants K highlighted with grey line/squares are extracted from NMR-based ligand exchange test reactions using 3,5-bis(trifluoromethyl) benzoic acid as shown in the ESI.

for 3 d reaction time. Due to the limited solubility of the used benzoic acids at ambient temperature, extensive washing with acetone was conducted to remove residual modulators from the MOF pores. Although this was done with repetitive cycles including longer decantation times, workup of larger quantities might be performed using continuous Soxhlet extraction techniques. Interestingly, all obtained MOF samples still inherited the colour shades of their respective precursors as displayed in Figure S14 in the ESI.

Phase purity and size of crystallite domains and particles

As shown in Figure 1, powder diffraction patterns indicate the successful synthesis of crystalline Ru-HKUST-1 with all used precursors. In line with previous reports, the acetate-derived MOFs give very broad reflections. In contrast, the other samples exhibit significantly narrower reflections peaking in the OBz-CF_3, the OBz and the L-mandelate-derived samples. All samples appear largely phase pure with additional minor reflections visible for the OBz and the OBz-CF_3 samples potentially arising from modulator residues. A PXRD comparison of MOF samples, their originating precursor and the related modulator is shown in Figures S15-21.

Full width at half maximum (FWHM) values of the three most intense reflections served to derive mean crystallite domain sizes using a simple estimation based on *Scherrer's* equation. Domain sizes are displayed as a function of precursor ligand/modulator pK_a in Figure 2. Note, that, instrument-related line broadening was neglected in this calculation. Thus, there is some intrinsic uncertainty and given size values should be regarded on a comparative basis only. Nonetheless, this instrument-related error might be neglectable regarding the comparably large FWHM values of PGM-MOFs in general. Therefore, and because the results are in very good agreement with the typical particle sizes obtained from HR-TEM (see below), we decided to provide absolute values in Figure 2. The OBz sample shows a remarkable fourfold increase in domain size (≈40 nm) compared to the established OAc PW precursor (≈10 nm). Also, the samples OBz-CF_3 (≈35 nm) and L-mandelate (≈30 nm) show lager crystallite domain sizes. The OBz-Me and OBz-F samples have domain sizes in the range of ≈15 nm.

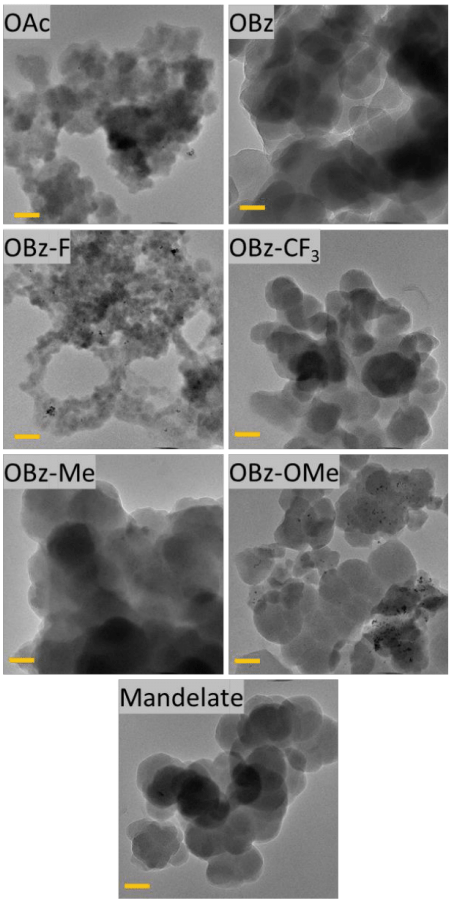

Figure 3: HR-TEM images of all Ru-MOF samples. Orange scale bars represent 50 nm. The increased primary particle size particularly of the samples OBz, OBz-CF_3, OBz-Me and mandelate is in line with results from FWHM analysis from PXRD patterns. The OAc and OBz-F samples contain few metal NPs while the OBz-OMe sample comprises higher amounts.

Generally, a combination of high ligand exchange rates and equilibrium constants K≈1 (both determined in the ligand exchange experiments mentioned above) seems to facilitate larger crystallites and better structural long-range order. At this point, it remains unclear why the ligand exchange rates and consequently the particle sizes of OBz and OBz-F differ significantly considering their relatively similar electronic (pK_a) and steric properties. Despite the clear particle size improvement, we were unable to obtain significantly larger crystallites. This may be possible by prolonged reaction times and using seed crystals.

HR-TEM images were recorded for all MOF samples to gain additional insights into particle size and morphology as well as the presence of metal nano particles (NPs) which are shown in Figure 3 and S30. First to mention, the general trends in primary particle size from FWHM analysis of the respective PXRD patterns is confirmed. The particle size increases from OAc toward OBz, OBz-CF_3, OBz-Me and mandelate-derived MOF samples. In addition, metal NPs are present in OAc and OBz-F samples in low amounts while the OBz-OMe sample contains larger concentrations of metal NPs. Their formation might be due to potential redox-active interactions with the methoxy modulator or with trace impurities thereof. This corroborates the higher metal content derived from TGA for this sample. To access the elemental distribution of some representative samples, elemental mappings were recorded from OBz, OBz-F, OBz-CF_3 and mandelate-derived samples. For the OBz and mandelate-derived samples, C, O and Ru contents are homogeneously distributed (see Figure S31-37). For the two samples OBz-F and OBz-CF_3, fluorine was monitored, too. The very small particle sizes of OBz-F hamper unambiguous conclusions on its elemental distribution. Macroscopically, the sample seems homogeneous. In contrast, mapping of the OBz-CF_3 sample comprising larger crystallites provides interesting insights into the location of residual modulator species. Notably, the 4-trifluormethylbenzoate preferentially locates at the surface of the primary particles as can be seen in Figure S34-35.

Composition

Elemental analysis was performed with all samples providing C and H values. For the F-containing samples OBz-F and OBz-CF_3, we derived F contents from Ru:F ratios based on triplicate EDS measurements. Metal contents were extracted from metal oxide residues of TGA measurements in analogy to earlier reports for these PGM-MOFs.[6, 7, 15] Theoretically, this set of C, H, F and Ru contents could provide a sufficient basis for a solver-assisted calculation of putative sum formulae as reported in our earlier studies.[6, 7, 15] However, uncertain F contents and relatively similar C:H ratios of BTC and the respective benzoate modulators render this approach less accurate and reliable. Putative sum formulae and their underlying elemental contents are displayed in Table S9. Irrespective of the solver approach, the elemental composition already allows for some conclusions all being in line with other conclusions drawn herein: Most of the samples comprise largely identical Ru ratios representative for a rather ideal Ru-HKUST-1 (42 wt-% Ru is expected in a "perfect" univalent [Ru_3BTC_2], see Table S9). However, the lower Ru contents of the OBz-CF_3 and OBz-Me samples originate from their modulator impurities also in line with surplus C and F contents. A higher Ru content for the OBz-OMe sample is caused by the presence of Ru nanoparticles as deduced from the HR-TEM images discussed above. This OBz-OMe sample also contains considerably smaller organic fractions. Regarding C, H and Ru contents, the samples OAc, OBz and L-mandelate contain quite ideal values compared to the empirical formula of stoichiometric [$Ru_3(BTC)_2$].

Oxidation State and IR & Raman Data

Vibrational spectroscopy (both FT-IR and Raman) was conducted for the whole series of materials to acquire insights

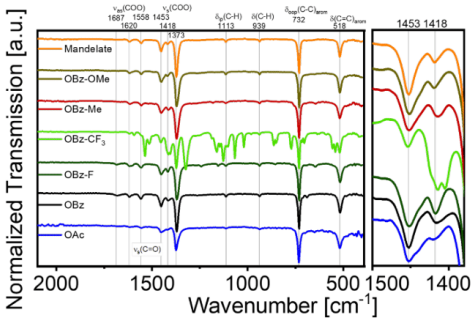

Figure 4: FT-IR spectra of all Ru-HKUST-1 samples. All spectra indicate overall similar bonding properties with all vibration bands associated to HKUST-1 being present. The zoom-in on the right shows ν_{as}(COO) providing strong indication for the $Ru^{II,II}$ oxidation state as demonstrated earlier.[7] The OBz-CF_3 sample features additional bands arising from substantial HOBz-CF_3 residue.

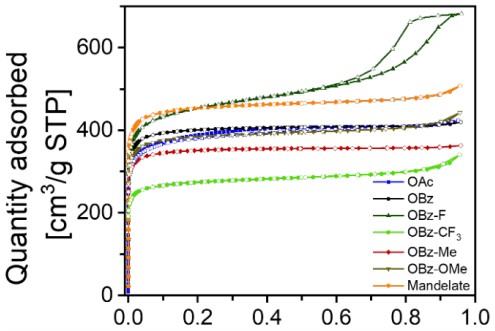

Figure 5: Nitrogen sorption isotherms recorded at 77 K indicate high permanent porosity of all samples. Close symbols refer to adsorption, open symbols to desorption branches respectively. The OBz-CF_3 sample shows reduced sorption capacity due to residual free carboxylic acid modulator partly occupying the pore volume. The OBz-F sample exhibits pronounced meso and macro porosity (type II isotherm). The mandelate-based sample has an unprecedented high BET surface area of ≈1790 m^2g^{-1} with well-defined micropores with a narrow PSD representing the most perfect $Ru^{II,II}$-HKUST-1 sample of this study. A comparison including molar surface areas and pore volumes of all samples in comparison with the ideal Cu-HKUST-1 structure is provided in Table S10.

into the linker/ligand bonding situation and in particular confirming the univalent $Ru^{II,II}$ oxidation state. Respective IR and Raman spectra are displayed in Figure 4 and Figures S22-29. In line with PXRD, the whole isostructural series exhibit largely identical vibrational spectra. For the HOBz-CF_3 sample, some residual modulator causing only minor reflections in PXRD has, however, a much stronger impact on the relative vibrational spectra as several additional strong signals appear. As highlighted in earlier studies, the ν(COO) valence modes of metal carboxylates are a sensitive probe for the coordination environment of the metal.[6, 7, 21] In detail, the Δν between ν_{as}(COO) and ν_s(COO) is a reliable probe for the metal oxidation states in PGM-PW compounds. [22, 23] In line with previous literature of PGM-HKUST-1 analogues, the band positions and shapes of the two bands displayed in Figure 4, right zoom-in, indicate the targeted $Ru^{II,II}$ oxidation state being dominant in all samples. Note that, this assignment can´t be unambiguously confirmed for the OBz-CF_3 sample due to overlapping bands from residual modulator. However, the band at 1453 cm^{-1} coincides with all other samples. Small amounts of loosely bound μ^1-carboxylates could be present in OBz and OBz-F samples as indicated by the weak absorption bands at 1687 cm^{-1}. In addition to standard FT-IR, we performed complementary Raman spectroscopy with all samples as displayed in Figure S22. In line with FT-IR and PXRD, the overall isostructurality is confirmed for the series. However, the present modulator impurity of OBz-CF_3 dominates its Raman spectrum with some MOF-related signals even not being visible.

Gas sorption studies, specific surface area and pore size distribution

Nitrogen sorption isotherms (see Figure 5) were recorded to investigate the porosity of all MOF samples including analysis of the pore size distribution derived from density functional theory (DFT) (see Figure 6). Most MOF samples show type I isotherms, the OBz-F sample shows a type II isotherm. All gravimetric surface areas (SA) according to *Brunauer, Emmett and Teller* (BET) are displayed in Table 1. Additional molar surface areas

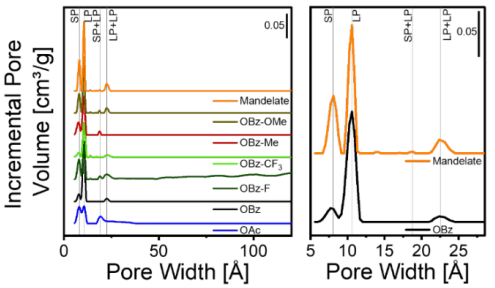

Figure 6: DFT-based pore size distributions indicate microporosity for all samples applying the model for cylindrical pores on oxide surfaces. Left: Most of the samples show additional defined pores resulting from pore wall removal merging two pores, Small pores (SP) or Large pores (LP). The OAc sample contains mesopores in the range of 2 nm with low definition. OBz-F sample contains considerable amounts of large highly diffuse meso and macro pores. OBz and OBz-CF_3 samples exhibit only small pore volume of SP relative to LP probably arising from pore blocking by residual modulator. Right: Zoom-in to the range of SP to LP+LP pore sizes shown for a selection of the two "best" samples: OBz and mandelate.

and molar total pore volumes (V_P, with respect to pores <387 Å) are provided in Table S10. The OAc, OBz, OBz-OMe and OBz-Me samples exhibit comparable SAs ranging from ≈1400 to ≈1520 m^2g^{-1} which is in general accordance with earlier reports on the univalent Ru-HKUST-1.[7, 10] All samples comprise the two HKUST-1 structure specific and distinct micropores with sizes of 8 Å (small pore; SP) and 10.5 Å (large pore; LP). Besides these pores of the ideal structure, larger pores occur probably induced by defects. They could result from pore wall removal (missing linker, missing node defect) and feature the merged pore sizes of SP+SP, SP+LP or LP+LP as indicated by vertical lines

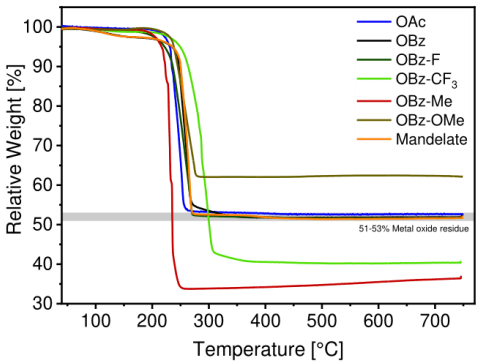

Figure 7: TGA curves of all MOF samples with decomposition in air (flow 20 mLmin^{-1}) and a constant temperature ramp of 10 Kmin^{-1}. The samples OBz-Me and OBz-CF_3 have lowered metal oxide residues indicating the excessive presence of organic compounds (residual modulator), while the OBz-OMe sample comprises higher metal amounts, indicating the presence of metal nanoparticles as confirmed by HR-TEM images. All other samples comprise organic / metal contents similar to the ideal Ru-HKUST-1 sum formula. Thermal stability is the lowest for the OBz-Me sample and the highest for the OBz-CF_3 sample. The mandelate-derived sample has the second highest thermal stability and shows a slight weight loss above 100 °C indicating the presence of residual water assumingly bound to the hydroxy groups of the mandelate ligand.

in Figure 6. Analysis of the PSD of the OBz-F sample reveals that the type II sorption isotherm with a hysteresis between adsorption and desorption branch is caused by some hierarchical porosity. Exclusively in the OBz-F sample, besides the defined micropores, there are meso and even macro pores without defined sizes starting from 50 Å resulting in the huge V_p of 0.706 cm³mmol^{-1}. In line with FT-IR, Raman and elemental analysis results, the OBz-CF_3 sample has a lower SA of ≈990 m²g^{-1} caused from pore occupancy by residual HOBz-CF_3 modulator (total pore volume of only 0.386 cm³mmol^{-1}). Perfectly matching the molecular size (max. 8.0 Å) of HOBz-CF_3, the 8 Å SPs are preferentially occupied as indicated by the PSD. A similar reduction of available Vp is observed for the OBz-OMe sample (0.352 cm³mmol^{-1}) due to the presence of dense Ru NPs. Notably, the l-mandelate sample has the highest SA ever reported for any Ru-HKUST-1 with ≈1790 m²g^{-1}. Expressed in molar values, its BET SA (1304 m²mmol^{-1}) as well as V_p (0.497 cm³mmol^{-1}) are perfectly in line with computational values of perfect Cu-HKUST-1 (1293 m²mmol^{-1} and 0.496 cm³mmol^{-1}) reported earlier.[24] In line with this, its porosity is characterized by clearly defined pores with the narrowest size distribution of this series. This is a clear indication for the high structural perfection of the Ru-HKUST-1 sample derived from coordination modulated CSA using the L-mandelate substituted Ru-PW precursor.

Thermal properties

Thermal stability of the MOF samples was investigated using thermogravimetric analysis (TGA). The respective graphs are displayed in Figure 7. TGA allows to access both thermal stability and a compositional determination of the organic / metal fractions within the samples as highlighted above. First, the thermal decomposition occurs between 200 and 300 °C for all samples of the series with the OBz-Me sample having the lowest and the OBz-CF_3 sample the highest thermal stability. All other samples exhibit very similar decomposition curves with the OBz and L-mandelate-derived samples having slightly higher stabilities compared to the other samples. These subtle differences might result from the different particle sizes as concluded from PXRD and HR-TEM data. Apparent in Figure 7 are the remarkable differences in the vertical plateaus of metal oxide residues after thermal decomposition. While the metal content is significantly higher for the OBz-OMe sample, it is much lower for the OBz-Me and OBz-CF_3 samples with respect to all other samples comprising relatively ideal metal contents (see chapter on sample compositions).

Conclusion and Outlook

In conclusion, a series of eight diruthenium tetracarboxylate complexes with $Ru^{II,II}$ oxidation state including some literature-known and some new examples of this structure motif were synthesized and characterized with ^{1}H-NMR, XRD, FT-IR and elemental analysis. New single crystal structures of four complexes namely $Ru_2(OBz\text{-}F)_4(Me_2CO)_2$, $Ru_2(OBz\text{-}Me)_4(Me_2CO)_2$, $Ru_2(OBz\text{-}OMe)_4(Me_2CO)_2$ and $Ru_2(OBz\text{-}(OMe)_2)_4(Me_2CO)_2$ were resolved. Seven of these molecular Ru-PW complexes were used as precursors for the coordination modulated synthesis of the univalent MOF $Ru^{II,II}$-HKUST-1 to investigate the specific impact of the precursor ligand and particularly its acidity. In all reactions, the used free carboxylic acid modulator additive was adopted according to the precursor ligand. The ruthenium benzoate and L-mandelate precursors in combination with using the excess of these ligands as coordination modulators in an optimized solvent mixture gave MOF materials with the most “perfect” structure, analytical composition, and sorption properties. The crystallite domain size was up to four times larger compared to the established acetate route. Further, the L-mandelate-derived MOF features the highest BET surface area reported for the univalent Ru-HKUST-1 with a rather perfect pore size distribution. Molar surface area and total pore volume perfectly coincide with previously computed values for stoichiometric and defect-free Cu-HKUST-1. Both MOF materials show HKUST-1 characteristic IR and Raman spectra, substantiating the univalent redox state of Ru^{II} and confirming high sample purity. The other utilized precursors OBz-F, OBz-CF_3, OBz-Me and OBz-OMe all resulted in particle sizes larger than the established OAc route but suffered either from high defectiveness, less defined PSDs, or impurities. In conclusion, the low or medium pK_a values of 4.19 and 3.37 from benzoate and mandelate turned out to be most suitable to obtain a rather ideal HKUST-1 structure with increasing crystallite sizes. As revealed by NMR kinetic experiments, particularly these two precursor ligands/ modulators feature a combination of high ligand exchange rates and equal coordination competition with the BTC linker. Our results underline the importance of matching the acidities of precursor ligand/modulator with the different BTC species as

linker of several well-known MOF materials such as HKUST-1, MIL-101 or MOF-808. The special ease of synthesis and its superior performance in MOF formation render the diruthenium tetramandelate an interesting precursor to access the univalent $Ru^{II,II}$-HKUST-1 analogue. We speculate that further optimizing the synthesis conditions in terms of solvent mixture, reaction time and temperature also including seed crystal techniques may further improve the sample quality in terms of accessible particle and crystallite domain sizes.

Experimental

General considerations about working procedures, used chemicals and solvents are listed in the supporting information. Detailed synthetic protocols and the analytical characterization data regarding all employed PW precursors, including the new single crystal structures of $Ru_2(OBz\text{-}F)_4(Me_2CO)_2$, $Ru_2(OBz\text{-}CF_3)_4(THF)_2$, $Ru_2(OBz\text{-}Me)_4(Me_2CO)_2$, $Ru_2(OBz\text{-}OMe)_4(Me_2CO)_2$ and $Ru_2(OBz\text{-}(OMe)_2)_4(Me_2CO)_2$, and as well the characterization data of the derived Ru-HKUST-1 samples using these precursors are compiled in the Supporting Information (Tables S1-5, Figures S4-8).

Instrumentation

All PW-complexes and MOFs were synthesized and handled under exclusion from air utilizing standard Schlenk techniques and Ar-filled gloveboxes. Used solvents were carefully degassed and stored in argon prior to use. Preparations for MOF syntheses and subsequent solvent exchange was conducted in a “wet glovebox” under oxygen-free conditions.
PXRD patterns were collected on a *PANalytical* Empyrean equipped with a Cu X-ray tube (λ = 0.154 nm) operated at 45 kV and 40 mA in a 2Θ range of 5-50° in steps of 0.0065651° (2Θ) with 0.175 s/step. Dried precursors and activated MOF samples were filled into 0.5 mm borosilicate glass capillaries and measured therein. SCXRD was measured on a *Bruker* D8 Venture diffractometer equipped with a Helios optic monochromator, a Photon 100 CMOS detector and either a Mo IMS microsource or a Mo rotating anode source (λ = 0.71073 Å). Single crystals were directly taken from the reaction solutions and prepared under inert conditions. Crystals were picked under a microscope in perfluorated ether and directly transported to the diffractometer. Elemental analysis of C and H content was carried out using a *Hekatech* EuroEA elemental analyzer. Ru contents were derived from TGA residues upon decomposition in synthetic air assuming Ru_2O_3. Ru:F ratios were obtained by EDS. Gas sorption experiments were conducted on a *Micromerictics* 3flex with additional sample activation at 150 °C for >10h. N_2 isotherms were recorded at 77K. FT-IR spectra were measured with finely ground activated powders on a *Bruker* ALPHA FTIR spectrometer with ATR unit at ambient temperature in the range of 400-4000 cm_{-1}. Raman spectra were measured on a *Renishaw* R04 Raman Micro-spectrometer with 532 nm laser wavelength. Liquid ^{1}H-NMR spectra were recorded with a *Bruker* AV400US at 400 MHz at 298 K. Kinetic measurements and 19F-spectra were recorded on a *Bruker* DRX400. LIFDI mass spectrometry was conducted on a *Waters* LCT Micromass TOF MS with additional LIFDI module. TGA measurements were conducted on a Mettler Toledo TGA/DSC 3+ in synthetic air using 10 $Kmin^{-1}$ heating rates. HR-TEM and respective elemental maps were recorded on a JEM NEOARM microscope from *JEOL* with a cold FEG electron source operated at 200 kV. Samples were prepared by depositing a drop of the crystalline products dispersed in ethanol onto carbon-coated copper grids (200 mesh) and dried in air. Images and maps are displayed in Figure 3 and S30-37. Dark field STEM images and respective EDS compositional maps were recorded for C, O, F and Ru. More experimental and instrumental details are provided in the ESI.

Kinetic NMR Experiments

Kinetics of ligand exchange reactions were monitored with *in-situ* ^{1}H-NMR of precursors. In an argon-filled glovebox, the specific precursor (0.008 mmol, 1 eq) was weighed into a centrifugation vial (45 mL) and dissolved in degassed deuterated acetone (5.5 mL). In another centrifugation vial, the co-ligand 3,5-bis(trifluoromethyl) benzoic acid (7.5 mg, 0.029 mmol, 4 eq) was placed. 5.0 mL of the precursor solution was added, quickly shacked and 0.5 mL of this solution was transferred into a J-Young-type NMR tube. The tube was excluded from the glovebox and immediately frozen in liquid nitrogen. In every case, the time between combining precursor and coligand until freezing was one minute. The frozen sample was transferred to the NMR spectrometer and the following sequence was measured: A new spectrum was recorded every 2 min (first 30 min) and then every 5 min (for another 60 min). The sample was then heated to 55 °C (reached within 2 min). At this temperature, spectra were recorded every 2 min (first 30 min) and then every 5 min (another 90 min).

Synthesis of MOF samples

All Ru-HKUST-1 samples were synthesized following an identical and optimized procedure: Samples of X mg Ru-PW precursor (0.36 mmol, 3 eq), 101 mg trimesic acid (H_3BTC, 0.48 mmol, 4 eq) and Y mg respective modulator (free carboxylic acid of the respective precursor, 12.2 mmol, 102 eq) were dissolved in 4 mL water and 4 mL acetone. The mixture was placed in a 20 mL Teflon inlet, tightly sealed in a steel autoclave and heated to 150 °C for 3 d. Upon cooldown to ambient temperature, the red brown supernatant was removed. Modulator removal and solvent exchange was achieved by 20 cycles of acetone wash (20x15 mL), settling for >6h and decantation subsequently. After solvent exchange, the MOF samples were desolvated at 150 °C in dynamic vacuo (≈10^{-2} mbar) for 24 h. The distinct weights of reagents used for every synthesis are provided in Table S8. All characterization data discussed in the main text are provided in the Supporting Information.

Conflicts of interest

The authors declare no competing financial interests.

Acknowledgements

This project was funded by Deutsche Forschungsgemeinschaft grant no. FI-502/32-1 („DEMOFs“). WRH would like to thank TUM Graduate School and GDCh for travel funding. All authors thank Jan Berger, Pia Vervoorts and Dardan Ukaj for experimental support with physisorption measurements, Maria Matthews and Patricia Heiß for technical support with NMR spectroscopy and Karina Hemmer for experimental support revising the manuscript.

References

1. I. Aguirrezabal-Telleria, I. Luz, M. A. Ortuño, M. Oregui-Bengoechea, I. Gandarias, N. López, M. A. Lail and M. Soukri, *Nat. Commun.*, 2019, **10**, 2076.
2. D. M. Shakya, O. A. Ejegbavwo, T. Rajeshkumar, S. D. Senanayake, A. J. Brandt, S. Farzandh, N. Acharya, A. M. Ebrahim, A. I. Frenkel, N. Rui, G. L. Tate, J. R. Monnier, K. D. Vogiatzis, N. B. Shustova and D. A. Chen, *Angew. Chem. Int. Ed.*, 2019, **58**, 16533-16537.
3. C.-H. Wang, W.-Y. Gao and D. C. Powers, *J. Am. Chem. Soc.*, 2019, **141**, 19203-19207.
4. K. Epp, I. Luz, W. R. Heinz, A. Rapeyko, F. X. Llabres i Xamena and R. A. Fischer, *ChemCatChem*, 2020, **12**, 1720-1725.
5. P. Guo, C. Froese, Q. Fu, Y.-T. Chen, B. Peng, W. Kleist, R. A. Fischer, M. Muhler and Y. Wang, *J. Phys. Chem. C*, 2018, **122**, 21433-21440.
6. W. R. Heinz, T. Kratky, M. Drees, A. Wimmer, O. Tomanec, S. Günther, M. Schuster and R. A. Fischer, *Dalton Trans.*, 2019, **48**, 12031-12039.
7. W. R. Heinz, I. Agirrezabal-Telleria, R. Junk, J. Berger, J. Wang, D. I. Sharapa, M. Gil-Calvo, I. Luz, M. Soukri, F. Studt, Y. Wang, C. Wöll, H. Bunzen, M. Drees and R. A. Fischer, *ACS Appl. Mater. Interfaces*, 2020, **12**, 40635-40647.
8. S. S.-Y. Chui, S. M.-F. Lo, J. P. H. Charmant, A. G. Orpen and I. D. Williams, *Science*, 1999, **283**, 1148-1150.
9. W. Zhang, O. Kozachuk, R. Medishetty, A. Schneemann, R. Wagner, K. Khaletskaya, K. Epp and R. A. Fischer, *Eur. J. Inorg. Chem.*, 2015, **2015**, 3913-3920.
10. W. Zhang, K. Freitag, S. Wannapaiboon, C. Schneider, K. Epp, G. Kieslich and R. A. Fischer, *Inorg. Chem.*, 2016, **55**, 12492-12495.
11. Z. Fang, B. Bueken, D. E. De Vos and R. A. Fischer, *Angew. Chem. Int. Ed.*, 2015, **54**, 7234-7254.
12. S. Dissegna, K. Epp, W. R. Heinz, G. Kieslich and R. A. Fischer, *Adv. Mater.*, 2018, **30**, 1704501.
13. O. Kozachuk, I. Luz, F. X. L. i. Xamena, H. Noei, M. Kauer, H. B. Albada, E. D. Bloch, B. Marler, Y. Wang, M. Muhler and R. A. Fischer, *Angew. Chem. Int. Ed.*, 2014, **53**, 7058-7062.
14. W. Zhang, M. Kauer, O. Halbherr, K. Epp, P. Guo, M. I. Gonzalez, D. J. Xiao, C. Wiktor, F. X. Liabrés i Xamena, C. Wöll, Y. Wang, M. Muhler and R. A. Fischer, *Chem. Eur. J.*, 2016, **22**, 14297-14307.
15. W. R. Heinz, R. Junk, I. Agirrezabal Telleria, B. Bueken, H. Bunzen, T. Gölz, M. Cokoja, D. E. De Vos and R. A. Fischer, *Catal. Sci. Technol.*, 2020, DOI: 10.1039/D0CY01479F.
16. T. Tsuruoka, S. Furukawa, Y. Takashima, K. Yoshida, S. Isoda and S. Kitagawa, *Angew. Chem. Int. Ed.*, 2009, **48**, 4739-4743.
17. S. Yuan, T.-F. Liu, D. Feng, J. Tian, K. Wang, J. Qin, Q. Zhang, Y.-P. Chen, M. Bosch, L. Zou, S. J. Teat, S. J. Dalgarno and H.-C. Zhou, *Chem. Sci.*, 2015, **6**, 3926-3930.
18. Y. Sun, D.-F. Lu, Y. Sun, M.-Y. Gao, N. Zheng, C. Gu, F. Wang and J. Zhang, *ACS Materials Letters*, 2021, **3**, 64-68.
19. D. Rose and G. Wilkinson, *Journal of the Chemical Society A: Inorganic, Physical, Theoretical*, 1970, DOI: 10.1039/J19700001791, 1791-1795.
20. F. A. Cotton, V. M. Miskowski and B. Zhong, *J. Am. Chem. Soc.*, 1989, **111**, 6177-6182.
21. M. A. S. Aquino, *Coord. Chem. Rev.*, 1998, **170**, 141-202.
22. M. Rusjan, E. E. Sileo and F. D. Cukiernik, *Solid State Ion.*, 2003, **159**, 389-396.
23. M. C. Rusjan, E. E. Sileo and F. D. Cukiernik, *Solid State Ion.*, 1999, **124**, 143-147.
24. J. Liu, J. T. Culp, S. Natesakhawat, B. C. Bockrath, B. Zande, S. G. Sankar, G. Garberoglio and J. K. Johnson, *J. Phys. Chem. C*, 2007, **111**, 9305-9313.

5 Lessons Learned & Outlook

The largely undiscovered chemistry of PGM-based MOFs was at the core of this PhD project. The low abundance of PGMs in MOF chemistry is rationalized by the challenging properties of these relatively inert elements hampering an efficient ligand exchange and thus, a vital self-assembly as precondition for structurally ordered MOFs. Regarding self-supported MOFs, the first PGM to be reported upon was ruthenium. Previous studies already established synthetic pathways; however, the pronounced inherent defectiveness has always been an inevitable companion. In former studies, the beneficial impact of DE on sorption and catalysis was exemplified using the *de novo* mixed-linker approach.

This thesis represents a continuation of these former works. First, the ambivalent role of the residual and unavoidable acetate content in these Ru-based mixed-component materials was investigated. As a byproduct from the CSA and modulated synthesis in aqueous acetic acid, large amounts of acetate-based defects are incorporated within the materials. In the lattice, each BTC linker can presumably be replaced by three acetate ligands lowering the overall framework connectivity and limiting the accessible MOF particle size during synthesis. In a mixture with chloride, acetate is also present as axial ligand in the mixed-valence $Ru^{II,III}$ system accounting for charge compensation.

The group of HKUST-1 analogues known so far was expanded by the monometallic Rh- and mixed-metal RuRh-HKUST-1 analogues herein. In the mixed-metal analogues, homogeneous solid-solutions of each monometallic $Ru^{II,III}$ and $Rh^{II,II}$ dimers are present. To gather more general insights into the chemistry of PGM-based MOFs and the impact of the chosen metal and its oxidation state, a selection of those samples namely the three monometallic $Ru^{II,II}$, $Ru^{II,III}$ and $Rh^{II,II}$ and one mixed-metal $Ru^{II,III}Rh^{II,II}$-HKUST-1 with equal metal ratios was further investigated.

The invention of **thermal defect-engineering** provided a valuable tool for the postsynthetic defect creation in MOFs. In contrast to earlier methods, TDE allows for the controlled and quantified introduction of defects by thermal decarboxylation of BTC linkers and/or removal of aforementioned acetate ligands. In this regard, the yet undesired companion acetate can be removed preferentially from axial positions in the mixed-valence $Ru^{II,III}$ MOF, giving rise to defined $Ru^{II,II}$ and more reduced modified PWs featuring increasing porosity and more OMS ready for catalysis. Significant differences between Ru and Rh were found during the process of TDE. While Ru exhibits an enormous redox flexibility tolerating partial metal reduction during defect incorporation, Rh turns out to be less flexible with concomitant NP formation. Ru was found to be a very active catalyst for the **dimerization of ethene** which could be attributed to the successive formation of metal hydrides during TDE. In this regard, the additionally investigated univalent $Ru^{II,II}$ sample exhibited a fourfold activity compared to previous reports. Rh showed only low activity for the dimerization of ethene.

In contrast, Rh is the prime element for the **catalytic cyclopropanation reaction**. Already the pristine Rh-HKUST-1 shows high activity in this reaction but TDE having almost no impact on the performance. Inversely, the pristine mixed-valent $Ru^{II,III}$ has only moderate catalytic activity with side products being formed. Both effects originate from axial ligands occupying half of the OMS and affecting the product outcome. However, the partial decarboxylation induced by TDE can boost both activity and chemoselectivity giving rise to a catalyst performance equally high as in the Rh case.

Besides representing another test reaction, the **cyclopropanation** reaction and its specific characteristics such as activity, chemo- and diastereoselectivity **can be utilized as analytical tool** to probe the defect chemistry of compositionally complex MOFs. The ease of experiment and the number of obtained

structural insights render this reaction a useful analytical method. This first proof-of-concept demonstration might inspire future research in the field.

Finally, the targeted defect minimization was studied. The rational and systematic selection of several precursor ligands / carboxylic acid modulators applied under standardized MOF synthesis conditions provided important insights into the growth behavior of MOFs and its underlying ligand exchange. In summary, complexes of unsubstituted benzoate, 4-methylbenzoate, 4-fluorobenzoate, 4-methoxybenzoate, 4-(trifluoromethyl)benzoate, and hydroxy(phenyl)acetate (L-mandelate) were prepared and investigated. Within the set of materials, the established acetate-derived MOF resulted in the smallest particle sizes, lowest structural order, and high defectiveness. The "best" results were obtained with both unsubstituted benzoate giving rise to fourfold particle and domain sizes and the mandelate-derived material having almost the same particle size and additionally an unprecedentedly high porosity with a pore size distribution matching the perfect HKUST-1 structure.

The insights gained in this thesis contribute to a more detailed comprehension of PGMs in MOFs. These metals are relevant in industrial catalysis which is where such PGM-MOFs could potentially find their application one day. The diverse **solid-gas interactions** with industrially most relevant gasses such as H_2, CO, CO_2, C_2H_6, C_2H_4, N_2, Ar and O_2 mark a fundamental basis for further investigations towards applications.

Regarding the metal, one could forecast the exploration of HKUST-1 analogues of even heavier metals such as tungsten, rhenium, osmium, or iridium. All those metals are known to readily form PW structures in molecular chemistry. Following the trend of progressively diminished kinetic reactivity regarding the ligand exchange, their self-assembly towards structurally ordered frameworks might be an even greater challenge than the Ru- and Rh-analogues studied herein. However, the results presented in **Study V** on the right choice of PW precursor might be applicable to these even heavier elements as well.

Of course, other metal nodes are interesting candidates for PGM-MOFs as well. Particularly, the trimeric metal nodes known from the MIL-series are present in the molecular so-called "basic ruthenium acetate". Its analogous utilization as MOF precursor could provide access to Ru-MIL derivatives.

The enormous design freedom associated with the diverse possibilities of **defect-engineering** can continue to find exploitation in future. In this regard, the author recommends TDE over other DE strategies due to its reproducible, controllable outcome which could be scaled to higher quantities with adequate setups. Another interesting point could be the incorporation of tailored metallo-defect linkers into Ru-/Rh-HKUST-1 following the mixed-linker approach. Such concept could facilitate a precise spatial allocation of a second metal in close proximity to the PGM dimer being of potential use in synergistic (photo)catalysis.

Finally, the field of zero-dimensional nanoobjects was somewhat revived by the works of *Furukawa et al.*, creating discrete Rh-PW-based cuboctahedra using isophthalate linkers.[96, 100, 110] Such molecular cages may once find their application in drug delivery concepts achieving local concentration of functional therapeutics in cancer therapies.

6 Author Contributions

Study I

Most of the work was done by *Konstantin Epp* involving planning, experiments, and paper writing. *Ignacio Luz* contributed with catalytic experiments, *Olesia Kozachuk* and *Wenhua Zhang* provided valuable contributions to the synthesis and characterization of the materials as well as conceptionally. *Werner R. Heinz*, the author of this thesis, was involved during the revision process of the manuscript and reproduced the materials, organized missing characterizations, and revised the manuscript. *Anastasia Rapeyko* and *Francesc X. Llabrés i Xamena* were involve in the catalysis part including recycling studies. *Roland A. Fischer* contributed to the overall concept, supervised the research, and was involved in manuscript writing. The TOC image was created by *WRH*.

Study II

Werner R. Heinz was involved in all parts of the study. He developed the overall concept, performed all syntheses and characterizations (except XPS and HR-TEM measurements) and wrote the manuscript. *WRH* designed and programmed the solver for sum formula calculations on the basis of the elemental contents. *Tim Kratky* and *Sebastian Günther* performed XPS measurements and contributed to the respective chapter. *Markus Drees* performed DFT calculations of model compounds. *Andreas Wimmer* and *Michael Schuster* contributed with ICP-MS measurements including data evaluation. *Ondřej Tomanec* recorded HR-TEM images and maps. *Roland A. Fischer* supervised the whole study and contributed to the manuscript. The cover page and the toc image were designed by *WRH*.

Study III

Werner R. Heinz developed the concept of the study and the process of TDE, performed syntheses and basic characterizations, coordinated all co-author contributions and wrote the manuscript. *Iker Agirrezabal-Telleria* contributed with previous experiences, performed (VT)-FT-IR measurements with H_2, D_2 and CO gases, performed catalytic experiments (with the assist from *Miryam Gil-Calvo*) and wrote the respective chapters in the manuscript. *Raphael Junk* was involved with synthesis, and performed TGA-MS, FT-IR and SLIR-measurements. He supported with data evaluation and created respective graphs and contributed with the writing of the manuscript. *Jan Berger* performed gas sorption measurements, performed the data evaluation, and contributed to the manuscript, *Junjun Wang*, *Yuemin Wang* and *Christof Wöll* contributed with UHV-SLIR measurements and wrote the respective chapter. *Dmitry I. Sharapa*, *Felix Studt* and *Markus Drees* performed DFT calculations and wrote the respective chapter. *Ignacio Luz* performed VT-PXRD measurements and contributed to the concept of the study supported by *Mustapha Soukri*. *Hana Bunzen* recorded HR-TEM measurements requested by the reviewers. *Roland A. Fischer* contributed intensively to the final touch of the manuscript. The TOC image was designed by *WRH*.

Study IV

Werner R. Heinz was involved in all aspects of the work and wrote the manuscript and designed the TOC image. *Raphael Junk* was involved in material synthesis, characterization and catalysis. He contributed with data evaluation. *Iker Agirrezabal-Telleria* performed the CO-TGA measurements. *Bart Bueken* and *Dirk De Vos* supported some catalytic works and contributed to the concept of the study. *Hana Bunzen* performed HR-TEM measurements and the respective interpretation. *Thorsten Gölz* contributed experimentally to the catalysis including recyclability of the materials and investigated (hot) filtration effects. *Mirza Cokoja* contributed to the manuscript. *Roland A. Fischer* supervised all activities and contributed to the final touch of the manuscript. The TOC image was created by *WRH*.

Study V

Werner R. Heinz designed the concept of the study, performed all MOF-related experiments, and wrote the manuscript. *Dominik Staude* performed all precursor syntheses, their characterizations, and the NMR-based ligand exchange experiments. *David Mayer* measured and evaluated the single crystal structures. *Hana Bunzen* performed HR-TEM and elemental mapping measurements of the materials. *Roland A. Fischer* contributed to the overall concept of the study, the supervision of the project, and improved the manuscript. The TOC image was designed by *WRH*.

7 Bibliography

All references used in the studies I to V listed in the results chapter are cited in the individual publications at the end of each study. Literature references in all other chapters appear in the following.

1. Harari, Y. N., *Sapiens: A Brief History of Humankind*. Vintage Books: 2015.
2. Zhou, H.-C.; Long, J. R.; Yaghi, O. M., Introduction to Metal–Organic Frameworks. *Chem. Rev.* **2012,** *112* (2), 673-674.
3. Furukawa, H.; Cordova, K. E.; O'Keeffe, M.; Yaghi, O. M., The Chemistry and Applications of Metal-Organic Frameworks. *Science* **2013,** *341* (6149), 1230444.
4. Fang, Z.; Bueken, B.; De Vos, D. E.; Fischer, R. A., Defect-Engineered Metal–Organic Frameworks. *Angew. Chem. Int. Ed.* **2015,** *54* (25), 7234-7254.
5. Dissegna, S.; Epp, K.; Heinz, W. R.; Kieslich, G.; Fischer, R. A., Defective Metal-Organic Frameworks. *Adv. Mater.* **2018,** *30* (37), 1704501.
6. Griffin, S. L.; Champness, N. R., A periodic table of metal-organic frameworks. *Coord. Chem. Rev.* **2020,** *414*, 213295.
7. Nicewicz, D. A.; MacMillan, D. W. C., Merging Photoredox Catalysis with Organocatalysis: The Direct Asymmetric Alkylation of Aldehydes. *Science* **2008,** *322* (5898), 77-80.
8. Narayanam, J. M. R.; Stephenson, C. R. J., Visible light photoredox catalysis: applications in organic synthesis. *Chem. Soc. Rev.* **2011,** *40* (1), 102-113.
9. Romero, N. A.; Nicewicz, D. A., Organic Photoredox Catalysis. *Chem. Rev.* **2016,** *116* (17), 10075-10166.
10. Skubi, K. L.; Blum, T. R.; Yoon, T. P., Dual Catalysis Strategies in Photochemical Synthesis. *Chem. Rev.* **2016,** *116* (17), 10035-10074.
11. Pagliaro, M.; Campestrini, S.; Ciriminna, R., Ru-based oxidation catalysis. *Chem. Soc. Rev.* **2005,** *34* (10), 837-845.
12. Heller, D.; Vries, A.; de Vries, J., *The Handbook of Homogeneous Hydrogenation*. 2008; p 1483-1516.
13. Tang, W.; Zhang, X., New Chiral Phosphorus Ligands for Enantioselective Hydrogenation. *Chem. Rev.* **2003,** *103* (8), 3029-3070.
14. Noyori, R., Facts are the Enemy of Truth—Reflections on Serendipitous Discovery and Unforeseen Developments in Asymmetric Catalysis. *Angew. Chem. Int. Ed.* **2013,** *52* (1), 79-92.
15. Jahangiri, H.; Bennett, J.; Mahjoubi, P.; Wilson, K.; Gu, S., A review of advanced catalyst development for Fischer–Tropsch synthesis of hydrocarbons from biomass derived syn-gas. *Catal. Sci. Technol.* **2014,** *4* (8), 2210-2229.
16. Herrmann, W. A., Organometallic Aspects of the Fischer-Tropsch Synthesis. *Angew. Chem. Int. Ed.* **1982,** *21* (2), 117-130.
17. Balcar, H.; Roth, W. J., Chapter 1 - Hybrid Catalysts for Olefin Metathesis and Related Polymerizations. In *New and Future Developments in Catalysis*, Suib, S. L., Ed. Elsevier: Amsterdam, 2013; pp 1-26.
18. Grubbs, R. H.; Khosravi, E., *Handbook of Metathesis, Volume 3: Polymer Synthesis*. Wiley: 2015.
19. Ainooson, M.; Meyer, F., 8.10 - Bimetallic Approaches in Olefin Polymerization and Metathesis. In *Comprehensive Inorganic Chemistry II (Second Edition)*, Reedijk, J.; Poeppelmeier, K., Eds. Elsevier: Amsterdam, 2013; pp 433-458.
20. Weskamp, T.; Kohl, F. J.; Hieringer, W.; Gleich, D.; Herrmann, W. A., Highly Active Ruthenium Catalysts for Olefin Metathesis: The Synergy of N-Heterocyclic Carbenes and Coordinatively Labile Ligands. *Angew. Chem. Int. Ed.* **1999,** *38* (16), 2416-2419.
21. Herrmann, W. A.; Schattenmann, W. C.; Nuyken, O.; Glander, S. C., Allylruthenium(IV) Complexes as Highly Efficient ROMP Catalysts. *Angew. Chem. Int. Ed.* **1996,** *35* (10), 1087-1088.

22. Noels, A. F.; Demonceau, A., From olefin cyclopropanation to olefin metathesis through catalyst engineering: recent applications of olefin metathesis to fine organic synthesis and to polymer chemistry. *J. Phys. Org. Chem.* **1998,** *11* (8-9), 602-609.
23. Weskamp, T.; Schattenmann, W. C.; Spiegler, M.; Herrmann, W. A., A Novel Class of Ruthenium Catalysts for Olefin Metathesis. *Angew. Chem. Int. Ed.* **1998,** *37* (18), 2490-2493.
24. Barral, M. C.; González-Prieto, R.; Jiménez-Aparicio, R.; Priego, J. L.; Torres, M. R.; Urbanos, Francisco A., Polymeric, Molecular, and Cation/Anion Arrangements in Chloro-, Bromo-, and Iododiruthenium(II,III) Carboxylate Compounds. *Eur. J. Inorg. Chem.* **2003,** *2003* (12), 2339-2347.
25. Aquino, M. A. S., Diruthenium and diosmium tetracarboxylates: synthesis, physical properties and applications. *Coord. Chem. Rev.* **1998,** *170* (1), 141-202.
26. Cotton, F. A.; Walton, R. A., *Multiple bonds between metal atoms*. Wiley: 1982.
27. Koberl, M.; Cokoja, M.; Herrmann, W. A.; Kuhn, F. E., From molecules to materials: Molecular paddle-wheel synthons of macromolecules, cage compounds and metal-organic frameworks. *Dalton Trans.* **2011,** *40* (26), 6834-6859.
28. Chui, S. S.-Y.; Lo, S. M.-F.; Charmant, J. P. H.; Orpen, A. G.; Williams, I. D., A Chemically Functionalizable Nanoporous Material [Cu3(TMA)2(H2O)3]n. *Science* **1999,** *283* (5405), 1148-1150.
29. Bhunia, M. K.; Hughes, J. T.; Fettinger, J. C.; Navrotsky, A., Thermochemistry of Paddle Wheel MOFs: Cu-HKUST-1 and Zn-HKUST-1. *Langmuir* **2013,** *29* (25), 8140-8145.
30. Duncan Lyngdoh, R. H.; Schaefer, H. F.; King, R. B., Metal–Metal (MM) Bond Distances and Bond Orders in Binuclear Metal Complexes of the First Row Transition Metals Titanium Through Zinc. *Chem. Rev.* **2018,** *118* (24), 11626-11706.
31. Santos, R. L. S. R.; van Eldik, R.; de Oliveira Silva, D., Thermodynamics of Axial Substitution and Kinetics of Reactions with Amino Acids for the Paddlewheel Complex Tetrakis(acetato)chloridodiruthenium(II,III). *Inorg. Chem.* **2012,** *51* (12), 6615-6625.
32. Drago, R. S.; Cosmano, R.; Telser, J., Quantitative studies on the coordination chemistry of tetrakis(n-butyrato)diruthenium chloride. *Inorg. Chem.* **1984,** *23* (26), 4514-4518.
33. Mitchell, R. W.; Spencer, A.; Wilkinson, G., Carboxylato-triphenylphosphine complexes of ruthenium, cationic triphenylphosphine complexes derived from them, and their behaviour as homogeneous hydrogenation catalysts for alkenes. *J. Chem. Soc., Dalton Trans.* **1973,** (8), 846-854.
34. Burchell, T. J.; Cameron, T. S.; Macartney, D. H.; Thompson, L. K.; Aquino, M. A. S., Kinetics and Magnetism of Phosphane Diadducts of Diruthenium(II,III) Tetraacetate. *Eur. J. Inorg. Chem.* **2007,** *2007* (25), 4021-4027.
35. Briand, G. G.; Cooke, M. W.; Cameron, T. S.; Farrell, H. M.; Burchell, T. J.; Aquino, M. A. S., An Axial Phosphine Diadduct of Diruthenium(II,III) Tetraacetate. *Inorg. Chem.* **2001,** *40* (14), 3267-3268.
36. Lindsay, A. J.; Wilkinson, G.; Motevalli, M.; Hursthouse, M. B., Reactions of tetra-μ-carboxylato-diruthenium(II,II) compounds. X-Ray crystal structures of Ru2(μ-O2CCF3)4(thf)2, Ru2(μ-O2CR)4(NO)2(R = Et or CF3), and {Na3[Ru2(μ-O2CO)4]·6H2O}. *J. Chem. Soc., Dalton Trans.* **1987,** (11), 2723-2736.
37. Vadavi, R.; Conrad, E. D.; Arbuckle, D. I.; Cameron, T. S.; Essoun, E.; Aquino, M. A. S., Chiral Induction via the Disassembly of Diruthenium(II,III) Tetraacetate by Chiral Diphosphines. *Inorg. Chem.* **2011,** *50* (23), 11862-11864.
38. Wyman, I. W.; Burchell, T. J.; Robertson, K. N.; Cameron, T. S.; Aquino, M. A. S., Structure and Electrochemistry of Heterobimetallic Ferrocenecarboxylatoruthenium(II) Complexes. *Organometallics* **2004,** *23* (22), 5353-5364.
39. Essoun, E.; Wang, R.; Aquino, M. A. S., Disassembly of diruthenium(II,III) tetraacetate with P–N donor ligands. *Inorg. Chim. Acta* **2017,** *454*, 97-106.
40. Ribeiro, G.; Benadiba, M.; Colquhoun, A.; de Oliveira Silva, D., Diruthenium(II,III) complexes of ibuprofen, aspirin, naproxen and indomethacin non-steroidal anti-inflammatory drugs: Synthesis, characterization and their effects on tumor-cell proliferation. *Polyhedron* **2008,** *27* (3), 1131-1137.
41. Bland, B. R. A.; Gilfoy, H. J.; Vamvounis, G.; Robertson, K. N.; Cameron, T. S.; Aquino, M. A. S., Hydrogen bonding in diruthenium(II,III) tetraacetate complexes with biologically relevant axial ligands. *Inorg. Chim. Acta* **2005,** *358* (13), 3927-3936.

42. Richens, D. T., Ligand Substitution Reactions at Inorganic Centers. *Chem. Rev.* **2005,** *105* (6), 1961-2002.
43. Boyar, E. B.; Robinson, S. D., Rhodium(II) carboxylates. *Coord. Chem. Rev.* **1983,** *50* (1), 109-208.
44. Kumar, D. K.; Filatov, A. S.; Napier, M.; Sun, J.; Dikarev, E. V.; Petrukhina, M. A., Dirhodium Paddlewheel with Functionalized Carboxylate Bridges: New Building Block for Self-Assembly and Immobilization on Solid Support. *Inorg. Chem.* **2012,** *51* (8), 4855-4861.
45. Chavan, M. Y.; Feldmann, F. N.; Lin, X. Q.; Bear, J. L.; Kadish, K. M., Generation of dinuclear ruthenium acetamidate complexes with variable ruthenium-ruthenium bond orders. *Inorg. Chem.* **1984,** *23* (16), 2373-2375.
46. Lindsay, A. J.; Wilkinson, G.; Motevalli, M.; Hursthouse, M. B., The synthesis, magnetic, electrochemical, and spectroscopic properties of diruthenium(II,II) tetra-[small micro]-carboxylates and their adducts. X-Ray structures of Ru2(O2CR)4L2(R = Me, L = H2O or tetrahydrofuran; R = Et, L = Me2CO). *J. Chem. Soc., Dalton Trans.* **1985,** (11), 2321-2326.
47. Spohn, M.; Strähle, J.; Hiller, W., Benzoatokomplexe des Rutheniums, 1. Mitt. Synthese, Eigenschaften und Kristallstruktur von Ru2(C6H5COO)4(C6H5COOH)2 und Ru2(C6H5COO)5 C6H5COOH. *Zeitschrift für Naturforschung* **1986,** *41b*, 541-547.
48. Cotton, F. A.; Miskowski, V. M.; Zhong, B., Chemistry, structure and bonding in diruthenium(II) tetracarboxylates. *J. Am. Chem. Soc.* **1989,** *111* (16), 6177-6182.
49. Maldivi, P.; Giroud-Godquin, A.-M.; Marchon, J.-C.; Guillon, D.; Skoulios, A., Diruthenium(II,II) tetra-μ-alkylcarboxylates: Magnetic susceptibility studies of their electronic configuration and thermotropic liquid crystalline mesophase. *Chem. Phys. Lett.* **1989,** *157* (6), 552-555.
50. Cooke, M. W.; Cameron, T. S.; Robertson, K. N.; Swarts, J. C.; Aquino, M. A. S., Structure and Electrochemistry of Various Diruthenium(II,III) Tetrametallocenecarboxylates. *Organometallics* **2002,** *21* (26), 5962-5971.
51. Barral, M. C.; de la Fuente, I.; Jiménez-Aparicio, R.; Priego, J. L.; Torres, M. R.; Urbanos, F. A., Synthesis of diruthenium(II,III) amidate compounds. Crystal structure of [Ru2(μ-HNOCC4H3S)4(thf)2]SbF6·0.5cyclohexane. *Polyhedron* **2001,** *20* (19), 2537-2544.
52. Cotton, F. A.; Murillo, C. A.; Walton, R. A., *Multiple Bonds between Metal Atoms*. Springer New York: 2005.
53. Doyle, M. P., Perspective on Dirhodium Carboxamidates as Catalysts. *J. Org. Chem.* **2006,** *71* (25), 9253-9260.
54. Sekine, Y.; Kosaka, W.; Kano, H.; Dou, C.; Yokoyama, T.; Miyasaka, H., trans-Heteroleptic carboxylate-bridged paddlewheel diruthenium(ii, ii) complexes with 2,6-bis(trifluoromethyl)benzoate ligands. *Dalton Trans.* **2016,** *45* (17), 7427-7434.
55. Barral, M. C.; Gallo, T.; Herrero, S.; Jiménez-Aparicio, R.; Torres, M. R.; Urbanos, F. A., Equatorially Connected Diruthenium(II,III) Units toward Paramagnetic Supramolecular Structures with Singular Magnetic Properties. *Inorg. Chem.* **2006,** *45* (9), 3639-3647.
56. Barral, M. C.; Herrero, S.; Jiménez-Aparicio, R.; Torres, M. R.; Urbanos, F. A., Preparation, characterization, and crystal structure of [Ru2Cl(μ-O2CMe)(μ-PhNCHNPh)3]: a way to tris(formamidinato)diruthenium(II,III) complexes. *Inorg. Chem. Commun.* **2004,** *7* (1), 42-46.
57. Angaridis, P.; Berry, J. F.; Cotton, F. A.; Lei, P.; Lin, C.; Murillo, C. A.; Villagrán, D., Dicarboxylato-bridged diruthenium units in two different oxidation states: the first step towards the synthesis of Creutz–Taube analogs with dinuclear Ru2n+ species. *Inorg. Chem. Commun.* **2004,** *7* (1), 9-13.
58. Lindsay, A. J.; Tooze, R. P.; Motevalli, M.; Hursthouse, M. B.; Wilkinson, G., The synthesis and structure of tetra-μ-acetatodiruthenium(II,II)–bis(tetrahydrofuran). *J. Chem. Soc., Chem. Commun.* **1984,** (20), 1383b-1384.
59. Cotton, F. A.; Datta, T.; Labella, L.; Shang, M., Stabilizing of the Ru26+ core. Use of highly charged ligands such as sulfate and phosphate. *Inorg. Chim. Acta* **1993,** *203* (1), 55-60.
60. Itoh, M.; Asai, Y.; Kamo, H.; Miura, A.; Miyasaka, H., A Dimer-of-dimers Composed of Paddlewheel Diruthenium(II, III) Complexes and a Bridge of Tetrachlorohydroquinonate(2−) Derived by Intramolecular Charge Transfers. *Chem. Lett.* **2012,** *41* (1), 26-28.

61. Barral, M. C.; González-Prieto, R.; Jiménez-Aparicio, R.; Priego, J. L.; Torres, M. R.; Urbanos, F. A., Reduction of diruthenium(II,III) carboxylate compounds with hydroquinone: a facile preparation of diruthenium(II) complexes. *Inorg. Chim. Acta* **2005,** *358* (1), 217-221.
62. Yoshioka, D.; Handa, M.; Azuma, H.; Mikuriya, M.; Hiromitsu, I.; Kasuga, K., Synthesis and Magnetic Property of Adducts of Ruthenium(II,III) Pivalate with 9,10-Anthraquinone. *Molecular Crystals and Liquid Crystals Science and Technology. Section A. Molecular Crystals and Liquid Crystals* **2000,** *342* (1), 133-138.
63. Thompson, D. J.; Barker Paredes, J. E.; Villalobos, L.; Ciclosi, M.; Elsby, R. J.; Liu, B.; Fanwick, P. E.; Ren, T., Diruthenium(II,III) tetracarboxylates catalyzed H2O2 oxygenation of organic sulfides. *Inorg. Chim. Acta* **2015,** *424*, 150-155.
64. Villalobos, L.; Barker Paredes, J. E.; Cao, Z.; Ren, T., tert-Butyl Hydroperoxide Oxygenation of Organic Sulfides Catalyzed by Diruthenium(II,III) Tetracarboxylates. *Inorg. Chem.* **2013,** *52* (21), 12545-12552.
65. Villalobos, L.; Cao, Z.; Fanwick, P. E.; Ren, T., Diruthenium(II,III) tetramidates as a new class of oxygenation catalysts. *Dalton Trans.* **2012,** *41* (2), 644-650.
66. Martin, D. S.; Newman, R. A.; Vlasnik, L. M., Crystal structure and polarized electronic spectra for diruthenium tetraacetate chloride. *Inorg. Chem.* **1980,** *19* (11), 3404-3407.
67. Epp, K.; Luz, I.; Heinz, W. R.; Rapeyko, A.; Llabres i Xamena, F. X.; Fischer, R. A., Defect Engineered Ruthenium MOFs as Versatile Hydrogenation Catalysts. *ChemCatChem* **2020,** *12* (6), 1720-1725.
68. Corcos, A. R.; Long, A. K. M.; Guzei, I. A.; Berry, J. F., A Synthetic Cycle for Nitrogen Atom Transfer Featuring a Diruthenium Nitride Intermediate. *Eur. J. Inorg. Chem.* **2013,** *2013* (22-23), 3808-3811.
69. Harvey, M. E.; Musaev, D. G.; Du Bois, J., A Diruthenium Catalyst for Selective, Intramolecular Allylic C–H Amination: Reaction Development and Mechanistic Insight Gained through Experiment and Theory. *J. Am. Chem. Soc.* **2011,** *133* (43), 17207-17216.
70. Rusjan, M.; Sileo, E. E.; Cukiernik, F. D., Thermal Stability of Mixed-Valent Diruthenium (II,III) Carboxylates. *Solid State Ion.* **2003,** *159* (3), 389-396.
71. Wang, Y.; Kuang, Y.; Wang, Y., Rh2(esp)2-catalyzed allylic and benzylic oxidations. *Chem. Commun.* **2015,** *51* (27), 5852-5855.
72. Savchenko, J.; Fanwick, P. E.; Hope, H.; Gao, Y.; Yerneni, C. K.; Ren, T., New diruthenium (II,III) compounds bearing terminal olefin groups. *Inorg. Chim. Acta* **2013,** *396*, 144-148.
73. Cummings, S. P.; Cao, Z.; Liskey, C. W.; Geanes, A. R.; Fanwick, P. E.; Hassell, K. M.; Ren, T., Diruthenium Phenylacetylide Complexes Bearing para-/meta-Amino Phenyl Substituents. *Organometallics* **2010,** *29* (12), 2783-2788.
74. Chakravarty, A. R.; Cotton, F. A., A new diruthenium(II,III) compound, Ru2(C・CPh)(PhNpy)4·2CH2Cl2, with an axial η1-acetylide ligand. *Inorg. Chim. Acta* **1986,** *113* (1), 19-26.
75. Cukiernik, F. D.; Ibn-Elhaj, M.; Chaia, Z. D.; Marchon, J.-C.; Giroud-Godquin, A.-M.; Guillon, D.; Skoulios, A.; Maldivi, P., Mixed-Valent Diruthenium (II,III) Long-Chain Carboxylates. 1. Molecular Design of Columnar Liquid-Crystalline Order. *Chem. Mater.* **1998,** *10* (1), 83-91.
76. Rose, D.; Wilkinson, G., The blue solutions of ruthenium(II) chloride: a cluster anion. *Journal of the Chemical Society A: Inorganic, Physical, Theoretical* **1970,** (0), 1791-1795.
77. Fourcroy, A. F. d.; Vauquelin, N. L., *Ann. Chim. (France)* **1804,** *48* (188), 5.
78. Jeannin, Y., Some new documents illuminating the controversy about the vestium-ruthenium discovery. *Comptes Rendus Chimie* **2012,** *15* (7), 580-584.
79. Rusjan, M. C.; Sileo, E. E.; Cukiernik, F. D., Thermal Decomposition of Mixed-Valent Diruthenium Pentakis(alkanoates) Enhanced by Their Liquid Crystalline State. *Solid State Ion.* **1999,** *124* (1), 143-147.
80. Barral, M. C.; Jiménez-Aparicio, R.; Royer, E. C.; Saucedo, M. J.; Urbanos, F. A.; Gutiérrez-Puebla, E.; Ruíz-valero, C., Reaction of tetraacetatochlorodiruthenium(II,III) with pyridine-2-carboxylic acid. X-Ray crystal structures of tris(pyridine-2-carboxylato-κN,O)ruthenium(III) monohydrate and trans-bis(pyridine-2-carboxylato-κN,O)bis(triphenylphosphine)ruthenium(II)–methanol(1/2). *J. Chem. Soc., Dalton Trans.* **1991,** (6), 1609-1613.
81. Barral, M. C.; Jiménez-Aparicio, R.; Priego, J. L.; Royer, E. C.; Urbanos, F. A.; Amador, U., Synthesis of tetracarboxylatediruthenium(II) compounds: reduction and disproportionation reactions of

diruthenium(II,III) units. Crystal structure of Ru2(μ-O2CCOPh)4(thf)2. *Inorg. Chim. Acta* **1998,** *279* (1), 30-36.
82. Barral, M. C.; Jimenez-Aparicio, R.; Priego, J. L.; Royer, E. C.; Saucedo, M. J.; Urbanos, F. A.; Amador, U., Influence of carboxylic acids on the reactions with chlorotetraacetatodiruthenium(II,III): X-ray crystal structure of [Ru2(μ-O2CC4H3S)4(OPPh3)2]BF4·2H2O. *Polyhedron* **1995,** *14* (17), 2419-2427.
83. Dikarev, E. V.; Li, B., Hitting Two Birds with One Stone: Crystal Containing Both Disproportionation Products of the Mixed-Valence Ruthenium(II, III) Carboxylate. *J. Cluster Sci.* **2004,** *15* (4), 437-449.
84. Werner, A., Beitrag zur Konstitution anorganischer Verbindungen. *Zeitschrift für anorganische Chemie* **1893,** *3* (1), 267-330.
85. Leininger, S.; Olenyuk, B.; Stang, P. J., Self-Assembly of Discrete Cyclic Nanostructures Mediated by Transition Metals. *Chem. Rev.* **2000,** *100* (3), 853-908.
86. Modrow, S., *Molekulare Virologie*. 2003.
87. Horne, R. W., *Virus Structure*. Academic Press: 1974.
88. Whitesides, G. M.; Mathias, J. P.; Seto, C. T., Molecular self-assembly and nanochemistry: a chemical strategy for the synthesis of nanostructures. *Science* **1991,** *254* (5036), 1312-9.
89. Kitagawa, S.; Kitaura, R.; Noro, S.-i., Functional Porous Coordination Polymers. *Angew. Chem. Int. Ed.* **2004,** *43* (18), 2334-2375.
90. Chen, X.-M., Chapter 10 - Assembly Chemistry of Coordination Polymers. In *Modern Inorganic Synthetic Chemistry*, Xu, R.; Pang, W.; Huo, Q., Eds. Elsevier: Amsterdam, 2011; pp 207-225.
91. Batten, S. R.; Champness, N. R., Coordination Polymers and Metal-Organic Frameworks: Materials by Design. *Philosophical Transactions of the Royal Society A: Mathematical, Physical and Engineering Sciences* **2017,** *375* (2084), 20160032.
92. Loukopoulos, E.; Kostakis, G. E., Review: Recent advances of one-dimensional coordination polymers as catalysts. *J. Coord. Chem.* **2018,** *71* (3), 371-410.
93. Yaghi, O. M.; Li, H.; Davis, C.; Richardson, D.; Groy, T. L., Synthetic Strategies, Structure Patterns, and Emerging Properties in the Chemistry of Modular Porous Solids. *Acc. Chem. Res.* **1998,** *31* (8), 474-484.
94. Eddaoudi, M.; Moler, D. B.; Li, H.; Chen, B.; Reineke, T. M.; O'Keeffe, M.; Yaghi, O. M., Modular Chemistry: Secondary Building Units as a Basis for the Design of Highly Porous and Robust Metal−Organic Carboxylate Frameworks. *Acc. Chem. Res.* **2001,** *34* (4), 319-330.
95. Yaghi, O. M.; O'Keeffe, M.; Ockwig, N. W.; Chae, H. K.; Eddaoudi, M.; Kim, J., Reticular Synthesis and the Design of New Materials. *Nature* **2003,** *423* (6941), 705-714.
96. Furukawa, S.; Horike, N.; Kondo, M.; Hijikata, Y.; Carné-Sánchez, A.; Larpent, P.; Louvain, N.; Diring, S.; Sato, H.; Matsuda, R.; Kawano, R.; Kitagawa, S., Rhodium–Organic Cuboctahedra as Porous Solids with Strong Binding Sites. *Inorg. Chem.* **2016,** *55* (21), 10843-10846.
97. Hoskins, B. F.; Robson, R., Infinite polymeric frameworks consisting of three dimensionally linked rod-like segments. *J. Am. Chem. Soc.* **1989,** *111* (15), 5962-5964.
98. Hoskins, B. F.; Robson, R., Design and construction of a new class of scaffolding-like materials comprising infinite polymeric frameworks of 3D-linked molecular rods. A reappraisal of the zinc cyanide and cadmium cyanide structures and the synthesis and structure of the diamond-related frameworks [N(CH3)4][CuIZnII(CN)4] and CuI[4,4',4'',4'''-tetracyanotetraphenylmethane]BF4.xC6H5NO2. *J. Am. Chem. Soc.* **1990,** *112* (4), 1546-1554.
99. Foster, J. A.; Henke, S.; Schneemann, A.; Fischer, R. A.; Cheetham, A. K., Liquid exfoliation of alkyl-ether functionalised layered metal–organic frameworks to nanosheets. *Chem. Commun.* **2016,** *52* (69), 10474-10477.
100. Carné-Sánchez, A.; Craig, G. A.; Larpent, P.; Hirose, T.; Higuchi, M.; Kitagawa, S.; Matsuda, K.; Urayama, K.; Furukawa, S., Self-assembly of metal–organic polyhedra into supramolecular polymers with intrinsic microporosity. *Nat. Commun.* **2018,** *9* (1), 2506.
101. Kosaka, W.; Yamagishi, K.; Hori, A.; Sato, H.; Matsuda, R.; Kitagawa, S.; Takata, M.; Miyasaka, H., Selective NO trapping in the pores of chain-type complex assemblies based on electronically activated paddlewheel-type [Ru2(II,II)]/[Rh2(II,II)] dimers. *J. Am. Chem. Soc.* **2013,** *135* (49), 18469-80.

102. Kosaka, W.; Yamagishi, K.; Zhang, J.; Miyasaka, H., Gate-Opening Gas Adsorption and Host-Guest Interacting Gas Trapping Behavior of Porous Coordination Polymers under Applied AC Electric Fields. *J. Am. Chem. Soc.* **2014,** *136* (35), 12304-12313.
103. Furukawa, S.; Ohba, M.; Kitagawa, S., Rational synthesis of a two-dimensional honeycomb structure based on a paramagnetic paddlewheel diruthenium complex. *Chem. Commun.* **2005,** (7), 865-867.
104. Liu, B.; Li, Y.-Z.; Zheng, L.-M., Na3Ru2(hedp)2·4H2O: A mixed valent diruthenium diphosphonate with three-dimensional structure. *Solid State Sciences* **2006,** *8* (9), 1041-1045.
105. Yi; Zheng, L.-M.; Xu, W.; Feng, S., Novel Layered Ruthenium Diphosphonate Containing a Mixed Valent Diruthenium Paddlewheel Core. *Inorg. Chem.* **2003,** *42* (9), 2827-2829.
106. Liu, B.; Li, B.-L.; Li, Y.-Z.; Chen, Y.; Bao, S.-S.; Zheng, L.-M., Lanthanide Diruthenium(II,III) Compounds Showing Layered and PtS-Type Open Framework Structures. *Inorg. Chem.* **2007,** *46* (21), 8524-8532.
107. Hashikawa, A.; Sawada, Y.; Yamamoto, Y.; Nishio, M.; Kosaka, W.; Hayashi, Y.; Miyasaka, H., Polyoxometalate-based frameworks with a linker of paddlewheel diruthenium(ii, iii) complexes. *CrystEngComm* **2013,** *15* (24), 4852-4859.
108. Sato, T.; Mori, W.; Kato, C. N.; Yanaoka, E.; Kuribayashi, T.; Ohtera, R.; Shiraishi, Y., Novel microporous rhodium(II) carboxylate polymer complexes containing metalloporphyrin: syntheses and catalytic performances in hydrogenation of olefins. *J. Catal.* **2005,** *232* (1), 186-198.
109. Liu, J.; Fasel, C.; Braga-Groszewicz, P.; Rothermel, N.; Lilly Thankamony, A. S.; Sauer, G.; Xu, Y.; Gutmann, T.; Buntkowsky, G., Heterogeneous self-supported dirhodium(ii) catalysts with high catalytic efficiency in cyclopropanation - a structural study. *Catal. Sci. Technol.* **2016,** *6* (21), 7830-7840.
110. Liu, G.; Wang, Y.; Zhu, B.; Zhang, L.; Su, C.-Y., A porous metal–organic aerogel based on dirhodium paddle-wheels as an efficient and stable heterogeneous catalyst towards the reduction reaction of aldehydes and ketones. *New J. Chem.* **2018,** *42* (14), 11358-11363.
111. Zhu, B.; Liu, G.; Chen, L.; Qiu, L.; Chen, L.; Zhang, J.; Zhang, L.; Barboiu, M.; Si, R.; Su, C.-Y., Metal–organic aerogels based on dinuclear rhodium paddle-wheel units: design, synthesis and catalysis. *Inorganic Chemistry Frontiers* **2016,** *3* (5), 702-710.
112. Nickerl, G.; Stoeck, U.; Burkhardt, U.; Senkovska, I.; Kaskel, S., A Catalytically Active Porous Coordination Polymer Based on a Dinuclear Rhodium Paddle-Wheel Unit. *J. Mater. Chem. A* **2014,** *2*, 144-148.
113. Blake, A. J.; Champness, N. R.; Hubberstey, P.; Li, W.-S.; Withersby, M. A.; Schröder, M., Inorganic crystal engineering using self-assembly of tailored building-blocks. *Coord. Chem. Rev.* **1999,** *183* (1), 117-138.
114. Horike, S.; Shimomura, S.; Kitagawa, S., Soft porous crystals. *Nat. Chem.* **2009,** *1* (9), 695-704.
115. Alhamami, M.; Doan, H.; Cheng, C.-H., A Review on Breathing Behaviors of Metal-Organic-Frameworks (MOFs) for Gas Adsorption. *Materials* **2014,** *7* (4), 3198-3250.
116. Schneemann, A.; Bon, V.; Schwedler, I.; Senkovska, I.; Kaskel, S.; Fischer, R. A., Flexible metal–organic frameworks. *Chem. Soc. Rev.* **2014,** *43* (16), 6062-6096.
117. Li, W.-J.; Liu, J.; Sun, Z.-H.; Liu, T.-F.; Lü, J.; Gao, S.-Y.; He, C.; Cao, R.; Luo, J.-H., Integration of metal-organic frameworks into an electrochemical dielectric thin film for electronic applications. *Nat. Commun.* **2016,** *7* (1), 11830.
118. Policicchio, A.; Florent, M.; Attia, M. F.; Whitehead, D. C.; Jagiello, J.; Bandosz, T. J., Effect of the Incorporation of Functionalized Cellulose Nanocrystals into UiO-66 on Composite Porosity and Surface Heterogeneity Alterations. *Advanced Materials Interfaces n/a* (n/a), 1902098.
119. Horcajada, P.; Serre, C.; Vallet-Regí, M.; Sebban, M.; Taulelle, F.; Férey, G., Metal–Organic Frameworks as Efficient Materials for Drug Delivery. *Angew. Chem. Int. Ed.* **2006,** *45* (36), 5974-5978.
120. Farrusseng, D.; Aguado, S.; Pinel, C., Metal–Organic Frameworks: Opportunities for Catalysis. *Angew. Chem. Int. Ed.* **2009,** *48* (41), 7502-7513.
121. Rösler, C.; Fischer, R. A., Metal–organic frameworks as hosts for nanoparticles. *CrystEngComm* **2015,** *17* (2), 199-217.

122. Drout, R. J.; Robison, L.; Farha, O. K., Catalytic applications of enzymes encapsulated in metal–organic frameworks. *Coord. Chem. Rev.* **2019,** *381*, 151-160.
123. Hu, C.; Bai, Y.; Hou, M.; Wang, Y.; Wang, L.; Cao, X.; Chan, C.-W.; Sun, H.; Li, W.; Ge, J.; Ren, K., Defect-induced activity enhancement of enzyme-encapsulated metal-organic frameworks revealed in microfluidic gradient mixing synthesis. *Science Advances* **2020,** *6* (5), eaax5785.
124. Chen, P., *Lanthanide Metal-Organic Frameworks*. 1 ed.; Springer-Verlag Berlin Heidelberg: Heidelberg, 2015; p IX, 371.
125. Wang, L.; Chu, Z.; Huang, W.; Gou, S., An enantiomeric pair of sodium(I) organic/inorganic frameworks having novel two-dimensional inorganic comb-like separating layers. *Inorg. Chem. Commun.* **2009,** *12* (1), 4-7.
126. Pichon, A., Making a meal of MOFs. *Nat. Chem.* **2010**.
127. Smaldone, R. A.; Forgan, R. S.; Furukawa, H.; Gassensmith, J. J.; Slawin, A. M. Z.; Yaghi, O. M.; Stoddart, J. F., Metal–Organic Frameworks from Edible Natural Products. *Angew. Chem. Int. Ed.* **2010,** *49* (46), 8630-8634.
128. Senthil Raja, D.; Luo, J.-H.; Wu, C.-Y.; Cheng, Y.-J.; Yeh, C.-T.; Chen, Y.-T.; Lo, S.-H.; Lai, Y.-L.; Lin, C.-H., Solvothermal Synthesis, Structural Diversity, and Properties of Alkali Metal–Organic Frameworks Based on V-shaped Ligand. *Cryst. Growth Des.* **2013,** *13* (8), 3785-3793.
129. Zhang, T.-Z.; Zhang, Z.-M.; Lu, Y.; Fu, H.; Wang, E.-B., Expansion of sodalite-type metal–organic frameworks with heterometallic metal–oxo cluster and its cation exchange property. *CrystEngComm* **2013,** *15* (3), 459-462.
130. Siman, P.; Trickett, C. A.; Furukawa, H.; Yaghi, O. M., l-Aspartate links for stable sodium metal–organic frameworks. *Chem. Commun.* **2015,** *51* (98), 17463-17466.
131. Cepeda, J.; Pérez-Yáñez, S.; Beobide, G.; Castillo, O.; Goikolea, E.; Aguesse, F.; Garrido, L.; Luque, A.; Wright, P. A., Scandium/Alkaline Metal–Organic Frameworks: Adsorptive Properties and Ionic Conductivity. *Chem. Mater.* **2016,** *28* (8), 2519-2528.
132. Seco, J. M.; San Sebastián, E.; Cepeda, J.; Biel, B.; Salinas-Castillo, A.; Fernández, B.; Morales, D. P.; Bobinger, M.; Gómez-Ruiz, S.; Loghin, F. C.; Rivadeneyra, A.; Rodríguez-Diéguez, A., A Potassium Metal-Organic Framework based on Perylene-3,4,9,10-tetracarboxylate as Sensing Layer for Humidity Actuators. *Scientific Reports* **2018,** *8* (1), 14414.
133. Zou, G.; Hou, H.; Ge, P.; Huang, Z.; Zhao, G.; Yin, D.; Ji, X., Metal–Organic Framework-Derived Materials for Sodium Energy Storage. *Small* **2018,** *14* (3), 1702648.
134. Kojima, D.; Sanada, T.; Wada, N.; Kojima, K., Synthesis, structure, and fluorescence properties of a calcium-based metal–organic framework. *RSC Adv.* **2018,** *8* (55), 31588-31593.
135. Li, L.; Guo, L.; Pu, S.; Wang, J.; Yang, Q.; Zhang, Z.; Yang, Y.; Ren, Q.; Alnemrat, S.; Bao, Z., A calcium-based microporous metal-organic framework for efficient adsorption separation of light hydrocarbons. *Chem. Eng. J.* **2019,** *358*, 446-455.
136. Li, L.; Guo, L.; Zheng, F.; Zhang, Z.; Yang, Q.; Yang, Y.; Ren, Q.; Bao, Z., Calcium-Based Metal–Organic Framework for Simultaneous Capture of Trace Propyne and Propadiene from Propylene. *ACS Appl. Mater. Interfaces* **2020,** *12* (14), 17147-17154.
137. Eddaoudi, M.; Kim, J.; Rosi, N.; Vodak, D.; Wachter, J.; O'Keeffe, M.; Yaghi, O. M., Systematic Design of Pore Size and Functionality in Isoreticular MOFs and Their Application in Methane Storage. *Science* **2002,** *295* (5554), 469-472.
138. Valvekens, P.; Vermoortele, F.; De Vos, D., Metal-Organic Frameworks as Catalysts: The Role of Metal Active Sites. *Catal. Sci. Technol.* **2013,** *3* (6), 1435-1445.
139. Doonan, C. J.; Sumby, C. J., Metal–organic framework catalysis. *CrystEngComm* **2017,** *19* (29), 4044-4048.
140. Dhakshinamoorthy, A.; Li, Z.; Garcia, H., Catalysis and Photocatalysis by Metal-Organic Frameworks. *Chem. Soc. Rev.* **2018,** *47* (22), 8134-8172.
141. Jiao, L.; Wang, Y.; Jiang, H.-L.; Xu, Q., Metal–Organic Frameworks as Platforms for Catalytic Applications. *Adv. Mater.* **2018,** *30* (37), 1703663.
142. Chapman, K. W.; Halder, G. J.; Chupas, P. J., Guest-Dependent High Pressure Phenomena in a Nanoporous Metal−Organic Framework Material. *J. Am. Chem. Soc.* **2008,** *130* (32), 10524-10526.

143. Howarth, A. J.; Liu, Y.; Li, P.; Li, Z.; Wang, T. C.; Hupp, J. T.; Farha, O. K., Chemical, Thermal and Mechanical Stabilities of Metal–Organic Frameworks. *Nat. Rev. Mater.* **2016,** *1* (3), 15018.
144. Valenzano, L.; Civalleri, B.; Chavan, S.; Bordiga, S.; Nilsen, M. H.; Jakobsen, S.; Lillerud, K. P.; Lamberti, C., Disclosing the Complex Structure of UiO-66 Metal Organic Framework: A Synergic Combination of Experiment and Theory. *Chem. Mater.* **2011,** *23* (7), 1700-1718.
145. Heinz, W. R.; Kratky, T.; Drees, M.; Wimmer, A.; Tomanec, O.; Günther, S.; Schuster, M.; Fischer, R. A., Mixed Precious-Group Metal–Organic Frameworks: A Case Study of the HKUST-1 Analogue [RuxRh3−x(BTC)2]. *Dalton Trans.* **2019,** *48* (32), 12031-12039.
146. Ji, W.; Xu, Z.; Liu, P.; Zhang, S.; Zhou, W.; Li, H.; Zhang, T.; Li, L.; Lu, X.; Wu, J.; Zhang, W.; Huo, F., Metal–Organic Framework Derivatives for Improving the Catalytic Activity of the CO Oxidation Reaction. *ACS Appl. Mater. Interfaces* **2017,** *9* (18), 15394-15398.
147. Lan, M.; Guo, R.-M.; Dou, Y.; Zhou, J.; Zhou, A.; Li, J.-R., Fabrication of porous Pt-doping heterojunctions by using bimetallic MOF template for photocatalytic hydrogen generation. *Nano Energy* **2017,** *33*, 238-246.
148. Lee, K. J.; Lee, J. H.; Jeoung, S.; Moon, H. R., Transformation of Metal–Organic Frameworks/Coordination Polymers into Functional Nanostructured Materials: Experimental Approaches Based on Mechanistic Insights. *Acc. Chem. Res.* **2017,** *50* (11), 2684-2692.
149. Zhou, J.; Dou, Y.; Zhou, A.; Guo, R.-M.; Zhao, M.-J.; Li, J.-R., MOF Template-Directed Fabrication of Hierarchically Structured Electrocatalysts for Efficient Oxygen Evolution Reaction. *Adv. Energy Mater.* **2017,** *7* (12), 1602643.
150. Hussain, M. Z.; Schneemann, A.; Fischer, R. A.; Zhu, Y.; Xia, Y., MOF Derived Porous ZnO/C Nanocomposites for Efficient Dye Photodegradation. *ACS Appl. Energy Mater.* **2018,** *1* (9), 4695-4707.
151. Yang, Y.; Dong, H.; Wang, Y.; He, C.; Wang, Y.; Zhang, X., Synthesis of Octahedral Like Cu-BTC Derivatives Derived from MOF Calcined under Different Atmosphere for Application in CO Oxidation. *J. Solid State Chem.* **2018,** *258*, 582-587.
152. Zhu, B.; Xia, D.; Zou, R., Metal-organic frameworks and their derivatives as bifunctional electrocatalysts. *Coord. Chem. Rev.* **2018,** *376*, 430-448.
153. Hussain, M. Z.; Pawar, G. S.; Huang, Z.; Tahir, A. A.; Fischer, R. A.; Zhu, Y.; Xia, Y., Porous ZnO/Carbon nanocomposites derived from metal organic frameworks for highly efficient photocatalytic applications: A correlational study. *Carbon* **2019,** *146*, 348-363.
154. Zhong, Y.; Xu, X.; Wang, W.; Shao, Z., Recent Advances in Metal-Organic Framework Derivatives as Oxygen Catalysts for Zinc-Air Batteries. *Batteries Supercaps* **2019,** *2* (4), 272-289.
155. Li, W.; Xue, S.; Watzele, S.; Hou, S.; Fichtner, J.; Semrau, A. L.; Zhou, L.; Welle, A.; Bandarenka, A. S.; Fischer, R. A., Advanced Bifunctional Oxygen Reduction and Evolution Electrocatalyst Derived from Surface-Mounted Metal–Organic Frameworks. *Angew. Chem. Int. Ed.* **2020,** *59* (14), 5837-5843.
156. Zhang, X.; Chen, Z.; Liu, X.; Hanna, S. L.; Wang, X.; Taheri-Ledari, R.; Maleki, A.; Li, P.; Farha, O. K., A historical overview of the activation and porosity of metal–organic frameworks. *Chem. Soc. Rev.* **2020**.
157. Zhuang, J.-L.; Ceglarek, D.; Pethuraj, S.; Terfort, A., Rapid Room-Temperature Synthesis of Metal–Organic Framework HKUST-1 Crystals in Bulk and as Oriented and Patterned Thin Films. *Adv. Funct. Mater.* **2011,** *21* (8), 1442-1447.
158. Nordin, N. A. H. M.; Ismail, A. F.; Mustafa, A.; Goh, P. S.; Rana, D.; Matsuura, T., Aqueous room temperature synthesis of zeolitic imidazole framework 8 (ZIF-8) with various concentrations of triethylamine. *RSC Adv.* **2014,** *4* (63), 33292-33300.
159. Tsai, C.-W.; Langner, E. H. G., The effect of synthesis temperature on the particle size of nano-ZIF-8. *Microporous Mesoporous Mater.* **2016,** *221*, 8-13.
160. Chen, D.; Zhao, J.; Zhang, P.; Dai, S., Mechanochemical synthesis of metal–organic frameworks. *Polyhedron* **2019,** *162*, 59-64.
161. Mueller, U.; Schubert, M.; Teich, F.; Puetter, H.; Schierle-Arndt, K.; Pastré, J., Metal–organic frameworks—prospective industrial applications. *J. Mater. Chem.* **2006,** *16* (7), 626-636.
162. Al-Kutubi, H.; Gascon, J.; Sudhölter, E. J. R.; Rassaei, L., Electrosynthesis of Metal–Organic Frameworks: Challenges and Opportunities. *ChemElectroChem* **2015,** *2* (4), 462-474.

163. Klinowski, J.; Almeida Paz, F. A.; Silva, P.; Rocha, J., Microwave-Assisted Synthesis of Metal–Organic Frameworks. *Dalton Trans.* **2011,** *40* (2), 321-330.
164. Demessence, A.; Horcajada, P.; Serre, C.; Boissière, C.; Grosso, D.; Sanchez, C.; Férey, G., Elaboration and properties of hierarchically structured optical thin films of MIL-101(Cr). *Chem. Commun.* **2009,** (46), 7149-7151.
165. Allendorf, M. D.; Schwartzberg, A.; Stavila, V.; Talin, A. A., A Roadmap to Implementing Metal–Organic Frameworks in Electronic Devices: Challenges and Critical Directions. *Chem. Eur. J.* **2011,** *17* (41), 11372-11388.
166. Stassen, I.; Burtch, N.; Talin, A.; Falcaro, P.; Allendorf, M.; Ameloot, R., An updated roadmap for the integration of metal-organic frameworks with electronic devices and chemical sensors. *Chem. Soc. Rev.* **2017,** *46* (11), 3185-3241.
167. Stassin, T.; Rodríguez-Hermida, S.; Schrode, B.; Cruz, A. J.; Carraro, F.; Kravchenko, D.; Creemers, V.; Stassen, I.; Hauffman, T.; De Vos, D.; Falcaro, P.; Resel, R.; Ameloot, R., Vapour-phase deposition of oriented copper dicarboxylate metal–organic framework thin films. *Chem. Commun.* **2019,** *55* (68), 10056-10059.
168. Stassen, I.; Styles, M.; Grenci, G.; Gorp, H. V.; Vanderlinden, W.; Feyter, S. D.; Falcaro, P.; Vos, D. D.; Vereecken, P.; Ameloot, R., Chemical vapour deposition of zeolitic imidazolate framework thin films. *Nat. Mater.* **2016,** *15* (3), 304-310.
169. Hermes, S.; Witte, T.; Hikov, T.; Zacher, D.; Bahnmüller, S.; Langstein, G.; Huber, K.; Fischer, R. A., Trapping Metal-Organic Framework Nanocrystals: An in-Situ Time-Resolved Light Scattering Study on the Crystal Growth of MOF-5 in Solution. *J. Am. Chem. Soc.* **2007,** *129* (17), 5324-5325.
170. Tsuruoka, T.; Furukawa, S.; Takashima, Y.; Yoshida, K.; Isoda, S.; Kitagawa, S., Nanoporous Nanorods Fabricated by Coordination Modulation and Oriented Attachment Growth. *Angew. Chem. Int. Ed.* **2009,** *48* (26), 4739-4743.
171. Pham, M.-H.; Vuong, G.-T.; Fontaine, F.-G.; Do, T.-O., Rational Synthesis of Metal–Organic Framework Nanocubes and Nanosheets Using Selective Modulators and Their Morphology-Dependent Gas-Sorption Properties. *Cryst. Growth Des.* **2012,** *12* (6), 3091-3095.
172. Forgan, R. S., Modulated self-assembly of metal–organic frameworks. *Chem. Sci.* **2020,** *11* (18), 4546-4562.
173. Zhang, W.; Kozachuk, O.; Medishetty, R.; Schneemann, A.; Wagner, R.; Khaletskaya, K.; Epp, K.; Fischer, R. A., Controlled SBU Approaches to Isoreticular Metal-Organic Framework Ruthenium-Analogues of HKUST-1. *Eur. J. Inorg. Chem.* **2015,** *2015* (23), 3913-3920.
174. Wade, C. R.; Dinca, M., Investigation of the synthesis, activation, and isosteric heats of CO2 adsorption of the isostructural series of metal-organic frameworks M3(BTC)2 (M = Cr, Fe, Ni, Cu, Mo, Ru). *Dalton Trans.* **2012,** *41* (26), 7931-7938.
175. Kozachuk, O.; Yusenko, K.; Noei, H.; Wang, Y.; Walleck, S.; Glaser, T.; Fischer, R. A., Solvothermal Growth of a Ruthenium Metal–Organic Framework Featuring HKUST-1 Structure Type as Thin Films on Oxide Surfaces. *Chem. Commun.* **2011,** *47* (30), 8509-8511.
176. Epp, K.; Semrau, A. L.; Cokoja, M.; Fischer, R. A., Dual Site Lewis-Acid Metal-Organic Framework Catalysts for CO2 Fixation: Counteracting Effects of Node Connectivity, Defects and Linker Metalation. *ChemCatChem* **2018,** *10* (16), 3506-3512.
177. Abednatanzi, S.; Gohari Derakhshandeh, P.; Depauw, H.; Coudert, F.-X.; Vrielinck, H.; Van Der Voort, P.; Leus, K., Mixed-metal metal–organic frameworks. *Chem. Soc. Rev.* **2019,** *48* (9), 2535-2565.
178. Das, M. C.; Xiang, S.; Zhang, Z.; Chen, B., Functional mixed metal-organic frameworks with metalloligands. *Angew. Chem. Int. Ed. Engl.* **2011,** *50* (45), 10510-20.
179. Das, M. C.; Guo, Q.; He, Y.; Kim, J.; Zhao, C. G.; Hong, K.; Xiang, S.; Zhang, Z.; Thomas, K. M.; Krishna, R.; Chen, B., Interplay of metalloligand and organic ligand to tune micropores within isostructural mixed-metal organic frameworks (M'MOFs) for their highly selective separation of chiral and achiral small molecules. *J. Am. Chem. Soc.* **2012,** *134* (20), 8703-10.
180. Epp, K.; Bueken, B.; Hofmann, B.; Cokoja, M.; Hemmer, K.; De Vos, D. E.; Fischer, R. A., Network topology and cavity confinement-controlled diastereoselectivity in cyclopropanation reactions catalyzed by porphyrin-based MOFs. *Catal. Sci. Technol.* **2019,** *9* (22), 6452-6459.

181. Liu, J.; Fan, Y.-Z.; Li, X.; Wei, Z.; Xu, Y.-W.; Zhang, L.; Su, C.-Y., A Porous Rhodium(III)-Porphyrin Metal-Organic Framework as an Efficient and Selective Photocatalyst for CO2 Reduction. *Applied Catalysis B: Environmental*.
182. Ahrenholtz, S. R.; Epley, C. C.; Morris, A. J., Solvothermal Preparation of an Electrocatalytic Metalloporphyrin MOF Thin Film and its Redox Hopping Charge-Transfer Mechanism. *J. Am. Chem. Soc.* **2014,** *136* (6), 2464-2472.
183. Liu, Y.; Howarth, A. J.; Hupp, J. T.; Farha, O. K., Selective Photooxidation of a Mustard-Gas Simulant Catalyzed by a Porphyrinic Metal–Organic Framework. *Angew. Chem. Int. Ed.* **2015,** *54* (31), 9001-9005.
184. Wang, Y.; Cui, H.; Wei, Z.-W.; Wang, H.-P.; Zhang, L.; Su, C.-Y., Engineering catalytic coordination space in a chemically stable Ir-porphyrin MOF with a confinement effect inverting conventional Si-H insertion chemoselectivity. *Chem. Sci.* **2017,** *8* (1), 775-780.
185. Matsunaga, S.; Hasada, K.-i.; Sugiura, K.; Kitamura, N.; Kudo, Y.; Endo, N.; Mori, W., Hetero Bi-Paddle-Wheel Coordination Networks: A New Synthetic Route to Rh-Containing Metal–Organic Frameworks. *Bull. Chem. Soc. Jpn.* **2012,** *85* (4), 433-438.
186. Kim, D.; Lee, G.; Oh, S.; Oh, M., Unbalanced MOF-on-MOF growth for the production of a lopsided core–shell of MIL-88B@MIL-88A with mismatched cell parameters. *Chem. Commun.* **2019,** *55* (1), 43-46.
187. Lee, G.; Lee, S.; Oh, S.; Kim, D.; Oh, M., Tip-To-Middle Anisotropic MOF-On-MOF Growth with a Structural Adjustment. *J. Am. Chem. Soc.* **2020,** *142* (6), 3042-3049.
188. Liu, C.; Lin, L.; Sun, Q.; Wang, J.; Huang, R.; Chen, W.; Li, S.; Wan, J.; Zou, J.; Yu, C., Site-specific growth of MOF-on-MOF heterostructures with controllable nano-architectures: beyond the combination of MOF analogues. *Chem. Sci.* **2020,** *11* (14), 3680-3686.
189. Wang, Z.; Wannapaiboon, S.; Henke, S.; Paulus, M.; Rodewald, K.; Rieger, B.; Fischer, R. A., Synergistic Effect of Heterostructured Dissimilar Metal-Organic Framework Thin Films on Adsorption Properties. *J. Mater. Chem. A* **2020**.
190. Ikigaki, K.; Okada, K.; Tokudome, Y.; Toyao, T.; Falcaro, P.; Doonan, C. J.; Takahashi, M., MOF-on-MOF: Oriented Growth of Multiple Layered Thin Films of Metal–Organic Frameworks. *Angew. Chem. Int. Ed.* **2019,** *58* (21), 6886-6890.
191. Yin, Z.; Wan, S.; Yang, J.; Kurmoo, M.; Zeng, M.-H., Recent advances in post-synthetic modification of metal–organic frameworks: New types and tandem reactions. *Coord. Chem. Rev.* **2019,** *378*, 500-512.
192. Cui, P.; Wang, P.; Zhao, Y.; Sun, W.-Y., Fabrication of Desired Metal–Organic Frameworks via Postsynthetic Exchange and Sequential Linker Installation. *Cryst. Growth Des.* **2019,** *19* (2), 1454-1470.
193. Kim, M.; Cahill, J. F.; Fei, H.; Prather, K. A.; Cohen, S. M., Postsynthetic Ligand and Cation Exchange in Robust Metal–Organic Frameworks. *J. Am. Chem. Soc.* **2012,** *134* (43), 18082-18088.
194. Shakya, D. M.; Ejegbavwo, O. A.; Rajeshkumar, T.; Senanayake, S. D.; Brandt, A. J.; Farzandh, S.; Acharya, N.; Ebrahim, A. M.; Frenkel, A. I.; Rui, N.; Tate, G. L.; Monnier, J. R.; Vogiatzis, K. D.; Shustova, N. B.; Chen, D. A., Selective Catalytic Chemistry at Rhodium(II) Nodes in Bimetallic Metal–Organic Frameworks. *Angew. Chem. Int. Ed.* **2019,** *58* (46), 16533-16537.
195. Nowacka, A.; Briantais, P.; Prestipino, C.; Llabrés i Xamena, F. X., Facile “green” aqueous synthesis of mono- and bimetallic trimesate metalorganic frameworks. *Cryst. Growth Des.* **2019**.
196. Ayoub, G.; Karadeniz, B.; Howarth, A. J.; Farha, O. K.; Đilović, I.; Germann, L. S.; Dinnebier, R. E.; Užarević, K.; Friscic, T., Rational synthesis of mixed-metal microporous metal-organic frameworks with controlled composition using mechanochemistry. *Chem. Mater.* **2019**.
197. Zhang, W.; Chen, Z.; Al-Naji, M.; Guo, P.; Cwik, S.; Halbherr, O.; Wang, Y.; Muhler, M.; Wilde, N.; Glaser, R.; Fischer, R. A., Simultaneous introduction of various palladium active sites into MOF via one-pot synthesis: Pd@[Cu3-xPdx(BTC)2]n. *Dalton Trans.* **2016,** *45* (38), 14883-14887.
198. Guo, P.; Froese, C.; Fu, Q.; Chen, Y.-T.; Peng, B.; Kleist, W.; Fischer, R. A.; Muhler, M.; Wang, Y., CuPd Mixed-Metal HKUST-1 as a Catalyst for Aerobic Alcohol Oxidation. *J. Phys. Chem. C* **2018,** *122* (37), 21433-21440.
199. Virmani, E.; Rotter, J. M.; Mähringer, A.; von Zons, T.; Godt, A.; Bein, T.; Wuttke, S.; Medina, D. D., On-Surface Synthesis of Highly Oriented Thin Metal–Organic Framework Films through Vapor-Assisted Conversion. *J. Am. Chem. Soc.* **2018,** *140* (14), 4812-4819.

200. Krishtab, M.; Stassen, I.; Stassin, T.; Cruz, A. J.; Okudur, O. O.; Armini, S.; Wilson, C.; De Gendt, S.; Ameloot, R., Vapor-deposited zeolitic imidazolate frameworks as gap-filling ultra-low-k dielectrics. *Nat. Commun.* **2019,** *10* (1), 3729.
201. Fischer, R. A.; Wöll, C., Layer-by-Layer Liquid-Phase Epitaxy of Crystalline Coordination Polymers at Surfaces. *Angew. Chem. Int. Ed.* **2009,** *48* (34), 6205-6208.
202. Thornton, A. W.; Jelfs, K. E.; Konstas, K.; Doherty, C. M.; Hill, A. J.; Cheetham, A. K.; Bennett, T. D., Porosity in metal-organic framework glasses. *Chem. Commun.* **2016,** *52* (19), 3750-3753.
203. Horike, S.; Nagarkar, S. S.; Ogawa, T.; Kitagawa, S., A New Dimension for Coordination Polymers and Metal–Organic Frameworks: Towards Functional Glasses and Liquids. *Angew. Chem. Int. Ed.* **2020,** *59* (17), 6652-6664.
204. Gaillac, R.; Pullumbi, P.; Beyer, K. A.; Chapman, K. W.; Keen, D. A.; Bennett, T. D.; Coudert, F.-X., Liquid metal–organic frameworks. *Nat. Mater.* **2017,** *16* (11), 1149-1154.
205. Bennett, T. D.; Horike, S., Liquid, glass and amorphous solid states of coordination polymers and metal–organic frameworks. *Nat. Rev. Mater.* **2018,** *3* (11), 431-440.
206. Hou, J.; Ashling, C. W.; Collins, S. M.; Krajnc, A.; Zhou, C.; Longley, L.; Johnstone, D. N.; Chater, P. A.; Li, S.; Coulet, M.-V.; Llewellyn, P. L.; Coudert, F.-X.; Keen, D. A.; Midgley, P. A.; Mali, G.; Chen, V.; Bennett, T. D., Metal-organic framework crystal-glass composites. *Nat. Commun.* **2019,** *10* (1), 2580.
207. Widmer, R. N.; Lampronti, G. I.; Anzellini, S.; Gaillac, R.; Farsang, S.; Zhou, C.; Belenguer, A. M.; Wilson, C. W.; Palmer, H.; Kleppe, A. K.; Wharmby, M. T.; Yu, X.; Cohen, S. M.; Telfer, S. G.; Redfern, S. A. T.; Coudert, F.-X.; MacLeod, S. G.; Bennett, T. D., Pressure promoted low-temperature melting of metal–organic frameworks. *Nat. Mater.* **2019,** *18* (4), 370-376.
208. Ma, L.; Haynes, C. J. E.; Grommet, A. B.; Walczak, A.; Parkins, C. C.; Doherty, C. M.; Longley, L.; Tron, A.; Stefankiewicz, A. R.; Bennett, T. D.; Nitschke, J. R., Coordination cages as permanently porous ionic liquids. *Nat. Chem.* **2020,** *12* (3), 270-275.
209. Yang, Q.; Liu, D.; Zhong, C.; Li, J.-R., Development of Computational Methodologies for Metal–Organic Frameworks and Their Application in Gas Separations. *Chem. Rev.* **2013,** *113* (10), 8261-8323.
210. Mellot-Draznieks, C., Computational exploration of metal–organic frameworks: examples of advances in crystal structure predictions and electronic structure tuning. *Molecular Simulation* **2015,** *41* (16-17), 1422-1437.
211. Coudert, F.-X.; Fuchs, A. H., Computational characterization and prediction of metal–organic framework properties. *Coord. Chem. Rev.* **2016,** *307*, 211-236.
212. Azar, A. N. V.; Velioglu, S.; Keskin, S., Large-Scale Computational Screening of Metal Organic Framework (MOF) Membranes and MOF-Based Polymer Membranes for H2/N2 Separations. *ACS Sustainable Chemistry & Engineering* **2019,** *7* (10), 9525-9536.
213. Rosen, A. S.; Notestein, J. M.; Snurr, R. Q., Identifying promising metal–organic frameworks for heterogeneous catalysis via high-throughput periodic density functional theory. *J. Comput. Chem.* **2019,** *40* (12), 1305-1318.
214. Lab, S. R.; Tracy-Amoroso, N.; Bucior, B.; Siderius, D.; Bobbitt, S. Metal-Organic Framework Database. https://mof.tech.northwestern.edu/ (accessed 19.10.).
215. Dürholt, J. P.; Keupp, J.; Schmid; Rochus, The Impact of Mesopores on the Mechanical Stability of HKUST-1: A Multiscale Investigation. *Eur. J. Inorg. Chem.* **2016,** *2016* (27), 4517-4523.
216. Klet, R. C.; Liu, Y.; Wang, T. C.; Hupp, J. T.; Farha, O. K., Evaluation of Bronsted acidity and proton topology in Zr- and Hf-based metal-organic frameworks using potentiometric acid-base titration. *J. Mater. Chem. A* **2016,** *4* (4), 1479-1485.
217. Liu, Y.; Klet, R. C.; Hupp, J. T.; Farha, O., Probing the correlations between the defects in metal-organic frameworks and their catalytic activity by an epoxide ring-opening reaction. *Chem. Comm.* **2016,** *52* (50), 7806-7809.
218. Mondal, S. S.; Dey, S.; Attallah, A. G.; Bhunia, A.; Kelling, A.; Schilde, U.; Krause-Rehberg, R.; Janiak, C.; Holdt, H.-J., Missing Building Blocks Defects in a Porous Hydrogen–bonded Amide-Imidazolate Network Proven by Positron Annihilation Lifetime Spectroscopy. *ChemistrySelect* **2016,** *1* (14), 4320-4325.
219. Cai, G.; Jiang, H.-L., A Modulator-Induced Defect-Formation Strategy to Hierarchically Porous Metal–Organic Frameworks with High Stability. *Angew. Chem. Int. Ed.* **2017,** *56* (2), 563-567.

220. Dissegna, S.; Hardian, R.; Epp, K.; Kieslich, G.; Coulet, M.-V.; Llewellyn, P.; Fischer, R. A., Using water adsorption measurements to access the chemistry of defects in the metal-organic framework UiO-66. *CrystEngComm* **2017**.
221. Fang, Z.; Bueken, B.; De Vos, D. E.; Fischer, R. A., Defect-Engineered Metal–Organic Frameworks. *Angew. Chem. Int. Ed.* **2015,** *54* (25), 7234-7254.
222. Canivet, J.; Fateeva, A.; Guo, Y.; Coasne, B.; Farrusseng, D., Water adsorption in MOFs: fundamentals and applications. *Chem. Soc. Rev.* **2014,** *43* (16), 5594-5617.
223. Rivera Torrente, M.; Filez, M.; Meirer, F.; Weckhuysen, B. M., Multi-spectroscopic Interrogation of the Spatial Linker Distribution in Defect-Engineered Metal-Organic Framework Crystals: The [Cu3(BTC)2-x(CYDC)x] Showcase. *Chem. Eur. J. n/a* (n/a).
224. Delen, G.; Ristanović, Z.; Mandemaker, L. D. B.; Weckhuysen, B. M., Mechanistic Insights into Growth of Surface-Mounted Metal-Organic Framework Films Resolved by Infrared (Nano-) Spectroscopy. *Chem. Eur. J.* **2018,** *24* (1), 187-195.
225. Thornton, A. W.; Babarao, R.; Jain, A.; Trousselet, F.; Coudert, F. X., Defects in metal-organic frameworks: a compromise between adsorption and stability? *Dalton Trans.* **2016,** *45* (10), 4352-4359.
226. Rogge, S. M. J.; Wieme, J.; Vanduyfhuys, L.; Vandenbrande, S.; Maurin, G.; Verstraelen, T.; Waroquier, M.; Van Speybroeck, V., Thermodynamic Insight in the High-Pressure Behavior of UiO-66: Effect of Linker Defects and Linker Expansion. *Chem. Mater.* **2016,** *28* (16), 5721-5732.
227. Bristow, J. K.; Svane, K. L.; Tiana, D.; Skelton, J. M.; Gale, J. D.; Walsh, A., Free Energy of Ligand Removal in the Metal–Organic Framework UiO-66. *J. Phys. Chem. C* **2016,** *120* (17), 9276-9281.
228. Sarkisov, L., Molecular simulation of low temperature argon adsorption in several models of IRMOF-1 with defects and structural disorder. *Dalton Trans.* **2016,** *45* (10), 4203-4212.
229. Dissegna, S.; Vervoorts, P.; Hobday, C. L.; Düren, T.; Daisenberger, D.; Smith, A. J.; Fischer, R. A.; Kieslich, G., Tuning the Mechanical Response of Metal–Organic Frameworks by Defect Engineering. *J. Am. Chem. Soc.* **2018,** *140* (37), 11581-11584.
230. Fang, Z.; Dürholt, J. P.; Kauer, M.; Zhang, W.; Lochenie, C.; Jee, B.; Albada, B.; Metzler-Nolte, N.; Pöppl, A.; Weber, B.; Muhler, M.; Wang, Y.; Schmid, R.; Fischer, R. A., Structural Complexity in Metal–Organic Frameworks: Simultaneous Modification of Open Metal Sites and Hierarchical Porosity by Systematic Doping with Defective Linkers. *J. Am. Chem. Soc.* **2014,** *136* (27), 9627-9636.
231. Kozachuk, O.; Luz, I.; Llabrés i Xamena, F. X.; Noei, H.; Kauer, M.; Albada, H. B.; Bloch, E. D.; Marler, B.; Wang, Y.; Muhler, M.; Fischer, R. A., Multifunctional, Defect-Engineered Metal–Organic Frameworks with Ruthenium Centers: Sorption and Catalytic Properties. *Angew. Chem. Int. Ed.* **2014,** *53* (27), 7058-7062.
232. Vermoortele, F.; Ameloot, R.; Alaerts, L.; Matthessen, R.; Carlier, B.; Fernandez, E. V. R.; Gascon, J.; Kapteijn, F.; De Vos, D. E., Tuning the Catalytic Performance of Metal-Organic Frameworks in Fine Chemistry by Active Site Engineering. *J. Mater. Chem.* **2012,** *22* (20), 10313-10321.
233. Vermoortele, F.; Bueken, B.; Le Bars, G.; Van de Voorde, B.; Vandichel, M.; Houthoofd, K.; Vimont, A.; Daturi, M.; Waroquier, M.; Van Speybroeck, V.; Kirschhock, C.; De Vos, D. E., Synthesis Modulation as a Tool To Increase the Catalytic Activity of Metal–Organic Frameworks: The Unique Case of UiO-66(Zr). *J. Am. Chem. Soc.* **2013,** *135* (31), 11465-11468.
234. Shearer, G. C.; Chavan, S.; Bordiga, S.; Svelle, S.; Olsbye, U.; Lillerud, K. P., Defect Engineering: Tuning the Porosity and Composition of the Metal–Organic Framework UiO-66 via Modulated Synthesis. *Chem. Mater.* **2016,** *28* (11), 3749-3761.
235. Kozachuk, O.; Luz, I.; Xamena, F. X. L. i.; Noei, H.; Kauer, M.; Albada, H. B.; Bloch, E. D.; Marler, B.; Wang, Y.; Muhler, M.; Fischer, R. A., Multifunctional, Defect-Engineered Metal–Organic Frameworks with Ruthenium Centers: Sorption and Catalytic Properties. *Angew. Chem. Int. Ed.* **2014,** *53* (27), 7058-7062.
236. Zhang, W.; Kauer, M.; Halbherr, O.; Epp, K.; Guo, P.; Gonzalez, M. I.; Xiao, D. J.; Wiktor, C.; Xamena, F. X. L. i.; Wöll, C.; Wang, Y.; Muhler, M.; Fischer, R. A., Ruthenium Metal–Organic Frameworks with Different Defect Types: Influence on Porosity, Sorption, and Catalytic Properties. *Chem. Eur. J.* **2016,** *22* (40), 14297-14307.
237. Wang, Z.; Henke, S.; paulus, M.; Welle, A.; Fan, Z.; Rodewald, K.; Rieger, B.; Fischer, R. A., Defect Creation in Surface Mounted Metal-Organic Framework Thin Films. *ACS Appl. Mater. Interfaces* **2019**.

238. Llabrés i Xamena, F. X.; Cirujano, F. G.; Corma, A., An unexpected bifunctional acid base catalysis in IRMOF-3 for Knoevenagel condensation reactions. *Microporous Mesoporous Mater.* **2012,** *157*, 112-117.
239. Behrens, K.; Mondal, S. S.; Nöske, R.; Baburin, I. A.; Leoni, S.; Günter, C.; Weber, J.; Holdt, H.-J., Microwave-Assisted Synthesis of Defects Metal-Imidazolate-Amide-Imidate Frameworks and Improved CO2 Capture. *Inorg. Chem.* **2015,** *54* (20), 10073-10080.
240. Liang, W.; Coghlan, C. J.; Ragon, F.; Rubio-Martinez, M.; D'Alessandro, D. M.; Babarao, R., Defect engineering of UiO-66 for CO2 and H2O uptake - a combined experimental and simulation study. *Dalton Trans.* **2016,** *45* (11), 4496-4500.
241. Bennett, T. D.; Todorova, T. K.; Baxter, E. F.; Reid, D. G.; Gervais, C.; Bueken, B.; Van de Voorde, B.; De Vos, D.; Keen, D. A.; Mellot-Draznieks, C., Connecting defects and amorphization in UiO-66 and MIL-140 metal-organic frameworks: a combined experimental and computational study. *Phys. Chem. Chem. Phys.* **2016,** *18* (3), 2192-2201.
242. Montoro, C.; Ocón, P.; Zamora, F.; Navarro, J. A. R., Metal–Organic Frameworks Containing Missing-Linker Defects Leading to High Hydroxide-Ion Conductivity. *Chem. Eur. J.* **2016,** *22* (5), 1646-1651.
243. Marshall, R. J.; Forgan, R. S., Postsynthetic Modification of Zirconium Metal-Organic Frameworks. *Eur. J. Inorg. Chem.* **2016,** *2016* (27), 4310-4331.
244. Karagiaridi, O.; Lalonde, M. B.; Bury, W.; Sarjeant, A. A.; Farha, O. K.; Hupp, J. T., Opening ZIF-8: A Catalytically Active Zeolitic Imidazolate Framework of Sodalite Topology with Unsubstituted Linkers. *J. Am. Chem. Soc.* **2012,** *134* (45), 18790-18796.
245. Lee, S. J.; Doussot, C.; Baux, A.; Liu, L.; Jameson, G. B.; Richardson, C.; Pak, J. J.; Trousselet, F.; Coudert, F.-X.; Telfer, S. G., Multicomponent Metal–Organic Frameworks as Defect-Tolerant Materials. *Chem. Mater.* **2016,** *28* (1), 368-375.
246. Shearer, G. C.; Chavan, S.; Ethiraj, J.; Vitillo, J. G.; Svelle, S.; Olsbye, U.; Lamberti, C.; Bordiga, S.; Lillerud, K. P., Tuned to Perfection: Ironing Out the Defects in Metal–Organic Framework UiO-66. *Chem. Mater.* **2014,** *26* (14), 4068-4071.
247. Karagiaridi, O.; Vermeulen, N. A.; Klet, R. C.; Wang, T. C.; Moghadam, P. Z.; Al-Juaid, S. S.; Stoddart, J. F.; Hupp, J. T.; Farha, O. K., Functionalized Defects through Solvent-Assisted Linker Exchange: Synthesis, Characterization, and Partial Postsynthesis Elaboration of a Metal–Organic Framework Containing Free Carboxylic Acid Moieties. *Inorg. Chem.* **2015,** *54* (4), 1785-1790.
248. Gadipelli, S.; Guo, Z., Postsynthesis Annealing of MOF-5 Remarkably Enhances the Framework Structural Stability and CO2 Uptake. *Chem. Mater.* **2014,** *26* (22), 6333-6338.
249. Bentley, J.; Foo, G. S.; Rungta, M.; Sangar, N.; Sievers, C.; Sholl, D. S.; Nair, S., Effects of Open Metal Site Availability on Adsorption Capacity and Olefin/Paraffin Selectivity in the Metal–Organic Framework Cu3(BTC)2. *Ind. Eng. Chem. Res.* **2016,** *55* (17), 5043-5053.
250. Luan, Y.; Qi, Y.; Gao, H.; Andriamitantsoa, R. S.; Zheng, N.; Wang, G., A general post-synthetic modification approach of amino-tagged metal-organic frameworks to access efficient catalysts for the Knoevenagel condensation reaction. *J. Mater. Chem. A* **2015,** *3* (33), 17320-17331.
251. Wang, Z.; Sezen, H.; Liu, J.; Yang, C.; Roggenbuck, S. E.; Peikert, K.; Fröba, M.; Mavrandonakis, A.; Supronowicz, B.; Heine, T.; Gliemann, H.; Wöll, C., Tunable coordinative defects in UHM-3 surface-mounted MOFs for gas adsorption and separation: A combined experimental and theoretical study. *Microporous and Mesoporous Mater.* **2015,** *207*, 53-60.
252. Aguirrezabal-Telleria, I.; Luz, I.; Ortuño, M. A.; Oregui-Bengoechea, M.; Gandarias, I.; López, N.; Lail, M. A.; Soukri, M., Gas Reactions Under Intrapore Condensation Regime within Tailored Metal–Organic Framework Catalysts. *Nat. Commun.* **2019,** *10* (1), 2076.
253. Wang, Y.; Wöll, C., Chemical Reactions at Isolated Single-Sites Inside Metal–Organic Frameworks. *Catal. Lett.* **2018,** *148* (8), 2201-2222.
254. Szilágyi, P. Á.; Serra-Crespo, P.; Gascon, J.; Geerlings, H.; Dam, B., The Impact of Post-Synthetic Linker Functionalization of MOFs on Methane Storage: The Role of Defects. *Front. Engergy Res.* **2016,** *4* (9).

255. Rodríguez-Albelo, L. M.; López-Maya, E.; Hamad, S.; Ruiz-Salvador, A. R.; Calero, S.; Navarro, J. A. R., Selective sulfur dioxide adsorption on crystal defect sites on an isoreticular metal organic framework series. *Nat. Commun.* **2017,** *8*, 14457.
256. Lu, A. X.; McEntee, M.; Browe, M. A.; Hall, M. G.; DeCoste, J. B.; Peterson, G. W., MOFabric: Electrospun Nanofiber Mats from PVDF/UiO-66-NH2 for Chemical Protection and Decontamination. *ACS Appl. Mater. Interfaces* **2017,** *9* (15), 13632-13636.
257. Plonka, A. M.; Wang, Q.; Gordon, W. O.; Balboa, A.; Troya, D.; Guo, W.; Sharp, C. H.; Senanayake, S. D.; Morris, J. R.; Hill, C. L.; Frenkel, A. I., In Situ Probes of Capture and Decomposition of Chemical Warfare Agent Simulants by Zr-Based Metal Organic Frameworks. *J. Am. Chem. Soc.* **2017,** *139* (2), 599-602.
258. Li, B.; Zhu, X.; Hu, K.; Li, Y.; Feng, J.; Shi, J.; Gu, J., Defect creation in metal-organic frameworks for rapid and controllable decontamination of roxarsone from aqueous solution. *J. Hazard. Mater.* **2016,** *302*, 57-64.
259. López-Maya, E.; Montoro, C.; Rodríguez-Albelo, L. M.; Aznar Cervantes, S. D.; Lozano-Pérez, A. A.; Cenís, J. L.; Barea, E.; Navarro, J. A. R., Textile/Metal–Organic-Framework Composites as Self-Detoxifying Filters for Chemical-Warfare Agents. *Angew. Chem. Int. Ed.* **2015,** *54* (23), 6790-6794.
260. Fernandez, C. A.; Nune, S. K.; Annapureddy, H. V.; Dang, L. X.; McGrail, B. P.; Zheng, F.; Polikarpov, E.; King, D. L.; Freeman, C.; Brooks, K. P., Hydrophobic and moisture-stable metal-organic frameworks. *Dalton Trans.* **2015,** *44* (30), 13490-13497.
261. Deria, P.; Mondloch, J. E.; Tylianakis, E.; Ghosh, P.; Bury, W.; Snurr, R. Q.; Hupp, J. T.; Farha, O. K., Perfluoroalkane Functionalization of NU-1000 via Solvent-Assisted Ligand Incorporation: Synthesis and CO2 Adsorption Studies. *J. Am. Chem. Soc.* **2013,** *135* (45), 16801-16804.
262. Xie, L.-H.; Xu, M.-M.; Liu, X.-M.; Zhao, M.-J.; Li, J.-R., Hydrophobic Metal–Organic Frameworks: Assessment, Construction, and Diverse Applications. *Adv. Sci.* **2020,** *n/a* (n/a), 1901758.
263. Jayaramulu, K.; Geyer, F.; Schneemann, A.; Kment, Š.; Otyepka, M.; Zboril, R.; Vollmer, D.; Fischer, R. A., Hydrophobic Metal–Organic Frameworks. *Adv. Mater.* **2019,** *31* (32), 1900820.
264. Kobayashi, Y.; Jacobs, B.; Allendorf, M. D.; Long, J. R., Conductivity, Doping, and Redox Chemistry of a Microporous Dithiolene-Based Metal−Organic Framework. *Chem. Mater.* **2010,** *22* (14), 4120-4122.
265. Sun, L.; Campbell, M. G.; Dincă, M., Electrically Conductive Porous Metal–Organic Frameworks. *Angew. Chem. Int. Ed.* **2016,** *55* (11), 3566-3579.
266. Kambe, T.; Sakamoto, R.; Kusamoto, T.; Pal, T.; Fukui, N.; Hoshiko, K.; Shimojima, T.; Wang, Z.; Hirahara, T.; Ishizaka, K.; Hasegawa, S.; Liu, F.; Nishihara, H., Redox Control and High Conductivity of Nickel Bis(dithiolene) Complex π-Nanosheet: A Potential Organic Two-Dimensional Topological Insulator. *J. Am. Chem. Soc.* **2014,** *136* (41), 14357-14360.
267. Wang, H.-Y.; Ge, J.-Y.; Hua, C.; Jiao, C.-Q.; Wu, Y.; Leong, C. F.; D'Alessandro, D. M.; Liu, T.; Zuo, J.-L., Photo- and Electronically Switchable Spin-Crossover Iron(II) Metal–Organic Frameworks Based on a Tetrathiafulvalene Ligand. *Angew. Chem. Int. Ed.* **2017,** *56* (20), 5465-5470.
268. Erickson, K. J.; Léonard, F.; Stavila, V.; Foster, M. E.; Spataru, C. D.; Jones, R. E.; Foley, B. M.; Hopkins, P. E.; Allendorf, M. D.; Talin, A. A., Thin Film Thermoelectric Metal–Organic Framework with High Seebeck Coefficient and Low Thermal Conductivity. *Adv. Mater.* **2015,** *27* (22), 3453-3459.
269. Talin, A. A.; Centrone, A.; Ford, A. C.; Foster, M. E.; Stavila, V.; Haney, P.; Kinney, R. A.; Szalai, V.; El Gabaly, F.; Yoon, H. P.; Léonard, F.; Allendorf, M. D., Tunable Electrical Conductivity in Metal-Organic Framework Thin-Film Devices. *Science* **2014,** *343* (6166), 66-69.
270. Allendorf, M. D.; Foster, M. E.; Léonard, F.; Stavila, V.; Feng, P. L.; Doty, F. P.; Leong, K.; Ma, E. Y.; Johnston, S. R.; Talin, A. A., Guest-Induced Emergent Properties in Metal–Organic Frameworks. *J. Phys. Chem. Lett.* **2015,** *6* (7), 1182-1195.
271. Sengupta, A.; Datta, S.; Su, C.; Herng, T. S.; Ding, J.; Vittal, J. J.; Loh, K. P., Tunable Electrical Conductivity and Magnetic Property of the Two Dimensional Metal Organic Framework [Cu(TPyP)Cu2(O2CCH3)4]. *ACS Appl. Mater. Interfaces* **2016,** *8* (25), 16154-16159.
272. Stavila, V.; Schneider, C.; Mowry, C.; Zeitler, T. R.; Greathouse, J. A.; Robinson, A. L.; Denning, J. M.; Volponi, J.; Leong, K.; Quan, W.; Tu, M.; Fischer, R. A.; Allendorf, M. D., Thin Film Growth of nbo MOFs and their Integration with Electroacoustic Devices. *Adv. Funct. Mater.* **2016,** *26* (11), 1699-1707.

273. Horike, S.; Umeyama, D.; Kitagawa, S., Ion Conductivity and Transport by Porous Coordination Polymers and Metal–Organic Frameworks. *Acc. Chem. Res.* **2013,** *46* (11), 2376-2384.
274. Yamada, T.; Otsubo, K.; Makiura, R.; Kitagawa, H., Designer coordination polymers: dimensional crossover architectures and proton conduction. *Chem. Soc. Rev.* **2013,** *42* (16), 6655-6669.
275. Taylor, J. M.; Dekura, S.; Ikeda, R.; Kitagawa, H., Defect Control To Enhance Proton Conductivity in a Metal–Organic Framework. *Chem. Mater.* **2015,** *27* (7), 2286-2289.
276. Goesten, M. G.; Juan-Alcañiz, J.; Ramos-Fernandez, E. V.; Sai Sankar Gupta, K. B.; Stavitski, E.; van Bekkum, H.; Gascon, J.; Kapteijn, F., Sulfation of metal–organic frameworks: Opportunities for acid catalysis and proton conductivity. *J. Catal.* **2011,** *281* (1), 177-187.
277. Ōkawa, H.; Sadakiyo, M.; Yamada, T.; Maesato, M.; Ohba, M.; Kitagawa, H., Proton-Conductive Magnetic Metal–Organic Frameworks, {NR3(CH2COOH)}[MaIIMbIII(ox)3]: Effect of Carboxyl Residue upon Proton Conduction. *J. Am. Chem. Soc.* **2013,** *135* (6), 2256-2262.
278. Hindelang, K.; Vagin, S. I.; Anger, C.; Rieger, B., Tandem post-synthetic modification for functionalized metal-organic frameworks viaepoxidation and subsequent epoxide ring-opening. *Chem. Commun.* **2012,** *48* (23), 2888-2890.
279. Fortea-Pérez, F. R.; Mon, M.; Ferrando-Soria, J.; Boronat, M.; Leyva-Pérez, A.; Corma, A.; Herrera, J. M.; Osadchii, D.; Gascon, J.; Armentano, D.; Pardo, E., The MOF-driven synthesis of supported palladium clusters with catalytic activity for carbene-mediated chemistry. *Nat. Mater.* **2017,** *16*, 760.
280. Kratzl, K.; Kratky, T.; Günther, S.; Tomanec, O.; Zbořil, R.; Michalička, J.; Macak, J. M.; Cokoja, M.; Fischer, R. A., Generation and Stabilization of Small Platinum Clusters Pt12±x Inside a Metal–Organic Framework. *J. Am. Chem. Soc.* **2019,** *141* (35), 13962-13969.
281. Ahlsten, N.; Lundberg, H.; Martín-Matute, B., Rhodium-catalysed isomerisation of allylic alcohols in water at ambient temperature. *Green Chemistry* **2010,** *12* (9), 1628-1633.
282. Cahard, D.; Gaillard, S.; Renaud, J.-L., Asymmetric isomerization of allylic alcohols. *Tetrahedron Lett.* **2015,** *56* (45), 6159-6169.
283. Xia, T.; Wei, Z.; Spiegelberg, B.; Jiao, H.; Hinze, S.; de Vries, J. G., Isomerization of Allylic Alcohols to Ketones Catalyzed by Well-Defined Iron PNP Pincer Catalysts. *Chem. Eur. J.* **2018,** *24* (16), 4043-4049.
284. Scalambra, F.; Lorenzo-Luis, P.; de los Rios, I.; Romerosa, A., Isomerization of allylic alcohols in water catalyzed by transition metal complexes. *Coord. Chem. Rev.* **2019,** *393*, 118-148.
285. Canivet, J.; Aguado, S.; Schuurman, Y.; Farrusseng, D., MOF-Supported Selective Ethylene Dimerization Single-Site Catalysts through One-Pot Postsynthetic Modification. *J. Am. Chem. Soc.* **2013,** *135* (11), 4195-4198.
286. Metzger, E. D.; Brozek, C. K.; Comito, R. J.; Dincă, M., Selective Dimerization of Ethylene to 1-Butene with a Porous Catalyst. *ACS Cent. Sci.* **2016,** *2* (3), 148-153.
287. Gonzalez, M. I.; Oktawiec, J.; Long, J. R., Ethylene oligomerization in metal–organic frameworks bearing nickel(ii) 2,2′-bipyridine complexes. *Faraday Discuss.* **2017,** *201* (0), 351-367.
288. Madrahimov, S. T.; Gallagher, J. R.; Zhang, G.; Meinhart, Z.; Garibay, S. J.; Delferro, M.; Miller, J. T.; Farha, O. K.; Hupp, J. T.; Nguyen, S. T., Gas-Phase Dimerization of Ethylene under Mild Conditions Catalyzed by MOF Materials Containing (bpy)NiII Complexes. *ACS Catal.* **2015,** *5* (11), 6713-6718.
289. Li, Z.; Schweitzer, N. M.; League, A. B.; Bernales, V.; Peters, A. W.; Getsoian, A. B.; Wang, T. C.; Miller, J. T.; Vjunov, A.; Fulton, J. L.; Lercher, J. A.; Cramer, C. J.; Gagliardi, L.; Hupp, J. T.; Farha, O. K., Sintering-Resistant Single-Site Nickel Catalyst Supported by Metal–Organic Framework. *J. Am. Chem. Soc.* **2016,** *138* (6), 1977-1982.
290. Liu, J.; Ye, J.; Li, Z.; Otake, K.-i.; Liao, Y.; Peters, A. W.; Noh, H.; Truhlar, D. G.; Gagliardi, L.; Cramer, C. J.; Farha, O. K.; Hupp, J. T., Beyond the Active Site: Tuning the Activity and Selectivity of a Metal–Organic Framework-Supported Ni Catalyst for Ethylene Dimerization. *J. Am. Chem. Soc.* **2018,** *140* (36), 11174-11178.
291. Angelescu, E.; Che, M.; Andruh, M.; Zăvoianu, R.; Costentin, G.; Miricã, C.; Dumitru Pavel, O., Ethylene selective dimerization on polymer complex catalyst of Ni(4,4′-bipyridine)Cl2 coactivated with AlCl(C2H5)2. *J. Mol. Catal. A: Chem.* **2004,** *219* (1), 13-19.
292. Brookhart, M.; Studabaker, W. B., Cyclopropanes from reactions of transition metal carbene complexes with olefins. *Chem. Rev.* **1987,** *87* (2), 411-432.

293. Doyle, M. P.; Forbes, D. C., Recent Advances in Asymmetric Catalytic Metal Carbene Transformations. *Chem. Rev.* **1998,** *98* (2), 911-936.
294. Lebel, H.; Marcoux, J.-F.; Molinaro, C.; Charette, A. B., Stereoselective Cyclopropanation Reactions. *Chem. Rev.* **2003,** *103* (4), 977-1050.
295. Corma, A.; Iglesias, M.; Llabrés i Xamena, F. X.; Sánchez, F., Cu and Au Metal–Organic Frameworks Bridge the Gap between Homogeneous and Heterogeneous Catalysts for Alkene Cyclopropanation Reactions. *Chem. Eur. J.* **2010,** *16* (32), 9789-9795.
296. Kim, J.; Cho, H.-Y.; Ahn, W.-S., Synthesis and Adsorption/Catalytic Properties of the Metal Organic Framework CuBTC. *Catalysis Surveys from Asia* **2012,** *16* (2), 106-119.
297. Heinz, W. R.; Junk, R.; Agirrezabal Telleria, I.; Bueken, B.; Bunzen, H.; Gölz, T.; Cokoja, M.; De Vos, D. E.; Fischer, R. A., Thermal Defect Engineering of Precious Group Metal-Organic Frameworks: Impact on the Catalytic Cyclopropanation Reaction. *Catal. Sci. Technol.* **2020**.
298. Doyle, M. P.; Ren, D., The Influence of Ligands on Dirhodium(II) on Reactivity and Selectivity in Metal Carbene Reactions. In *Prog. Inorg. Chem.*, 2007; pp 113-168.
299. Padwa, A.; Austin, D. J.; Hornbuckle, S. F.; Semones, M. A.; Doyle, M. P.; Protopopova, M. N., Control of chemoselectivity in catalytic carbenoid reactions. Dirhodium(II) ligand effects on relative reactivities. *J. Am. Chem. Soc.* **1992,** *114* (5), 1874-1876.
300. Doyle, M. P.; Westrum, L. J.; Wolthuis, W. N. E.; See, M. M.; Boone, W. P.; Bagheri, V.; Pearson, M. M., Electronic and steric control in carbon-hydrogen insertion reactions of diazoacetoacetates catalyzed by dirhodium(II) carboxylates and carboxamides. *J. Am. Chem. Soc.* **1993,** *115* (3), 958-964.
301. Anciaux, A. J.; Hubert, A. J.; Noels, A. F.; Petiniot, N.; Teyssie, P., Transition-metal-catalyzed reactions of diazo compounds. 1. Cyclopropanation of double bonds. *J. Org. Chem.* **1980,** *45* (4), 695-702.
302. Maas, G., Ruthenium-catalysed carbenoid cyclopropanation reactions with diazo compounds. *Chem. Soc. Rev.* **2004,** *33* (3), 183-190.
303. Cotton, F. A.; Dunbar, K. R.; Verbruggen, M. G., New directions in the chemistry of dirhodium(II) compounds. *J. Am. Chem. Soc.* **1987,** *109* (18), 5498-5506.
304. Simal, F.; Demonceau, A.; Noels, A. F.; Knowles, D. R. T.; O'Leary, S.; Maitlis, P. M.; Gusev, O., Cp*Ru(II) and Cp*Ru(IV)-catalyzed reactions of CHX with vinyl C–H bonds: competition between double bond homologation and olefin cyclopropanation by alkyl diazoacetate. *J. Organomet. Chem.* **1998,** *558* (1), 163-170.
305. Heinz, W. R.; Agirrezabal-Telleria, I.; Junk, R.; Berger, J.; Wang, J.; Sharapa, D. I.; Gil-Calvo, M.; Luz, I.; Soukri, M.; Studt, F.; Wang, Y.; Wöll, C.; Bunzen, H.; Drees, M.; Fischer, R. A., Thermal Defect-Engineering of Precious Group Metal-Organic Frameworks: A Case Study on Ru/Rh-HKUST-1 Analogues. *ACS Appl. Mater. Interfaces* **2020,** *12* (36), 40635-40647.
306. Wong-Foy, A. G.; Matzger, A. J.; Yaghi, O. M., Exceptional H2 Saturation Uptake in Microporous Metal−Organic Frameworks. *J. Am. Chem. Soc.* **2006,** *128* (11), 3494-3495.
307. Liu, J.; Culp, J. T.; Natesakhawat, S.; Bockrath, B. C.; Zande, B.; Sankar, S. G.; Garberoglio, G.; Johnson, J. K., Experimental and Theoretical Studies of Gas Adsorption in Cu3(BTC)2: An Effective Activation Procedure. *J. Phys. Chem. C* **2007,** *111* (26), 9305-9313.
308. Farrusseng, D.; Daniel, C.; Gaudillère, C.; Ravon, U.; Schuurman, Y.; Mirodatos, C.; Dubbeldam, D.; Frost, H.; Snurr, R. Q., Heats of Adsorption for Seven Gases in Three Metal−Organic Frameworks: Systematic Comparison of Experiment and Simulation. *Langmuir* **2009,** *25* (13), 7383-7388.
309. Yazaydın, A. Ö.; Benin, A. I.; Faheem, S. A.; Jakubczak, P.; Low, J. J.; Willis, R. R.; Snurr, R. Q., Enhanced CO2 Adsorption in Metal-Organic Frameworks via Occupation of Open-Metal Sites by Coordinated Water Molecules. *Chem. Mater.* **2009,** *21* (8), 1425-1430.
310. Hartmann, M.; Kunz, S.; Himsl, D.; Tangermann, O.; Ernst, S.; Wagener, A., Adsorptive Separation of Isobutene and Isobutane on Cu3(BTC)2. *Langmuir* **2008,** *24* (16), 8634-8642.
311. Bureekaew, S.; Amirjalayer, S.; Schmid, R., Orbital directing effects in copper and zinc based paddle-wheel metal organic frameworks: the origin of flexibility. *J. Mater. Chem.* **2012,** *22* (20), 10249-10254.

312. Zhang, W.; Kauer, M.; Guo, P.; Kunze, S.; Cwik, S.; Muhler, M.; Wang, Y.; Epp, K.; Kieslich, G.; Fischer, R. A., Impact of Synthesis Parameters on the Formation of Defects in HKUST-1. *Eur. J. Inorg. Chem.* **2017,** *2017* (5), 925-931.
313. Turano, P., NMR of Paramagnetic Species. In *Encyclopedia of Spectroscopy and Spectrometry (Third Edition)*, Lindon, J. C.; Tranter, G. E.; Koppenaal, D. W., Eds. Academic Press: Oxford, 2017; pp 164-169.
314. Wee, L. H.; Lohe, M. R.; Janssens, N.; Kaskel, S.; Martens, J. A., Fine tuning of the metal–organic framework Cu3(BTC)2 HKUST-1 crystal size in the 100 nm to 5 micron range. *J. Mater. Chem.* **2012,** *22* (27), 13742-13746.
315. Schneider, C.; Bodesheim, D.; Keupp, J.; Schmid, R.; Kieslich, G., Retrofitting metal-organic frameworks. *Nat. Commun.* **2019,** *10* (1), 4921.
316. Schneider, C.; Ukaj, D.; Koerver, R.; Talin, A. A.; Kieslich, G.; Pujari, S. P.; Zuilhof, H.; Janek, J.; Allendorf, M. D.; Fischer, R. A., High electrical conductivity and high porosity in a Guest@MOF material: evidence of TCNQ ordering within Cu3BTC2 micropores. *Chem. Sci.* **2018,** *9* (37), 7405-7412.
317. Rivera-Torrente, M.; Filez, M.; Schneider, C.; van der Feltz, E. C.; Wolkersdörfer, K.; Taffa, D. H.; Wark, M.; Fischer, R. A.; Weckhuysen, B. M., Micro-spectroscopy of HKUST-1 metal–organic framework crystals loaded with tetracyanoquinodimethane: effects of water on host–guest chemistry and electrical conductivity. *PCCP* **2019,** *21* (46), 25678-25689.
318. Schneider, C.; Bodesheim, D.; Ehrenreich, M. G.; Crocellà, V.; Mink, J.; Fischer, R. A.; Butler, K. T.; Kieslich, G., Tuning the Negative Thermal Expansion Behavior of the Metal–Organic Framework Cu3BTC2 by Retrofitting. *J. Am. Chem. Soc.* **2019,** *141* (26), 10504-10509.
319. Schneider, C.; Mendt, M.; Pöppl, A.; Crocellà, V.; Fischer, R. A., Scrutinizing the Pore Chemistry and the Importance of Cu(I) Defects in TCNQ-Loaded Cu3(BTC)2 by a Multitechnique Spectroscopic Approach. *ACS Appl. Mater. Interfaces* **2020,** *12* (1), 1024-1035.
320. St. Petkov, P.; Vayssilov, G. N.; Liu, J.; Shekhah, O.; Wang, Y.; Wöll, C.; Heine, T., Defects in MOFs: A Thorough Characterization. *ChemPhysChem* **2012,** *13* (8), 2025-2029.
321. Al-Janabi, N.; Hill, P.; Torrente-Murciano, L.; Garforth, A.; Gorgojo, P.; Siperstein, F.; Fan, X., Mapping the Cu-BTC metal–organic framework (HKUST-1) stability envelope in the presence of water vapour for CO2 adsorption from flue gases. *Chem. Eng. J.* **2015,** *281*, 669-677.
322. Guo, P.; Fu, Q.; Yildiz, C.; Chen, Y.-T.; Ollegott, K.; Froese, C.; Kleist, W.; Fischer, R. A.; Wang, Y.; Muhler, M.; Peng, B., Regulating the size and spatial distribution of Pd nanoparticles supported by the defect engineered metal–organic framework HKUST-1 and applied in the aerobic oxidation of cinnamyl alcohol. *Catal. Sci. Technol.* **2019,** *9* (14), 3703-3710.
323. Rivera-Torrente, M.; Filez, M.; Hardian, R.; Reynolds, E.; Seoane, B.; Coulet, M.-V.; Oropeza Palacio, F. E.; Hofmann, J. P.; Fischer, R. A.; Goodwin, A. L.; Llewellyn, P. L.; Weckhuysen, B. M., Metal-Organic Frameworks as Catalyst Supports: Influence of Lattice Disorder on Metal Nanoparticle Formation. *Chem. Eur. J.* **2018,** *24* (29), 7498-7506.
324. Marx, S.; Kleist, W.; Baiker, A., Synthesis, structural properties, and catalytic behavior of Cu-BTC and mixed-linker Cu-BTC-PyDC in the oxidation of benzene derivatives. *J. Catal.* **2011,** *281* (1), 76-87.
325. Albolkany, M. K.; Wang, Y.; Li, W.; Arooj, S.; Chen, C.-H.; Wu, N.; Wang, Y.; Zbořil, R.; Fischer, R. A.; Liu, B., Dual-Function HKUST-1: Templating and Catalyzing Formation of Graphitic Carbon Nitride Quantum Dots Under Mild Conditions. *Angew. Chem. Int. Ed. n/a* (n/a).
326. Fang, Q.; Zhu, G.; Xin, M.; Zhang, D.; Shi, Z.; Wu, G.; Tian, G.; Tang, Z.; Xue, M.; Zuo, S., Synthesis and Crystal Structure of a 3D Inorganic-Organic Hybrid Compound [Zn3(BTC)2(H2O)3]n with Micropores *Chem. J. Univ.-Chin.* **2004,** (6), 1016-1018.
327. Kramer, M.; Schwarz, U.; Kaskel, S., Synthesis and properties of the metal-organic framework Mo3(BTC)2 (TUDMOF-1). *J. Mater. Chem.* **2006,** *16* (23), 2245-2248.
328. Xie, L.; Liu, S.; Gao, C.; Cao, R.; Cao, J.; Sun, C.; Su, Z., Mixed-Valence Iron(II, III) Trimesates with Open Frameworks Modulated by Solvents. *Inorg. Chem.* **2007,** *46* (19), 7782-7788.
329. Murray, L. J.; Dinca, M.; Yano, J.; Chavan, S.; Bordiga, S.; Brown, C. M.; Long, J. R., Highly-Selective and Reversible O2 Binding in Cr3(1,3,5-benzenetricarboxylate)2. *J. Am. Chem. Soc.* **2010,** *132* (23), 7856-7857.

330. Maniam, P.; Stock, N., Investigation of Porous Ni-Based Metal–Organic Frameworks Containing Paddle-Wheel Type Inorganic Building Units via High-Throughput Methods. *Inorg. Chem.* **2011,** *50* (11), 5085-5097.
331. Zhang, W.; Freitag, K.; Wannapaiboon, S.; Schneider, C.; Epp, K.; Kieslich, G.; Fischer, R. A., Elaboration of a Highly Porous RuII,II Analogue of HKUST-1. *Inorg. Chem.* **2016,** *55* (24), 12492-12495.
332. Valvekens, P.; Jonckheere, D.; De Baerdemaeker, T.; Kubarev, A. V.; Vandichel, M.; Hemelsoet, K.; Waroquier, M.; Van Speybroeck, V.; Smolders, E.; Depla, D.; Roeffaers, M. B. J.; De Vos, D., Base catalytic activity of alkaline earth MOFs: a (micro)spectroscopic study of active site formation by the controlled transformation of structural anions. *Chem. Sci.* **2014,** *5* (11), 4517-4524.

8 Curriculum Vitae

9 List of all Publications and Conference Contributions

Publications used in this thesis:

"Mixed Precious-Group Metal–Organic Frameworks: A Case Study of the HKUST-1 Analogue $[Ru_xRh_{3-x}(BTC)_2]$", W. R. Heinz, T. Kratky, M. Drees, A. Wimmer, O. Tomanec, S. Günther, M. Schuster and R. A. Fischer, *Dalton Transactions* **2019**, *48*, 12031-12039.

Contributions: Concept, project management, experimental works of synthesis and characterization, data evaluation and interpretation, manuscript writing and revision, preparation of graphics, images and illustrations, design of the journal front cover artwork.

"Thermal Defect-Engineering of Precious Group Metal-Organic Frameworks: A Case Study on Ru/Rh-HKUST-1 Analogues", W. R. Heinz, I. Agirrezabal-Telleria, R. Junk, J. Berger, J. Wang, D. I. Sharapa, M. Gil-Calvo, I. Luz, M. Soukri, F. Studt, Y. Wang, Ch. Wöll, M. Drees and R. A. Fischer, *ACS Applied Materials & Interfaces* **2020**, 12, 36, 40635–40647.

Contributions: Concept, project management, experimental works of synthesis and characterization, data evaluation and interpretation, manuscript writing and revision, preparation of graphics, images and illustrations.

"Thermal Defect Engineering of Precious Group Metal-Organic Frameworks: Impact on the Catalytic Cyclopropanation Reaction", W. R. Heinz, R. Junk, I. Agirrezabal-Telleria, B. Bueken, H. Bunzen, T. Gölz, M. Cokoja, D. De Vos and R. A. Fischer, *Catalysis: Science and Technology* **2020**, 10, 8077 – 8085.

Contributions: Concept, project management, experimental works of synthesis, characterization and catalysis, data evaluation and interpretation, manuscript writing and revision, preparation of graphics, images and illustrations.

"Defect Engineered Ruthenium MOFs as Versatile Hydrogenation Catalysts", K. Epp, I. Luz, W. R. Heinz, A. Rapeyko, F. X. Llabres i Xamena and R. A. Fischer, *ChemCatChem* **2020**, 12, 1720-1725.

Contributions: Synthesis and characterization of the samples requested by the reviewers, revision of the manuscript, preparation of figures and schemes, design of the TOC image.

"Scrutinizing Ligand Exchange Reactions in the Formation of the Precious Group Metal-Organic Framework $Ru^{II,II}$-HKUST-1: The Impact of Diruthenium Tetracarboxylate Precursor and Modulator Choice", W. R. Heinz, D. Staude, H. Bunzen, D. Mayer and R. A. Fischer, *Dalton Transactions* **2021**, accepted manuscript, https://doi.org/10.1039/D1DT00118C.

Contributions: Concept, project management, experimental works of MOF synthesis and characterization, manuscript writing and revision, design and preparation of all graphics, images and illustrations. Design of the TOC image.

"Defective Metal-Organic Frameworks", S. Dissegna,* K. Epp,* W. R. Heinz,* G. Kieslich and R. A. Fischer, *Advanced Materials* **2018**, 1704501. *equally contributing.

Contributions: Literature search and classification, manuscript writing (Preparation of chapters 2.3, 3.3, 3.4, 3.6, and Table 1), revision of the manuscript, design of the journal cover artwork.

Other Publications:

"Wide-Gamut Lasing from a Single Organic Chromophore", S. Lane, S. I. Vagin, H. Wang, W. R. Heinz, W. Morrish, Y. Zhao, B. Rieger and A. Meldrum, *Light: Science & Applications* **2018,** *7* (1), 101.

Contributions: Synthesis and characterization, fundamental investigation of the chromophore, writing of parts of the manuscript.

"Studies on the Biocompatibility of Poly(diethyl vinyl-phosphonate) with a New Fluorescent Marker", C. Schwarzenböck, S. I. Vagin, W. R. Heinz, P. J. Nelson and B. Rieger, *Macromolecular Rapid Communications* **2018,** *39* (15), 1800259.

Contributions: Idea & concept, synthesis and characterization, writing of parts of the manuscript.

"Metal–Organic Framework with Color-Switching and Strongly Polarized Emission", H. Wang, S. I. Vagin, S. Lane, W. Lin, V. Shyta, W. R. Heinz, C. Van Dyck, A. J. Bergren, K. Gardner, B. Rieger and A. Meldrum, *Chemistry of Materials* **2019,** *31* (15), 5816-5823.

Contributions: Synthesis and characterization, basic investigation of the optical properties and the anisotropy, writing of parts of the manuscript.

"An in situ Investigation of the Thermal Decomposition of Metal-Organic Framework NH_2-MIL-125 (Ti)", M. Z. Hussain, M. Bahri, W. R. Heinz, Q. Jia, O. Ersen, T. Kratky, R. A. Fischer, Y. Zhu and Y. Xia, *Microporous and Mesoporous Materials* **2021,** *316*, 110957.

Contributions: Design, execution, evaluation, and manuscript writing regarding thermogravimetric analysis.

List of Conference Contributions:

[1] 2nd European Conference on Metal-Organic Frameworks and Porous Polymers (EuroMOF 2017), Delft, Netherlands, October 2017, Poster presentation: **"Paddle-Wheel based 3D-Connected MOFs: Defect-Engineering and Metal Substitution"**.

[2] 6th International Conference on Metal-Organic Frameworks (MOF 2018), Auckland, New Zealand, December 2018, Poster presentation: **"$[Ru_xRh_{3-x}(BTC)_2]$ – Adding Precious to Mixed-Metal MOFs"**.

[3] Symposium on Porous Coordination Polymers and Metal-Organic Frameworks (docMOF), Munich, Germany, May 2019, Poster presentation: **"Ru-BTC – A Mixed Component HKUST-1 Analogue"**.

[4] *3rd European Conference on Metal-Organic Frameworks and Porous Polymers (EuroMOF 2017)*, Paris, France, October 2019, Poster presentation: **"Thermal Defect-Engineering (TDE) of Precious Metal-based HKUST-1 Analogues $[Ru_xRh_{3-x}(BTC)_2]$"**.

Appendix

ESI Study I

CHEMCATCHEM

Supporting Information

Defect-Engineered Ruthenium MOFs as Versatile Heterogeneous Hydrogenation Catalysts

Konstantin Epp, Ignacio Luz, Werner R. Heinz, Anastasia Rapeyko, Francesc X. Llabrés i Xamena,* and Roland A. Fischer*

S1. ^{1}H NMR analysis

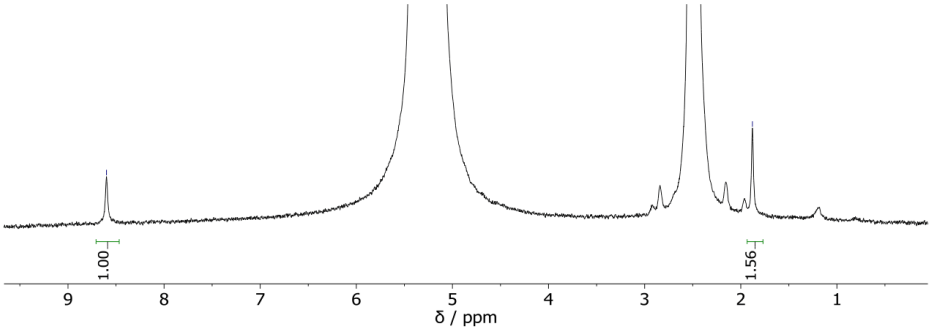

Figure S1a. Acid-digested ^{1}H NMR spectra of thermally activated RuMOF **1** in DMSO-d_6.

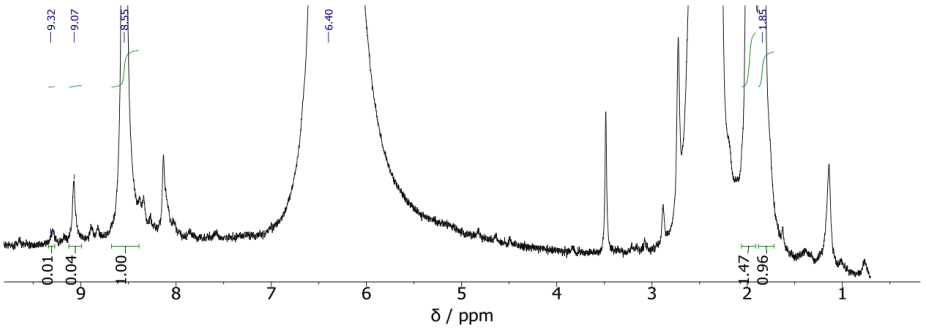

Figure S1b. Acid-digested ^{1}H NMR spectra of **D30** in DMSO-d_6.

S2. Elemental analysis

Table S2. Results obtained from element analysis of **D30**.

atom	calc. [%]	found [%]
N	0.99	0.89
C	30.71	31.77
H	1.94	2.84

S3. Powder X-ray diffraction (PXRD)

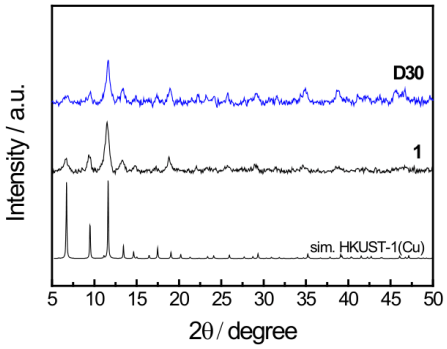

Figure S3. Diffraction pattern of activated Ru-MOF **1** and defect engineered **D30** in comparison to simulated pattern of HKUST-1(Cu).

S4. Nitrogen Physisorption

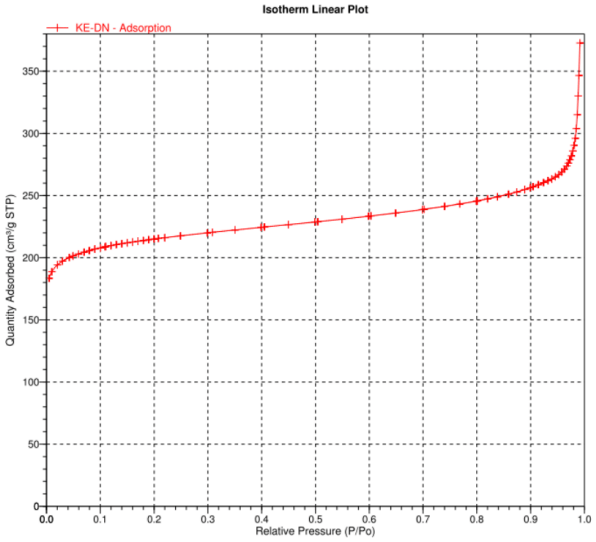

Figure S4. N_2-physisorption of defect engineered sample **D30.**

S5. Thermal gravimetric analysis (TGA)

TGA studies were performed for parent Ru-MOF **1** and **D30** (30% PYDC feed ratio) under oxidizing atmosphere using a N_2/O_2 flow (80/20), revealing their relatively high thermal

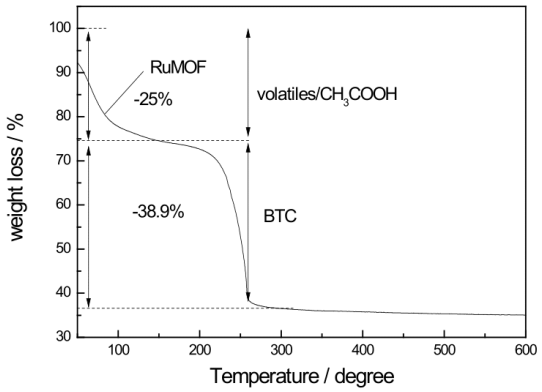

robustness up to ~220 °C.

S5a. Thermogravimetric analysis (TGA) of as synthesized **1** performed under oxidizing N_2/O_2 (80/20) flow using a heating ramp of 10°/min.

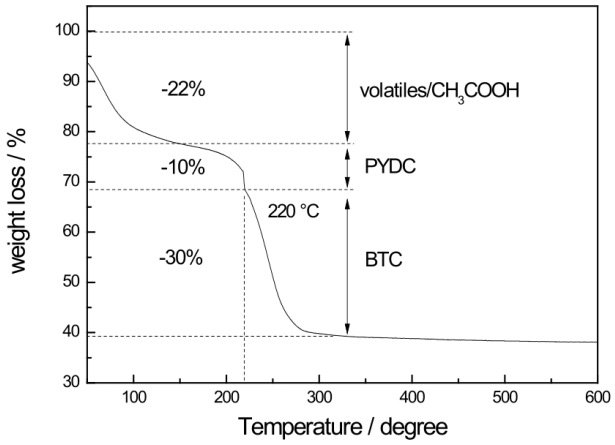

S5b. Thermogravimetric analysis (TGA) of as synthesized **D30** performed under oxidizing N_2/O_2 (80/20) flow using a heating ramp of 10°/min, revealing a third decomposition event (PYDC linker).

Notably, the nature of the TGA experiment changes, when oxidizing conditions are applied as opposed to more frequently used inert atmosphere utilizing N_2 as a carrier gas. Consecutively, the decomposition events of the organic compounds proceed on a faster time scale, due to the fact that the incorporated organic fraction may react with oxygen and release i.e. CO/CO_2. This exothermic decomposition ignites rupture of adjacent structures leading to accelerated framework pyrolysis. **D30** sample shows an additional decomposition event which lays near the decomposition temperature of BTC (~220 °C). The observed total loss in mass of about -10% is 1/3 in terms of total linker amount and is in good agreement to the feeding ratio of 30% PYDC and also to the data obtained by elemental analysis.

S6. Hot filtration test

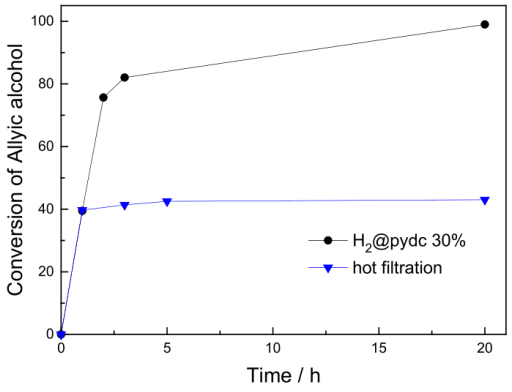

Figure S6. Hot-filtration test of H_2 pre-treated **D30** in the isomerization of 3-octene-1-ol.

S7. Reusability tests

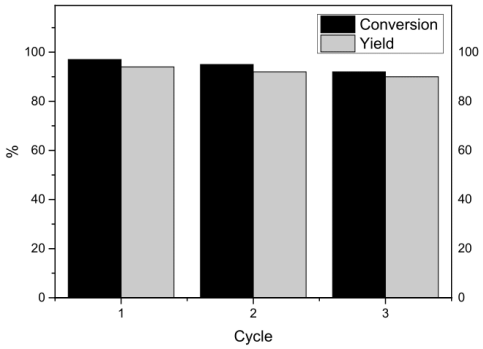

Figure S7. Results for the reusability experiment of the isomerization of allylic alcohols (after 17 h) under **D30** catalyst in 1 mL *i*-PrOH under 120 °C at 2 bar N_2.

S8. PXRD measurements before and after catalysis

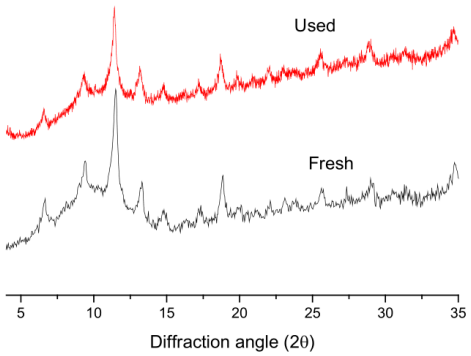

Figure S8. X-ray diffraction pattern (CuKα radiation) of fresh **D3** sample (bottom), and after being used in catalysis for 5 consecutive catalytic cycles (bottom).

S9. Transmission Electron Microscopy before and after Catalysis

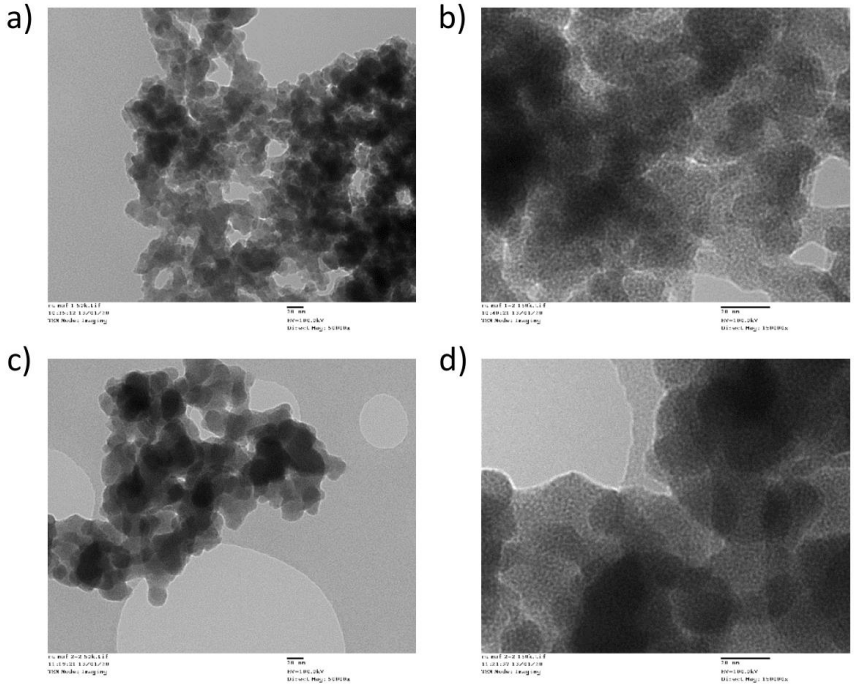

Figure S9. Transmission electron microscopy images of fresh **D3** sample (a and b), and after being used in catalysis for 5 consecutive catalytic cycles (c and d).

ESI Study II

Supporting Information

Mixed Precious-Group Metal-Organic Frameworks:

Case Study of the HKUST-1 Analogue $[Ru_xRh_{3-x}(BTC)_2]$

Werner R. Heinz,[a] Tim Kratky,[b] Markus Drees,[a] Andreas Wimmer,[c] Ondřej Tomanec,[d] Sebastian Günther,[b] Michael Schuster,[c] and Roland A. Fischer[a]

[a] Chair of Inorganic and Metal-Organic Chemistry, Department of Chemistry, Technical University of Munich, Lichtenbergstraße 4, 85748 Garching, Germany. E-mail: roland.fischer@tum.de

[b] Chair of Physical Chemistry with Focus on Catalysis, Department of Chemistry, Technical University of Munich, Lichtenbergstraße 4, 85748 Garching, Germany. E-mail: sebastian.guenther@tum.de

[c] Chair of Analytical Chemistry, Department of Chemistry, Technical University of Munich, Lichtenbergstraße 4, 85748 Garching, Germany. E-mail: michael.schuster@ch.tum.de

[d] Group of Carbon nanostructures and biomacromolecules, Regional Centre of Advanced Technology and Materials, Šlechtitelů 27, 78371 Olomouc, Czech Republic. E-mail: ondrej.tomanec@upol.cz

Table of contents

Experimental Details

General considerations

Trimesic acid (Sigma-Aldrich), $RuCl_3 \cdot x\ H_2O$ (Precious Metals Online), $Rh_2(OAc)_4$ (Sigma-Aldrich) and HPLC-grade acetone and ethanol (VWR Chemicals) were purchased commercially and used without further purification. Ultra-pure water was obtained using a Milli-Q purification system (18.2 MΩ cm^{-1}). Technical dichloromethane was purified using a MBraun SPS-800. $Ru_2(OAc)_4Cl$ was synthesized following literature procedures.[1] Desolvated MOFs were handled in a glovebox using argon (>99.996%; Westfalen).

Instrumentation

Powder X-Ray diffraction

All diffraction patterns were collected on a PANalytical Empyrean equipped with a Cu X-ray tube (λ = 0.154 nm) operated at 45 kV and 40 mA in a 2Θ range of 5-50° in steps of 0.0065651° (2Θ) with 6.3025 s/step. The incident beam was focussed on the sample through a focusing beam mirror with a 1/16° divergence slit and a nickel beta filter (0.2 mm). A PIXcel1D detector was used in receiving mode with a 1/8° anti-scatter slit and 0.04 rad soller slits. The activated samples were filled in borosilicate capillaries of 0.5 mm inner diameter and mounted onto a capillary spinner.

Elemental Analysis & ICP-MS

Determination of the elemental composition was performed together with the microanalytical laboratories of the chemistry department at the Technical University of Munich. Determination of C, H, N and S was carried out with a Hekatech EuroEA elemental analyser. Ru and Rh were initially determined after digestion of activated MOF samples in sulfuric acid at up to 200 °C with both atomic absorption spectroscopy (AAS) as well as inductively coupled plasma – mass spectrometry detection (ICP-MS). Those digestions at ambient pressure turned out to provide underestimated metal contents. This was potentially due to formation of volatile ruthenium oxide and chloride species.[2, 3]

1. R. W. Mitchell, A. Spencer and G. Wilkinson, *J. Chem. Soc., Dalton Trans.*, 1973, DOI: 10.1039/DT9730000846, 846-854.
2. Y. D. Kim, H. Over, G. Krabbes and G. Ertl, *Top. Catal.*, 2000, **14**, 95-100.
3. M. Binnewies, R. Glaum, M. Schmidt and P. Schmidt, *Chemical Vapor Transport Reactions*, 2012.

Thus, microwave-assisted digestions were developed, and quantitative analysis was performed using ICP-MS:

Microwave assisted sample digestion

Prior to quantitative measurements, all samples were digested adding a mixture of 1 mL HCl (30% (w/w), suprapur, Merck, Darmstadt, Germany) and 8 mL HNO_3 (65% (w/w), suprapur, Merck) to 1 to 3 mg of the Ru and Rh containing sample. All samples were weighted under inert gas to avoid hygroscopic mass effects. Samples and reagents were filled in a PTFE liner fixed in a closed pressure vessel. The digestion was performed in an ETHOS.lab microwave system (MLS, Leutkirch, Germany). After subjecting the samples to the digestion process including a ramp time of 10 min to 240 °C

followed by 30 min holding this temperature and a cooling step for another 120 min, clear orange solutions were obtained. These solutions were filled up to 50 mL using ultra-pure water (UPW) with a resistivity of 18.2 MΩ cm^{-1} provided by a Milli-Q-Gradient-System (Millipore GmbH, Billerica, MA, USA). For quantification, all digests were diluted 1:200 in a 1.625% HNO_3 (w/w) solution.

Quantification of Ru and Rh in digested samples

Quantitative analysis of Ru and Rh in the digested samples was carried out using an Agilent 7900 ICP-Q-MS (Agilent, Santa Clara, CA, USA) equipped with a collision cell technique (CCT) and an autosampler SPS4 (Agilent). Argon 4.8 was used as plasma gas. ^{101}Ru and ^{103}Rh were chosen as target masses to avoid potential isobaric interferences and measured in triplicate. ^{115}In was used as internal standard by adding traces of a stock solution containing 400 µg L^{-1} In (in 1.625% HNO_3 (w/w), Merck) *via* a Y-connecting tubing to the sample immediately before nebulization. Integration time for detection of ^{101}Ru and ^{103}Rh was set to 0.1 s, whereby ^{101}Ru was measured in He-CCT and ^{103}Rh in high-energy He-CCT to overcome polyatomic interferences. For calibration, solutions containing simultaneously Ru and Rh in a range of 1 to 50 µg L^{-1} (in 1.625% HNO_3) were prepared from the stock solution Periodic Table Mix II (Sigma Aldrich, St. Louis, MO, USA). UPW was used for all kinds of dilutions, HNO_3 (65% (w/w), suprapur) was used for acidification. All calibration solutions were measured under the same conditions as used for the samples.

Calculation of the sum formula

Based on determined elemental contents and assuming oxygen to complete the 100 wt-%, sum formulas were calculated and normalized to three metal atoms per repeating unit. The GRG-nonlinear solver function implemented in Microsoft Excel was used for compositional fittings assuming acetate and BTC as exclusive organic framework components. It should be mentioned, that other efforts to determine organic ligand ratios (BTC to acetate) have not been successful as typical sample digestions in diluted acids were not quantitative.

MAS-NMR spectroscopy

Magic angle spinning-NMR spectra were recorded on a Bruker Avance 300 with measurement frequencies of 300.130 MHz (^{1}H) and 75.468 MHz (^{13}C) in 4 mm ZrO_2 rotors at ambient temperature with D1 = 2 s. Sample tubes were rotated with 15 kHz. Proton spectra were recorded with single pulse technique (250 ppm spectral width, each 200 scans), ^{13}C spectra with cross polarisation (CPMAS) (0%, 50%, 100% Rh sample with 84,104; 30,440 and 9,800 scans respectively). Adamantane was used as external (secondary) reference with 2.00 ppm (^{1}H) / 29.472 ppm (^{13}C) chemical shift versus tetramethylsilane.

HR-TEM with EDS mapping

Samples were measured by High Resolution Transmission Electron Microscope (HRTEM) Titan G2 (FEI) with image corrector on accelerating voltage 80 kV. Images were taken with BM UltraScan CCD camera (Gatan). Energy Dispersive Spectroscopy (EDS) was performed in Scanning TEM (STEM) mode by Super-X system with four silicon drift detectors (Bruker). STEM images were taken with HAADF detector 3000 (Fishione). Spectra acquisition time was set to 600 s.

X-ray photoelectron spectroscopy (XPS)

X-ray photoelectron spectra were recorded on a *Leybold-Heraeus* LHS 10 spectrometer using a non-monochromatized Al K_α source (1486.7 eV). The powder samples were pressed into cavities and measured as pellets. Sample preparation and transfer into the XPS spectrometer were carried out under argon atmosphere. All spectra were recorded in an ultra-high vacuum chamber at a pressure below 5×10^{-8} mbar. The analyzer was operated at a constant pass energy of 100 eV leading to an

energy resolution with a full width at half-maximum (FWHM) of ~1.1 eV. In addition, a constant pass energy of 20 eV was used for the Ru 3d/C 1s region to gain spectral resolution (~0.8 eV FWHM). The energy scale of the spectra was corrected for sample charging by using the O 1s main signal (531 eV). Core level spectra were deconvoluted by using Doniach-Sunjic functions and linear background subtraction. To quantify the molar Rh/Ru ratio the Rh 3d and the Ru $3p_{3/2}$ signals were integrated due the overlap of Ru 3d and C 1s. Depth profiling was carried out by removing the top layers of the samples using Ar ion sputtering and subsequent XPS measurements. For sputtering, a *Leybold-Heraeus* IQE 12 ion gun was operated at an Ar ion current of 0.6 µA and a kinetic energy of 2 kV leading to a sputtering rate of ~ 1 Å/min.

Nitrogen and carbon dioxide sorption measurements

Sorption experiments were conducted using a Micromeritics 3Flex with 50 to 80 mg of desolvated sample. Prior to the measurement each sample was additionally degassed at 150°C for >10h. Nitrogen isotherms were recorded at 77K, CO_2 isotherms at 195K respectively. The BET surface area was calculated using data points in the relative pressure range of 0.01 to 0.1 in the adsorption branch with the Rouquerol consistency criteria taken into account.

Fourier-transform infrared spectroscopy

FT-IR spectra were recorded from finely ground activated powder samples under argon atmosphere in a glovebox using a Bruker ALPHA FTIR spectrometer equipped with a Pt attenuated total reflectance (ATR) unit at room temperature in the range of 400 to 4000 cm^{-1} with a resolution of 2 cm^{-1} and 24 scans per measurement. A pyroelectric deuterated L-alanine doped triglycine sulfate (RT-DLaTGS) detector was used.

Raman spectroscopy

Raman spectroscopy was measured with an inVia Reflex Raman System with an optical microscope (Leica DM2700M, 50x magnification) coupled to a Renishaw R04 Raman spectrometer with 532 nm laser wavelength (Laser: RL532C, Class 3B) with activated samples filled into Borosilicate glass capillaries (0.5 mm inner diameter) under argon atmosphere. A Renishaw 266n10 detector was used. All samples were measured with 10 s exposure time, 5 % laser power and 10 accumulations (exception 0%Rh sample: 10s exposure, 1% laser Power, 10 accumulations).

Solid-state UV / Vis spectroscopy

Absorption spectra were recorded with a Shimadzu UV3600Plus UV VIS NIR spectrophotometer from 300 to 800 nm. The system is equipped with halogen and deuterium lamps. R-928 photomultiplier tube (UV & VIS <700 nm) and InGaAs photodiode (VIS >700 nm) were used to detect the light. Automatic change of the lamp and the integrated detector occurred at 395 nm and 700 nm respectively. Samples were pressed between two optical glass plates and boundaries sealed with Teflon® grease under argon.

DFT calculations of Ru- and Rh-paddle-wheel complexes

All calculations have been performed with the Gaussian 16 suite of software[4]. The level of theory included the use of the hybrid DFT functional B3LYP together with the basis set 6-31+G** for C,H,O, Cl.[5,6] Ru and Rh have been described by the Stuttgart-Dresden97-ECP[7].

All structures have been optimized until no negative frequencies haven been calculated by frequency analysis. Frequencies calculation have been also used to determine unscaled frequencies and IR and Raman intensities. UV-VIS spectra of selected singlet state compounds have been calculated by time-dependent DFT[8] taking into account the three most probable electon transitions to singlet and triplet excited states.

4. Gaussian 16, Revision B.01, M. J. Frisch, G. W. Trucks, H. B. Schlegel, G. E. Scuseria, M. A. Robb, J. R. Cheeseman, G. Scalmani, V. Barone, G. A. Petersson, H. Nakatsuji, X. Li, M. Caricato, A. V. Marenich, J. Bloino, B. G. Janesko, R. Gomperts, B. Mennucci, H. P. Hratchian, J. V. Ortiz, A. F. Izmaylov, J. L. Sonnenberg, D. Williams-Young, F. Ding, F. Lipparini, F. Egidi, J. Goings, B. Peng, A. Petrone, T. Henderson, D. Ranasinghe, V. G. Zakrzewski, J. Gao, N. Rega, G. Zheng, W. Liang, M. Hada, M. Ehara, K. Toyota, R. Fukuda, J. Hasegawa, M. Ishida, T. Nakajima, Y. Honda, O. Kitao, H. Nakai, T. Vreven, K. Throssell, J. A. Montgomery, Jr., J. E. Peralta, F. Ogliaro, M. J. Bearpark, J. J. Heyd, E. N. Brothers, K. N. Kudin, V. N. Staroverov, T. A. Keith, R. Kobayashi, J. Normand, K. Raghavachari, A. P. Rendell, J. C. Burant, S. S. Iyengar, J. Tomasi, M. Cossi, J. M. Millam, M. Klene, C. Adamo, R. Cammi, J. W. Ochterski, R. L. Martin, K. Morokuma, O. Farkas, J. B. Foresman, and D. J. Fox, Gaussian, Inc., Wallingford CT, **2016**.

5. a) A.D. Becke, *J. Chem. Phys*. **1993**, 98, 5648-5652; b) C. Lee, W. Yang, R.G. Parr, *Phys. Rev. B* **1988**, *37*, 785-789; c) S.H. Vosko, L. Wilk, M. Nusair, *Can. J. Phys.* **1980**, *58*, 1200-1211; d) P.J. Stephens, F.J. Devlin, C.F. Chabalowski, M.J. Frisch, *J.Phys.Chem.* **1994**, 98, 11623-11627.

6. a) W.J. Hehre, R. Ditchfield and J.A. Pople, J. Chem. Phys. **1972**, *56,* 2257-2261 (1972); b) T. Clark, J. Chandrasekhar, G. W. Spitznagel, and P. v. R. Schleyer, *J. Comp. Chem.*, **1983**, *4*, 294-301; c) M.M. Francl, W.J. Petro, W.J. Hehre, J.S. Binkley, M.S. Gordon, D.J. DeFrees and J.A. Pople, *J. Chem. Phys.* **1982**, *77*, 3654-3665.

7. a) A. Bergner, M. Dolg, W. Kuechle, H. Stoll, H. Preuss, *Mol. Phys.* **1993**, *80*,1431-1441 ; b) M. Kaupp, P. v. R. Schleyer, H. Stoll, H. Preuss, *J. Chem. Phys.* **1991**, *94*, 1360-1366; c) M. Dolg, H. Stoll, H. Preuss, R.M. Pitzer, *J. Phys. Chem.* **1993**, *97*, 5852-5859.

8. a) R. E. Stratmann, G. E. Scuseria, M. J. Frisch, *J. Chem. Phys.*, **1998**, *109*, 8218-24. b) F. Furche and R. Ahlrichs, *J. Chem. Phys.*, **2002**, *117*, 7433-7447.

Thermogravimetric analysis

Thermal stability of the materials was determined with a Mettler Toledo TGA/DSC 1 in aluminium oxide pans (70 µL with lid) with sample amounts of 1 to 5 mg. Samples of activated materials were taken under inert conditions in a glovebox and transferred to the measurement chamber in screw capped vials immediately prior to the measurement. The following thermal program was applied using synthetic air (20 mL min^{-1}, Westfalen, 80% N_2; 20% O_2): At 30 °C isothermal equilibration (15 min), ramp from 30 °C to 700 °C with 10 K min^{-1}, at 700 °C isothermal equilibration (15 min).

Additional information

Composition

Table S 1: Comparison of total metal contents determined by TG analysis and ICP-MS after digestion.

Sample	TGA residue (metal oxide) [%]	M_{total} (TGA) [%]	M_{total} (ICP) [%]
0 % Rh	48.2	38.9	38.9
5 % Rh	47.7	38.5	37.5
10 % Rh	48.3	39.0	38.2
20 % Rh	47.9	38.7	35.7
50 % Rh	49.9	40.4	39.6
75 % Rh	49.4	40.0	40.2
95 % Rh	48.3	39.2	41.0
100 % Rh	49.6	40.2	40.5

MAS-NMR spectroscopy

To confirm the findings of elemental analysis fittings regarding organic constituents, MAS-NMR was performed with 0%, 50% and 100% Rh samples. Ruthenium containing samples did not produce spectra with valuable information due to paramagnetism of the Ru_2 cores. However, the obtained spectra for 100% Rh sample (pure Rh-BTC) reveal some interesting information. In the ^{1}H-NMR spectrum, two singlets at 1.88 ppm and 8.74 ppm appear together with a set of rotation side bands shifted by the rotational frequency (15 kHz). Unambiguously, the set of signals centred at 1.88 ppm can be assigned to acetate protons while the one centred at 8.74 ppm originates from aromatic BTC protons. Total signal integration (including rotational side bands) indicates a molar BTC to acetate ratio (≈1.4) which is in accordance with the calculated composition based on EA values (≈1.3). The ^{13}C-NMR spectrum shows mainly three independent singlets. These signals can be assigned to carboxylate (182.4 ppm), aromatic (130.5 ppm) and aliphatic (19.4 ppm) carbon atoms representing BTC and acetate as framework constituents. Due to cross-polarization excitation, a quantitative comparison based on ^{13}C-NMR is not suitable. Low intensity signals (191.2; 174.2; 163.2 ppm) may be attributed to traces of carboxylates bound differently.

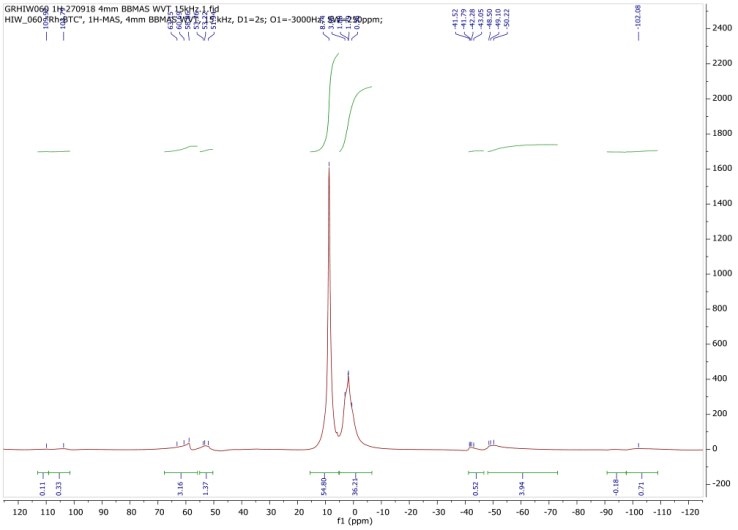

Figure S 1: Proton MAS-NMR spectrum of 100% Rh sample with signal integration.

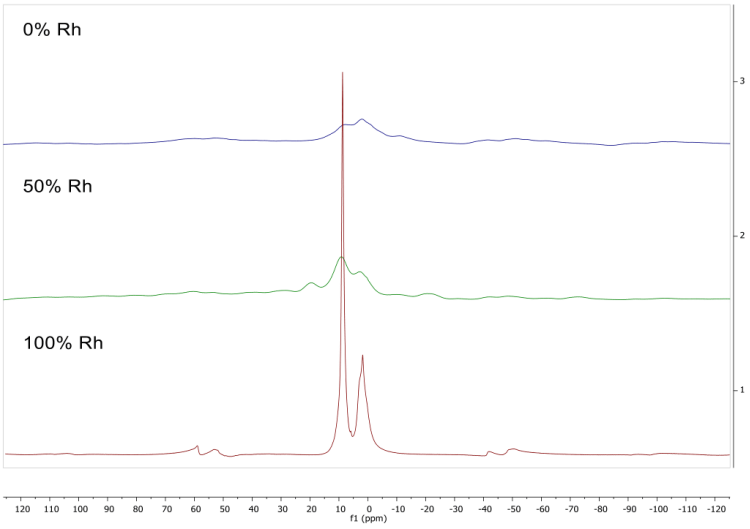

Figure S 2: Proton MAS-NMR spectra of 0%, 50% and 100% Rh samples.

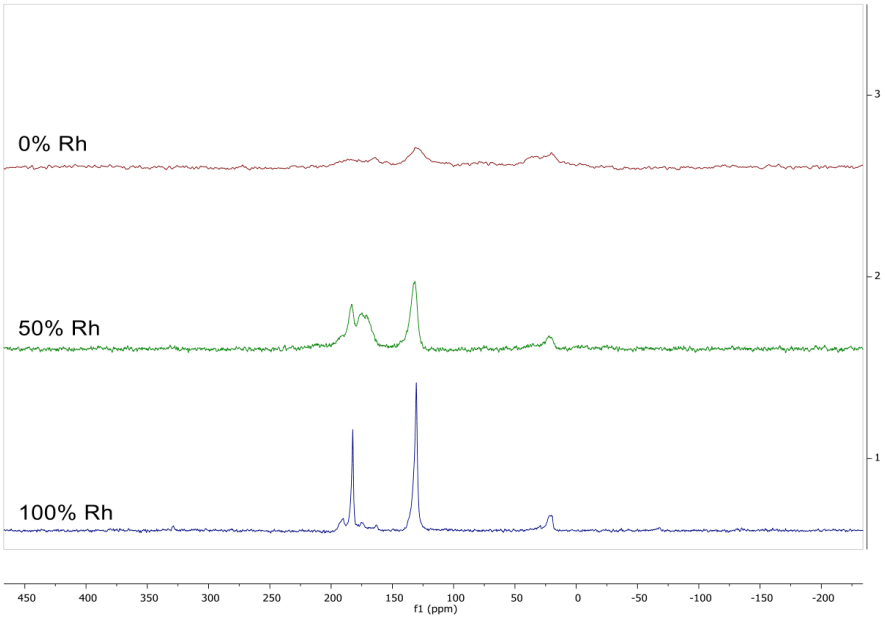

Figure S 3: ^{13}C-MAS-NMR spectra of 0, 50 and 100% Rh samples. Cross polarization was used.

HR-TEM-based elemental mapping

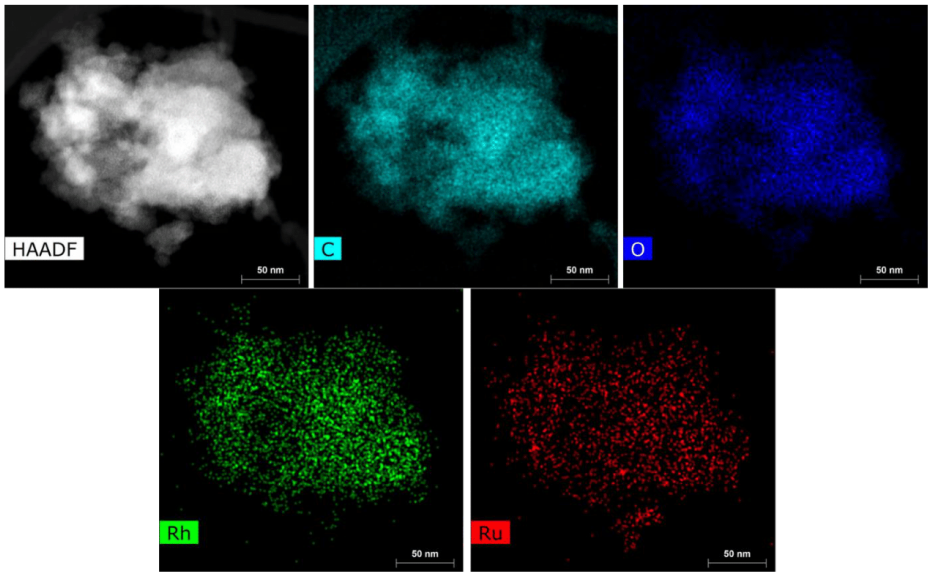

Figure S 4: HR-STEM images of representative particle of 75% Rh sample: From left to right: HAADF image and elemental mapping for C, O, Ru and Rh (map1).

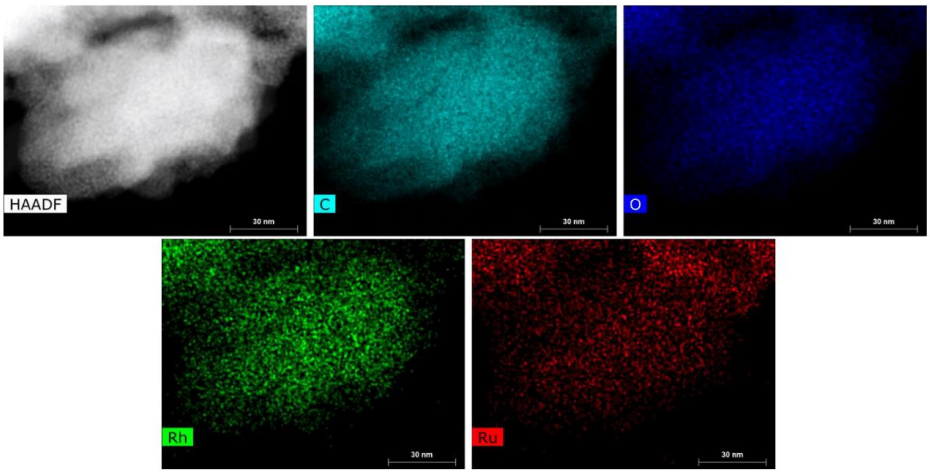

Figure S 5: HR-STEM images of representative particle of 75% Rh sample: From left to right: HAADF image and elemental mapping for C, O, Ru and Rh (map2).

HR-TEM images

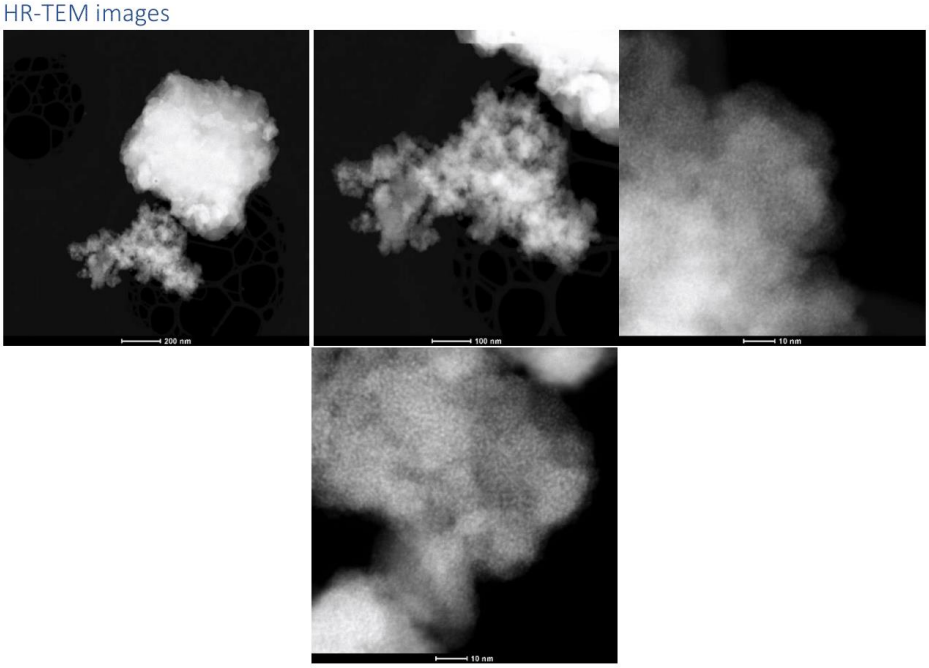

Figure S 6: HAADF-TEM images of 50% Rh sample.

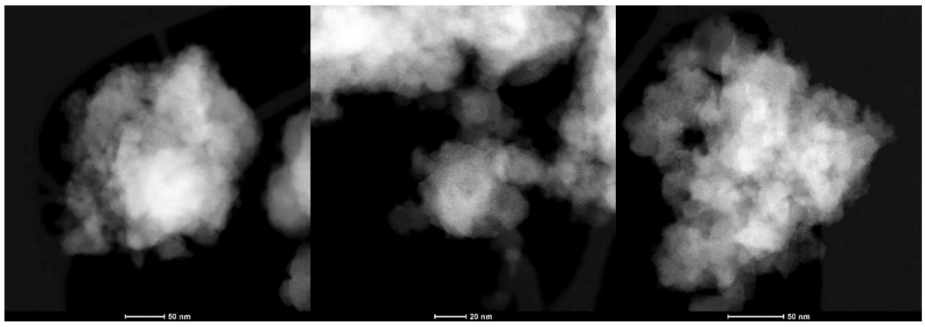

Figure S 7: HAADF-TEM images of 75% Rh sample.

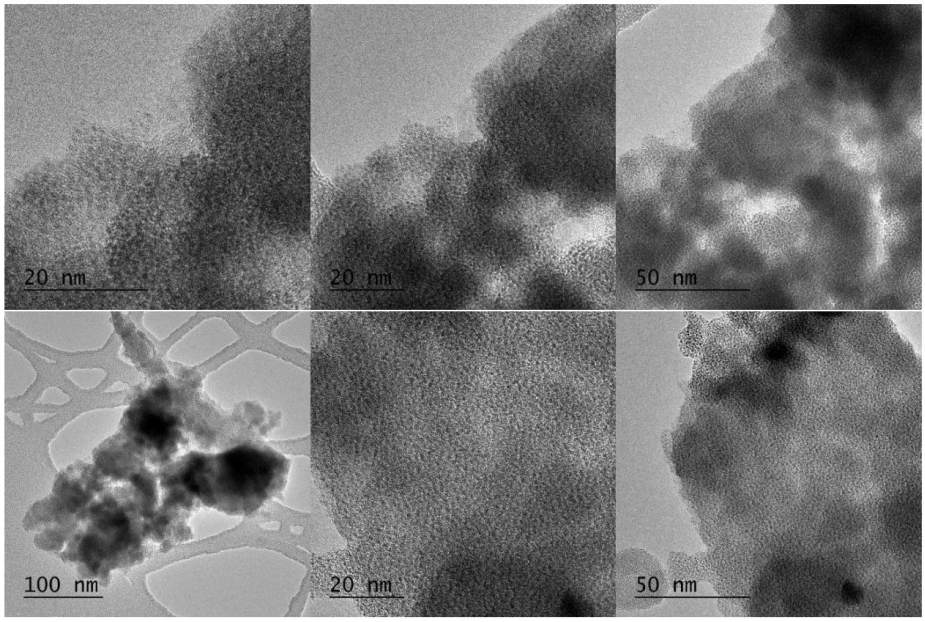

Figure S 8: HR-TEM images of 50% Rh sample.

XPS

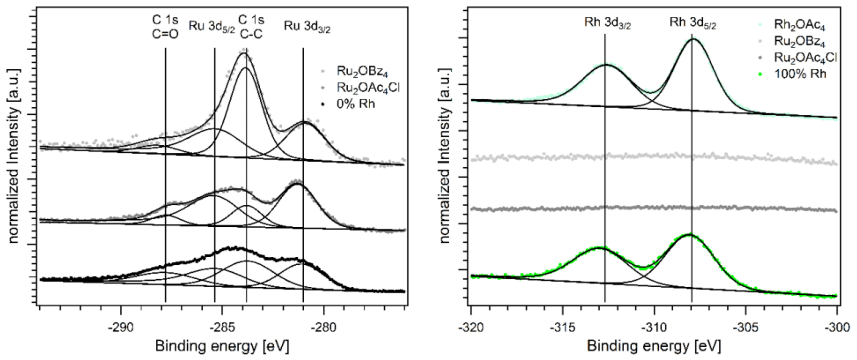

Figure S 9: Left: XP spectra showing Ru 3d and C 1s region of Ru-BTC and Ru containing reference substances. Right: XP spectra showing Rh 3d region of Rh-BTC and Rh-containing and Rh-free reference compounds.

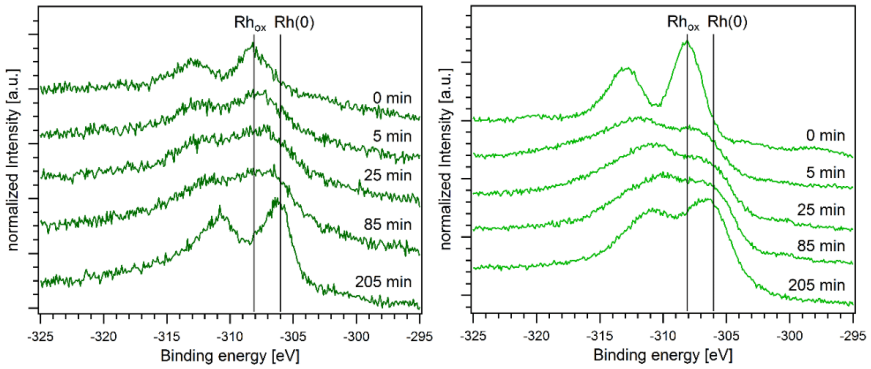

Figure S 10: XP spectra of Rh 3d peaks indicating sputter-induced metalation: Left: 20%Rh sample; Right: 75%Rh sample.

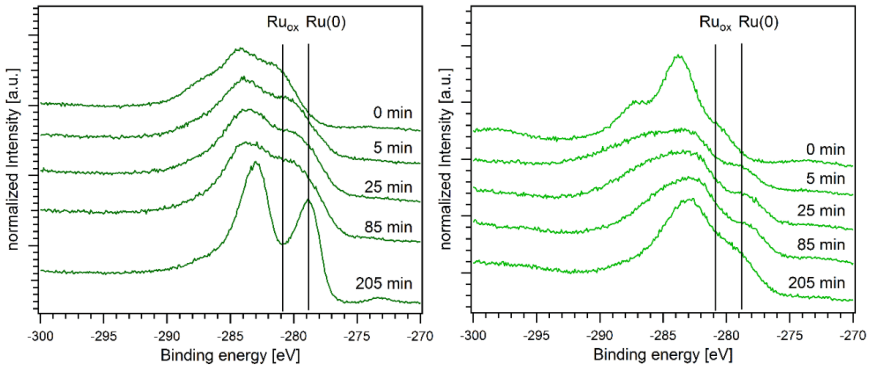

Figure S 11: XP spectra of Ru 3d peaks indicating sputter-induced metalation: Left: 20%Rh sample; Right: 75%Rh sample.

Table S 2: Found Rh content of selected MPG-MOFs related to the total metal content based on XPS.

Sample	Found Rh : M_{total} ratio
0% Rh	0%
20% Rh	21±2%
50% Rh	45±3%
75% Rh	75±2%
100% Rh	100%

Table S 3: Depth profiling of 20% Rh and 75% Rh samples and found Rh contents related to the total metal content

Overall sputtering time	Found Rh : M_{total} ratio	
	20% Rh sample	75% Rh sample
0 min	21±2%	75±2%
5 min	22±2%	76±2%
25 min	21±2%	75±2%
85 min	24±4%	75±2%
205 min	24±4%	76±2%

Sorption experiments

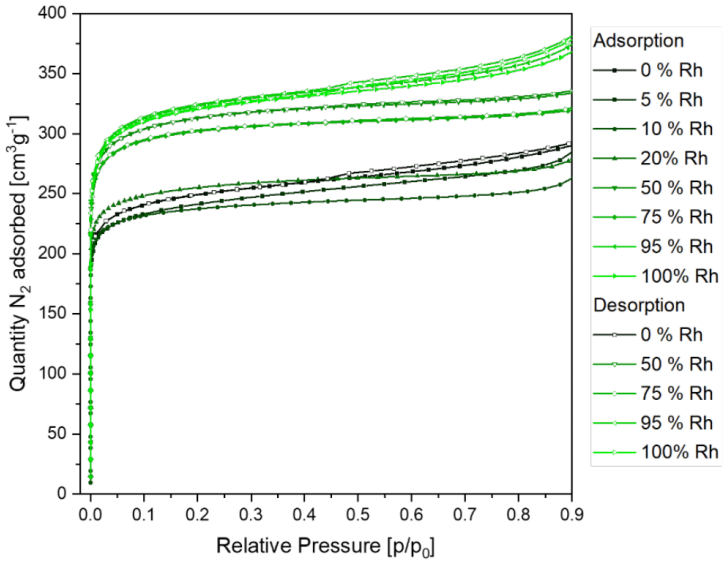

Figure S 12: Nitrogen sorption isotherms showing both adsorption and desorption branches. Isotherms were recorded at 77K. Closed symbols represent data points from adsorption branch, open symbols represent data points from desorption branch.

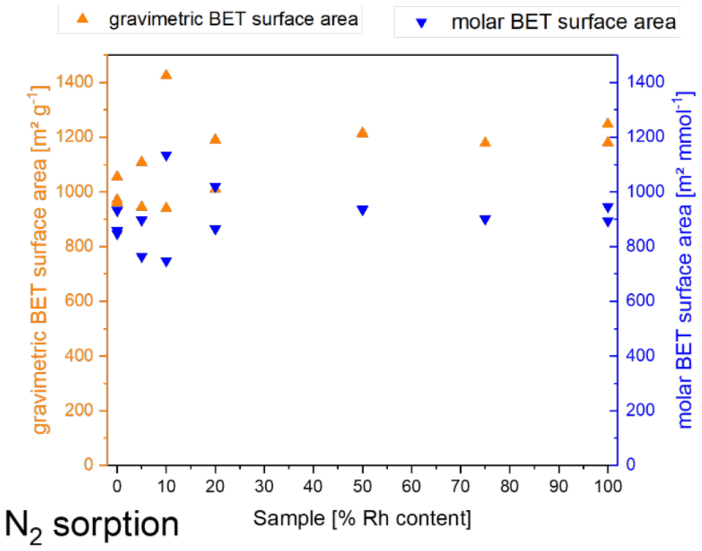

Figure S 13: Trend of gravimetric and molar BET surface areas of samples from different batches. Data was obtained with nitrogen as sorptive at 77 K.

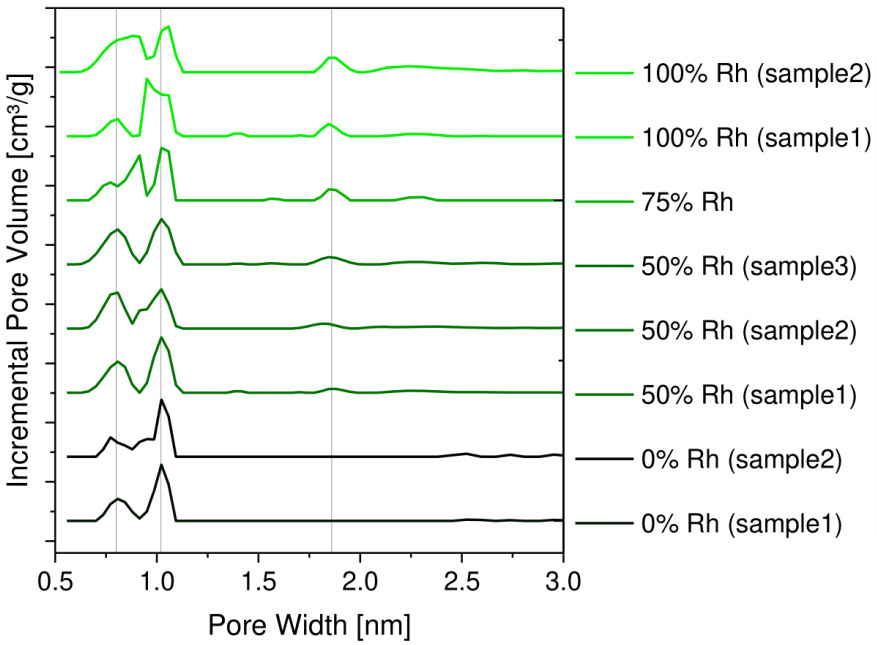

Figure S 14: DFT-based pore size distribution of different RuRh-BTC samples calculated from adsorption branches of sorption experiments. Broadening of pore size distribution and evolution of mesopore fractions occur upon Rh increase. Absolute pore size values might be shifted due to the chosen parameters (cylindrical pores on a silicon oxide substrate)

Vibrational spectroscopy

Table S 4: Experimental vibration frequencies in RuRh-MPG-MOFs and calculated modes based on the following model compounds: [a] $[Rh_2(OBz)_4(H_2O)_2]$, [b] $[Rh_2(H_2BTC)_4]$, [c] $[Rh_2(OBz)_4Cl_2]^{2-}$, [d] $[Rh_2(OBz)_4Cl]^-$, [e] $[Rh_2(OAc)_4]$, [f] $[Rh_2(OAc)_3(OBz)]$, [g] cis-$[Rh_2(OAc)_2(OBz)_2]$, [h] trans-$[Rh_2(OAc)_2(OBz)_2]$, [i] $[Rh_2(OAc)(OBz)_3]$.

Experimental frequencies [cm^{-1}]		Calculated frequencies [cm^{-1}]		Assigned vibration mode
IR mode	Raman mode	IR mode	Raman mode	
		1767[b]	1767[b]	$\nu_{as}(COOH)_{free\ acid}$
1687	1688			$\nu_{as}(COO)_{low\ coord}$
1622	1606	1622[b], 1627[d], 1604[e], 1609[f], 1612[i]	1611[b],	$\nu_{as}(COO) + \delta_{ip}(C\text{-}H_{arom})$
		1617[a]	1617[a]	$\nu_{as}(COO) + \nu_s(C\text{=}C_{arom})$
1577		1575		$\nu_{as}(COO) + \nu_s(C\text{=}C_{arom})$
	1503		1508[a], 1511[e], 1510[f]	$\nu_{as}(COO)$
	1452		1453[b]	$\nu_s(COO) + \delta_{ip}(C\text{-}H_{arom})$
1448		1446[b]		$\delta_{ip}(C\text{-}H_{arom})$
		1457[e]		$\delta(C\text{-}H_{OAc})$
1438		1439[e], 1434[i], 1425[i]		$\delta(C\text{-}H_{OAc})$
	1383	1395[a]	1395, 1411[a]	$\nu_s(COO)$
1366		1351[b]		$\nu_s(COO)$
1115		1176[a], 1151[b], 1113[b]	1141[a]	$\delta_{ip}(C\text{-}H_{arom})$
	1003		997[a]	$\nu_s(C\text{=}C_{arom})$
939		942[b]		$\delta_{oop}(C\text{-}H_{arom})$
	845		852, 859[a], 845[f]	$\delta_{ip}(COO)$
	792		804[a]	$\delta_{oop}(COO\ \&C\text{-}H_{arom})$
732-738		712[a], 740[b]		$\delta_{oop}(C\text{-}R_{arom})$
		685[e]		$\delta_{ip}(COO)$
523		515[a], 521[c], 524[c], 515[g]	515[c]	$\nu_{as}(ORhO)$
		529[b]		$\delta(C\text{=}C_{arom}) + \nu_{as}(ORhO)$
	375		357[c]	$\nu(Rh\text{-}Rh\text{-}Cl)$
			357[f], 358[g], 357[i]	$\nu_s(ORhO)$
	333		345[a], 318, 346[e], 340[f], 344[h]	$\nu(Rh\text{-}Rh)$
	278			$\nu(Rh\text{-}Cl)$
			245[d]	$\nu(Rh\text{-}Rh\text{-}Cl)$
	250 (Rh-BTC)		225[c]	$\nu_s(Rh\text{-}Rh) + \delta_{oop}(COO)$
	150			$\nu(Rh\text{-}Rh)$
			148[c]	$\nu_s(Rh\text{-}Cl)_2$
			148[e], 150[f], 149[g], 152[i]	$\delta(PW)$

FT-IR spectroscopy

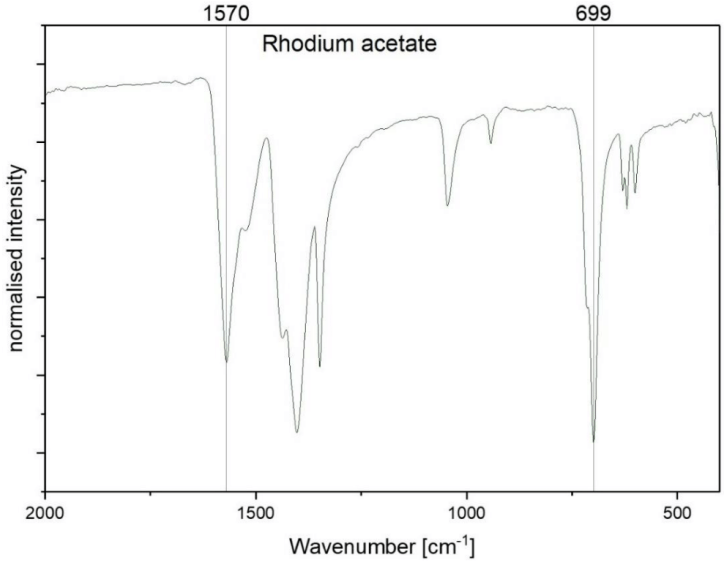

Figure S 15: FT-IR spectrum of dirhodium tetraacetate.

SS-UV / VIS spectroscopy

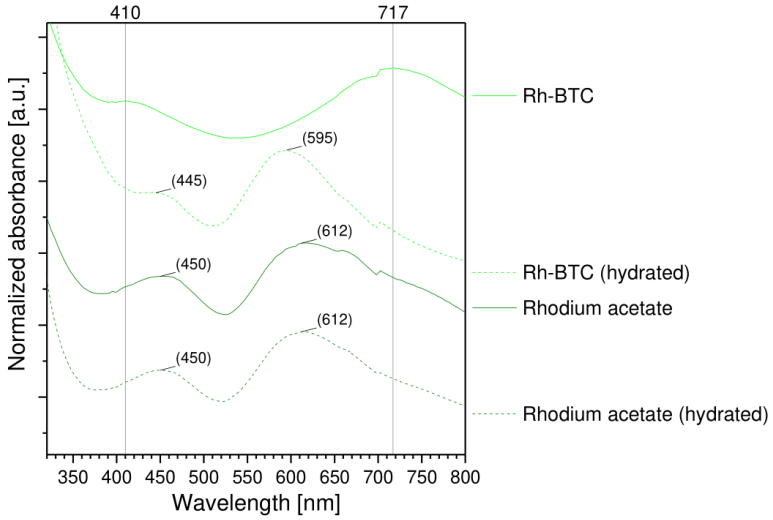

Figure S 16: SS-UV / VIS spectra of activated Rh-BTC and after rehydration in comparison with Rhodium acetate.

Table S 5: Comparison of optical properties between experimental and theoretical results (this work) and the literature from different dirhodium tetracarboxylates. [a] experimental result, this work; [b] theoretical result, this work; [c] experimental result from Kitchens et al.

Compound	Wavelength band **I** [nm]	Wavelength band **II** [nm]
Rh-BTC activated[a]	410	717
Rh-BTC rehydrated[a]	445	595
$[Rh_2(OAc)_4]$[a]	450	612
$[Rh_2(OAc)_4(H_2O)_2]$[a]	450	612
$[Rh_2(OBz)_4(H_2O)_2]$[b] (singlet)		601
$[Rh_2(OBz)_4(H_2O)_2]$[b] (triplet)		1230
$[Rh_2(OBz)_4]$[b] (singlet)		916
$[Rh_2(OBz)_4]$[b] (triplet)		1025
$[Rh_2(OBz)_4Cl_2]^{2-}$ [b] (singlet)		620
$[Rh_2(OBz)_4Cl]^-$ [b] (singlet)		677
$[Rh_2(OAc)_4]$[b] (singlet)		910
$[Rh_2(OAc)_3(OBz)_1]$[b] (singlet)		912
cis-$[Rh_2(OAc)_2(OBz)_2]$[b] (singlet)		913
Trans-$[Rh_2(OAc)_2(OBz)_2]$[b] (singlet)		914
$[Rh_2(OAc)_1(OBz)_3]$[b] (singlet)		914
$[Rh_2(OAc)_4]$[c]	442	617
$[Rh_2(OAc)_4(H_2O)_2]$[c]	441	584
$[Rh_2(OAc)_4(NH_3)_2]$[c]	442	528

Calculated vibration modes of selected model compounds

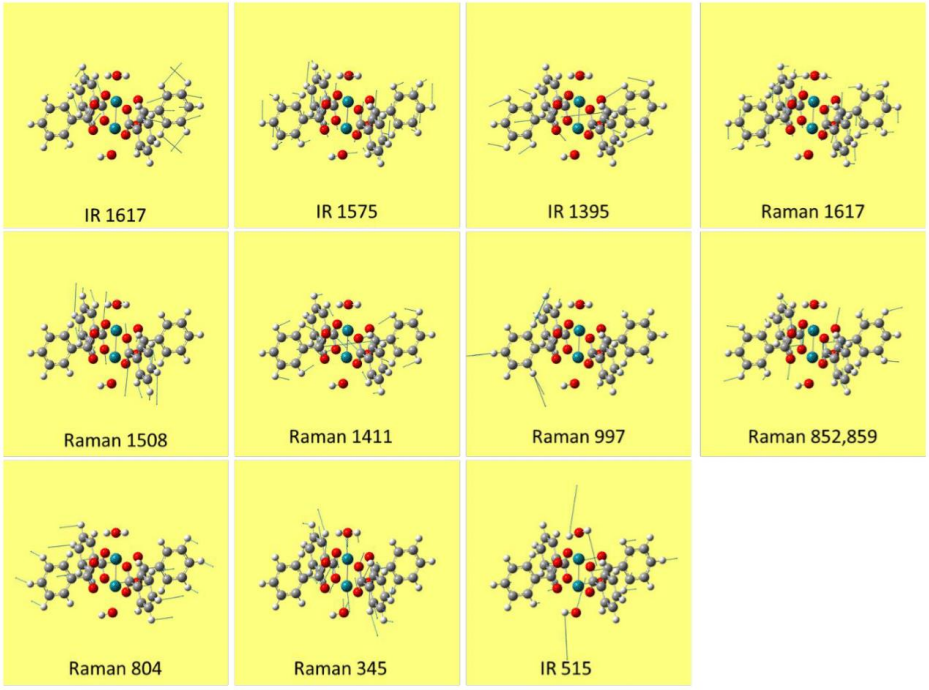

Figure S 17: Most prominent calculated vibrational modes of $[Rh_2(OBz)_4(H_2O)_2]$.

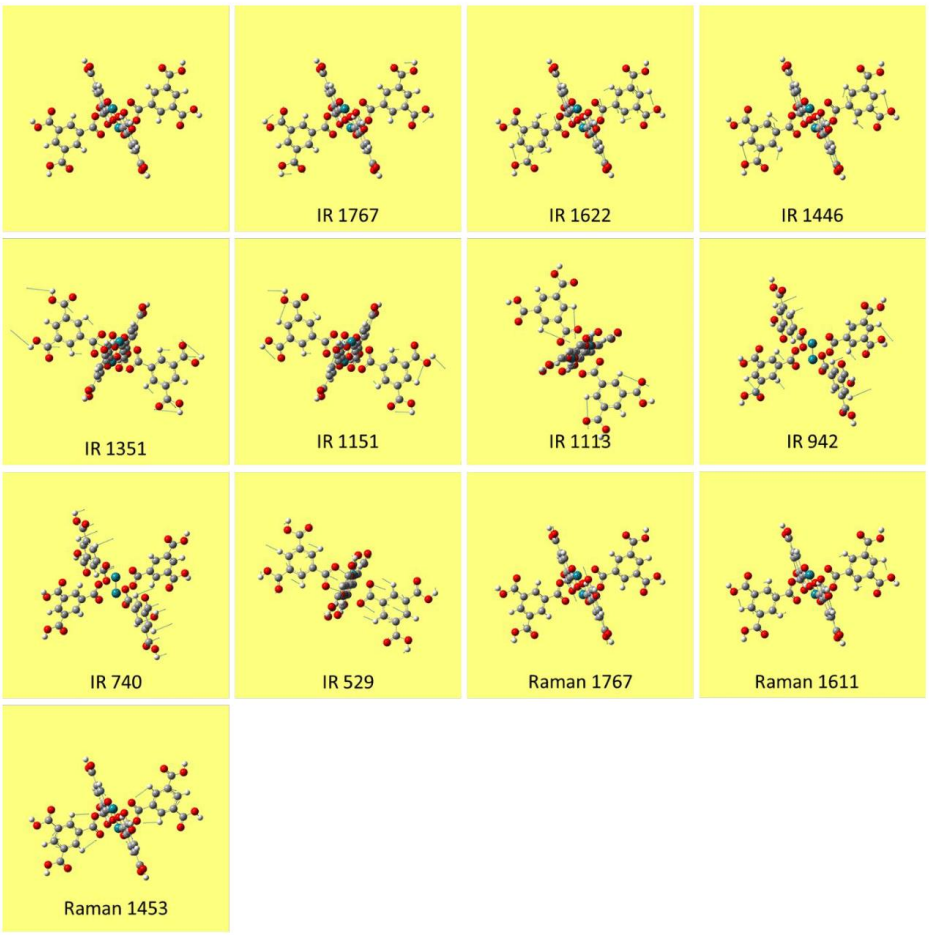

Figure S 18: Most prominent calculated vibrational modes of $[Rh_2(H_2BTC)_4]$.

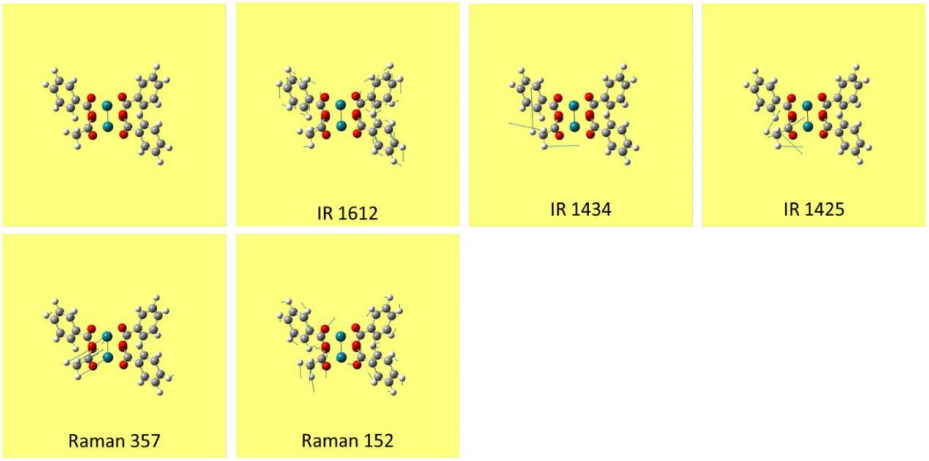

Figure S 19: Most prominent calculated vibrational modes of $[Rh_2(OBz)_3(OAc)]$.

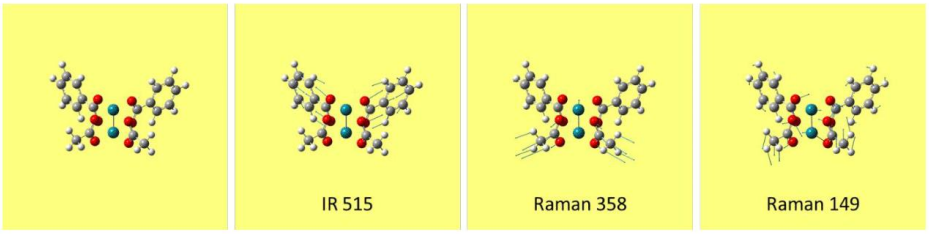

Figure S 20: Most prominent calculated vibrational modes of cis-$[Rh_2(OBz)_2(OAc)_2]$.

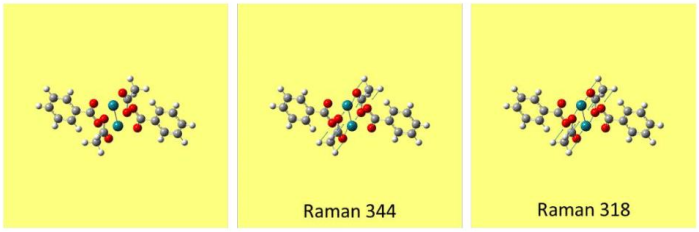

Figure S 21: Most prominent calculated vibrational modes of trans-$[Rh_2(OBz)_2(OAc)_2]$.

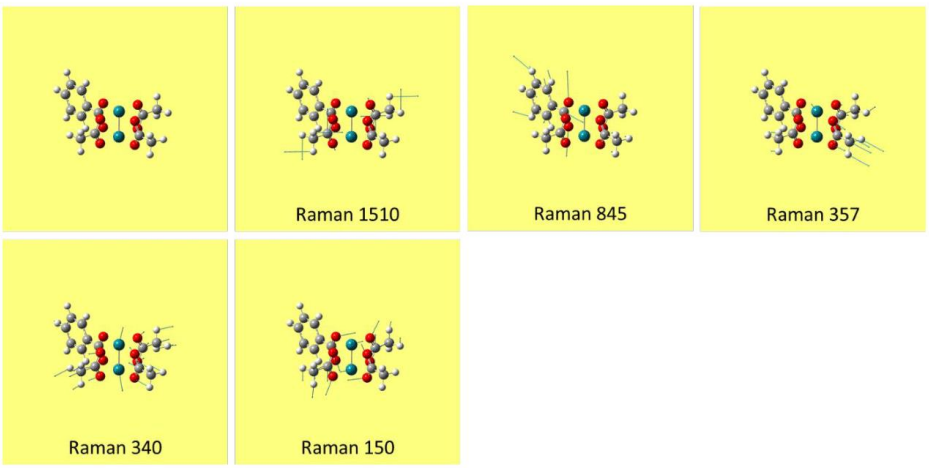

Figure S 22: Most prominent calculated vibrational modes of $[Rh_2(OBz)(OAc)_3]$.

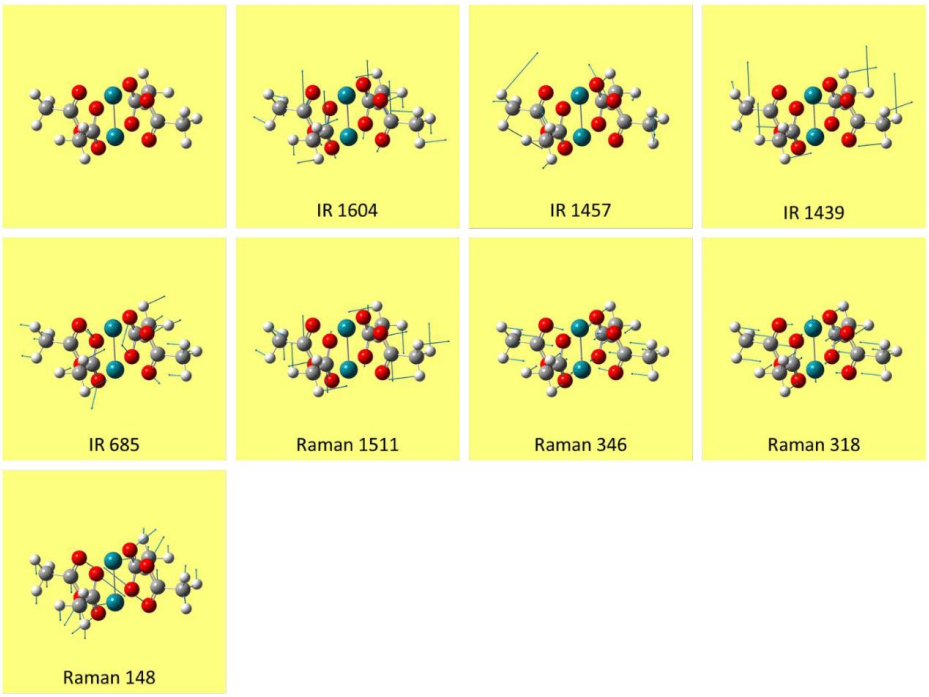

Figure S 23: Most prominent calculated vibrational modes of $[Rh_2(OAc)_4]$.

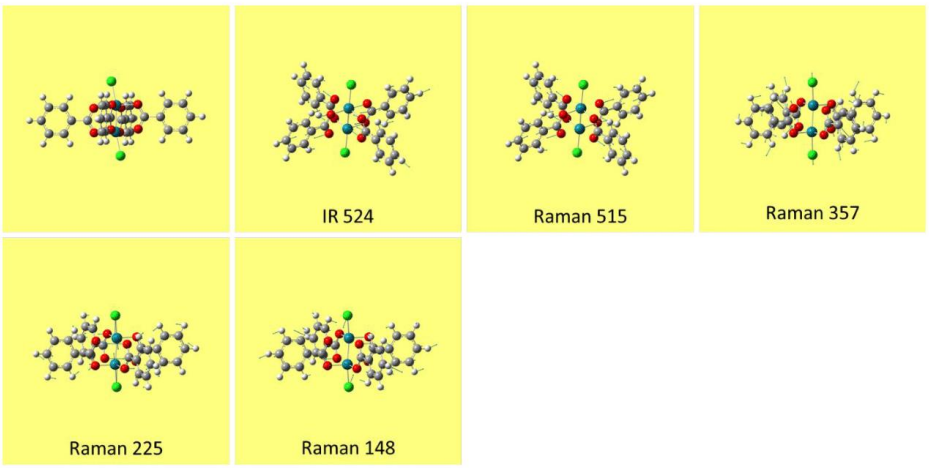

Figure S 24: Most prominent calculated vibrational modes of $[Rh_2(OBz)_4CL_2]^{2-}$.

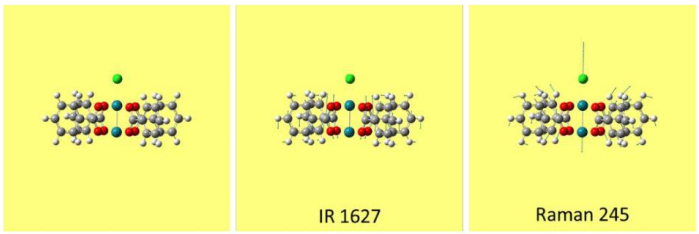

Figure S 25: Most prominent calculated vibrational modes of $[Rh_2(OBz)_4Cl]^{-}$.

Calculated molecules for the comparison of vibrational and UV/VIS spectra

Geometries and energies

$[Rh_2(OBz)_4(H_2O)_2]$ (singlet)

Charge=0, Multiplicity=1

Center Number	Atomic Number	Atomic Type	Coordinates (Angstroms) X	Y	Z
1	6	0	-2.863670	6.328446	-0.049415
2	6	0	-2.561080	5.715196	1.170524
3	6	0	-1.986406	4.444238	1.190181
4	6	0	-1.709466	3.778066	-0.012294
5	6	0	-2.013857	4.396048	-1.234147
6	6	0	-2.589397	5.666629	-1.250528
7	6	0	-1.093569	2.414807	0.001859
8	8	0	-0.854186	1.888338	1.142127
9	45	0	-0.011569	0.001451	1.203582
10	8	0	0.045219	0.193758	3.588471
11	8	0	-0.850695	1.875089	-1.125223
12	45	0	-0.006639	-0.009389	-1.203581
13	8	0	0.175927	-0.095563	-3.588470
14	8	0	1.885016	0.832811	-1.133073
15	6	0	2.416419	1.081374	0.000084
16	6	0	3.781576	1.693595	0.000064
17	6	0	4.460808	1.904462	1.208828
18	6	0	5.734037	2.474180	1.207455
19	6	0	6.336748	2.840703	-0.000024
20	6	0	5.662296	2.633773	-1.207461
21	6	0	4.390478	2.060925	-1.208747
22	8	0	1.877211	0.850175	1.133216
23	8	0	0.838279	-1.895232	-1.142190
24	6	0	1.072056	-2.424233	-0.001920
25	6	0	1.681110	-3.790562	0.012220
26	6	0	1.941740	-4.428225	1.234083
27	6	0	2.509651	-5.702236	1.250458
28	6	0	2.821699	-6.347069	0.049329
29	6	0	2.563197	-5.713992	-1.170622
30	6	0	1.994468	-4.440364	-1.190270
31	8	0	0.830569	-1.883895	1.125155
32	8	0	-1.884869	-0.858659	-1.134240
33	6	0	-2.423794	-1.084556	-0.000048
34	6	0	-3.788350	-1.696739	-0.000018
35	6	0	-4.405305	-2.041686	1.211325
36	6	0	-5.677277	-2.614470	1.209409
37	6	0	-6.341427	-2.843564	0.000087
38	6	0	-5.729164	-2.499201	-1.209285
39	6	0	-4.456125	-1.928781	-1.211307
40	8	0	-1.896601	-0.832527	1.134169
41	1	0	3.982825	1.615008	2.137727
42	1	0	3.856437	1.896175	-2.137590
43	1	0	6.256345	2.632119	2.146533
44	1	0	6.127325	2.919142	-2.146574
45	1	0	7.327770	3.285669	-0.000061
46	1	0	1.693195	-3.915425	2.156516
47	1	0	1.788061	-3.938470	-2.128783
48	1	0	2.708467	-6.192423	2.199054
49	1	0	2.804260	-6.213057	-2.104753
50	1	0	3.264006	-7.339254	0.063732
51	1	0	-3.877301	-1.858704	2.140484
52	1	0	-3.968644	-1.655789	-2.140528
53	1	0	-6.150410	-2.882514	2.149638

54	1	0	-6.243843	-2.674942	-2.149472
55	1	0	-7.332447	-3.288789	0.000131
56	1	0	-1.747730	3.956843	2.128687
57	1	0	-1.796172	3.869367	-2.156555
58	1	0	-2.773598	6.227100	2.104638
59	1	0	-2.824565	6.140473	-2.199112
60	1	0	-3.311964	7.317940	-0.063826
61	1	0	1.102439	0.141956	-3.736666
62	1	0	0.838206	0.728368	3.737348
63	1	0	-0.704195	0.770604	3.793438
64	1	0	0.109557	-1.039144	-3.792523

HF=-2055.2282792

$[Rh_2(OBz)_4(H_2O)_2]$ (triplet)

Charge=0, Multiplicity=3

Center Number	Atomic Number	Atomic Type	Coordinates (Angstroms) X	Y	Z
1	6	0	6.977156	0.111825	-0.165867
2	6	0	6.308462	0.167578	1.061018
3	6	0	4.914482	0.141144	1.098272
4	6	0	4.179303	0.060253	-0.093239
5	6	0	4.853705	0.007820	-1.322530
6	6	0	6.247680	0.032198	-1.356385
7	6	0	2.685974	0.033333	-0.064496
8	8	0	2.102791	0.032892	1.072321
9	45	0	-0.009058	0.011360	1.232447
10	8	0	0.983055	-0.315980	3.635019
11	8	0	2.080360	0.010424	-1.184381
12	45	0	0.009124	0.011464	-1.232527
13	8	0	-0.981449	-0.323733	-3.634492
14	8	0	-0.001435	-2.066266	-1.136158
15	6	0	0.007225	-2.648942	0.000008
16	6	0	0.011571	-4.145053	-0.000023
17	6	0	-0.135990	-4.850971	1.203033
18	6	0	-0.134468	-6.245818	1.201182
19	6	0	0.019778	-6.945060	-0.000049
20	6	0	0.169925	-6.244904	-1.201267
21	6	0	0.163272	-4.850072	-1.203091
22	8	0	0.012516	-2.066283	1.136185
23	8	0	-2.102842	0.021892	-1.072217
24	6	0	-2.685998	0.018921	0.064613
25	6	0	-4.179458	0.037258	0.093355
26	6	0	-4.853562	-0.019934	1.322596
27	6	0	-6.247657	-0.003728	1.356438
28	6	0	-6.977566	0.072459	0.165960
29	6	0	-6.309189	0.132985	-1.060871
30	6	0	-4.915077	0.114693	-1.098116
31	8	0	-2.080258	-0.000625	1.184489
32	8	0	0.009183	2.074082	-1.137430
33	6	0	-0.007193	2.654588	-0.000127
34	6	0	-0.011696	4.149597	-0.000137
35	6	0	-0.055407	4.852677	1.212891
36	6	0	-0.060080	6.247572	1.210417
37	6	0	-0.020300	6.946946	-0.000154
38	6	0	0.023794	6.247816	-1.210717
39	6	0	0.027695	4.852919	-1.213173
40	8	0	-0.020107	2.073991	1.137155
41	1	0	-0.256383	-4.296926	2.127028
42	1	0	0.280454	-4.295322	-2.127075
43	1	0	-0.253873	-6.787378	2.134961
44	1	0	0.292516	-6.785737	-2.135055

45	1	0	0.022967	-8.031354	-0.000059
46	1	0	-4.274312	-0.075072	2.237385
47	1	0	-4.388885	0.166615	-2.044326
48	1	0	-6.764729	-0.048810	2.310342
49	1	0	-6.873569	0.196066	-1.986519
50	1	0	-8.063407	0.086595	0.194043
51	1	0	-0.085942	4.296058	2.142885
52	1	0	0.061636	4.296492	-2.143163
53	1	0	-0.094810	6.788953	2.151318
54	1	0	0.055184	6.789391	-2.151624
55	1	0	-0.023653	8.033381	-0.000160
56	1	0	4.388017	0.189323	2.044527
57	1	0	4.274769	-0.050074	-2.237348
58	1	0	6.872485	0.233293	1.986701
59	1	0	6.764987	-0.009190	-2.310330
60	1	0	8.062895	0.132337	-0.193958
61	1	0	-0.865818	-1.280895	-3.709147
62	1	0	0.872754	-1.273604	3.711689
63	1	0	1.855389	-0.190593	3.230791
64	1	0	-1.854464	-0.202408	-3.230494

HF=-2055.1797223

$[Rh_2(H_2BTC)_4]$

Charge=0, Multiplicity=1

Center Number	Atomic Number	Atomic Type	Coordinates (Angstroms) X	Y	Z
1	6	0	-4.880995	4.928438	0.000058
2	6	0	-4.386301	4.429072	-1.211395
3	6	0	-3.401303	3.434697	-1.211222
4	6	0	-2.908436	2.937103	0.000047
5	6	0	-3.401360	3.434631	1.211323
6	6	0	-4.386350	4.429010	1.211508
7	6	0	-1.856365	1.875053	0.000045
8	8	0	-1.445428	1.460114	-1.133673
9	45	0	0.000034	-0.000002	-1.195222
10	8	0	-1.445398	1.460152	1.133778
11	45	0	0.000003	0.000026	1.195216
12	8	0	-1.460129	-1.445401	1.133722
13	6	0	-1.875025	-1.856370	-0.000005
14	6	0	-2.937110	-2.908410	-0.000002
15	6	0	-3.434818	-3.401166	-1.211272
16	6	0	-4.429205	-4.386150	-1.211445
17	6	0	-4.928499	-4.880918	0.000010
18	6	0	-4.428973	-4.386368	1.211458
19	6	0	-3.434555	-3.401416	1.211272
20	8	0	-1.460087	-1.445441	-1.133731
21	8	0	1.445427	-1.460128	1.133668
22	6	0	1.856389	-1.875043	-0.000050
23	6	0	2.908430	-2.937122	-0.000049
24	6	0	3.401270	-3.434741	-1.211322
25	6	0	4.386245	-4.429134	-1.211501
26	6	0	4.880948	-4.928498	-0.000048
27	6	0	4.386324	-4.429054	1.211403
28	6	0	3.401355	-3.434652	1.211223
29	8	0	1.445465	-1.460099	-1.133783
30	8	0	1.460137	1.445440	1.133722
31	6	0	1.875063	1.856392	-0.000002
32	6	0	2.937138	2.908434	-0.000004
33	6	0	3.434659	3.401365	-1.211278
34	6	0	4.429069	4.386326	-1.211461
35	6	0	4.928515	4.880951	-0.000011

36	6	0	4.429150	4.386254	1.211442
37	6	0	3.434765	3.401269	1.211268
38	8	0	1.460141	1.445436	-1.133727
39	1	0	-3.053959	-3.023692	-2.153026
40	1	0	-3.053490	-3.024138	2.153021
41	1	0	-5.697547	-5.642609	0.000015
42	1	0	3.023858	-3.053812	-2.153073
43	1	0	3.024010	-3.053657	2.152974
44	1	0	5.642645	-5.697542	-0.000047
45	1	0	3.053655	3.024026	-2.153027
46	1	0	3.053847	3.023851	2.153020
47	1	0	5.697560	5.642646	-0.000014
48	1	0	-3.023894	3.053772	-2.152975
49	1	0	-3.023994	3.053651	2.153071
50	1	0	-5.642704	5.697469	0.000062
51	6	0	4.926111	4.878357	2.527803
52	8	0	4.529901	4.486256	3.607093
53	8	0	5.886586	5.829408	2.409269
54	1	0	6.143652	6.084043	3.311176
55	6	0	4.925936	4.878512	-2.527826
56	8	0	4.529928	4.486197	-3.607112
57	8	0	5.886316	5.829661	-2.409299
58	1	0	6.143401	6.084268	-3.311208
59	6	0	-4.878532	4.925879	2.527873
60	8	0	-4.486313	4.529777	3.607160
61	8	0	-5.829729	5.886212	2.409348
62	1	0	-6.084387	6.143246	3.311258
63	6	0	-4.878424	4.926013	-2.527755
64	8	0	-4.486247	4.529879	-3.607046
65	8	0	-5.829624	5.886342	-2.409220
66	1	0	-6.084280	6.143386	-3.311127
67	6	0	-4.926254	-4.878164	-2.527804
68	8	0	-4.530097	-4.486013	-3.607096
69	8	0	-5.886802	-5.829143	-2.409269
70	1	0	-6.143943	-6.083701	-3.311177
71	6	0	-4.925754	-4.878635	2.527824
72	8	0	-4.529732	-4.486332	3.607110
73	8	0	-5.886099	-5.829821	2.409301
74	1	0	-6.143135	-6.084473	3.311212
75	6	0	4.878345	-4.926093	-2.527863
76	8	0	4.486201	-4.529923	-3.607152
77	8	0	5.829443	-5.886524	-2.409332
78	1	0	6.084073	-6.143590	-3.311240
79	6	0	4.878515	-4.925919	2.527766
80	8	0	4.486346	-4.529770	3.607054
81	8	0	5.829648	-5.886316	2.409237
82	1	0	6.084312	-6.143345	3.311146

HF=3411.0011819

$[Rh_2(OBz)_4Cl_2]^{2-}$

Charge=-2, Multiplicity=1

Center Number	Atomic Number	Atomic Type	Coordinates (Angstroms) X	Y	Z
1	17	0	-0.000652	0.000114	3.885340
2	8	0	-1.417688	1.520315	1.137845
3	6	0	-1.800154	1.930608	-0.000080
4	8	0	-1.417494	1.520286	-1.137984
5	6	0	-2.829139	3.034280	-0.000216
6	6	0	-3.309187	3.549346	-1.212204
7	6	0	-3.309754	3.549085	1.211661
8	6	0	-4.261847	4.570863	-1.210961
9	1	0	-2.921468	3.133812	-2.136802
10	6	0	-4.262407	4.570599	1.210225
11	1	0	-2.922459	3.133364	2.136356
12	6	0	-4.741149	5.084387	-0.000428
13	1	0	-4.630463	4.966343	-2.154662
14	1	0	-4.631443	4.965889	2.153840
15	1	0	-5.483314	5.880096	-0.000520
16	8	0	-1.520485	-1.417556	1.137870
17	6	0	-1.930811	-1.799988	-0.000049
18	8	0	-1.520394	-1.417486	-1.137967
19	6	0	-3.034553	-2.828924	-0.000155
20	6	0	-3.549234	-3.309418	-1.212132
21	6	0	-3.549845	-3.308995	1.211730
22	6	0	-4.570865	-4.261955	-1.210871
23	1	0	-3.133327	-2.922119	-2.136738
24	6	0	-4.571470	-4.261529	1.210314
25	1	0	-3.134383	-2.921396	2.136414
26	6	0	-5.084885	-4.740699	-0.000327
27	1	0	-4.966064	-4.630890	-2.154565
28	1	0	-4.967124	-4.630154	2.153938
29	1	0	-5.880702	-5.482749	-0.000400
30	8	0	1.417662	-1.520614	1.138044
31	6	0	1.800070	-1.930884	0.000155
32	8	0	1.417707	-1.520666	-1.137860
33	6	0	2.829212	-3.034626	0.000131
34	6	0	3.309750	-3.549382	-1.211801
35	6	0	3.309383	-3.549768	1.212032
36	6	0	4.262397	-4.570903	-1.210485
37	1	0	2.922380	-3.133594	-2.136436
38	6	0	4.262029	-4.571288	1.210697
39	1	0	2.921735	-3.134250	2.136678
40	6	0	4.741233	-5.084764	0.000099
41	1	0	4.631349	-4.966137	-2.154158
42	1	0	4.630717	-4.966816	2.154352
43	1	0	5.483376	-5.880496	0.000103
44	8	0	1.520399	1.417884	1.138035
45	6	0	1.930661	1.800313	0.000142
46	8	0	1.520524	1.417812	-1.137860
47	6	0	3.034559	2.829257	0.000107
48	6	0	3.549840	3.309220	-1.211829
49	6	0	3.549301	3.309862	1.212007
50	6	0	4.571463	4.261759	-1.210517
51	1	0	3.134356	2.921519	-2.136461
52	6	0	4.570922	4.262400	1.210665
53	1	0	3.133417	2.922619	2.136657
54	6	0	5.084908	4.741048	0.000062
55	1	0	4.967083	4.630293	-2.154191
56	1	0	4.966150	4.631417	2.154317
57	1	0	5.880702	5.483124	0.000059
58	45	0	-0.000139	0.000019	1.246821

59	45	0	0.000086	-0.000010	-1.246591
60	17	0	0.000504	-0.000085	-3.885160

HF=-2822.875789

$[Rh_2(OBz)_4Cl]^-$

Charge=-1, Multiplicity=1

Center Number	Atomic Number	Atomic Type	Coordinates (Angstroms) X	Y	Z
1	17	0	0.000028	0.000029	3.514139
2	8	0	-1.668754	1.226604	0.946049
3	6	0	-2.128365	1.564622	-0.187968
4	8	0	-1.667596	1.225408	-1.327798
5	6	0	-3.338820	2.455152	-0.180212
6	6	0	-3.914926	2.878896	-1.385607
7	6	0	-3.896555	2.866414	1.038635
8	6	0	-5.038940	3.706644	-1.372357
9	1	0	-3.469875	2.550987	-2.318741
10	6	0	-5.020513	3.694143	1.048792
11	1	0	-3.436009	2.527886	1.960638
12	6	0	-5.594132	4.116027	-0.155324
13	1	0	-5.481698	4.032451	-2.310007
14	1	0	-5.448716	4.010068	1.996296
15	1	0	-6.469437	4.760748	-0.145501
16	8	0	-1.226571	-1.668706	0.946108
17	6	0	-1.564611	-2.128354	-0.187897
18	8	0	-1.225440	-1.667611	-1.327723
19	6	0	-2.455157	-3.338827	-0.180060
20	6	0	-2.878930	-3.914966	-1.385422
21	6	0	-2.866372	-3.896510	1.038822
22	6	0	-3.706677	-5.038983	-1.372108
23	1	0	-2.551052	-3.469950	-2.318585
24	6	0	-3.694102	-5.020470	1.049042
25	1	0	-2.527819	-3.435937	1.960801
26	6	0	-4.116021	-5.594131	-0.155042
27	1	0	-4.032513	-5.481775	-2.309733
28	1	0	-4.009996	-5.448641	1.996571
29	1	0	-4.760741	-6.469437	-0.145170
30	8	0	1.668751	-1.226594	0.946095
31	6	0	2.128355	-1.564620	-0.187929
32	8	0	1.667567	-1.225427	-1.327752
33	6	0	3.338816	-2.455140	-0.180171
34	6	0	3.914917	-2.878892	-1.385566
35	6	0	3.896565	-2.866385	1.038676
36	6	0	5.038938	-3.706629	-1.372317
37	1	0	3.469854	-2.550996	-2.318700
38	6	0	5.020530	-3.694105	1.048832
39	1	0	3.436025	-2.527850	1.960679
40	6	0	5.594143	-4.115995	-0.155284
41	1	0	5.481692	-4.032441	-2.309968
42	1	0	5.448744	-4.010016	1.996336
43	1	0	6.469454	-4.760709	-0.145462
44	8	0	1.226567	1.668722	0.946116
45	6	0	1.564605	2.128343	-0.187906
46	8	0	1.225416	1.667584	-1.327716
47	6	0	2.455160	3.338809	-0.180094
48	6	0	2.878934	3.914919	-1.385470
49	6	0	2.866384	3.896514	1.038774
50	6	0	3.706691	5.038930	-1.372182
51	1	0	2.551049	3.469887	-2.318623

52	6	0	3.694122	5.020468	1.048968
53	1	0	2.527831	3.435962	1.960764
54	6	0	4.116042	5.594100	-0.155129
55	1	0	4.032528	5.481698	-2.309818
56	1	0	4.010023	5.448656	1.996487
57	1	0	4.760770	6.469400	-0.145277
58	45	0	0.000003	0.000008	1.055903
59	45	0	-0.000017	-0.000012	-1.402999

HF=-2362.6553196

$[Rh_2(OAc)_4]$

Charge=0, Multiplicity=1

Center Number	Atomic Number	Atomic Type	Coordinates (Angstroms) X	Y	Z
1	8	0	-1.456440	-1.461190	1.133361
2	6	0	-1.872802	-1.870710	-0.000010
3	8	0	-1.455896	-1.461711	-1.133374
4	8	0	1.452763	-1.458322	1.133372
5	6	0	1.869333	-1.867649	0.000025
6	8	0	1.453315	-1.457788	-1.133332
7	8	0	1.449745	1.454577	1.133368
8	6	0	1.865941	1.864273	0.000032
9	8	0	1.449228	1.455119	-1.133315
10	8	0	-1.461456	1.449430	1.133338
11	6	0	-1.870357	1.866401	-0.000021
12	8	0	-1.461964	1.448903	-1.133367
13	45	0	-0.003619	-0.003711	1.194876
14	45	0	-0.003601	-0.003705	-1.194867
15	6	0	2.963380	2.900403	-0.000026
16	1	0	3.930901	2.386112	-0.002491
17	1	0	2.902008	3.517427	-0.897971
18	1	0	2.904856	3.514640	0.899996
19	6	0	2.965866	-2.904668	0.000037
20	1	0	2.905035	-3.520448	-0.898777
21	1	0	3.933867	-2.391279	-0.000236
22	1	0	2.905322	-3.520145	0.899072
23	6	0	-2.970678	-2.906170	-0.000069
24	1	0	-2.911803	-3.520977	0.899533
25	1	0	-3.937782	-2.391105	-0.001635
26	1	0	-2.909974	-3.522736	-0.898357
27	6	0	-2.904542	2.965556	-0.000002
28	1	0	-3.521096	2.905904	0.898379
29	1	0	-2.388210	3.931984	0.001479
30	1	0	-3.519435	2.907578	-0.899614

HF=-1135.3253968

$[Rh_2(OAc)_3(OBz)]$

Charge=0, Multiplicity=1

Center Number	Atomic Number	Atomic Type	Coordinates (Angstroms) X	Y	Z

1	8	0	0.765394	-2.065196	1.133226
2	6	0	0.752797	-2.649125	-0.000169
3	8	0	0.765803	-2.065046	-1.133485
4	8	0	2.835120	-0.021707	1.133372
5	6	0	3.419156	-0.021225	0.000007
6	8	0	2.835124	-0.021175	-1.133361
7	8	0	0.789987	2.050933	1.133482
8	6	0	0.795253	2.635092	0.000191
9	8	0	0.789568	2.051093	-1.133187
10	8	0	-1.278650	0.005335	1.133296
11	6	0	-1.868011	0.009483	0.000005
12	8	0	-1.278654	0.005087	-1.133287
13	6	0	-3.360335	0.019854	0.000007
14	6	0	-4.063502	0.024899	-1.213941
15	6	0	-4.063499	0.024951	1.213956
16	6	0	-5.458215	0.035086	-1.211444
17	1	0	-3.507892	0.021018	-2.145002
18	6	0	-5.458213	0.035137	1.211462
19	1	0	-3.507888	0.021110	2.145016
20	6	0	-6.157210	0.040216	0.000009
21	1	0	-5.999833	0.039128	-2.152731
22	1	0	-5.999829	0.039217	2.152750
23	1	0	-7.243524	0.048264	0.000010
24	45	0	0.777953	-0.007380	1.194494
25	45	0	0.777950	-0.007217	-1.194487
26	6	0	0.841431	4.143521	0.000231
27	1	0	1.889729	4.462361	-0.002143
28	1	0	0.361838	4.536934	-0.897502
29	1	0	0.365705	4.536856	0.900032
30	6	0	4.928002	0.009166	0.000002
31	1	0	5.316577	-0.472500	-0.898753
32	1	0	5.257650	1.054103	-0.000378
33	1	0	5.316591	-0.471910	0.899061
34	6	0	0.689663	-4.156762	-0.000308
35	1	0	1.161224	-4.555975	0.899139
36	1	0	-0.362588	-4.462241	-0.001539
37	1	0	1.163180	-4.555847	-0.898794

HF=-1327.0755005

cis-[$Rh_2(OAc)_2(OBz)_2$]

Charge=0, Multiplicity=1

Center Number	Atomic Number	Atomic Type	Coordinates (Angstroms) X	Y	Z
1	8	0	-1.454599	0.483648	1.133234
2	6	0	-1.870907	0.900980	-0.000094
3	8	0	-1.454784	0.483334	-1.133373
4	6	0	-2.926003	1.956139	-0.000154
5	6	0	-3.423592	2.452875	-1.214090
6	6	0	-3.423494	2.453111	1.213725
7	6	0	-4.410512	3.438373	-1.211668
8	1	0	-3.030219	2.060456	-2.145117
9	6	0	-4.410414	3.438610	1.211190
10	1	0	-3.030047	2.060874	2.144797
11	6	0	-4.905113	3.932396	-0.000267
12	1	0	-4.793564	3.821238	-2.152983
13	1	0	-4.793389	3.821660	2.152461
14	1	0	-5.673652	4.700185	-0.000311

15	8	0	-1.455525	-2.423169	1.133296
16	6	0	-1.867300	-2.837512	-0.000065
17	8	0	-1.455122	-2.423474	-1.133391
18	8	0	1.455105	-2.423474	1.133437
19	6	0	1.867286	-2.837525	0.000121
20	8	0	1.455514	-2.423196	-1.133249
21	8	0	1.454798	0.483333	1.133372
22	6	0	1.870919	0.900969	0.000087
23	8	0	1.454610	0.483622	-1.133236
24	6	0	2.926010	1.956131	0.000134
25	6	0	3.423495	2.453096	-1.213751
26	6	0	3.423604	2.452877	1.214064
27	6	0	4.410411	3.438598	-1.211228
28	1	0	3.030044	2.060851	-2.144818
29	6	0	4.410521	3.438379	1.211630
30	1	0	3.030236	2.060464	2.145096
31	6	0	4.905115	3.932394	0.000224
32	1	0	4.793380	3.821643	-2.152504
33	1	0	4.793575	3.821252	2.152941
34	1	0	5.673651	4.700186	0.000258
35	45	0	-0.000061	-0.969515	1.193893
36	45	0	0.000061	-0.969528	-1.193876
37	6	0	2.908796	-3.929539	0.000117
38	1	0	2.399747	-4.899808	-0.002389
39	1	0	3.525730	-3.864120	-0.897546
40	1	0	3.522849	-3.866999	0.899938
41	6	0	-2.908810	-3.929524	-0.000118
42	1	0	-3.524540	-3.865262	-0.898684
43	1	0	-2.399760	-4.899796	-0.000594
44	1	0	-3.524070	-3.865828	0.898804

HF=-1518.8254229

trans-[$Rh_2(OAc)_2(OBz)_2$]

Charge=0, Multiplicity=1

Center Number	Atomic Number	Atomic Type	Coordinates (Angstroms) X	Y	Z
1	8	0	0.003415	2.057689	1.133342
2	6	0	0.011277	2.641873	-0.000004
3	8	0	0.003269	2.057681	-1.133347
4	8	0	-2.055419	0.003451	1.133323
5	6	0	-2.644825	0.004985	0.000002
6	8	0	-2.055418	0.003293	-1.133318
7	6	0	-4.137075	0.008527	0.000002
8	6	0	-4.840263	0.010135	-1.213943
9	6	0	-4.840264	0.010250	1.213947
10	6	0	-6.234998	0.013529	-1.211447
11	1	0	-4.284679	0.008894	-2.145026
12	6	0	-6.234999	0.013644	1.211449
13	1	0	-4.284680	0.009097	2.145029
14	6	0	-6.934010	0.015286	0.000001
15	1	0	-6.776623	0.014897	-2.152737
16	1	0	-6.776624	0.015100	2.152738
17	1	0	-8.020351	0.018025	0.000001
18	8	0	-0.003415	-2.057710	1.133364
19	6	0	-0.011274	-2.641906	0.000025
20	8	0	-0.003268	-2.057724	-1.133325
21	8	0	2.055418	-0.003476	1.133324
22	6	0	2.644825	-0.005048	0.000003
23	8	0	2.055419	-0.003338	-1.133317
24	6	0	4.137075	-0.008513	0.000004

25	6	0	4.840264	-0.010091	-1.213941
26	6	0	4.840263	-0.010193	1.213949
27	6	0	6.234999	-0.013423	-1.211443
28	1	0	4.284680	-0.008882	-2.145023
29	6	0	6.234998	-0.013525	1.211453
30	1	0	4.284679	-0.009063	2.145032
31	6	0	6.934011	-0.015141	0.000005
32	1	0	6.776625	-0.014770	-2.152733
33	1	0	6.776623	-0.014953	2.152742
34	1	0	8.020352	-0.017831	0.000005
35	45	0	-0.000000	-0.000011	1.194002
36	45	0	0.000000	-0.000022	-1.193996
37	6	0	-0.062791	-4.149879	-0.000020
38	1	0	-1.112602	-4.463627	-0.002002
39	1	0	0.414880	-4.545079	-0.897994
40	1	0	0.411687	-4.545098	0.899619
41	6	0	0.062786	4.149847	-0.000041
42	1	0	-0.412361	4.545066	0.899249
43	1	0	1.112597	4.463600	-0.001197
44	1	0	-0.414222	4.545042	-0.898366

HF=-1518.8255919

$[Rh_2(OAc)(OBz)_3]$.

Charge=0, Multiplicity=1

Center Number	Atomic Number	Atomic Type	Coordinates (Angstroms) X	Y	Z
1	8	0	0.004941	1.441576	1.133279
2	6	0	0.006526	2.031163	-0.000021
3	8	0	0.004832	1.441551	-1.133307
4	6	0	0.010465	3.523233	-0.000037
5	6	0	0.012241	4.226324	-1.213921
6	6	0	0.012306	4.226352	1.213831
7	6	0	0.015888	5.621002	-1.211474
8	1	0	0.010769	3.670717	-2.144943
9	6	0	0.015953	5.621029	1.211352
10	1	0	0.010883	3.670765	2.144865
11	6	0	0.017754	6.320026	-0.000069
12	1	0	0.017283	6.162615	-2.152773
13	1	0	0.017400	6.162663	2.152640
14	1	0	0.020612	7.406374	-0.000081
15	8	0	-2.054951	-0.611588	1.133280
16	6	0	-2.644469	-0.609740	-0.000035
17	8	0	-2.054913	-0.611697	-1.133328
18	6	0	-4.136605	-0.608504	-0.000059
19	6	0	-4.839749	-0.608441	-1.213983
20	6	0	-4.839790	-0.608359	1.213840
21	6	0	-6.234460	-0.607998	-1.211526
22	1	0	-4.284157	-0.608108	-2.145043
23	6	0	-6.234501	-0.607916	1.211336
24	1	0	-4.284230	-0.607964	2.144919
25	6	0	-6.933494	-0.607787	-0.000107
26	1	0	-6.776064	-0.607456	-2.152829
27	1	0	-6.776137	-0.607311	2.152620
28	1	0	-8.019841	-0.607117	-0.000126
29	8	0	-0.003431	-2.670861	1.133387
30	6	0	-0.010790	-3.255147	0.000047
31	8	0	-0.003261	-2.670889	-1.133311
32	8	0	2.055305	-0.620201	1.133361
33	6	0	2.644870	-0.621500	0.000051

34	8	0	2.055343	-0.620142	-1.133279
35	6	0	4.136942	-0.627321	0.000077
36	6	0	4.840103	-0.630528	-1.213815
37	6	0	4.840061	-0.630584	1.213993
38	6	0	6.234791	-0.636860	-1.211314
39	1	0	4.284560	-0.627612	-2.144894
40	6	0	6.234749	-0.636916	1.211540
41	1	0	4.284485	-0.627711	2.145052
42	6	0	6.933774	-0.640103	0.000125
43	1	0	6.776421	-0.638986	-2.152599
44	1	0	6.776347	-0.639086	2.152843
45	1	0	8.020112	-0.644803	0.000144
46	45	0	0.000402	-0.614384	1.193529
47	45	0	0.000443	-0.614410	-1.193512
48	6	0	-0.060723	-4.763068	0.000012
49	1	0	-1.110140	-5.078020	-0.002053
50	1	0	0.417521	-5.157680	-0.897862
51	1	0	0.414186	-5.157687	0.899632

HF=-1710.5754439

$[Rh_2(OBz)_4]$ (singlet)

Charge=0, Multiplicity=1

Center Number	Atomic Number	Atomic Type	Coordinates (Angstroms) X	Y	Z
1	8	0	-1.052893	1.764491	-1.133306
2	6	0	-1.354949	2.270894	0.000015
3	8	0	-1.052827	1.764531	1.133339
4	6	0	-2.119331	3.552168	0.000026
5	6	0	-2.479668	4.155910	1.213904
6	6	0	-2.479507	4.156026	-1.213842
7	6	0	-3.194280	5.353581	1.211457
8	1	0	-2.195069	3.678760	2.144947
9	6	0	-3.194117	5.353697	-1.211375
10	1	0	-2.194775	3.678972	-2.144894
11	6	0	-3.552378	5.953893	0.000046
12	1	0	-3.471854	5.818662	2.152752
13	1	0	-3.471568	5.818867	-2.152663
14	1	0	-4.109022	6.886796	0.000052
15	8	0	1.764454	1.052890	-1.133336
16	6	0	2.270854	1.354982	-0.000020
17	8	0	1.764506	1.052831	1.133331
18	6	0	3.552171	2.119305	-0.000034
19	6	0	4.155949	2.479630	1.213830
20	6	0	4.156030	2.479441	-1.213914
21	6	0	5.353652	3.194187	1.211357
22	1	0	3.678800	2.195064	2.144883
23	6	0	5.353733	3.193998	-1.211473
24	1	0	3.678949	2.194721	-2.144956
25	6	0	5.953963	3.552246	-0.000066
26	1	0	5.818759	3.471751	2.152643
27	1	0	5.818903	3.471419	-2.152771
28	1	0	6.886892	4.108847	-0.000079
29	8	0	1.052844	-1.764464	-1.133302
30	6	0	1.354885	-2.270881	0.000014
31	8	0	1.052797	-1.764513	1.133333
32	6	0	2.119314	-3.552123	0.000024
33	6	0	2.479690	-4.155841	1.213903
34	6	0	2.479496	-4.155976	-1.213844
35	6	0	3.194344	-5.353486	1.211455
36	1	0	2.195085	-3.678695	2.144945

37	6	0	3.194150	-5.353621	-1.211377
38	1	0	2.194733	-3.678941	-2.144896
39	6	0	3.552449	-5.953795	0.000044
40	1	0	3.471948	-5.818550	2.152751
41	1	0	3.471605	-5.818789	-2.152665
42	1	0	4.109127	-6.886678	0.000050
43	8	0	-1.764493	-1.052858	-1.133330
44	6	0	-2.270927	-1.354894	-0.000014
45	8	0	-1.764545	-1.052792	1.133340
46	6	0	-3.552176	-2.119334	-0.000030
47	6	0	-4.155923	-2.479713	1.213834
48	6	0	-4.156003	-2.479523	-1.213910
49	6	0	-5.353564	-3.194373	1.211360
50	1	0	-3.678799	-2.195106	2.144888
51	6	0	-5.353645	-3.194182	-1.211470
52	1	0	-3.678946	-2.194761	-2.144951
53	6	0	-5.953845	-3.552482	-0.000063
54	1	0	-5.818648	-3.471978	2.152645
55	1	0	-5.818790	-3.471642	-2.152768
56	1	0	-6.886726	-4.109163	-0.000078
57	45	0	-0.000020	0.000015	-1.193005
58	45	0	-0.000014	0.000011	1.193018

HF=-1902.3252607

$[Rh_2(OBz)_4]$ (triplet)

Charge=0, Multiplicity=3

Center Number	Atomic Number	Atomic Type	Coordinates (Angstroms) X	Y	Z
1	8	0	-2.067372	0.026140	-1.136528
2	6	0	-2.650504	0.033810	-0.000000
3	8	0	-2.067372	0.026159	1.136527
4	6	0	-4.144484	0.053379	-0.000001
5	6	0	-4.847844	0.062833	1.213661
6	6	0	-4.847844	0.062848	-1.213662
7	6	0	-6.242472	0.081611	1.211299
8	1	0	-4.292013	0.055405	2.144510
9	6	0	-6.242472	0.081627	-1.211301
10	1	0	-4.292012	0.055431	-2.144511
11	6	0	-6.941573	0.091092	-0.000001
12	1	0	-6.783933	0.088910	2.152697
13	1	0	-6.783932	0.088940	-2.152699
14	1	0	-8.027849	0.105780	-0.000001
15	8	0	0.026083	2.053355	-1.129483
16	6	0	0.033972	2.650002	-0.000002
17	8	0	0.026101	2.053356	1.129481
18	6	0	0.053507	4.139548	-0.000002
19	6	0	0.062949	4.841850	1.214380
20	6	0	0.062964	4.841849	-1.214384
21	6	0	0.081742	6.236218	1.211682
22	1	0	0.055518	4.286415	2.145527
23	6	0	0.081757	6.236218	-1.211686
24	1	0	0.055543	4.286414	-2.145532
25	6	0	0.091227	6.934772	-0.000002
26	1	0	0.089054	6.777930	2.152813
27	1	0	0.089082	6.777929	-2.152818
28	1	0	0.105933	8.020992	-0.000002
29	8	0	2.067359	-0.026140	-1.136528
30	6	0	2.650490	-0.033822	-0.000000
31	8	0	2.067359	-0.026156	1.136527
32	6	0	4.144471	-0.053386	-0.000001
33	6	0	4.847832	-0.062836	1.213660

34	6	0	4.847830	-0.062855	-1.213663
35	6	0	6.242460	-0.081612	1.211297
36	1	0	4.292002	-0.055408	2.144509
37	6	0	6.242458	-0.081633	-1.211303
38	1	0	4.291998	-0.055441	-2.144511
39	6	0	6.941560	-0.091093	-0.000003
40	1	0	6.783921	-0.088909	2.152695
41	1	0	6.783918	-0.088946	-2.152701
42	1	0	8.027836	-0.105780	-0.000004
43	8	0	-0.026101	-2.053354	-1.129480
44	6	0	-0.034002	-2.649999	0.000002
45	8	0	-0.026118	-2.053352	1.129484
46	6	0	-0.053498	-4.139546	0.000004
47	6	0	-0.062919	-4.841847	1.214387
48	6	0	-0.062936	-4.841849	-1.214378
49	6	0	-0.081680	-6.236216	1.211690
50	1	0	-0.055501	-4.286410	2.145533
51	6	0	-0.081697	-6.236218	-1.211678
52	1	0	-0.055530	-4.286415	-2.145526
53	6	0	-0.091149	-6.934771	0.000007
54	1	0	-0.088979	-6.777926	2.152822
55	1	0	-0.089011	-6.777931	-2.152808
56	1	0	-0.105830	-8.020991	0.000009
57	45	0	-0.000007	0.000001	-1.221671
58	45	0	-0.000007	0.000002	1.221671

HF=-1902.2952939

ESI Study III

Supporting Information

Thermal Defect-Engineering of Precious Group Metal-Organic Frameworks: A Case Study on Ru/Rh-HKUST-1 Analogues

Werner R. Heinz,[a] Iker Agirrezabal-Telleria,[b] Raphael Junk,[a] Jan Berger,[a] Junjun Wang,[d] Dmitry I. Sharapa,[e] Miryam Gil-Calvo,[b] Ignacio Luz,[c] , Mustapha Soukri[c], Felix Studt,[e] Yuemin Wang,[d] Christof Wöll[d], Hana Bunzen,[f] Markus Drees[a] and Roland A. Fischer[a*]

[a] Chair of Inorganic and Metal-Organic Chemistry, Department of Chemistry, Technical University of Munich, Lichtenbergstraße 4, 85748 Garching, Germany. E-mail: roland.fischer@tum.de

[*]Corresponding Author

[b] Department of Chemical and Environmental Engineering, Engineering School of the University of the Basque Country (UPV/EHU), Plaza Torres Quevedo 1, 48013 Bilbao, Spain. E-mail: iker.aguirrezabal@ehu.eus

[c] RTI International, 3040 E Cornwallis Road, Research Triangle Park, NC 27709, USA. E-mail: iluzminguez@rti.org

[d] Chemistry of oxidic and organic interfaces, Institute of Functional Interfaces, Karlsruhe Institute of Technology, Hermann-von-Helmholtz-Platz 1, 76344 Eggenstein-Leopoldshafen. E-mail: yuemin.wang@kit.edu and christof.woell@kit.edu

[e] Institute of Catalysis Research and Technology (IKFT), Karlsruhe Institute of Technology (KIT), Hermann-von-Helmholtz-Platz 1, 76344 Eggenstein-Leopoldshafen, Germany. E-mail: felix.studt@kit.edu

[f] Chair of Solid State and Materials Chemistry, Institute of Physics, University of Augsburg, Universitätsstraße 1, 86159 Augsburg, Germany. E-mail: hana.bunzen@physik.uni-augsburg.de

Table of Contents

Experimental Details

General considerations

Trimesic acid (Sigma-Aldrich), $RuCl_3 \cdot x\ H_2O$ (Precious Metals Online), $Rh_2(OAc)_4$ (Sigma-Aldrich, Carbolution) and HPLC-grade acetone and ethanol (VWR Chemicals) were purchased commercially and used without further purification. Ultrapure water was obtained using a Milli-Q purification system (18.2 MΩ cm). Technical dichloromethane was purified using a MBraun SPS-800. $Ru_2(OAc)_4Cl$ was synthesized following literature procedures.[1] Desolvated MOFs were handled in a glovebox using argon (>99.996%; Westfalen).

Instrumentation

Thermal syntheses

Post-synthetic treatments of the pristine MOF samples to yield the TDE-MOFs were conducted with a Netzsch TG209 F1 Libra in an argon-filled glovebox. Decomposition gasses were analyzed in-situ using a Netzsch QMS 403C Aëolos mass spectrometer. The voltage of the mass spectrometer was set to 2300 V for the most abundant ions (m/z =18, 28 and 44) and to 2800 V for the less abundant ions (m/z = 2, 14, 16, 25, 30, 31, 35, 37, 46, 56, 58, 60 and 70). The transfer line, the inlet system and the adapter head were heated to 250 °C, 200 °C and 160 °C, respectively. Argon served both as the purge gas and the protective gas of the measurement set-up. Flow rates were set to 20 mL min^{-1}. The following heating protocols were used:

Targeted weight loss of 5.5 wt-% (denoted as 10% defects): Ramp from 15 °C to 150 °C, subsequent isothermal equilibration (30 min), ramp to 200 °C, subsequent isothermal equilibration (30 min), ramp to 220 °C, subsequent isothermal equilibration (30 min), ramp to 240 °C, subsequent isothermal equilibration (20 min), ramp to 260 °C, subsequent isothermal equilibration (20 min).

Targeted weight loss of 10 wt-% and 15 wt-% (denoted as 20% and 30% defects): Ramp from 15 °C to 150 °C, subsequent isothermal equilibration (30 min), ramp to 200 °C, subsequent isothermal equilibration (20 min), ramp to 250 °C, subsequent isothermal equilibration (60 min), ramp to 270 °C, subsequent isothermal equilibration (20 min), ramp to 290 °C, subsequent isothermal equilibration (60 min).

All ramps were programmed with a heating rate of 10 K min^{-1}. The thermal treatment was terminated as soon as the targeted mass loss had been reached and the material was cooled to room temperature.

Powder X-Ray diffraction

All diffraction patterns were collected on a PANalytical Empyrean equipped with a Cu X-ray tube (λ = 0.154 nm) operated at 45 kV and 40 mA in a 2Θ range of 5-50° in steps of 0.0065651° (2Θ) with 0.175 s/step. The incident beam was focussed on the sample through a focusing beam mirror with a

1/8° divergence slit and a nickel beta filter (0.2 mm). A PIXcel1D detector was used in receiving mode with a 1/8° anti-scatter slit and 0.04 rad soller slits. The activated samples were filled in borosilicate capillaries of 0.5 mm inner diameter and mounted onto a capillary spinner. **VT-PXRD measurements** were conducted on a PANalytical Empyrean X-ray diffractometer with Cu Kα radiation (λ=1.54778 Å). The samples were prepared by filling the holder with the dry powder. Crystalline phase stabilities were investigated using an XRK900 high temperature oven chamber. Sample was heated in the chamber from 25 °C to 800 °C with a heating rate of 3 °C/min under a stream of nitrogen. Diffraction patterns were measured throughout the whole heat treatment using Cu Kα x-ray radiation with a wavelength of 1.5418 Å and a 2θ range of 4.5° – 60°. Each pattern was measured for 4 minutes using a step size and count time of 2θ = 0.0263° and 0.1147 sec/step, respectively.

Elemental Analysis

Determination of the elemental composition was performed together with the microanalytical laboratories of the chemistry department at the Technical University of Munich. Determination of C, H, N and S was carried out with a Hekatech EuroEA elemental analyser. As shown in our previous publication, metal oxide residues determined by TGA provide sufficient accuracy for metal content determination as confirmed by ICP-MS. Furthermore, the actual metal ratio in the 50% Rh sample nicely represents the feed ratio, thus a 48:52 ratio served as basis for sum formula calculations (normalized to 3 metal atoms per repeating unit gives $Ru_{1.44}Rh_{1.56}$ respectively).[2] Chlorine contents were determined by potentiometric titration of HCl after thermal decomposition.

Calculation of the sum formula

Based on determined elemental contents and assuming exclusively the oxygen mass fraction missing to complete the 100 wt-%, sum formulas were calculated and normalized to three metal atoms per repeating unit. The GRG nonlinear solver function implemented in *Microsoft Excel®* was used for compositional fittings assuming acetate and BTC as the only organic framework components of the pristine MOF samples. To account for BTC decarboxylation in TDE-MOFs, isophthalate was added to this protocol optimizing the fitting results. A potential formation of benzoic acid according to a double decarboxylation of a single BTC unit could take place. However, such process results in identical changes in elemental composition and thus, could not be accounted for. For TDE-MOFs, the ceiling amounts of IPA + BTC and OAc^- was restricted to the respective parental BTC and OAc^- amounts. It should be mentioned that other efforts to determine organic ligand ratios (BTC to acetate) have not been successful as typical sample digestions in diluted acids do not proceed quantitatively and paramagnetic ruthenium obstruct NMR quantification. MAS-NMR of (100/0) sample confirms the general viability of the fitting approach.

Gas sorption measurements

Sorption experiments were conducted using a Micromeritics 3Flex with each 20 to 80 mg of desolvated sample. Samples were transferred under dry Ar atmosphere into preweighed sample tubes and capped with Micromeritics CheckSeals. Prior to the measurement each sample was additionally degassed at 150°C for >10h using a SmartVac Prep by Micromeritics Instrument Corp. to ensure unwanted adsorbates and identical pre-measurement states of all samples. The sample weight was then recorded. Free space of the sample tube is determined prior to measurements using helium. Nitrogen isotherms were recorded at 77 K, ethane and ethene isotherms for the heat of adsorption at 278 K, 288 K and 298 K, respectively. Temperature adjustment was achieved utilizing a water bath (278 K,

288 K, 298 K) or liquid nitrogen (77 K) Adsorption data was processed using the 3Flex Software Version 5.01 by Micromeritics Instrument Corp. and plotted in OriginPro 2019b by OriginLab Corp. The BET surface area was calculated using data points in the relative pressure range of 0.01 to 0.1 in the adsorption branch with the *Rouquerol* consistency criteria considered. The pore size distribution (PSD) was derived by fitting N_2 isotherms measured at 77 K with DFT-calculated sets of isotherms (kernel) of specific pore sizes and geometry. As approximation, cylindrical pores on an oxide surface are assumed for all materials to allow comparability within this series. Fitting was done using the respective kernel available *via* the 3Flex Software Version 5.01 by Micromeritics Instrument Corp.

The binding energy of ethane and ethene to the adsorption sites (isosteric enthalpy of adsorption, -ΔH_{ads}) within the materials was determined from the temperature dependence of the adsorption isotherms using the *Clausius–Clapeyron* expression. The isosteric energy of adsorption can be derived at a constant loading by

Equation S 1: Isosteric energy of adsorption.

$$\Delta H_{ads} = -R\frac{d(ln\ p)}{d(1/T)}$$

where *R* is the ideal gas constant, *p* is the pressure at a given loading and *T* is the temperature (278 K, 288 K and 298 K) at which the isotherm was measured. To obtain a description of *p* at any given loading, isotherms were fitted using a dual-site *Langmuir–Freundlich* equation, given by

Equation S 2: Langmuir-Freundlich equation.

$$V_{ads} = \frac{q_{sat,1}\ K_1\, p^{v_1}}{1 + K_1\, p^{v_1}} + \frac{q_{sat,2}\ K_2\, p^{v_2}}{1 + K_2\, p^{v_2}}$$

where V_{ads} is the amount adsorbed in cm^3/g, q_{sat} is the amount adsorbed when saturated with the gas in cm^3/g, *K* is the *Langmuir–Freundlich* constant in bar^{-1}, *p* is the gas pressure in bar, *v* is the dimensionless *Freundlich* parameter and subscripts *1* and *2* correspond to two different site identities. These parameters and fits are given in Figure S 26 - Figure S 28.

Fourier-transform infrared spectroscopy

FT-IR spectra were recorded from finely ground activated powder samples under argon atmosphere in a glovebox using a Bruker ALPHA FTIR spectrometer equipped with a Platinum attenuated total reflectance (ATR) unit at room temperature in the range of 400 to 4000 cm^{-1} with a resolution of 2 cm^{-1} and 24 scans per measurement. A pyroelectric deuterated L-alanine doped triglycine sulfate (RT-DLaTGS) detector was used.

VT-FT-IR spectra and CO-probe measurements **at ambient conditions** were recorded in a diffuse reflectance cell (Harrick, Praying Mantis, HVC-DRP-5) using a Bruker Vertex V70 module and a liquid-nitrogen cooled MCT detector. Samples were sieved into fine powders (<30 µm particle size) and treated (in N_2, H_2 or CO) following the procedures as described in the main text. Temperature was controlled with a temperature controller (Harrick, ATK-024-4). Elevated temperatures (150 / 300 °C) were held for 10 min during thermal pretreatments. Consecutive CO adsorption experiments were carried out using controlled flows of 1 % CO in He at 30 °C. All IR spectra were measured under inert conditions (N_2) to avoid signal-disturbance due to gaseous H_2 or CO.

UHV-FTIR was recorded using a *Bruker Vertex 80v* FTIR spectrometer coupled to a UHV system fabricated by *Prevac*. The spectrometer was operated in transmission mode with a base pressure of ≈10^{-10} mbar in the measurement chamber. A sample of 30-50 mg was pressed onto a metal grid with the help of an evacuable die and a hydraulic press (5 tonnes, 2 min). After removing of loose material, the grid was mounted onto a sample holder equipped with a thermocouple and then introduced into the set-up. Inside the measurement chamber, the sample was treated at 373 K to desorb any remaining adsorbates. The sample was then cooled to 105 K before 0.01 mbar CO was dosed and the transmission FTIR spectra recorded. Subsequently, a procedure consisting of the following steps was repeated: heating, isothermal treatment at a temperature higher than the previous, cooling, dosing of CO and measuring. The treatments were conducted at 373 K, 423 K, 453 K, 483 K, 523 K and 543 K (Rh MOF also 563 K) each for 20 min. The $Ru^{II,II}$ MOF sample was prepared in a nitrogen-filled glovebox. The material was pressed onto the metal grid using a screw clamp to exert force onto the die. After removing the loose particles, the sample was placed in a mobile transportation chamber specifically designed for the purpose of transferring samples into the measurement set-up under inert conditions.

Raman spectroscopy

Raman spectroscopy was measured with an inVia Reflex Raman System with an optical microscope (Leica DM2700M, 50x magnification) coupled to a Renishaw R04 Raman spectrometer with 532 nm laser wavelength (Laser: RL532C, Class 3B) with activated samples filled into Borosilicate glass capillaries (0.5 mm inner diameter) under argon atmosphere. A Renishaw 266n10 detector was used. All samples were measured with 10 s exposure time, 1 % laser power and 10 accumulations.

DFT calculations of isolated Ru- and Rh-paddle-wheel complexes

Calculations for IR frequencies of isolated ideal PW complexes comprising different combinations of acetate and BTC ligands have been performed with the Gaussian 16 suite of software[1]. The level of theory included the use of the hybrid DFT functional B3LYP together with the basis set 6-31+G** for C, H, O, Cl.[2,3] Ru and Rh have been described by the Stuttgart-Dresden97-ECP[4].

All structures have been optimized until no negative frequencies haven been calculated by frequency analysis. Frequencies calculation have been also used to determine unscaled frequencies and IR and Raman intensities. UV-VIS spectra of selected singlet state compounds have been calculated by time-dependent DFT[5] considering the three most probable electron transitions to singlet and triplet excited states.

1. Gaussian 16, Revision B.01, M. J. Frisch, G. W. Trucks, H. B. Schlegel, G. E. Scuseria, M. A. Robb, J. R. Cheeseman, G. Scalmani, V. Barone, G. A. Petersson, H. Nakatsuji, X. Li, M. Caricato, A. V. Marenich, J. Bloino, B. G. Janesko, R. Gomperts, B. Mennucci, H. P. Hratchian, J. V. Ortiz, A. F. Izmaylov, J. L. Sonnenberg, D. Williams-Young, F. Ding, F. Lipparini, F. Egidi, J. Goings, B. Peng, A. Petrone, T. Henderson, D. Ranasinghe, V. G. Zakrzewski, J. Gao, N. Rega, G. Zheng, W. Liang, M. Hada, M. Ehara, K. Toyota, R. Fukuda, J. Hasegawa, M. Ishida, T. Nakajima, Y. Honda, O. Kitao, H. Nakai, T. Vreven, K. Throssell, J. A. Montgomery, Jr., J. E. Peralta, F. Ogliaro, M. J. Bearpark, J. J. Heyd, E. N. Brothers, K. N. Kudin, V. N. Staroverov, T. A. Keith, R. Kobayashi, J. Normand, K. Raghavachari, A. P. Rendell, J. C. Burant, S. S. Iyengar, J. Tomasi, M. Cossi, J. M. Millam, M. Klene, C. Adamo, R. Cammi, J. W. Ochterski, R. L. Martin, K. Morokuma, O. Farkas, J. B. Foresman, and D. J. Fox, Gaussian, Inc., Wallingford CT, **2016**.

2. a) A.D. Becke, *J. Chem. Phys*. **1993**, 98, 5648-5652; b) C. Lee, W. Yang, R.G. Parr, *Phys. Rev. B* **1988**, *37*, 785-789; c) S.H. Vosko, L. Wilk, M. Nusair, *Can. J. Phys.* **1980**, *58*, 1200-1211; d) P.J. Stephens, F.J. Devlin, C.F. Chabalowski, M.J. Frisch, *J.Phys.Chem.* **1994**, 98, 11623-11627.

3. a) W.J. Hehre, R. Ditchfield and J.A. Pople, J. Chem. Phys. **1972**, *56,* 2257-2261 (1972); b) T. Clark, J. Chandrasekhar, G. W. Spitznagel, and P. v. R. Schleyer, *J. Comp. Chem.*, **1983**, *4*, 294-301; c) M.M. Francl, W.J. Petro, W.J. Hehre, J.S. Binkley, M.S. Gordon, D.J. DeFrees and J.A. Pople, *J. Chem. Phys.* **1982**, *77*, 3654-3665.

4. a) A. Bergner, M. Dolg, W. Kuechle, H. Stoll, H. Preuss, *Mol. Phys.* **1993**, *80*,1431-1441 ; b) M. Kaupp, P. v. R. Schleyer, H. Stoll, H. Preuss, *J. Chem. Phys.* **1991**, *94*, 1360-1366; c) M. Dolg, H. Stoll, H. Preuss, R.M. Pitzer, *J. Phys. Chem.* **1993**, *97*, 5852-5859.

5. a) R. E. Stratmann, G. E. Scuseria, M. J. Frisch, *J. Chem. Phys.*, **1998**, *109*, 8218-24. b) F. Furche and R. Ahlrichs, *J. Chem. Phys.*, **2002**, *117*, 7433-7447.

Details of DFT calculations for CO frequencies of pristine and defective Rh-PWs

All calculations performed in ORCA 4.2.0. Minnesota DFT functionals (M06 and M06L) were used with def2-TZVP basis set and RIJCOSX approximation. DFT calculations show almost degenerated doublet, quartet and sextet spin states of defect system without CO (Table S 8, see page 41). FOD-analysis shows significant NFOD, however CASSCF demonstrates that each spin state can be described by single electron configuration and thus DFT-methods can be applied (Table S 10, see page 42). Also, CASSCF full optimization of basic defect in sextet spin ends up in significant change of geometry that is impossible in MOF. For detailed investigation of this case, extended system with 3 dicyanobenzoate instead of acetic ligands were used. Adsorption of CO significantly stabilize the low-spin state. Adsorption energies of CO to different systems in lowest corresponding spin state are shown in Table S 9 (see page 41).

Thermogravimetric analysis

Thermal analysis of the materials was determined with a Mettler Toledo TGA/DSC 3 in aluminium oxide crucibles (70 µL with lid) with sample amounts of 1 to 5 mg. Samples of activated materials were taken under inert conditions in a glovebox and transferred to the measurement chamber in screw capped vials immediately prior to the measurement. The following thermal program was applied using synthetic air (20 mL min^{-1}, Westfalen, 80% N_2; 20% O_2): At 30 °C isothermal equilibration (15 min), ramp from 30 °C to 700 °C with 10 K min^{-1}, at 700 °C isothermal equilibration (15 min).

Catalytic Experiments

Ethylene dimerization reactions into butene products were measured in a high-pressure stainless-steel tubular reactor (300 mm long, 12.5 mm diameter) integrated in a fully-automated lab-scale reaction unit from *Demede*. As-prepared MOF samples (25 mg) were diluted with inert SiO_2 (1:20 mass, Davisil-62, Sigma-Aldrich). MOF samples were activated following the procedures as described in the main text using N_2 (2.0 $cm^3g^{-1}s^{-1}$, 99.999%), H_2 (99.9%, 2.0 $cm^3g^{-1}s^{-1}$) or D_2 (99.5%, 2.0 $cm^3g^{-1}s^{-1}$). Thermal defect-engineered MOF samples were treated in N_2 for 1 h at each reaction temperature. Prior to the

catalysis conditions at 50 °C, the reactor was flushed with N_2 and pressurized in N_2 until 5 bar of pressure. Ethylene (99.9%, *Air Liquide*) was then introduced at 10–20 mol g^{-1} h^{-1}. Temperatures were measured with a K-type thermocouple (K-type, Omega) and controlled electronically. Pressure was electronically controlled with a servometer designed by *Demede*. The concentrations of ethylene and products were measured via flame ionization detection after chromatography separation (Agilent 6890; HP-5 methyl silicone).

Transmission Electron Microscopy

Of pristine [(0/0), (50/0) and (100/0)] and most defective samples [(0/30), (50/30) and (100/30)] TEM images were recorded using a JEM NEOARM microscope (JEOL) with a cold FEG electron source operated at 200 kV. Samples were prepared by depositing a drop of the crystalline products dispersed in ethanol onto carbon-coated copper grids (200 mesh) and dried in air.

Additional information

Definitions for “defect amount or “defectiveness” used in the manuscript

In this manuscript, the terms “defectiveness” and “defect amount” are used. Although, *Dissegna et al.* have provided a generally accepted definition of “defect” in a recent review on Defective MOFs, that definition is very general and not sufficiently precise for the work presented herein. For this reason and to prevent the readers from confusion, further explanations shall be provided in the following. A tripartite definition appears most suitable for the point defects discussed herein depending on a.) the sample preparation, b.) the network connectivity and c.) the organometallic perspective.

The first definition is related to the experimental procedure and the chosen sample denotation using an (XX/YY) nomenclature. XX refers to the fraction of rhodium PWs as part of the total metal content comprising ruthenium and rhodium (0%, 50% or 100%). YY refers to the **thermally introduced number of defects** (0%, 10%, 20% or 30%). The mentioned values best reflect the defectiveness throughout the three series of TDE materials and results from different calculative approaches (whether a.) the total amount of organics, b.) the ligands or c.) specifically carboxylates are considered). All different values are depicted in Table S3 (see page 21), respectively. In general, thermal treatments result in the removal of exclusively organic constituents (representing ≈50% of the whole framework). Concluded from mass spectrometry, acetate and carbon dioxide are the major components being removed during TDE. There are no indications for the removal of any aromatic fragments. To reach the arbitrarily chosen defectiveness (YY%), weight losses of 5.5, 10 and 15 wt-% were targeted respectively. At this point, it should be mentioned that “defectiveness” in this context quantifies only defects which were introduced to the framework postsynthetically. Defects originating from modulated synthesis and already being present in the pristine samples are not covered in this first definition.

Secondly, the defectiveness of a MOF sample could be qualitatively defined according to the **network connectivity**. In the ideal HKUST-1 structure, each PW is coordinated by four BTC linkers while each of them interconnects three PWs. Modulated synthesis of PGM-MOFs results in relatively large acetate amounts incorporated to the structure. Even if all equatorial coordination sites are occupied, three acetate ligands can replace one BTC linker resulting in a **“connectivity defect”**. Its occurrence has several effects: The lower connectivity hampers the mechanical stability of the framework and its crystallinity. Further the clearly defined size of the micropores is dispersed and mesopore formation occurs. In contrast to decarboxylation of BTC, any removal of monotopic acetates during TDE does not increase the number of these connectivity defects. Since both acetate and aromatic carboxylate ligands have rather similar electronic and steric effects to the metal nodes, strong impacts on the reactivity of PWs is not to be expected for connectivity defects. This situation changes for the **third definition**:

Defects from an organometallic point of view (**“coordination defect”**) are often called ligand vacancies, **open metal sites** or coordinatively unsaturated sites (CUS). As usual MOF activation facilitates removal of neutral solvent molecules coordinated to the axial positions of a PW, anionic ligands remain strongly bound. This holds true for axial anions accounting for additional charge compensation in the mixed-valent $Ru^{II,III}$-BTC but also for equatorial bridging carboxylates. For instance, a connectivity defect according to our second definition is not necessarily considered defective in this third definition as all equatorial metal sites are coordinated with bridging carboxylates. In this work, TDE-induced decarboxylation results in a strong increase in coordination defects. This is accompanied by altered electronic and steric properties such as (partial) metal reduction or increased accessibility of the metal

nodes. Changes in reactivity of these “coordination defects” are observed for instance in ethylene sorption and dimerization.

Selection of Supplementary Literature

(find bibliography at the end of the document)
Structural tunability[3-6]
Fields of potential MOF applications[7-19]
Mixed-metal MOFs[20-26]
MOF functionalization[20, 27-28]
Catalysis in MOFs[29-36]
PW complexes and HKUST-1 derivatives of copper,[37] ruthenium (mixed- and univalent),[38-39] molybdenum[40-41] and rhodium[42-46], mixed-metallic MOF containing $Rh^{II,II}$ and $Ru^{II,III}$ nodes[2]
Further characterization of the Ru-based MOF[47-49]
Modulator-induced framework-inherent defects[50-51]
Works on defects as opportunities[33, 51-57]
Defect-engineering in MOFs[58-59]
Defect-engineering of Cu and Ru HKUST-1 following the mixed-linker approach[47, 49, 60-61]
Catalysis with Ru-HKUST-1: Hydrogen transfer[62], ethylene dimerization[49, 63]
Thermal annealing of $Zn_4(BDC)_3$ (MOF-5)[64]
Study of the MOF activation temperature,[33, 65-67] and pyrolysis of MOF structures to yield metal (oxide) / carbon composites (termed MOF derivatives)[9, 24, 68-76]
Relevance of process parameters in thermal treatments.[77]
Most recent studies on precious metal-based PWs[78-80] and their HKUST-1 analogues.[63, 81-82]

Syntheses: Thermal Programs & Volatile Analysis

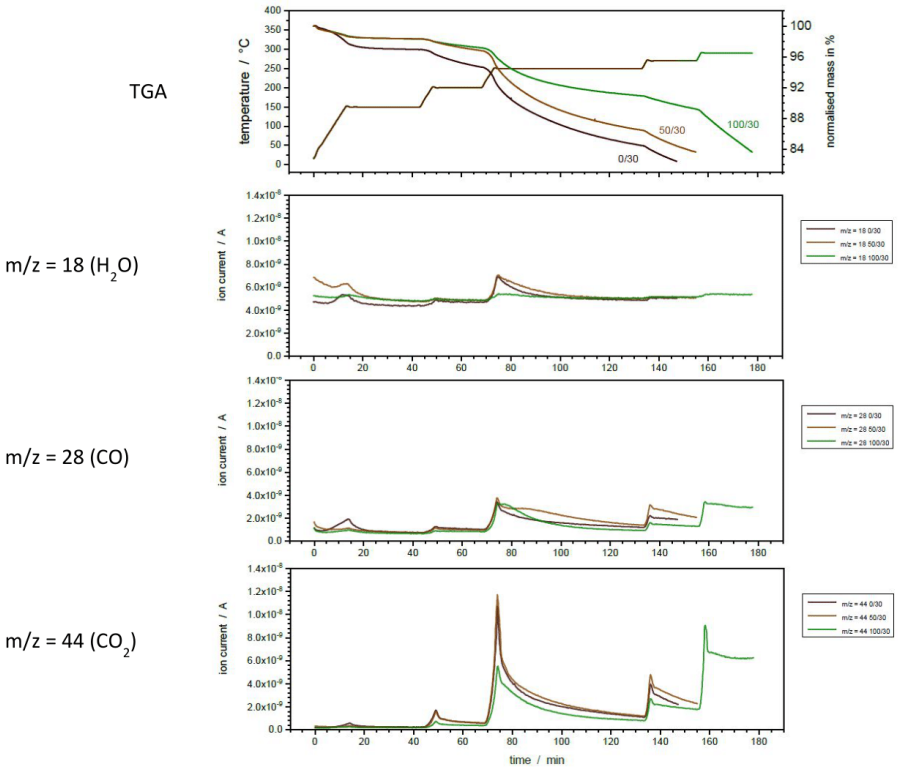

Figure S 1: Top graph: TGA curves for thermal defect engineering temperature programs including respective weight process. Other graphs display mass spectrometric ion currents of 18 (H_2O), 28 (CO), 44 (CO_2), 35 (^{35}Cl) and 37 (putative C_3H fragment instead of expected ^{37}Cl specifity). The presence of peaks at m/z = 37 even in Cl free material (100/30) indicates the lack of specifity while detected peaks at m/z = 35 are exclusive for Ru-based materials.

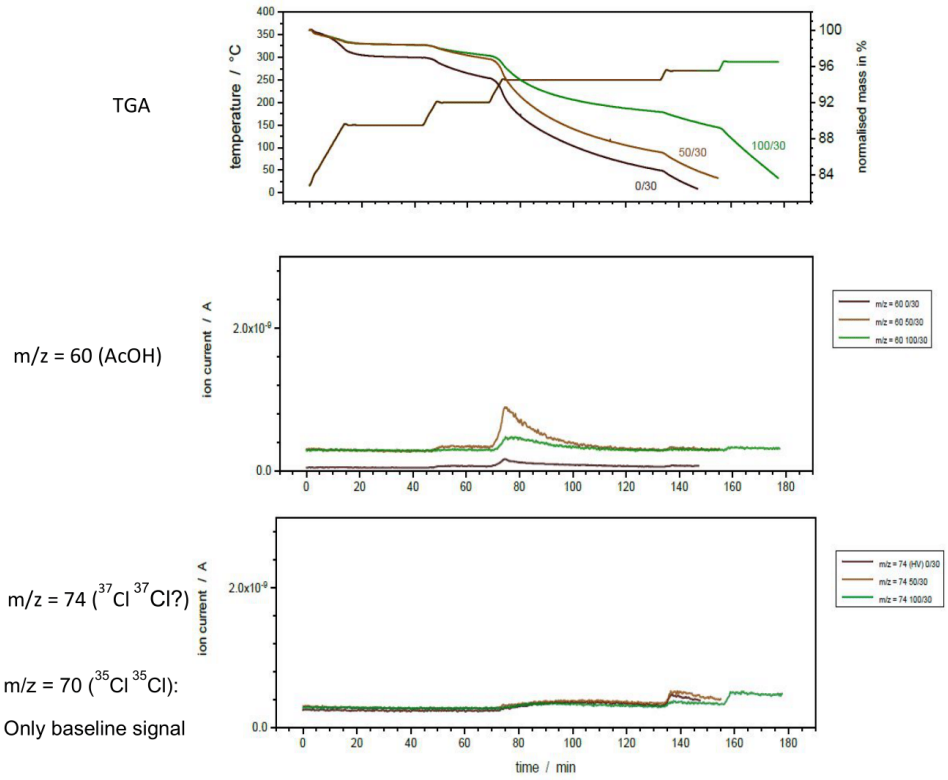

Figure S 2: Top graph: TGA curves for thermal defect engineering temperature programs including respective weight process. Other graphs display mass spectrometric ion currents of 60 (HOAc), 74 (expected Cl_2 specifity (both Cl-37 isotopes), but as identical peaks occur in Cl free sample (0/30), observation of carbon-based fragments are likely. Note that observation of m/z = 70 (Cl_2 with Cl-35 isotopes) did not result in any peaks.

The specific processes occurring during hydride generation were further elucidated utilizing TGA-MS with flow of different gasses. Based on the previous findings that axial acetates are readily removed upon TDE and result in $Ru^{II,II}$ sites, we investigated the role of an hydrogen atmosphere onto the release of volatile HCl within the TGA-MS setup. The results are depicted in Figure S 3 and suggest an increase HCl release in H_2 atmosphere at only 150 °C even if the sample was already pretreated in N_2 at 300 °C. Therefrom, we conclude that axial Cl ligands are rather inert to removal during TDE in inert atmosphere, but H_2 readily removes them. A respective metal hydride formation is assumed to accompany the HCl evolution.

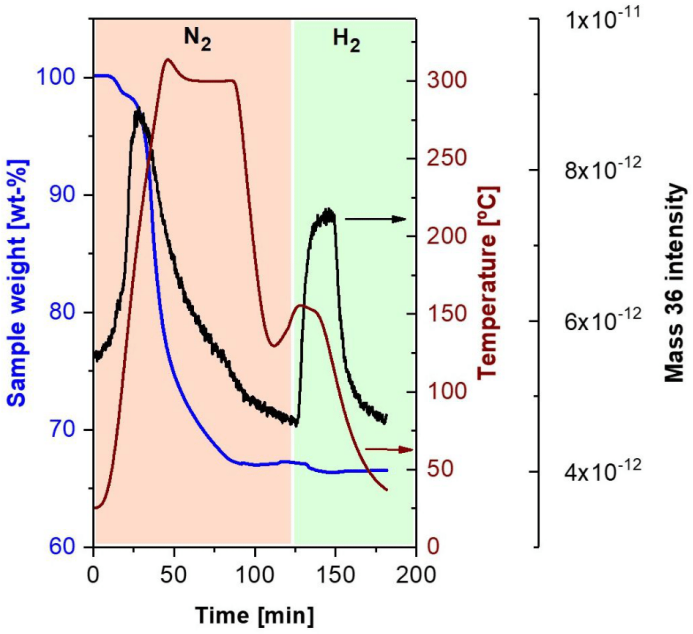

Figure S 3: TGA-MS experiment supporting the assumed chlorine-releasing effect of the hydrogen treatment. Residual weight (blue curve), the observed HCl ion current (black curve) and the temperature program (brown curve) are displayed. In the red region N_2 served as atmosphere which was then switched to H_2 (green region).

PXRD

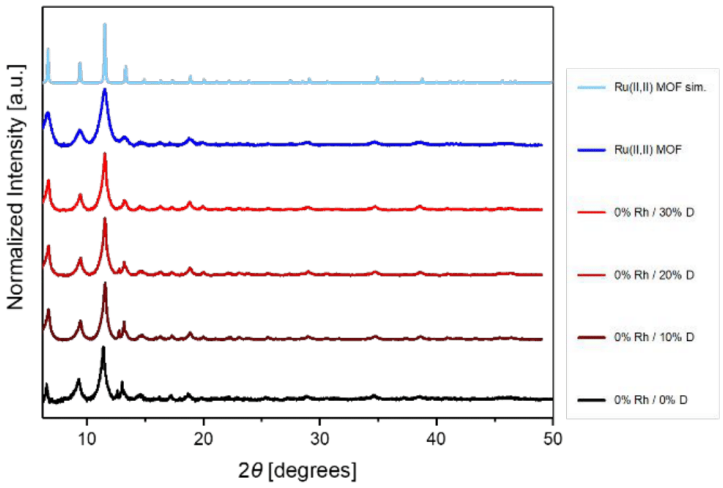

Figure S 4: PXRD pattern of 0% Rh pristine and TDE-materials indicating preserved crystallinity.

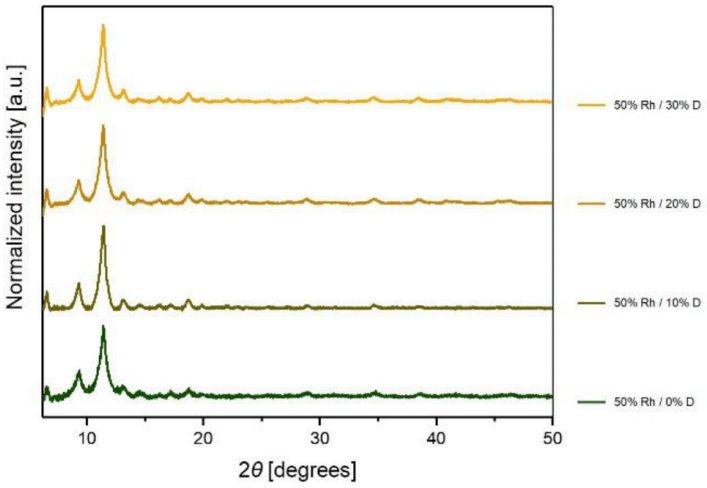

Figure S 5: PXRD patterns of 50%Rh pristine and TDE-materials indicate preserved crystallinity.

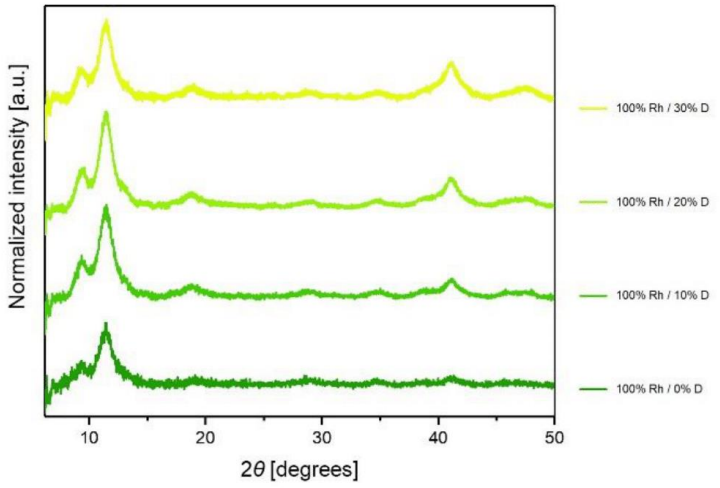

Figure S 6: PXRD patterns of 100%Rh pristine and TDE-materials indicating preserved crystallinity and nanoparticle formation.

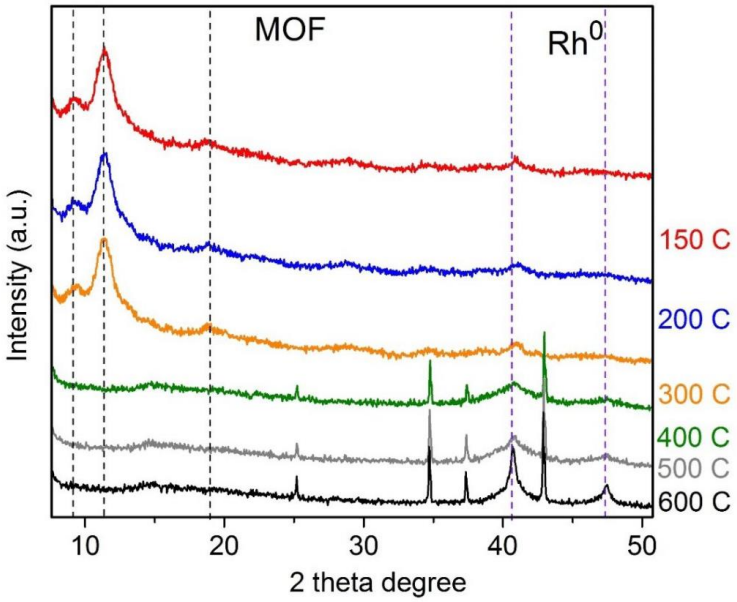

Figure S 7: VT-PXRD pattern of Rh-BTC indicating loss of crystallinity (black hashed lines on main reflections) between 300 °C and 400 °C and formation of Rh^0 NPs (grey hashed lines).

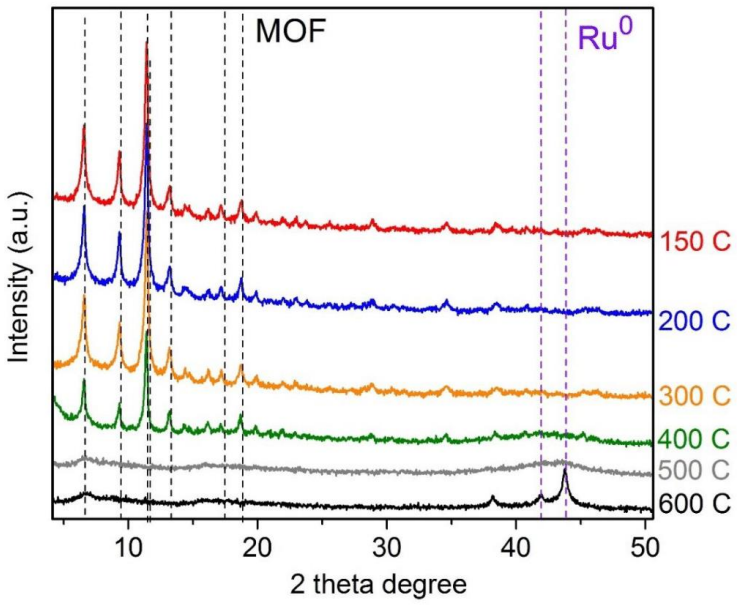

Figure S 8: VT-PXRD pattern of Ru-BTC indicating loss of crystallinity (black hashed lines on main reflections) between 300 °C and 400 °C and complete amorphization until 500 °C accompanied by the formation of Ru^0 NPs (grey hashed lines).

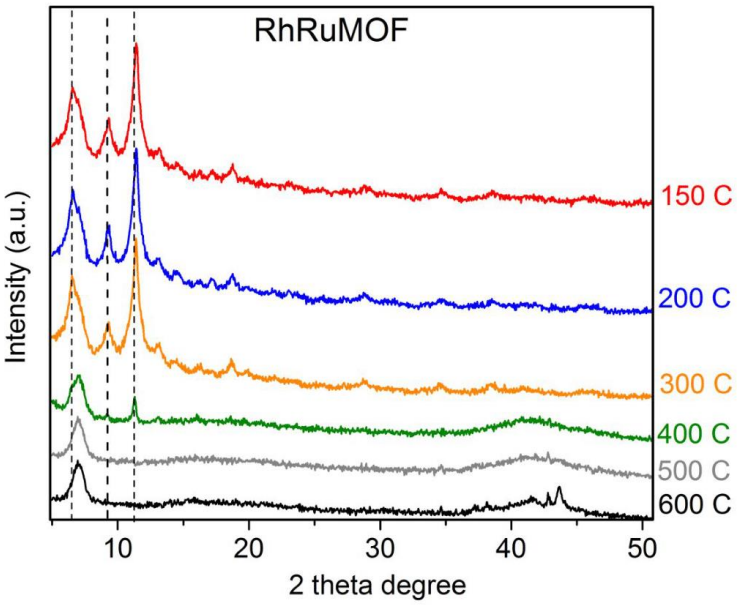

Figure S 9: VT-PXRD pattern of Ru-BTC indicating loss of crystallinity (black hashed lines on main reflections) between 300 °C and 400 °C and complete amorphization until 500 °C accompanied by the formation of metallic NPs (broad reflection around 40° 2Θ. An unidentified reflection at 7 ° emerges.

Thermogravimetric Analysis

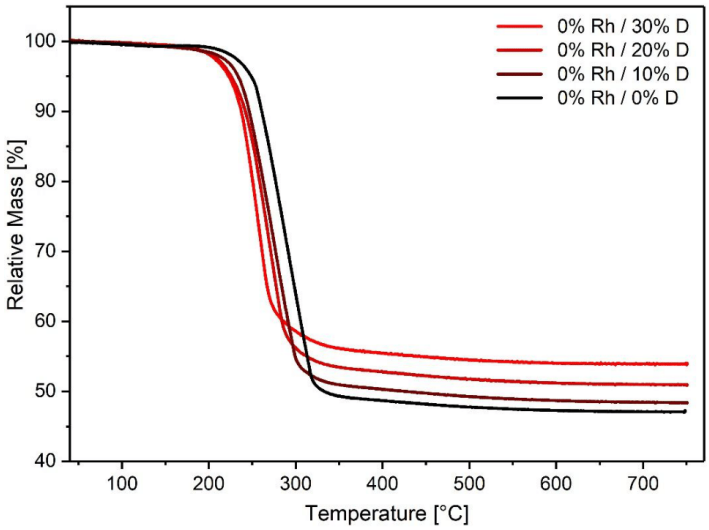

Figure S 10: TGA curves of 0%Rh samples with different defect amounts. Increasing metal oxide contents indicate successful TDE processes due to thermal organic constituent removal and allow metal content determination. Slightly decreased thermal stabilities may result from weakened structural stability of the defective frameworks.

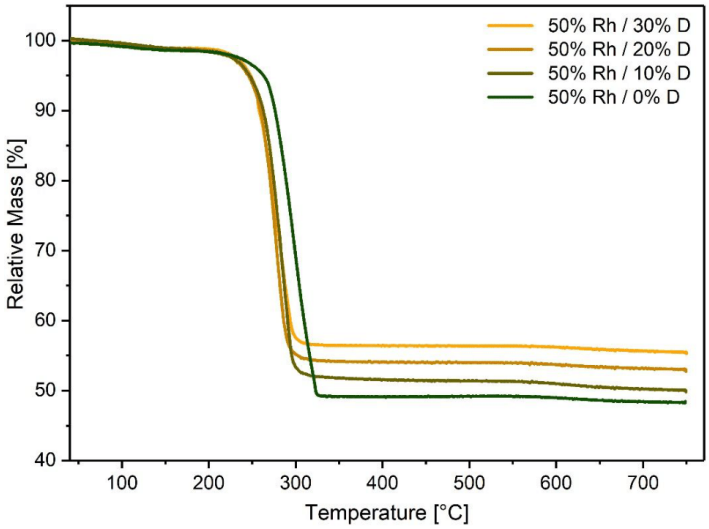

Figure S 11: TGA curves of 50%Rh samples with different defect amounts. Increasing metal oxide contents indicate successful TDE processes due to thermal organic constituent removal and allow metal content determination. Slightly decreased thermal stabilities may result from weakened structural stability of the defective frameworks.

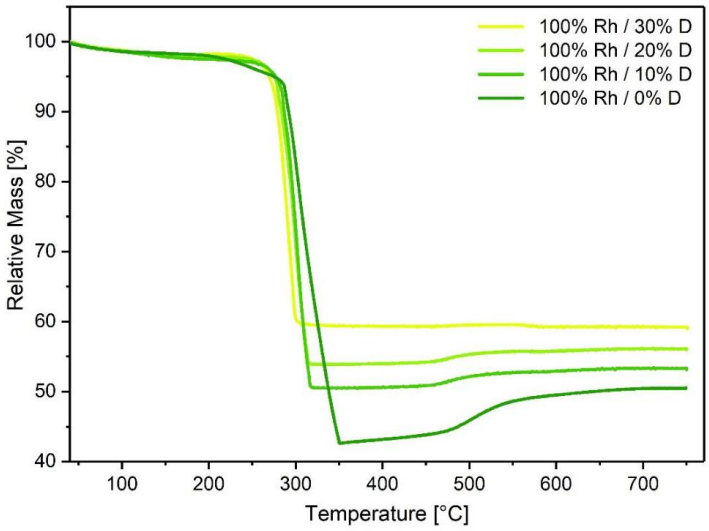

Figure S 12: TGA curves of 100%Rh samples with different defect amounts. Increasing metal oxide contents indicate successful TDE processes due to thermal organic constituent removal and allow metal content determination. Slightly decreased thermal stabilities may result from weakened structural stability of the defective frameworks. Weight increase at ~500°C results from reoxidation of elemental rhodium to Rh_2O_3.

Additionally, we performed a CO-based TGA experiment to "titrate" open metal sites in $Ru^{II,III}$, $Ru^{II,II}$ and Rh-MOFs. Thus, the gravimetric quantity of adsorbed CO detected by the weight increase upon CO dosing was transformed into a molar amount per PW.

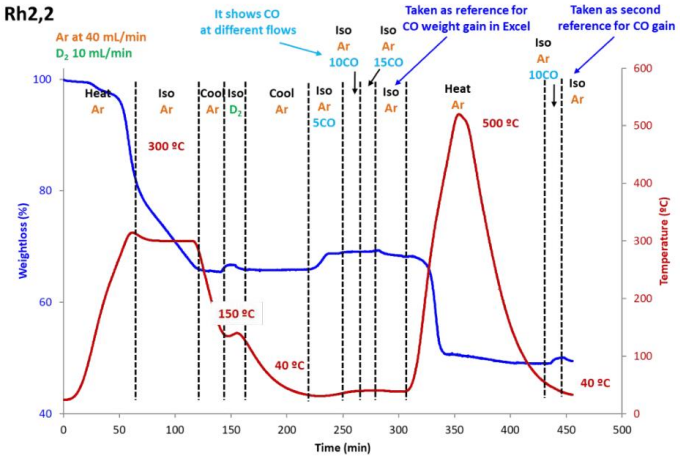

Figure S 13: TGA-based CO titration experiment with Rh-BTC treated at 300 °C. Weight curve (blue) and temperature program curve (red) with different gas streams (displayed on top). The CO induced weight gain represents sorption of 0.30 molecules CO per metal atom. This refers to roughly one CO rather strongly bound to a PW indicating the little weaker interaction of CO with Rh compared to Ru-BTC. As a reference sample was completely pyrolyzed at 500°C to exclusively form Rh NPs and load them with CO respectively. The much smaller uptake of CO proves the remaining presence of active Rh sites after treatment at 300 °C.

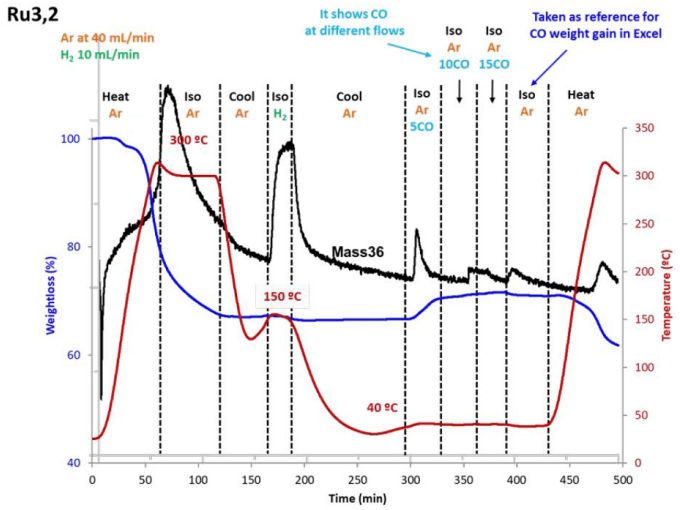

Figure S 14: TGA-based CO titration experiment with mixed-valent $Ru^{II,III}$-BTC treated at 300 °C. Weight curve (blue) and temperature program curve (red) with different gas streams (displayed on top). The CO induced weight gain represents sorption of 0.48 molecules CO per metal atom or one CUS per PW.

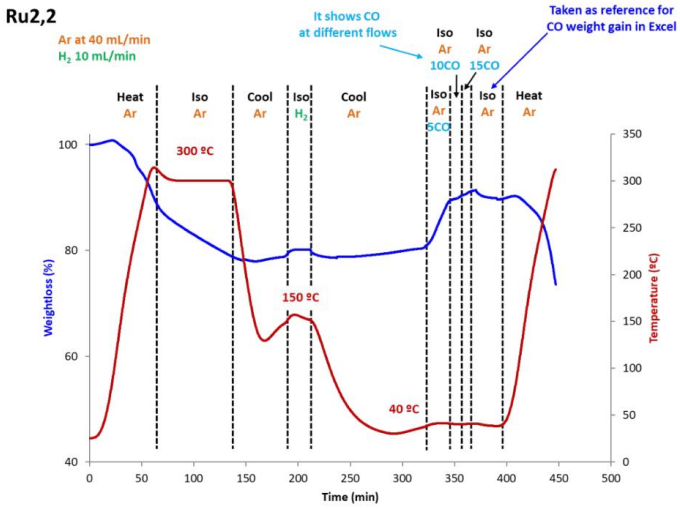

Figure S 15: TGA-based CO titration experiment with mixed-valent $Ru^{II,III}$-BTC treated at 300 °C. Weight curve (blue) and temperature program curve (red) with different gas streams (displayed on top). The CO induced weight gain represents sorption of 0.93 molecules CO per metal atom or two CUS per PW.

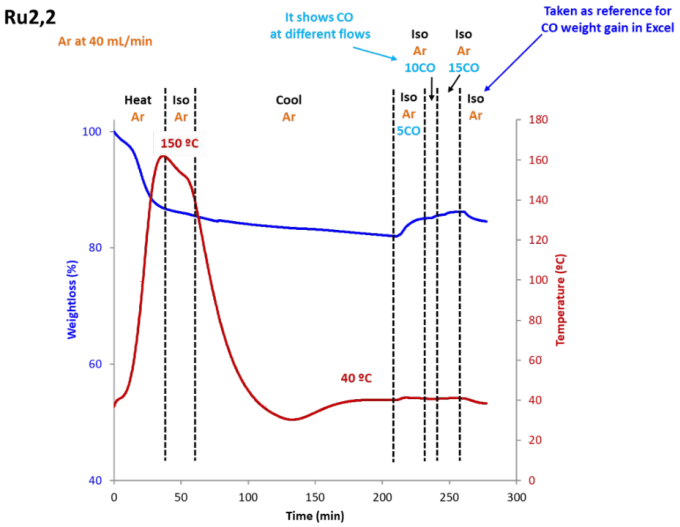

Figure S 16: TGA-based CO titration experiment with univalent $Ru^{II,II}$-BTC treated at 150 °C. Weight curve (blue) and temperature program curve (red) with different gas streams (displayed on top). The CO induced weight gain represents sorption of 0.36 molecules CO per metal atom. This refers to roughly one CO rather strongly bound to a PW.

Table S 1: Summarized CO uptake per PW of each MOF system and respective pretreatment conditions.

MOF system	Pretreatment temperature [°C]	CO uptake per PW
$Rh^{II,II}$	300	0.59
$Ru^{II,III}$	300	0.97
$Ru^{II,II}$	300	1.86
$Ru^{II,II}$	150	0.72

Calculated Composition

Table S 2: Calculated sum formulae based on EA and TGA results and putative assignment of axial and equatorial acetates. As observed in PXRD: Pristine MOF samples with low crystallinity and increasing defectiveness also have a higher putative OAc fraction within the equatorial ligators reducing the network connectivity.

Sample	Calculated Sum Formulae	Assumed fractions*				Molecular Weight
		OAc_{eq}	OAc_{ax}	Axial Occupancy	OAc fraction of total eq. ligators	
(100 / 0)	$[Rh_3(BTC)_{1.61}(OAc)_{1.89}]$	1.17	0.71	24 %	20 %	753.35
(100 / 10)	$[Rh_3(BTC)_{1.22}(IPA)_{0.39}(OAc)_{1.34}]$					704.08
(100 / 20)	$[Rh_3(BTC)_{0.86}(IPA)_{0.74}(OAc)_{1.01}]$					669.74
(100 / 30)	$[Rh_3(BTC)_{0.61}(IPA)_{0.99}(OAc)_{0.64}]$					637.14
(50 / 0)	$[Ru_{1.44}Rh_{1.56}(BTC)_{1.52}(OAc)_{2.69}Cl_{0.3}]$	1.44	1.25	53 %	24 %	791.44
(50 / 10)	$[Ru_{1.44}Rh_{1.56}(BTC)_{1.36}(IPA)_{0.57}(OAc)_{1.03}Cl_{0.3}]$					753.18
(50 / 20)	$[Ru_{1.44}Rh_{1.56}(BTC)_{0.64}(IPA)_{1.27}(OAc)_{0.64}Cl_{0.3}]$					695.69
(50 / 30)	$[Ru_{1.44}Rh_{1.56}(BTC)_{0.54}(IPA)_{1.27}(OAc)_{0.52}Cl_{0.3}]$					667.45
(0 / 0)	$[Ru_3(BTC)_{1.89}(OAc)_{1.55}Cl_{0.7}]$	0.33	1.22	64 %	6 %	810.73
(0 / 10)	$[Ru_3(BTC)_{0.56}(IPA)_{1.32}(OAc)_{1.55}Cl_{0.65}]$					751.88
(0 / 20)	$[Ru_3(BTC)_{0.82}(IPA)_{1.44}(OAc)_0Cl_{0.61}]$					730.18
(0 / 30)	$[Ru_3(BTC)_{1.12}(IPA)_{0.76}(OAc)_{0.24}Cl_{0.57}]$					695.75
$Ru^{II,II}$-BTC	$[Ru_3(BTC)_{1.32}(OAc)_{2.22}]$	2.05	0.17	<1 %	34 %	707.28

* Assuming perfect equatorial saturation of PW nodes of $M:L_{eq}$ = 3:6 in $[M_3(BTC)_2]$. OAc is assumed to occupy the missing fraction of equatorial sites.

Table S 3: Quantification of the term "defectiveness" in TDE samples depending on metal type and reference.

(XX/YY) Nomenclature			Removed Fraction of:			
Sample	XX % Rh	YY %* Defects	Removed wt-%	Total Organics	Total Ligands	CO_2^-
(0/0)	0	0	0		0%	0%
(0/10)	0	10	5.50%	-9%	-18%	-19%
(0/20)	0	20	10%	-16%	-25%	-26%
(0/30)	0	30	15%	-24%	-28%	-29%
(50/0)	50	0	0		0%	0%
(50/10)	50	10	5.50%	-9%	-13%	-14%
(50/20)	50	20	10%	-16%	-28%	-30%
(50/30)	50	30	15%	-25%	-34%	-35%

(100/0)	100	0	0		0%	0%
(100/10)	100	10	5.50%	-9%	-14%	-14%
(100/20)	100	20	10%	-17%	-25%	-25%
(100/30)	100	30	15%	-25%	-34%	-34%
		Predefined		Based on TGA / sum formulae		

Structural Complexity in Pristine PGM-MOFs

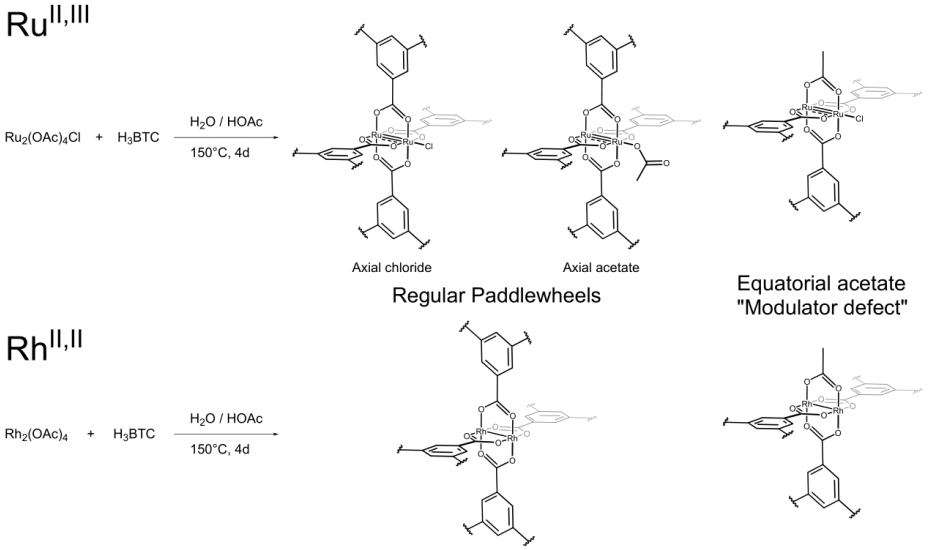

Scheme S 1: Structural complexity in pristine PGM-HKUST-1 derivatives. The mixed-valent Ru-HKUST-1 comprises one axial ligand per PW which is either chloride or acetate for compensation of the additional charge. Modulator-based acetate incorporation on equatorial positions (up to three equatorial acetates per PW) occurs in both metal derivatives.

Assumed Reactions during TDE

a.) Mixed valent Ru-MOF:

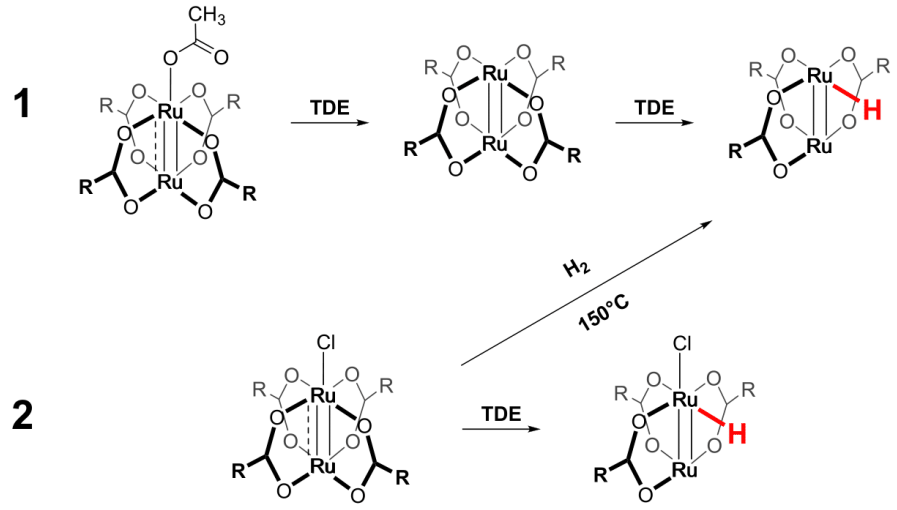

b.) Univalent Rh-MOF:

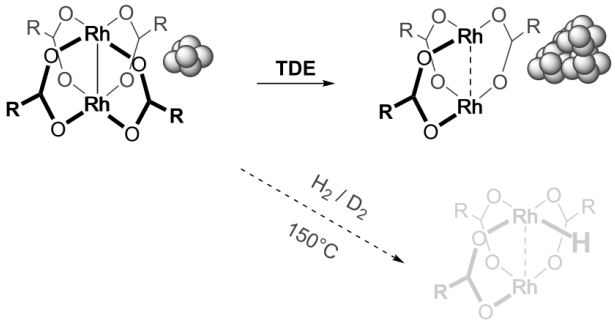

Scheme S 2: Assumed molecular reactions during TDE of the highly complex PGM-MOFs. Organic residues R represent either CH_3 (acetate) or $C_8H_3O_4$ (BTC). Each univalent PW could carry x= 1-4 BTC ligands and 4-x acetate ligands according to Scheme S1. ***a.)*** *Mixed-valent Ru-MOF. Either acetate (**1**) or chloride (**2**) can coordinate one axial position for charge compensation. **1** displays the case when acetate is the additional axial ligand: Temperature-induced removal first generates a univalent Ru-PW which further undergoes ligand removal/fragmentation under subsequent Ru-H formation. **2** displays the case of an axially bound chloride ligand: TDE under inert atmosphere retains the chloride while hydrogen treatment facilitates its removal.* ***b.)*** *The assumed TDE of the univalent Rh-MOF features much less flexibility. While few Rh NPs are already present in the pristine MOF, their agglomeration leads to larger NPs during TDE. No Rh-H formation is observed in inert atmosphere TDE, while low Rh-H formation is visible under harsher H_2 / D_2 treatment. Overall Ru-MOF seems more tolerant towards TDE-induced ligand removal / fragmentation. Hypothetically the higher bond order in Ru dimers allows more progressive ligand removal since M-M bonds could potentially prevent NP formation.*

Sorption experiments

Nitrogen Sorption

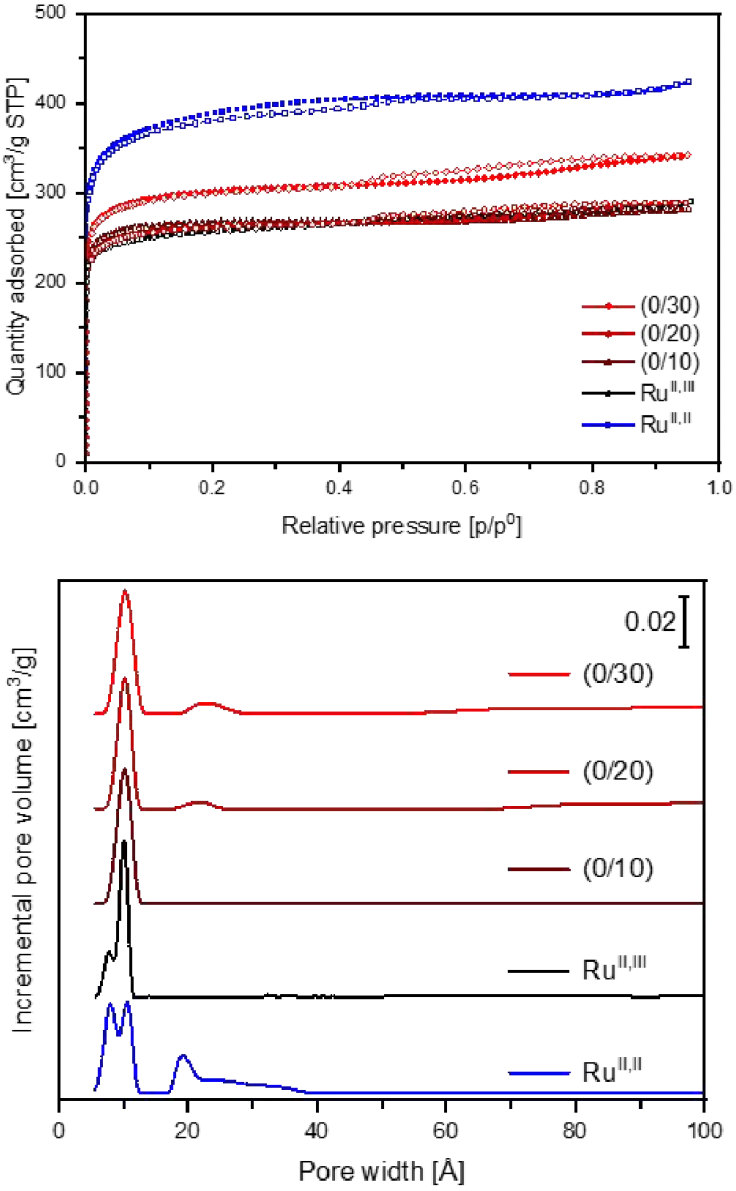

Figure S 17: Top: Nitrogen sorption isotherms of 0%Rh samples and $Ru^{II,II}$-MOF displaying both adsorption and desorption branches. Isotherms were recorded at 77K. Closed symbols represent data points from adsorption branch, open symbols represent data points from desorption branch. Hystereses indicate upcoming mesoporosity. Bottom: Pore size distributions of ruthenium-based samples assuming cylindrical pores on oxide surfaces.

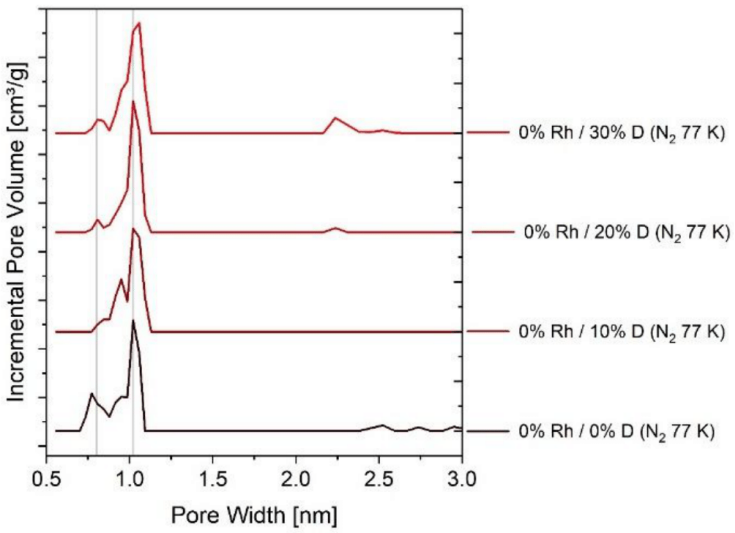

Figure S 18: DFT-based pore size distribution of 0%Rh samples (pristine and TDE) calculated assuming cylindrical pores and silicon oxide adsorption properties. Data obtained from nitrogen sorption experiments recorded at 77K. Extinction of small pores due to TDE induced pore wall removal and the formation of mesopores can be observed with increasing defectiveness. Medium-sized micropore (~0.9 nm) may result from pore size reduction through axial ligands in mixed-valent Ru-MOF.

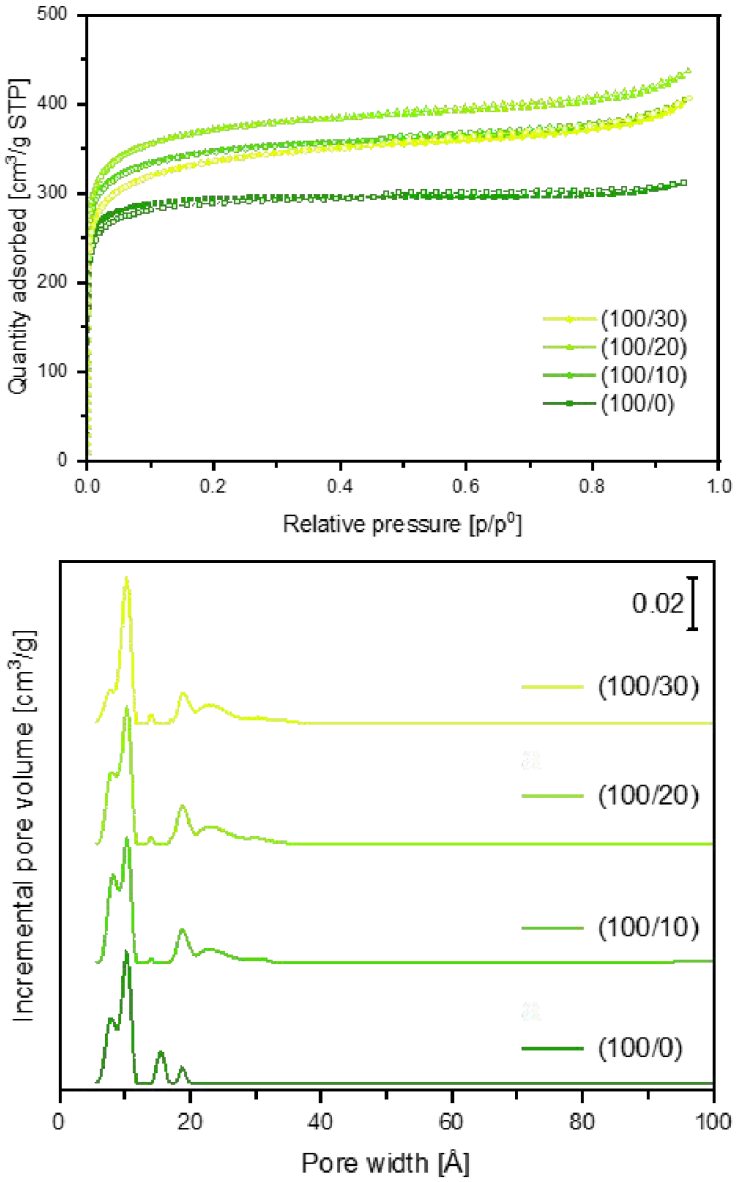

Figure S 19: Top: N_2 sorption isotherms for 100%Rh series recorded at 77K. Bottom: DFT-calculated pore size distributions assuming cylindrical pores on oxide surfaces. Increasing porosity emerges due to fusion of small sized micropores into larger pores.

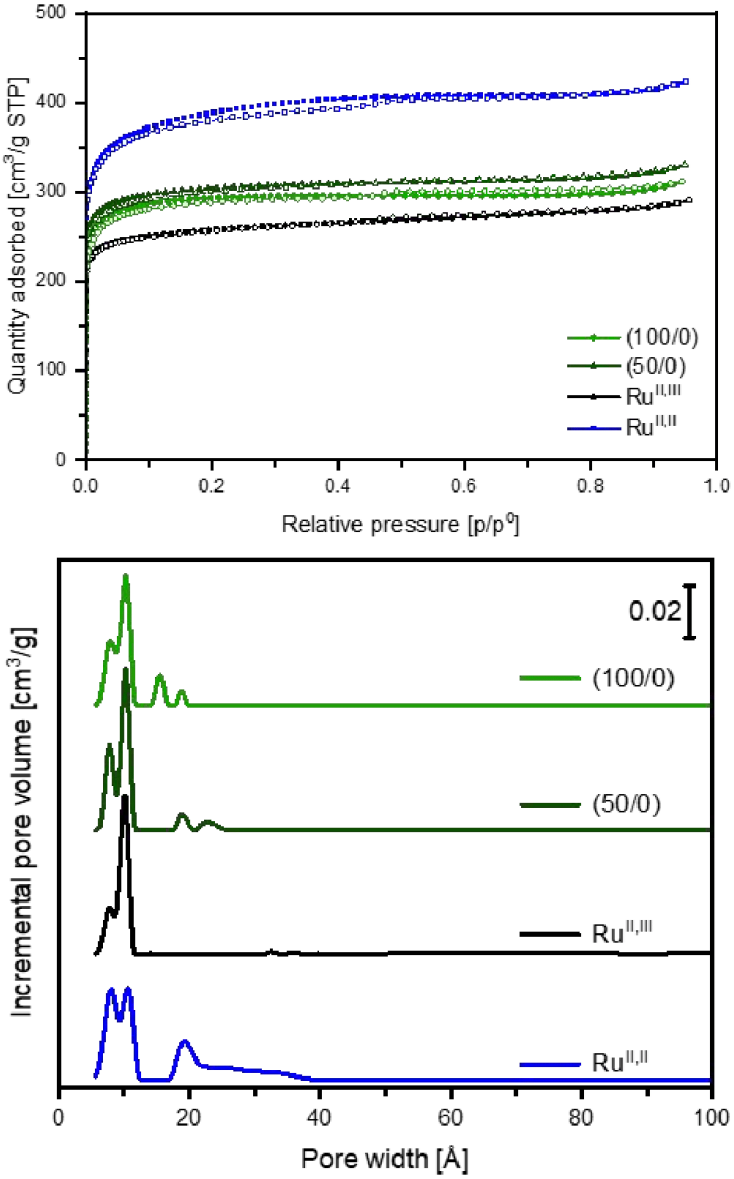

Figure S 20: Top: N_2 sorption isotherms for pristine Ru-, Rh- and bimetallic (50:50 Ru:Rh)-MOFs recorded at 77K. Bottom: DFT-calculated pore size distributions assuming cylindrical pores on oxide surfaces.

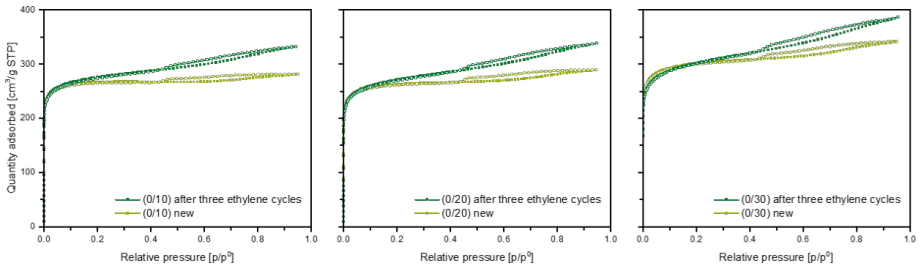

Figure S 21: Comparison of Ru-TDE-MOFs (0/10), (0/20) and (0/30) before and after three cycles of ethylene sorption. Increasing slope of type I isotherms suggests broad range of different sized mesopores after repeated ethylene cycles.

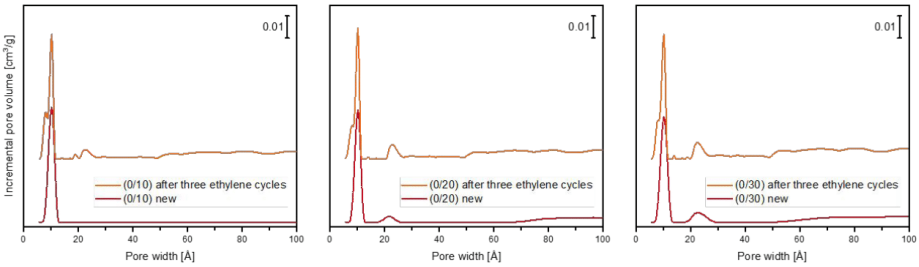

Figure S 22: Comparison of DFT-calculated pore size distribution of Ru-TDE-MOFs (0/10), (0/20) and (0/30) before and after three cycles of ethylene sorption. The formation of a narrow micro pore suggests axial coordination of PWs reducing the size of one of the two large micro pores. Further formation of a wide range of meso pores takes place after several cycles of ethylene sorption indicating etching of the materials.

Ethane Sorption

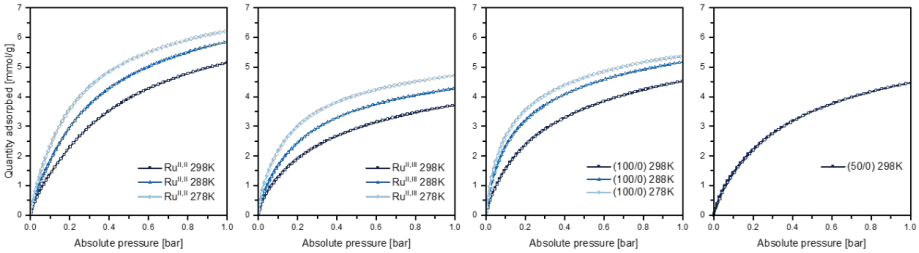

Figure S 23: Ethane sorption isotherms of pristine MOF samples Ru^{II,II} reference, (0/0), (50/0) and (100/0) recorded at 298K, 288K and 278K respectively. Expected temperature effects are observed and not affected by chemisorption allowing derivation of heat of adsorptions.

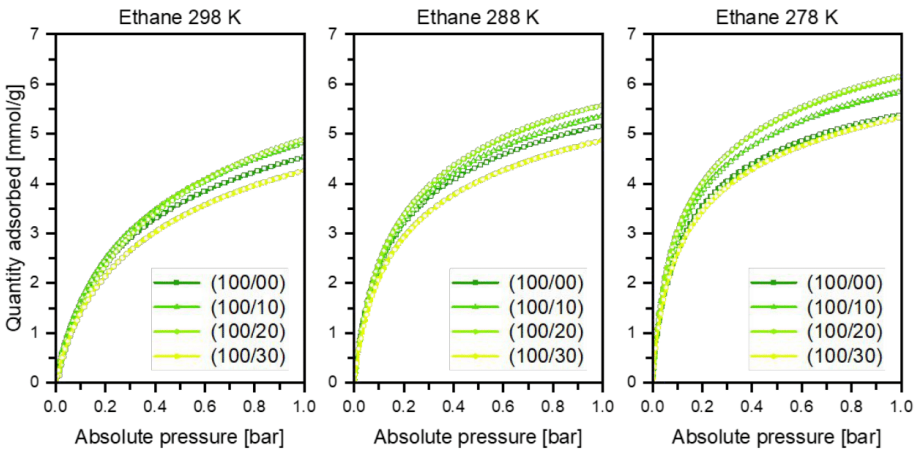

Figure S 24: Ethane sorption isotherms of Rh-based MOF samples (100/0), (100/10), (100/20) and (100/30) recorded at 298K, 288K and 278K respectively. Expected temperature effects are observed and not affected by chemisorption allowing derivation of heat of adsorptions.

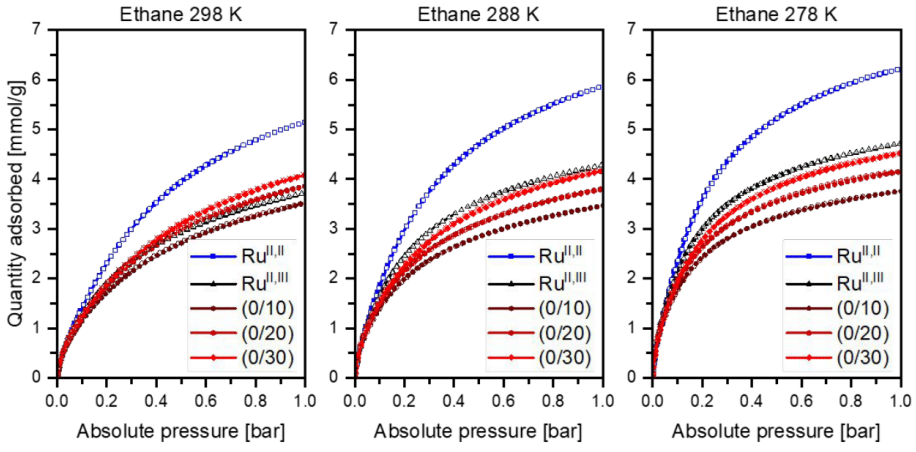

Figure S 25: Ethane sorption isotherms of Ru-based MOF samples recorded at 298K, 288K and 278K respectively. Increased sorption capacities with decreased temperatures reflect ideal non-reactive sorption behaviour.

Table S 4: Volumetric and molar uptake for ethane sorption.

Ethane Uptake [cm³ g^{-1}]	Sample								
	0/0	0/10	0/20	0/30	Ru^{II,II}	100/0	100/10	100/20	100/30
298 K	83.66	79.04	86.49	91.46	115.39	101.48	108.32	109.79	95.65
288 K	96.34	77.66	85.63	93.84	131.74	116.11	120.07	124.79	109.20
278 K	105.66	84.31	93.35	101.29	139.74	120.73	131.22	138.17	119.98
Ethane Uptake [mmol g^{-1}]	Sample								
	0/0	0/10	0/20	0/30	Ru^{II,II}	100/0	100/10	100/20	100/30

298 K	3.73	3.53	3.86	4.01	5.15	4.53	4.83	4.90	4.27
288 K	4.30	3.46	3.82	4.19	5.88	5.18	5.36	5.57	4.87
278 K	4.71	3.76	4.16	4.52	6.23	5.39	5.85	6.16	5.35

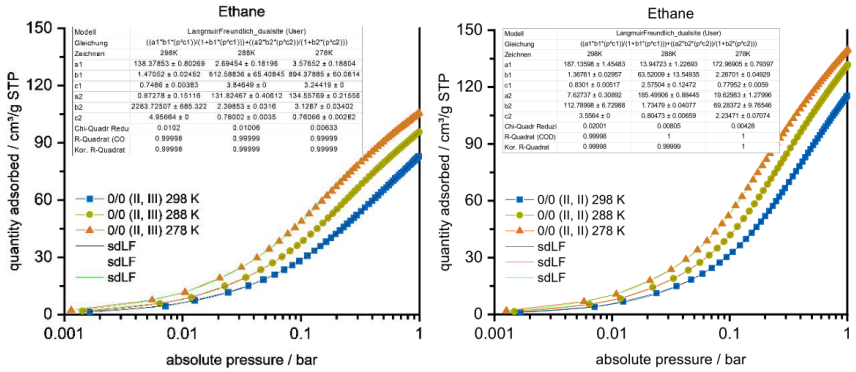

Figure S 26: Fits for the calculation of the energy of adsorptions for pristine Ru-MOFs. Left: Mixed-valent, right: univaltent Ru-MOF.

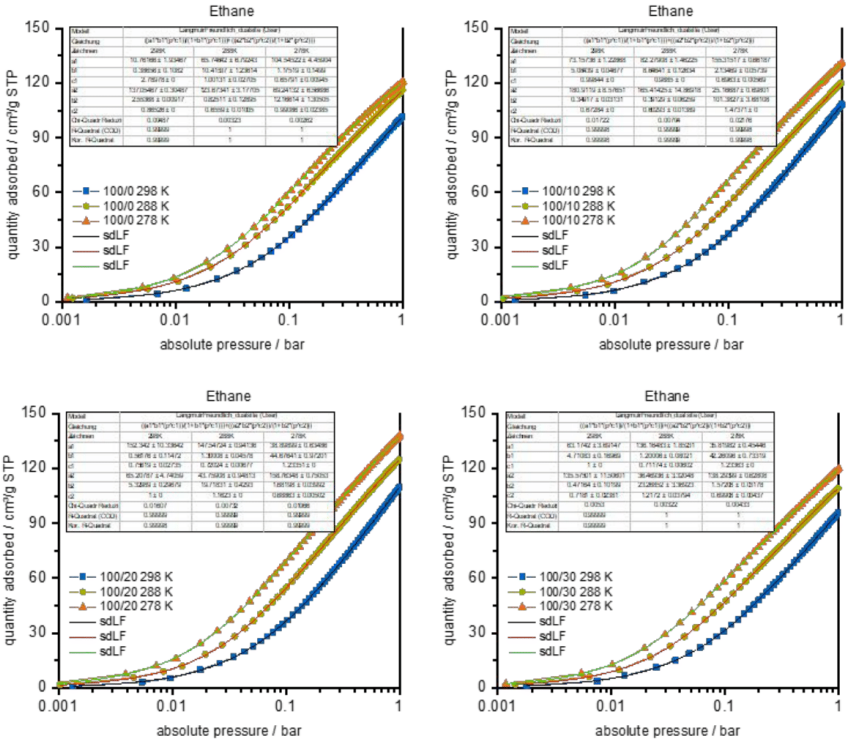

Figure S 27: Fits for the calculation of the energy of adsorptions for TDE-Rh-MOFs. Top left: (100/0), right: (100/10), bottom left: (100/20), right: (100/30).

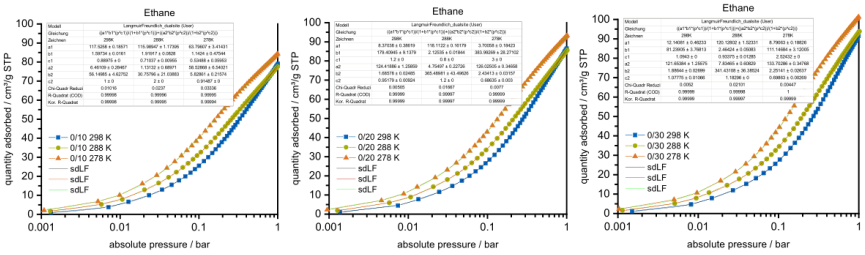

Figure S 28: Fits for the calculation of the energy of adsorptions for Ru-TDE-MOFs.

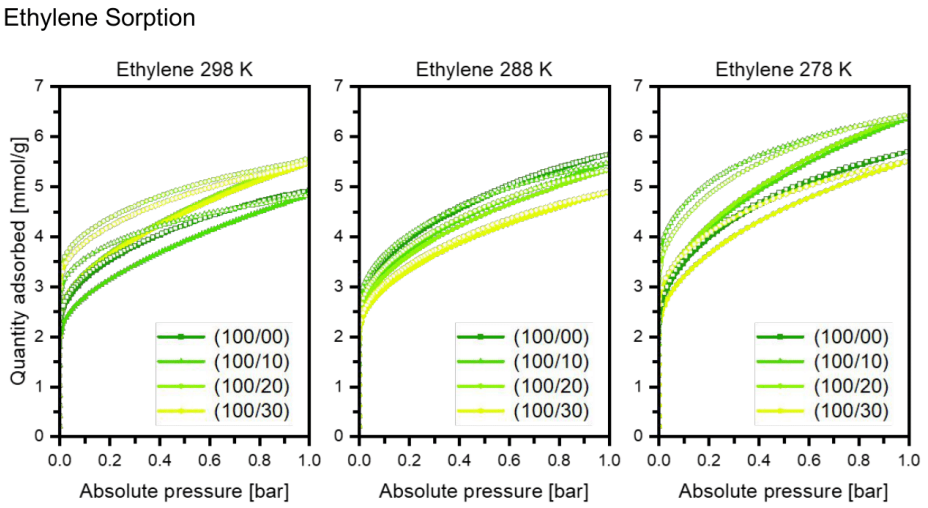

Figure S 29: Ethylene sorption isotherms of rhodium samples at 298K, 288K and 278K respectively. While pristine Rh-MOF features slightly increasing uptake with decreasing temperatures no clear trend can be extracted for defective samples. Irreversible coordination or reactivity of ethylene can be concluded from non-"closing" isotherms with residual uptake at the end of the desorption branch which correlates with sorption temperature and defectiveness of the samples. Each isotherm was performed with a fresh sample.

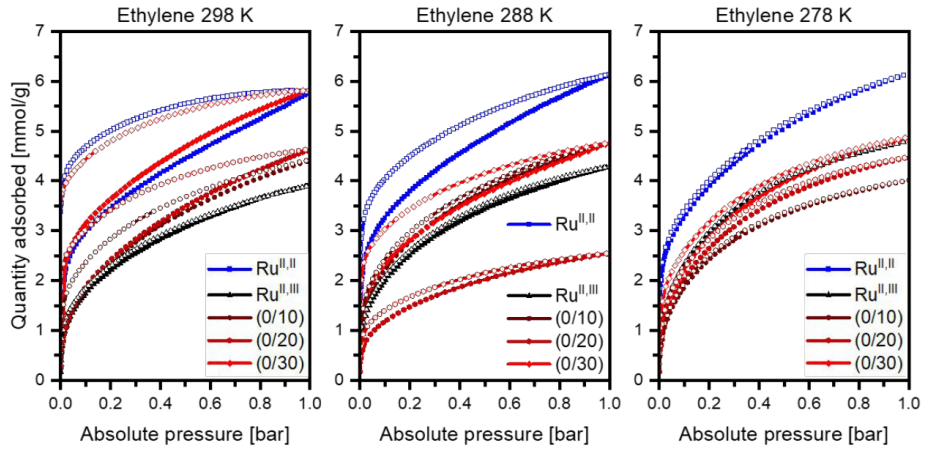

Figure S 30: Ethylene sorption isotherms of ruthenium samples at 298K, 288K and 278K respectively. While pristine Ru-MOF features increasing uptake with decreasing temperatures, the opposite trend occurs with defective samples peaking in huge chemisorption on (0/30) at 298 K. Irreversible coordination or reactivity of ethylene can be concluded from non-"closing" isotherms with residual uptake at the end of the desorption branch which correlates with sorption temperature and defectiveness of the samples. Each isotherm was performed with a fresh sample.

Table S 5: Volumetric (top row) and molar (middle row) uptake for ethylene sorption and calculated molecules per paddlewheel (bottom row).

Ethylene Uptake [$cm^3\ g^{-1}$]	Sample								
	0/0	0/10	0/20	0/30	$Ru^{II,II}$	100/0	100/10	100/20	100/30
298 K	87.68	99.42	104.06	130.57	129.95	110.34	108.27	124.59	122.54
288 K	96.05	107.56	57.38	107.11	137.55	126.54	123.00	119.83	110.11
278 K	107.83	89.99	100.53	108.58	137.94	128.24	143.06	144.44	123.99
Ethylene Uptake [$mmol\ g^{-1}$]	Sample								
	0/0	0/10	0/20	0/30	$Ru^{II,II}$	100/0	100/10	100/20	100/30
298 K	3.91	4.44	4.64	5.83	5.80	4.92	4.83	5.56	5.47
288 K	4.29	4.78	2.56	4.78	6.14	5.65	5.49	5.35	4.91
278 K	4.81	4.01	4.49	4.87	6.15	5.72	6.38	6.44	5.53
Ethylene Uptake [molecules per PW]	Sample								
	0/0	0/10	0/20	0/30	$Ru^{II,II}$	100/0	100/10	100/20	100/30
298 K	2.11	2.23	2.26	2.70	2.73	2.47	2.27	2.48	2.32
288 K	2.32	2.40	1.25	2.22	2.90	2.84	2.58	2.39	2.09
278 K	2.60	2.01	2.19	2.26	2.90	2.87	2.99	2.88	2.35

Table S 6: Residues of ethylene sorption representative for chemisorption. Volumetric (top row), molar (middle row) and stoichiometric (middle row, molecules ethylene per paddlewheel) ethylene residues.

Ethylene Residues [$cm^3\ g^{-1}$]	Sample								
	0/0	0/10	0/20	0/30	$Ru^{II,II}$	100/0	100/10	100/20	100/30
298 K	9.09	23.25	44.06	79.78	75.95	46.12	57.42	66.78	66.65
288 K	18.31	12.37	10.69	33.94	47.96	51.82	55.07	52.53	43.63
278 K	10.85	7.24	12.03	15.34	27.98	47.07	74.6	67.19	59.13
Ethylene Residue [$mmol\ g^{-1}$]	Sample								
	0/0	0/10	0/20	0/30	$Ru^{II,II}$	100/0	100/10	100/20	100/30
298 K	0.41	1.04	1.97	3.56	3.39	2.06	2.56	2.98	2.97
288 K	0.82	0.55	0.48	1.51	2.14	2.31	2.46	2.34	1.95
278 K	0.48	0.32	0.54	0.68	1.15	2.10	3.33	3.00	2.64
Ethylene Residue [molecules per PW]	Sample								
	0/0	0/10	0/20	0/30	$Ru^{II,II}$	100/0	100/10	100/20	100/30
298 K	0.22	0.52	0.96	1.65	1.60	1.03	1.20	1.33	1.26
288 K	0.44	0.28	0.23	0.70	1.01	1.16	1.15	1.04	0.83
278 K	0.26	0.16	0.26	0.32	0.54	1.05	1.56	1.34	1.12

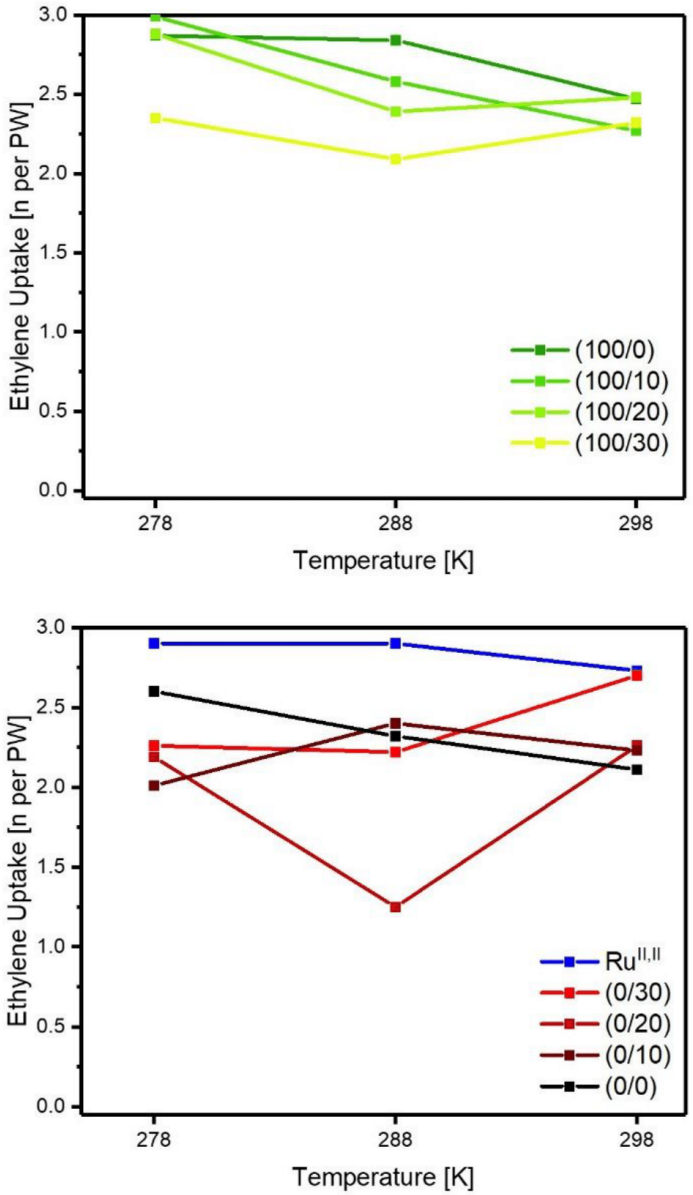

Figure S 31: Ethylene sorption uptakes at the end of adsorption branches. Top: Rh-TDE-MOFs, Bottom: Ru-TDE-MOFs. Total uptake is comparable between Rh and Ru-MOFs and no strong temperature dependency with defectiveness can be concluded. In Ru samples with higher defectiveness have increasing uptakes at 298 K.

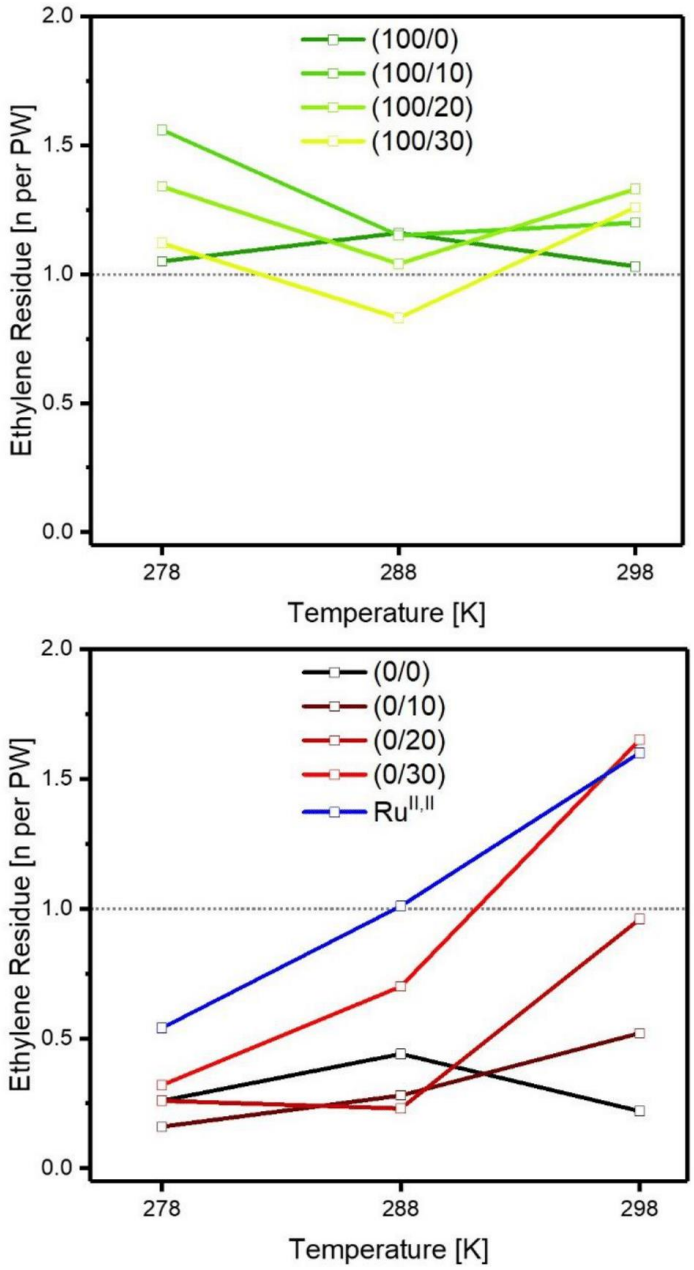

Figure S 32: Ethylene sorption residues at the end of desorption branches. Top: Rh-TDE-MOFs, Bottom: Ru-TDE-MOFs. Dotted line indicates adsorption of one molecule ethylene per PW unit. No temperature-defect correlation for Rh occurs. Strong increase in residues at higher temperature for Ru suggesting emerging reactivity upon metal reduction as indicated by $Ru^{II,II}$ reference sample.

35

Vibrational spectroscopy

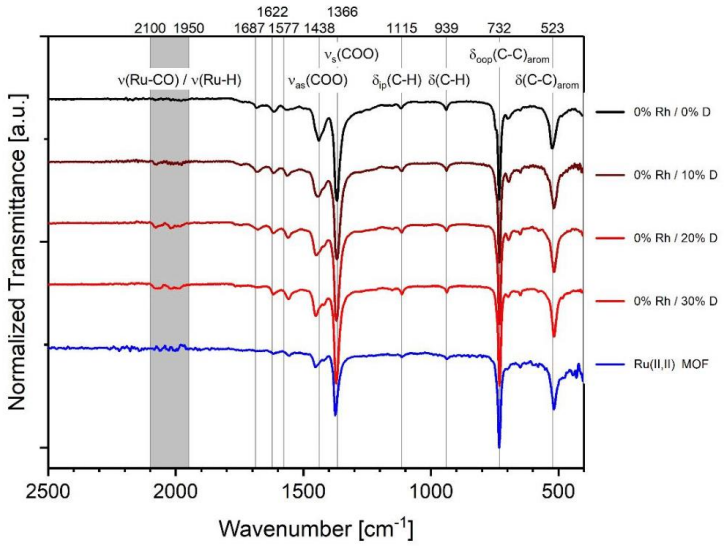

Figure S 33: Stacked FT-IR spectra of 0%Rh samples (pristine and TDE samples, $Ru^{II,II}$-BTC reference sample). Spectra reveal the formation of metal hydride and carbonyl species (1950 – 2100 cm^{-1}). A subsequent shift of ν_{as}(COO) (1438 cm^{-1}) and occurrence of a slight shoulder indicates metal reduction upon thermal defect-engineering e.g. through axial ligand removal.

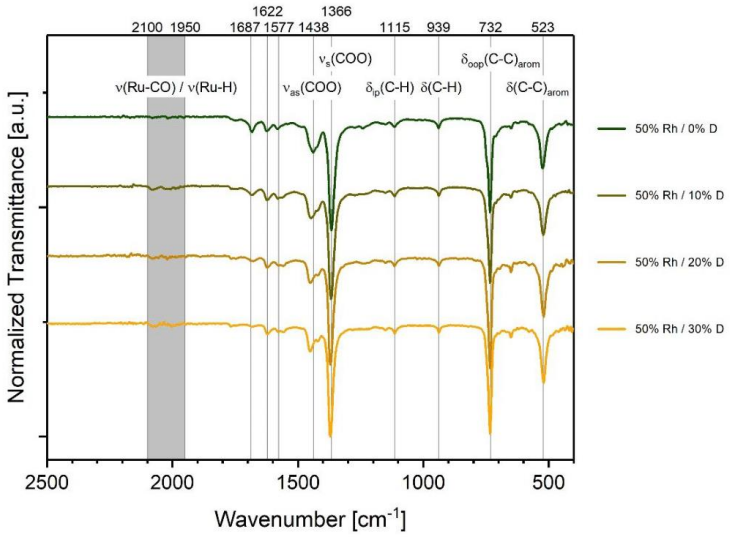

Figure S 34: Stacked FT-IR spectra of 50%Rh samples (pristine and TDE samples).

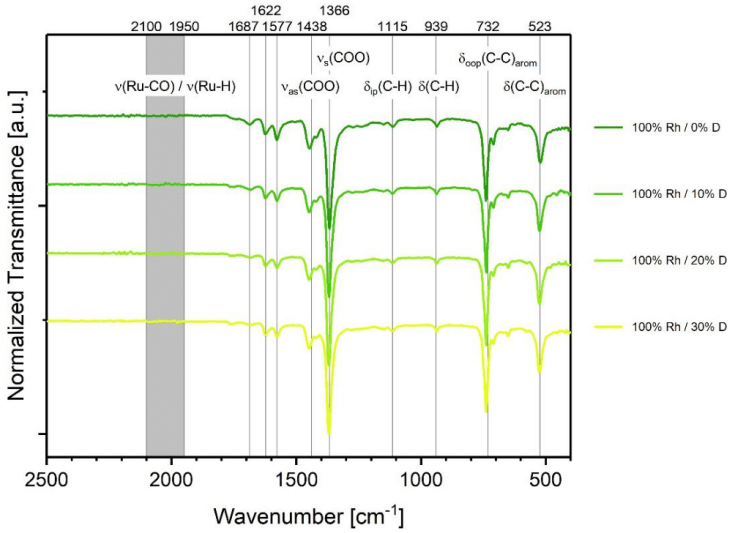

Figure S 35: Stacked FT-IR spectra of 100%Rh samples (pristine and TDE samples). Spectra do not reveal metal hydride or carbonyl formation with rhodium.

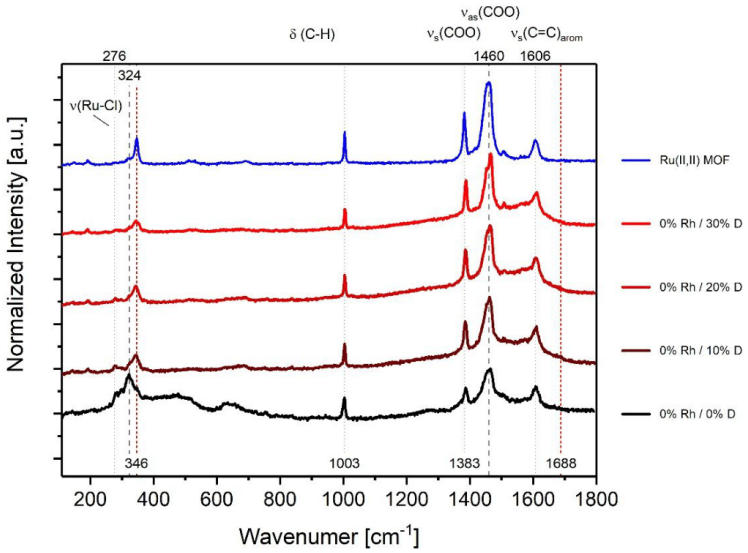

Figure S 36: Stacked Raman spectra of 0%Rh samples (pristine, TDE and $Ru^{II,II}$ reference sample). Spectra reveal the removal of axial Ru-OAc bands (324 cm^{-1}) suggesting partial metal reduction through axial ligand removal. Almost identical spectra of (0/30) and $Ru^{II,II}$ indicate their chemical similarity. Broadening of the aromatic valence mode at 1606 cm^{-1} indicates modification of the intact BTC moiety potentially towards isophthalate species via decarboxylation.

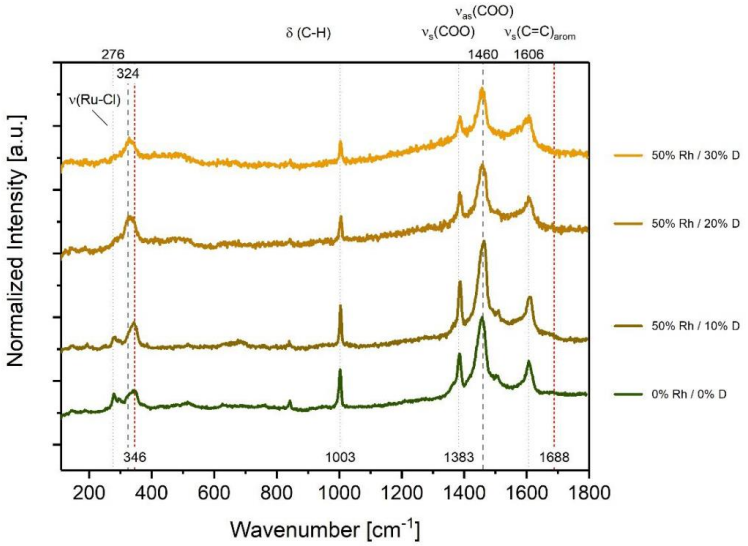

Figure S 37: Stacked Raman spectra of 50%Rh samples (pristine and TDE samples). Broadening of the aromatic valence mode at 1606 cm^{-1} indicates modification of the intact BTC moiety potentially towards isophthalate species via decarboxylation.

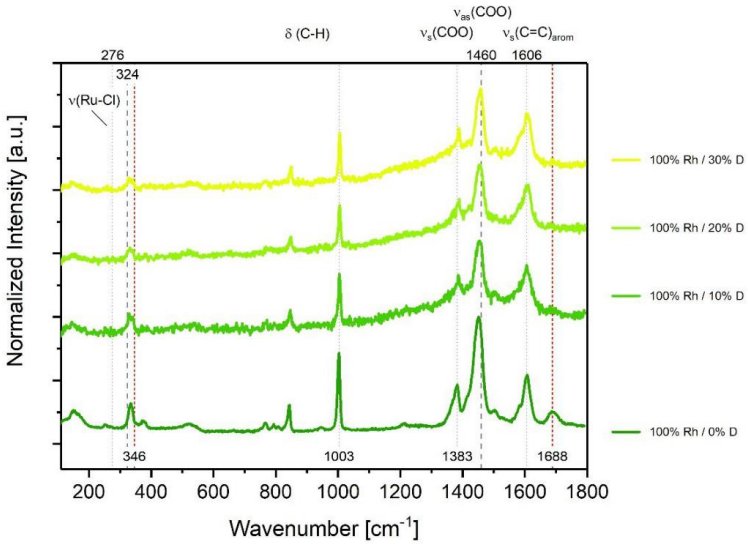

Figure S 38: Stacked Raman spectra of 100%Rh samples (pristine and TDE samples). Spectra reveal the removal of free carboxylates (1688 cm^{-1}) as well as a significant line broadening of aromatic C=C stretching modes (1606 cm^{-1}) indicates BTC decarboxylation towards isophthalate upon TDE.

Table S 7: Comparison of selected experimental vibration frequencies with the following DFT calculated model compounds: [a] $[Rh_2(OBz)_4(H_2O)_2]$, [b] $[Rh_2(H_2BTC)_4]$, [c] $[Rh_2(OBz)_4Cl_2]^{2-}$, [d] $[Rh_2(OBz)_4Cl]^-$, [e] $[Rh_2(OAc)_4]$, [f] $[Rh_2(OAc)_3(OBz)]$, [g] cis-$[Rh_2(OAc)_2(OBz)_2]$, [h] trans-$[Rh_2(OAc)_2(OBz)_2]$, [i] $[Rh_2(OAc)(OBz)_3]$, [j] $[Rh_2(H_2BTC)_4(H_2O)_2]$

Experimental frequencies [cm^{-1}]	Calculated frequencies [cm^{-1}]	Assigned vibration mode
Raman mode	Raman mode	
	1767[b]	$\nu_{as}(COOH)_{free\ acid}$
1688		$\nu_{as}(COO)_{\ low\ coord}$
1606	1611[b],	$\nu_{as}(COO) + \delta_{ip}(C\text{-}H_{arom})$
	1617[a]	$\nu_{as}(COO) + \nu_s(C{=}C_{arom})$
		$\nu_{as}(COO) + \nu_s(C{=}C_{arom})$
1503	1508[a], 1511[e], 1510[f]	$\nu_{as}(COO)$
1452	1453[b]	$\nu_s(COO) + \delta_{ip}(C\text{-}H_{arom})$
		$\delta_{ip}(C\text{-}H_{arom})$
		$\delta(C\text{-}H_{OAc})$
		$\delta(C\text{-}H_{OAc})$
1383	1395, 1411[a]	$\nu_s(COO)$
		$\nu_s(COO)$
	1141[a]	$\delta_{ip}(C\text{-}H_{arom})$
1003	997[a]	$\nu_s(C{=}C_{arom})$
		$\delta_{oop}(C\text{-}H_{arom})$
845	852, 859[a], (862&874)[f]	$\delta_{ip}(COO)$
792	804[a]	$\delta_{oop}(COO\ \&C\text{-}H_{arom})$
		$\delta_{oop}(C\text{-}R_{arom})$
		$\delta_{ip}(COO)$
	515[c]	$\nu_{as}(ORhO)$
		$\delta(C{=}C_{arom}) + \nu_{as}(ORhO)$
375	357[c]	$\nu(Rh\text{-}Rh\text{-}Cl)$
346	357[f], 358[g], 357[i]	$\nu_s(ORhO)$
	349[b],	$\nu(C\text{-}CO_2)$
333	345[a], 318, 346[e], 340[f], 344[h]	$\nu(Rh\text{-}Rh)$
324	326[d]	$\nu(Rh\text{-}Cl)$
276	268[j]	$\delta(PW)$
	250[d]	$\nu(Rh\text{-}Rh\text{-}Cl)$
250	225[c]	$\nu_s(Rh\text{-}Rh) + \delta_{oop}(COO)$
191	191,[b] 181,[i]	$\delta_{oop}(arom), \nu(BzO\text{-}Rh_2)_{trans\text{-}syn}$
150		$\nu(Rh\text{-}Rh)$
	148[c]	$\nu_s(Rh\text{-}Cl)_2$
	148[e], 150[f], 149[g], 152[i]	$\delta(PW)$

Hydride Evolution

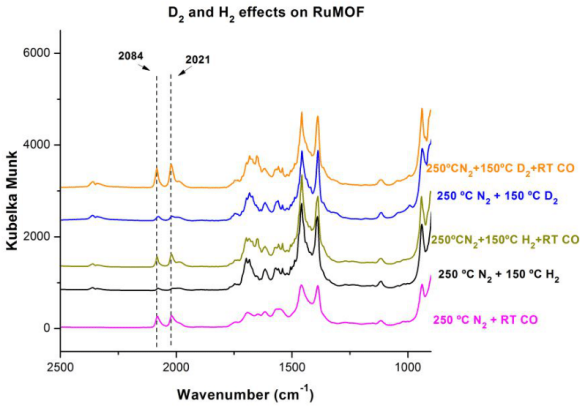

Figure S 39: FT-IR spectra indicating the generation of ruthenium hydride and deuteride species upon related treatments.

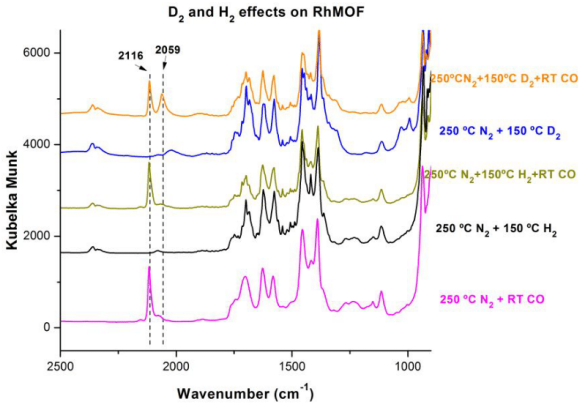

Figure S 40: FT-IR spectra indicating low generation of rhodium hydride and deuteride species upon related treatments.

CO sorption experiments

After sorption of 5% CO in He stream, desorption was investigated in N2 stream dependent on desorption temperatures. Consecutive IR spectra were recorded, and the areas of CO bands integrated and referenced to the C=C bands. This served as a basis for the desorption plots displayed in the main manuscript. In the following, the CO desorption IR spectra are displayed for each material.

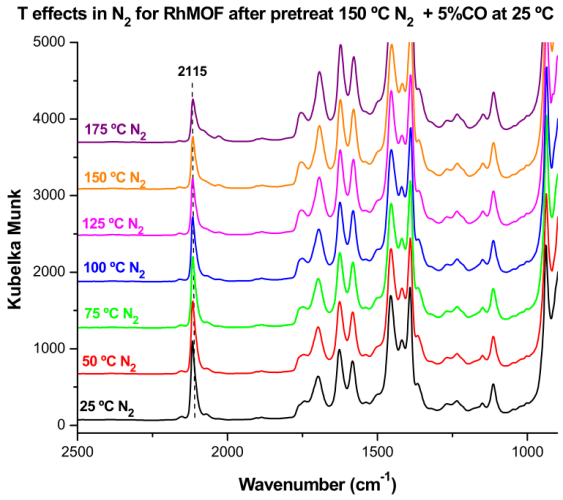

Figure S 41: CO desorption experiments using IR spectroscopy and controlled temperature induced desorption for Rh-BTC pretreated at 150 °C (10 min) in nitrogen and 5% CO in He at 25 °C.

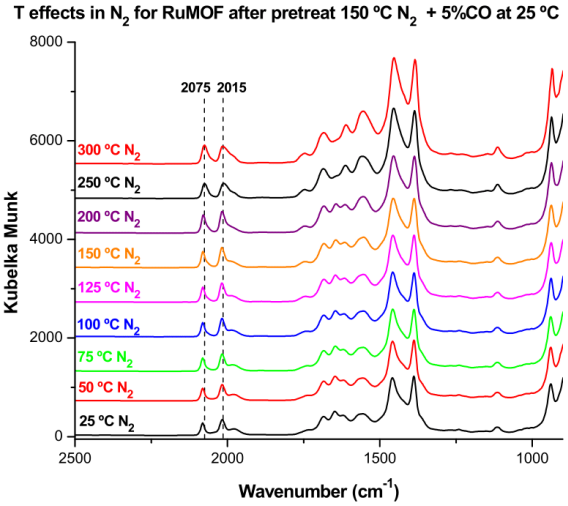

Figure S 42: CO desorption experiments using IR spectroscopy and controlled temperature induced desorption for Ru-BTC pretreated at 150 °C (10 min) in nitrogen and 5% CO in He at 25 °C.

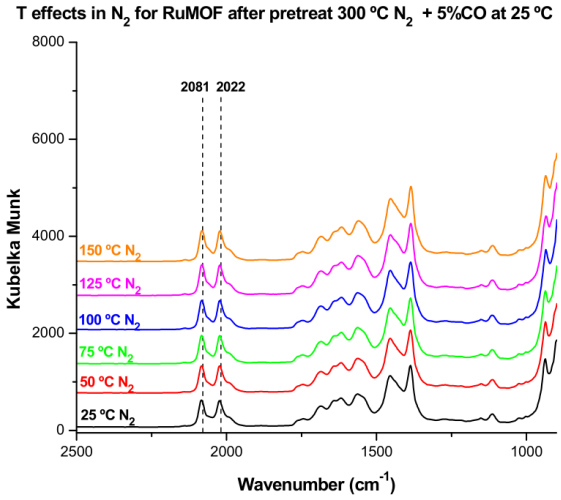

Figure S 43: CO desorption experiments using IR spectroscopy and controlled temperature induced desorption for Ru-BTC pretreated at 300 °C (10 min) in nitrogen and 5% CO in He at 25 °C.

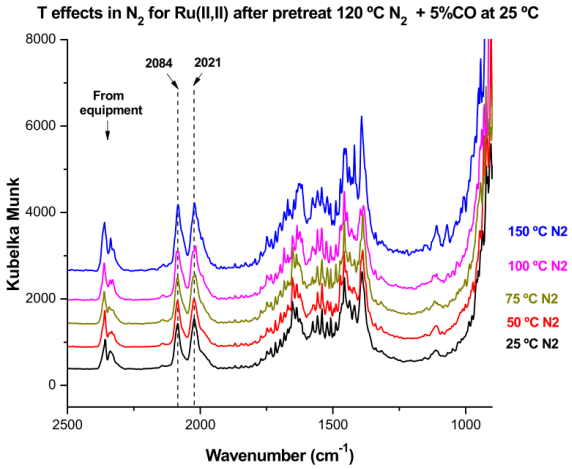

Figure S 44: CO desorption experiments using IR spectroscopy and controlled temperature induced desorption for $Ru^{II,II}$-BTC pretreated at 120 °C (10 min) in nitrogen and 5% CO in He at 25 °C.

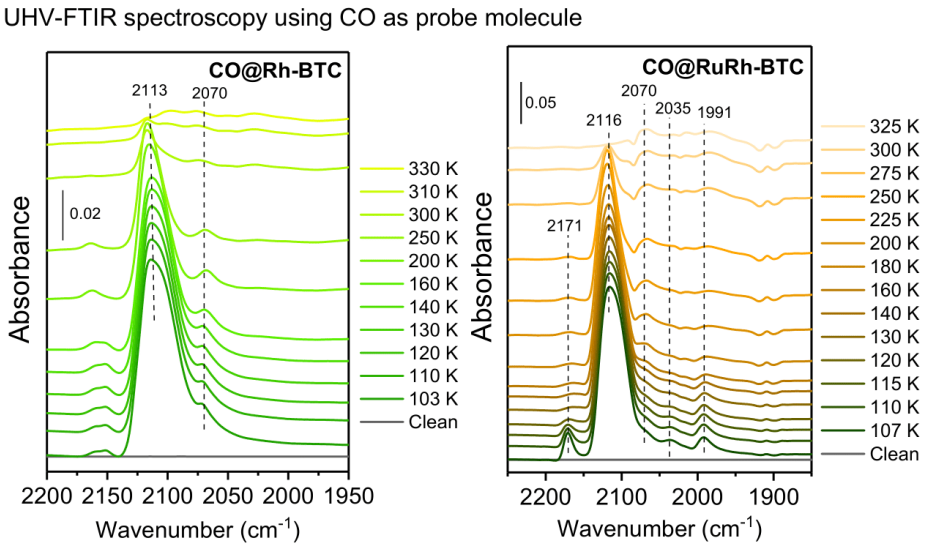

Figure S 45: UHV-FTIRS data obtained after exposing Rh-BTC (left) and RuRh-BTC (right) to CO (0.01 mbar) at 105 K and subsequently annealing to indicated temperatures.

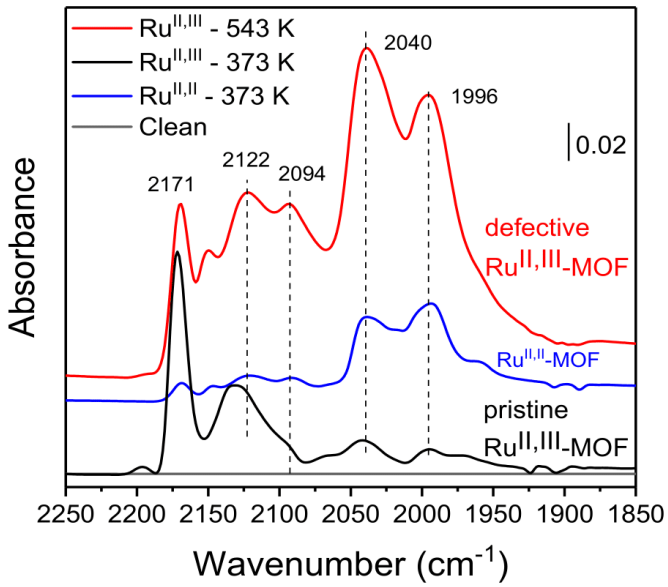

Figure S 46: Comparison of Ru-MOFs (univalent, mixed valent and thermally treated) using CO probe FT-IR spectroscopy. The univalent $Ru^{II,II}$ sample seems to be dominated by reduced $Ru^{\delta+}$sites. We attribute this to the high level of intrinsic defects resulting from the modulated synthesis and the small particle size. Besides this and according to the literature, the excitation efficiency of CO bound to reduced metal sites seems to be strongly increased and thus pretending enormous amounts of defective sites.[83]Still, a clear reduction of the pristine mixed-valent Ru-MOF upon thermal treatment can be deduced.

Transmission Electron Microscopy

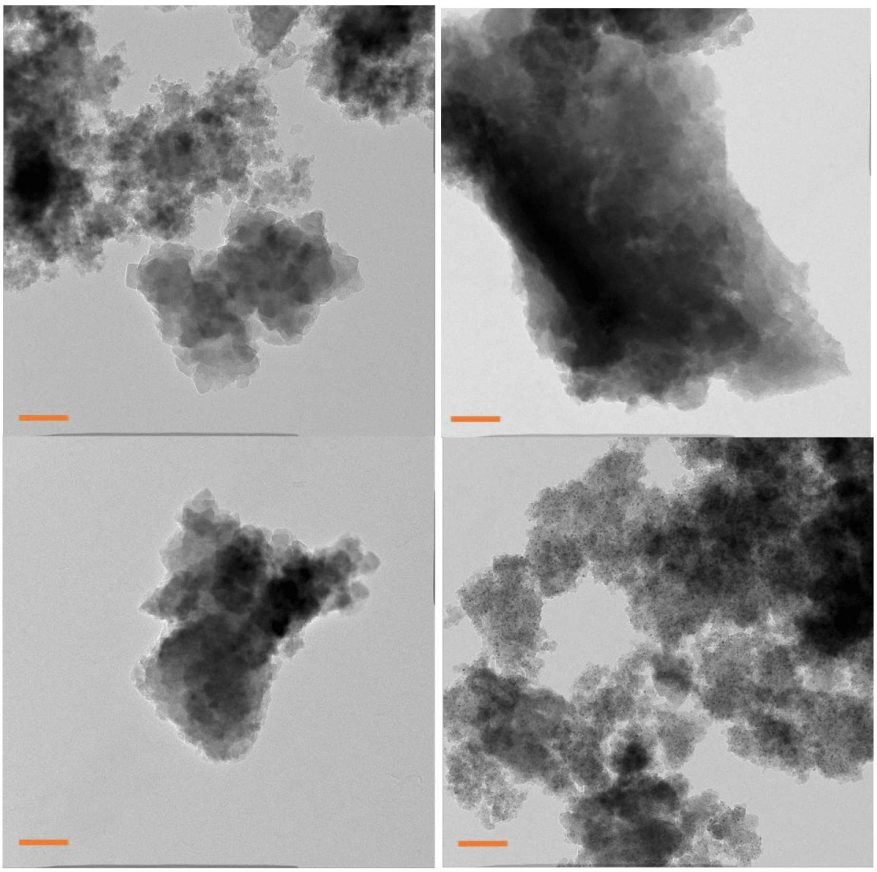

Figure S 47: HR-TEM images of Ru- and RuRh-MOF samples. Left top: (0/0); left bottom (0/30); right top (50/0), right bottom (50)30). Scale bars represent 100 nm each. While Ru-MOF samples do not show or produce metal NPs, the thermal treatment of the mixed-metal sample yields metal NP in the (50/30) sample.

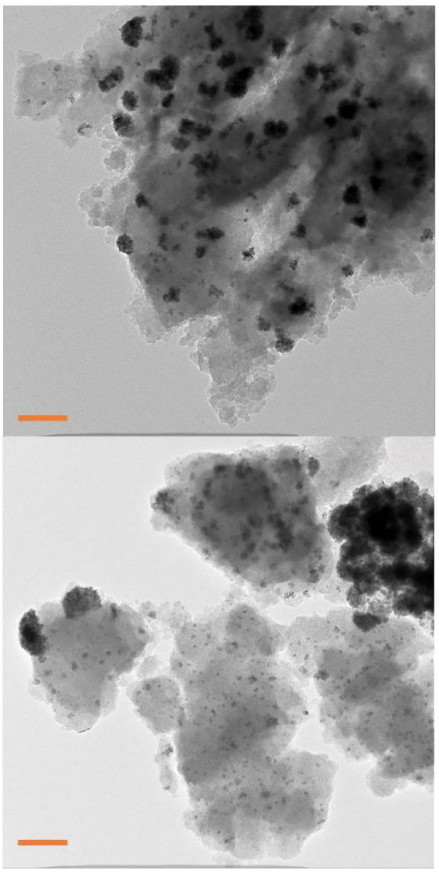

Figure S 48: HR-TEM images of Rh-MOF samples. Top: (100/0); bottom: (100/30) sample. The scale bars represent 100 nm each. While Rh NPs are already present in the pristine MOF in several sizes and agglomerations, TDE yields ingreasing formation of small size metal NPs homogeneously dispersed throughout the material.

DFT calculations for CO adducts of perfect and defective PWs

Table S 8: DFT-based results regarding multiplicity and relative energy differences of selected perfect and defective PW complexes and their CO adducts.

System (multiplicity)	E_{Total} a.u.	$E_{Relative}$ kJ/mol
M06L/def2-TZVP		
Pristine (Singlet)	*-1135.669926*	*0*
Pristine (Triplet)	-1135.649755	53
Pristine (Quintet)	-1135.621885	126
Defect (Doublet)	*-907.01718*	*0*
Defect (Quartet)	*-907.01716*	*0*
Defect (Sextet)	-907.01452	7
Defect-CO (Doublet)	*-1020.452799*	*0*
Defect-CO (Quartet)	-1020.432731	53
Defect-CO (Sextet)	-1020.389328	167
Defect-2CO (Singlet)	*-1133.881799*	*0*
Defect-BiCO	-1133.836858	118
Defect-3CO (Singlet)	-1247.250273	0
CO	-113.3440327	0

Table S 9: DFT-based results regarding CO adsorption energies of computed Rh_2 model complexes.

System (multiplicity)	a.u.	E_{ads}(CO) kJ/mol
M06L/def2-TZVP		
Pristine (s)	-1135.669821	
Pristine-CO (s)	-1249.05727	-114
Pristine-2CO (s)	-1362.429247	-73
Defect (d)	-907.0171791	
Defect-CO (d)	-1020.452799	-240
Defect-2CO (d)	-1133.881799	-223
Defect-BiCO (d)	-1133.836858	-105
Defect-3CO (d)	-1247.250273	-64
CO	-113.3440327	

Table S 10: Multireference treatment of defects.

Basic system:

```
-----------------------------------------------
CAS-SCF STATES FOR BLOCK  1 MULT= 8 NROOTS= 1
-----------------------------------------------

ROOT   0:  E=    -900.3672613050 Eh
      1.00000 [     0]: 1111111


-----------------------------------------------
CAS-SCF STATES FOR BLOCK  2 MULT= 6 NROOTS= 1
-----------------------------------------------

ROOT   0:  E=    -900.5798244534 Eh
      0.99370 [     0]: 2111110
      0.00623 [     2]: 2111011


-----------------------------------------------
CAS-SCF STATES FOR BLOCK  3 MULT= 4 NROOTS= 1
-----------------------------------------------

ROOT   0:  E=    -900.5957944640 Eh
      0.84435 [     0]: 2211100
      0.13316 [     3]: 2210110
      0.00788 [     2]: 2211001
      0.00641 [   101]: 1122100
      0.00339 [   105]: 1121110


-----------------------------------------------
CAS-SCF STATES FOR BLOCK  4 MULT= 2 NROOTS= 1
-----------------------------------------------

ROOT   0:  E=    -900.6387300892 Eh
      0.86589 [     0]: 2221000
      0.12822 [     2]: 2220010
```

Extended system.

```
-----------------------------------------------
CAS-SCF STATES FOR BLOCK  1 MULT= 6 NROOTS= 1
-----------------------------------------------

ROOT   0:  E=   -2021.7114231546 Eh
      0.99843 [     0]: 2111110


-----------------------------------------------
CAS-SCF STATES FOR BLOCK  2 MULT= 4 NROOTS= 1
-----------------------------------------------

ROOT   0:  E=   -2021.7242144016 Eh
      0.89076 [     0]: 2211100
      0.07399 [    20]: 2111110
      0.01887 [    54]: 2011120
      0.00376 [    49]: 2012110


-----------------------------------------------
CAS-SCF STATES FOR BLOCK  3 MULT= 2 NROOTS= 1
-----------------------------------------------

ROOT   0:  E=   -2021.7115956728 Eh
      0.86553 [     0]: 2221000
      0.03586 [    32]: 2121010
      0.02462 [    17]: 2201200
      0.01898 [    81]: 2021020
      0.01608 [     5]: 2211100
      0.00669 [    76]: 2022010
      0.00440 [     2]: 2220010
      0.00361 [    37]: 2120020
      0.00349 [     9]: 2210110
      0.00278 [    40]: 2112100
```

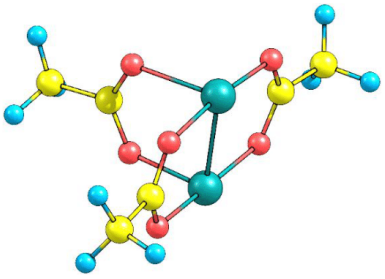

Figure S 49: Computed molecular structure of modified PW defect of rhodium acetate.

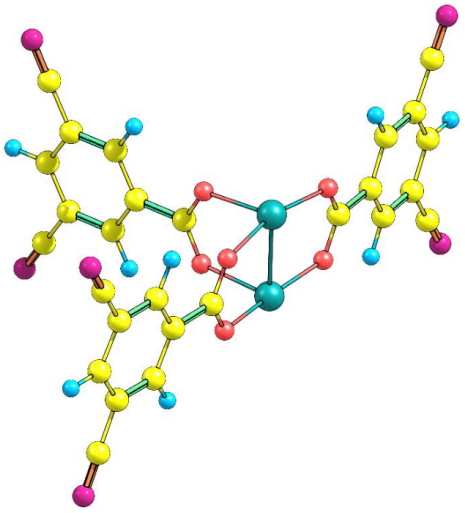

Figure S 50: Computed molecular structure of extended defect PW.

Structures of Rh-PW complexes

Structure RhRh-Pristine, M06

Table S 11: Atom coordinates of computed structure M06, dirhodium tetraacetate.

30

O	0.781295000	-1.483605000	-1.811291000
C	1.543520000	-1.876277000	-0.888230000
O	1.530499000	-1.471499000	0.304009000
Rh	-0.570438000	-0.015398000	-1.401437000
Rh	0.188036000	-0.018818000	0.839888000
O	1.547067000	1.410798000	0.311145000
C	1.610931000	1.768666000	-0.894910000
O	0.873313000	1.360762000	-1.830964000
O	-1.958722000	-1.422550000	-0.852660000
O	-1.856515000	1.490715000	-0.893762000
C	-1.977591000	-1.820110000	0.341853000
O	-1.204219000	-1.440641000	1.261286000
O	-1.197868000	1.428700000	1.250501000
C	-1.890895000	1.883969000	0.301886000
C	-3.024600000	-2.816910000	0.726196000
H	-3.484401000	-3.263105000	-0.153107000
H	-2.587011000	-3.584497000	1.363158000
H	-3.791819000	-2.301644000	1.307428000
C	-2.850575000	2.981250000	0.639920000
H	-2.341493000	3.745393000	1.226831000
H	-3.278482000	3.416887000	-0.260762000
H	-3.651770000	2.571185000	1.256584000
C	2.653369000	2.783970000	-1.233274000
H	3.555983000	2.593653000	-0.654921000
H	2.869516000	2.777266000	-2.299607000
H	2.279397000	3.771018000	-0.953683000
C	2.570282000	-2.898589000	-1.261292000
H	3.341866000	-2.409233000	-1.858846000
H	3.028844000	-3.335266000	-0.376552000
H	2.115227000	-3.671810000	-1.879134000

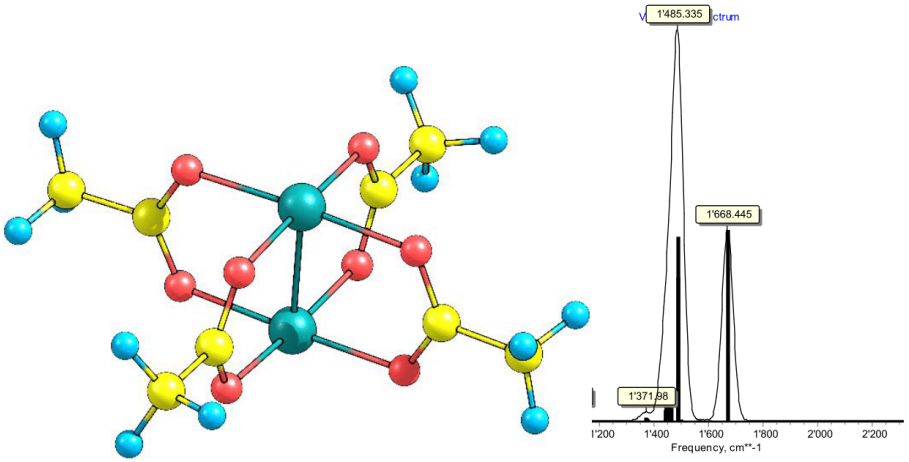

Figure S 51: Left: Computed molecular structure of ideal PW. Right: respective IR frequencies.

Structure RhRh-Pristine-CO, M06

Table S 12: Atom coordinates of computed structure M06, dirhodium tetraacetate mono CO adduct.

32

O	0.796176000	-1.483356000	-1.807351000
C	1.525967000	-1.897928000	-0.877391000
O	1.515181000	-1.492770000	0.320860000
Rh	-0.567523000	-0.010461000	-1.414063000
Rh	0.218062000	0.003141000	0.870026000
O	1.592799000	1.410549000	0.275673000
C	1.601185000	1.803650000	-0.926582000
O	0.844034000	1.406685000	-1.842223000
O	-1.937074000	-1.427090000	-0.864219000
O	-1.888246000	1.464322000	-0.899212000
C	-1.972999000	-1.807052000	0.328914000
O	-1.226124000	-1.403048000	1.266537000
O	-1.148732000	1.496505000	1.221663000
C	-1.891711000	1.893006000	0.277942000
C	-2.991068000	-2.836911000	0.706722000
H	-3.575379000	-3.135846000	-0.160150000
H	-2.489163000	-3.704285000	1.136519000
H	-3.648397000	-2.430470000	1.476204000
C	-2.859733000	2.980365000	0.624847000
H	-2.312786000	3.847736000	0.995965000
H	-3.451769000	3.258663000	-0.243682000
H	-3.513643000	2.641972000	1.429196000
C	2.616697000	2.850471000	-1.262115000
H	3.604868000	2.520229000	-0.941782000
H	2.616333000	3.057698000	-2.329524000
H	2.385634000	3.763187000	-0.711046000
C	2.524603000	-2.966234000	-1.195405000
H	3.526478000	-2.534533000	-1.169458000
H	2.486887000	-3.747882000	-0.437272000
H	2.338604000	-3.383207000	-2.182350000
C	0.876199000	0.016757000	2.759495000
O	1.255602000	0.028539000	3.821425000

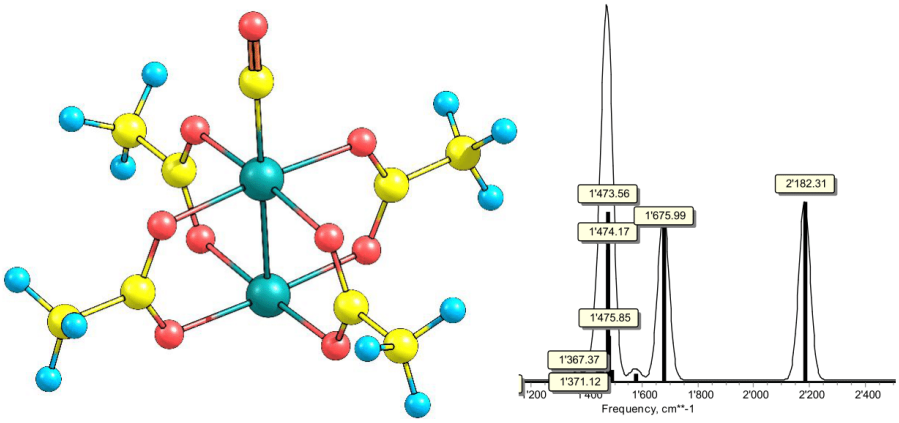

Figure S 52: Left: Computed molecular structure of ideal PW mono CO adduct. Right: respective IR frequencies.

Structure RhRh-Pristine-2CO, M06

Table S 13: Atom coordinates of computed structure M06, dirhodium tetraacetate bis CO adduct.

34

O	0.768829000	-1.508521000	-1.807538000
C	1.541643000	-1.888990000	-0.890940000
O	1.547787000	-1.476997000	0.296660000
Rh	-0.591838000	-0.016445000	-1.443310000
Rh	0.202946000	-0.018525000	0.877017000
O	1.549957000	1.429851000	0.314286000
C	1.614280000	1.778226000	-0.892538000
O	0.887647000	1.362462000	-1.830715000
O	-1.981065000	-1.428936000	-0.851582000
O	-1.865295000	1.510993000	-0.899204000
C	-1.983389000	-1.831851000	0.339292000
O	-1.203269000	-1.461447000	1.253698000
O	-1.213562000	1.435094000	1.246434000
C	-1.897590000	1.896411000	0.296942000
C	-3.026084000	-2.833610000	0.728987000
H	-3.491495000	-3.279058000	-0.147699000
H	-2.581408000	-3.601487000	1.360724000
H	-3.789915000	-2.321351000	1.317247000
C	-2.850469000	3.000578000	0.639410000
H	-2.331718000	3.763837000	1.219192000
H	-3.284329000	3.436319000	-0.258235000
H	-3.647030000	2.596289000	1.265735000
C	2.651143000	2.801639000	-1.231103000
H	3.550453000	2.626939000	-0.642983000
H	2.876783000	2.787226000	-2.295398000
H	2.262689000	3.786789000	-0.964713000
C	2.564606000	-2.914297000	-1.272542000
H	3.331862000	-2.425056000	-1.875744000
H	3.030024000	-3.352471000	-0.392145000
H	2.102914000	-3.685923000	-1.887398000
C	0.869678000	0.002064000	2.857001000
O	1.214206000	0.038542000	3.929440000
C	-1.256704000	-0.015005000	-3.425976000

O -1.601118000 -0.011438000 -4.499026000

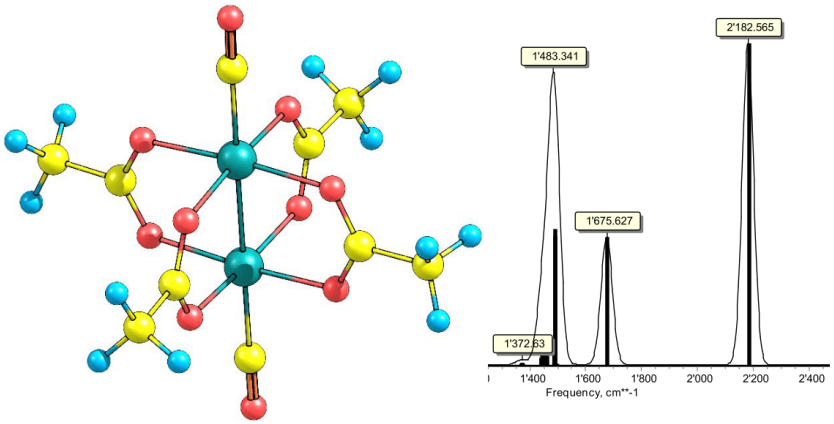

Figure S 53: Left: Computed molecular structure of ideal PW bis CO adduct. Right: respective IR frequencies.

Structure RhRh-Defect, Doublet, M06

Table S 14: Atom coordinates of computed structure M06, dirhodium triacetate, Doublet.

23

O	1.006254000	-1.682644000	-1.776957000
C	1.698966000	-2.016741000	-0.756740000
O	1.607783000	-1.545789000	0.380002000
Rh	-0.376403000	-0.294418000	-1.694184000
Rh	0.108050000	0.055990000	0.690597000
O	1.447508000	1.496533000	0.102301000
C	1.581922000	1.755855000	-1.120662000
O	0.995802000	1.179236000	-2.080785000
O	-1.795861000	-1.646110000	-1.094009000
C	-1.992237000	-1.844945000	0.138454000
O	-1.359890000	-1.322534000	1.091074000
C	-3.126200000	-2.753402000	0.490536000
H	-3.251783000	-3.523860000	-0.267147000
H	-2.972941000	-3.194768000	1.473449000
H	-4.043113000	-2.159600000	0.520019000
C	2.490561000	2.894348000	-1.461614000
H	3.244162000	3.006932000	-0.683494000
H	2.950712000	2.745502000	-2.436372000
H	1.896132000	3.811873000	-1.475624000
C	2.710543000	-3.083564000	-1.049926000
H	3.445612000	-2.693531000	-1.754587000
H	3.206684000	-3.394845000	-0.133863000
H	2.220853000	-3.933906000	-1.524436000

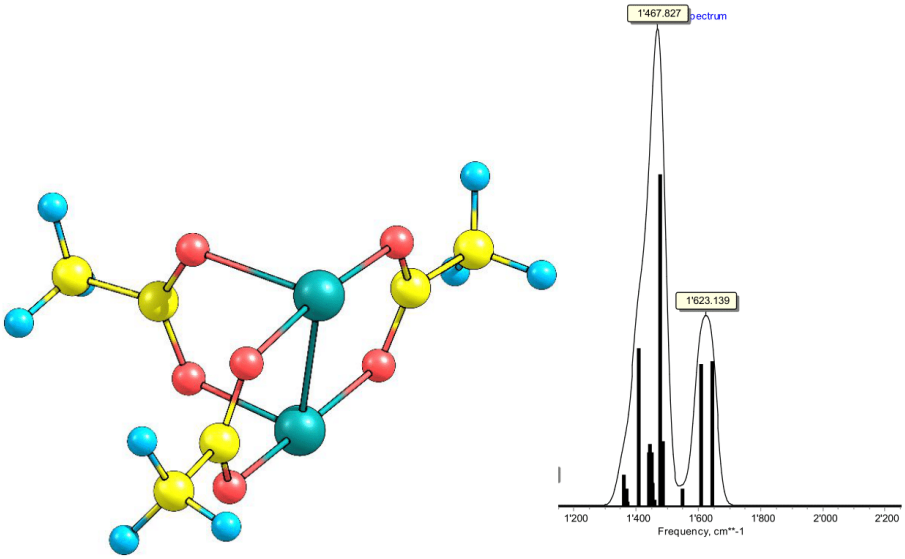

Figure S 54: Left: Computed molecular structure of defective PW, doublet. Right: respective IR frequencies.

Structure RhRh-Defect, Quartet, M06

Table S 15: Atom coordinates of computed structure M06, dirhodium triacetate, Quartet.

23

O	1.091560000	-1.816434000	-1.922638000
C	1.758001000	-2.127439000	-0.912212000
O	1.653905000	-1.619655000	0.239596000
Rh	-0.441394000	-0.266261000	-1.849636000
Rh	0.299886000	-0.159783000	0.594561000
O	1.611523000	1.317064000	0.069134000
C	1.509530000	1.844028000	-1.069726000
O	0.689975000	1.507236000	-1.967313000
O	-2.072396000	-1.299905000	-1.005756000
C	-2.041758000	-1.765342000	0.165994000
O	-1.168615000	-1.510624000	1.036619000
C	-3.159921000	-2.681689000	0.551427000
H	-3.165258000	-3.543857000	-0.116673000
H	-3.064198000	-3.010921000	1.583066000
H	-4.110040000	-2.164081000	0.411078000
C	2.425358000	2.982364000	-1.392171000
H	3.022216000	3.266261000	-0.528927000
H	3.081623000	2.690359000	-2.213524000
H	1.836498000	3.831582000	-1.740699000
C	2.788886000	-3.205192000	-1.066213000
H	3.528177000	-2.885292000	-1.801505000
H	3.278287000	-3.422863000	-0.120190000
H	2.310399000	-4.103421000	-1.457382000

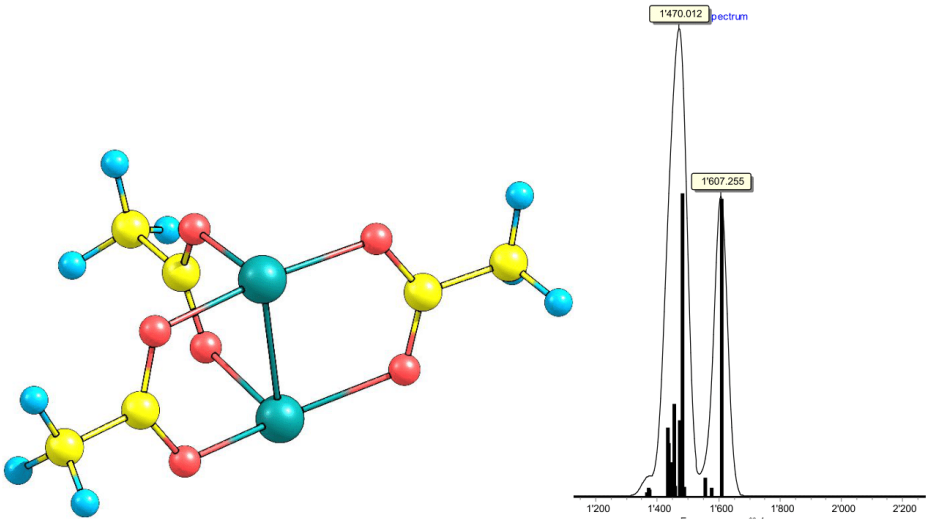

Figure S 55: Left: Computed molecular structure of defective PW, quartet. Right: respective IR frequencies.

Structure RhRh-Defect-CO, M06

Table S 16: Atom coordinates of computed structure M06, dirhodium triacetate mono CO adduct.

25

O	0.955199000	-1.385138000	-1.825291000
C	1.563738000	-1.891104000	-0.851977000
O	1.452190000	-1.532025000	0.349353000
Rh	-0.598610000	0.000542000	-1.657371000
Rh	0.167453000	0.059395000	0.732852000
O	1.549068000	1.454226000	0.150353000
C	1.586129000	1.826331000	-1.053241000
O	0.823723000	1.455686000	-1.987909000
O	-1.844373000	-1.532936000	-1.047594000
C	-1.957557000	-1.800697000	0.182353000
O	-1.316649000	-1.281799000	1.133146000
C	-2.968517000	-2.846963000	0.528622000
H	-2.608284000	-3.814257000	0.173972000
H	-3.131072000	-2.893260000	1.602866000
H	-3.902515000	-2.635143000	0.008568000
C	2.653939000	2.805563000	-1.431467000
H	3.117196000	3.239720000	-0.547657000
H	3.415084000	2.279258000	-2.010589000
H	2.235068000	3.584616000	-2.067072000
C	2.512307000	-3.011896000	-1.150766000
H	3.324775000	-2.629756000	-1.770248000
H	2.920869000	-3.440840000	-0.238451000
H	1.993643000	-3.777105000	-1.728715000
C	-2.004410000	1.169299000	-1.557656000
O	-2.910894000	1.853726000	-1.478323000

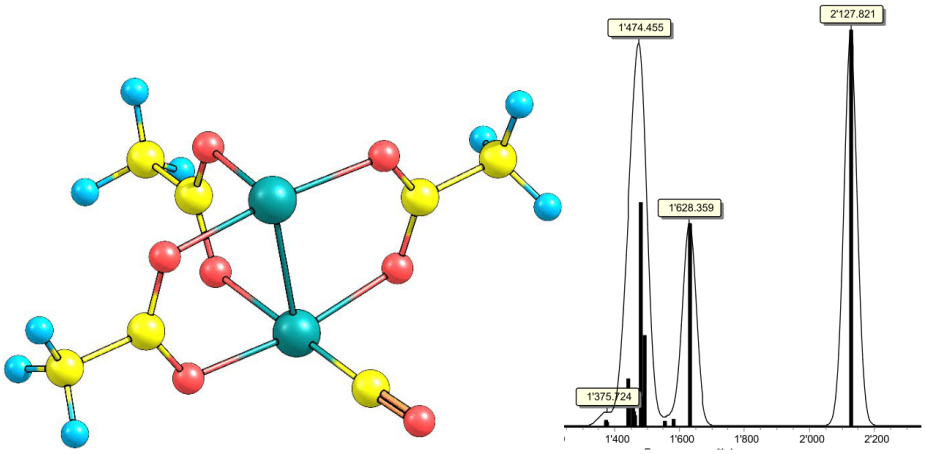

Figure S 56: Left: Computed molecular structure of defective PW mono CO adduct. Right: respective IR frequencies.

Structure RhRh-Defect-2CO, M06

Table S 17: Atom coordinates of computed structure M06, dirhodium triacetate bis CO adduct.

27

O	0.707440000	-1.409988000	-1.806692000
C	1.478796000	-1.858594000	-0.922803000
O	1.509554000	-1.465242000	0.268547000
Rh	-0.667633000	0.096302000	-1.439704000
Rh	0.251199000	0.018933000	0.983871000
O	1.661634000	1.386545000	0.321480000
C	1.678054000	1.756502000	-0.882871000
O	0.866799000	1.446332000	-1.796529000
O	-1.971497000	-1.391910000	-0.818352000
C	-1.907069000	-1.852457000	0.353181000
O	-1.161044000	-1.468136000	1.293355000
C	-2.808631000	-3.011428000	0.653576000
H	-2.316628000	-3.926097000	0.316561000
H	-2.989626000	-3.092413000	1.723095000
H	-3.744640000	-2.916187000	0.106294000
C	2.800977000	2.661694000	-1.290770000
H	3.348407000	3.019923000	-0.422386000
H	3.479321000	2.106382000	-1.940749000
H	2.410322000	3.498132000	-1.869403000
C	2.428615000	-2.938937000	-1.334046000
H	3.088383000	-2.557009000	-2.114250000
H	3.018422000	-3.285921000	-0.489348000
H	1.868200000	-3.768054000	-1.766938000
C	-1.929536000	1.423085000	-1.258402000
O	-2.708795000	2.243617000	-1.145768000
C	-0.803612000	1.317723000	1.749455000
O	-1.458846000	2.119600000	2.219242000

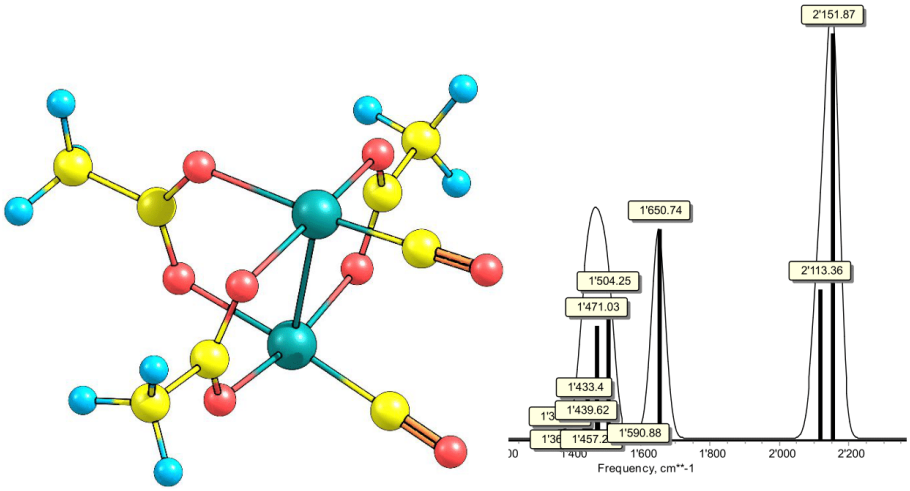

Figure S 57: Left: Computed molecular structure of defective PW bis CO adduct. Right: respective IR frequencies.

Structure RhRh-ExtendedPristine, M06L (all atoms relaxed)

Table S 18: Atom coordinates of computed structure M06L, dirhodium tetra(3,5-dinitrilobenzoate) all atoms relaxed.

66

Rh	-0.565026000	-0.001203000	-1.398974000
Rh	0.221322000	0.001888000	0.834921000
O	0.789262000	-1.497728000	-1.817938000
C	1.539668000	-1.906223000	-0.882384000
O	1.543628000	-1.490239000	0.314420000
O	1.610922000	1.421356000	0.287678000
C	1.629353000	1.810571000	-0.918000000
O	0.865607000	1.414149000	-1.847852000
O	-1.959568000	-1.414857000	-0.850376000
O	-1.883060000	1.495808000	-0.879637000
C	-1.975137000	-1.807821000	0.354147000
O	-1.205927000	-1.417907000	1.282224000
O	-1.137397000	1.493743000	1.255800000
C	-1.883616000	1.906804000	0.318874000
C	-2.997723000	-2.824448000	0.712316000
C	-3.873763000	-3.294756000	-0.256545000
C	-3.076150000	-3.298935000	2.014533000
C	-4.835663000	-4.245608000	0.078369000
C	-4.037353000	-4.249940000	2.351348000
C	-4.919212000	-4.724978000	1.383493000
H	-3.805199000	-2.919488000	-1.267570000
H	-2.390101000	-2.926926000	2.761998000
H	-5.665259000	-5.462179000	1.644315000
C	2.648750000	2.830563000	-1.275623000
C	3.519214000	3.307747000	-0.305108000
C	2.729791000	3.301311000	-2.579036000
C	4.478087000	4.261820000	-0.639550000
C	3.687964000	4.255522000	-2.915380000
C	4.564197000	4.737512000	-1.945853000
H	3.448704000	2.935284000	0.706822000
H	2.048174000	2.923846000	-3.327818000
H	5.307916000	5.477189000	-2.206306000
C	-2.855468000	2.978143000	0.658395000
C	-3.694545000	3.487141000	-0.323527000
C	-2.922660000	3.466041000	1.956316000
C	-4.607072000	4.491232000	-0.006397000
C	-3.835386000	4.469320000	2.275644000
C	-4.679347000	4.984057000	1.294377000
H	-3.635268000	3.100969000	-1.331030000
H	-2.265702000	3.063634000	2.714080000
H	-5.387397000	5.762374000	1.541361000
C	2.511350000	-2.977818000	-1.221517000
C	3.354726000	-3.482199000	-0.240903000
C	2.574304000	-3.470324000	-2.517912000
C	4.267308000	-4.486314000	-0.557804000
C	3.487002000	-4.473712000	-2.836987000
C	4.335242000	-4.983858000	-1.857017000
H	3.298841000	-3.092333000	0.765368000
H	1.914111000	-3.071367000	-3.274690000
H	5.043292000	-5.762234000	-2.103807000
C	-3.906683000	4.970181000	3.607288000
N	-3.963647000	5.375886000	4.688807000

Structure RhRh-ExtendedPristine, M06L (all atoms relaxed)

Table S 18: Atom coordinates of computed structure M06L, dirhodium tetra(3,5-dinitrilobenzoate) all atoms relaxed.

66

Rh	-0.565026000	-0.001203000	-1.398974000
Rh	0.221322000	0.001888000	0.834921000
O	0.789262000	-1.497728000	-1.817938000
C	1.539668000	-1.906223000	-0.882384000
O	1.543628000	-1.490239000	0.314420000
O	1.610922000	1.421356000	0.287678000
C	1.629353000	1.810571000	-0.918000000
O	0.865607000	1.414149000	-1.847852000
O	-1.959568000	-1.414857000	-0.850376000
O	-1.883060000	1.495808000	-0.879637000
C	-1.975137000	-1.807821000	0.354147000
O	-1.205927000	-1.417907000	1.282224000
O	-1.137397000	1.493743000	1.255800000
C	-1.883616000	1.906804000	0.318874000
C	-2.997723000	-2.824448000	0.712316000
C	-3.873763000	-3.294756000	-0.256545000
C	-3.076150000	-3.298935000	2.014533000
C	-4.835663000	-4.245608000	0.078369000
C	-4.037353000	-4.249940000	2.351348000
C	-4.919212000	-4.724978000	1.383493000
H	-3.805199000	-2.919488000	-1.267570000
H	-2.390101000	-2.926926000	2.761998000
H	-5.665259000	-5.462179000	1.644315000
C	2.648750000	2.830563000	-1.275623000
C	3.519214000	3.307747000	-0.305108000
C	2.729791000	3.301311000	-2.579036000
C	4.478087000	4.261820000	-0.639550000
C	3.687964000	4.255522000	-2.915380000
C	4.564197000	4.737512000	-1.945853000
H	3.448704000	2.935284000	0.706822000
H	2.048174000	2.923846000	-3.327818000
H	5.307916000	5.477189000	-2.206306000
C	-2.855468000	2.978143000	0.658395000
C	-3.694545000	3.487141000	-0.323527000
C	-2.922660000	3.466041000	1.956316000
C	-4.607072000	4.491232000	-0.006397000
C	-3.835386000	4.469320000	2.275644000
C	-4.679347000	4.984057000	1.294377000
H	-3.635268000	3.100969000	-1.331030000
H	-2.265702000	3.063634000	2.714080000
H	-5.387397000	5.762374000	1.541361000
C	2.511350000	-2.977818000	-1.221517000
C	3.354726000	-3.482199000	-0.240903000
C	2.574304000	-3.470324000	-2.517912000
C	4.267308000	-4.486314000	-0.557804000
C	3.487002000	-4.473712000	-2.836987000
C	4.335242000	-4.983858000	-1.857017000
H	3.298841000	-3.092333000	0.765368000
H	1.914111000	-3.071367000	-3.274690000
H	5.043292000	-5.762234000	-2.103807000
C	-3.906683000	4.970181000	3.607288000
N	-3.963647000	5.375886000	4.688807000

56

C	-5.468060000	5.015068000	-1.013128000
N	-6.166578000	5.439446000	-1.831375000
C	3.553936000	-4.979311000	-4.167062000
N	3.607359000	-5.388867000	-5.247308000
C	5.132834000	-5.005268000	0.447560000
N	5.835023000	-5.425655000	1.264722000
C	3.772967000	4.739309000	-4.252490000
N	3.840863000	5.131178000	-5.338467000
C	5.372687000	4.751333000	0.355120000
N	6.098320000	5.147691000	1.163757000
C	-4.119735000	-4.737519000	3.687247000
N	-4.185486000	-5.132469000	4.772240000
C	-5.735887000	-4.728147000	-0.914645000
N	-6.466059000	-5.118838000	-1.721951000

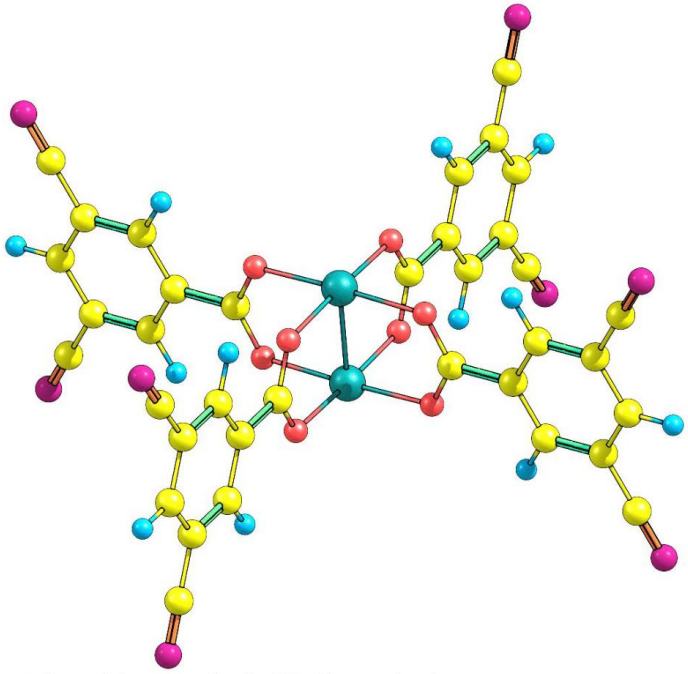

Figure S 58: Computed extended structure of perfect PW, all atoms relaxed.

Structure RhRh-ExtendedDefect, M06L (N atoms frozen in pristine geometry)

Table S 19: Atom coordinates of computed structure M06L, dirhodium tetra(3,5-dinitrilobenzoate), N atoms frozen.

50			
Rh	-0.654736000	0.117425000	-1.346661000
Rh	0.152385000	0.107320000	0.962297000
O	0.770338000	-1.459909000	-1.759783000
C	1.500046000	-1.888507000	-0.866942000
O	1.473538000	-1.474172000	0.295841000
O	1.410952000	1.683488000	0.328440000
C	1.467190000	2.037756000	-0.852778000
O	0.705959000	1.644518000	-1.741286000
O	-2.145113000	-1.206593000	-0.729367000
C	-2.192018000	-1.602055000	0.439273000
O	-1.479680000	-1.176597000	1.352826000
C	-3.146894000	-2.689407000	0.763950000
C	-3.970024000	-3.202446000	-0.222215000
C	-3.180117000	-3.202503000	2.048665000
C	-4.836659000	-4.237520000	0.090571000
C	-4.047680000	-4.242029000	2.341804000
C	-4.883644000	-4.768075000	1.369893000
H	-3.935730000	-2.792512000	-1.219024000
H	-2.534949000	-2.791143000	2.808188000
H	-5.570038000	-5.566934000	1.608684000
C	2.543705000	2.982114000	-1.237784000
C	3.444635000	3.411792000	-0.280174000
C	2.656816000	3.400530000	-2.551658000
C	4.468151000	4.268957000	-0.648855000
C	3.684953000	4.261215000	-2.901823000
C	4.599311000	4.702020000	-1.958475000
H	3.343224000	3.079813000	0.740539000
H	1.946833000	3.059212000	-3.288021000
H	5.391998000	5.380799000	-2.236382000
C	2.485566000	-2.969680000	-1.211605000
C	3.332856000	-3.474648000	-0.234519000
C	2.554747000	-3.460386000	-2.508727000
C	4.248317000	-4.469969000	-0.560538000
C	3.473553000	-4.456654000	-2.822905000
C	4.323685000	-4.965849000	-1.853052000
H	3.274499000	-3.089297000	0.771502000
H	1.893579000	-3.063647000	-3.263501000
H	5.035039000	-5.739793000	-2.101146000
C	3.553936000	-4.979311000	-4.167062000
N	3.607359000	-5.388867000	-5.247308000
C	5.132834000	-5.005268000	0.447560000
N	5.835023000	-5.425655000	1.264722000
C	3.772967000	4.739309000	-4.252490000
N	3.840863000	5.131178000	-5.338467000
C	5.372687000	4.751333000	0.355120000
N	6.098320000	5.147691000	1.163757000
C	-4.119735000	-4.737519000	3.687247000
N	-4.185486000	-5.132469000	4.772240000
C	-5.735887000	-4.728147000	-0.914645000
N	-6.466059000	-5.118838000	-1.721951000

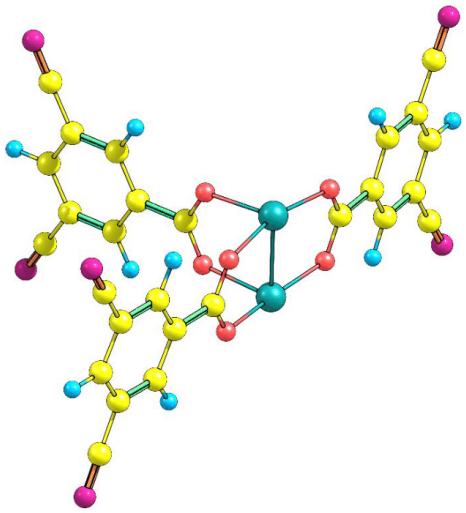

Figure S 59: Computed extended structure of defective PW, only N atoms frozen.

Catalytic Ethene Dimerization

In this study, the relative impact of TDE and related changes in oxidation states and OMS on the catalytic activity was shown. To embed our results in the broader context of state-of-the art catalytic systems for this reactions, Table S11 summarizes activities and related reaction conditions of this and previous studies.

Table S 20: Different MOF-catalyzed ethene dimerization systems and their turnovers, selectivities and required activators. Table adapted from Ref.[63] with modifications.

System	Activator / metal	Phase	TOF [mol_{butene} mol_{metal}^{-1} h^{-1}]	Butene selectivity [%]	Conditions		Ref.
					Temperature [°C]	Pressure [bar]	
Ni-(Fe) MIL-101	70 (MAO)	Liquid (batch)	10’455	95	25	30	[84]
Ni-MFU4L	500 (MAO)	Liquid (batch)	41’500	96	25	50	[85]
$Zr_6O_4(OH)_4(bypydc)_6$	100 (MAO)	Liquid (batch)	36’000	73	55	59	[86]
$(bpy)Ni^{II}$@NU1000	Et_2AlCl	Liquid (batch)	1’560	82**	21	15	[87]
Ni-AIM	HCl	Gas (flow)	252	46**	50	1.5	[88]
Ni-F-acac-AIM-NU1000	Et_2AlCl	Gas (flow)	16	99**	45	2	[89]
$Ni(bpy)Cl_2$@zeolites	5 Et_2AlCl	Solid (batch)	<110	<93**	25	12	[90]
Ni-MCM-36	--	Liquid (batch)	16’000	45**	150	40	[91]
Ni-MCM-36	--	Liquid (batch)	4’200	81**	70	40	[91]
Ni-MCM-41	5 Et_2AlCl	Solid (batch)	305	84**	25	12	[90]
DE-$Ru^{II,III}$-HKUST-1	Et_2AlCl	Liquid (batch)	4	99	80	55	[49]
DE-$Ru^{II,III}$-HKUST-1*	--	Gas (flow)***	200	99	60	42	[63]
TDE-$Rh^{II,II}$-HKUST-1	--	Gas (flow)	1	99	50	5	This work
TDE-RuRh-HKUST-1	--	Gas (flow)	23	99	50	5	
TDE-$Ru^{II,III}$-HKUST-1*	--	Gas (flow)	53	99	50	5	
TDE-$Ru^{II,II}$-HKUST-1	--	Gas (flow)	204	99	50	5	

* Identical sample preparation but controlled TDE. **mixtures of butenes were obtained. ***under intrapore condensation regime.

Bibliography of Supporting Information

1. Mitchell, R. W.; Spencer, A.; Wilkinson, G., Carboxylato-triphenylphosphine complexes of ruthenium, cationic triphenylphosphine complexes derived from them, and their behaviour as homogeneous hydrogenation catalysts for alkenes. *J. Chem. Soc., Dalton Trans.* **1973,** (8), 846-854.
2. Heinz, W. R.; Kratky, T.; Drees, M.; Wimmer, A.; Tomanec, O.; Günther, S.; Schuster, M.; Fischer, R. A., Mixed precious-group metal–organic frameworks: a case study of the HKUST-1 analogue [RuxRh3−x(BTC)2]. *Dalton Trans.* **2019,** *48* (32), 12031-12039.
3. Zhou, H.-C.; Long, J. R.; Yaghi, O. M., Introduction to Metal–Organic Frameworks. *Chem. Rev.* **2012,** *112* (2), 673-674.
4. Zhou, H.-C. J.; Kitagawa, S., Metal–Organic Frameworks (MOFs). *Chem. Soc. Rev.* **2014,** *43* (16), 5415-5418.
5. Han, S. S.; Deng, W.-Q.; Goddard III, W. A., Improved Designs of Metal–Organic Frameworks for Hydrogen Storage. *Angew. Chem. Int. Ed.* **2007,** *46* (33), 6289-6292.
6. Alhamami, M.; Doan, H.; Cheng, C.-H., A Review on Breathing Behaviors of Metal-Organic-Frameworks (MOFs) for Gas Adsorption. *Materials* **2014,** *7* (4), 3198-3250.
7. Horcajada, P.; Serre, C.; Vallet-Regí, M.; Sebban, M.; Taulelle, F.; Férey, G., Metal–Organic Frameworks as Efficient Materials for Drug Delivery. *Angew. Chem. Int. Ed.* **2006,** *45* (36), 5974-5978.
8. Dias, E. M.; Petit, C., Towards the use of metal–organic frameworks for water reuse: a review of the recent advances in the field of organic pollutants removal and degradation and the next steps in the field. *J. Mater. Chem. A* **2015,** *3* (45), 22484-22506.
9. Dang, S.; Zhu, Q.-L.; Xu, Q., Nanomaterials derived from metal–organic frameworks. *Nat. Rev. Mater.* **2017,** *3* (1), 17075.
10. Müller-Buschbaum, K.; Beuerle, F.; Feldmann, C., MOF based luminescence tuning and chemical/physical sensing. *Microporous Mesoporous Mater.* **2015,** *216*, 171-199.
11. Sun, L.; Campbell, M. G.; Dincă, M., Electrically Conductive Porous Metal–Organic Frameworks. *Angew. Chem. Int. Ed.* **2016,** *55* (11), 3566-3579.
12. Ramaswamy, P.; Wong, N. E.; Shimizu, G. K. H., MOFs as proton conductors - challenges and opportunities. *Chem. Soc. Rev.* **2014,** *43* (16), 5913-5932.
13. Schneemann, A.; Bon, V.; Schwedler, I.; Senkovska, I.; Kaskel, S.; Fischer, R. A., Flexible metal-organic frameworks. *Chem. Soc. Rev.* **2014,** *43* (16), 6062-6096.
14. Xia, W.; Mahmood, A.; Zou, R.; Xu, Q., Metal-organic frameworks and their derived nanostructures for electrochemical energy storage and conversion. *Energy Environ. Sci.* **2015,** *8* (7), 1837-1866.
15. Wang, H.; Vagin, S. I.; Lane, S.; Lin, W.; Shyta, V.; Heinz, W. R.; Van Dyck, C.; Bergren, A. J.; Gardner, K.; Rieger, B.; Meldrum, A., Metal–Organic Framework with Color-Switching and Strongly Polarized Emission. *Chem. Mater.* **2019,** *31* (15), 5816-5823.
16. Medishetty, R.; Nemec, L.; Nalla, V.; Henke, S.; Samoć, M.; Reuter, K.; Fischer, R. A., Multi-Photon Absorption in Metal–Organic Frameworks. *Angew. Chem. Int. Ed.* **2017,** *56* (46), 14743-14748.
17. Medishetty, R.; Zaręba, J. K.; Mayer, D.; Samoć, M.; Fischer, R. A., Nonlinear optical properties, upconversion and lasing in metal–organic frameworks. *Chem. Soc. Rev.* **2017,** *46* (16), 4976-5004.
18. Jayaramulu, K.; Geyer, F.; Schneemann, A.; Kment, Š.; Otyepka, M.; Zboril, R.; Vollmer, D.; Fischer, R. A., Hydrophobic Metal–Organic Frameworks. *Adv. Mater.* **2019,** *31* (32), 1900820.
19. Kim, H.; Rao, S. R.; Kapustin, E. A.; Zhao, L.; Yang, S.; Yaghi, O. M.; Wang, E. N., Adsorption-based atmospheric water harvesting device for arid climates. *Nat. Commun.* **2018,** *9* (1), 1191.
20. Abednatanzi, S.; Gohari Derakhshandeh, P.; Depauw, H.; Coudert, F.-X.; Vrielinck, H.; Van Der Voort, P.; Leus, K., Mixed-metal metal–organic frameworks. *Chem. Soc. Rev.* **2019,** *48* (9), 2535-2565.
21. Ayoub, G.; Karadeniz, B.; Howarth, A. J.; Farha, O. K.; Đilović, I.; Germann, L. S.; Dinnebier, R. E.; Užarević, K.; Friscic, T., Rational synthesis of mixed-metal microporous metal-organic frameworks with controlled composition using mechanochemistry. *Chem. Mater.* **2019**.
22. Dhakshinamoorthy, A.; Asiri, A. M.; Garcia, H., Mixed-metal or mixed-linker metal organic frameworks as heterogeneous catalysts. *Catal. Sci. Technol.* **2016,** *6* (14), 5238-5261.
23. Guo, P.; Froese, C.; Fu, Q.; Chen, Y.-T.; Peng, B.; Kleist, W.; Fischer, R. A.; Muhler, M.; Wang, Y., CuPd Mixed-Metal HKUST-1 as a Catalyst for Aerobic Alcohol Oxidation. *J. Phys. Chem. C* **2018,** *122* (37), 21433-21440.
24. Lan, M.; Guo, R.-M.; Dou, Y.; Zhou, J.; Zhou, A.; Li, J.-R., Fabrication of porous Pt-doping heterojunctions by using bimetallic MOF template for photocatalytic hydrogen generation. *Nano Energy* **2017,** *33*, 238-246.
25. Nowacka, A.; Briantais, P.; Prestipino, C.; Llabrés i Xamena, F. X., Facile “green” aqueous synthesis of mono- and bimetallic trimesate metalorganic frameworks. *Cryst. Growth Des.* **2019**.
26. Yang, X.; Xu, Q., Bimetallic Metal–Organic Frameworks for Gas Storage and Separation. *Cryst. Growth Des.* **2017,** *17* (4), 1450-1455.
27. Baumann, A. E.; Burns, D. A.; Liu, B.; Thoi, V. S., Metal-organic framework functionalization and design strategies for advanced electrochemical energy storage devices. *Commun. Chem.* **2019,** *2* (1), 86.
28. Park, J.-H.; Park, K.; Han, D.; Yeon, D.-H.; Jung, H.; Choi, B.; Park, S. Y.; Ahn, S.-J.; Park, J.-H.; Han, H. N.; Lee, K. H., Structure- and porosity-tunable, thermally reactive metal organic frameworks for high-performance Ni-rich layered oxide cathode materials with multi-scale pores. *J. Mater. Chem. A* **2019,** *7* (25), 15190-15197.
29. Farrusseng, D.; Aguado, S.; Pinel, C., Metal–Organic Frameworks: Opportunities for Catalysis. *Angew. Chem. Int. Ed.* **2009,** *48* (41), 7502-7513.
30. Doonan, C. J.; Sumby, C. J., Metal–organic framework catalysis. *CrystEngComm* **2017,** *19* (29), 4044-4048.
31. Vermoortele, F.; Ameloot, R.; Alaerts, L.; Matthessen, R.; Carlier, B.; Fernandez, E. V. R.; Gascon, J.; Kapteijn, F.; De Vos, D. E., Tuning the catalytic performance of metal-organic frameworks in fine chemistry by active site engineering. *J. Mater. Chem.* **2012,** *22* (20), 10313-10321.
32. Valvekens, P.; Vermoortele, F.; De Vos, D., Metal-organic frameworks as catalysts: the role of metal active sites. *Catal. Sci. Technol.* **2013,** *3* (6), 1435-1445.
33. Vermoortele, F.; Bueken, B.; Le Bars, G.; Van de Voorde, B.; Vandichel, M.; Houthoofd, K.; Vimont, A.; Daturi, M.; Waroquier, M.; Van Speybroeck, V.; Kirschhock, C.; De Vos, D. E., Synthesis Modulation as a Tool To Increase the Catalytic Activity of Metal–Organic Frameworks: The Unique Case of UiO-66(Zr). *J. Am. Chem. Soc.* **2013,** *135* (31), 11465-11468.
34. Dhakshinamoorthy, A.; Li, Z.; Garcia, H., Catalysis and photocatalysis by metal organic frameworks. *Chem. Soc. Rev.* **2018,** *47* (22), 8134-8172.

35. Wang, Y.; Wöll, C., Chemical Reactions at Isolated Single-Sites Inside Metal–Organic Frameworks. *Catal. Lett.* **2018,** *148* (8), 2201-2222.
36. Dincă, M.; Gabbaï, F. P.; Long, J. R., Organometallic Chemistry within Metal–Organic Frameworks. *Organometallics* **2019,** *38* (18), 3389-3391.
37. Chui, S. S.-Y.; Lo, S. M.-F.; Charmant, J. P. H.; Orpen, A. G.; Williams, I. D., A Chemically Functionalizable Nanoporous Material [Cu3(TMA)2(H2O)3]n. *Science* **1999,** *283* (5405), 1148-1150.
38. Zhang, W.; Freitag, K.; Wannapaiboon, S.; Schneider, C.; Epp, K.; Kieslich, G.; Fischer, R. A., Elaboration of a Highly Porous RuII,II Analogue of HKUST-1. *Inorg. Chem.* **2016,** *55* (24), 12492-12495.
39. Kozachuk, O.; Yusenko, K.; Noei, H.; Wang, Y.; Walleck, S.; Glaser, T.; Fischer, R. A., Solvothermal growth of a ruthenium metal–organic framework featuring HKUST-1 structure type as thin films on oxide surfaces. *Chem. Commun.* **2011,** *47* (30), 8509-8511.
40. Cotton, F. A.; Norman, J. G., Molybdenum(II) trifluoroacetate dimer. Bispyridine adduct. *J. Am. Chem. Soc.* **1972,** *94* (16), 5697-5702.
41. Lawton, D.; Mason, R., The Molecular Structure of Molybdenum(II) Acetate. *J. Am. Chem. Soc.* **1965,** *87* (4), 921-922.
42. Dubicki, L.; Martin, R. L., Metal-metal bond in binuclear rhodium(II) acetate monohydrate. *Inorg. Chem.* **1970,** *9* (3), 673-675.
43. Boyar, E. B.; Robinson, S. D., Rhodium(II) carboxylates. *Coord. Chem. Rev.* **1983,** *50* (1), 109-208.
44. Kumar, D. K.; Filatov, A. S.; Napier, M.; Sun, J.; Dikarev, E. V.; Petrukhina, M. A., Dirhodium Paddlewheel with Functionalized Carboxylate Bridges: New Building Block for Self-Assembly and Immobilization on Solid Support. *Inorg. Chem.* **2012,** *51* (8), 4855-4861.
45. Kitamura, H.; Ozawa, T.; Jitsukawa, K.; Masuda, H.; Aoyama, Y.; Einaga, H., Syntheses, structures, and properties of tetrakis(mu-acetato)dirhodium(II) complexes with axial pyridine nitrogen donor ligands with or without assistance of hydrogen bonds. *Inorg. Chem.* **2000,** *39* (15), 3294-300.
46. Nickerl, G.; Stoeck, U.; Burkhardt, U.; Senkovska, I.; Kaskel, S., A catalytically active porous coordination polymer based on a dinuclear rhodium paddle-wheel unit. *J. Mater. Chem. A* **2014,** *2*, 144-148.
47. Noei, H.; Kozachuk, O.; Amirjalayer, S.; Bureekaew, S.; Kauer, M.; Schmid, R.; Marler, B.; Muhler, M.; Fischer, R. A.; Wang, Y., CO Adsorption on a Mixed-Valence Ruthenium Metal–Organic Framework Studied by UHV-FTIR Spectroscopy and DFT Calculations. *J. Phys. Chem. C* **2013,** *117* (11), 5658-5666.
48. Zhang, W.; Kozachuk, O.; Medishetty, R.; Schneemann, A.; Wagner, R.; Khaletskaya, K.; Epp, K.; Fischer, R. A., Controlled SBU Approaches to Isoreticular Metal-Organic Framework Ruthenium-Analogues of HKUST-1. *Eur. J. Inorg. Chem.* **2015,** *2015* (23), 3913-3920.
49. Zhang, W.; Kauer, M.; Halbherr, O.; Epp, K.; Guo, P.; Gonzalez, M. I.; Xiao, D. J.; Wiktor, C.; Xamena, F. X. L. i.; Wöll, C.; Wang, Y.; Muhler, M.; Fischer, R. A., Ruthenium Metal–Organic Frameworks with Different Defect Types: Influence on Porosity, Sorption, and Catalytic Properties. *Chem. Eur. J.* **2016,** *22* (40), 14297-14307.
50. Fang, Z.; Bueken, B.; De Vos, D. E.; Fischer, R. A., Defect-Engineered Metal–Organic Frameworks. *Angew. Chem. Int. Ed.* **2015,** *54* (25), 7234-7254.
51. Dissegna, S.; Epp, K.; Heinz, W. R.; Kieslich, G.; Fischer, R. A., Defective Metal-Organic Frameworks. *Adv. Mater.* **2018,** *30* (37), 1704501.
52. Gutov, O. V.; Hevia, M. G.; Escudero-Adán, E. C.; Shafir, A., Metal–Organic Framework (MOF) Defects under Control: Insights into the Missing Linker Sites and Their Implication in the Reactivity of Zirconium-Based Frameworks. *Inorg. Chem.* **2015,** *54* (17), 8396-8400.
53. Tu, B.; Pang, Q.; Wu, D.; Song, Y.; Weng, L.; Li, Q., Ordered Vacancies and Their Chemistry in Metal–Organic Frameworks. *J. Am. Chem. Soc.* **2014,** *136* (41), 14465-14471.
54. Canivet, J.; Vandichel, M.; Farrusseng, D., Origin of highly active metal-organic framework catalysts: defects? Defects! *Dalton Trans.* **2016,** *45* (10), 4090-4099.
55. Sholl, D. S.; Lively, R. P., Defects in Metal–Organic Frameworks: Challenge or Opportunity? *J. Phys. Chem. Lett.* **2015,** *6* (17), 3437-3444.
56. Cheetham, A. K.; Bennett, T. D.; Coudert, F.-X.; Goodwin, A. L., Defects and disorder in metal organic frameworks. *Dalton Trans.* **2016,** *45* (10), 4113-4126.
57. Montoro, C.; Ocón, P.; Zamora, F.; Navarro, J. A. R., Metal–Organic Frameworks Containing Missing-Linker Defects Leading to High Hydroxide-Ion Conductivity. *Chem. Eur. J.* **2016,** *22* (5), 1646-1651.
58. Shearer, G. C.; Chavan, S.; Bordiga, S.; Svelle, S.; Olsbye, U.; Lillerud, K. P., Defect Engineering: Tuning the Porosity and Composition of the Metal–Organic Framework UiO-66 via Modulated Synthesis. *Chem. Mater.* **2016,** *28* (11), 3749-3761.
59. Ye, G.; Zhang, D.; Li, X.; Leng, K.; Zhang, W.; Ma, J.; Sun, Y.; Xu, W.; Ma, S., Boosting Catalytic Performance of Metal–Organic Framework by Increasing the Defects via a Facile and Green Approach. *ACS Appl. Mater. Interfaces* **2017,** *9* (40), 34937-34943.
60. Kozachuk, O.; Luz, I.; Xamena, F. X. L. i.; Noei, H.; Kauer, M.; Albada, H. B.; Bloch, E. D.; Marler, B.; Wang, Y.; Muhler, M.; Fischer, R. A., Multifunctional, Defect-Engineered Metal–Organic Frameworks with Ruthenium Centers: Sorption and Catalytic Properties. *Angew. Chem. Int. Ed.* **2014,** *53* (27), 7058-7062.
61. Fang, Z.; Dürholt, J. P.; Kauer, M.; Zhang, W.; Lochenie, C.; Jee, B.; Albada, B.; Metzler-Nolte, N.; Pöppl, A.; Weber, B.; Muhler, M.; Wang, Y.; Schmid, R.; Fischer, R. A., Structural Complexity in Metal–Organic Frameworks: Simultaneous Modification of Open Metal Sites and Hierarchical Porosity by Systematic Doping with Defective Linkers. *J. Am. Chem. Soc.* **2014,** *136* (27), 9627-9636.
62. Fischer, R. A.; Epp, K.; Luz, I.; Heinz, W. R.; Rapeyko, A.; Llabres i Xamena, F. X., Defect Engineered Ruthenium MOFs as Versatile Hydrogenation Catalysts. *ChemCatChem* **2020,** *n/a* (n/a).
63. Agirrezabal-Telleria, I.; Luz, I.; Ortuño, M. A.; Oregui-Bengoechea, M.; Gandarias, I.; López, N.; Lail, M. A.; Soukri, M., Gas reactions under intrapore condensation regime within tailored metal–organic framework catalysts. *Nat. Commun.* **2019,** *10* (1), 2076.
64. Gadipelli, S.; Guo, Z., Postsynthesis Annealing of MOF-5 Remarkably Enhances the Framework Structural Stability and CO2 Uptake. *Chem. Mater.* **2014,** *26* (22), 6333-6338.
65. Bentley, J.; Foo, G. S.; Rungta, M.; Sangar, N.; Sievers, C.; Sholl, D. S.; Nair, S., Effects of Open Metal Site Availability on Adsorption Capacity and Olefin/Paraffin Selectivity in the Metal–Organic Framework Cu3(BTC)2. *Ind. Eng. Chem. Res.* **2016,** *55* (17), 5043-5053.
66. Lee, S. J.; Doussot, C.; Baux, A.; Liu, L.; Jameson, G. B.; Richardson, C.; Pak, J. J.; Trousselet, F.; Coudert, F.-X.; Telfer, S. G., Multicomponent Metal–Organic Frameworks as Defect-Tolerant Materials. *Chem. Mater.* **2016,** *28* (1), 368-375.
67. Chun, H.; Bak, W.; Hong, K.; Moon, D., A Simple and Rational Approach for Binodal Metal–Organic Frameworks with Tetrahedral Nodes and Unexpected Multimodal Porosities from Nonstoichiometric Defects. *Cryst. Growth Des.* **2014,** *14* (4), 1998-2002.
68. Yang, S. J.; Im, J. H.; Kim, T.; Lee, K.; Park, C. R., MOF-derived ZnO and ZnO@C composites with high photocatalytic activity and adsorption capacity. *J. Hazard. Mater.* **2011,** *186* (1), 376-382.
69. Ji, W.; Xu, Z.; Liu, P.; Zhang, S.; Zhou, W.; Li, H.; Zhang, T.; Li, L.; Lu, X.; Wu, J.; Zhang, W.; Huo, F., Metal–Organic Framework Derivatives for Improving the Catalytic Activity of the CO Oxidation Reaction. *ACS Appl. Mater. Interfaces* **2017,** *9* (18), 15394-15398.
70. Zhou, J.; Dou, Y.; Zhou, A.; Guo, R.-M.; Zhao, M.-J.; Li, J.-R., MOF Template-Directed Fabrication of Hierarchically Structured Electrocatalysts for Efficient Oxygen Evolution Reaction. *Adv. Energy Mater.* **2017,** *7* (12), 1602643.
71. Hussain, M. Z.; Schneemann, A.; Fischer, R. A.; Zhu, Y.; Xia, Y., MOF Derived Porous ZnO/C Nanocomposites for Efficient Dye Photodegradation. *ACS Appl. Energy Mater.* **2018,** *1* (9), 4695-4707.

72. Yang, Y.; Dong, H.; Wang, Y.; He, C.; Wang, Y.; Zhang, X., Synthesis of octahedral like Cu-BTC derivatives derived from MOF calcined under different atmosphere for application in CO oxidation. *J. Solid State Chem.* **2018,** *258*, 582-587.
73. Zhu, B.; Xia, D.; Zou, R., Metal-organic frameworks and their derivatives as bifunctional electrocatalysts. *Coord. Chem. Rev.* **2018,** *376*, 430-448.
74. Hussain, M. Z.; Pawar, G. S.; Huang, Z.; Tahir, A. A.; Fischer, R. A.; Zhu, Y.; Xia, Y., Porous ZnO/Carbon nanocomposites derived from metal organic frameworks for highly efficient photocatalytic applications: A correlational study. *Carbon* **2019,** *146*, 348-363.
75. Zhong, Y.; Xu, X.; Wang, W.; Shao, Z., Recent Advances in Metal-Organic Framework Derivatives as Oxygen Catalysts for Zinc-Air Batteries. *Batteries Supercaps* **2019,** *2* (4), 272-289.
76. Lee, K. J.; Lee, J. H.; Jeoung, S.; Moon, H. R., Transformation of Metal–Organic Frameworks/Coordination Polymers into Functional Nanostructured Materials: Experimental Approaches Based on Mechanistic Insights. *Acc. Chem. Res.* **2017,** *50* (11), 2684-2692.
77. Picheau, E.; Hof, F.; Derré, A.; Daffos, B.; Pénicaud, A., Thermal Oxidation of Carbonaceous Nanomaterials Revisited: Evidence of Mechanism Changes. *Angew. Chem. Int. Ed.* **2019,** *58* (45), 16013-16017.
78. Gao, W.-Y.; Ezazi, A. A.; Wang, C.-H.; Moon, J.; Abney, C.; Wright, J.; Powers, D. C., Metallopolymerization as a Strategy to Translate Ligand-Modulated Chemoselectivity to Porous Catalysts. *Organometallics* **2019,** *38* (18), 3436-3443.
79. Das, A.; Maher, A. G.; Telser, J.; Powers, D. C., Observation of a Photogenerated Rh2 Nitrenoid Intermediate in C–H Amination. *J. Am. Chem. Soc.* **2018,** *140* (33), 10412-10415.
80. Das, A.; Chen, Y.-S.; Reibenspies, J. H.; Powers, D. C., Characterization of a Reactive Rh2 Nitrenoid by Crystalline Matrix Isolation. *J. Am. Chem. Soc.* **2019,** *141* (41), 16232-16236.
81. Wang, C.-H.; Gao, W.-Y.; Powers, D. C., Measuring and Modulating Substrate Confinement during Nitrogen-Atom Transfer in a Ru2-Based Metal-Organic Framework. *J. Am. Chem. Soc.* **2019,** *141* (49), 19203-19207.
82. Shakya, D. M.; Ejegbavwo, O. A.; Rajeshkumar, T.; Senanayake, S. D.; Brandt, A. J.; Farzandh, S.; Acharya, N.; Ebrahim, A. M.; Frenkel, A. I.; Rui, N.; Tate, G. L.; Monnier, J. R.; Vogiatzis, K. D.; Shustova, N. B.; Chen, D. A., Selective Catalytic Chemistry at Rhodium(II) Nodes in Bimetallic Metal–Organic Frameworks. *Angew. Chem. Int. Ed.* **2019,** *58* (46), 16533-16537.
83. St. Petkov, P.; Vayssilov, G. N.; Liu, J.; Shekhah, O.; Wang, Y.; Wöll, C.; Heine, T., Defects in MOFs: A Thorough Characterization. *ChemPhysChem* **2012,** *13* (8), 2025-2029.
84. Canivet, J.; Aguado, S.; Schuurman, Y.; Farrusseng, D., MOF-Supported Selective Ethylene Dimerization Single-Site Catalysts through One-Pot Postsynthetic Modification. *J. Am. Chem. Soc.* **2013,** *135* (11), 4195-4198.
85. Metzger, E. D.; Brozek, C. K.; Comito, R. J.; Dincă, M., Selective Dimerization of Ethylene to 1-Butene with a Porous Catalyst. *ACS Cent. Sci.* **2016,** *2* (3), 148-153.
86. Gonzalez, M. I.; Oktawiec, J.; Long, J. R., Ethylene oligomerization in metal–organic frameworks bearing nickel(ii) 2,2′-bipyridine complexes. *Faraday Discuss.* **2017,** *201* (0), 351-367.
87. Madrahimov, S. T.; Gallagher, J. R.; Zhang, G.; Meinhart, Z.; Garibay, S. J.; Delferro, M.; Miller, J. T.; Farha, O. K.; Hupp, J. T.; Nguyen, S. T., Gas-Phase Dimerization of Ethylene under Mild Conditions Catalyzed by MOF Materials Containing (bpy)NiII Complexes. *ACS Catal.* **2015,** *5* (11), 6713-6718.
88. Li, Z.; Schweitzer, N. M.; League, A. B.; Bernales, V.; Peters, A. W.; Getsoian, A. B.; Wang, T. C.; Miller, J. T.; Vjunov, A.; Fulton, J. L.; Lercher, J. A.; Cramer, C. J.; Gagliardi, L.; Hupp, J. T.; Farha, O. K., Sintering-Resistant Single-Site Nickel Catalyst Supported by Metal–Organic Framework. *J. Am. Chem. Soc.* **2016,** *138* (6), 1977-1982.
89. Liu, J.; Ye, J.; Li, Z.; Otake, K.-i.; Liao, Y.; Peters, A. W.; Noh, H.; Truhlar, D. G.; Gagliardi, L.; Cramer, C. J.; Farha, O. K.; Hupp, J. T., Beyond the Active Site: Tuning the Activity and Selectivity of a Metal–Organic Framework-Supported Ni Catalyst for Ethylene Dimerization. *J. Am. Chem. Soc.* **2018,** *140* (36), 11174-11178.
90. Angelescu, E.; Che, M.; Andruh, M.; Zăvoianu, R.; Costentin, G.; Miricã, C.; Dumitru Pavel, O., Ethylene selective dimerization on polymer complex catalyst of Ni(4,4′-bipyridine)Cl2 coactivated with AlCl(C2H5)2. *J. Mol. Catal. A: Chem.* **2004,** *219* (1), 13-19.
91. Lallemand, M.; Rusu, O. A.; Dumitriu, E.; Finiels, A.; Fajula, F.; Hulea, V., Ni-MCM-36 and Ni-MCM-22 catalysts for the ethylene oligomerization. In *Stud. Surf. Sci. Catal.*, Gédéon, A.; Massiani, P.; Babonneau, F., Eds. Elsevier: 2008; Vol. 174, pp 1139-1142.

ESI Study IV

Electronic Supplementary Material (ESI) for Catalysis Science & Technology.

Supporting Information

Thermal Defect Engineering of Precious Group Metal-Organic Frameworks: Impact on the Catalytic Cyclopropanation Reaction

Werner R. Heinz,[a] Raphael Junk,[a] Iker Agirrezabal-Telleria,[b] Bart Bueken,[c] Hana Bunzen,[d] Thorsten Gölz,[a] Mirza Cokoja,[a] Dirk De Vos,[c] and Roland A. Fischer[a]

[a] Chair of Inorganic and Metal-Organic Chemistry, Department of Chemistry, Technical University of Munich, Lichtenbergstraße 4, 85748 Garching, Germany. E-mail: roland.fischer@tum.de

[b] Department of Chemical and Environmental Engineering, Engineering School of the University of the Basque Country (UPV/EHU), Plaza Torres Quevedo 1, 48013 Bilbao, Spain. E-mail: iker.aguirrezabal@ehu.eus

[c] Centre for Membrane Separations, Adsorption, Catalysis and Spectroscopy for Sustainable Solutions (CMACs), Department of Microbial and Molecular Systems (M2S), KU Leuven, Celestijnenlaan 200F p.o. box 2461, 3001 Leuven, Belgium. E-mail: dirk.devos@kuleuven.be

[d] Chair of Solid State Materials Chemistry, University of Augsburg, Universitätsstraße 1, 86159 Augsburg, Germany. E-mail: hana.bunzen@physik.uni-augsburg.de

Table of Contents

Experimental Details

General considerations

Trimesic acid (Sigma-Aldrich), $RuCl_3 \cdot x\ H_2O$ (Precious Metals Online), $Rh_2(OAc)_4$ (Sigma-Aldrich, Carbolution) and HPLC-grade acetone and ethanol (VWR Chemicals) were purchased commercially and used without further purification. Ultra-pure water was obtained using a Milli-Q purification system (18.2 MΩ cm^{-1}). Dichloromethane was purified and dried using a MBraun SPS-800. $Ru_2(OAc)_4Cl$ was synthesized following literature procedures.[1] Desolvated MOFs were handled in a glovebox using argon (>99.996%; Westfalen).

Instrumentation

Thermal syntheses

Post-synthetic treatments of the pristine MOF samples to yield the TDE-MOFs were conducted with a Netzsch TG209 F1 Libra in an argon-filled glovebox. Decomposition gases were analyzed *in-situ* using a Netzsch QMS 403C Aëolos mass spectrometer. The acceleration voltage of the mass spectrometer was set to 2300 V for the most abundant ions (m/z =18, 28 and 44) and to 2800 V for the less abundant ions (m/z = 2, 14, 16, 25, 30, 31, 35, 37, 46, 56, 58, 60 and 70). The transfer line, the inlet system and the adapter head were heated to 250 °C, 200 °C and 160 °C, respectively. Argon served both as the purge gas and the protective gas of the measurement set-up. Flow rates were set to 20 mL min^{-1}. The following heating protocols were used:

Targeted weight loss of 5.5 wt-% (denoted as 10% defects): Ramp from 15 °C to 150 °C, subsequent isothermal equilibration (30 min), ramp to 200 °C, subsequent isothermal equilibration (30 min), ramp to 220 °C, subsequent isothermal equilibration (30 min), ramp to 240 °C, subsequent isothermal equilibration (20 min), ramp to 260 °C, subsequent isothermal equilibration (20 min).

Targeted weight loss of 10 wt-% and 15 wt-% (denoted as 20% and 30% defects): Ramp from 15 °C to 150 °C, subsequent isothermal equilibration (30 min), ramp to 200 °C, subsequent isothermal equilibration (20 min), ramp to 250 °C, subsequent isothermal equilibration (60 min), ramp to 270 °C, subsequent isothermal equilibration (20 min), ramp to 290 °C, subsequent isothermal equilibration (60 min).

All ramps were programmed with a heating rate of 10 K min^{-1}. The thermal treatment was terminated as soon as the targeted mass loss had been reached and the material was cooled to room temperature.

Powder X-Ray diffraction

All diffraction patterns were collected on a PANalytical Empyrean equipped with a Cu X-ray tube (λ = 0.154 nm) operated at 45 kV and 40 mA in a 2Θ range of 5-50° in steps of 0.0065651° (2Θ) with 0.175 s/step. The incident beam was focussed on the sample through a focusing beam mirror with a 1/8° divergence slit and a nickel beta filter (0.2 mm). A PIXcel1D detector was used in receiving mode with a 1/8° anti-scatter slit and 0.04 rad soller slits. The activated samples were filled in borosilicate capillaries of 0.5 mm inner diameter and mounted onto a capillary spinner.

Elemental Analysis

Determination of the elemental composition was performed together with the microanalytical laboratories of the chemistry department at the Technical University of Munich. Determination of C, H, N and S was carried out with a Hekatech EuroEA elemental analyser. Metal contents were derived from TGA-based metal oxide residues as reported earlier.[2] Chlorine contents were determined by potentiometric titration of HCl after thermal decomposition.

Calculation of the sum formula

Based on determined elemental contents and assuming exclusively the oxygen mass fraction missing to complete the 100 wt-%, sum formulas were calculated and normalized to three metal atoms per repeating unit. The GRG nonlinear solver function implemented in *Microsoft Excel®* was used for compositional fittings assuming acetate and BTC as the only organic framework components of the pristine MOF samples. To account for BTC decarboxylation in TDE-MOFs, isophthalate (IPA) was added to this protocol optimizing the fitting results. For TDE-MOFs, the ceiling amounts of IPA + BTC and OAc^- was restricted to the respective parental BTC and OAc^- amounts. It should be mentioned, that other efforts to determine organic ligand ratios (BTC to acetate) have not been successful as typical sample digestions in diluted acids do not proceed quantitatively and paramagnetic ruthenium obstruct qNMR. MAS-NMR of (100/0) sample was used to confirm the general viability of the fitting approach.

Gas sorption measurements

Sorption experiments were conducted using a Micromeritics 3Flex with each 20 to 80 mg of desolvated sample. Prior to the measurement each sample was additionally degassed at 150°C for >10h. Nitrogen isotherms were recorded at 77 K. The BET surface area was calculated using data points in the relative pressure range of 0.01 to 0.1 in the adsorption branch with the *Rouquerol* consistency criteria considered.

Fourier-transform infrared spectroscopy

FT-IR spectra were recorded from finely ground activated powder samples under argon atmosphere in a glovebox using a Bruker ALPHA FTIR spectrometer equipped with a Pt attenuated total reflectance (ATR) unit at room temperature in the range of 400 to 4000 cm^{-1} with a resolution of 2 cm^{-1} and 24 scans per measurement. A pyroelectric deuterated L-alanine doped triglycine sulfate (RT-DLaTGS) detector was used.

Raman spectroscopy

Raman spectroscopy was measured with an inVia Reflex Raman System with an optical microscope (Leica DM2700M, 50x magnification) coupled to a Renishaw R04 Raman spectrometer with 532 nm laser wavelength (Laser: RL532C, Class 3B) with activated samples filled into Borosilicate glass capillaries (0.5 mm inner diameter) under argon atmosphere. A Renishaw 266n10 detector was used. All samples were measured with 10 s exposure time, 1 % laser power and 10 accumulations.

DFT calculations of Ru- and Rh-paddle-wheel complexes

All calculations have been performed with the Gaussian 16 suite of software[4]. The level of theory included the use of the hybrid DFT functional B3LYP together with the basis set 6-31+G** for C,H,O, Cl.[5,6] Ru and Rh have been described by the Stuttgart-Dresden97-ECP[7].

All structures have been optimized until no negative frequencies haven been calculated by frequency analysis. Frequencies calculation have been also used to determine unscaled frequencies and IR and Raman intensities. UV-VIS spectra of selected singlet state compounds have been calculated by time-dependent DFT[8] taking into account the three most probable electon transitions to singlet and triplet excited states.

4. Gaussian 16, Revision B.01, M. J. Frisch, G. W. Trucks, H. B. Schlegel, G. E. Scuseria, M. A. Robb, J. R. Cheeseman, G. Scalmani, V. Barone, G. A. Petersson, H. Nakatsuji, X. Li, M. Caricato, A. V. Marenich, J. Bloino, B. G. Janesko, R. Gomperts, B. Mennucci, H. P. Hratchian, J. V. Ortiz, A. F. Izmaylov, J. L. Sonnenberg, D. Williams-Young, F. Ding, F. Lipparini, F. Egidi, J. Goings, B. Peng, A. Petrone, T. Henderson, D. Ranasinghe, V. G. Zakrzewski, J. Gao, N. Rega, G. Zheng, W. Liang, M. Hada, M. Ehara, K. Toyota, R. Fukuda, J. Hasegawa, M. Ishida, T. Nakajima, Y. Honda, O. Kitao, H. Nakai, T. Vreven, K. Throssell, J. A. Montgomery, Jr., J. E. Peralta, F. Ogliaro, M. J. Bearpark, J. J. Heyd, E. N. Brothers, K. N. Kudin, V. N. Staroverov, T. A. Keith, R. Kobayashi, J. Normand, K. Raghavachari, A. P. Rendell, J. C. Burant, S. S. Iyengar, J. Tomasi, M. Cossi, J. M. Millam, M. Klene, C. Adamo, R. Cammi, J. W. Ochterski, R. L. Martin, K. Morokuma, O. Farkas, J. B. Foresman, and D. J. Fox, Gaussian, Inc., Wallingford CT, **2016**.

5. a) A.D. Becke, *J. Chem. Phys*. **1993**, 98, 5648-5652; b) C. Lee, W. Yang, R.G. Parr, *Phys. Rev. B* **1988**, *37*, 785-789; c) S.H. Vosko, L. Wilk, M. Nusair, *Can. J. Phys.* **1980**, *58*, 1200-1211; d) P.J. Stephens, F.J. Devlin, C.F. Chabalowski, M.J. Frisch, *J.Phys.Chem.* **1994**, 98, 11623-11627.

6. a) W.J. Hehre, R. Ditchfield and J.A. Pople, J. Chem. Phys. **1972**, *56,* 2257-2261 (1972); b) T. Clark, J. Chandrasekhar, G. W. Spitznagel, and P. v. R. Schleyer, *J. Comp. Chem.*, **1983**, *4*, 294-301; c) M.M. Francl, W.J. Petro, W.J. Hehre, J.S. Binkley, M.S. Gordon, D.J. DeFrees and J.A. Pople, *J. Chem. Phys.* **1982**, *77*, 3654-3665.

7. a) A. Bergner, M. Dolg, W. Kuechle, H. Stoll, H. Preuss, *Mol. Phys.* **1993**, *80*,1431-1441 ; b) M. Kaupp, P. v. R. Schleyer, H. Stoll, H. Preuss, *J. Chem. Phys.* **1991**, *94*, 1360-1366; c) M. Dolg, H. Stoll, H. Preuss, R.M. Pitzer, *J. Phys. Chem.* **1993**, *97*, 5852-5859.

8. a) R. E. Stratmann, G. E. Scuseria, M. J. Frisch, *J. Chem. Phys.*, **1998**, *109*, 8218-24. b) F. Furche and R. Ahlrichs, *J. Chem. Phys.*, **2002**, *117*, 7433-7447.

Thermogravimetric analysis

Thermal analysis of the materials was determined with a Mettler Toledo TGA/DSC 1 in aluminium oxide crucibles (70 µL with lid) with sample amounts of 1 to 5 mg. Samples of activated materials were taken under inert conditions in a glovebox and transferred to the measurement chamber in screw capped vials immediately prior to the measurement. The following thermal program was applied using synthetic air (20 mL min^{-1}, Westfalen, 80% N_2; 20% O_2): At 30 °C isothermal equilibration (15 min), ramp from 30 °C to 700 °C with 10 K min^{-1}, at 700 °C isothermal equilibration (15 min).

High-resolution transmission electron microscopy

TEM and STEM micrographs and EDS elemental mappings were recorded with a JEM NEOARM microscope (JEOL) with a cold FEG electron source operated at 200 kV. Samples were prepared by depositing a drop of the crystalline products dispersed in ethanol onto carbon-coated copper grids (200 mesh) and dried in air.

Catalytic Experiments

4.0 to 5.0 mg MOF material (referring to ≈1.3 mol-% catalyst loading) was weighed directly into a 20 mL glass vial in an argon-filled glovebox with a *Sartorius Entris* laboratory balance. The vial was then equipped with a cross-shaped stir bar and sealed using a polypropylene screw cap with a PTFE/silicone septum. A second empty vial was equipped with a stir bar and sealed accordingly. Outside the glovebox, 2.4 mL styrene, 2.4 mL dichloromethane, 0.2 mL toluene and 0.2 mL EDA solution (containing ≥ 13 wt-% CH_2Cl_2) were introduced into this empty vial. Dichloromethane and toluene had been degassed by argon purging prior to their use and were stored over activated 3 Å molecular sieves under inert conditions. 0.5 mL styrene and 0.5 mL dichloromethane, both dry and degassed, were introduced into the vial containing the MOF sample. The contents of both vials were stirred for approximately 20 min at 150 min^{-1} before the entire EDA solution was drawn up into a 5 ml syringe. Using a New Era Pump Systems NE-1010 syringe pump, which was set to a syringe diameter of 12.52 mm and an addition rate of 0.087 mL min^{-1}, the EDA solution was drop-wise introduced into the vial containing the MOF sample over 60 min. A long syringe needle was used to release the pressure that would otherwise build up by the formation of dinitrogen. The first sample was taken when the addition process had been completed, 60 min after starting the syringe pump. This moment was defined as the starting point of the time scale (0 h). Subsequent samples were taken at 20 min, 40 min, 60 min, 2 h, 3 h, 4 h and 24 h. The sampling process was performed by drawing 0.7 mL HPLC grade dichloromethane up into a 1 mL syringe and then taking a 0.1 mL aliquot of the reaction mixture by pulling the plunger to the 0.8 mL mark. The resulting suspension was filtered into a GC vial using a 13 mm PTFE membrane syringe filter with a pore size of 0.2 µm. Reusability experiments were conducted in a similar way using the same MOF catalyst for five cycles. Every sampling was conducted after 4 h of reaction time. Catalytic parameters were calculated using the following formulae: The conversion X was calculated using $X = \frac{\Sigma n_{products,\,normalized}}{\Sigma n_{products,\,normalized} + n_{EDA,\,normalized}}$, with the sum (Σ) of product moles being $n = \frac{I_{GC}}{\#_{carbon}}$ comprising the GC-based intensity (I) of each product divided by its carbon number ($\#_{carbon}$). Chemoselectivities S were calculated using $S = \frac{n_{product}}{\Sigma n_{products}}$ with the amount n of the particular product divided by the sum of all product amounts. Similarly, diastereoselectivities (DS) are calculated relating to the trans product as follows: $DS_{trans} = \frac{I_{trans}}{I_{trans} + I_{cis}}$ being irrespective of any normalization as both diastereoisomers contain identical carbon contents. Initial TOFs are calculated according to $TOF\left[h^{-1}\right] = \frac{X_{t\,=\,0min} \cdot n_{EDA}}{n_{metal} \cdot 0.5\ h}$ using the initial conversion $X_{t=0min}$, the mean reaction time (0.5 h) of EDA molecules during the EDA addition and the molar ratio of EDA and the total metal content used for the reaction. The internal standard toluene was used to derive a continuity factor f assuring constant molarity of EDA and EDA-derived products during each catalytic run. The continuity factor was calculated according to $f = \frac{n_{toluene,\,normalized}}{\Sigma n_{products} + n_{EDA}}$ and remained constant during each run. This validates the chosen data evaluation as no undetected EDA-derived species emerge.

Additional Information – Material Descriptions

Definitions for "defect amount or "defectiveness" used in the manuscript

In this manuscript, the terms "defectiveness" and "defect amount" are used. Although, Dissegna *et al.* have provided a generally accepted definition of "defect" in a recent review on Defective MOFs, that definition is very general and not sufficiently precise for the work presented herein. For this reason and to prevent the readers from confusion, further explanations shall be provided in the following. A tripartite definition appears most suitable for the point defects discussed herein depending on a.) the sample preparation, b.) the network connectivity and c.) the organometallic perspective.

The first definition is related to the experimental procedure and the chosen sample denotation using an (XX/YY) nomenclature. XX refers to the fraction of rhodium PWs as part of the total metal content comprising ruthenium and rhodium (0%, 50% or 100%). YY refers to the **thermally introduced number of defects** (0%, 10%, 20% or 30%). The mentioned values best reflect the defectiveness throughout the three series of TDE materials and results from different calculative approaches (whether a.) the total amount of organics, b.) the ligands or c.) specifically carboxylates are considered). All different values are depicted in Table S3 (see page 11), respectively. In general, thermal treatments result in the removal of exclusively organic constituents (representing ≈50% of the whole framework). Concluded from mass spectrometry, acetate and carbon dioxide are the major components being removed during TDE. There are no indications for the removal of any aromatic fragments. To reach the arbitrarily chosen defectiveness (YY%), weight losses of 5.5, 10 and 15 wt-% were targeted respectively. At this point, it should be mentioned that "defectiveness" in this context quantifies only defects which were introduced to the framework postsynthetically. Defects originating from modulated synthesis and already being present in the pristine samples are not covered in this first definition.

Secondly, the defectiveness of a MOF sample could be qualitatively defined according to the **network connectivity**. In the ideal HKUST-1 structure, each PW is coordinated by four BTC linkers while each of them interconnects three PWs. Modulated synthesis of PGM-MOFs results in relatively large acetate amounts incorporated to the structure. Even if all equatorial coordination sites are occupied, three acetate ligands can replace one BTC linker resulting in a **"connectivity defect"**. Its occurrence has several effects: The lower connectivity hampers the mechanical stability of the framework and its crystallinity. Further the clearly defined size of the micropores is dispersed and mesopore formation (due to missing node defects) occurs. In contrast to decarboxylation of BTC, any removal of monotopic acetates during TDE does not increase the number of these connectivity defects. Since both acetate and aromatic carboxylate ligands have rather similar electronic and steric effects to the metal nodes, strong impacts on the reactivity of PWs is not to be expected for connectivity defects. This situation changes for the **third definition**:

Defects from an organometallic point of view (**"coordination defect"**) are often called ligand vacancies, **open metal sites** (OMS) or coordinatively unsaturated sites (CUS). As usual MOF activation facilitates removal of neutral solvent molecules coordinated to the axial positions of a PW, anionic ligands remain strongly bound. This holds true for axial anions accounting for additional charge compensation in the mixed-valent $Ru^{II,III}$ -BTC but also for equatorial bridging carboxylates. For instance, a connectivity defect according to our second definition is not necessarily considered defective in this third definition as all equatorial metal sites are coordinated with bridging carboxylates. In this work, TDE-induced decarboxylation results in a strong increase in coordination defects. This is accompanied by altered electronic and steric properties such as (partial) metal reduction or increased accessibility of the metal nodes and potential mesopore formation (removal of "pore walls"). Changes in reactivity of these "coordination defects" are observed for instance in ethylene sorption and dimerization.

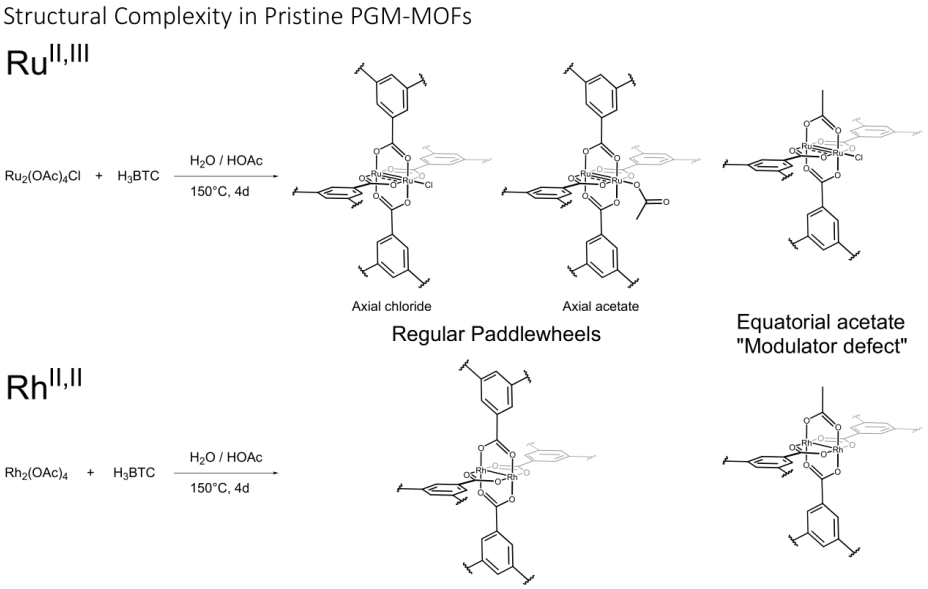

Scheme S 1: Structural complexity in pristine PGM-HKUST-1 derivatives. The mixed-valent Ru-HKUST-1 comprises one axial ligand per PW which is either chloride or acetate for compensation of the additional charge. Modulator-based acetate incorporation on equatorial positions (up to three equatorial acetates per PW) occurs in both metal derivatives.

Assumed Reactions during TDE

a.) Mixed valent Ru-MOF:

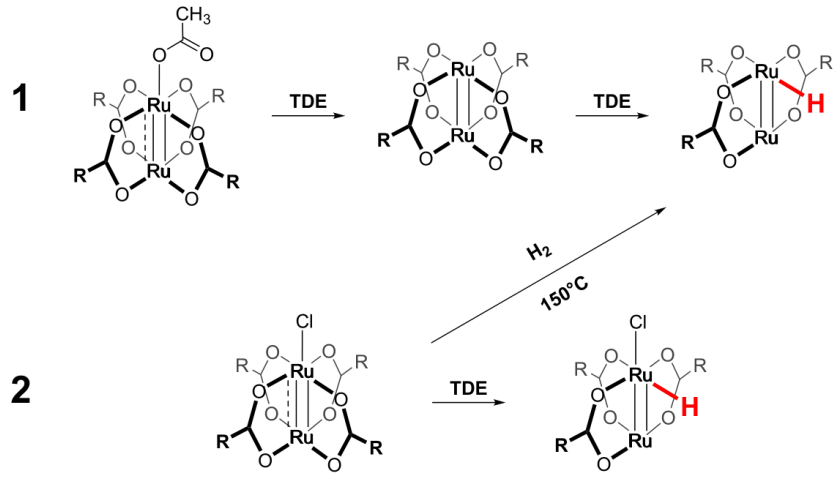

b.) Univalent Rh-MOF:

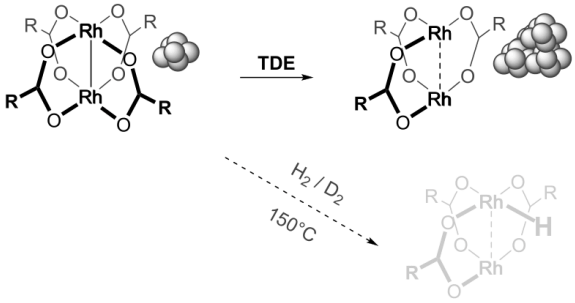

Scheme S 2: Assumed molecular reactions during TDE of the highly complex PGM-MOFs. Organic residues R represent either CH_3 (acetate) or $C_8H_3O_4$ (BTC). Each univalent PW could carry x= 1-4 BTC ligands and 4-x acetate ligands according to Scheme S1. ***a.)*** *Mixed-valent Ru-MOF. Either acetate (**1**) or chloride (**2**) can coordinate one axial position for charge compensation. **1** displays the case when acetate is the additional axial ligand: Temperature-induced removal first generates a univalent Ru-PW which further undergoes ligand removal/fragmentation under subsequent Ru-H formation. **2** displays the case of an axially bound chloride ligand: TDE under inert atmosphere retains the chloride while hydrogen treatment facilitates its removal.* ***b.)*** *The assumed TDE of the univalent Rh-MOF features much less flexibility. While few Rh NPs are already present in the pristine MOF, their agglomeration leads to larger NPs during TDE. No Rh-H formation is observed in inert atmosphere TDE, while low Rh-H formation is visible under harsher H_2 / D_2 treatment. Overall Ru-MOF seems more tolerant towards TDE-induced ligand removal / fragmentation. Hypothetically the higher bond order in Ru dimers allows more progressive ligand removal since M-M bonds could potentially prevent NP formation.*

Additional Information – Material Characterization

Thermal Defect-Engineering – Temperature Program

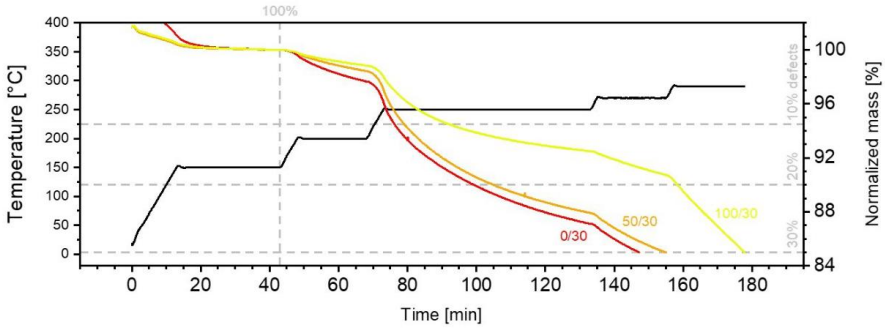

Figure S 1: Weight profiles and the underlying temperature program for TDE-MOF syntheses in 20mL min^{-1} argon stream. Thermal syntheses were performed in an Ar-filled glovebox to prevent deactivation of generated open metal sites by oxygen or moisture after the treatment. The dashed vertical line indicates the point of weight-referencing. The dashed horizontal lines indicate the targeted weight-loss for 10%, 20% and 30% defect amounts.

Powder X-Ray Diffraction

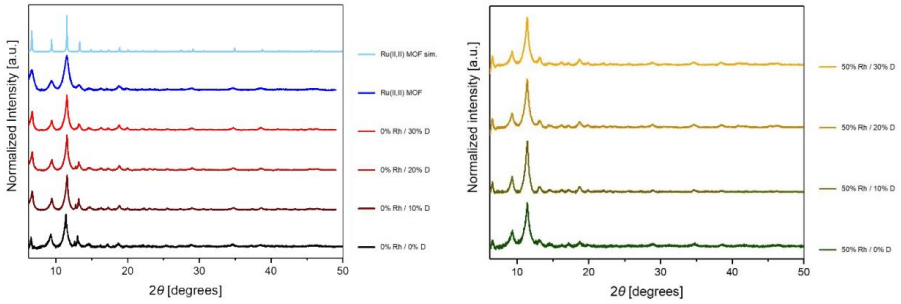

Figure S 2: PXRD patterns of 0%Rh and 50%Rh pristine and TDE-materials indicate preserved crystallinity.

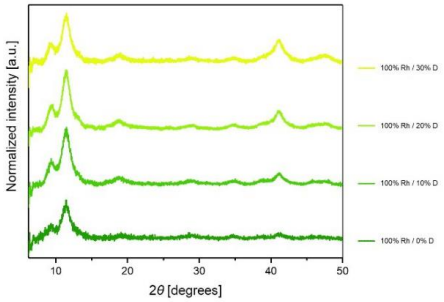

Figure S 3: PXRD patterns of 100%Rh pristine and TDE-materials indicating preserved crystallinity and increasing scattering of nanoparticles. In combination with TEM images, existing small NPs merge into larger ones which increases their X-ray scattering.

Elemental Analysis & Surface Areas

*Table S 1: Found elementary contents, derived sum formulae, respective molecular weights, metal contents and nitrogen-based BET surface areas of all samples. *Based on duplicate analyses.*

Sample	Found C*,H*,Cl,M_{total} values [wt-%]	Calculated Sum Formulae	Molecular Weight [g mol^{-1}]	Metal Content [%]	N2 Surface Area [m^2 g^{-1}]
(100 / 0)	29.1/1.56/0/41.0	$[Rh_3(BTC)_{1.61}(OAc)_{1.89}]$	753.35	41.0	1360
(100 / 10)	28.1/1.30/0/43.1	$[Rh_3(BTC)_{1.22}(IPA)_{0.39}(OAc)_{1.34}]$	704.08	43.1	1340
(100 / 20)	27.9/1.28/0/45.5	$[Rh_3(BTC)_{0.86}(IPA)_{0.74}(OAc)_{1.01}]$	669.74	45.5	1424
(100 / 30)	27.6/1.22/0/48.0	$[Rh_3(BTC)_{0.61}(IPA)_{0.99}(OAc)_{0.64}]$	637.14	48.0	1274
(50 / 0)	30.4/1.66/1.5/39.2	$[Ru_{1.44}Rh_{1.56}(BTC)_{1.52}(OAc)_{2.69}Cl_{0.3}]$	791.44	18.4 / 20.8	1211
(50 / 10)	30.0/1.26/1.5/40.4	$[Ru_{1.44}Rh_{1.56}(BTC)_{1.36}(IPA)_{0.57}(OAc)_{1.03}Cl_{0.3}]$	753.18	19.0 / 21.4	n.d.
(50 / 20)	28.9/1.26/1.5/42.8	$[Ru_{1.44}Rh_{1.56}(BTC)_{0.64}(IPA)_{1.27}(OAc)_{0.64}Cl_{0.3}]$	695.69	20.1 / 22.7	n.d.
(50 / 30)	28.26/1.22/1.45/44.8	$[Ru_{1.44}Rh_{1.56}(BTC)_{0.54}(IPA)_{1.27}(OAc)_{0.52}Cl_{0.3}]$	667.45	21.0 / 23.7	n.d.
(0 / 0)	29.8/1.34/3.0/37.4	$[Ru_3(BTC)_{1.89}(OAc)_{1.55}Cl_{0.7}]$	810.73	37.4	1018
(0 / 10)	29.1/1.67/3.0/39.1	$[Ru_3(BTC)_{0.56}(IPA)_{1.32}(OAc)_{1.55}Cl_{0.65}]$	751.88	39.1	1065
(0 / 20)	30.8/0.93/2.9/41.2	$[Ru_3(BTC)_{0.82}(IPA)_{1.44}(OAc)_0Cl_{0.61}]$	730.18	41.2	1034
(0 / 30)	28.8/1.04/2.9/43.6	$[Ru_3(BTC)_{1.12}(IPA)_{0.76}(OAc)_{0.24}Cl_{0.57}]$	695.75	43.6	1173
$Ru^{II,II}$-BTC	27.4/1.50/0/42.5	$[Ru_3(BTC)_{1.32}(OAc)_{2.22}]$	707.28	42.5	1493

Table S 2: Quantification of the term "defectiveness" in TDE samples depending on metal type and reference.

(XX/YY) Nomenclature			Removed wt-%	Removed Fraction of:		
Sample	XX % Rh	YY %* Defects		Total Organics	Total Ligands	CO_2^-
(0/0)	0	0	0		0%	0%
(0/10)	0	10	5.50%	-9%	-18%	-19%
(0/20)	0	20	10%	-16%	-25%	-26%
(0/30)	0	30	15%	-24%	-28%	-29%
(50/0)	50	0	0		0%	0%
(50/10)	50	10	5.50%	-9%	-13%	-14%
(50/20)	50	20	10%	-16%	-28%	-30%
(50/30)	50	30	15%	-25%	-34%	-35%
(100/0)	100	0	0		0%	0%
(100/10)	100	10	5.50%	-9%	-14%	-14%
(100/20)	100	20	10%	-17%	-25%	-25%
(100/30)	100	30	15%	-25%	-34%	-34%
		Predefined		Based on TGA / sum formulae		

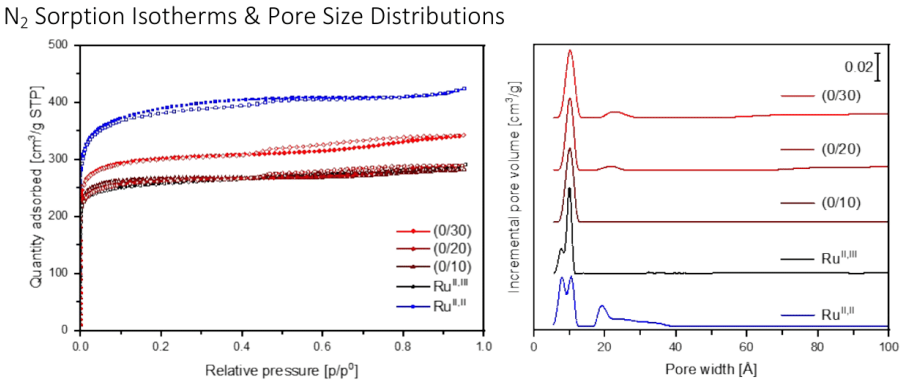

Figure S 4: Left: Nitrogen sorption isotherms of 0%Rh samples and $Ru^{II,II}$-MOF displaying both adsorption and desorption branches. Isotherms were recorded at 77K. Closed symbols represent data points from adsorption branch, open symbols represent data points from desorption branch. Hystereses indicate upcoming mesoporosity. Right: Pore size distributions of ruthenium-based samples assuming cylindrical pores on oxide surfaces.

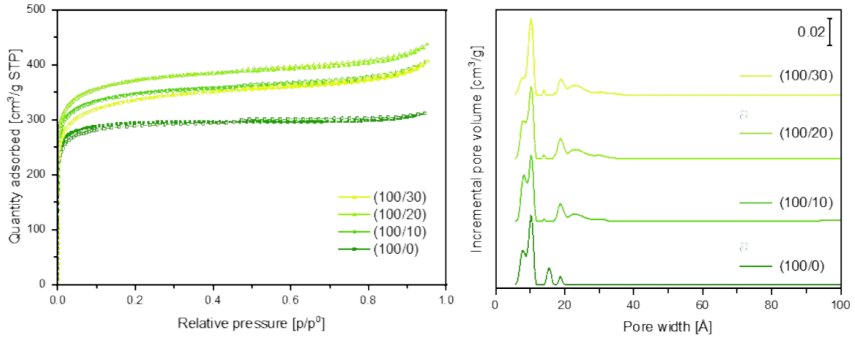

Figure S 5: Left: N_2 sorption isotherms for 100%Rh series recorded at 77K. Right: DFT-calculated pore size distributions assuming cylindrical pores on oxide surfaces. Increasing porosity emerges due to fusion of small sized micropores into larger pores.

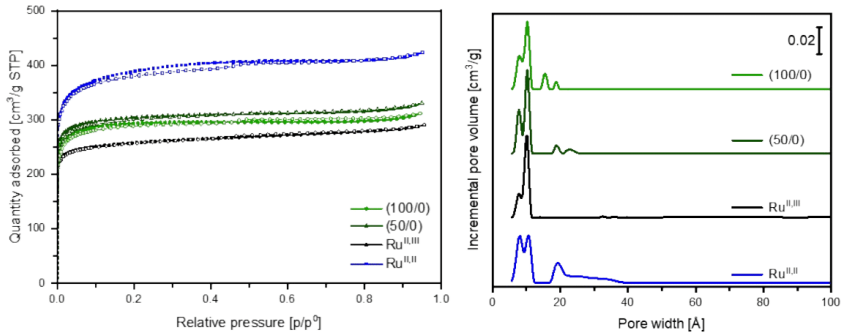

Figure S 6: Left: N_2 sorption isotherms for pristine Ru-, Rh- and bimetallic (50:50 Ru:Rh)-MOFs recorded at 77K. Right: DFT-calculated pore size distributions assuming cylindrical pores on oxide surfaces.

Thermogravimetric Analysis

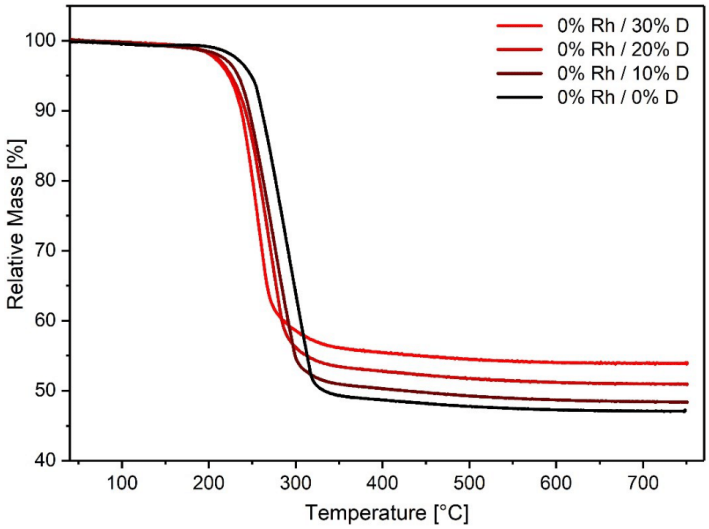

Figure S 7: TGA curves of 0%Rh samples (=Ru-MOF) with different defect amounts. Increasing metal oxide contents indicate successful TDE processes due to thermal organic constituent removal and allow for the metal content determination. Slightly decreased thermal stabilities may result from weakened structural stability of the defective frameworks.

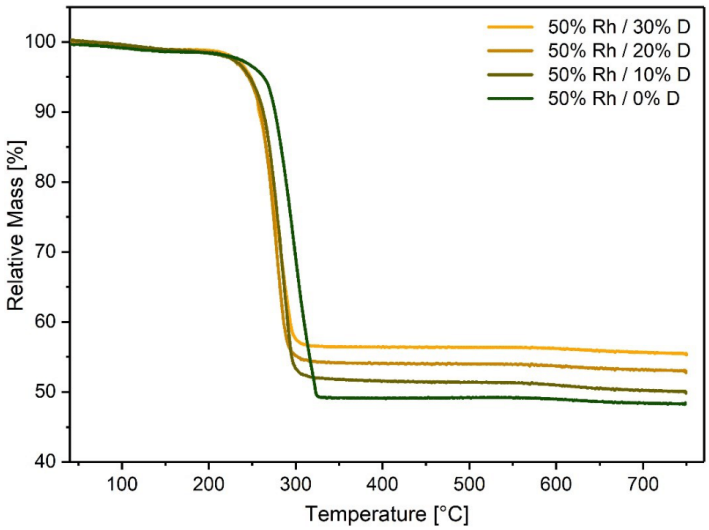

Figure S 8: TGA curves of 50%Rh samples with different defect amounts. Increasing metal oxide contents indicate successful TDE processes due to thermal organic constituent removal and allow for the metal content determinations. Slightly decreased thermal stabilities may result from weakened structural stability of the defective frameworks.

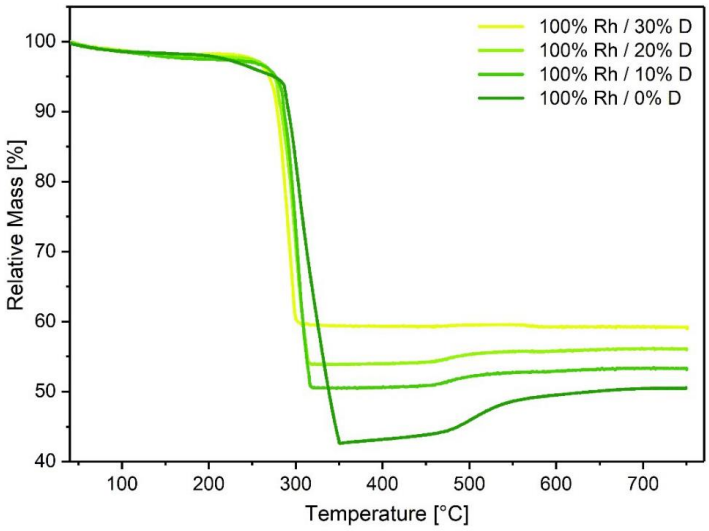

Figure S 9: TGA curves of 100%Rh samples with different defect amounts. Increasing metal oxide contents indicate successful TDE processes due to thermal organic constituent removal and allow for metal content determinations. Slightly decreased thermal stabilities may result from weakened structural stability of the defective frameworks. The weight increase at ~500°C results from reoxidation of elemental rhodium to Rh_2O_3.

FT-IR spectroscopy

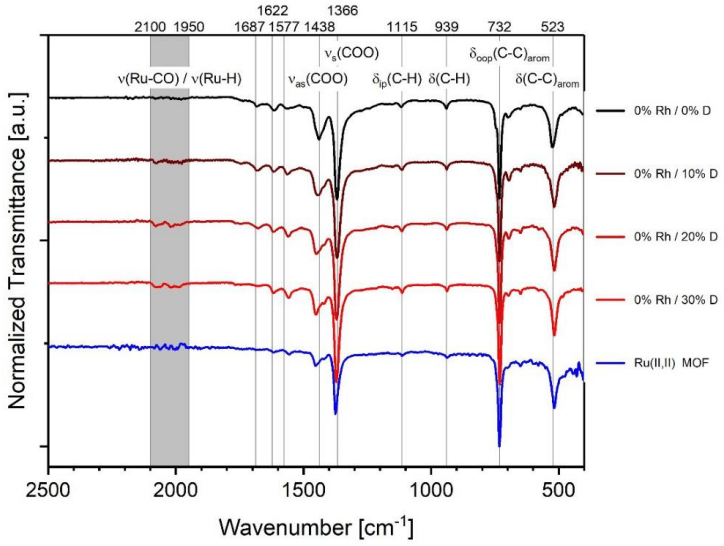

Figure S 10: Stacked FT-IR spectra of 0%Rh samples (pristine and TDE samples, $Ru^{II,II}$-BTC reference sample). Spectra reveal the formation of metal hydride and carbonyl species (1950 – 2100 cm^{-1}). A subsequent shift of ν_{as}(COO) (1438 cm^{-1}) and occurrence of a slight shoulder indicates metal reduction upon thermal defect-engineering e.g. through axial ligand removal.

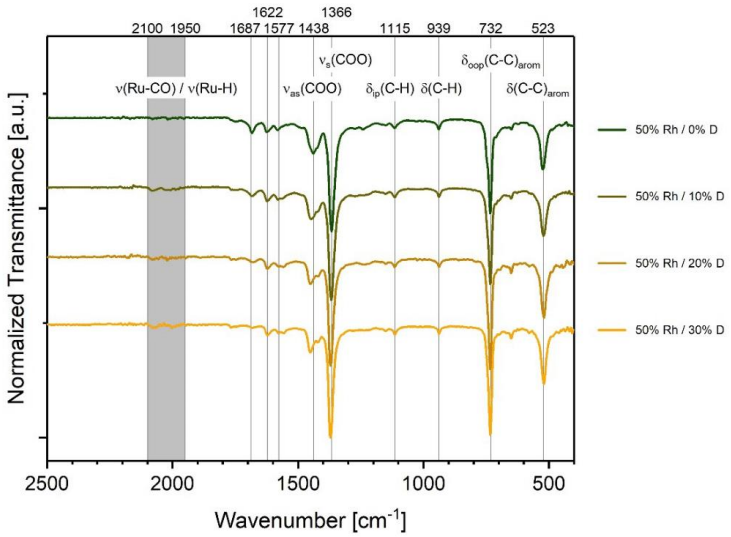

Figure S 11: Stacked FT-IR spectra of 50%Rh samples (pristine and TDE samples).

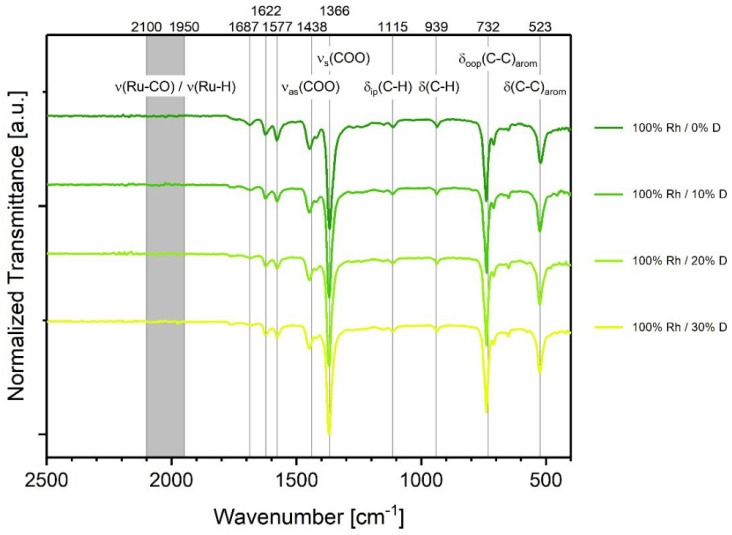

Figure S 12: Stacked FT-IR spectra of 100%Rh samples (pristine and TDE samples). Spectra do not reveal metal hydride or carbonyl formation with rhodium.

Raman Spectroscopy

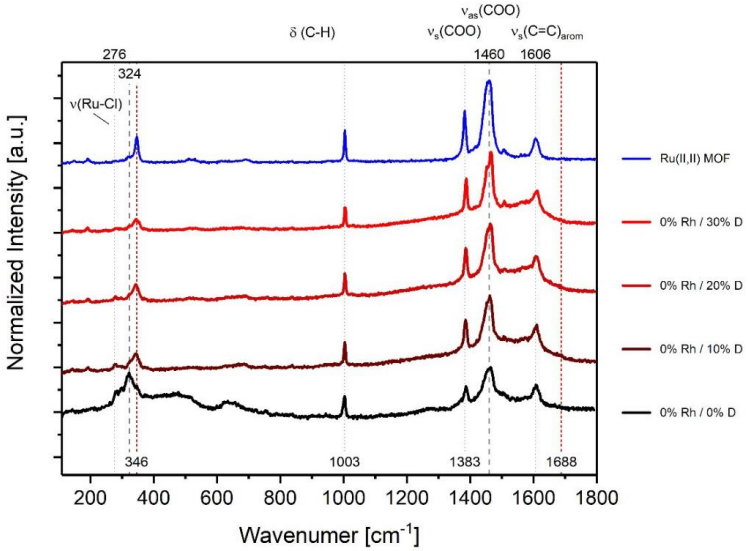

Figure S 13: Stacked Raman spectra of 0%Rh samples (pristine, TDE and $Ru^{II,II}$ reference sample). Spectra reveal slight reduction of Ru-Cl bands (276 cm^{-1}) and removal of axial Ru-OAc species (324 cm^{-1}) suggesting partial metal reduction through axial ligand removal.

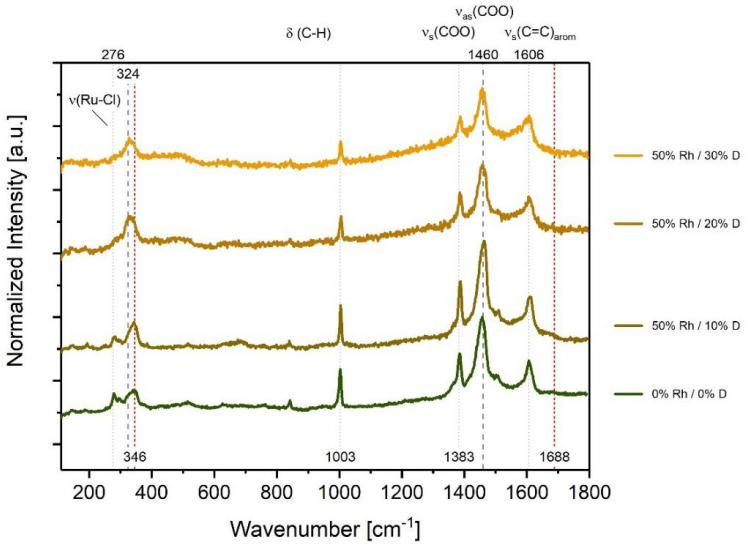

Figure S 14: Stacked Raman spectra of 50%Rh samples (pristine and TDE samples). Spectra reveal slight reduction of Ru-Cl bands (276 cm^{-1}) and removal of axial Ru-OAc species (324 cm^{-1}) suggesting partial metal reduction through axial ligand removal. Effects are considerably weaker compared with 0%Rh samples.

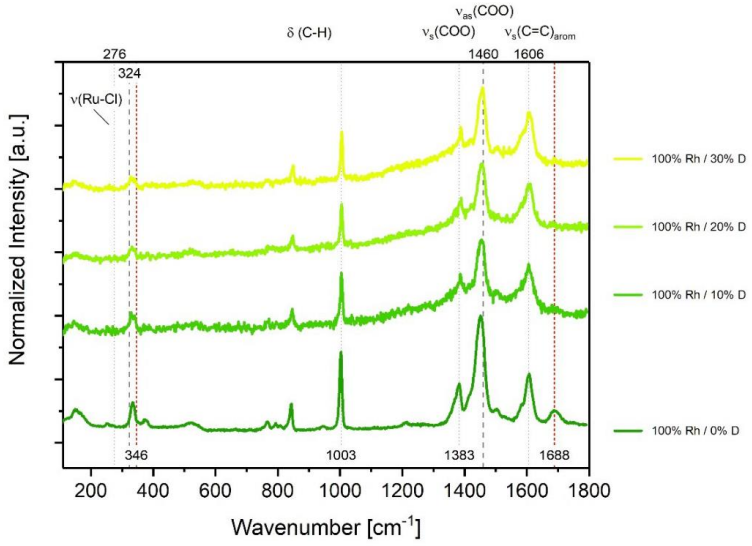

Figure S 15: Stacked Raman spectra of 100%Rh samples (pristine and TDE samples). Spectra reveal the removal of free carboxylates (1688 cm^{-1}) as well as a significant line broadening of aromatic C=C stretching modes (1606 cm^{-1}) indicating BTC decarboxylation towards isophthalate upon TDE.

TGA-Based Titration of OMS using CO

In the following, a graph summarizing the findings of the CO titration experiment using TGA is shown first. The entire, individual TGA curves are displayed then. Finally, quantitative values extracted from these experiments on the amounts of bound CO molecules per PW is shown in a table.

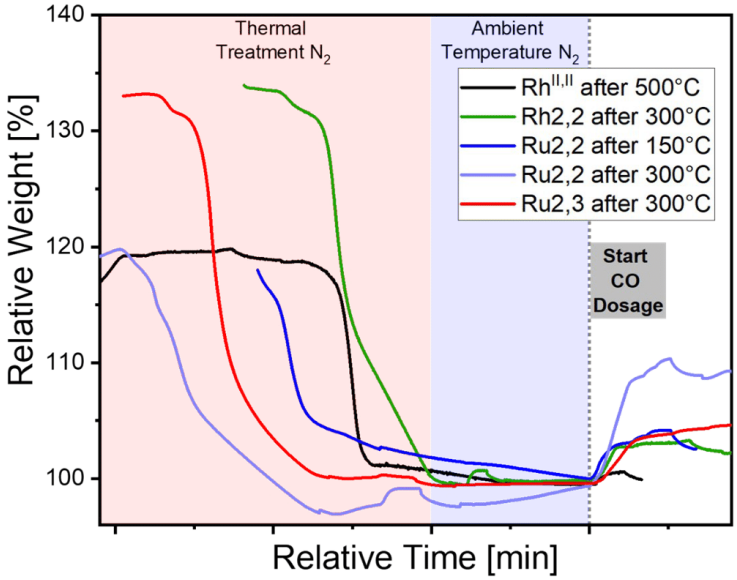

Figure S 16: TGA curves for CO-based titration experiments of selected MOF samples supporting an increased number of OMS upon thermal treatment. The investigated materials gave the following molecules CO per PW (treatment temperature in brackets): $Rh^{II,II}$ (300°C) 0.59, $Ru^{II,III}$ (300°C) 0.97, $Ru^{II,II}$ (150°C) 0.72, $Ru^{II,II}$ (300°C) 1.86. Note, the time of each experiment was adjusted to the start of CO dosage irrespective of the varying sample pretreatment. Relative weights are referenced to the start of the CO dosage as 100 wt-%.

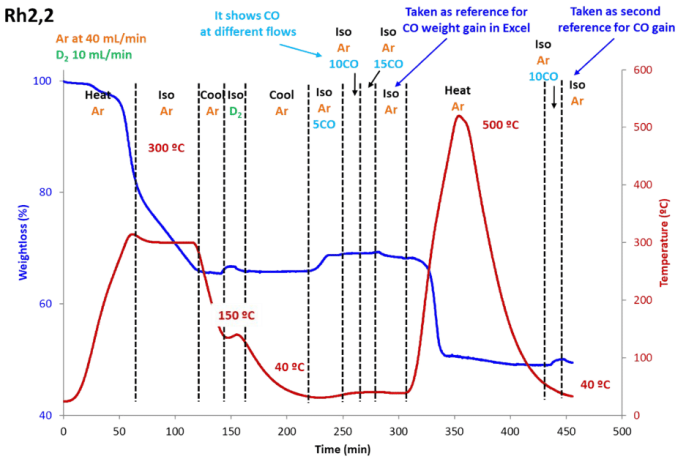

Figure S 17: TGA-based CO titration experiment with Rh-BTC treated at 300 °C. Weight curve (blue) and temperature program curve (red) with different gas streams (displayed on top). CO gas streams are given in mL/min. D_2 treatment serves for additional defect creation. The CO induced weight gain represents sorption of 0.30 molecules CO per metal atom. This refers

to roughly one CO rather strongly bound to a PW indicating the little weaker interaction of CO with Rh compared to Ru-BTC. As a reference, the sample was completely pyrolyzed at 500°C to exclusively form Rh NPs and load them with CO respectively. The then much smaller uptake of CO confirms the presence of active Rh sites after treatment at 300 °C.

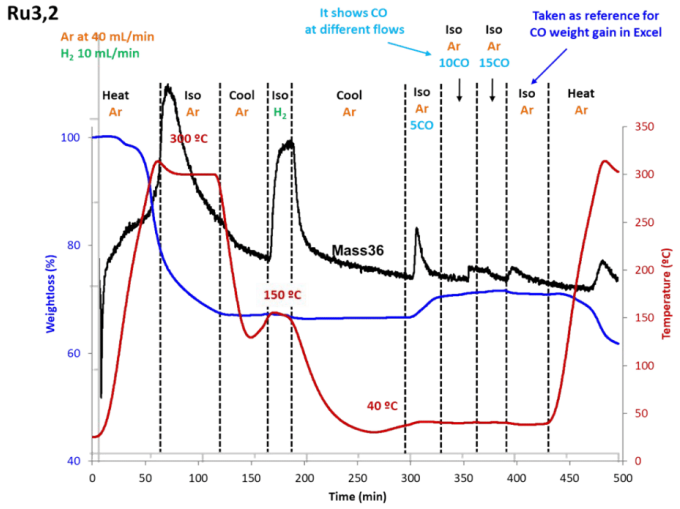

Figure S 18: TGA-based CO titration experiment with mixed-valent $Ru^{II,III}$-BTC treated at 300 °C. CO gas streams are given in mL/min. Weight curve (blue) and temperature program curve (red) with different gas streams (displayed on top). H_2 treatment serves for additional defect creation and shows the release of axial chlorides. The CO induced weight gain represents sorption of 0.48 molecules CO per metal atom. This translates to one CUS per PW.

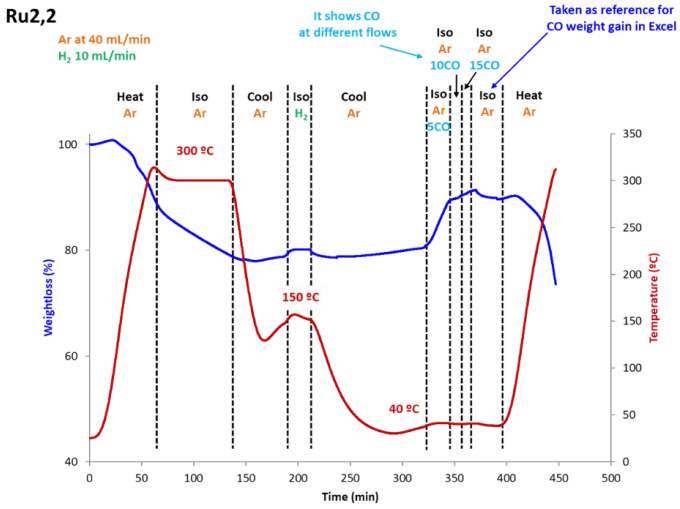

Figure S 19: TGA-based CO titration experiment with mixed-valent $Ru^{II,III}$-BTC treated at 300 °C. CO gas streams are given in mL/min. H_2 treatment serves for additional defect creation. Weight curve (blue) and temperature program curve (red) with different gas streams (displayed on top). The CO induced weight gain represents sorption of 0.93 molecules CO per metal atom. This translates to two CUS per PW.

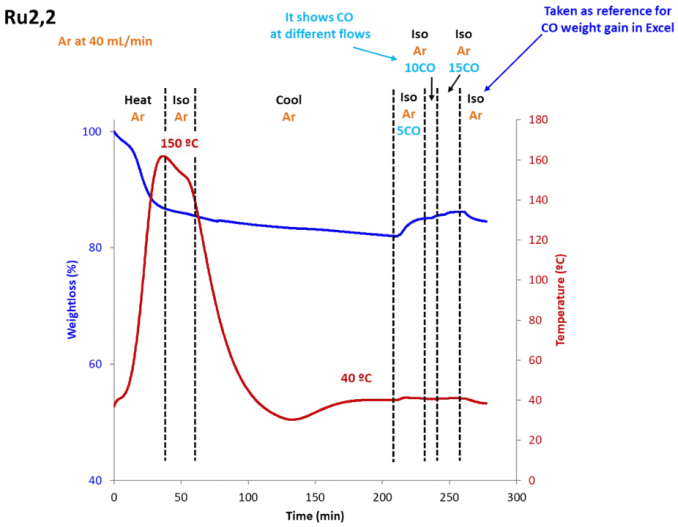

Figure S 20: TGA-based CO titration experiment with univalent $Ru^{II,II}$-BTC treated at 150 °C. CO gas streams are given in mL/min. Weight curve (blue) and temperature program curve (red) with different gas streams (displayed on top). The CO induced weight gain represents sorption of 0.36 molecules CO per metal atom. This refers to roughly one CO molecule rather strongly bound to a PW.

Table S 3: Summarized CO uptake per PW of each MOF system and respective pretreatment conditions.

MOF system	Pretreatment temperature [°C]	CO uptake per PW
$Rh^{II,II}$	300	0.59
$Ru^{II,III}$	300	0.97
$Ru^{II,II}$	300	1.86
$Ru^{II,II}$	150	0.72

Transmission Electron Microscopy

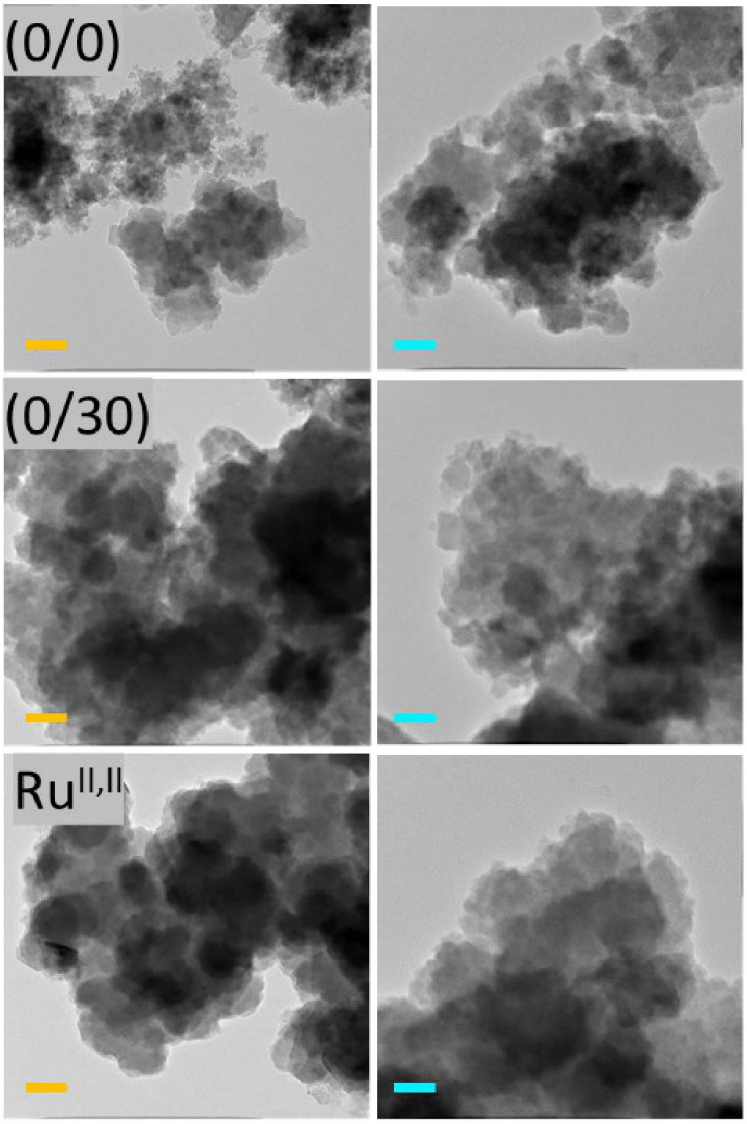

Figure S 21: HR-TEM images of ruthenium-based MOFs samples. Yellow scale bars represent 100 nm, blue ones 50 nm.

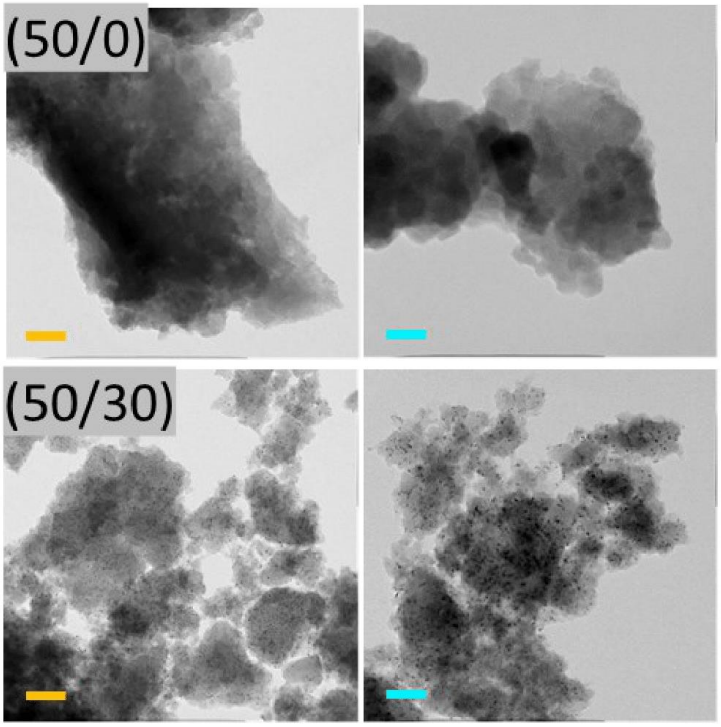

Figure S 22: HR-TEM images of 50% Rh MOFs samples. Yellow scale bars represent 100 nm, blue ones 50 nm. While pristine 50% Rh MOF sample is free of detectable NPs, upon TDE homogeneously dispersed metal NPs are observable (50/30).

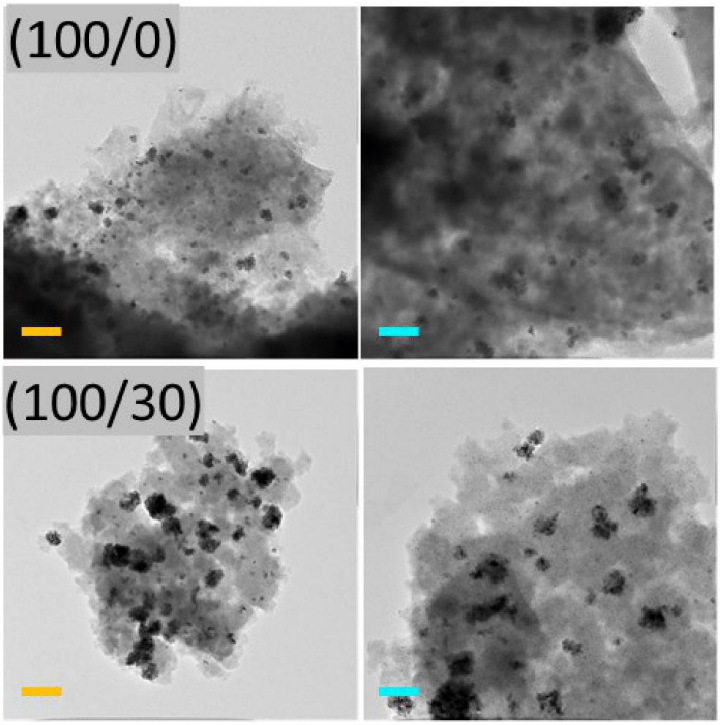

Figure S 23: HR-TEM images of 100% Rh MOFs samples. Yellow scale bars represent 100 nm, blue ones 50 nm. Presence of Rh NPs already in pristine MOFs (100/0), but increase upon TDE (100/30).

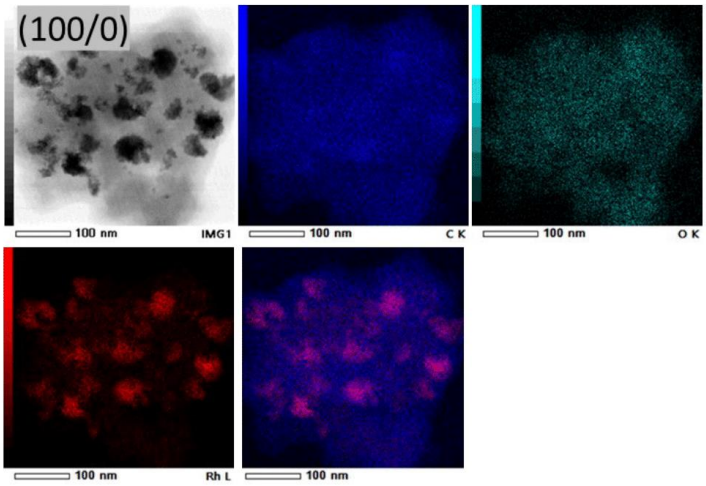

Figure S 24: Bright field STEM images of (100/0) sample and the respective EDX elemental mappings of C, O, Rh and an overlay of C&Rh (bottom middle) indicating a homogeneous MOF matrix with incorporated metal NPs.

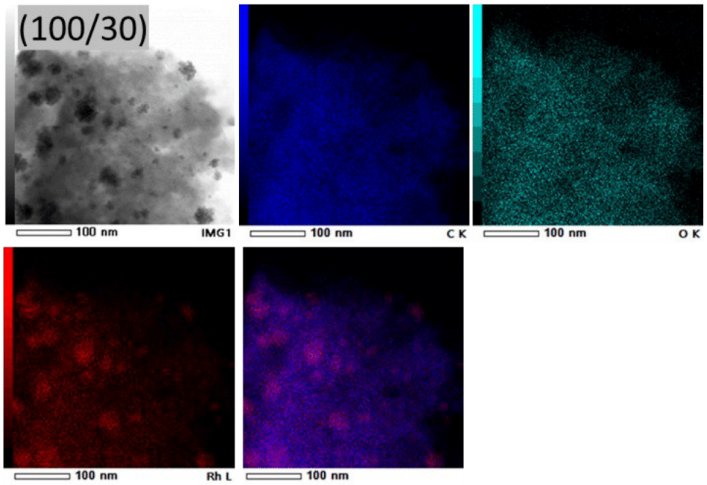

Figure S 25: Bright field STEM images of (100/30) sample and the respective EDX elemental mappings of C, O, Rh and an overlay of C&Rh (bottom middle) indicating a homogeneous MOF matrix with incorporated metal NPs.

Additional Information – Cyclopropanation Catalysis

Mechanistic Aspects relevant for this Study

This paragraph should provide the interested reader with additional background knowledge on the mechanisms and important parameters of the cyclopropanation reaction as briefly mentioned in the introduction of the main manuscript.

It is general knowledge that transition metal carbenoids play an important role as active species or intermediates in many catalytic reactions, such as olefin metathesis, O-H, N-H and C-H bond activation just to name a few.[3, 4] For PW complexes, the CP is probably the most investigated reaction. Almost any imaginary combination (both inter- and intramolecularly) of Rh-PW catalyst, diazo compound, and olefin was screened to achieve deeper mechanistic comprehension of important parameters.[5]

The first, rate-determining step (r.d.s.) of transition metal-catalyzed CP is the denitrification of diazo compounds and formation of a metal-carbene, which then transfers the carbene to the olefin in an outer-sphere fashion, which is fast, since the carbenes are highly reactive. For the r.d.s. and the catalytic activity, respectively, the availability of open metal sites (OMS) is thus most decisive. For styrene and EDA as reactants, the nature of the equatorial PW ligands was found to guide the diastereoselectivity. While strongly binding electron-rich carboxylates or carbamates at the PW give 64-68% *trans* selectivity, electron-poor fluorinated carboxylates lack any preference with 50% *trans* selectivity.[6] Labile ligands temporarily dissociate yielding defective PWs. At those defective or modified PWs, more trajectories for styrene to approach the carbene are possible obstructing higher diastereoselectivities.[4, 6] In contrast, the steric demand of the carboxylates (like acetate, pivalate or benzoate) has only minor impact on diastereoselectivities since the PW-inherent square planar geometry spanned by the metal atom and its four adjacent O ligator atoms governs the diastereomeric preference and more distant side groups perpendicular to the axially bound carbene do not play a decisive role. Unwanted side-products resulting from homocoupling of two carbenes or from C–H activation are known to occur.[3] Homocoupling is usually suppressed by process control *via* slow addition of a diluted EDA solution over time and the excessive use of olefin.[7] Other side products can emerge from C-H activation of styrene.[3] Such a carbene-transfer results in linear allyl species which are further denoted as linear products. Other, non-PW complexes are known to produce cyclopropanes and linear products in different ratios.[8, 9] In contrast to the CP formation, these linear products could emerge via metallacyclobutane intermediates requiring additional OMS at the metal centre.[3, 9] From this fact, we conclude that their formation (which is not observed in perfect PW systems like $Rh_2(OAc)_4$ or $Cu_3(BTC)_2$) is indicative for the presence of modified PWs in PGM-MOFs as presented earlier by several other analytical techniques.[10]

Additional Catalysis Data

*Table S 4: Summary of catalysis data of all samples. Initial turnover frequencies (TOFs) are given in h^{-1} and are calculated as outlined above using 1.3 mol-% catalyst loading with respect to the total metal content and EDA. Chemoselectivities refer to conversions after 24 h. The given diastereoselectivity (DS) in % refers to the trans-cyclopropane. *The $Rh_2(OAc)_4$ sample reached quantitative conversion already at the first measurement upon complete EDA addition. Thus, the TOF is experimentally limited to this value. **In contrast to all other MOF samples, the Ru and Rh NPs differed significantly in their 24h selectivity values compared to earlier data points. To avoid misinterpretation, both values are presented: 24 h values as similar to the other samples, 4 h values are marked with **.*

Sample	TOF [h^{-1}]	Chemoselectivity of			DS of *trans*-CP [%]
		CPs [%]	Homo-coupling [%]	Linear products [%]	
(0/0)	49.9	68.7	29.3	2.0	56
(0/10)	64.2	70.3	27.6	2.0	54.4
(0/20)	83.8	77.4	20.9	1.8	55.2
(0/30)	92.3	81.0	17.0	2.0	55.4
$Ru^{II,II}$-MOF	110.3	83.4	14.3	2.3	53.6
(50/0)	112	82.8	2.1	15.1	51.4
(50/10)	107.2	83.5	1.9	14.6	50.9
(50/20)	108.2	83.4	1.7	14.8	49.5
(50/30)	113.7	82.8	1.7	15.5	48
(100/0)	88	81.5	0.7	17.7	51
(100/10)	78	82.5	1.7	15.8	49.3
(100/20)	93.6	82.5	1.3	16.2	48.7
(100/30)	92.3	81.4	0	18.6	48.9
Cu-HKUST-1	18.2	83.7	16.3	0	65
$Rh_2(OAc)_4$	145*	100	0	0	64.2
Ru NPs	11.3	83.6	16.4	0	61.8
Ru NPs**	11.3	69.4	30.6	0	60.1
Rh NPs	8.7	78.5	16.6	4.8	61.8
Rh NPs**	8.7	68.9	31.1	0	61.2

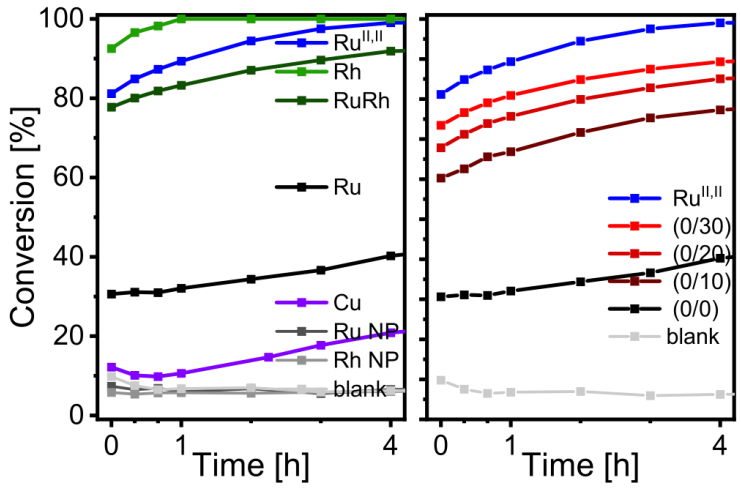

Figure S 26: Early activity in the cyclopropanation reaction of styrene with EDA. Left: Time conversion plots comparing different pristine HKUST-1 analogues of Cu (purple), Ru (mixed-valent (black) and univalent (blue)) and Rh (green) and respective NPs (grey) as catalysts. Right: Activity comparison of different ruthenium-based MOFs: The moderate activity of the mixed-valent $Ru^{II,III}$-MOF (0/0) is strongly enhanced by TDE (0/10→30) (brown to red curves). This Figure contains the data from Figure 3 in the main text but highlights the evolution of conversion for the initial period. Sampling was repeated every 20 min within the first hour, and then on an hourly interval.

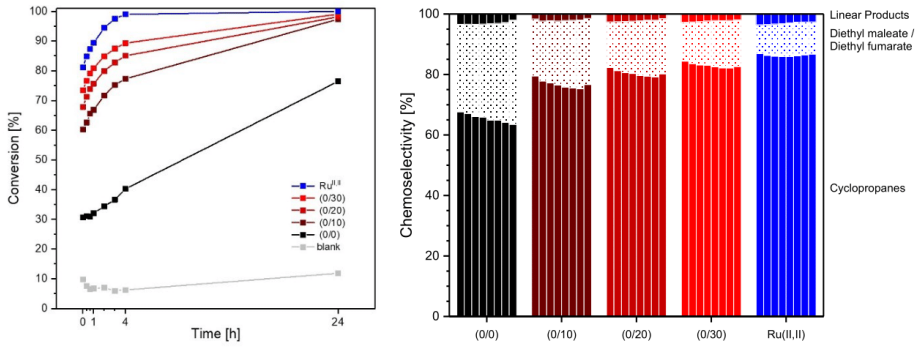

Figure S 27: Left: Time-Conversion plots for Ru-MOF samples (each 5 mg) and the blank reaction. The beneficial effect of TDE on Ru-MOF is clearly to be seen. $Ru^{II,II}$-MOF exhibits the highest activity. Right: Stacked chemoselectivities for each data point within the series of Ru-MOFs. Each group represents the development during the reaction. The top fraction is for linear products, the middle for the homocoupling products, the bottom and main fraction are the cyclopropanes. A clear improvement of the selectivity towards CP products can be extracted. Homocoupling products represent the main side products. As TDE accounts for a successive removal of mostly axial ligands, their presence might account for the homocoupling side reaction.

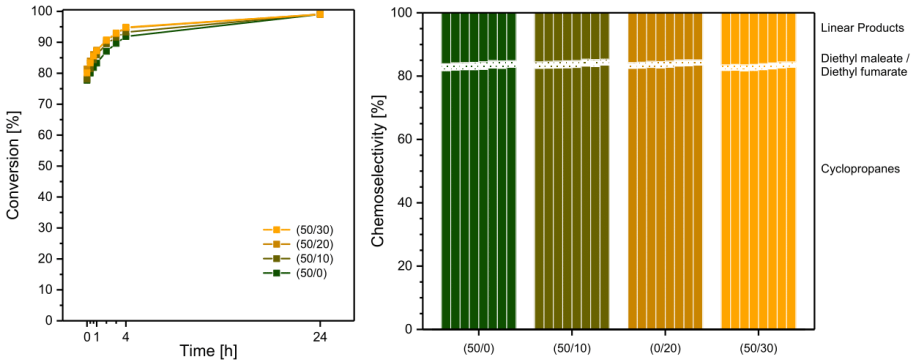

Figure S 28: Left: Time-Conversion plots for mixed-metallic RuRh-MOF samples (each 5 mg). Almost identical activity can be seen irrespective of the TDE. However, The (50/30) sample exhibits the highest activity. Right: Stacked chemoselectivities for each data point within the series of RuRh-MOFs. Each group represents the development during the reaction. The top fraction is for linear products, the middle for the homocoupling products, the bottom and main fraction are the cyclopropanes. Linear propene species account for the main side products from RuRh-MOF catalysis. The product distribution seems unaffected by TDE.

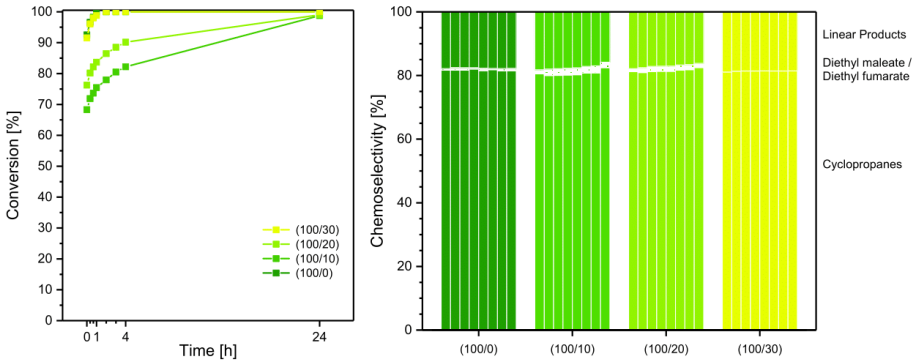

Figure S 29: Left: Time-Conversion plots for Rh-MOF samples (each 5 mg). A first activity drop for the (100/10) sample is visible with again rising activity for (100/20) and (100/30) samples. The (100/30) sample exhibits comparable activity as the pristine Rh-MOF. Right: Stacked chemoselectivities for each data point within the series of Rh-MOFs. Each group represents the development during the reaction. The top fraction is for linear products, the middle for the homocoupling products, the bottom and main fraction are the cyclopropanes. Linear propene species account for the main side products from RuRh-MOF catalysis. The product distribution seems unaffected by TDE.

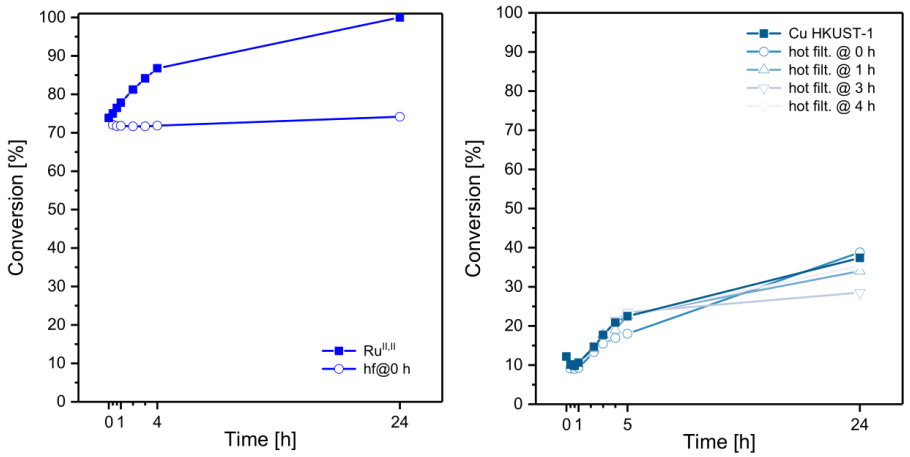

Figure S 30: Hot filtration experiments indicating the differences between $Ru^{II,II}$-MOF sample representing the precious-metal analogues of the parent Cu-HKUST-1 (depicted on the right). Cu-HKUST-1 exhibits significantly lower performance which can even be attributed to leaching species into the solutions as hot filtration tests performed after different reaction times clearly indicate. The Ru-MOF does not exhibit leaching. For both graphs, equal metal loadings of 1.3 mol-% were applied to allow comparable data.

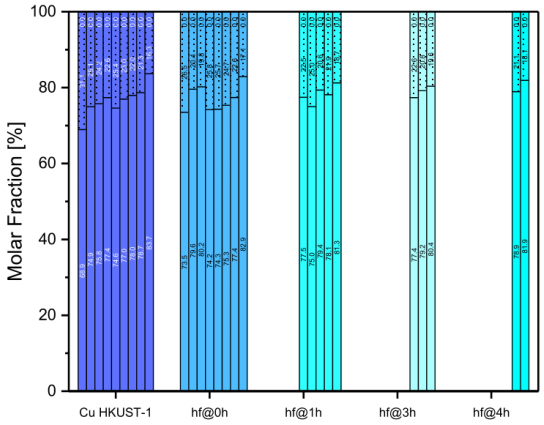

Figure S 31: Chemoselectivty of Cu-HKUST-1 and the respective hot filtration experiments with respect to the time-conversion plots of the right graph in Figure S 30.

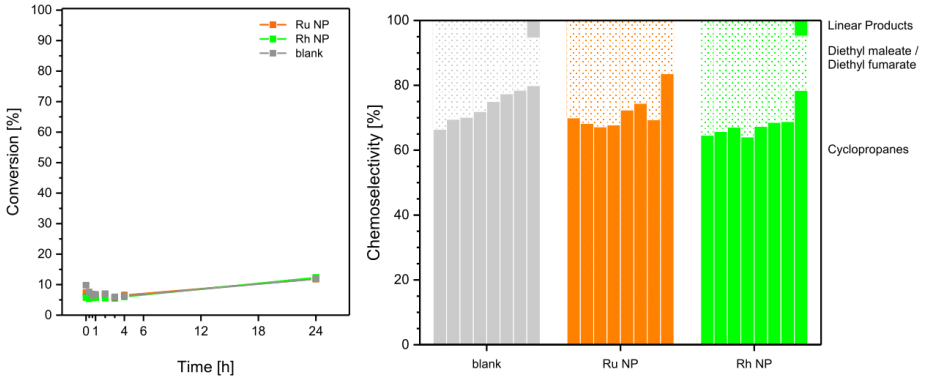

Figure S 32: Left: Time-conversion plots for metal nanoparticles and the blank reaction indicating the particles inactivity. Right: Chemoselectivity of blank and NPs in the course of the reaction indicating mostly the homocoupling as side reaction.

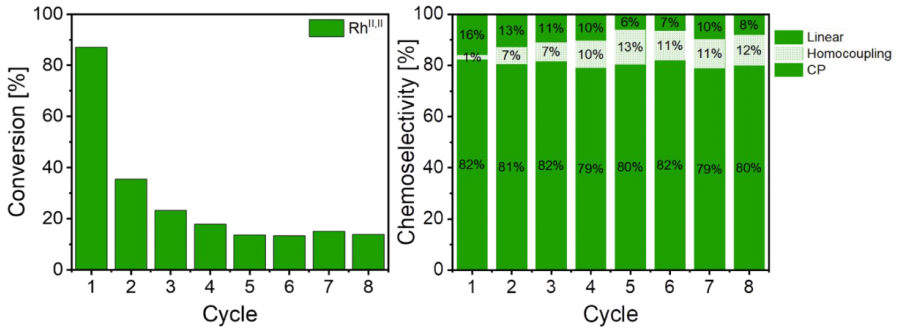

Figure S 33: Recycling of pristine Rh-MOF sample: Cycle dependent evolution of activity (left) and chemoselectivity (right). The data indicates reduced catalytic activity presumably due to pore blocking phenomena or competing adsorption of polar reaction products on OMS while the chemoselectivity of the catalyst remains mostly unaffected. Reduced linear product formation presumably due to regeneration of perfect PWs from modified PWs.

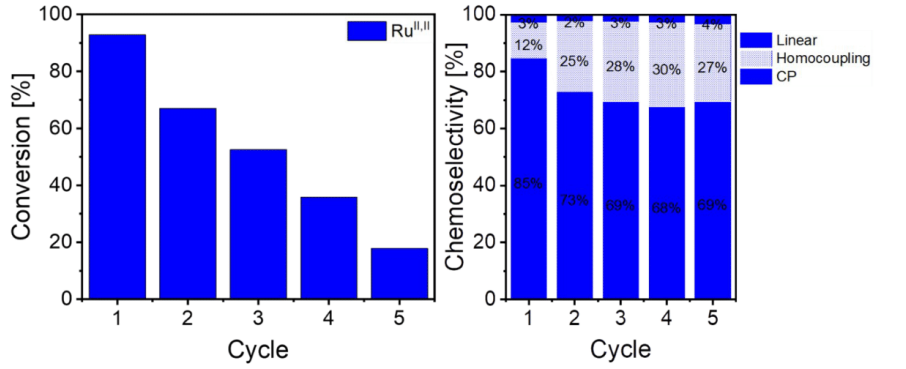

Figure S 34: Recycling of pristine Ru^{II,II}-MOF sample: Cycle dependent evolution of activity (left) and chemoselectivity (right). The data indicates reduced catalytic activity with cycling which can presumably be attributed to pore blocking phenomena or competing adsorption of polar reaction products on OMS. In contrast to Rh-BTC, the evolution of the chemoselectivity with

cycling indicates oxidation towards $Ru^{II,III}$ PWs displaying the reversed process of TDE. Thus the reduced activity also stems from oxidation and its concomitant reduction of OMS.

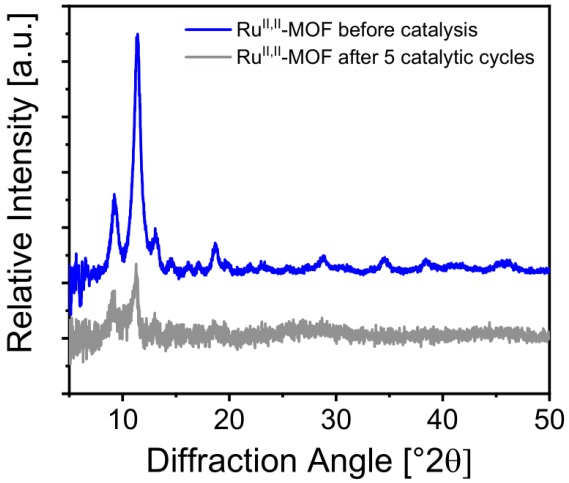

Figure S 35: PXRD pattern of univalent $Ru^{II,II}$-MOF sample before and after catalysis indicating mostly preserved structural order. The low signal intensity and high level of noise is assigned to the very low sample amount available after catalysis.

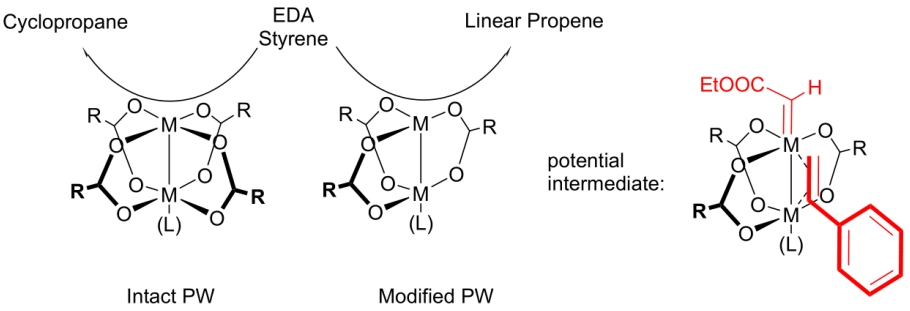

Scheme S 3: Proposed intermediate for the formation of linear propene species observed in rhodium catalysed reactions. The formation presumably takes place on defective PWs offering two coordination sites.

1. R. W. Mitchell, A. Spencer and G. Wilkinson, *J. Chem. Soc., Dalton Trans.*, 1973, DOI: 10.1039/DT9730000846, 846-854.
2. W. R. Heinz, T. Kratky, M. Drees, A. Wimmer, O. Tomanec, S. Günther, M. Schuster and R. A. Fischer, *Dalton Trans.*, 2019, **48**, 12031-12039.
3. M. P. Doyle and D. Ren, in *Prog. Inorg. Chem.*, 2007, DOI: 10.1002/9780470166512.ch2, pp. 113-168.
4. M. P. Doyle, *J. Org. Chem.*, 2006, **71**, 9253-9260.
5. M. Brookhart and W. B. Studabaker, *Chem. Rev.*, 1987, **87**, 411-432; A. Padwa, D. J. Austin, S. F. Hornbuckle, M. A. Semones, M. P. Doyle and M. N. Protopopova, *J. Am. Chem. Soc.*, 1992, **114**, 1874-1876; M. P. Doyle, L. J. Westrum, W. N. E. Wolthuis, M. M. See, W. P. Boone, V. Bagheri and M. M. Pearson, *J. Am. Chem. Soc.*, 1993, **115**, 958-964; M. P. Doyle and D. C. Forbes, *Chem. Rev.*, 1998, **98**, 911-936.
6. A. J. Anciaux, A. J. Hubert, A. F. Noels, N. Petiniot and P. Teyssie, *J. Org. Chem.*, 1980, **45**, 695-702.
7. K. Epp, B. Bueken, B. Hofmann, M. Cokoja, K. Hemmer, D. E. De Vos and R. A. Fischer, *Catal. Sci. Technol.*, 2019, **9**, 6452-6459.
8. G. Maas, *Chem. Soc. Rev.*, 2004, **33**, 183-190; F. A. Cotton, K. R. Dunbar and M. G. Verbruggen, *J. Am. Chem. Soc.*, 1987, **109**, 5498-5506; F. Simal, A. Demonceau, A. F. Noels, D. R. T. Knowles, S. O'Leary, P. M. Maitlis and O. Gusev, *J. Organomet. Chem.*, 1998, **558**, 163-170.
9. A. F. Noels and A. Demonceau, *J. Phys. Org. Chem.*, 1998, **11**, 602-609.
10. W. R. Heinz, I. Aguirrezabal-Telleria, R. Junk, J. Berger, J. Wang, D. I. Sharapa, M. Gil-Calvo, I. Luz, M. Soukri, F. Studt, Y. Wang, C. Wöll, H. Bunzen, M. Drees and R. A. Fischer, *ACS Appl. Mater. Interfaces*, 2020, DOI: 10.1021/acsami.0c10721.

ESI Study V

Supporting Information

Scrutinizing Ligand Exchange Reactions in the Formation of the Precious Group Metal-Organic Framework $Ru^{II,II}$-HKUST-1: The Impact of Diruthenium Tetracarboxylate Precursor and Modulator Choice

Werner R. Heinz,[a] Dominik Staude,[a] David Mayer,[a] Hana Bunzen,[b] and Roland A. Fischer[a,*]

[a] Chair of Inorganic and Metal-Organic Chemistry, Department of Chemistry, Technical University of Munich, Lichtenbergstraße 4, 85748 Garching, Germany. E-mail: roland.fischer@tum.de

[b] Chair of Solid State and Materials Chemistry, Institute of Physics, University of Augsburg, Universitätsstraße 1, 86159 Augsburg, Germany. E-mail: hana.bunzen@physik.uni-augsburg.de

Table of Contents

Experimental Details

General considerations

Trimesic acid (Sigma-Aldrich), $RuCl_3 \cdot x\ H_2O$ (Precious Metals Online) and HPLC-grade acetone and ethanol (VWR Chemicals) were purchased commercially and used without further purification. Substituted benzoic acid derivatives were purchased from Sigma-Aldrich (analytical grade) and used without further purification. 4-Methyl benzoic acid sodium salt was prepared by neutralization of the acid in aqueous NaOH and subsequent solvent removal. Ultra-pure water was obtained using a Milli-Q purification system (18.2 MΩ cm^{-1}). Dichloromethane, diethyl ether and tetrahydrofurane were purified and dried using a MBraun SPS-800 and additionally degassed and stored under argon atmosphere. All complexes and MOFs were synthesized under exclusion from air and handled in a using argon-filled (>99.996%; Westfalen) glovebox.

Instrumentation

Gloveboxes

MOF synthesis including degassed solvent and water were performed in an MBraun 500 glovebox operated under wet conditions in argon atmosphere. Activated MOF samples were stored and handled in another glovebox under dry Ar atmosphere conditions.

Powder X-Ray diffraction

All diffraction patterns were collected on a PANalytical Empyrean equipped with a Cu X-ray tube (λ = 0.154 nm) operated at 45 kV and 40 mA in a 2Θ range of 5-50° in steps of 0.0065651° (2Θ) with 0.175 s/step. The incident beam was focussed on the sample through a focusing beam mirror with a 1/8° divergence slit and a nickel beta filter (0.2 mm). A PIXcel1D detector was used in receiving mode with a 1/8° anti-scatter slit and 0.04 rad soller slits. The activated MOF samples and dried precursor adducts were filled in borosilicate capillaries of 0.5 mm inner diameter and mounted onto a capillary spinner. Free carboxylic acid reference spectra were measured with reflection-transmission-spinner (RTS) mode.

Single crystal X-Ray diffraction

Single crystal structures of related precursor complexes were either measured on a Bruker D8 Venture diffractometer equipped with a Helios optic monochromator, a Photon 100 CMOS detector and a Mo IMS microsource (λ = 0.71073 Å), or on a Bruker D8 Venture diffractometer equipped with a Helios optic monochromator, a Photon 100 CMOS detector and a Mo rotating anode source (λ = 0.71073 Å), at 100(2) K. The raw area detector data frames were reduced and corrected for absorption effects using the SAINT and SADABS programs with multi-scan absorption correction. Final unit cell parameters were determined by least-squares refinement of the respective independent reflections taken from the data sets. The structures were solved by intrinsic phasing with SHELXT. Difference Fourier calculations and full-matrix least-squares refinements against F^2 were performed by SHELXL-2014/7 (Sheldrick, 2014). All non-hydrogen atoms were refined with anisotropic displacement parameters. Hydrogen atoms throughout could not be located in the Fourier maps and were calculated in ideal positions using a riding model (d(C-H) = 0.95 Å, $U_{ISO}(H) = U_{EQ}(C)$). Disordered solvent molecules, which could not properly be refined were treated as diffuse contribution to the overall scattering without specific positions using the Squeeze routine in Platon. Single crystals were directly taken from the reaction solution and fixed on microsampler using perfluorated ether under an Ar counterflow. Crystal structure graphics were created using Mercury software.

Elemental Analysis

Determination of the elemental composition was performed together with the microanalytical laboratories of the chemistry department at the Technical University of Munich. Determination of C, H, N and S was carried out with a Hekatech EuroEA elemental analyser with samples of 1-3 mg. Samples were decomposed at T >1000 °C in oxygen atmosphere and decomposition gases purified and separated through a GC column. Detection and quantification of CO_2, H_2O, NO_2 and SO_2 allowed to derive elemental contents. Metal contents were derived from TGA-based metal oxide residues as reported earlier.[1] Low sample amounts obstructed the analysis of F contents in OBz-F and OBz-CF_3 samples.

Gas sorption measurements

Sorption experiments were conducted using a *Micromeritics 3Flex* with each ~50 mg of desolvated sample. Prior to the measurement each sample was additionally degassed at 150°C for >10h. Nitrogen isotherms were recorded at 77 K. The BET surface area was calculated using data points in the relative pressure range of 0.01 to 0.1 in the adsorption branch with the *Rouquerol* consistency criteria considered.

Fourier-transform infrared spectroscopy

FT-IR spectra were recorded from finely ground activated powder samples under argon atmosphere in a glovebox using a *Bruker ALPHA* FTIR spectrometer equipped with a Pt attenuated total reflectance (ATR) unit at room temperature in the range of 400 to 4000 cm^{-1} with a resolution of 2 cm^{-1} and 24 scans per measurement. A pyroelectric deuterated L-alanine doped triglycine sulfate (RT-DLaTGS) detector was used.

Raman spectroscopy

Raman spectroscopy was measured with an inVia Reflex Raman System with an optical microscope (Leica DM2700M, 50x magnification) coupled to a *Renishaw R04* Raman spectrometer with 532 nm laser wavelength (Laser: RL532C, Class 3B) with activated samples filled into Borosilicate glass capillaries (0.5 mm inner diameter) under argon atmosphere. A Renishaw 266n10 detector was used. All samples were measured with 10 s exposure time, 1 % laser power and 10 accumulations.

NMR spectroscopy

Standard liquid ^{1}H-NMR spectra were recorded with a *Bruker AV400US* at 400 MHz at 298 K. Kinetic measurements and ^{19}F-NMR were measured using a *Bruker DRX400* (400 MHz) with implemented heating module at 298 K unless otherwise stated. Sensitive samples were prepared using degassed deuterated solvents. MestreNova was used for data analysis applying manual phase correction and automated baseline correction (Whittaker Smoother). Chemical shifts are given in parts per million (ppm) and calibrated to the residual proton signal of the deuterated solvent. Multiplicity is given as s – singlet as paramagnetic ruthenium accounts for significant line broadening.

LIFDI mass spectrometry

Liquid injection field desorption ionization mass spectrometry was measured on a *Waters LCT Micromass* TOF MS with additional LIFDI module using a current of 80 mA for sample evaporation. Prior to measurements, dissolved samples were filtered through 0.2 µm syringe filter (PTFE). Instrument control and data analysis was performed using *MassLynx NT* software package.

Thermogravimetric analysis

Thermal analysis of the materials was determined with a Mettler Toledo TGA/DSC 3+ in aluminium oxide crucibles (70 µL with lid) with sample amounts of 1 to 5 mg. Samples of activated materials were taken under inert conditions in a glovebox and transferred to the measurement chamber in screw capped vials immediately prior to the measurement. The following thermal program was applied using

synthetic air (20 mL min^{-1}, Westfalen, 80% N_2; 20% O_2): At 30 °C isothermal equilibration (15 min), ramp from 30 °C to 700 °C with 10 K min^{-1}, at 700 °C isothermal equilibration (15 min).

High-resolution transmission electron microscopy

TEM and STEM micrographs and EDS elemental mappings were recorded with a JEM NEOARM microscope (JEOL) with a cold FEG electron source operated at 200 kV. Samples were prepared by depositing a drop of the crystalline products dispersed in ethanol onto carbon-coated copper grids (200 mesh) and dried in air.

Synthesis of Precursor Complexes

All syntheses were performed under exclusion from air and with degassed solvents and solutions. The obtained powders crystallize as adducts coordinating two solvent molecules (THF or acetone) on the axial positions of the PW. XRD measurements were performed with these adducts, while all other characterizations (yield, NMR, IR, EA) were performed with the amorphized desolvated complexes after thermal activation at 80 °C for 12 h. Reaction yields of isolated complexes refer to $RuCl_3$ assumed as dihydrate.

General Procedure via the “blue solutions of ruthenium (II)

Acetate and benzoate precursor complexes were synthesized according to literature procedures via the “blue solutions” of Ru^{2+} with slight modifications.[2] The blue solutions were prepared in a *Fisher Porter* bottle using carefully degassed dispersions of $RuCl_3 \cdot x\ H_2O$ (1-3 g, 1.0 eq.) and PtO_2 (17.9 mg) in MeOH (10-30 mL). The black mixtures were stirred for 3 h under hydrogen atmosphere (3 bar). The resulting deep blue solution was filtered through a Schlenk frit into a solution of the respective carboxylic acid alkali metal salt (2.5-2.8 eq for sodium benzoates, 5.8 eq for lithium acetate) in MeOH (10-30 mL). The whole mixture was heated to reflux for 24 h. Workup of the $Ru_2(OAc)_4$ was performed by removal of the supernatant by *Whatman* filtration and successive drying of the formed microcrystalline powder in argon stream. Workup of methyl benzoate and methoxy benzoate complexes was achieved by an additional washing step of the precipitate with hot MeOH. All other diruthenium tetrabenzoate complexes were isolated by removal of the solvent in vacuo and subsequent extraction with hot acetone, concentration of the extract, and crystallisation at -32 °C.

Additional Information – Precursor Characterization

Diruthenium tetraacetate

$Ru_2(OAc)_4$ was synthesized according to above-mentioned modified literature procedure.[2] Yield: 43 % of a brown powder. ^{1}H-NMR: (400 MHz, THF-d^8, 298 K): δ [ppm] = 1.09 (s, 12H, CH_3); EA: (calc / found %): C (21.9/21.3), H (2.76/2.68); LIFDI-MS (THF): (calc/found) m/z = (438.32/438.68).

Diruthenium tetrabenzoate

$Ru_2(OBz)_4$ was synthesized according to above-mentioned modified literature procedure.[2] Yield: 17 % of a brown powder. ^{1}H-NMR: (400 MHz, THF-d^8, 298 K): δ [ppm] = 16.50 (s, 8H, *ortho*-H), 10.71 (s, 4H, *para*-H), 9.26 (s, 8H, *meta*-H); EA: (calc / found %): C (49.0/49.0), H (2.94/3.00); LIFDI-MS (THF): (calc/found) m/z = (686.6/687.1).

Diruthenium tetra (4-fluoro benzoate)

$Ru_2(OBz\text{-}F)_4$ was synthesized according to above-mentioned modified literature procedure.[2] Yield: 40 % of a dark brown powder. ^{1}H-NMR: (400 MHz, THF-d^8, 298 K): δ [ppm] = 16.47 (s, 8H, *ortho*-H), 9.00 (s, 8H, *meta*-H); EA: (calc / found %): C (44.3/43.5), H (2.13/2.15); LIFDI-MS (THF): (calc/found) m/z = (758.6/759.6).

Diruthenium tetrakis (4-trifluoromethyl benzoate)

$Ru_2(OBz\text{-}CF_3)_4$ was synthesized according to above-mentioned modified literature procedure.[2] Yield: 18 % of an orange powder. ^{1}H-NMR: (400 MHz, THF-d^8, 298 K): δ [ppm] = 16.63 (s, 8H, *ortho*-H), 9.64 (s, 8H, *meta*-H); EA: (calc / found %): C (40.1/39.9), H (1.68/1.64); LIFDI-MS (THF): (calc/found) m/z = (958.6/959.9).

Diruthenium tetra (4-methyl benzoate)

$Ru_2(OBz\text{-}Me)_4$ was synthesized according to above-mentioned modified literature procedure.[2] Yield: 47 % of a light brown powder. ^{1}H-NMR: (400 MHz, THF-d^8, 298 K): δ [ppm] = 16.45 (s, 8H, *ortho*-H), 9.20 (s, 8H, *meta*-H) 2.96 (s, 12H, CH_3); EA: (calc / found %): C (51.8/50.0), H (3.80/3.76); LIFDI-MS (THF): (calc/found) m/z = (742.7/743.1).

Diruthenium tetra (4-methoxy benzoate)

$Ru_2(OBz\text{-}OMe)_4$ was synthesized adopting the above-mentioned procedure. Yield: 34 % of a brown powder. ^{1}H-NMR: (400 MHz, THF-d^8, 298 K): δ [ppm] = 16.66 (s, 8H, *ortho*-H), 8.75 (s, 8H, *meta*-H) 4.79 (s, 12H, OCH_3); EA: (calc / found %): C (47.6/45.4), H (3.50/3.32).

Diruthenium tetrakis (3,5-dimethoxy benzoate)

$Ru_2(OBz\text{-}(OMe)_2)_4$ was synthesized by adopting the above-mentioned procedure via the blue solutions. Yield: 34 % of a light brown powder (86% purity according to NMR and 14% free acid impurity). ^{1}H-NMR: (400 MHz, THF-d^8, 298 K): δ [ppm] = 15.53 (s, 8H, *ortho*-H), 9.63 (s, 4H, *para*-H) 4.69 (s, 24H, OCH_3); EA: (calc / found %): C (46.7/45.2), H (3.92/3.82).

Diruthenium tetraacetate chloride

$Ru_2(OAc)_4Cl$ was synthesized according to modified literature procedures.[3] A mixture of $RuCl_3 \cdot x\ H_2O$ (7.5 g, 28.7 mmol, 1.0 eq.) and LiCl (7.5 g, XX mmol, XX eq), acetic acid (190 mL) and acetic anhydride (100 mL) was degassed by a stream of argon over 30 min and subsequently heated to reflux for 3 d in argon atmosphere. After cooldown to ambient temperature, the red brown precipitate was collected by filtration in air. The crude product was washed with cold acetone until the washing solution remained colorless and subsequently dried in vacuo. Yield: 73 % of a red brown powder. EA: (calc / found %): C (20.3/20.1), H (2.55/2.49).

Diruthenium tetra (L-mandelate)

$Ru_2(mand)_4$ was synthesized according to a literature procedure.[4] $Ru_2(OAc)_4Cl$ (202 mg, 0.43 mmol, 1 eq.) and L-mandelic acid (1.6 g, 10.52 mmol, 24 eq.) were dissolved in H_2O (125 mL) and heated to reflux for 90 min. The resulting yellow green solution was slowly cooled down to 4 °C. After 8 d, the supernatant was removed via *Whatman* filtration and the golden microcrystalline powder carefully dried under reduced pressure. After sampling for PXRD, the remaining solid was desolvated at 80 °C for 60 h. Yield: 21 % of a golden powder. ^{1}H-NMR: (400 MHz, CD_3CN, 298 K): δ [ppm] = 14.30 (s, 8H, *ortho*-H), 11.50 (s, 4H, *para*-H) 9.91 (s, 8H, *meta*-H) 9.48 (s, 4H, CH_{aliph}) 9.19 (s, 4H, OH); EA: (calc / found %): C (47.6/46.1), H (3.50/3.34).

PXRD

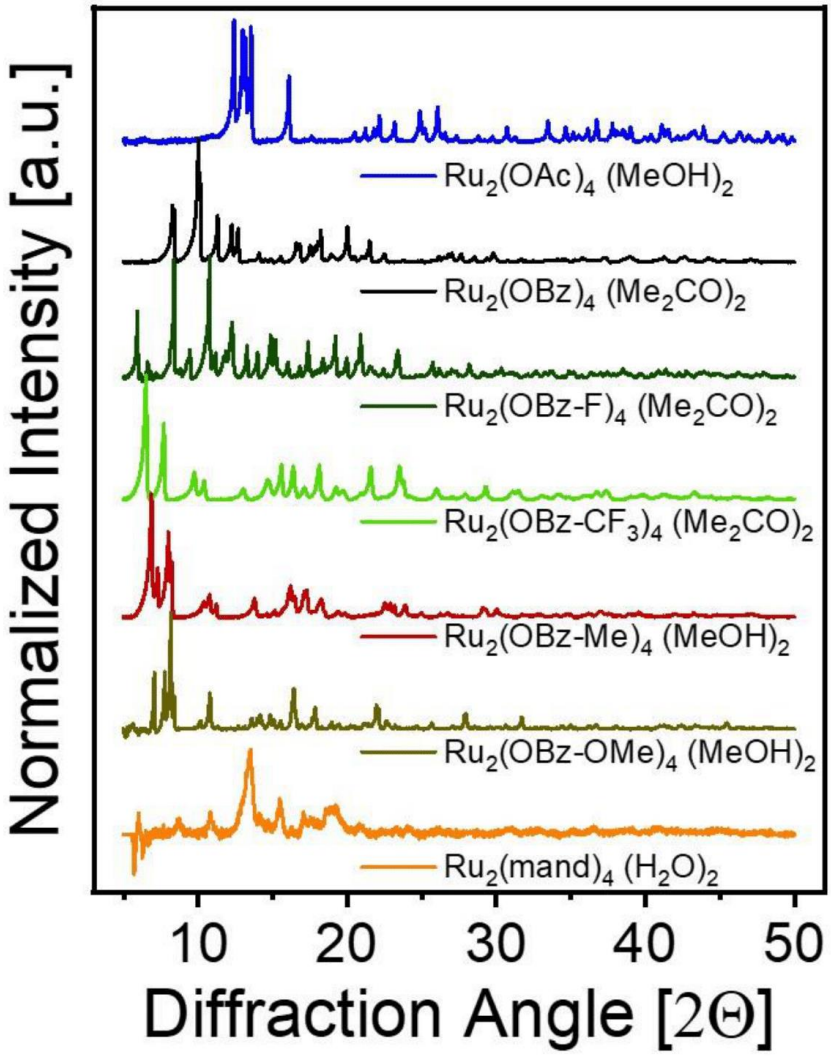

Figure S 1: Background-corrected and normalized PXRD pattern of the obtained univalent Ru-PW precursor adducts of methanol, water or acetone as indicated. Note that, low signal intensity and instrumental reasons caused a negative baseline for $Ru_2(mand)_4(H_2O)_2$ sample. Precursors were desolvated prior to usage in MOF syntheses.

FT-IR spectra

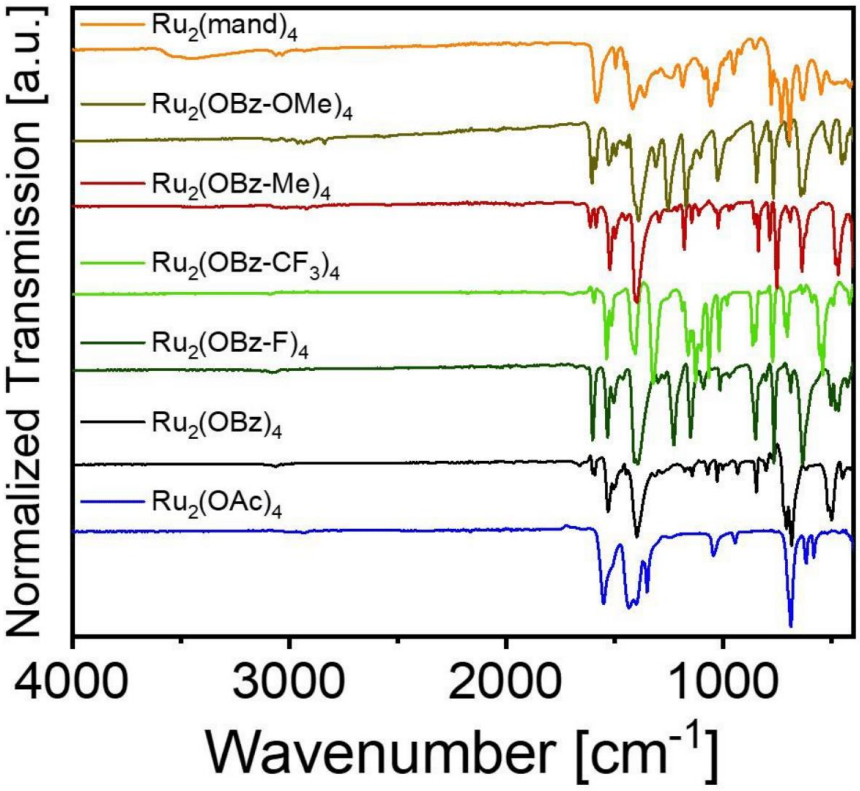

Figure S 2: Stacked and normalized FT-IR spectra of the Ru-PW precursors complexes used for MOF syntheses.

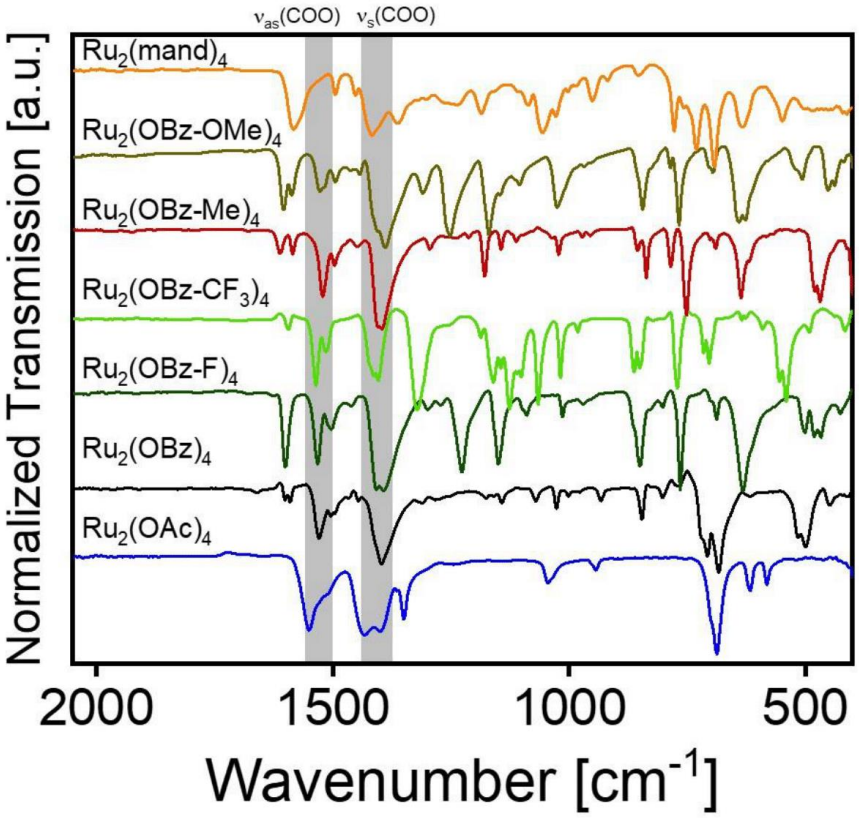

Figure S 3: Selected region (2000-400 cm^{-1}) of FT-IR spectra of the univalent Ru-PW precursor complexes. The highlighted regions indicate the asymmetric and symmetric carboxylate stretch vibrations indicating the +II / +II valency. Note that, apparently the adjacent hydroxy side groups of the ruthenium mandelate precursor cause a blue shift of ν_{as}(COO) towards absorption at 1583 cm^{-1}.

SC-XRD Structures

Single crystal X-ray crystallography of the diruthenium(II,II) tetra-μ-carboxylate paddlewheel complexes were mainly affected by their crystallization behavior (solubility issues) and their air sensitivity, which required single crystal search under inert conditions. All single crystals were directly taken from the respective reaction solutions, which were slowly cooled to -32 °C. The compounds throughout tend to crystallize as small plates or long needles, showing a crystallization behavior to form multiple stacking layers. Thus, the compounds showed a pronounced tendency to form twinned structures. For each compound, we therefore tested a couple of different single crystals until good quality for a full subsequent measurement was achieved. For the compound $Ru_2(OBz\text{-}CF_3)_4(THF)_2$, however, we were not able to improve the crystallization protocol in a way to achieve higher-quality crystals, showing less intergrowth behavior. We, nevertheless, were able to achieve a structure model of the paddlewheel complex by SC-XRD analysis, which showed sufficient quality for discussion of bond-lengths, angles etc. to be compared to the other complexes. For the sake of completeness and as further characterization detail, we here are providing the found structure model (crystal system, atom coordinates).

$Ru_2(OBz\text{-}CF_3)_4(THF)_2$

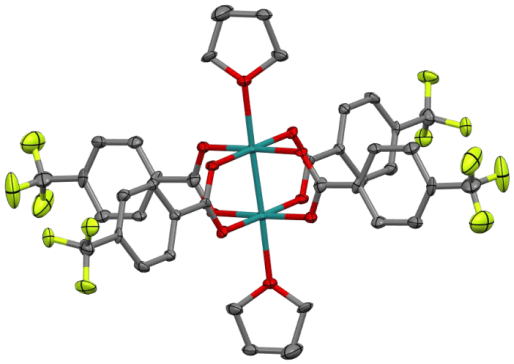

Figure S 4: ORTEP representation of $Ru_2(OBz\text{-}CF_3)_4(Me_2CO)_2$ with 50% probability level.

Table S 1: SC-XRD data of the complex $Ru_2(OBz\text{-}CF_3)_4(Me_2CO)_2$.

compound	**$Ru_2(OBz\text{-}CF_3)_4(Me_2CO)_2$**
Formula	$C_{40}H_{32}F_6O_{10}Ru_2$
Formula weight	1112.80
Temperature (K)	100(2)
Wavelength (Å)	0.7103 (Mo-K_α)

Crystal system	monoclinic
Space group	C 1 2/c 1
Z	8
a (Å)	24.756(6)
b (Å)	14.090(3)
c (Å)	16.243(3)
α (°)	90
β (°)	110.200(7)
γ (°)	90
Volume (Å^3)	5317(2)

Symbol	x/a	y/b	z/c	U
Ru1	0.53315(2)	0.48847(5)	0.56760(3)	0.0141836
F1	0.3338(3)	-0.0114(6)	0.6468(4)	0.072389
F2	0.2741(3)	0.0049(6)	0.5197(3)	0.0734417
F3	0.2671(3)	0.0914(6)	0.6233(4)	0.0783953
F4	0.25209(19)	0.8500(5)	0.6684(3)	0.0394186
F5	0.32436(19)	0.8656(4)	0.7884(3)	0.0351291
F6	0.27172(17)	0.7412(4)	0.7674(3)	0.0351291
O1	0.48884(19)	0.3710(5)	0.5830(3)	0.020146
O2	0.42380(18)	0.3908(4)	0.4491(2)	0.0171187
O3	0.48374(19)	0.5681(4)	0.6207(3)	0.0191009
O4	0.4186(2)	0.5927(4)	0.4874(3)	0.0194071
O5	0.6020(2)	0.4711(5)	0.7046(3)	0.0218944
C1	0.3037(4)	0.0546(9)	0.5892(5)	0.0420945
C2	0.3418(3)	0.1274(8)	0.5718(5)	0.0343539
C3	0.3968(3)	0.1420(8)	0.6284(5)	0.0328046
H3	0.41171	0.10435	0.67980	0.039
C4	0.4300(3)	0.2102(7)	0.6109(4)	0.025048
H4	0.46873	0.21784	0.64896	0.03
C5	0.4078(3)	0.2701(6)	0.5368(4)	0.0200749
C6	0.3522(3)	0.2553(7)	0.4792(4)	0.0230204
H6	0.33732	0.29390	0.42831	0.027
C7	0.3180(3)	0.1844(8)	0.4954(4)	0.0307509
H7	0.27978	0.17423	0.45639	0.037
C8	0.4431(3)	0.3502(7)	0.5224(4)	0.0228942
C9	0.2953(4)	0.8053(8)	0.7260(5)	0.0328228
C10	0.3335(3)	0.7524(6)	0.6859(4)	0.0180736
C11	0.3809(3)	0.7068(7)	0.7378(4)	0.0241645
H11	0.39064	0.70837	0.79974	0.029
C12	0.4156(3)	0.6571(6)	0.7007(4)	0.0172297
H12	0.44897	0.62434	0.73663	0.021

C13	0.4002(3)	0.6566(6)	0.6096(4)	0.0171747
C14	0.3523(3)	0.7031(6)	0.5577(4)	0.0179712
H14	0.34192	0.70035	0.49568	0.021
C15	0.3184(3)	0.7543(7)	0.5942(4)	0.0219123
H15	0.28606	0.78942	0.55847	0.021
C16	0.4366(3)	0.6013(6)	0.5693(4)	0.0140649
C17	0.5974(3)	0.4089(7)	0.7713(4)	0.0283364
H17A	0.58244	0.34613	0.74623	0.034
H17B	0.57110	0.43588	0.79938	0.034
C18	0.6571(4)	0.3999(11)	0.8364(5)	0.0667195
H18A	0.65737	0.41397	0.89624	0.08
H18B	0.67179	0.33473	0.83564	0.08
C19	0.6933(3)	0.4697(7)	0.8101(4)	0.0304985
H19A	0.73270	0.44501	0.82191	0.037
H19B	0.69558	0.53089	0.84111	0.037
C20	0.6615(3)	0.4803(8)	0.7135(4)	0.0342819
H20A	0.66914	0.54309	0.69241	0.041
H20B	0.67295	0.43010	0.68008	0.041

Atom1	Atom2	Length
Ru1	O1	2.048(7)
Ru1	O3	2.056(6)
Ru1	O5	2.302(4)
F1	C1	1.35(1)
F2	C1	1.32(1)
F3	C1	1.32(1)
F4	C9	1.31(1)
F5	C9	1.33(1)
F6	C9	1.37(1)
O1	C8	1.252(7)
O2	C8	1.257(8)
O3	C16	1.267(8)
O4	C16	1.254(8)
O5	C17	1.43(1)
O5	C20	1.435(9)
C1	C2	1.49(2)
C2	C3	1.370(9)
C2	C7	1.42(1)
C3	H3	0.950
C3	C4	1.36(1)
C4	H4	0.951
C4	C5	1.42(1)
C5	C6	1.387(9)
C5	C8	1.49(1)
C6	H6	0.951
C6	C7	1.39(1)
C7	H7	0.950
C9	C10	1.52(1)

C10	C11	1.35(1)
C10	C15	1.405(9)
C11	H11	0.950
C11	C12	1.40(1)
C12	H12	0.950
C12	C13	1.395(9)
C13	C14	1.362(9)
C13	C16	1.50(1)
C14	H14	0.951
C14	C15	1.39(1)
C15	H15	0.950
C17	H17A	0.990
C17	H17B	0.991
C17	C18	1.50(1)
C18	H18A	0.990
C18	H18B	0.99
C18	C19	1.49(2)
C19	H19A	0.990
C19	H19B	0.990
C19	C20	1.500(8)
C20	H20A	0.99
C20	H20B	0.99

$Ru_2(OBz\text{-}Me)_4(Me_2CO)_2$

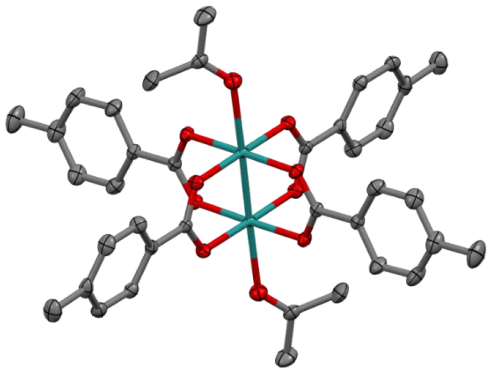

Figure S 5: ORTEP representation of $Ru_2(OBz\text{-}Me)_4(Me_2CO)_2$ with 50% probability level.

Table S 2: SC-XRD data of the complex $Ru_2(OBz\text{-}Me)_4(Me_2CO)_2$.

Compound	**$Ru_2(OBz\text{-}Me)_4(Me_2CO)_2$**
Formula	$C_{38}H_{40}O_{10}Ru_2$
CCDC	2043844
Formula weight	858.84
Temperature (K)	100(2)
Wavelength (Å)	0.7103 (Mo-K_α)
Crystal system	triclinic
Space group	P -1
Z	1
a (Å)	6.6721(13)
b (Å)	11.701(2)
c (Å)	12.113(2)
α (°)	96.337(8)
β (°)	104.603(8)
γ (°)	103.407(8)

Volume (Å^3)	875.7(3)
μ (mm^{-1})	0.921
d_{calc} (g/cm^3)	1.629
F (000)	436
Crystal size (mm^3)	0.045x 0.133 x 0.280
Theta range	2.30° to 25.35°
Index range	-8 ≤ h ≤ 8
	-14 ≤ k ≤ 14
	-14 ≤ l ≤ 14
Refl. collected	34266
Independent reflections	3196 (R_{int} = 0.1059)
Data/restraints/parameters	3195 / 0 / 230
GOF on F^2	1.034
R_1/wR_2[a]	0.0425 / 0.1172
[I ≥ 2σ(I)][b]	
R_1/wR_2	0.0487 / 0.1218
[all data]	
Largest diff. peak and hole	1.642 and -0.757 eÅ^{-3}

a: $w = 1/[\sigma^2(F_o^2) + (0.0733P)^2 + 2.19991P]$ where $P = (F_o^2 + 2F_c^2)/3$

b: $R_1 = \sum||F_o|-|F_c||/\sum|F_o|$; $wR_2 = \{\sum[w(F_o^2 - F_c^2)^2]/\sum[w(F_o^2)^2]\}^{1/2}$

Atom1	Atom2	Length
Ru1	O1	2.056(3)
Ru1	O3	2.047(4)
Ru1	O5	2.350(4)
O1	C1	1.274(5)
O2	C1	1.247(6)
O3	C9	1.256(5)
O4	C9	1.271(6)
O5	C18	1.205(6)
C1	C2	1.475(7)
C2	C3	1.387(7)
C2	C7	1.380(6)
C3	C4	1.373(7)
C3	H3	0.950
C4	C5	1.390(8)

C4	H4	0.950
C5	C6	1.392(7)
C5	C8	1.495(7)
C6	C7	1.376(7)
C6	H6	0.951
C7	H7	0.950
C8	H8A	0.980
C8	H8B	0.980
C8	H8C	0.980
C9	C10	1.483(7)
C10	C11	1.393(8)
C10	C15	1.384(6)
C11	C12	1.368(8)
C11	H11	0.950
C12	C13	1.381(7)
C12	H12	0.949
C13	C14	1.390(9)
C13	C16	1.501(9)
C14	C15	1.371(8)
C14	H14	0.950
C15	H15	0.950
C16	H16A	0.980
C16	H16B	0.979
C16	H16C	0.980
C17	C18	1.486(9)
C17	H17A	0.981
C17	H17B	0.980
C17	H17C	0.980
C18	C19	1.483(8)
C19	H19A	0.980
C19	H19B	0.981
C19	H19C	0.979

$Ru_2(OBz\text{-}OMe)_4(Me_2CO)_2$

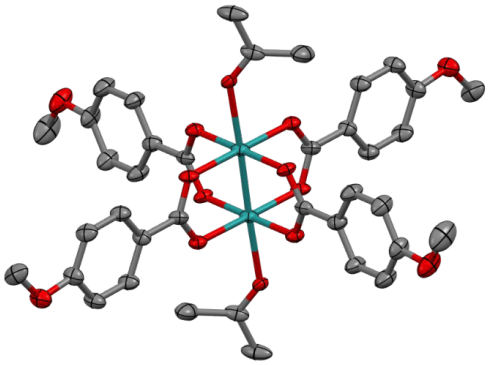

Figure S 6: ORTEP representation of $Ru_2(OBz\text{-}OMe)_4(Me_2CO)_2$ with 50% probability level.

Table S 3: SC-XRD data of the complex $Ru_2(OBz\text{-}OMe)_4(Me_2CO)_2$.

Compound	**$Ru_2(OBz\text{-}OMe)_4(Me_2CO)_2$**
Formula	$C_{38}H_{40}O_{14}Ru_2$
CCDC	2043845
Formula weight	922.84
Temperature (K)	100(2)
Wavelength (Å)	0.7103 (Mo-K_α)
Crystal system	monoclinic
Space group	C 1 2/c 1
Z	4
a (Å)	24.3485(18)
b (Å)	9.9212(7)
c (Å)	23.6907(11)
α (°)	90
β (°)	117.401(2)
γ (°)	90

Volume (Å^3)	5080.8(6)
μ (mm^{-1})	0.645
d_{calc} (g/cm^3)	1.206
F (000)	1827
Crystal size (mm^3)	0.049 x 0.175 x 0.365
Theta range	2.26° to 25.35°
Index range	-29 ≤ h ≤ 29
	-11 ≤ k ≤ 11
	-28 ≤ l ≤ 28
Refl. collected	101964
Independent reflections	4638 (R_{int} = 0.0802)
Data/restraints/parameters	4638 / 0 / 244
GOF on F^2	1.197
R_1/wR_2[a]	0.0574 / 0.1190
[I ≥ 2σ(I)][b]	
R_1/wR_2	0.0690 / 0.1258
[all data]	
Largest diff. peak and hole	1.366 and -1.107 eÅ^{-3}

a: $w = 1/[\sigma^2(F_o^2) + 71.3381P]$ where $P = (F_o^2 + 2F_c^2)/3$

b: $R_1 = \sum||F_o|-|F_c||/\sum|F_o|$; $wR_2 = \{\sum[w(F_o^2 - F_c^2)^2]/\sum[w(F_o^2)^2]\}^{1/2}$

Atom1	Atom2	Length
Ru1	O1	2.057(4)
Ru1	O4	2.047(4)
Ru1	O7	2.342(3)
O1	C1	1.266(6)
O2	C1	1.280(8)
O3	C5	1.359(8)
O3	C8	1.434(7)
O4	C9	1.264(8)
O5	C9	1.275(6)
O6	C13	1.352(9)
O6	C16	1.416(8)
O7	C18	1.218(6)
C1	C2	1.479(8)
C2	C3	1.394(8)

C2	C7	1.397(9)
C3	C4	1.38(1)
C3	H3	0.950
C4	C5	1.38(1)
C4	H4	0.950
C5	C6	1.391(8)
C6	C7	1.38(1)
C6	H6	0.951
C7	H7	0.950
C8	H8A	0.981
C8	H8B	0.980
C8	H8C	0.979
C9	C10	1.49(1)
C10	C11	1.39(1)
C10	C15	1.394(8)
C11	C12	1.38(1)
C11	H11	0.950
C12	C13	1.394(8)
C12	H12	0.949
C13	C14	1.38(1)
C14	C15	1.36(1)
C14	H14	0.951
C15	H15	0.949
C16	H16A	0.979
C16	H16B	0.98
C16	H16C	0.979
C17	C18	1.494(8)
C17	H17A	0.980
C17	H17B	0.979
C17	H17C	0.979
C18	C19	1.492(9)
C19	H19A	0.979
C19	H19B	0.98
C19	H19C	0.980

$Ru_2(OBz\text{-}(OMe)_2)_4(Me_2CO)_2$

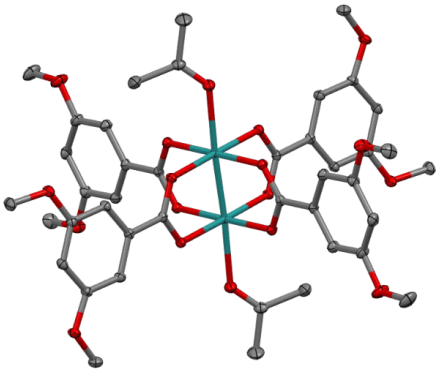

Figure S 7: ORTEP representation of $Ru_2(OBz\text{-}(OMe)_2)_4(Me_2CO)_2$ with 50% probability level.

Table S 4: SC-XRD data of the complex $Ru_2(OBz\text{-}(OMe)_2)_4(Me_2CO)_2$.

Compound	**$Ru_2(OBz\text{-}(OMe)_2)_4(Me_2CO)_2$**
Formula	$C_{48}H_{60}O_{20}Ru_2$
CCDC	2043847
Formula weight	1159.10
Temperature (K)	100(2)
Wavelength (Å)	0.7103 (Mo-K_α)
Crystal system	triclinic
Space group	P -1
Z	1
a (Å)	9.6301(5)
b (Å)	11.2950(6)
c (Å)	12.4945(6)
α (°)	99.576(2)
β (°)	107.789(2)
γ (°)	97.983(2)
Volume ($Å^3$)	1249.72(11)

μ (mm^{-1})	0.682
d_{calc} (g/cm^3)	1.540
F (000)	596
Crystal size (mm^3)	0.068 x 0.110 x 0.176
Theta range	2.26° to 30.56°
Index range	-13 ≤ h ≤ 13
	-16 ≤ k ≤ 16
	-17 ≤ l ≤ 17
Refl. collected	7602
Independent reflections	7096 (R_{int} = 0.0144)
Data/restraints/parameters	7602 / 6 / 334
GOF on F^2	1.037
R_1/wR_2[a]	0.0224 / 0.0544
[I ≥ 2σ(I)][b]	
R_1/wR_2	0.0198 / 0.0529
[all data]	
Largest diff. peak and hole	0.071 and -0.894 eÅ^{-3}

a: $w = 1/[\sigma^2(F_o^2) + (0.0306P)^2 + 0.0689P]$ where $P = (F_o^2 + 2F_c^2)/3$

b: $R_1 = \sum||F_o|-|F_c||/\sum|F_o|$; $wR_2 = \{\sum[w(F_o^2 - F_c^2)^2]/\sum[w(F_o^2)^2]\}^{1/2}$

Atom1	Atom2	Length
Ru1	O1	2.0566(7)
Ru1	O3	2.0645(9)
Ru1	O5	2.335(1)
O1	C1	1.273(2)
C1	O2	1.267(1)
C1	C2	1.493(1)
C2	C3	1.394(2)
C2	C7	1.392(2)
O3	C10	1.267(2)
C3	H3	0.950
C3	C4	1.394(1)
O4	C10	1.271(2)
C4	C5	1.396(2)
C4	O7	1.366(2)
O5	C19	1.223(2)
C5	H5	0.950

C5	C6	1.396(2)
O6	C6	1.365(2)
O6	C8	1.427(1)
C6	C7	1.387(1)
O7	C9	1.426(1)
C7	H7	0.950
O8	C15	1.363(2)
O8	C18	1.432(2)
C8	H8A	0.980
C8	H8AB	0.980
C8	H8AC	0.980
O9	C13	1.365(2)
O9	C17	1.430(2)
C9	H9A	0.980
C9	H9AB	0.980
C9	H9AC	0.980
C10	C11	1.493(2)
C11	C12	1.402(2)
C11	C16	1.385(2)
C12	H12	0.950
C12	C13	1.388(2)
C13	C14	1.402(2)
C14	H14	0.950
C14	C15	1.388(2)
C15	C16	1.400(2)
C16	H16	0.950
C17	H17A	0.980
C17	H17B	0.980
C17	H17C	0.980
C18	H18A	0.980
C18	H18B	0.980
C18	H18C	0.980
C19	C20	1.493(2)
C19	C21	1.498(2)
C20	H20A	0.980
C20	H20B	0.980
C20	H20C	0.980
C21	H21A	0.980
C21	H21B	0.980
C21	H21C	0.980
C22	C23	1.503(4)
C22	C24	1.473(3)
C22	O10	1.255(4)
C23	H23A	0.980
C23	H23B	0.980
C23	H23C	0.980
C24	H24A	0.980
C24	H24B	0.980
C24	H24C	0.980

$Ru_2(OBz\text{-}F)_4(Me_2CO)_2$

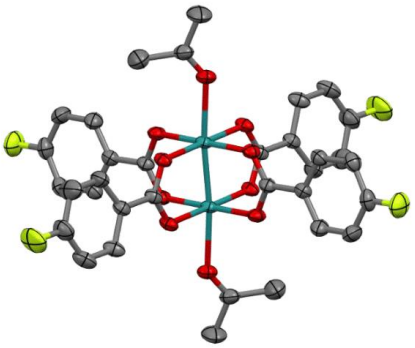

Figure S 8: ORTEP representation of $Ru_2(OBz\text{-}F)_4(Me_2CO)_2$ with 50% probability level.

Table S 5: SC-XRD data of the complex $Ru_2(OBz\text{-}F)_4(Me_2CO)_2$.

Compound	**$Ru_2(OBz\text{-}F)_4(Me_2CO)_2$**
Formula	$C_{34}H_{28}F_4O_{10}Ru_2$
CCDC	2043846
Formula weight	874.70
Temperature (K)	100(2)
Wavelength (Å)	0.7103 (Mo-K_α)
Crystal system	monoclinic
Space group	C 1 2/c 1
Z	8
a (Å)	29.179(10)
b (Å)	18.400(7)
c (Å)	17.212(6)
α (°)	90
β (°)	113.270(11)
γ (°)	90
Volume ($Å^3$)	8489.0(5)
μ (mm^{-1})	0.775

d_{calc} (g/cm^3)	1.639
F (000)	3488
Crystal size (mm^3)	0.049 x 0.185 x 0.345
Theta range	2.21° to 25.35°
Index range	-35 ≤ h ≤ 35
	-22 ≤ k ≤ 22
	-20 ≤ l ≤ 20
Refl. collected	131612
Independent reflections	7767 (R_{int} = 0.0553)
Data/restraints/parameters	7767 / 0 / 422
GOF on F^2	1.139
R_1/wR_2[a]	0.0773 / 0.2202
[I ≥ 2σ(I)][b]	
R_1/wR_2	0.0843 / 0.2320
[all data]	
Largest diff. peak and hole	2.592 and -2.341 eÅ^{-3}

a: $w = 1/[\sigma^2(F_o^2) + (0.1582P)^2 + 57.6731P]$ where $P = (F_o^2 + 2F_c^2)/3$

b: $R_1 = \sum||F_o|-|F_c||/\sum|F_o|$; $wR_2 = \{\sum[w(F_o^2 - F_c^2)^2]/\sum[w(F_o^2)^2]\}^{1/2}$

Atom1	Atom2	Length
Ru1	O1	2.070(4)
Ru1	O3	2.074(5)
Ru1	O10	2.346(6)
F1	C5	1.361(8)
F2	C12	1.38(1)
O1	C1	1.269(7)
O2	C1	1.279(8)
O3	C8	1.276(9)
O4	C8	1.266(8)
O10	C32	1.216(9)
C1	C2	1.477(7)
C2	C3	1.388(9)
C2	C7	1.40(1)
C3	C4	1.37(1)
C3	H3	0.950
C4	C5	1.39(1)
C4	H4	0.950

C5	C6	1.37(1)
C6	C7	1.381(9)
C6	H6	0.949
C7	H7	0.950
C8	C9	1.48(1)
C9	C10	1.39(2)
C9	C14	1.38(2)
C10	C11	1.40(2)
C10	H10	0.95
C11	C12	1.34(1)
C11	H11	0.95
C12	C13	1.40(2)
C13	C14	1.38(2)
C13	H13	0.95
C14	H14	0.95
C32	C33	1.50(1)
C32	C34	1.51(1)
C33	H33A	0.980
C33	H33B	0.982
C33	H33C	0.978
C34	H34A	0.98
C34	H34B	0.98
C34	H34C	0.981
Ru02	O5	2.069(4)
Ru02	O7	2.076(6)
Ru02	O9	2.316(4)
F3	C19	1.371(9)
F4	C26	1.36(1)
O5	C15	1.264(7)
O6	C15	1.265(6)
O7	C22	1.279(8)
O8	C22	1.262(7)
O9	C29	1.212(8)
C15	C16	1.497(8)
C16	C17	1.37(1)
C16	C21	1.410(9)
C17	C18	1.40(1)
C17	H17	0.950
C18	C19	1.38(1)
C18	H18	0.949
C19	C20	1.36(1)
C20	C21	1.370(9)
C20	H20	0.949
C21	H21	0.949
C22	C23	1.49(1)
C23	C24	1.391(9)
C23	C28	1.37(1)
C24	C25	1.40(1)
C24	H24	0.950

C25	C26	1.38(1)
C25	H25	0.950
C26	C27	1.37(1)
C27	C28	1.40(1)
C27	H27	0.951
C28	H28	0.951
C29	C30	1.53(1)
C29	C31	1.48(1)
C30	H30A	0.98
C30	H30B	0.98
C30	H30C	0.98
C31	H31A	0.98
C31	H31B	0.98
C31	H31C	0.98

Structural Properties of Diruthenium Tetracarboxylates – Bond Lengths and Angles

*Table S 6: Overview on selected bond lengths and angles found in diruthenium tetracarboxylates in literature and presented in this work. *Always the angle <90° was selected, **Average value (there are two Ru atoms in the asymmetric unit, belonging to two complexes).*

Equatorial carboxylate	Axial ligand	d_{Ru-Ru} [Å]	$d_{Ru-O(eq)}$ [Å]**	$d_{Ru-L(ax)}$ [Å]	$\omega_{O(eq)-Ru-O(eq)}$ [°]*	$\tau_{Oeq-Ru-Ru-Oeq}$ [°]	Ref.
Univalent $Ru^{II,II}$ PWs							
Acetate	H_2O	2.262	2.068	2.335	87.75	1.18	[2]
Acetate	MeOH	2.265	2.073	2.333	89.65	0.21	[5]
Trifluoroacetate	THF	2.277	2.074	2.268	87.69	0.16	[6]
Propionate	Acetone	2.2595	2.0675	1.363	89.74	0.40	[2]
Benzoate	Benzoic acid	2.2634	2.0535	2.356	89.65	0.53	[7]
Benzoate	Acetone	2.2608	2.0650	2.3467	98.66	3.92	[5]
Benzoate	THF	2.2667	2.0585	2.353	87.61	0.59	[8]
4-fluoro benzoate	Acetone	2.2698**	2.0698	2.3317**	89.31	0.55	This work
4-fluoro benzoate	THF	2.2677	2.061	2.354	89.80	0.85	[9]
3,5-difluoro benzoate	THF	2.2708	2.073	2.310	88.58	0.59	[9]
2,4,6-trifluoro benzoate	THF	2.2723	2.071	2.283	89.42	0.25	[9]
4-trifluoro-methyl benzoate	THF	2.2656	2.0610	2.3019	89.04	0.82	This work
4-trifluoro-methyl benzoate	THF (THF solvate)	2.2662	2.065	2.298	88.72	0.30	[10]
4-methoxy benzoate	Acetone	2.2687	2.0558	2.3415	89.29	0.24	This work
3,5-dimethoxy benzoate	Acetone	2.2679	2.0628	2.3342	89.43	0.49	This work
4-methyl benzoate	Acetone	2.2585	2.0550	2.3503	89.73	0.37	This work
Mixed-valence $Ru^{II,III}$ PWs							
Acetate	Chloride	2.2800	2.0229	2.5722	89.50	0.58	[11]
Acetate	Pyridine (PF_6^- anion)	2.2805	2.03	2.27	89.19	1.65	[12]
Acetate	4-methyl Pyridine (PF_6^- anion)	2.2786	2.019	2.291	88.76	0.43	[12]
Acetate	Quinuclidine (PF_6^- anion)	2.2918	2.025	2.338	88.72	0.83	[12]

Additional Information – Ligand Exchange Test Reaction

To systematically unveil ligand exchange properties of the obtained series of diruthenium tetrabenzoate derivatives, we conducted additional NMR-based ligand exchange reactions. Best mimicking the properties of BTC with electron withdrawing groups in meta position but being chemically inert, we selected 3,5-bis(trifluoromethyl) benzoic acid as competing ligand (coligand) for this test reaction. In Figure S 9, initial ligand exchange rates (black circles) and the found equilibrium constants (grey squares) are displayed as a function of the respective ligand pK_a. Details on procedure and data evaluation are provided in the ESI. Although not in a very strict order, a general trend towards lower exchange rates for more acidic precursor ligands can be extracted. It remains unclear why OBz-Me has a comparably low rate. Overall, exchange rates between 1 and 8 h^{-1} (at ambient temperature) confirm the slow ligand exchange kinetics for PGM-PW complexes. Equilibrium constants were extracted from the ratio of free precursor acid to the acid of the coligand after thermodynamic equilibration for 120 min at 55 °C. Entropic contribution is not to be expected for such a stoichiometric exchange reaction. A general correlation can be seen. Following chemical intuition, rather basic ligands are substituted preferentially as they tend to be protonated upon their dissociation and thus, are partially removed from the equilibrium.

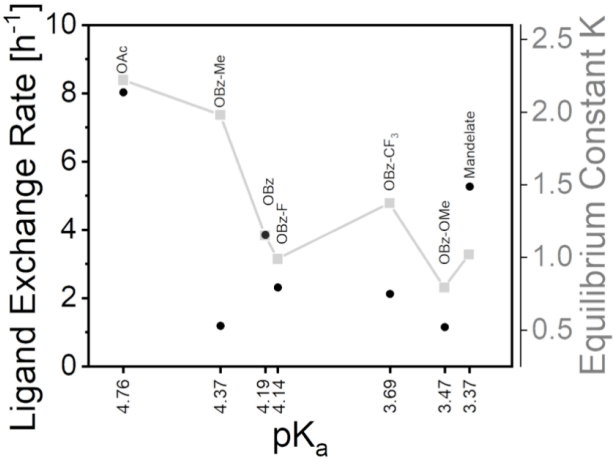

Figure S 9: Correlation between the ligand exchange rate (black circular data points), the equilibrium constant K (grey square data points) and the respective precursor ligand acidity (pK_a). The ligand exchange was performed with 3,5-bis(trifluoromethyl) benzoic acid as monofunctional BTC simulant. Ligand exchange rates were determined using the maximum initial slopes at ambient temperature. Equilibrium constants are determined using the ratio of released precursors ligand to free coligand (equimolar feed) upon equilibration at 55 °C.

Generally, the ligand exchange is controlled by the acidity of the respective carboxylic acids. Although more basic ligands form stronger bonds to the metal rendering them more difficult to dissociated, their basicity prevents them from reversible coordination as their protonation occurs upon release. On the contrary, more acidic ligands are preferentially deprotonated but might form relatively weak coordination bonds to the metal. Due to these competing effects, a final decision on the ideal MOF precursor on the basis of this NMR-based simulating experiment is not substantiated but requires the experimental MOF syntheses and careful analysis of the respective materials as outlined in the following. However, the the two samples OBz and mandelate seem to have higher ligand exchange rates compared to the other investigated benzoate ligands.

As follows, Figure S 10 shows an exemplary NMR spectrum how the calculation of kinetic and thermodynamic data was extracted from the primary data. Figure S 11 gives an impression on the

evolution of related NMR spectra throughout the experiment exemplified by $Ru_2(OBz)_4$. Figure S 12 summarizes the evolution of the ratio of free precursor ligand to coligand for the whole series of diruthenium benzoate precursors.

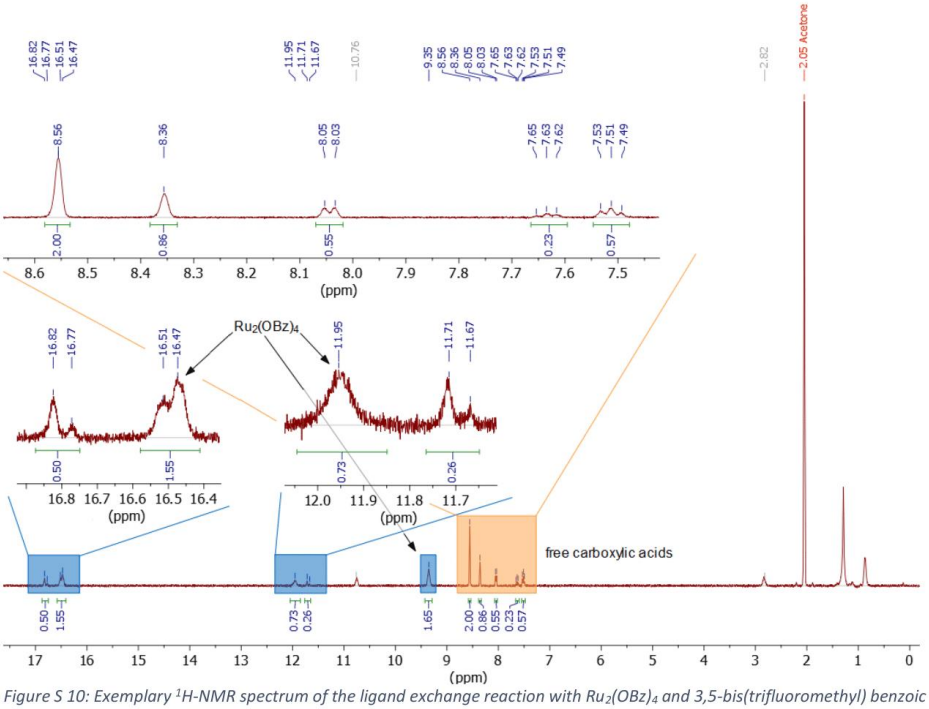

Figure S 10: Exemplary ^{1}H-NMR spectrum of the ligand exchange reaction with $Ru_2(OBz)_4$ and 3,5-bis(trifluoromethyl) benzoic acid as competitive coligand after 6min 27s at ambient temperature. The signals of ligands bound to complexes are highlighted with blue, the region of free acids is highlighted in orange. Equilibrium konstants were determined using the ratios of the free acids as paramagnetism of the diruthenium core obstructs quantification of bound ligands.

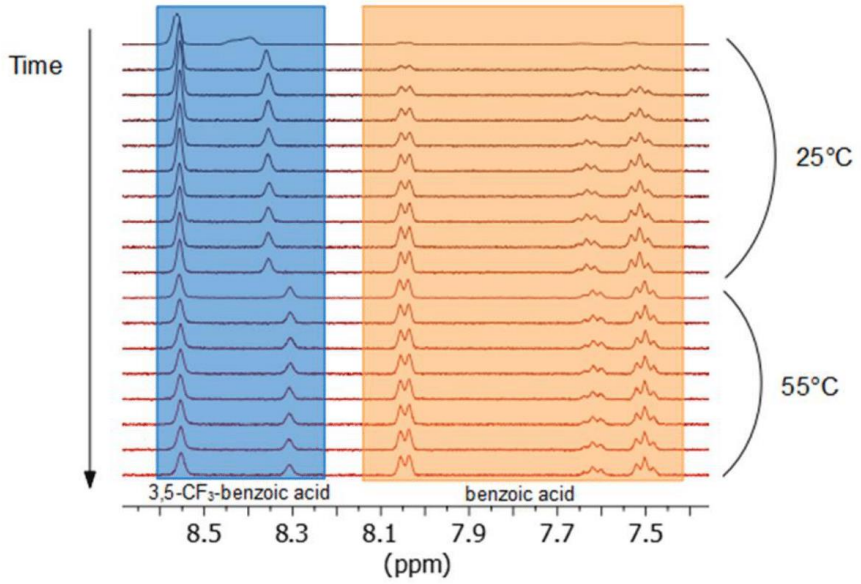

Figure S 11: Stacked ^{1}H-NMR spectra of the kinetic series recorded for $Ru_2(OBz)_4$ as example.

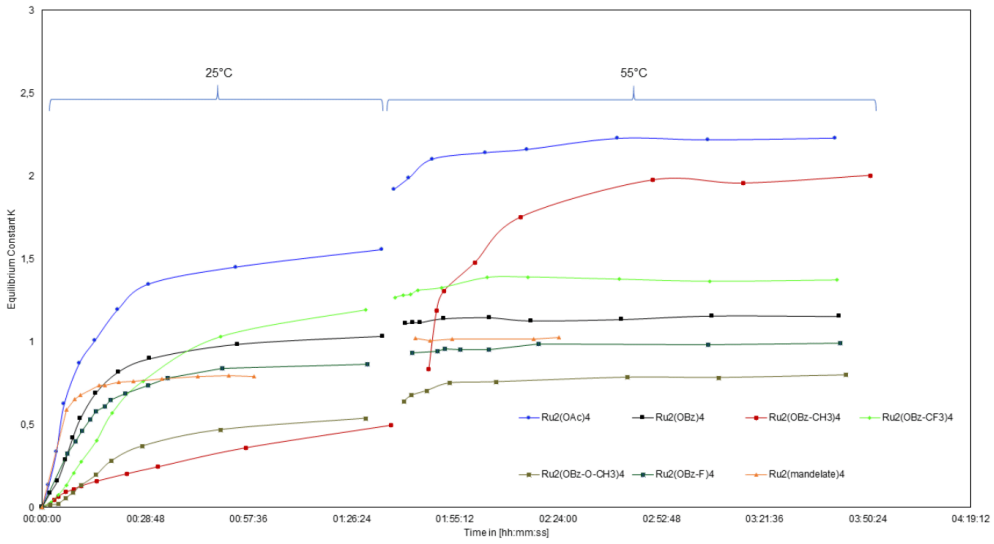

Figure S 12: Evolution of the ligand exchange reaction between precursor complexes and 3,5-bis(trifluoromethyl) benzoic acid as monotopic BTC simulant. The graphs display the ratio of the released precursor ligand to free coligand as a function of time. The gap at 1:30 h between the curves represents the transition from r.t. to 55 °C. Horizontal plateaus of the curves indicate reached equilibria. The steepest slopes in the beginning of the reactions were taken to calculate the exchange rates.

Additional Information – MOF Characterization

Development of a Modified MOF Synthesis Procedure

On the basis of the established Ru-HKUST-1 synthesis procedure utilizing $Ru_2(OAc)_4$ precursor and HOAc modulator, we developed a modified procedure to account for the different solubility of benzoate-derived precursors and benzoic acid derivatives as modulator. In contrast to the acetic acid, any solubilizing effect and function as cosolvent enhancing H_3BTC dissolution is absent for benzoic acids. Thus, we investigated the suitability of a water acetone mixture for MOF syntheses.

The following Table S 7 summarizes the outcome of MOF syntheses dedicated to extract the ideal synthetic procedure for this study. In each reaction, 158 mg $Ru_2(OAc)_4$ precursor and 101 mg H_3BTC were dissolved in the stated solvent / modulator mixture and heated to 150 °C over 3 d. Test reactions A, B and C yielded crystalline powders featuring the HKUST-1 structure, while reaction D resulted in an amorphous gel. Respective PXRD patterns are provided in Figure S 13. To avoid gel formation and to minimize the modulator loading, we selected the conditions of test reaction C for the study. For reasons of comprehensiveness, test reaction B was included in the results section of the main manuscript denoted as “OAc (x2 Mod)”.

*Table S 7: Solvent amounts used to extract the ideal MOF synthesis conditions for this study. For each reaction, 158 mg $Ru_2(OAc)_4$ precursor and 101 mg H_3BTC were dissolved in the stated solvent / modulator mixture and heated to 150 °C for 3 d. *related PXRD patterns are displayed in Figure S 13 below.*

Test reaction	H_2O [mL]	Me_2CO [mL]	HOAc [mL]	Outcome
A	2	2	0.7	Crystalline powder*
B	4	4	1.4	Crystalline powder*
C	4	4	0.7	Crystalline powder*
D	4	4	0.3	Amorphous gel

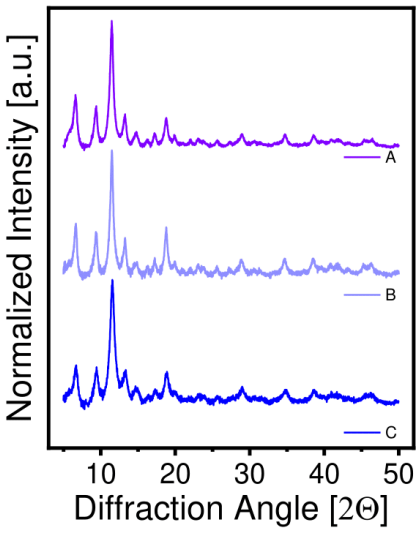

Figure S 13: Comparison of PXRD patterns for the MOF synthesis optimisation following test reactions A, B and C. All three patterns indicate crystalline and phase pure MOF materials.

MOF Synthesis Details

Table S 8: Used reagent amounts for the synthesis of Ru-HKUST-1 samples. All syntheses using 4 mL water and 4 mL acetone were performed under inert conditions in steel autoclaves with Teflon liners at 150 °C over 3 days.

MOF sample	Precursor (Ru_2R_4)			Linker H_3BTC			Modulator		
	Molar weight [$gmol^{-1}$]	Mass [mg]	Eq	Molar weight [$gmol^{-1}$]	Mass [mg]	Eq	Species	Mass [mg]	Eq
OAc	438.32	158.0	3	210.14	101	4	HOAc	735	102
OAc (x2mod)	438.32	158.0	3	210.14	101	4	HOAc	1470	204
OBz	686.60	247.5	3	210.14	101	4	HOBz	1490	102
OBz-F	758.56	273.1	3	210.14	101	4	HOBz-F	1710	102
OBz-CF_3	958.59	345.1	3	210.14	101	4	HOBz-CF_3	2320	102
OBz-Me	742.71	267.4	3	210.14	101	4	HOBz-Me	1660	102
OBz-OMe	806.70	290.4	3	210.14	101	4	HOBz-OMe	1860	102
L-mandelate	806.70	290.4	3	210.14	101	4	L-mandelic acid	1860	102

Sample Appearance

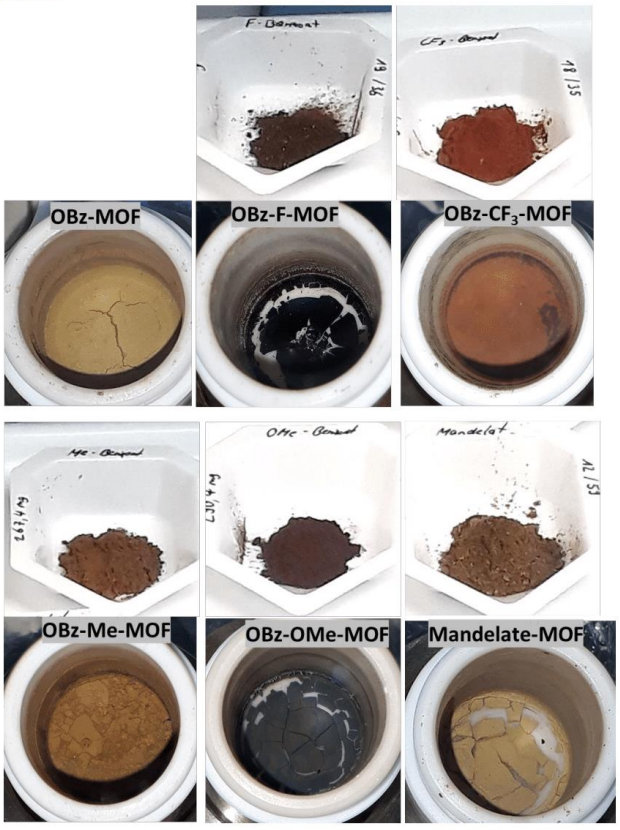

Figure S 14: Similarity of color shade between precursor complex and derived activated MOF.

Powder X-Ray Diffraction

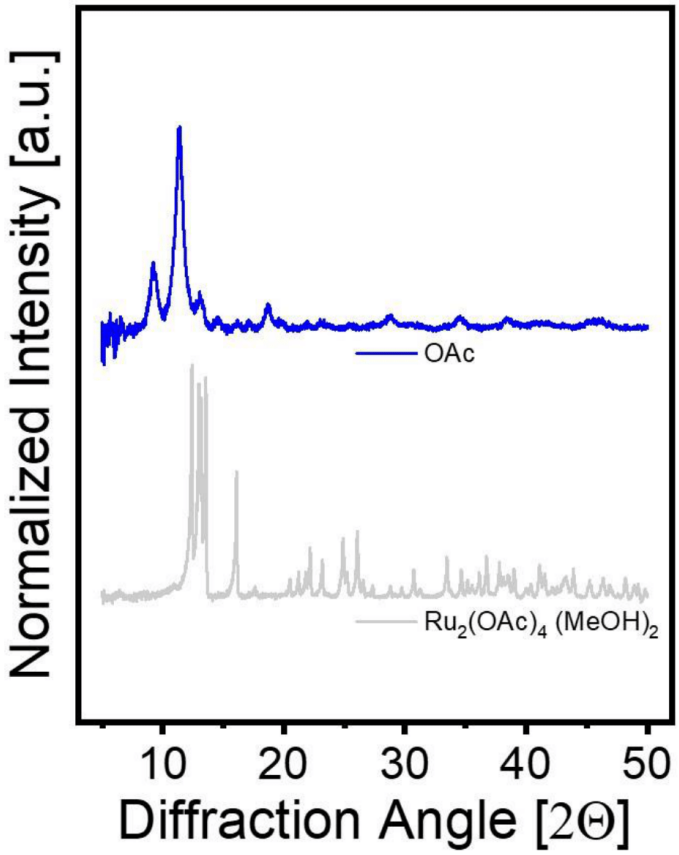

Figure S 15: PXRD comparison of Ru-HKUST-1 (top trace, blue) with its acetate precursor (bottom trace, light grey). Note that the crystalline precursor adduct was desolvated prior to use in MOF syntheses.

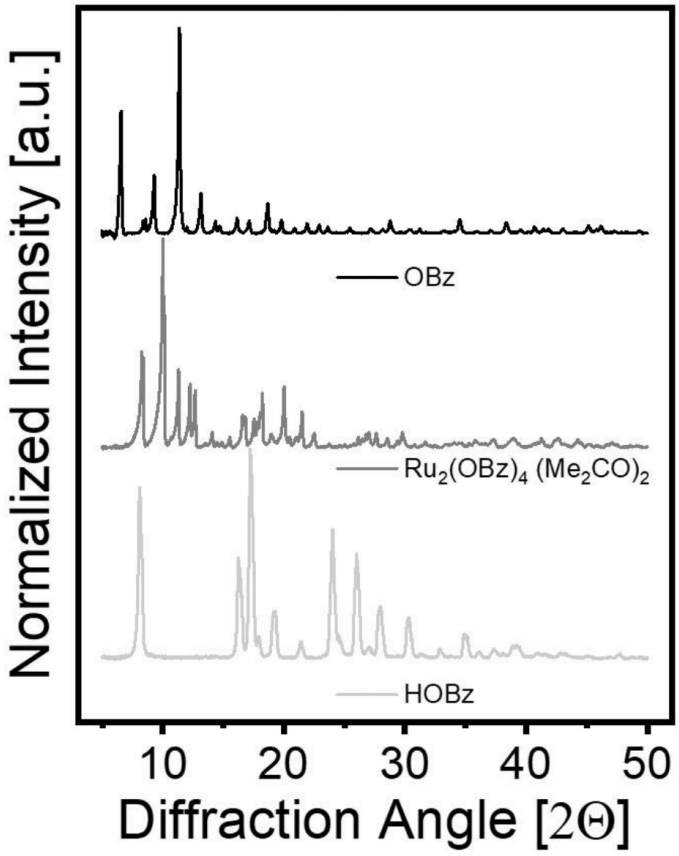

Figure S 16: PXRD comparison of Ru-HKUST-1 (top trace, black) with its benzoate precursor (middle trace, dark grey) and the used free acid modulator (bottom trace, light grey). Note that the crystalline precursor adduct was desolvated prior to use in MOF syntheses.

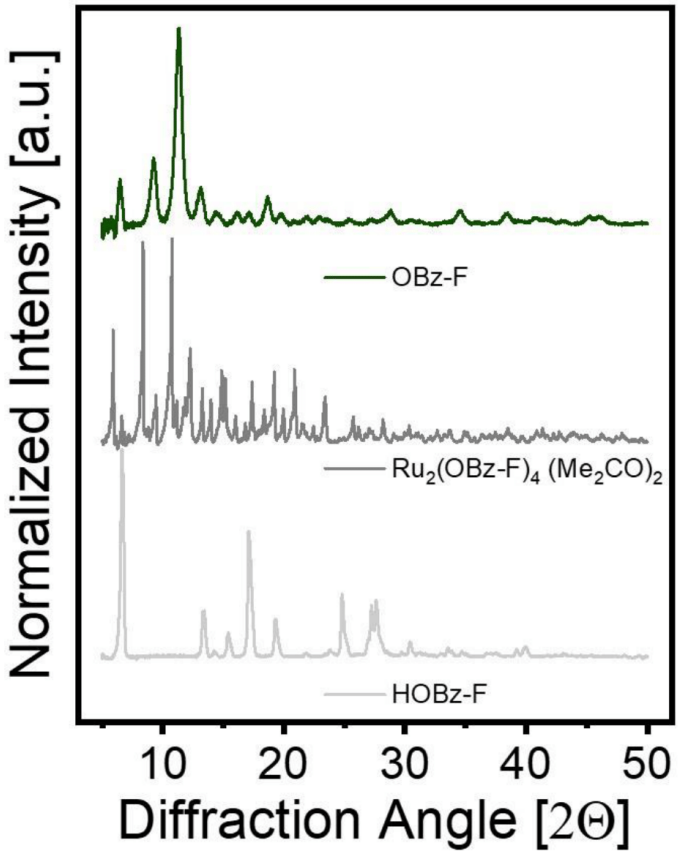

Figure S 17: PXRD comparison of Ru-HKUST-1 (top trace, emerald) with its 4-fluoro benzoate precursor (middle trace, dark grey) and the used free acid modulator (bottom trace, light grey). Note that the crystalline precursor adduct was desolvated prior to use in MOF syntheses.

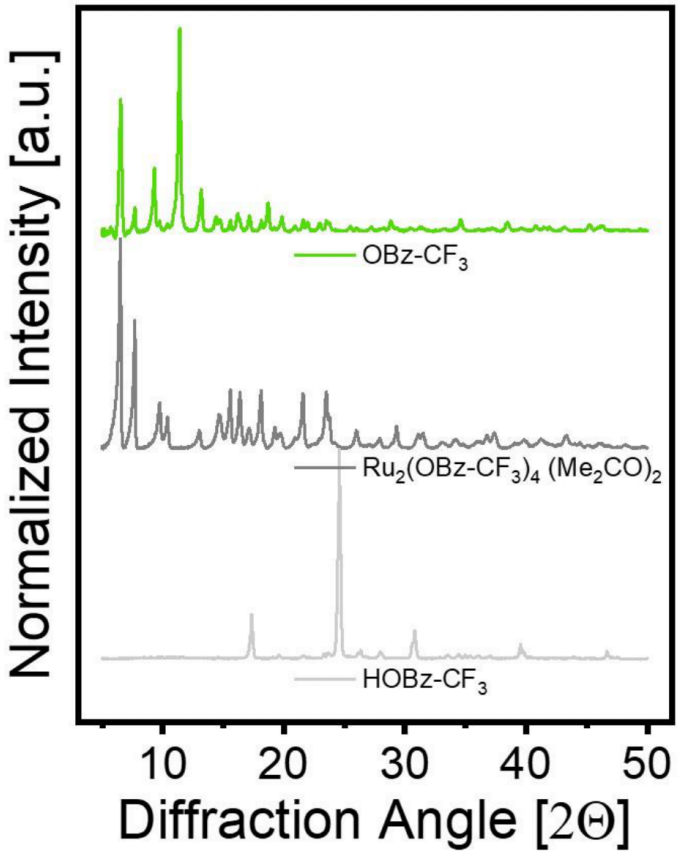

Figure S 18: PXRD comparison of Ru-HKUST-1 (top trace, green) with its 4-trifluoromethyl benzoate precursor (middle trace, dark grey) and the used free acid modulator (bottom trace, light grey). Note that the crystalline precursor adduct was desolvated prior to use in MOF syntheses.

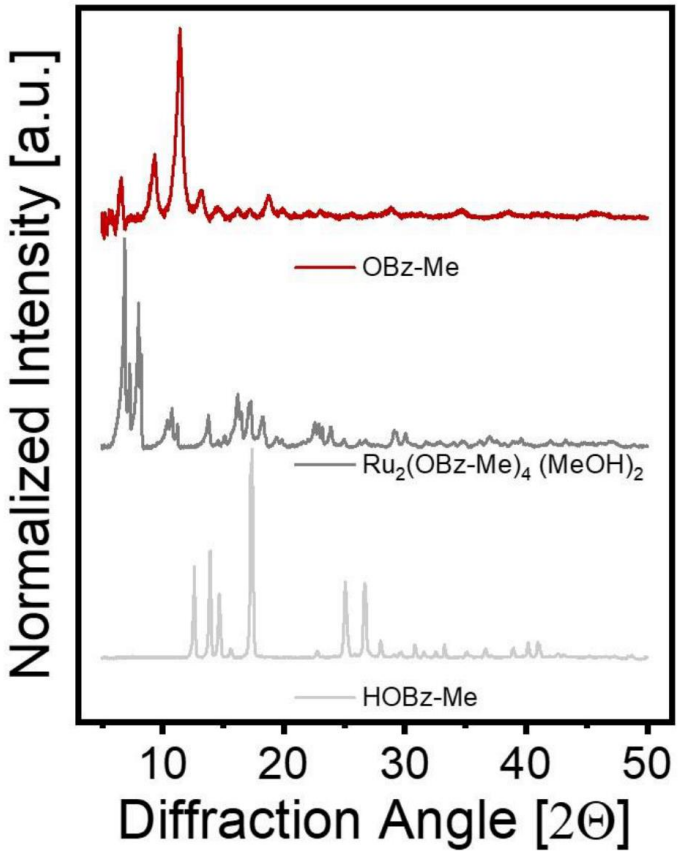

Figure S 19: PXRD comparison of Ru-HKUST-1 (top trace, red) with its 4-methyl benzoate precursor (middle trace, dark grey) and the used free acid modulator (bottom trace, light grey). Note that the crystalline precursor adduct was desolvated prior to use in MOF syntheses.

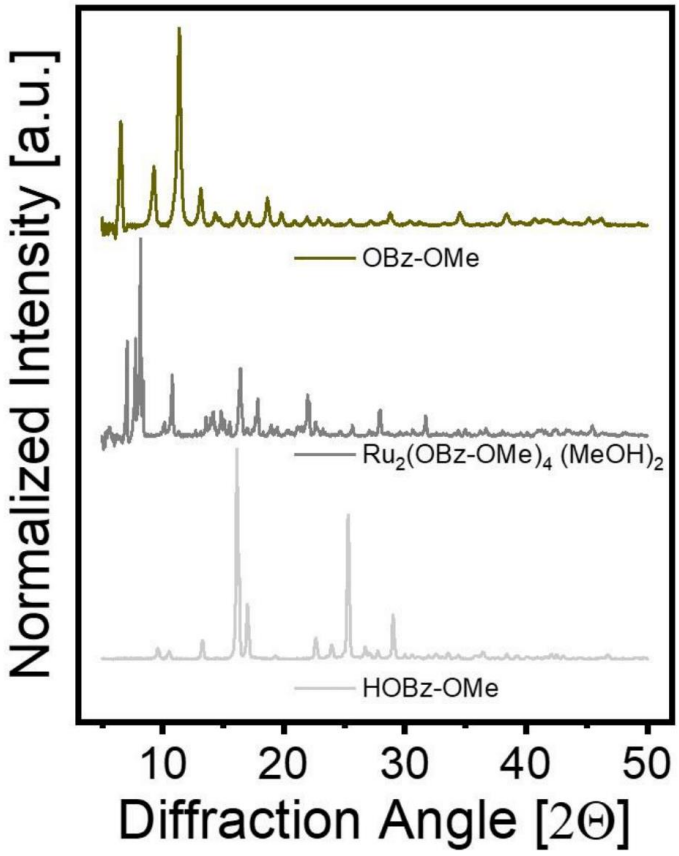

Figure S 20: PXRD comparison of Ru-HKUST-1 (top trace, olive) with its 4-methoxy benzoate precursor (middle trace, dark grey) and the used free acid modulator (bottom trace, light grey). Note that the crystalline precursor adduct was desolvated prior to use in MOF syntheses.

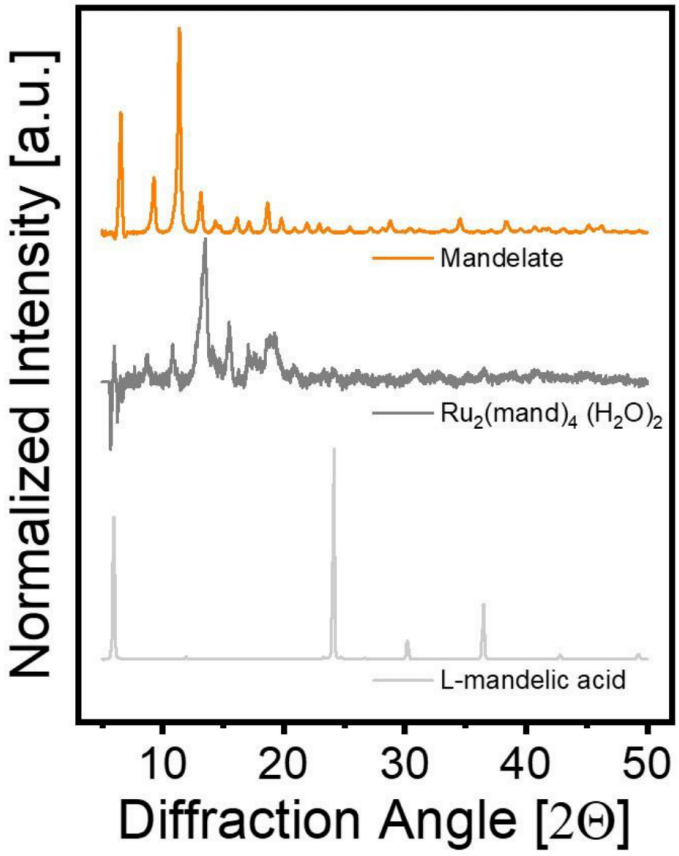

Figure S 21: PXRD comparison of Ru-HKUST-1 (top trace, orange) with its L-mandelate precursor (middle trace, dark grey) and the used free acid modulator (bottom trace, light grey). Note that the crystalline precursor adduct was desolvated prior to use in MOF syntheses.

Composition & Porosity

C and H elemental analysis was combined with Ru contents derived from TGA-based metal oxide residues and Ru:F ratios obtained from EDS analysis. The residual unknown elemental content is assigned to oxygen assumed as the only missing elemental component. A summary of all elemental contents together with the theoretical values of an ideal $[Ru_3(BTC)_2]$ structure is shown in Table S 9. Solver-derived sum formulae putatively describing the found experimental values are provided with several assumptions: Neither oxides, nor hydroxides, nor fluorides were considered as additional counterions. All calculations were limited to BTC^{3-}, $RCOO^-$ and H^+ with R being characteristic for each modulator/precursor ligand. No localisation of calculated protons to any counterions is possible from the obtained data, thus H^+ are involved in the sum formulae independently. Note, that the sum of organic charges (involving BTC^{3-}, $RCOO^-$ and H^+) was set to be ≥-6. This condition is based on the assumed $Ru^{II,II}$ sites and potential presence of Ru^0-NPs in some samples. Each sum formula was set to three Ru atoms per repeating unit.

*Table S 9: Summary of compositions of all samples. The experimentally determined elemental C, H, F and Ru contents served for a solver-approach using Microsoft Excel to derive the stated putative sum formulae. However, fitting did not provide unambiguous results for all samples. *the fitting of this sample gave inconsistencies or bad fitting quality. Elemental contents close to the ideal composition are highlighted in green, those very different from the ideal value are highlighted in red. Note, that the H^+ content of each sample calculated by this method is highly sensitive to experimental fluctuations and should not be overinterpreted. Considerably lower anion amounts per sum formula found for the OBz-OMe sample is in line with pronounced Ru^0-NP formation.*

Sample	Elemental contents [%]					Putative sum formula	Molar weight of repeating unit
	C	H	F	O*	Ru		
OAc	30.48	1.33	- -	27.8	40.4	$[Ru_3(BTC)_{1.83}(OAc)_{0.49}H_{2.09}]$	713.27
OAc (modx2)	30.60	1.28	- -	27.0	41.2	$[Ru_3(BTC)_{1.77}(OAc)_{1.17}H_{0.48}]$*	739.37
OBz	31.40	1.26	- -	25.4	41.9	$[Ru_3(BTC)_{1.78}(OBz)_{0.41}H_{1.63}]$	723.18
OBz-F	30.70	1.19	0.46	25.8	41.8	$[Ru_3(BTC)_{1.91}(OBz\text{-}F)_{0.18}H_{2.13}]$*	725.99
OBz-CF_3	33.74	1.42	3.03	29.2	32.6	$[Ru_3(BTC)_{2.58}(OBz\text{-}CF_3)_{0.5}H_{3.35}]$*	935.51
OBz-Me	31.67	1.47	- -	37.71	29.2	$[Ru_3(BTC)_{3.58}(OBz\text{-}Me)_0H_{4.74}]$*	1184.61
OBz-OMe	25.94	0.98	- -	22.7	50.4	$[Ru_3(BTC)_{1.40}(OBz\text{-}OMe)_{0.05}H_{1.28}]$	602.02
Mandelate	30.67	1.22	- -	26.4	41.7	$[Ru_3(BTC)_{1.93}(mand)_{0.16}H_{1.94}]$	729.08
Ideal $[Ru_3(BTC)_2]$	30.13	0.84	- -	26.76	42.26	$[Ru_3(BTC)_2]$	713.27

On the basis of these idealized (bottom row) and putative sum formulae (all other lines), their respective molecular weight of the repeating unit was used to normalize the found BET surface areas. The following Table S 10 provides an overview on molar BET surface areas [m^2mmol^{-1}] and the molar pore volumes [cm^3mmol^{-1}] of all samples. For comparison values of the ideal Cu-HKUST-1 structure are supplemented.

Table S 10: Gravimetric BET surface areas (SA) and molar SAs [m^2mmol^{-1}] and pore volumes (PV) [cm^3mmol^{-1}] derived from idealized and calculated putative sum formulae. Total pore volumes refer to pores <387 Å. For comparison, the ideal Cu-HKUST-1 data is also provided. The ideal sum formula refers to 717.44 mg $mmol^{-1}$ for Ru and 604.87 mg $mmol^{-1}$ for Cu. The calculated sum formulae and respective molar weights are given in Table S 9 (right column). The values for the ideal Cu-HKUST-1 are derived from DFT simulations conducted in Ref.[13] The enormous coincidence of surface area and pore volume of the mandelate-based Ru-MOF sample is highlighted in comparison with the structural simulation (bottom row). Note, that both ideal and calculated sum formulae give very similar molar values supporting the general approach used herein.

Sample	Gravimetric		Based on ideal sum formula $[Ru_3(BTC)_2]$		Based on calculated sum formulae*	
	BET SA [m^2g^{-1}]	BET PV [cm^3g^{-1}]	SA [m^2mmol^{-1}]	PV [cm^3mmol^{-1}]	SA [m^2mmol^{-1}]	PV [cm^3mmol^{-1}]
OAc	1493	0.618	1071.13792	0.444	1065	0.441
OAc (modx2)	n.d.		n.d.	n.d.	n.d.	0.000
OBz	1432	0.584	1027	0.420	1036	0.423
OBz-F	1516	0.973	1088	0.701	1101	0.706
OBz-CF_3	987	0.413	708	0.298	923	0.386
OBz-Me	1401	0.516	1005	0.372	1660	0.611
OBz-OMe	1505	0.585	1080	0.423	906	0.352
Mandelate	1789	0.681	1284	0.493	1304	0.497
Ideal $[Cu_3(BTC)_2]$	2137	0.820	1293	0.496	1293	0.496

Vibrational spectroscopy

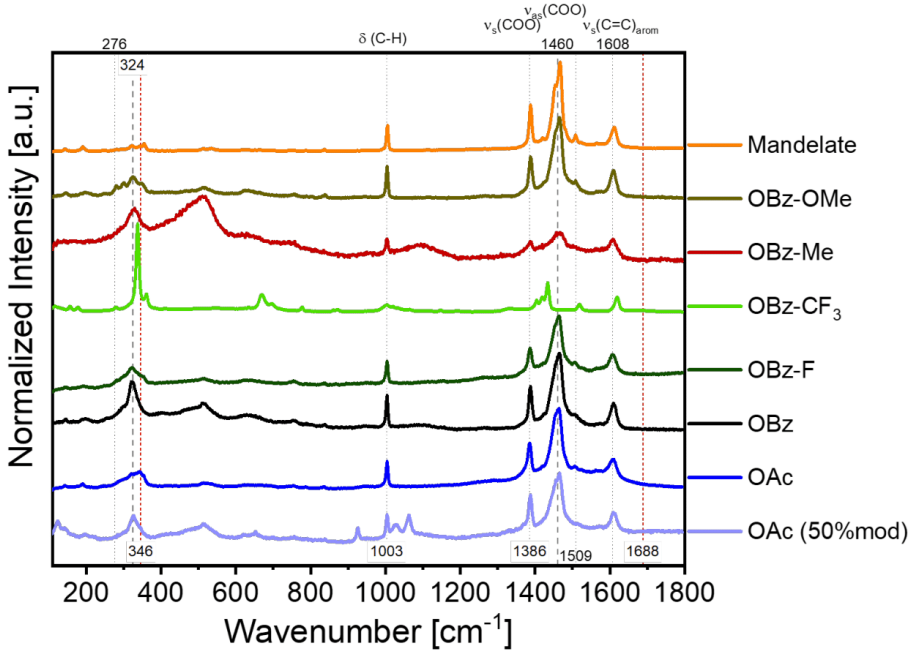

Figure S 22: Raman spectra of the whole $Ru^{II,II}$-HKUST-1 series indicate a generally identical bonding situation in all samples. However, the spectrum of OBz-CF_3 is dominated by strong signals arising from the respective modulator residues with the usually strong ν_{as}(COO) at 1460 cm^{-1} even not being visible. According to the absence of peaks around 1688 cm^{-1}, no free carboxylic acids are present in the samples.

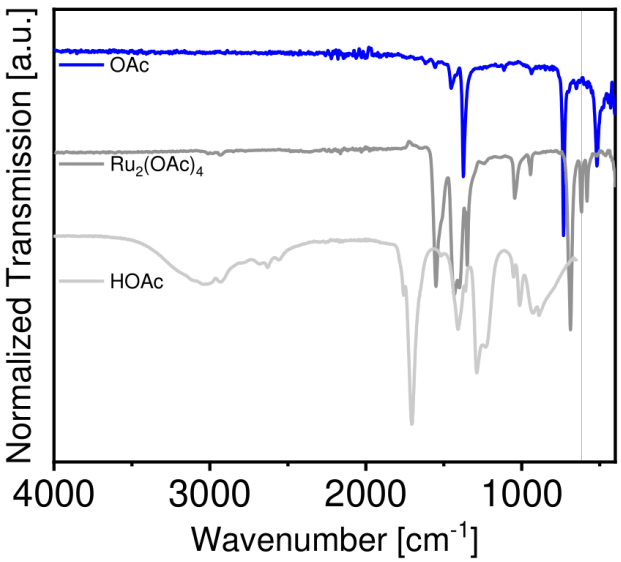

Figure S 23: Comparison of Ru-HKUST-1 (blue trace), the used OAc precursor (dark grey trace) and the free carboxylic acid (light grey trace). Vertical lines highlight vibration bands of the respective MOF sample which can not be assigned to the ideal MOF structure and thus, have to be associated with either precursor or modulator.

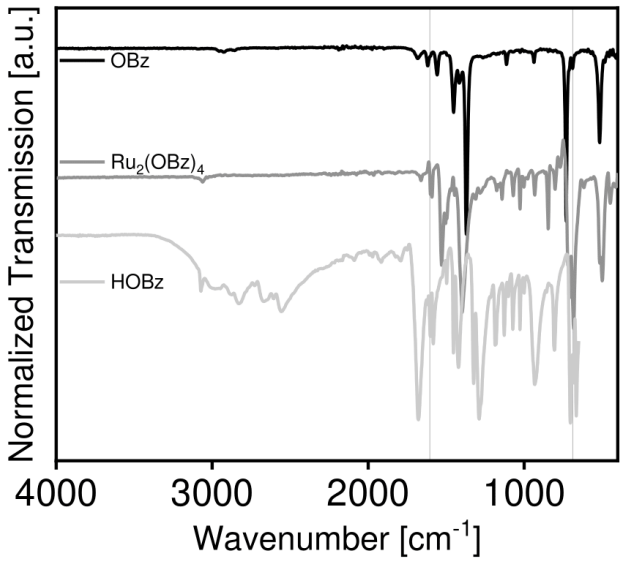

Figure S 24: Comparison of Ru-HKUST-1 (black trace), the used OBz precursor (dark grey trace) and the free carboxylic acid (light grey trace). Vertical lines highlight vibration bands of the respective MOF sample which can not be assigned to the ideal MOF structure and thus, have to be associated with either precursor or modulator.

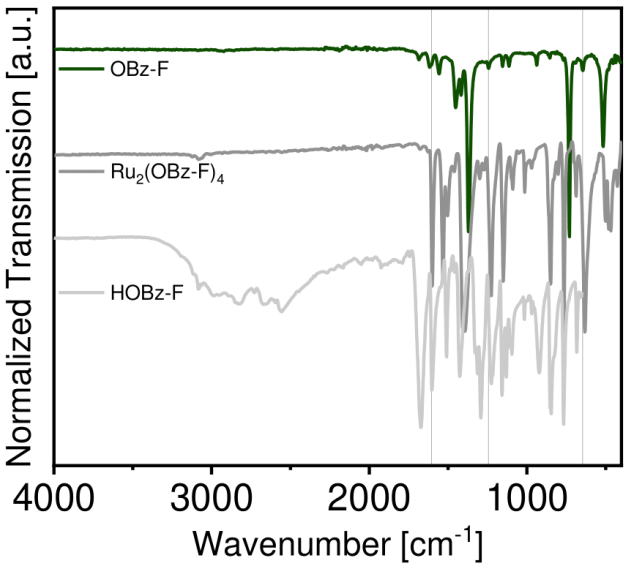

Figure S 25: Comparison of Ru-HKUST-1 (dark green trace), the used OBz-F precursor (dark grey trace) and the free carboxylic acid (light grey trace). Vertical lines highlight vibration bands of the respective MOF sample which can not be assigned to the ideal MOF structure and thus, have to be associated with either precursor or modulator.

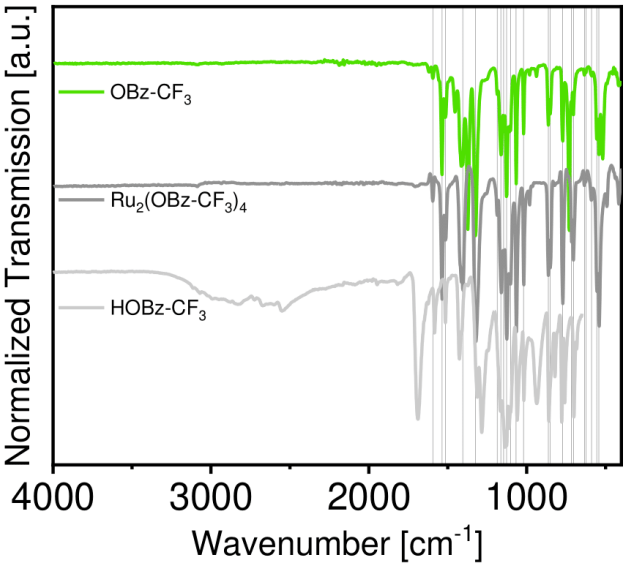

Figure S 26: Comparison of Ru-HKUST-1 (green trace), the used OBz-CF_3 precursor (dark grey trace) and the free carboxylic acid (light grey trace). Vertical lines highlight vibration bands of the respective MOF sample which can not be assigned to the ideal MOF structure and thus, have to be associated with either precursor or modulator. As compared to other samples of this series, the OBz-CF_3 spectra contain large amounts of residual precursor/modulator.

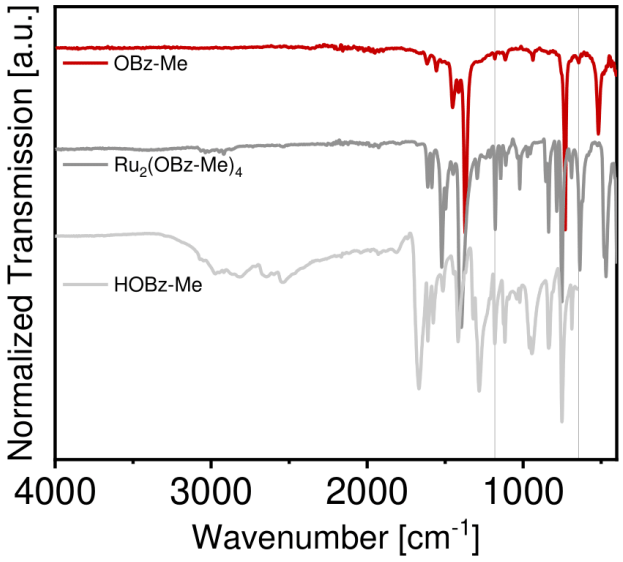

Figure S 27: Comparison of Ru-HKUST-1 (red trace), the used OBz-CF_3 precursor (dark grey trace) and the free carboxylic acid (light grey trace). Vertical lines highlight vibration bands of the respective MOF sample which can not be assigned to the ideal MOF structure and thus, have to be associated with either precursor or modulator.

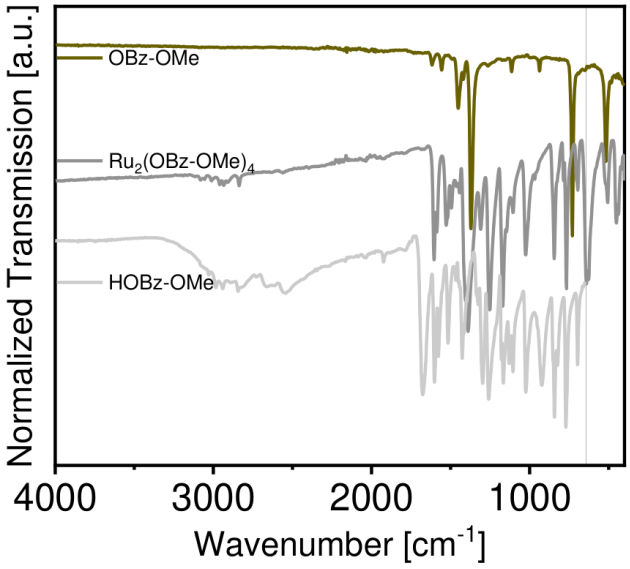

Figure S 28: Comparison of Ru-HKUST-1 (olive trace), the used OBz-CF_3 precursor (dark grey trace) and the free carboxylic acid (light grey trace). Vertical lines highlight vibration bands of the respective MOF sample which can not be assigned to the ideal MOF structure and thus, have to be associated with either precursor or modulator.

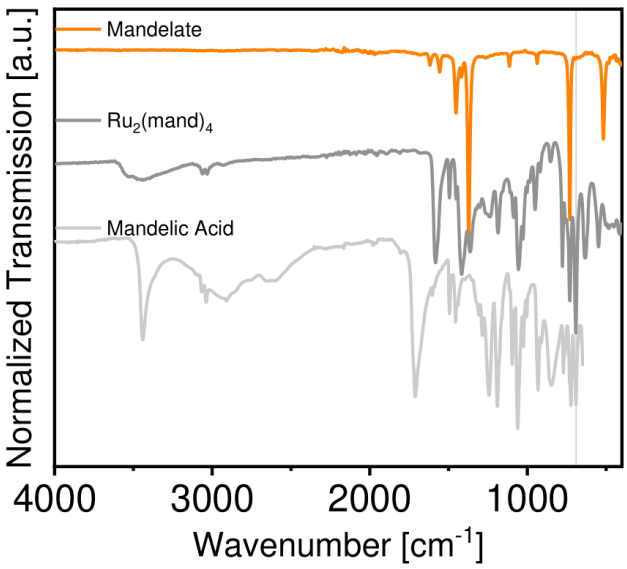

Figure S 29: Comparison of Ru-HKUST-1 (orange trace), the used OBz-CF_3 precursor (dark grey trace) and the free carboxylic acid (light grey trace). Vertical lines highlight vibration bands of the respective MOF sample which can not be assigned to the ideal MOF structure and thus, have to be associated with either precursor or modulator.

HR-TEM

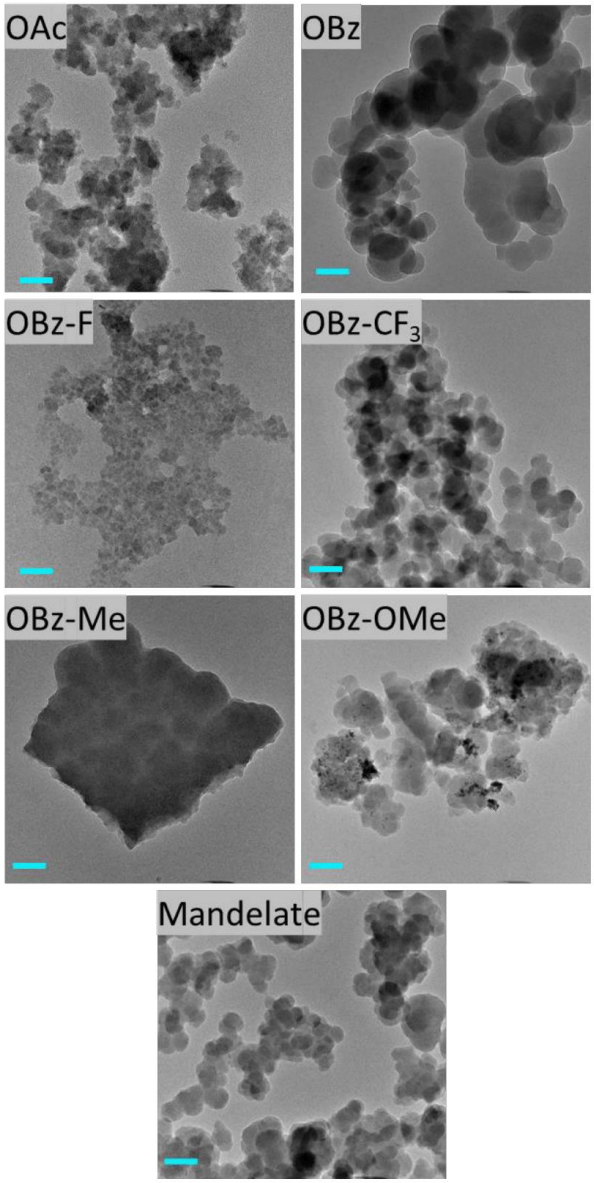

Figure S 30: HR-TEM images of all Ru-MOF samples. Blue scale bars represent 100 nm. The increased primary particle size particularly of the samples OBz, OBz-CF_3, OBz-Me and Mandelate is in line with results from FWHM analysis from PXRD patterns. The OAc and OBz-F samples contain few metal NPs while the OBz-OMe sample comprises higher amounts.

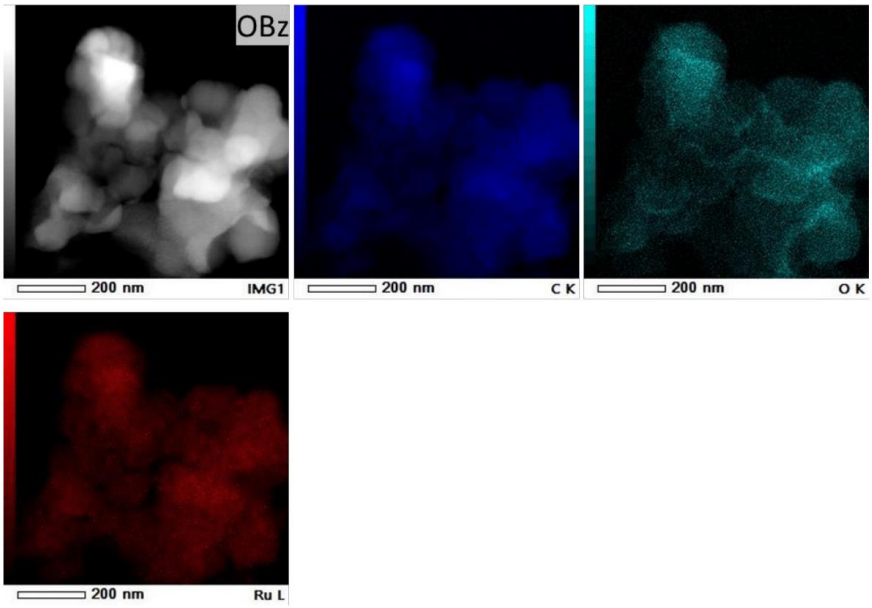

Figure S 31: A dark field STEM image of a representative particles of the OBz sample and corresponding EDS compositional maps of C, O and Ru indicates a homogeneous elemental distribution. Scale bars represent 200 nm.

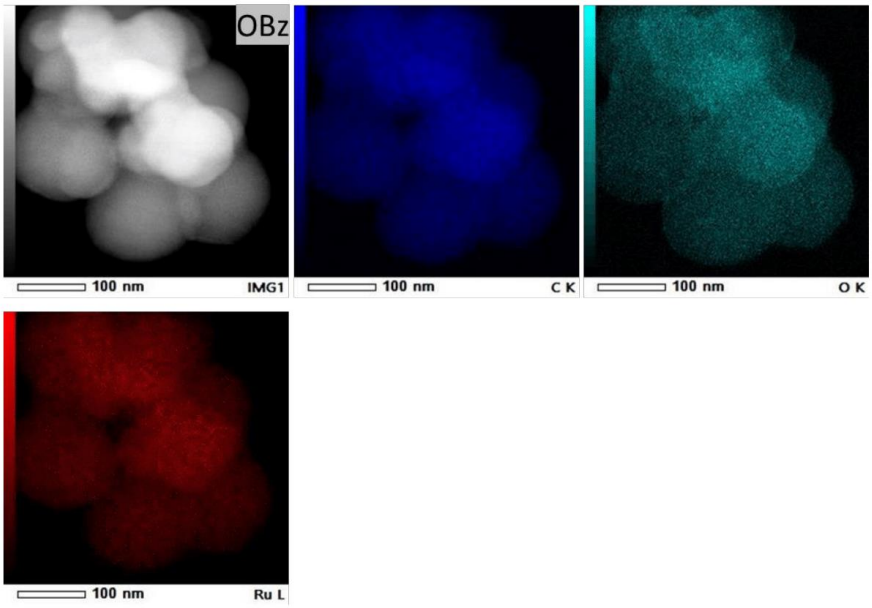

Figure S 32: A dark field STEM image of a representative particles of the OBz sample and corresponding EDS compositional maps of C, O and Ru indicates a homogeneous elemental distribution. Scale bars represent 100 nm.

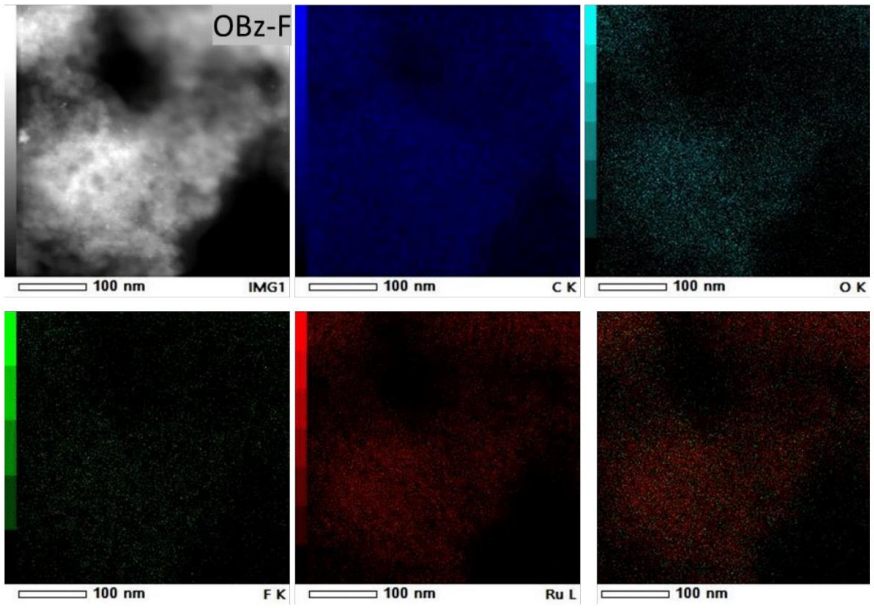

Figure S 33: A dark field STEM image of a representative particles of the OBz-F sample and corresponding EDS compositional maps of C, O and Ru indicates relatively homogeneous elemental distribution. Scale bars represent 100 nm. The bottom right image is an overlay of fluorine (green) and ruthenium (red). Due to the small particle size, clear conclusions on elemental inhomogeneities are difficult to draw.

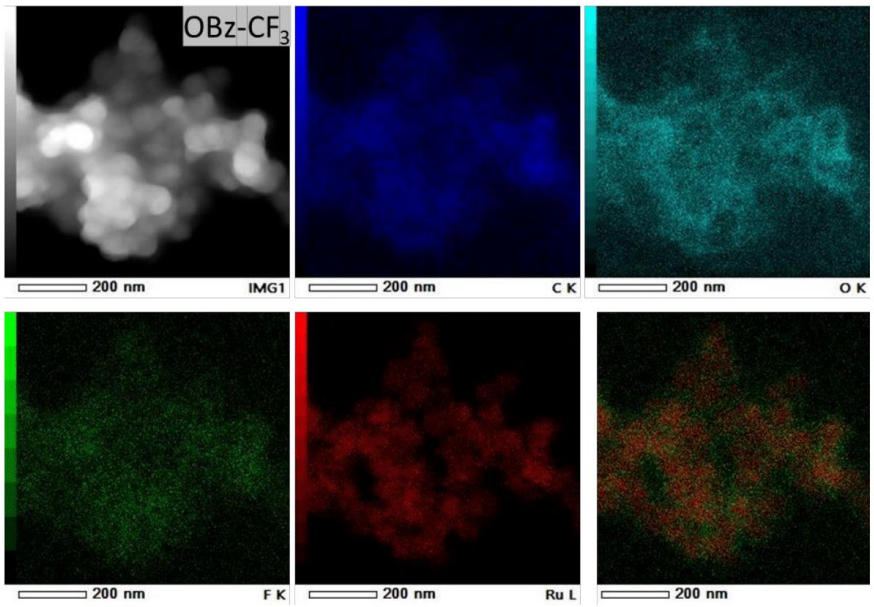

Figure S 34: A dark field STEM image of a representative particles of the OBz-CF_3 sample and corresponding EDS compositional maps of C, O, F and Ru and an overlay of F/Ru. Scale bars represent 200 nm. The bottom right image is an overlay of fluorine (green) and ruthenium (red). The images suggest the modulator to be preferentially located at the surface of the particles.

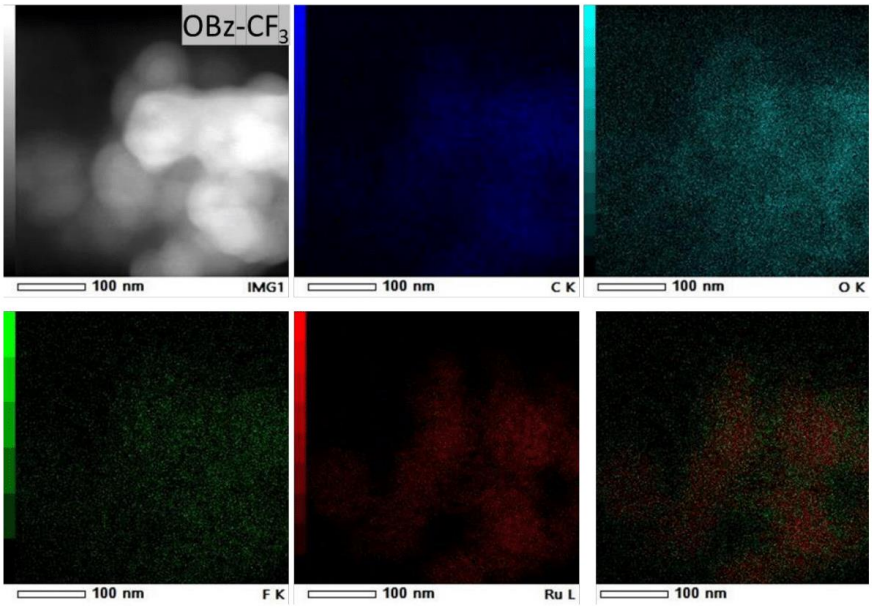

Figure S 35: A dark field STEM image of a representative particles of the OBz-CF_3 sample and corresponding EDS compositional maps of C, O, F and Ru and an overlay of F/Ru. Scale bars represent 100 nm. The bottom right image is an overlay of fluorine (green) and ruthenium (red). The images suggest the modulator to be preferentially located at the surface of the particles.

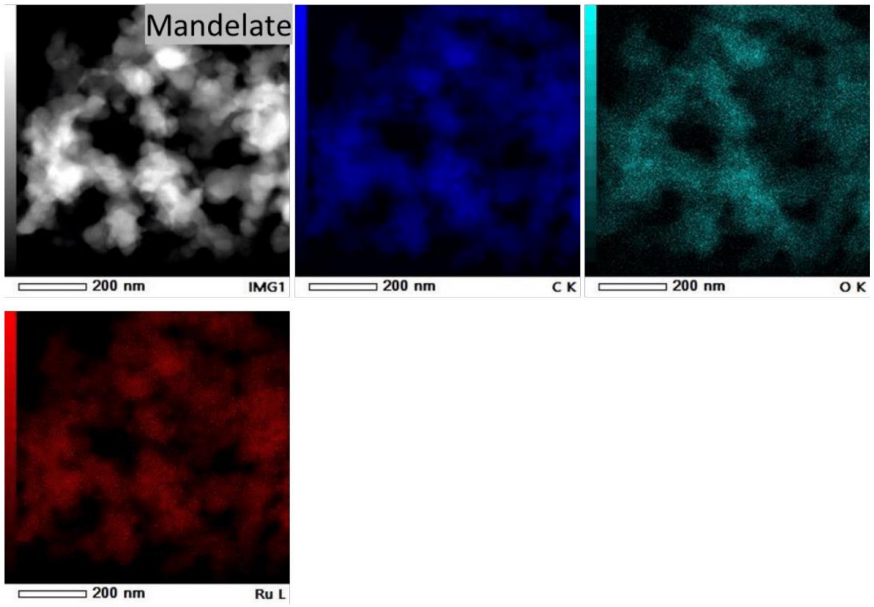

Figure S 36: A dark field STEM image of a representative particles of the mandelate-derived MOF sample and corresponding EDS compositional maps of C, O and Ru indicates a homogeneous elemental distribution. Scale bars represent 200 nm.

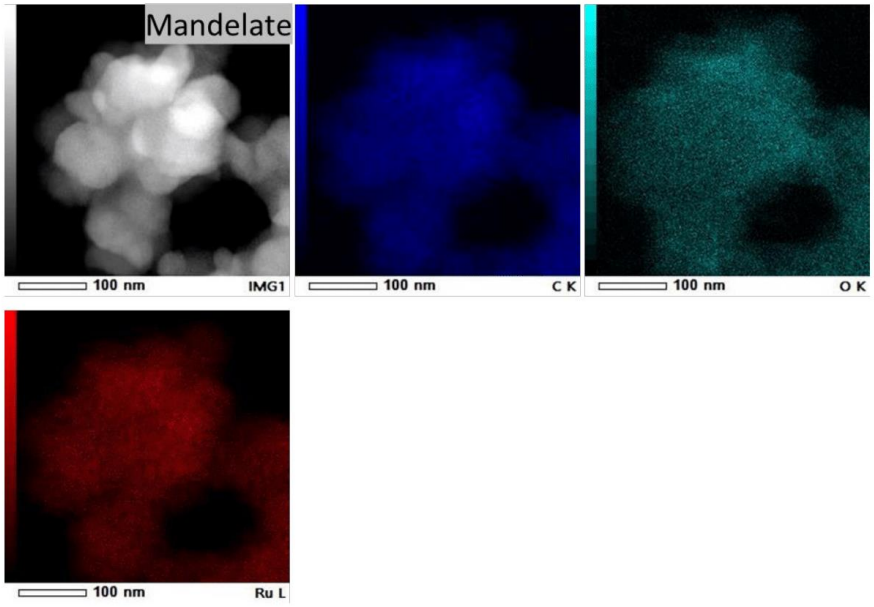

Figure S 37: A dark field STEM image of a representative particles of the mandelate-derived MOF sample and corresponding EDS compositional maps of C, O and Ru indicates a homogeneous elemental distribution. Scale bars represent 200 nm.

1. W. R. Heinz, T. Kratky, M. Drees, A. Wimmer, O. Tomanec, S. Günther, M. Schuster and R. A. Fischer, *Dalton Trans.*, 2019, **48**, 12031-12039.
2. A. J. Lindsay, G. Wilkinson, M. Motevalli and M. B. Hursthouse, *J. Chem. Soc., Dalton Trans.*, 1985, DOI: 10.1039/DT9850002321, 2321-2326.
3. R. W. Mitchell, A. Spencer and G. Wilkinson, *J. Chem. Soc., Dalton Trans.*, 1973, DOI: 10.1039/DT9730000846, 846-854.
4. F. A. Cotton, V. M. Miskowski and B. Zhong, *J. Am. Chem. Soc.*, 1989, **111**, 6177-6182.
5. V.F.Kuznetsov, H.Alper and G.P.A.Yap, CCDC 136234: Experimental Crystal Structure Determination, 2000, DOI: 10.5517/cc4krn2
6. A. J. Lindsay, G. Wilkinson, M. Motevalli and M. B. Hursthouse, *J. Chem. Soc., Dalton Trans.*, 1987, DOI: 10.1039/DT9870002723, 2723-2736.
7. M. Spohn, J. Strähle and W. Hiller, *Zeitschrift für Naturforschung*, 1986, **41b**, 541-547.
8. M. C. Barral, R. González-Prieto, R. Jiménez-Aparicio, J. L. Priego, M. R. Torres and F. A. Urbanos, *Inorg. Chim. Acta*, 2005, **358**, 217-221.
9. H. Miyasaka, N. Motokawa, R. Atsuumi, H. Kamo, Y. Asai and M. Yamashita, *Dalton Trans.*, 2011, **40**, 673-682.
10. Y. Sekine, K. H. Aliyah, T. Shimada, J. Zhang, W. Kosaka and H. Miyasaka, *Chem. Lett.*, 2018, **47**, 693-696.
11. D. S. Martin, R. A. Newman and L. M. Vlasnik, *Inorg. Chem.*, 1980, **19**, 3404-3407.
12. G. Vamvounis, J. F. Caplan, T. S. Cameron, K. N. Robertson and M. A. S. Aquino, *Inorg. Chim. Acta*, 2000, **304**, 87-98.
13. J. Liu, J. T. Culp, S. Natesakhawat, B. C. Bockrath, B. Zande, S. G. Sankar, G. Garberoglio and J. K. Johnson, *J. Phys. Chem. C*, 2007, **111**, 9305-9313.

Reprint Permissions

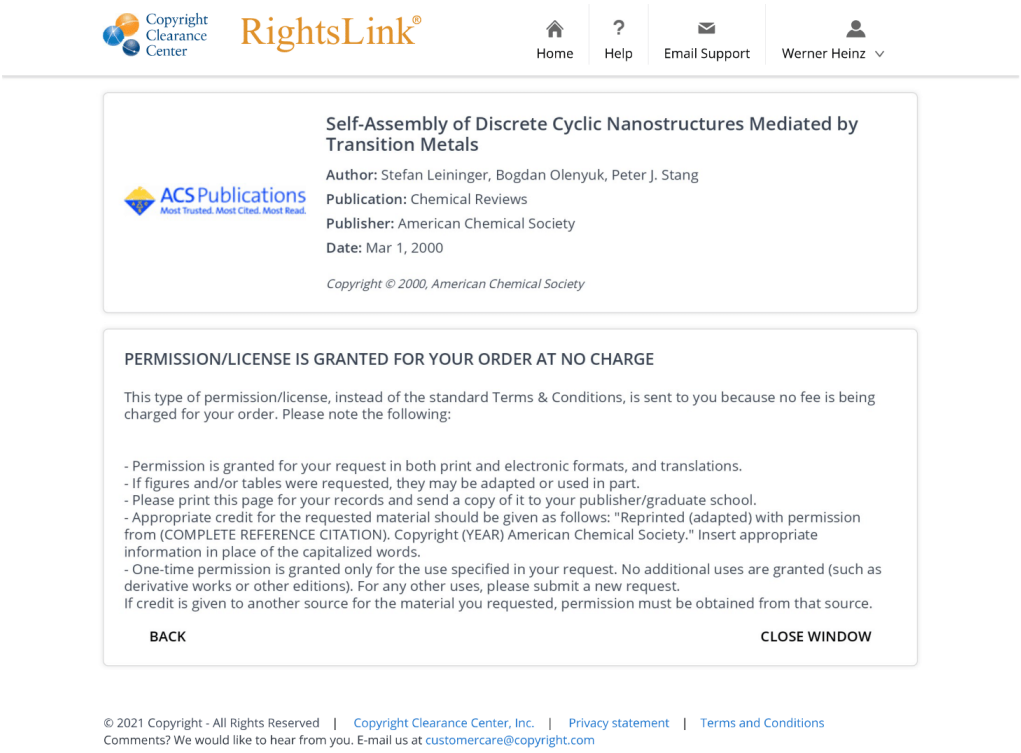

Copyright Clearance Center RightsLink®

Home | Help | Email Support | Werner Heinz

ACS Publications
Most Trusted. Most Cited. Most Read.

Self-Assembly of Discrete Cyclic Nanostructures Mediated by Transition Metals

Author: Stefan Leininger, Bogdan Olenyuk, Peter J. Stang
Publication: Chemical Reviews
Publisher: American Chemical Society
Date: Mar 1, 2000

Copyright © 2000, American Chemical Society

PERMISSION/LICENSE IS GRANTED FOR YOUR ORDER AT NO CHARGE

This type of permission/license, instead of the standard Terms & Conditions, is sent to you because no fee is being charged for your order. Please note the following:

- Permission is granted for your request in both print and electronic formats, and translations.
- If figures and/or tables were requested, they may be adapted or used in part.
- Please print this page for your records and send a copy of it to your publisher/graduate school.
- Appropriate credit for the requested material should be given as follows: "Reprinted (adapted) with permission from (COMPLETE REFERENCE CITATION). Copyright (YEAR) American Chemical Society." Insert appropriate information in place of the capitalized words.
- One-time permission is granted only for the use specified in your request. No additional uses are granted (such as derivative works or other editions). For any other uses, please submit a new request.

If credit is given to another source for the material you requested, permission must be obtained from that source.

BACK CLOSE WINDOW

THE AMERICAN ASSOCIATION FOR THE ADVANCEMENT OF SCIENCE LICENSE TERMS AND CONDITIONS

Jan 31, 2021

This Agreement between Werner Heinz ("You") and The American Association for the Advancement of Science ("The American Association for the Advancement of Science") consists of your license details and the terms and conditions provided by The American Association for the Advancement of Science and Copyright Clearance Center.

License Number	4999490942948
License date	Jan 31, 2021
Licensed Content Publisher	The American Association for the Advancement of Science
Licensed Content Publication	Science
Licensed Content Title	Systematic Design of Pore Size and Functionality in Isoreticular MOFs and Their Application in Methane Storage
Licensed Content Author	Mohamed Eddaoudi,Jaheon Kim,Nathaniel Rosi,David Vodak,Joseph Wachter,Michael O'Keeffe,Omar M. Yaghi
Licensed Content Date	Jan 18, 2002
Licensed Content Volume	295
Licensed Content Issue	5554
Volume number	295
Issue number	5554
Type of Use	Thesis / Dissertation
Requestor type	Scientist/individual at a research institution
Format	Print and electronic
Portion	Figure
Number of figures/tables	2
Title	Defects in Functional Porous Materials Ruthenium and Rhodium HKUST-1 Analogues as a Case Study for Precious Group Metal-Organic Frameworks - Synthesis, Characterization, Defect-Engineering and Catalysis
Institution name	Technical University of Munich
Expected presentation date	Feb 2021
Portions	Figure 1
	Werner Heinz

other than those specifically identified in your request above.

The following credit line must be printed along with the AAAS material: "From [Full Reference Citation]. Reprinted with permission from AAAS."

All required credit lines and notices must be visible any time a user accesses any part of the AAAS material and must appear on any printed copies and authorized user might make.

This permission does not apply to figures / photos / artwork or any other content or materials included in your work that are credited to non-AAAS sources. If the requested material is sourced to or references non-AAAS sources, you must obtain authorization from that source as well before using that material. You agree to hold harmless and indemnify AAAS against any claims arising from your use of any content in your work that is credited to non-AAAS sources.

If the AAAS material covered by this permission was published in Science during the years 1974 - 1994, you must also obtain permission from the author, who may grant or withhold permission, and who may or may not charge a fee if permission is granted. See original article for author's address. This condition does not apply to news articles.

The AAAS material may not be modified or altered except that figures and tables may be modified with permission from the author. Author permission for any such changes must be secured prior to your use.

Whenever possible, we ask that electronic uses of the AAAS material permitted herein include a hyperlink to the original work on AAAS's website (hyperlink may be embedded in the reference citation).

AAAS material reproduced in your work identified herein must not account for more than 30% of the total contents of that work.

AAAS must publish the full paper prior to use of any text.

AAAS material must not imply any endorsement by the American Association for the Advancement of Science.

This permission is not valid for the use of the AAAS and/or Science logos.

AAAS makes no representations or warranties as to the accuracy of any information contained in the AAAS material covered by this permission, including any warranties of

merchantability or fitness for a particular purpose.

If permission fees for this use are waived, please note that AAAS reserves the right to charge for reproduction of this material in the future.

Permission is not valid unless payment is received within sixty (60) days of the issuance of this permission. If payment is not received within this time period then all rights granted herein shall be revoked and this permission will be considered null and void.

In the event of breach of any of the terms and conditions herein or any of CCC's Billing and Payment terms and conditions, all rights granted herein shall be revoked and this permission will be considered null and void.

AAAS reserves the right to terminate this permission and all rights granted herein at its discretion, for any purpose, at any time. In the event that AAAS elects to terminate this permission, you will have no further right to publish, publicly perform, publicly display, distribute or otherwise use any matter in which the AAAS content had been included, and all fees paid hereunder shall be fully refunded to you. Notification of termination will be sent to the contact information as supplied by you during the request process and termination shall be immediate upon sending the notice. Neither AAAS nor CCC shall be liable for any costs, expenses, or damages you may incur as a result of the termination of this permission, beyond the refund noted above.

This Permission may not be amended except by written document signed by both parties.

The terms above are applicable to all permissions granted for the use of AAAS material. Below you will find additional conditions that apply to your particular type of use.

FOR A THESIS OR DISSERTATION
If you are using figure(s)/table(s), permission is granted for use in print and electronic versions of your dissertation or thesis. A full text article may be used in print versions only of a dissertation or thesis.

Permission covers the distribution of your dissertation or thesis on demand by ProQuest / UMI, provided the AAAS material covered by this permission remains in situ.

If you are an Original Author on the AAAS article being reproduced, please refer to your License to Publish for rules on reproducing your paper in a dissertation or thesis.

FOR JOURNALS:
Permission covers both print and electronic versions of your journal article, however the AAAS material may not be used in any manner other than within the context of your article.

FOR BOOKS/TEXTBOOKS:
If this license is to reuse figures/tables, then permission is granted for non-exclusive world rights in all languages in both print and electronic formats (electronic formats are defined below).

If this license is to reuse a text excerpt or a full text article, then permission is granted for non-exclusive world rights in English only. You have the option of securing either print or electronic rights or both, but electronic rights are not automatically granted and do garner additional fees. Permission for translations of text excerpts or full text articles into other languages must be obtained separately.

Licenses granted for use of AAAS material in electronic format books/textbooks are valid only in cases where the electronic version is equivalent to or substitutes for the print version of the book/textbook. The AAAS material reproduced as permitted herein must remain in situ and must not be exploited separately (for example, if permission covers the use of a full text article, the article may not be offered for access or for purchase as a stand-alone unit), except in the case of permitted textbook companions as noted below.

You must include the following notice in any electronic versions, either adjacent to the reprinted AAAS material or in the terms and conditions for use of your electronic products: "Readers may view, browse, and/or download material for temporary copying purposes only, provided these uses are for noncommercial personal purposes. Except as provided by law, this material may not be further reproduced, distributed, transmitted, modified, adapted, performed, displayed, published, or sold in whole or in part, without prior written permission from the publisher."

If your book is an academic textbook, permission covers the following companions to your textbook, provided such companions are distributed only in conjunction with your textbook at no additional cost to the user:

- Password-protected website
- Instructor's image CD/DVD and/or PowerPoint resource
- Student CD/DVD

All companions must contain instructions to users that the AAAS material may be used for non-commercial, classroom purposes only. Any other uses require the prior written permission from AAAS.

If your license is for the use of AAAS Figures/Tables, then the electronic rights granted herein permit use of the Licensed Material in any Custom Databases that you distribute the electronic versions of your textbook through, so long as the Licensed Material remains within the context of a chapter of the title identified in your request and cannot be downloaded by a user as an independent image file.

Rights also extend to copies/files of your Work (as described above) that you are required to provide for use by the visually and/or print disabled in compliance with state and federal laws.

This permission only covers a single edition of your work as identified in your request.

FOR NEWSLETTERS:
Permission covers print and/or electronic versions, provided the AAAS material reproduced as permitted herein remains in situ and is not exploited separately (for example, if permission covers the use of a full text article, the article may not be offered for access or for purchase as a stand-alone unit)

FOR ANNUAL REPORTS:
Permission covers print and electronic versions provided the AAAS material reproduced as permitted herein remains in situ and is not exploited separately (for example, if permission covers the use of a full text article, the article may not be offered for access or for purchase as a stand-alone unit)

FOR PROMOTIONAL/MARKETING USES:
Permission covers the use of AAAS material in promotional or marketing pieces such as information packets, media kits, product slide kits, brochures, or flyers limited to a single print run. The AAAS Material may not be used in any manner which implies endorsement or promotion by the American Association for the Advancement of Science (AAAS) or Science of any product or service. AAAS does not permit the reproduction of its name, logo or text on promotional literature.

If permission to use a full text article is permitted, The Science article covered by this permission must not be altered in any way. No additional printing may be set onto an article copy other than the copyright credit line required above. Any alterations must be approved in advance and in writing by AAAS. This includes, but is not limited to, the placement of sponsorship identifiers, trademarks, logos, rubber stamping or self-adhesive stickers onto the article copies.

Additionally, article copies must be a freestanding part of any information package (i.e. media kit) into which they are inserted. They may not be physically attached to anything, such as an advertising insert, or have anything attached to them, such as a sample product. Article copies must be easily removable from any kits or informational packages in which they are used. The only exception is that article copies may be inserted into three-ring binders.

FOR CORPORATE INTERNAL USE:
The AAAS material covered by this permission may not be altered in any way. No additional printing may be set onto an article copy other than the required credit line. Any alterations must be approved in advance and in writing by AAAS. This includes, but is not limited to the placement of sponsorship identifiers, trademarks, logos, rubber stamping or self-adhesive stickers onto article copies.

If you are making article copies, copies are restricted to the number indicated in your request and must be distributed only to internal employees for internal use.

If you are using AAAS Material in Presentation Slides, the required credit line must be visible on the slide where the AAAS material will be reprinted

If you are using AAAS Material on a CD, DVD, Flash Drive, or the World Wide Web, you must include the following notice in any electronic versions, either adjacent to the reprinted AAAS material or in the terms and conditions for use of your electronic products: "Readers may view, browse, and/or download material for temporary copying purposes only, provided these uses are for noncommercial personal purposes. Except as provided by law, this material may not be further reproduced, distributed, transmitted, modified, adapted, performed, displayed, published, or sold in whole or in part, without prior written permission from the publisher." Access to any such CD, DVD, Flash Drive or Web page must be restricted to your organization's employees only.

FOR CME COURSE and SCIENTIFIC SOCIETY MEETINGS:
Permission is restricted to the particular Course, Seminar, Conference, or Meeting indicated in your request. If this license covers a text excerpt or a Full Text Article, access to the reprinted AAAS material must be restricted to attendees of your event only (if you have been granted electronic rights for use of a full text article on your website, your website must be password protected, or access restricted so that only attendees can access the content on your site).

If you are using AAAS Material on a CD, DVD, Flash Drive, or the World Wide Web, you must include the following notice in any electronic versions, either adjacent to the reprinted AAAS material or in the terms and conditions for use of your electronic products: "Readers may view, browse, and/or download material for temporary copying purposes only, provided these uses are for noncommercial personal purposes. Except as provided by law, this material may not be further reproduced, distributed, transmitted, modified, adapted, performed, displayed, published, or sold in whole or in part, without prior written permission from the publisher."

FOR POLICY REPORTS:
These rights are granted only to non-profit organizations and/or government agencies. Permission covers print and electronic versions of a report, provided the required credit line appears in both versions and provided the AAAS material reproduced as permitted herein remains in situ and is not exploited separately.

FOR CLASSROOM PHOTOCOPIES:
Permission covers distribution in print copy format only. Article copies must be freestanding and not part of a course pack. They may not be physically attached to anything or have anything attached to them.

FOR COURSEPACKS OR COURSE WEBSITES:
These rights cover use of the AAAS material in one class at one institution. Permission is valid only for a single semester after which the AAAS material must be removed from the Electronic Course website, unless new permission is obtained for an additional semester. If the material is to be distributed online, access must be restricted to students and instructors enrolled in that particular course by some means of password or access control.

FOR WEBSITES:
You must include the following notice in any electronic versions, either adjacent to the reprinted AAAS material or in the terms and conditions for use of your electronic products: "Readers may view, browse, and/or download material for temporary copying purposes only, provided these uses are for noncommercial personal purposes. Except as provided by law, this material may not be further reproduced, distributed, transmitted, modified, adapted, performed, displayed, published, or sold in whole or in part, without prior written permission from the publisher."

Permissions for the use of Full Text articles on third party websites are granted on a case by case basis and only in cases where access to the AAAS Material is restricted by some means of password or access control. Alternately, an E-Print may be purchased through our reprints department (brocheleau@rockwaterinc.com).

REGARDING FULL TEXT ARTICLE USE ON THE WORLD WIDE WEB IF YOU ARE AN 'ORIGINAL AUTHOR' OF A SCIENCE PAPER

If you chose "Original Author" as the Requestor Type, you are warranting that you are one of authors listed on the License Agreement as a "Licensed content author" or that you are acting on that author's behalf to use the Licensed content in a new work that one of the authors listed on the License Agreement as a "Licensed content author" has written.

Original Authors may post the 'Accepted Version' of their full text article on their personal or on their University website and not on any other website. The 'Accepted Version' is the version of the paper accepted for publication by AAAS including changes resulting from peer review but prior to AAAS's copy editing and production (in other words not the AAAS published version).

FOR MOVIES / FILM / TELEVISION:
Permission is granted to use, record, film, photograph, and/or tape the AAAS material in connection with your program/film and in any medium your program/film may be shown or heard, including but not limited to broadcast and cable television, radio, print, world wide web, and videocassette.

The required credit line should run in the program/film's end credits.

FOR MUSEUM EXHIBITIONS:
Permission is granted to use the AAAS material as part of a single exhibition for the duration of that exhibit. Permission for use of the material in promotional materials for the exhibit must be cleared separately with AAAS (please contact us at permissions@aaas.org).

FOR TRANSLATIONS:
Translation rights apply only to the language identified in your request summary above.

The following disclaimer must appear with your translation, on the first page of the article, after the credit line: "This translation is not an official translation by AAAS staff, nor is it endorsed by AAAS as accurate. In crucial matters, please refer to the official English-language version originally published by AAAS."

FOR USE ON A COVER:
Permission is granted to use the AAAS material on the cover of a journal issue, newsletter issue, book, textbook, or annual report in print and electronic formats provided the AAAS material reproduced as permitted herein remains in situ and is not exploited separately

By using the AAAS Material identified in your request, you agree to abide by all the terms and conditions herein.

Questions about these terms can be directed to the AAAS Permissions department permissions@aaas.org.

Other Terms and Conditions:

v 2

Questions? customercare@copyright.com or +1-855-239-3415 (toll free in the US) or +1-978-646-2777.

SPRINGER NATURE LICENSE
TERMS AND CONDITIONS

Jan 31, 2021

This Agreement between Werner Heinz ("You") and Springer Nature ("Springer Nature") consists of your license details and the terms and conditions provided by Springer Nature and Copyright Clearance Center.

License Number	4999500028301
License date	Jan 31, 2021
Licensed Content Publisher	Springer Nature
Licensed Content Publication	Nature Chemistry
Licensed Content Title	Soft porous crystals
Licensed Content Author	Satoshi Horike et al
Licensed Content Date	Nov 23, 2009
Type of Use	Thesis/Dissertation
Requestor type	academic/university or research institute
Format	print and electronic
Portion	figures/tables/illustrations
Number of figures/tables /illustrations	1
High-res required	no
Will you be translating?	no
Circulation/distribution	1 - 29
Author of this Springer Nature content	no
Title	Defects in Functional Porous Materials Ruthenium and Rhodium HKUST-1 Analogues as a Case Study for Precious Group Metal-Organic Frameworks - Synthesis, Characterization, Defect-Engineering and Catalysis
Institution name	Technical University of Munich
Expected presentation date	Feb 2021
Portions	Figure 1
	Werner Heinz

licence to reproduce the Licensed Material for the purpose specified in your order only. Licences are granted for the specific use requested in the order and for no other use, subject to the conditions below.

1. 2. The Licensor warrants that it has, to the best of its knowledge, the rights to license reuse of the Licensed Material. However, you should ensure that the material you are requesting is original to the Licensor and does not carry the copyright of another entity (as credited in the published version).

1. 3. If the credit line on any part of the material you have requested indicates that it was reprinted or adapted with permission from another source, then you should also seek permission from that source to reuse the material.

2. Scope of Licence

2. 1. You may only use the Licensed Content in the manner and to the extent permitted by these Ts&Cs and any applicable laws.

2. 2. A separate licence may be required for any additional use of the Licensed Material, e.g. where a licence has been purchased for print only use, separate permission must be obtained for electronic re-use. Similarly, a licence is only valid in the language selected and does not apply for editions in other languages unless additional translation rights have been granted separately in the licence. Any content owned by third parties are expressly excluded from the licence.

2. 3. Similarly, rights for additional components such as custom editions and derivatives require additional permission and may be subject to an additional fee. Please apply to Journalpermissions@springernature.com/bookpermissions@springernature.com for these rights.

2. 4. Where permission has been granted **free of charge** for material in print, permission may also be granted for any electronic version of that work, provided that the material is incidental to your work as a whole and that the electronic version is essentially equivalent to, or substitutes for, the print version.

2. 5. An alternative scope of licence may apply to signatories of the STM Permissions Guidelines, as amended from time to time.

3. Duration of Licence

3. 1. A licence for is valid from the date of purchase ('Licence Date') at the end of the relevant period in the below table:

Scope of Licence	Duration of Licence
Post on a website	12 months
Presentations	12 months
Books and journals	Lifetime of the edition in the language purchased

4. Acknowledgement

4. 1. The Licensor's permission must be acknowledged next to the Licenced Material in print. In electronic form, this acknowledgement must be visible at the same time as the figures/tables/illustrations or abstract, and must be hyperlinked to the journal/book's homepage. Our required acknowledgement format is in the Appendix below.

5. Restrictions on use

5. 1. Use of the Licensed Material may be permitted for incidental promotional use and minor editing privileges e.g. minor adaptations of single figures, changes of format, colour and/or style where the adaptation is credited as set out in Appendix 1 below. Any other changes including but not limited to, cropping, adapting, omitting material that affect the meaning, intention or moral rights of the author are strictly prohibited.

5. 2. You must not use any Licensed Material as part of any design or trademark.

5. 3. Licensed Material may be used in Open Access Publications (OAP) before publication by Springer Nature, but any Licensed Material must be removed from OAP sites prior to final publication.

6. Ownership of Rights

6. 1. Licensed Material remains the property of either Licensor or the relevant third party and any rights not explicitly granted herein are expressly reserved.

7. Warranty

IN NO EVENT SHALL LICENSOR BE LIABLE TO YOU OR ANY OTHER PARTY OR ANY OTHER PERSON OR FOR ANY SPECIAL, CONSEQUENTIAL, INCIDENTAL OR INDIRECT DAMAGES, HOWEVER CAUSED, ARISING OUT OF OR IN CONNECTION WITH THE DOWNLOADING, VIEWING OR USE OF THE MATERIALS REGARDLESS OF THE FORM OF ACTION, WHETHER FOR BREACH OF CONTRACT, BREACH OF WARRANTY, TORT, NEGLIGENCE, INFRINGEMENT OR OTHERWISE (INCLUDING, WITHOUT LIMITATION, DAMAGES BASED ON LOSS OF PROFITS, DATA, FILES, USE, BUSINESS OPPORTUNITY OR CLAIMS OF THIRD PARTIES), AND
WHETHER OR NOT THE PARTY HAS BEEN ADVISED OF THE POSSIBILITY OF SUCH DAMAGES. THIS LIMITATION SHALL APPLY NOTWITHSTANDING ANY FAILURE OF ESSENTIAL PURPOSE OF ANY LIMITED REMEDY PROVIDED HEREIN.

8. Limitations

8. 1. ***BOOKS ONLY:*** Where **'reuse in a dissertation/thesis'** has been selected the following terms apply: Print rights of the final author's accepted manuscript (for clarity, NOT the published version) for up to 100 copies, electronic rights for use only on a personal website or institutional repository as defined by the Sherpa guideline (www.sherpa.ac.uk/romeo/).

8. 2. For content reuse requests that qualify for permission under the STM Permissions Guidelines, which may be updated from time to time, the STM Permissions Guidelines supersede the terms and conditions contained in this licence.

9. Termination and Cancellation

9. 1. Licences will expire after the period shown in Clause 3 (above).

9. 2. Licensee reserves the right to terminate the Licence in the event that payment is not received in full or if there has been a breach of this agreement by you.

Appendix 1 — Acknowledgements:

For Journal Content:
Reprinted by permission from [**the Licensor**]: [**Journal Publisher** (e.g. Nature/Springer/Palgrave)] [**JOURNAL NAME**] [**REFERENCE CITATION** (Article name, Author(s) Name), [**COPYRIGHT**] (year of publication)

For **Advance Online Publication papers:**
Reprinted by permission from [**the Licensor**]: [**Journal Publisher** (e.g. Nature/Springer/Palgrave)] [**JOURNAL NAME**] [**REFERENCE CITATION** (Article name, Author(s) Name), [**COPYRIGHT**] (year of publication), advance online publication, day month year (doi: 10.1038/sj.[JOURNAL ACRONYM].)

For Adaptations/Translations:
Adapted/Translated by permission from [**the Licensor**]: [**Journal Publisher** (e.g. Nature/Springer/Palgrave)] [**JOURNAL NAME**] [**REFERENCE CITATION** (Article name, Author(s) Name), [**COPYRIGHT**] (year of publication)

Note: For any republication from the British Journal of Cancer, the following credit line style applies:

Reprinted/adapted/translated by permission from [**the Licensor**]: on behalf of Cancer Research UK: : [**Journal Publisher** (e.g. Nature/Springer/Palgrave)] [**JOURNAL NAME**] [**REFERENCE CITATION** (Article name, Author(s) Name), [**COPYRIGHT**] (year of publication)

For **Advance Online Publication** papers:
Reprinted by permission from The [**the Licensor**]: on behalf of Cancer Research UK: [**Journal Publisher** (e.g. Nature/Springer/Palgrave)] [**JOURNAL NAME**] [**REFERENCE CITATION** (Article name, Author(s) Name), [**COPYRIGHT**] (year of publication), advance online publication, day month year (doi: 10.1038/sj.[JOURNAL ACRONYM])

For Book content:
Reprinted/adapted by permission from [**the Licensor**]: [**Book Publisher** (e.g. Palgrave Macmillan, Springer etc) [**Book Title**] by [**Book author**(s)] [**COPYRIGHT**] (year of publication)

Other Conditions:

Version 1.3

Questions? customercare@copyright.com or +1-855-239-3415 (toll free in the US) or +1-978-646-2777.

Copyright Clearance Center Marketplace™

Royal Society of Chemistry - License Terms and Conditions

This is a License Agreement between Werner Heinz ("You") and Royal Society of Chemistry ("Publisher") provided by Copyright Clearance Center ("CCC"). The license consists of your order details, the terms and conditions provided by Royal Society of Chemistry, and the CCC terms and conditions.

All payments must be made in full to CCC.

Order Date	31-Jan-2021	Type of Use	Republish in a thesis/dissertation
Order license ID	1094352-1		
ISSN	1460-4744	Publisher	ROYAL SOCIETY OF CHEMISTRY
		Portion	Image/photo/illustration

LICENSED CONTENT

Publication Title	Chemical Society reviews	Country	United Kingdom of Great Britain and Northern Ireland
Author/Editor	Royal Society of Chemistry (Great Britain)	Rightsholder	Royal Society of Chemistry
Date	01/01/1972	Publication Type	e-Journal
Language	English	URL	http://www.rsc.org/csr

REQUEST DETAILS

Portion Type	Image/photo/illustration	Distribution	Worldwide
Number of images / photos / illustrations	1	Translation	Original language of publication
Format (select all that apply)	Print, Electronic	Copies for the disabled?	No
Who will republish the content?	Academic institution	Minor editing privileges?	No
		Incidental promotional use?	No
Duration of Use	Life of current edition	Currency	EUR
Lifetime Unit Quantity	Up to 499		
Rights Requested	Main product		

NEW WORK DETAILS

Title	Defects in Functional Porous Materials Ruthenium and Rhodium HKUST-1 Analogues as Case Study for Precious Group Metal-Organic Frameworks - Synthesis, Characterization, Defect-Engineering and Catalysis	Institution name	Technical University of Munich
		Expected presentation date	2021-02-28
Instructor name	Werner Heinz		

ADDITIONAL DETAILS

Order reference number	N/A	The requesting person / organization to appear on the license	Werner Heinz

REUSE CONTENT DETAILS

Title, description or numeric reference of the portion(s)	Scheme 1	Title of the article/chapter the portion is from	A historical overview of the activation and porosity of metal–organic frameworks
Editor of portion(s)	N/A		
Volume of serial or monograph	N/A	Author of portion(s)	Royal Society of Chemistry (Great Britain)
Page or page range of portion	7	Issue, if republishing an article from a serial	N/A

Publication date of portion 1972-01-01

CCC Republication Terms and Conditions

1. Description of Service; Defined Terms. This Republication License enables the User to obtain licenses for republication of one or more copyrighted works as described in detail on the relevant Order Confirmation (the "Work(s)"). Copyright Clearance Center, Inc. ("CCC") grants licenses through the Service on behalf of the rightsholder identified on the Order Confirmation (the "Rightsholder"). "Republication", as used herein, generally means the inclusion of a Work, in whole or in part, in a new work or works, also as described on the Order Confirmation. "User", as used herein, means the person or entity making such republication.

2. The terms set forth in the relevant Order Confirmation, and any terms set by the Rightsholder with respect to a particular Work, govern the terms of use of Works in connection with the Service. By using the Service, the person transacting for a republication license on behalf of the User represents and warrants that he/she/it (a) has been duly authorized by the User to accept, and hereby does accept, all such terms and conditions on behalf of User, and (b) shall inform User of all such terms and conditions. In the event such person is a "freelancer" or other third party independent of User and CCC, such party shall be deemed jointly a "User" for purposes of these terms and conditions. In any event, User shall be deemed to have accepted and agreed to all such terms and conditions if User republishes the Work in any fashion.

3. Scope of License; Limitations and Obligations.

    3.1. All Works and all rights therein, including copyright rights, remain the sole and exclusive property of the Rightsholder. The license created by the exchange of an Order Confirmation (and/or any invoice) and payment by User of the full amount set forth on that document includes only those rights expressly set forth in the Order Confirmation and in these terms and conditions, and conveys no other rights in the Work(s) to User. All rights not expressly granted are hereby reserved.

    3.2. General Payment Terms: You may pay by credit card or through an account with us payable at the end of the month. If you and we agree that you may establish a standing account with CCC, then the following terms apply: Remit Payment to: Copyright Clearance Center, 29118 Network Place, Chicago, IL 60673-1291. Payments Due: Invoices are payable upon their delivery to you (or upon our notice to you that they are available to you for downloading). After 30 days, outstanding amounts will be subject to a service charge of 1-1/2% per month or, if less, the maximum rate allowed by applicable law. Unless otherwise specifically set forth in the Order Confirmation or in a separate written agreement signed by CCC, invoices are due and payable on "net 30" terms. While User may exercise the rights licensed immediately upon issuance of the Order Confirmation, the license is automatically revoked and is null and void, as if it had never been issued, if complete payment for the license is not received on a timely basis either from User directly or through a payment agent, such as a credit card company.

    3.3. Unless otherwise provided in the Order Confirmation, any grant of rights to User (i) is "one-time" (including the editions and product family specified in the license), (ii) is non-exclusive and non-transferable and (iii) is subject to any and all limitations and restrictions (such as, but not limited to, limitations on duration of use or circulation) included in the Order Confirmation or invoice and/or in these terms and conditions. Upon completion of the licensed use, User shall either secure a new permission for further use of the Work(s) or immediately cease any new use of the Work(s) and shall render inaccessible (such as by deleting or by removing or severing links or other locators) any further copies of the Work (except for copies printed on paper in accordance with this license and still in User's stock at the end of such period).

    3.4. In the event that the material for which a republication license is sought includes third party materials (such as photographs, illustrations, graphs, inserts and similar materials) which are identified in such material as having been used by permission, User is responsible for identifying, and seeking separate licenses (under this Service or otherwise) for, any of such third party materials; without a separate license, such third party materials may not be used.

    3.5. Use of proper copyright notice for a Work is required as a condition of any license granted under the Service. Unless otherwise provided in the Order Confirmation, a proper copyright notice will read substantially as follows: "Republished with permission of [Rightsholder's name], from [Work's title, author, volume, edition number and year of copyright]; permission conveyed through Copyright Clearance Center, Inc. " Such notice must be provided in a reasonably legible font size and must be placed either immediately adjacent to the Work as used (for example, as part of a by-line or footnote but not as a separate electronic link) or in the place where substantially all other credits or notices for the new work containing the republished Work are located. Failure to include the required notice results in loss to the Rightsholder and CCC, and the User shall be liable to pay liquidated damages for each such failure equal to twice the use fee specified in the Order Confirmation, in addition to the use fee itself and any other fees and charges specified.

    3.6. User may only make alterations to the Work if and as expressly set forth in the Order Confirmation. No Work may be used in any way that is defamatory, violates the rights of third parties (including such third parties' rights of copyright, privacy, publicity, or other tangible or intangible property), or is otherwise illegal, sexually explicit or obscene. In addition, User may not conjoin a Work with any other material that may result in damage to the reputation of the Rightsholder. User agrees to inform CCC if it becomes aware of any infringement of any rights in a Work and to cooperate with any reasonable request of CCC or the Rightsholder in connection therewith.

4. Indemnity. User hereby indemnifies and agrees to defend the Rightsholder and CCC, and their respective employees and directors, against all claims, liability, damages, costs and expenses, including legal fees and expenses, arising out of any use of a Work beyond the scope of the rights granted herein, or any use of a Work which has been altered in any unauthorized way by User, including claims of defamation or infringement of rights of copyright, publicity, privacy or other tangible or intangible property.

5. Limitation of Liability. UNDER NO CIRCUMSTANCES WILL CCC OR THE RIGHTSHOLDER BE LIABLE FOR ANY DIRECT, INDIRECT, CONSEQUENTIAL OR INCIDENTAL DAMAGES (INCLUDING WITHOUT LIMITATION DAMAGES FOR LOSS OF BUSINESS PROFITS OR INFORMATION, OR FOR BUSINESS INTERRUPTION) ARISING OUT OF THE USE OR INABILITY TO USE A WORK, EVEN IF ONE OF THEM HAS BEEN ADVISED OF THE POSSIBILITY OF SUCH DAMAGES. In any event, the total liability of the Rightsholder and CCC (including their respective employees and directors) shall not exceed the total amount actually paid by User for this license. User assumes full liability for the actions and omissions of its principals, employees, agents, affiliates, successors and assigns.

6. Limited Warranties. THE WORK(S) AND RIGHT(S) ARE PROVIDED "AS IS". CCC HAS THE RIGHT TO GRANT TO USER THE RIGHTS GRANTED IN THE ORDER CONFIRMATION DOCUMENT. CCC AND THE RIGHTSHOLDER DISCLAIM ALL OTHER WARRANTIES RELATING TO THE WORK(S) AND RIGHT(S), EITHER EXPRESS OR IMPLIED, INCLUDING WITHOUT LIMITATION IMPLIED WARRANTIES OF MERCHANTABILITY OR FITNESS FOR A PARTICULAR PURPOSE. ADDITIONAL RIGHTS MAY BE REQUIRED TO USE ILLUSTRATIONS, GRAPHS, PHOTOGRAPHS, ABSTRACTS, INSERTS OR OTHER PORTIONS OF THE WORK (AS OPPOSED TO THE ENTIRE WORK) IN A MANNER CONTEMPLATED BY USER; USER UNDERSTANDS AND AGREES THAT NEITHER CCC NOR THE RIGHTSHOLDER MAY HAVE SUCH ADDITIONAL RIGHTS TO GRANT.

7. Effect of Breach. Any failure by User to pay any amount when due, or any use by User of a Work beyond the scope of the license set forth in the Order Confirmation and/or these terms and conditions, shall be a material breach of the license created by the Order Confirmation and these terms and conditions. Any breach not cured within 30 days of written notice thereof shall result in immediate termination of such license without further notice. Any unauthorized (but licensable) use of a Work that is terminated immediately upon notice thereof may be liquidated by payment of the Rightsholder's ordinary license price therefor; any unauthorized (and unlicensable) use that is not terminated immediately for any reason (including, for example, because materials containing the Work cannot reasonably be recalled) will be subject to all remedies available at law or in equity, but in no event to a payment of less than three times the Rightsholder's ordinary license price for the most closely analogous licensable use plus Rightsholder's and/or CCC's costs and expenses incurred in collecting such payment.

8. Miscellaneous.

    8.1. User acknowledges that CCC may, from time to time, make changes or additions to the Service or to these terms and conditions, and CCC reserves the right to send notice to the User by electronic mail or otherwise for the purposes of notifying User of such changes or additions; provided that any such changes or additions shall not apply to permissions already secured and paid for.

    8.2. Use of User-related information collected through the Service is governed by CCC's privacy policy, available online here:https://marketplace.copyright.com/rs-ui-web/mp/privacy-policy

    8.3. The licensing transaction described in the Order Confirmation is personal to User. Therefore, User may not assign or transfer to any other person (whether a natural person or an organization of any kind) the license created by the Order Confirmation and these terms and conditions or any rights granted hereunder; provided, however, that User may assign such license in its entirety on written notice to CCC in the event of a transfer of all or substantially all of User's rights in the new material which includes the Work(s) licensed under this Service.

    8.4. No amendment or waiver of any terms is binding unless set forth in writing and signed by the parties. The Rightsholder and CCC hereby object to any terms contained in any writing prepared by the User or its principals, employees, agents or affiliates and purporting to govern or otherwise relate to the licensing transaction described in the Order Confirmation, which terms are in any way inconsistent with any terms set forth in the Order Confirmation and/or in these terms and conditions or CCC's standard operating procedures, whether such writing is prepared prior to, simultaneously with or subsequent to the Order Confirmation, and whether such writing appears on a copy of the Order Confirmation or in a separate instrument.

    8.5. The licensing transaction described in the Order Confirmation document shall be governed by and construed under the law of the State of New York, USA, without regard to the principles thereof of conflicts of law. Any case, controversy, suit, action, or proceeding arising out of, in connection with, or related to such licensing transaction shall be brought, at CCC's sole discretion, in any federal or state court located in the County of New York, State of New York, USA, or in any federal or state court whose geographical jurisdiction covers the location of the Rightsholder set forth in the Order Confirmation. The parties expressly submit to the personal jurisdiction and venue of each such federal or state court.If you have any comments or questions about the Service or Copyright Clearance Center, please contact us at 978-750-8400 or send an e-mail to support@copyright.com.

v 1.1

Copyright Clearance Center RightsLink®

Home | Help | Email Support | Werner Heinz

ACS Publications
Most Trusted. Most Cited. Most Read.

Rational Synthesis of Metal–Organic Framework Nanocubes and Nanosheets Using Selective Modulators and Their Morphology-Dependent Gas-Sorption Properties

Author: Minh-Hao Pham, Gia-Thanh Vuong, Frédéric-Georges Fontaine, et al
Publication: Crystal Growth and Design
Publisher: American Chemical Society
Date: Jun 1, 2012

PERMISSION/LICENSE IS GRANTED FOR YOUR ORDER AT NO CHARGE

This type of permission/license, instead of the standard Terms & Conditions, is sent to you because no fee is being charged for your order. Please note the following:

- Permission is granted for your request in both print and electronic formats, and translations.
- If figures and/or tables were requested, they may be adapted or used in part.
- Please print this page for your records and send a copy of it to your publisher/graduate school.
- Appropriate credit for the requested material should be given as follows: "Reprinted (adapted) with permission from (COMPLETE REFERENCE CITATION). Copyright (YEAR) American Chemical Society." Insert appropriate information in place of the capitalized words.
- One-time permission is granted only for the use specified in your request. No additional uses are granted (such as derivative works or other editions). For any other uses, please submit a new request.

If credit is given to another source for the material you requested, permission must be obtained from that source.

BACK CLOSE WINDOW

JOHN WILEY AND SONS LICENSE
TERMS AND CONDITIONS

Feb 07, 2021

This Agreement between Werner Heinz ("You") and John Wiley and Sons ("John Wiley and Sons") consists of your license details and the terms and conditions provided by John Wiley and Sons and Copyright Clearance Center.

License Number	5003641025625
License date	Feb 07, 2021
Licensed Content Publisher	John Wiley and Sons
Licensed Content Publication	Advanced Materials
Licensed Content Title	Metal–Organic Frameworks: Defective Metal-Organic Frameworks (Adv. Mater. 37/2018)
Licensed Content Author	Roland A. Fischer, Gregor Kieslich, Werner R. Heinz, et al
Licensed Content Date	Sep 10, 2018
Licensed Content Volume	30
Licensed Content Issue	37
Licensed Content Pages	1
Type of use	Dissertation/Thesis
Requestor type	Author of this Wiley article
Format	Print and electronic
Portion	Figure/table
Number of figures/tables	2
Will you be translating?	No
Title	Defects in Functional Porous Materials Ruthenium and Rhodium HKUST-1 Analogues as a Case Study for Precious Group Metal-Organic Frameworks - Synthesis, Characterization, Defect-Engineering and Catalysis

Institution name	Technical University of Munich
Expected presentation date	Feb 2021
Portions	Figure 2, Cover Artwork
	Werner Heinz

basis, or any of the rights granted to you hereunder to any other person.

- The Wiley Materials and all of the intellectual property rights therein shall at all times remain the exclusive property of John Wiley & Sons Inc, the Wiley Companies, or their respective licensors, and your interest therein is only that of having possession of and the right to reproduce the Wiley Materials pursuant to Section 2 herein during the continuance of this Agreement. You agree that you own no right, title or interest in or to the Wiley Materials or any of the intellectual property rights therein. You shall have no rights hereunder other than the license as provided for above in Section 2. No right, license or interest to any trademark, trade name, service mark or other branding ("Marks") of WILEY or its licensors is granted hereunder, and you agree that you shall not assert any such right, license or interest with respect thereto

- NEITHER WILEY NOR ITS LICENSORS MAKES ANY WARRANTY OR REPRESENTATION OF ANY KIND TO YOU OR ANY THIRD PARTY, EXPRESS, IMPLIED OR STATUTORY, WITH RESPECT TO THE MATERIALS OR THE ACCURACY OF ANY INFORMATION CONTAINED IN THE MATERIALS, INCLUDING, WITHOUT LIMITATION, ANY IMPLIED WARRANTY OF MERCHANTABILITY, ACCURACY, SATISFACTORY QUALITY, FITNESS FOR A PARTICULAR PURPOSE, USABILITY, INTEGRATION OR NON-INFRINGEMENT AND ALL SUCH WARRANTIES ARE HEREBY EXCLUDED BY WILEY AND ITS LICENSORS AND WAIVED BY YOU.

- WILEY shall have the right to terminate this Agreement immediately upon breach of this Agreement by you.

- You shall indemnify, defend and hold harmless WILEY, its Licensors and their respective directors, officers, agents and employees, from and against any actual or threatened claims, demands, causes of action or proceedings arising from any breach of this Agreement by you.

- IN NO EVENT SHALL WILEY OR ITS LICENSORS BE LIABLE TO YOU OR ANY OTHER PARTY OR ANY OTHER PERSON OR ENTITY FOR ANY SPECIAL, CONSEQUENTIAL, INCIDENTAL, INDIRECT, EXEMPLARY OR PUNITIVE DAMAGES, HOWEVER CAUSED, ARISING OUT OF OR IN CONNECTION WITH THE DOWNLOADING, PROVISIONING, VIEWING OR USE OF THE MATERIALS REGARDLESS OF THE FORM OF ACTION, WHETHER FOR BREACH OF CONTRACT, BREACH OF WARRANTY, TORT, NEGLIGENCE, INFRINGEMENT OR OTHERWISE (INCLUDING, WITHOUT LIMITATION, DAMAGES BASED ON LOSS OF PROFITS, DATA, FILES, USE, BUSINESS OPPORTUNITY OR CLAIMS OF THIRD PARTIES), AND WHETHER OR NOT THE PARTY HAS BEEN ADVISED OF THE POSSIBILITY OF SUCH DAMAGES. THIS LIMITATION SHALL APPLY NOTWITHSTANDING ANY FAILURE OF ESSENTIAL PURPOSE OF ANY LIMITED REMEDY PROVIDED HEREIN.

- Should any provision of this Agreement be held by a court of competent jurisdiction to be illegal, invalid, or unenforceable, that provision shall be deemed amended to achieve as nearly as possible the same economic effect as the original provision, and the legality, validity and enforceability of the remaining provisions of this Agreement shall not be affected or impaired thereby.

- The failure of either party to enforce any term or condition of this Agreement shall not constitute a waiver of either party's right to enforce each and every term and condition of this Agreement. No breach under this agreement shall be deemed waived or excused by either party unless such waiver or consent is in writing signed by the party granting such waiver or consent. The waiver by or consent of a party to a breach of any provision of this Agreement shall not operate or be construed as a waiver of or consent to any other or subsequent breach by such other party.

- This Agreement may not be assigned (including by operation of law or otherwise) by you without WILEY's prior written consent.

- Any fee required for this permission shall be non-refundable after thirty (30) days from receipt by the CCC.

- These terms and conditions together with CCC's Billing and Payment terms and conditions (which are incorporated herein) form the entire agreement between you and WILEY concerning this licensing transaction and (in the absence of fraud) supersedes all prior agreements and representations of the parties, oral or written. This Agreement may not be amended except in writing signed by both parties. This Agreement shall be binding upon and inure to the benefit of the parties' successors, legal representatives, and authorized assigns.

- In the event of any conflict between your obligations established by these terms and conditions and those established by CCC's Billing and Payment terms and conditions, these terms and conditions shall prevail.

- WILEY expressly reserves all rights not specifically granted in the combination of (i) the license details provided by you and accepted in the course of this licensing transaction, (ii) these terms and conditions and (iii) CCC's Billing and Payment terms and conditions.
- This Agreement will be void if the Type of Use, Format, Circulation, or Requestor Type was misrepresented during the licensing process.
- This Agreement shall be governed by and construed in accordance with the laws of the State of New York, USA, without regards to such state's conflict of law rules. Any legal action, suit or proceeding arising out of or relating to these Terms and Conditions or the breach thereof shall be instituted in a court of competent jurisdiction in New York County in the State of New York in the United States of America and each party hereby consents and submits to the personal jurisdiction of such court, waives any objection to venue in such court and consents to service of process by registered or certified mail, return receipt requested, at the last known address of such party.

WILEY OPEN ACCESS TERMS AND CONDITIONS

Wiley Publishes Open Access Articles in fully Open Access Journals and in Subscription journals offering Online Open. Although most of the fully Open Access journals publish open access articles under the terms of the Creative Commons Attribution (CC BY) License only, the subscription journals and a few of the Open Access Journals offer a choice of Creative Commons Licenses. The license type is clearly identified on the article.

The Creative Commons Attribution License

The Creative Commons Attribution License (CC-BY) allows users to copy, distribute and transmit an article, adapt the article and make commercial use of the article. The CC-BY license permits commercial and non-

Creative Commons Attribution Non-Commercial License

The Creative Commons Attribution Non-Commercial (CC-BY-NC)License permits use, distribution and reproduction in any medium, provided the original work is properly cited and is not used for commercial purposes.(see below)

Creative Commons Attribution-Non-Commercial-NoDerivs License

The Creative Commons Attribution Non-Commercial-NoDerivs License (CC-BY-NC-ND) permits use, distribution and reproduction in any medium, provided the original work is properly cited, is not used for commercial purposes and no modifications or adaptations are made. (see below)

Use by commercial "for-profit" organizations

Use of Wiley Open Access articles for commercial, promotional, or marketing purposes requires further explicit permission from Wiley and will be subject to a fee.

Further details can be found on Wiley Online Library http://olabout.wiley.com/WileyCDA/Section/id-410895.html

Other Terms and Conditions:

v1.10 Last updated September 2015

Questions? customercare@copyright.com or +1-855-239-3415 (toll free in the US) or +1-978-646-2777.

JOHN WILEY AND SONS LICENSE
TERMS AND CONDITIONS

Feb 07, 2021

This Agreement between Werner Heinz ("You") and John Wiley and Sons ("John Wiley and Sons") consists of your license details and the terms and conditions provided by John Wiley and Sons and Copyright Clearance Center.

License Number	5003641494768
License date	Feb 07, 2021
Licensed Content Publisher	John Wiley and Sons
Licensed Content Publication	Angewandte Chemie International Edition
Licensed Content Title	Defect-Engineered Metal–Organic Frameworks
Licensed Content Author	Zhenlan Fang, Bart Bueken, Dirk E. De Vos, et al
Licensed Content Date	Jun 3, 2015
Licensed Content Volume	54
Licensed Content Issue	25
Licensed Content Pages	21
Type of use	Dissertation/Thesis
Requestor type	University/Academic
Format	Print and electronic
Portion	Figure/table
Number of figures/tables	1
Will you be translating?	No
Title	Defects in Functional Porous Materials Ruthenium and Rhodium HKUST-1 Analogues as a Case Study for Precious Group Metal-Organic Frameworks - Synthesis, Characterization, Defect-Engineering and Catalysis

Institution name	Technical University of Munich
Expected presentation date	Feb 2021
Portions	Figure 1
	Werner Heinz

basis, or any of the rights granted to you hereunder to any other person.

- The Wiley Materials and all of the intellectual property rights therein shall at all times remain the exclusive property of John Wiley & Sons Inc, the Wiley Companies, or their respective licensors, and your interest therein is only that of having possession of and the right to reproduce the Wiley Materials pursuant to Section 2 herein during the continuance of this Agreement. You agree that you own no right, title or interest in or to the Wiley Materials or any of the intellectual property rights therein. You shall have no rights hereunder other than the license as provided for above in Section 2. No right, license or interest to any trademark, trade name, service mark or other branding ("Marks") of WILEY or its licensors is granted hereunder, and you agree that you shall not assert any such right, license or interest with respect thereto

- NEITHER WILEY NOR ITS LICENSORS MAKES ANY WARRANTY OR REPRESENTATION OF ANY KIND TO YOU OR ANY THIRD PARTY, EXPRESS, IMPLIED OR STATUTORY, WITH RESPECT TO THE MATERIALS OR THE ACCURACY OF ANY INFORMATION CONTAINED IN THE MATERIALS, INCLUDING, WITHOUT LIMITATION, ANY IMPLIED WARRANTY OF MERCHANTABILITY, ACCURACY, SATISFACTORY QUALITY, FITNESS FOR A PARTICULAR PURPOSE, USABILITY, INTEGRATION OR NON-INFRINGEMENT AND ALL SUCH WARRANTIES ARE HEREBY EXCLUDED BY WILEY AND ITS LICENSORS AND WAIVED BY YOU.

- WILEY shall have the right to terminate this Agreement immediately upon breach of this Agreement by you.

- You shall indemnify, defend and hold harmless WILEY, its Licensors and their respective directors, officers, agents and employees, from and against any actual or threatened claims, demands, causes of action or proceedings arising from any breach of this Agreement by you.

- IN NO EVENT SHALL WILEY OR ITS LICENSORS BE LIABLE TO YOU OR ANY OTHER PARTY OR ANY OTHER PERSON OR ENTITY FOR ANY SPECIAL, CONSEQUENTIAL, INCIDENTAL, INDIRECT, EXEMPLARY OR PUNITIVE DAMAGES, HOWEVER CAUSED, ARISING OUT OF OR IN CONNECTION WITH THE DOWNLOADING, PROVISIONING, VIEWING OR USE OF THE MATERIALS REGARDLESS OF THE FORM OF ACTION, WHETHER FOR BREACH OF CONTRACT, BREACH OF WARRANTY, TORT, NEGLIGENCE, INFRINGEMENT OR OTHERWISE (INCLUDING, WITHOUT LIMITATION, DAMAGES BASED ON LOSS OF PROFITS, DATA, FILES, USE, BUSINESS OPPORTUNITY OR CLAIMS OF THIRD PARTIES), AND WHETHER OR NOT THE PARTY HAS BEEN ADVISED OF THE POSSIBILITY OF SUCH DAMAGES. THIS LIMITATION SHALL APPLY NOTWITHSTANDING ANY FAILURE OF ESSENTIAL PURPOSE OF ANY LIMITED REMEDY PROVIDED HEREIN.

- Should any provision of this Agreement be held by a court of competent jurisdiction to be illegal, invalid, or unenforceable, that provision shall be deemed amended to achieve as nearly as possible the same economic effect as the original provision, and the legality, validity and enforceability of the remaining provisions of this Agreement shall not be affected or impaired thereby.

- The failure of either party to enforce any term or condition of this Agreement shall not constitute a waiver of either party's right to enforce each and every term and condition of this Agreement. No breach under this agreement shall be deemed waived or excused by either party unless such waiver or consent is in writing signed by the party granting such waiver or consent. The waiver by or consent of a party to a breach of any provision of this Agreement shall not operate or be construed as a waiver of or consent to any other or subsequent breach by such other party.

- This Agreement may not be assigned (including by operation of law or otherwise) by you without WILEY's prior written consent.

- Any fee required for this permission shall be non-refundable after thirty (30) days from receipt by the CCC.

- These terms and conditions together with CCC's Billing and Payment terms and conditions (which are incorporated herein) form the entire agreement between you and WILEY concerning this licensing transaction and (in the absence of fraud) supersedes all prior agreements and representations of the parties, oral or written. This Agreement may not be amended except in writing signed by both parties. This Agreement shall be binding upon and inure to the benefit of the parties' successors, legal representatives, and authorized assigns.

- In the event of any conflict between your obligations established by these terms and conditions and those established by CCC's Billing and Payment terms and conditions, these terms and conditions shall prevail.

- WILEY expressly reserves all rights not specifically granted in the combination of (i) the license details provided by you and accepted in the course of this licensing transaction, (ii) these terms and conditions and (iii) CCC's Billing and Payment terms and conditions.
- This Agreement will be void if the Type of Use, Format, Circulation, or Requestor Type was misrepresented during the licensing process.
- This Agreement shall be governed by and construed in accordance with the laws of the State of New York, USA, without regards to such state's conflict of law rules. Any legal action, suit or proceeding arising out of or relating to these Terms and Conditions or the breach thereof shall be instituted in a court of competent jurisdiction in New York County in the State of New York in the United States of America and each party hereby consents and submits to the personal jurisdiction of such court, waives any objection to venue in such court and consents to service of process by registered or certified mail, return receipt requested, at the last known address of such party.

WILEY OPEN ACCESS TERMS AND CONDITIONS

Wiley Publishes Open Access Articles in fully Open Access Journals and in Subscription journals offering Online Open. Although most of the fully Open Access journals publish open access articles under the terms of the Creative Commons Attribution (CC BY) License only, the subscription journals and a few of the Open Access Journals offer a choice of Creative Commons Licenses. The license type is clearly identified on the article.

The Creative Commons Attribution License

The Creative Commons Attribution License (CC-BY) allows users to copy, distribute and transmit an article, adapt the article and make commercial use of the article. The CC-BY license permits commercial and non-

Creative Commons Attribution Non-Commercial License

The Creative Commons Attribution Non-Commercial (CC-BY-NC)License permits use, distribution and reproduction in any medium, provided the original work is properly cited and is not used for commercial purposes.(see below)

Creative Commons Attribution-Non-Commercial-NoDerivs License

The Creative Commons Attribution Non-Commercial-NoDerivs License (CC-BY-NC-ND) permits use, distribution and reproduction in any medium, provided the original work is properly cited, is not used for commercial purposes and no modifications or adaptations are made. (see below)

Use by commercial "for-profit" organizations

Use of Wiley Open Access articles for commercial, promotional, or marketing purposes requires further explicit permission from Wiley and will be subject to a fee.

Further details can be found on Wiley Online Library http://olabout.wiley.com/WileyCDA/Section/id-410895.html

Other Terms and Conditions:

v1.10 Last updated September 2015

Questions? customercare@copyright.com or +1-855-239-3415 (toll free in the US) or +1-978-646-2777.

JOHN WILEY AND SONS LICENSE
TERMS AND CONDITIONS

Feb 07, 2021

This Agreement between Werner Heinz ("You") and John Wiley and Sons ("John Wiley and Sons") consists of your license details and the terms and conditions provided by John Wiley and Sons and Copyright Clearance Center.

License Number	5003650437412
License date	Feb 07, 2021
Licensed Content Publisher	John Wiley and Sons
Licensed Content Publication	European Journal of Inorganic Chemistry
Licensed Content Title	The Impact of Mesopores on the Mechanical Stability of HKUST-1: A Multiscale Investigation
Licensed Content Author	and Rochus Schmid, Julian Keupp, Johannes P. Dürholt
Licensed Content Date	Jul 27, 2016
Licensed Content Volume	2016
Licensed Content Issue	27
Licensed Content Pages	7
Type of use	Dissertation/Thesis
Requestor type	University/Academic
Format	Print and electronic
Portion	Figure/table
Number of figures/tables	1
Will you be translating?	No
Title	Defects in Functional Porous Materials Ruthenium and Rhodium HKUST-1 Analogues as a Case Study for Precious Group Metal-Organic Frameworks - Synthesis, Characterization, Defect-Engineering and Catalysis

Institution name	Technical University of Munich
Expected presentation date	Feb 2021
Portions	Figure 1
	Werner Heinz

basis, or any of the rights granted to you hereunder to any other person.

- The Wiley Materials and all of the intellectual property rights therein shall at all times remain the exclusive property of John Wiley & Sons Inc, the Wiley Companies, or their respective licensors, and your interest therein is only that of having possession of and the right to reproduce the Wiley Materials pursuant to Section 2 herein during the continuance of this Agreement. You agree that you own no right, title or interest in or to the Wiley Materials or any of the intellectual property rights therein. You shall have no rights hereunder other than the license as provided for above in Section 2. No right, license or interest to any trademark, trade name, service mark or other branding ("Marks") of WILEY or its licensors is granted hereunder, and you agree that you shall not assert any such right, license or interest with respect thereto

- NEITHER WILEY NOR ITS LICENSORS MAKES ANY WARRANTY OR REPRESENTATION OF ANY KIND TO YOU OR ANY THIRD PARTY, EXPRESS, IMPLIED OR STATUTORY, WITH RESPECT TO THE MATERIALS OR THE ACCURACY OF ANY INFORMATION CONTAINED IN THE MATERIALS, INCLUDING, WITHOUT LIMITATION, ANY IMPLIED WARRANTY OF MERCHANTABILITY, ACCURACY, SATISFACTORY QUALITY, FITNESS FOR A PARTICULAR PURPOSE, USABILITY, INTEGRATION OR NON-INFRINGEMENT AND ALL SUCH WARRANTIES ARE HEREBY EXCLUDED BY WILEY AND ITS LICENSORS AND WAIVED BY YOU.

- WILEY shall have the right to terminate this Agreement immediately upon breach of this Agreement by you.

- You shall indemnify, defend and hold harmless WILEY, its Licensors and their respective directors, officers, agents and employees, from and against any actual or threatened claims, demands, causes of action or proceedings arising from any breach of this Agreement by you.

- IN NO EVENT SHALL WILEY OR ITS LICENSORS BE LIABLE TO YOU OR ANY OTHER PARTY OR ANY OTHER PERSON OR ENTITY FOR ANY SPECIAL, CONSEQUENTIAL, INCIDENTAL, INDIRECT, EXEMPLARY OR PUNITIVE DAMAGES, HOWEVER CAUSED, ARISING OUT OF OR IN CONNECTION WITH THE DOWNLOADING, PROVISIONING, VIEWING OR USE OF THE MATERIALS REGARDLESS OF THE FORM OF ACTION, WHETHER FOR BREACH OF CONTRACT, BREACH OF WARRANTY, TORT, NEGLIGENCE, INFRINGEMENT OR OTHERWISE (INCLUDING, WITHOUT LIMITATION, DAMAGES BASED ON LOSS OF PROFITS, DATA, FILES, USE, BUSINESS OPPORTUNITY OR CLAIMS OF THIRD PARTIES), AND WHETHER OR NOT THE PARTY HAS BEEN ADVISED OF THE POSSIBILITY OF SUCH DAMAGES. THIS LIMITATION SHALL APPLY NOTWITHSTANDING ANY FAILURE OF ESSENTIAL PURPOSE OF ANY LIMITED REMEDY PROVIDED HEREIN.

- Should any provision of this Agreement be held by a court of competent jurisdiction to be illegal, invalid, or unenforceable, that provision shall be deemed amended to achieve as nearly as possible the same economic effect as the original provision, and the legality, validity and enforceability of the remaining provisions of this Agreement shall not be affected or impaired thereby.

- The failure of either party to enforce any term or condition of this Agreement shall not constitute a waiver of either party's right to enforce each and every term and condition of this Agreement. No breach under this agreement shall be deemed waived or excused by either party unless such waiver or consent is in writing signed by the party granting such waiver or consent. The waiver by or consent of a party to a breach of any provision of this Agreement shall not operate or be construed as a waiver of or consent to any other or subsequent breach by such other party.

- This Agreement may not be assigned (including by operation of law or otherwise) by you without WILEY's prior written consent.

- Any fee required for this permission shall be non-refundable after thirty (30) days from receipt by the CCC.

- These terms and conditions together with CCC's Billing and Payment terms and conditions (which are incorporated herein) form the entire agreement between you and WILEY concerning this licensing transaction and (in the absence of fraud) supersedes all prior agreements and representations of the parties, oral or written. This Agreement may not be amended except in writing signed by both parties. This Agreement shall be binding upon and inure to the benefit of the parties' successors, legal representatives, and authorized assigns.

- In the event of any conflict between your obligations established by these terms and conditions and those established by CCC's Billing and Payment terms and conditions, these terms and conditions shall prevail.

- WILEY expressly reserves all rights not specifically granted in the combination of (i) the license details provided by you and accepted in the course of this licensing transaction, (ii) these terms and conditions and (iii) CCC's Billing and Payment terms and conditions.
- This Agreement will be void if the Type of Use, Format, Circulation, or Requestor Type was misrepresented during the licensing process.
- This Agreement shall be governed by and construed in accordance with the laws of the State of New York, USA, without regards to such state's conflict of law rules. Any legal action, suit or proceeding arising out of or relating to these Terms and Conditions or the breach thereof shall be instituted in a court of competent jurisdiction in New York County in the State of New York in the United States of America and each party hereby consents and submits to the personal jurisdiction of such court, waives any objection to venue in such court and consents to service of process by registered or certified mail, return receipt requested, at the last known address of such party.

WILEY OPEN ACCESS TERMS AND CONDITIONS

Wiley Publishes Open Access Articles in fully Open Access Journals and in Subscription journals offering Online Open. Although most of the fully Open Access journals publish open access articles under the terms of the Creative Commons Attribution (CC BY) License only, the subscription journals and a few of the Open Access Journals offer a choice of Creative Commons Licenses. The license type is clearly identified on the article.

The Creative Commons Attribution License

The Creative Commons Attribution License (CC-BY) allows users to copy, distribute and transmit an article, adapt the article and make commercial use of the article. The CC-BY license permits commercial and non-

Creative Commons Attribution Non-Commercial License

The Creative Commons Attribution Non-Commercial (CC-BY-NC)License permits use, distribution and reproduction in any medium, provided the original work is properly cited and is not used for commercial purposes.(see below)

Creative Commons Attribution-Non-Commercial-NoDerivs License

The Creative Commons Attribution Non-Commercial-NoDerivs License (CC-BY-NC-ND) permits use, distribution and reproduction in any medium, provided the original work is properly cited, is not used for commercial purposes and no modifications or adaptations are made. (see below)

Use by commercial "for-profit" organizations

Use of Wiley Open Access articles for commercial, promotional, or marketing purposes requires further explicit permission from Wiley and will be subject to a fee.

Further details can be found on Wiley Online Library http://olabout.wiley.com/WileyCDA/Section/id-410895.html

Other Terms and Conditions:

v1.10 Last updated September 2015

Questions? customercare@copyright.com or +1-855-239-3415 (toll free in the US) or +1-978-646-2777.

JOHN WILEY AND SONS LICENSE
TERMS AND CONDITIONS

Feb 07, 2021

This Agreement between Werner Heinz ("You") and John Wiley and Sons ("John Wiley and Sons") consists of your license details and the terms and conditions provided by John Wiley and Sons and Copyright Clearance Center.

License Number	5003650899429
License date	Feb 07, 2021
Licensed Content Publisher	John Wiley and Sons
Licensed Content Publication	Angewandte Chemie International Edition
Licensed Content Title	Multifunctional, Defect-Engineered Metal–Organic Frameworks with Ruthenium Centers: Sorption and Catalytic Properties
Licensed Content Author	Roland A. Fischer, Martin Muhler, Yuemin Wang, et al
Licensed Content Date	May 18, 2014
Licensed Content Volume	53
Licensed Content Issue	27
Licensed Content Pages	5
Type of use	Dissertation/Thesis
Requestor type	University/Academic
Format	Print and electronic
Portion	Figure/table
Number of figures/tables	1
Will you be translating?	No
Title	Defects in Functional Porous Materials Ruthenium and Rhodium HKUST-1 Analogues as a Case Study for Precious Group Metal-Organic Frameworks - Synthesis, Characterization, Defect-Engineering and Catalysis

Institution name	Technical University of Munich
Expected presentation date	Feb 2021
Portions	Figure 1
	Werner Heinz

basis, or any of the rights granted to you hereunder to any other person.

- The Wiley Materials and all of the intellectual property rights therein shall at all times remain the exclusive property of John Wiley & Sons Inc, the Wiley Companies, or their respective licensors, and your interest therein is only that of having possession of and the right to reproduce the Wiley Materials pursuant to Section 2 herein during the continuance of this Agreement. You agree that you own no right, title or interest in or to the Wiley Materials or any of the intellectual property rights therein. You shall have no rights hereunder other than the license as provided for above in Section 2. No right, license or interest to any trademark, trade name, service mark or other branding ("Marks") of WILEY or its licensors is granted hereunder, and you agree that you shall not assert any such right, license or interest with respect thereto

- NEITHER WILEY NOR ITS LICENSORS MAKES ANY WARRANTY OR REPRESENTATION OF ANY KIND TO YOU OR ANY THIRD PARTY, EXPRESS, IMPLIED OR STATUTORY, WITH RESPECT TO THE MATERIALS OR THE ACCURACY OF ANY INFORMATION CONTAINED IN THE MATERIALS, INCLUDING, WITHOUT LIMITATION, ANY IMPLIED WARRANTY OF MERCHANTABILITY, ACCURACY, SATISFACTORY QUALITY, FITNESS FOR A PARTICULAR PURPOSE, USABILITY, INTEGRATION OR NON-INFRINGEMENT AND ALL SUCH WARRANTIES ARE HEREBY EXCLUDED BY WILEY AND ITS LICENSORS AND WAIVED BY YOU.

- WILEY shall have the right to terminate this Agreement immediately upon breach of this Agreement by you.

- You shall indemnify, defend and hold harmless WILEY, its Licensors and their respective directors, officers, agents and employees, from and against any actual or threatened claims, demands, causes of action or proceedings arising from any breach of this Agreement by you.

- IN NO EVENT SHALL WILEY OR ITS LICENSORS BE LIABLE TO YOU OR ANY OTHER PARTY OR ANY OTHER PERSON OR ENTITY FOR ANY SPECIAL, CONSEQUENTIAL, INCIDENTAL, INDIRECT, EXEMPLARY OR PUNITIVE DAMAGES, HOWEVER CAUSED, ARISING OUT OF OR IN CONNECTION WITH THE DOWNLOADING, PROVISIONING, VIEWING OR USE OF THE MATERIALS REGARDLESS OF THE FORM OF ACTION, WHETHER FOR BREACH OF CONTRACT, BREACH OF WARRANTY, TORT, NEGLIGENCE, INFRINGEMENT OR OTHERWISE (INCLUDING, WITHOUT LIMITATION, DAMAGES BASED ON LOSS OF PROFITS, DATA, FILES, USE, BUSINESS OPPORTUNITY OR CLAIMS OF THIRD PARTIES), AND WHETHER OR NOT THE PARTY HAS BEEN ADVISED OF THE POSSIBILITY OF SUCH DAMAGES. THIS LIMITATION SHALL APPLY NOTWITHSTANDING ANY FAILURE OF ESSENTIAL PURPOSE OF ANY LIMITED REMEDY PROVIDED HEREIN.

- Should any provision of this Agreement be held by a court of competent jurisdiction to be illegal, invalid, or unenforceable, that provision shall be deemed amended to achieve as nearly as possible the same economic effect as the original provision, and the legality, validity and enforceability of the remaining provisions of this Agreement shall not be affected or impaired thereby.

- The failure of either party to enforce any term or condition of this Agreement shall not constitute a waiver of either party's right to enforce each and every term and condition of this Agreement. No breach under this agreement shall be deemed waived or excused by either party unless such waiver or consent is in writing signed by the party granting such waiver or consent. The waiver by or consent of a party to a breach of any provision of this Agreement shall not operate or be construed as a waiver of or consent to any other or subsequent breach by such other party.

- This Agreement may not be assigned (including by operation of law or otherwise) by you without WILEY's prior written consent.

- Any fee required for this permission shall be non-refundable after thirty (30) days from receipt by the CCC.

- These terms and conditions together with CCC's Billing and Payment terms and conditions (which are incorporated herein) form the entire agreement between you and WILEY concerning this licensing transaction and (in the absence of fraud) supersedes all prior agreements and representations of the parties, oral or written. This Agreement may not be amended except in writing signed by both parties. This Agreement shall be binding upon and inure to the benefit of the parties' successors, legal representatives, and authorized assigns.

- In the event of any conflict between your obligations established by these terms and conditions and those established by CCC's Billing and Payment terms and conditions, these terms and conditions shall prevail.

- WILEY expressly reserves all rights not specifically granted in the combination of (i) the license details provided by you and accepted in the course of this licensing transaction, (ii) these terms and conditions and (iii) CCC's Billing and Payment terms and conditions.
- This Agreement will be void if the Type of Use, Format, Circulation, or Requestor Type was misrepresented during the licensing process.
- This Agreement shall be governed by and construed in accordance with the laws of the State of New York, USA, without regards to such state's conflict of law rules. Any legal action, suit or proceeding arising out of or relating to these Terms and Conditions or the breach thereof shall be instituted in a court of competent jurisdiction in New York County in the State of New York in the United States of America and each party hereby consents and submits to the personal jurisdiction of such court, waives any objection to venue in such court and consents to service of process by registered or certified mail, return receipt requested, at the last known address of such party.

WILEY OPEN ACCESS TERMS AND CONDITIONS

Wiley Publishes Open Access Articles in fully Open Access Journals and in Subscription journals offering Online Open. Although most of the fully Open Access journals publish open access articles under the terms of the Creative Commons Attribution (CC BY) License only, the subscription journals and a few of the Open Access Journals offer a choice of Creative Commons Licenses. The license type is clearly identified on the article.

The Creative Commons Attribution License

The Creative Commons Attribution License (CC-BY) allows users to copy, distribute and transmit an article, adapt the article and make commercial use of the article. The CC-BY license permits commercial and non-

Creative Commons Attribution Non-Commercial License

The Creative Commons Attribution Non-Commercial (CC-BY-NC)License permits use, distribution and reproduction in any medium, provided the original work is properly cited and is not used for commercial purposes.(see below)

Creative Commons Attribution-Non-Commercial-NoDerivs License

The Creative Commons Attribution Non-Commercial-NoDerivs License (CC-BY-NC-ND) permits use, distribution and reproduction in any medium, provided the original work is properly cited, is not used for commercial purposes and no modifications or adaptations are made. (see below)

Use by commercial "for-profit" organizations

Use of Wiley Open Access articles for commercial, promotional, or marketing purposes requires further explicit permission from Wiley and will be subject to a fee.

Further details can be found on Wiley Online Library http://olabout.wiley.com/WileyCDA/Section/id-410895.html

Other Terms and Conditions:

v1.10 Last updated September 2015

Questions? customercare@copyright.com or +1-855-239-3415 (toll free in the US) or +1-978-646-2777.

JOHN WILEY AND SONS LICENSE
TERMS AND CONDITIONS

Feb 07, 2021

This Agreement between Werner Heinz ("You") and John Wiley and Sons ("John Wiley and Sons") consists of your license details and the terms and conditions provided by John Wiley and Sons and Copyright Clearance Center.

License Number	5003651194909
License date	Feb 07, 2021
Licensed Content Publisher	John Wiley and Sons
Licensed Content Publication	Advanced Materials
Licensed Content Title	Metal–Organic Frameworks as Platforms for Catalytic Applications
Licensed Content Author	Long Jiao, Yang Wang, Hai-Long Jiang, et al
Licensed Content Date	Nov 27, 2017
Licensed Content Volume	30
Licensed Content Issue	37
Licensed Content Pages	23
Type of use	Dissertation/Thesis
Requestor type	University/Academic
Format	Print and electronic
Portion	Figure/table
Number of figures/tables	1
Will you be translating?	No
Title	Defects in Functional Porous Materials Ruthenium and Rhodium HKUST-1 Analogues as a Case Study for Precious Group Metal-Organic Frameworks - Synthesis, Characterization, Defect-Engineering and Catalysis

Institution name	Technical University of Munich
Expected presentation date	Feb 2021
Portions	Figure 1
	Werner Heinz

basis, or any of the rights granted to you hereunder to any other person.

- The Wiley Materials and all of the intellectual property rights therein shall at all times remain the exclusive property of John Wiley & Sons Inc, the Wiley Companies, or their respective licensors, and your interest therein is only that of having possession of and the right to reproduce the Wiley Materials pursuant to Section 2 herein during the continuance of this Agreement. You agree that you own no right, title or interest in or to the Wiley Materials or any of the intellectual property rights therein. You shall have no rights hereunder other than the license as provided for above in Section 2. No right, license or interest to any trademark, trade name, service mark or other branding ("Marks") of WILEY or its licensors is granted hereunder, and you agree that you shall not assert any such right, license or interest with respect thereto

- NEITHER WILEY NOR ITS LICENSORS MAKES ANY WARRANTY OR REPRESENTATION OF ANY KIND TO YOU OR ANY THIRD PARTY, EXPRESS, IMPLIED OR STATUTORY, WITH RESPECT TO THE MATERIALS OR THE ACCURACY OF ANY INFORMATION CONTAINED IN THE MATERIALS, INCLUDING, WITHOUT LIMITATION, ANY IMPLIED WARRANTY OF MERCHANTABILITY, ACCURACY, SATISFACTORY QUALITY, FITNESS FOR A PARTICULAR PURPOSE, USABILITY, INTEGRATION OR NON-INFRINGEMENT AND ALL SUCH WARRANTIES ARE HEREBY EXCLUDED BY WILEY AND ITS LICENSORS AND WAIVED BY YOU.

- WILEY shall have the right to terminate this Agreement immediately upon breach of this Agreement by you.

- You shall indemnify, defend and hold harmless WILEY, its Licensors and their respective directors, officers, agents and employees, from and against any actual or threatened claims, demands, causes of action or proceedings arising from any breach of this Agreement by you.

- IN NO EVENT SHALL WILEY OR ITS LICENSORS BE LIABLE TO YOU OR ANY OTHER PARTY OR ANY OTHER PERSON OR ENTITY FOR ANY SPECIAL, CONSEQUENTIAL, INCIDENTAL, INDIRECT, EXEMPLARY OR PUNITIVE DAMAGES, HOWEVER CAUSED, ARISING OUT OF OR IN CONNECTION WITH THE DOWNLOADING, PROVISIONING, VIEWING OR USE OF THE MATERIALS REGARDLESS OF THE FORM OF ACTION, WHETHER FOR BREACH OF CONTRACT, BREACH OF WARRANTY, TORT, NEGLIGENCE, INFRINGEMENT OR OTHERWISE (INCLUDING, WITHOUT LIMITATION, DAMAGES BASED ON LOSS OF PROFITS, DATA, FILES, USE, BUSINESS OPPORTUNITY OR CLAIMS OF THIRD PARTIES), AND WHETHER OR NOT THE PARTY HAS BEEN ADVISED OF THE POSSIBILITY OF SUCH DAMAGES. THIS LIMITATION SHALL APPLY NOTWITHSTANDING ANY FAILURE OF ESSENTIAL PURPOSE OF ANY LIMITED REMEDY PROVIDED HEREIN.

- Should any provision of this Agreement be held by a court of competent jurisdiction to be illegal, invalid, or unenforceable, that provision shall be deemed amended to achieve as nearly as possible the same economic effect as the original provision, and the legality, validity and enforceability of the remaining provisions of this Agreement shall not be affected or impaired thereby.

- The failure of either party to enforce any term or condition of this Agreement shall not constitute a waiver of either party's right to enforce each and every term and condition of this Agreement. No breach under this agreement shall be deemed waived or excused by either party unless such waiver or consent is in writing signed by the party granting such waiver or consent. The waiver by or consent of a party to a breach of any provision of this Agreement shall not operate or be construed as a waiver of or consent to any other or subsequent breach by such other party.

- This Agreement may not be assigned (including by operation of law or otherwise) by you without WILEY's prior written consent.

- Any fee required for this permission shall be non-refundable after thirty (30) days from receipt by the CCC.

- These terms and conditions together with CCC's Billing and Payment terms and conditions (which are incorporated herein) form the entire agreement between you and WILEY concerning this licensing transaction and (in the absence of fraud) supersedes all prior agreements and representations of the parties, oral or written. This Agreement may not be amended except in writing signed by both parties. This Agreement shall be binding upon and inure to the benefit of the parties' successors, legal representatives, and authorized assigns.

- In the event of any conflict between your obligations established by these terms and conditions and those established by CCC's Billing and Payment terms and conditions, these terms and conditions shall prevail.

- WILEY expressly reserves all rights not specifically granted in the combination of (i) the license details provided by you and accepted in the course of this licensing transaction, (ii) these terms and conditions and (iii) CCC's Billing and Payment terms and conditions.
- This Agreement will be void if the Type of Use, Format, Circulation, or Requestor Type was misrepresented during the licensing process.
- This Agreement shall be governed by and construed in accordance with the laws of the State of New York, USA, without regards to such state's conflict of law rules. Any legal action, suit or proceeding arising out of or relating to these Terms and Conditions or the breach thereof shall be instituted in a court of competent jurisdiction in New York County in the State of New York in the United States of America and each party hereby consents and submits to the personal jurisdiction of such court, waives any objection to venue in such court and consents to service of process by registered or certified mail, return receipt requested, at the last known address of such party.

WILEY OPEN ACCESS TERMS AND CONDITIONS

Wiley Publishes Open Access Articles in fully Open Access Journals and in Subscription journals offering Online Open. Although most of the fully Open Access journals publish open access articles under the terms of the Creative Commons Attribution (CC BY) License only, the subscription journals and a few of the Open Access Journals offer a choice of Creative Commons Licenses. The license type is clearly identified on the article.

The Creative Commons Attribution License

The Creative Commons Attribution License (CC-BY) allows users to copy, distribute and transmit an article, adapt the article and make commercial use of the article. The CC-BY license permits commercial and non-

Creative Commons Attribution Non-Commercial License

The Creative Commons Attribution Non-Commercial (CC-BY-NC)License permits use, distribution and reproduction in any medium, provided the original work is properly cited and is not used for commercial purposes.(see below)

Creative Commons Attribution-Non-Commercial-NoDerivs License

The Creative Commons Attribution Non-Commercial-NoDerivs License (CC-BY-NC-ND) permits use, distribution and reproduction in any medium, provided the original work is properly cited, is not used for commercial purposes and no modifications or adaptations are made. (see below)

Use by commercial "for-profit" organizations

Use of Wiley Open Access articles for commercial, promotional, or marketing purposes requires further explicit permission from Wiley and will be subject to a fee.

Further details can be found on Wiley Online Library http://olabout.wiley.com/WileyCDA/Section/id-410895.html

Other Terms and Conditions:

v1.10 Last updated September 2015

Questions? customercare@copyright.com or +1-855-239-3415 (toll free in the US) or +1-978-646-2777.

JOHN WILEY AND SONS LICENSE
TERMS AND CONDITIONS

Feb 07, 2021

This Agreement between Werner Heinz ("You") and John Wiley and Sons ("John Wiley and Sons") consists of your license details and the terms and conditions provided by John Wiley and Sons and Copyright Clearance Center.

License Number	5003660101622
License date	Feb 07, 2021
Licensed Content Publisher	John Wiley and Sons
Licensed Content Publication	ChemCatChem
Licensed Content Title	Defect-Engineered Ruthenium MOFs as Versatile Heterogeneous Hydrogenation Catalysts
Licensed Content Author	Roland A. Fischer, Francesc X. Llabrés i Xamena, Anastasia Rapeyko, et al
Licensed Content Date	Feb 19, 2020
Licensed Content Volume	12
Licensed Content Issue	6
Licensed Content Pages	6
Type of use	Dissertation/Thesis
Requestor type	Author of this Wiley article
Format	Print and electronic
Portion	Full article
Will you be translating?	No
Title	Defects in Functional Porous Materials Ruthenium and Rhodium HKUST-1 Analogues as a Case Study for Precious Group Metal-Organic Frameworks - Synthesis, Characterization, Defect-Engineering and Catalysis
Institution name	Technical University of Munich

Expected presentation date	Feb 2021
	Werner Heinz

continuance of this Agreement. You agree that you own no right, title or interest in or to the Wiley Materials or any of the intellectual property rights therein. You shall have no rights hereunder other than the license as provided for above in Section 2. No right, license or interest to any trademark, trade name, service mark or other branding ("Marks") of WILEY or its licensors is granted hereunder, and you agree that you shall not assert any such right, license or interest with respect thereto

- NEITHER WILEY NOR ITS LICENSORS MAKES ANY WARRANTY OR REPRESENTATION OF ANY KIND TO YOU OR ANY THIRD PARTY, EXPRESS, IMPLIED OR STATUTORY, WITH RESPECT TO THE MATERIALS OR THE ACCURACY OF ANY INFORMATION CONTAINED IN THE MATERIALS, INCLUDING, WITHOUT LIMITATION, ANY IMPLIED WARRANTY OF MERCHANTABILITY, ACCURACY, SATISFACTORY QUALITY, FITNESS FOR A PARTICULAR PURPOSE, USABILITY, INTEGRATION OR NON-INFRINGEMENT AND ALL SUCH WARRANTIES ARE HEREBY EXCLUDED BY WILEY AND ITS LICENSORS AND WAIVED BY YOU.

- WILEY shall have the right to terminate this Agreement immediately upon breach of this Agreement by you.

- You shall indemnify, defend and hold harmless WILEY, its Licensors and their respective directors, officers, agents and employees, from and against any actual or threatened claims, demands, causes of action or proceedings arising from any breach of this Agreement by you.

- IN NO EVENT SHALL WILEY OR ITS LICENSORS BE LIABLE TO YOU OR ANY OTHER PARTY OR ANY OTHER PERSON OR ENTITY FOR ANY SPECIAL, CONSEQUENTIAL, INCIDENTAL, INDIRECT, EXEMPLARY OR PUNITIVE DAMAGES, HOWEVER CAUSED, ARISING OUT OF OR IN CONNECTION WITH THE DOWNLOADING, PROVISIONING, VIEWING OR USE OF THE MATERIALS REGARDLESS OF THE FORM OF ACTION, WHETHER FOR BREACH OF CONTRACT, BREACH OF WARRANTY, TORT, NEGLIGENCE, INFRINGEMENT OR OTHERWISE (INCLUDING, WITHOUT LIMITATION, DAMAGES BASED ON LOSS OF PROFITS, DATA, FILES, USE, BUSINESS OPPORTUNITY OR CLAIMS OF THIRD PARTIES), AND WHETHER OR NOT THE PARTY HAS BEEN ADVISED OF THE POSSIBILITY OF SUCH DAMAGES. THIS LIMITATION SHALL APPLY NOTWITHSTANDING ANY FAILURE OF ESSENTIAL PURPOSE OF ANY LIMITED REMEDY PROVIDED HEREIN.

- Should any provision of this Agreement be held by a court of competent jurisdiction to be illegal, invalid, or unenforceable, that provision shall be deemed amended to achieve as nearly as possible the same economic effect as the original provision, and the legality, validity and enforceability of the remaining provisions of this Agreement shall not be affected or impaired thereby.

- The failure of either party to enforce any term or condition of this Agreement shall not constitute a waiver of either party's right to enforce each and every term and condition of this Agreement. No breach under this agreement shall be deemed waived or excused by either party unless such waiver or consent is in writing signed by the party granting such waiver or consent. The waiver by or consent of a party to a breach of any provision of this Agreement shall not operate or be construed as a waiver of or consent to any other or subsequent breach by such other party.

- This Agreement may not be assigned (including by operation of law or otherwise) by you without WILEY's prior written consent.

- Any fee required for this permission shall be non-refundable after thirty (30) days from receipt by the CCC.

- These terms and conditions together with CCC's Billing and Payment terms and conditions (which are incorporated herein) form the entire agreement between you and WILEY concerning this licensing transaction and (in the absence of fraud) supersedes all prior agreements and representations of the parties, oral or written. This Agreement may not be amended except in writing signed by both parties. This Agreement shall be binding upon and inure to the benefit of the parties' successors, legal representatives, and authorized assigns.

- In the event of any conflict between your obligations established by these terms and conditions and those established by CCC's Billing and Payment terms and conditions, these terms and conditions shall prevail.

- WILEY expressly reserves all rights not specifically granted in the combination of (i) the license details provided by you and accepted in the course of this licensing transaction, (ii) these terms and conditions and (iii) CCC's Billing and Payment terms and conditions.

- This Agreement will be void if the Type of Use, Format, Circulation, or Requestor Type was misrepresented during the licensing process.
- This Agreement shall be governed by and construed in accordance with the laws of the State of New York, USA, without regards to such state's conflict of law rules. Any legal action, suit or proceeding arising out of or relating to these Terms and Conditions or the breach thereof shall be instituted in a court of competent jurisdiction in New York County in the State of New York in the United States of America and each party hereby consents and submits to the personal jurisdiction of such court, waives any objection to venue in such court and consents to service of process by registered or certified mail, return receipt requested, at the last known address of such party.

WILEY OPEN ACCESS TERMS AND CONDITIONS

Wiley Publishes Open Access Articles in fully Open Access Journals and in Subscription journals offering Online Open. Although most of the fully Open Access journals publish open access articles under the terms of the Creative Commons Attribution (CC BY) License only, the subscription journals and a few of the Open Access Journals offer a choice of Creative Commons Licenses. The license type is clearly identified on the article.

The Creative Commons Attribution License

The Creative Commons Attribution License (CC-BY) allows users to copy, distribute and transmit an article, adapt the article and make commercial use of the article. The CC-BY license permits commercial and non-

Creative Commons Attribution Non-Commercial License

The Creative Commons Attribution Non-Commercial (CC-BY-NC)License permits use, distribution and reproduction in any medium, provided the original work is properly cited and is not used for commercial purposes.(see below)

Creative Commons Attribution-Non-Commercial-NoDerivs License

The Creative Commons Attribution Non-Commercial-NoDerivs License (CC-BY-NC-ND) permits use, distribution and reproduction in any medium, provided the original work is properly cited, is not used for commercial purposes and no modifications or adaptations are made. (see below)

Use by commercial "for-profit" organizations

Use of Wiley Open Access articles for commercial, promotional, or marketing purposes requires further explicit permission from Wiley and will be subject to a fee.

Further details can be found on Wiley Online Library http://olabout.wiley.com/WileyCDA/Section/id-410895.html

Other Terms and Conditions:

v1.10 Last updated September 2015

Questions? customercare@copyright.com or +1-855-239-3415 (toll free in the US) or +1-978-646-2777.

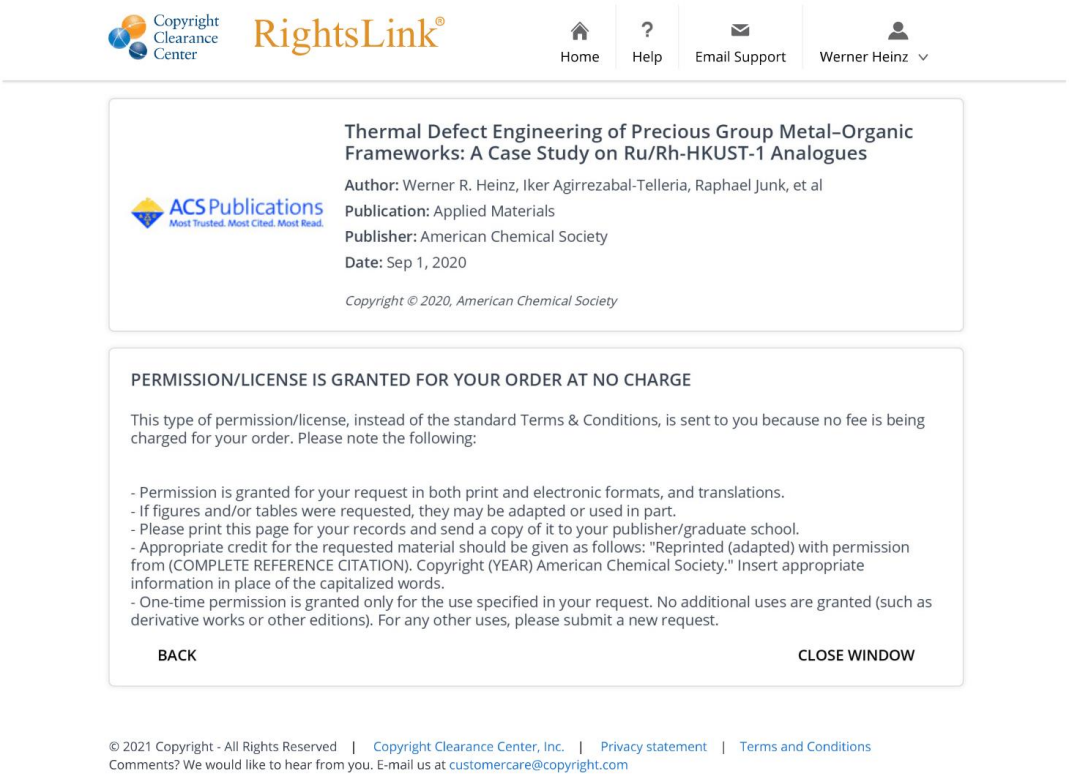

Copyright Clearance Center RightsLink®

Home | Help | Email Support | Werner Heinz

ACS Publications
Most Trusted. Most Cited. Most Read.

Thermal Defect Engineering of Precious Group Metal–Organic Frameworks: A Case Study on Ru/Rh-HKUST-1 Analogues

Author: Werner R. Heinz, Iker Agirrezabal-Telleria, Raphael Junk, et al
Publication: Applied Materials
Publisher: American Chemical Society
Date: Sep 1, 2020

Copyright © 2020, American Chemical Society

PERMISSION/LICENSE IS GRANTED FOR YOUR ORDER AT NO CHARGE

This type of permission/license, instead of the standard Terms & Conditions, is sent to you because no fee is being charged for your order. Please note the following:

- Permission is granted for your request in both print and electronic formats, and translations.
- If figures and/or tables were requested, they may be adapted or used in part.
- Please print this page for your records and send a copy of it to your publisher/graduate school.
- Appropriate credit for the requested material should be given as follows: "Reprinted (adapted) with permission from (COMPLETE REFERENCE CITATION). Copyright (YEAR) American Chemical Society." Insert appropriate information in place of the capitalized words.
- One-time permission is granted only for the use specified in your request. No additional uses are granted (such as derivative works or other editions). For any other uses, please submit a new request.

BACK CLOSE WINDOW